

Dario Di Maio *Editor*

# Rotating Machinery, Vibro-Acoustics & Laser Vibrometry, Volume 7

Proceedings of the 36th IMAC, A Conference and Exposition  
on Structural Dynamics 2018



# **Conference Proceedings of the Society for Experimental Mechanics Series**

*Series Editor*

Kristin B. Zimmerman, Ph.D.  
Society for Experimental Mechanics, Inc.,  
Bethel, CT, USA

More information about this series at <http://www.springer.com/series/8922>

Dario Di Maio  
Editor

# Rotating Machinery, Vibro-Acoustics & Laser Vibrometry, Volume 7

Proceedings of the 36th IMAC, A Conference and Exposition  
on Structural Dynamics 2018

*Editor*  
Dario Di Maio  
Faculty of Engineering  
Queen's Building  
University of Bristol  
Bristol, UK

ISSN 2191-5644                      ISSN 2191-5652 (electronic)  
Conference Proceedings of the Society for Experimental Mechanics Series  
ISBN 978-3-319-74692-0              ISBN 978-3-319-74693-7 (eBook)  
<https://doi.org/10.1007/978-3-319-74693-7>

Library of Congress Control Number: 2018939785

© The Society for Experimental Mechanics, Inc. 2019

This work is subject to copyright. All rights are reserved by the Publisher, whether the whole or part of the material is concerned, specifically the rights of translation, reprinting, reuse of illustrations, recitation, broadcasting, reproduction on microfilms or in any other physical way, and transmission or information storage and retrieval, electronic adaptation, computer software, or by similar or dissimilar methodology now known or hereafter developed.

The use of general descriptive names, registered names, trademarks, service marks, etc. in this publication does not imply, even in the absence of a specific statement, that such names are exempt from the relevant protective laws and regulations and therefore free for general use.

The publisher, the authors and the editors are safe to assume that the advice and information in this book are believed to be true and accurate at the date of publication. Neither the publisher nor the authors or the editors give a warranty, express or implied, with respect to the material contained herein or for any errors or omissions that may have been made. The publisher remains neutral with regard to jurisdictional claims in published maps and institutional affiliations.

Printed on acid-free paper

This Springer imprint is published by the registered company Springer International Publishing AG part of Springer Nature.  
The registered company address is: Gewerbestrasse 11, 6330 Cham, Switzerland

# Preface

*Rotating Machinery, Vibro-Acoustics and Laser Vibrometry* represents one of nine volumes of technical papers presented at the 36th IMAC, A Conference and Exposition on Structural Dynamics, organized by the Society for Experimental Mechanics, and held in Orlando, Florida, February 12–15, 2018. The full proceedings also include volumes on Nonlinear Dynamics; Dynamics of Civil Structures; Model Validation and Uncertainty Quantification; Dynamics of Coupled Structures; Special Topics in Structural Dynamics; Structural Health Monitoring, Photogrammetry and DIC; Sensors and Instrumentation, Aircraft/Aerospace and Energy Harvesting; and Topics in Modal Analysis and Testing.

Each collection presents early findings from experimental and computational investigations on an important area within structural dynamics. Topics represent papers on enabling technologies, rotating machinery, vibro-acoustics and laser vibrometry, and advances in wind energy.

The organizers would like to thank the authors, presenters, session organizers, and session chairs for their participation in this track.

Bristol, UK

D. Di Maio

# Contents

<b>1</b>	<b>Summarizing Results for Scaling OMA Mode Shapes by the OMAH Technique</b> .....	<b>1</b>
	Anders Brandt, Marta Berardengo, Stefano Manzoni, Marcello Vanali, and Alfredo Cigada	
<b>2</b>	<b>Delamination Identification of Laminated Composite Plates Using a Continuously Scanning Laser Doppler Vibrometer System</b> .....	<b>9</b>
	Da-Ming Chen, Y. F. Xu, and W. D. Zhu	
<b>3</b>	<b>Rapid and Dense 3D Vibration Measurement by Three Continuously Scanning Laser Doppler Vibrometers</b> .....	<b>19</b>
	Da-Ming Chen and W. D. Zhu	
<b>4</b>	<b>Modal Control of Magnetic Suspended Rotors</b> .....	<b>31</b>
	Marcus Vinicius Fernandes de Oliveira, Felipe Carmo Carvalho, Adriano Borges Silva, Aldemir Ap Cavalini Jr., and Valder Steffen Jr.	
<b>5</b>	<b>On the Implementation of Metastructures in Rotordynamics</b> .....	<b>43</b>
	Carlo Rosso, Elvio Bonisoli, and Fabio Bruzzone	
<b>6</b>	<b>Analysis of the Dynamic Response of Coupled Coaxial Rotors</b> .....	<b>53</b>
	Alexander H. Haslam, Christoph W. Schwingshackl, and Andrew I. J. Rix	
<b>7</b>	<b>Operational Modal Analysis of Rotating Machinery</b> .....	<b>67</b>
	S. Gres, P. Andersen, and L. Damkilde	
<b>8</b>	<b>Characterization of Torsional Vibrations: Torsional-Order Based Modal Analysis</b> .....	<b>77</b>
	Emilio Di Lorenzo, C. Colantoni, F. Bianciardi, S. Manzato, K. Janssens, and B. Peeters	
<b>9</b>	<b>Long-Term Automatic Tracking of the Modal Parameters of an Offshore Wind Turbine Drivetrain System in Standstill Condition</b> .....	<b>91</b>
	Mahmoud El-Kafafy, Nicoletta Gioia, Patrick Guillaume, and Jan Helsen	
<b>10</b>	<b>Dynamic Modelling and Vibration Control of a Turbomolecular Pump with Magnetic Bearings in the Presence of Blade Flexibility</b> .....	<b>101</b>
	Alysson B. Barbosa Moreira and Fabrice Thouverez	
<b>11</b>	<b>Pushing 3D Scanning Laser Doppler Vibrometry to Capture Time Varying Dynamic Characteristics</b> .....	<b>111</b>
	Bryan Witt and Brandon Zwink	
<b>12</b>	<b>Dynamic Measurements on Miniature Springs for Flaw and Damage Detection</b> .....	<b>123</b>
	Daniel P. Rohe	
<b>13</b>	<b>Using High-Resolution Measurements to Update Finite Element Substructure Models</b> .....	<b>137</b>
	Daniel P. Rohe	
<b>14</b>	<b>Determination of Representative Offshore Wind Turbine Locations for Fatigue Load Monitoring by Means of Hierarchical Clustering</b> .....	<b>149</b>
	Andreas Ehrmann, Cristian Guillermo Gebhardt, and Raimund Rolfes	

<b>15</b>	<b>Effect of Friction-Induced Nonlinearity on OMA-Identified Dynamic Characteristics of Offshore Platform Models</b> .....	153
	Tobias Friis, Antonios Orfanos, Evangelos Katsanos, Sandro Amador, and Rune Brincker	
<b>16</b>	<b>Remote Damage Detection of Rotating Machinery</b> .....	163
	Peter H. Fickenwirth, Charles H. Liang, Tyrel C. Rupp, Eric B. Flynn, and Adam J. Wachtor	
<b>17</b>	<b>Experimental Demonstration of a Tunable Acoustoelastic System</b> .....	179
	Deborah Fowler, Garrett Lopp, Dhiraj Bansal, Ryan Schultz, Matthew Brake, and Micah Shepherd	
<b>18</b>	<b>Numerical Modeling of an Enclosed Cylinder</b> .....	191
	Ryan Schultz and Micah Shepherd	
<b>19</b>	<b>Exploiting Laser Doppler Vibrometry in Large Displacement Tests</b> .....	199
	E. Copertaro, P. Chiariotti, M. Martarelli, and P. Castellini	
<b>20</b>	<b>A Rational Basis for Determining Vibration Signature of Shaft/Coupling Misalignment in Rotating Machinery</b> .....	207
	Changrui Bai, Surendra (Suri) Ganeriwala, and Nader Sawalhi	
<b>21</b>	<b>Parametric Experimental Modal Analysis of a Modern Violin Based on a Guarneri del Gesù Model</b> .....	219
	Elvio Bonisoli, Marco Casazza, Domenico Lisitano, and Luca Dimauro	
<b>22</b>	<b>Influence of the Harmonics on the Modal Behavior of Wind Turbine Drivetrains</b> .....	231
	N. Gioia, P. J. Daems, C. Peeters, M. El-Kafafy, P. Guillaume, and J. Helsen	
<b>23</b>	<b>The Influence of Geometrical Correlation in Modal Validation Using Automated 3D Metrology</b> .....	239
	Tarun Teja Mallareddy, Daniel J. Alarcón, Sarah Schneider, and Peter G. Blaschke	





# Chapter 1

## Summarizing Results for Scaling OMA Mode Shapes by the OMAH Technique

Anders Brandt, Marta Berardengo, Stefano Manzoni, Marcello Vanali, and Alfredo Cigada

**Abstract** Methods for scaling mode shapes determined by operational modal analysis (OMA) have been extensively investigated in the last years. A recent addition to the range of methods for scaling OMA mode shapes is the so-called OMAH technique, which is based on exciting the structure by harmonic forces applied by an actuator. By applying harmonic forces in at least one degree-of-freedom (DOF), and measuring the response in at least one response DOF, while using at least as many frequencies as the number of mode shapes to be scaled, the mode shape scaling (modal mass) of all modes of interest may be determined. In previous publications on the method the authors have proven that the technique is easy and robust to apply to both small scale and large scale structures. Also, it has been shown that the technique is capable of scaling highly coupled modes by using an extended multiple reference formulation. The present paper summarizes the theory of the OMAH method and gives recommendations of how to implement the method for best results. It is pointed out, as has been shown in previous papers, that the accuracy of the mode scaling is increased by using more than one response DOF, and by selecting DOFs with high mode shape coefficients. To determine the harmonic force and responses, it is recommended to use the three-parameter sine fit method. It is shown that by using this method, the measurement time can be kept short by using high sampling frequency and bandpass filtering whereas spectrum based methods require long measurement times. This means that even for structures with low natural frequencies, the extra measurement time for scaling the mode shapes can be kept relatively short.

**Keywords** Operational modal analysis · OMA · Mode shape scaling · OMAH · Sine excitation

### 1.1 Introduction

Operational modal analysis (OMA) naturally leads to unscaled mode shapes, since the forces acting on the structure are not measured. It is not uncommon that scaled mode shapes are desired, however. In such cases, several methods exist by which the mode shapes obtained by the OMA parameter extraction may be scaled. Most of the methods developed to scale OMA mode shapes can be divided into the following categories:

1. methods based on several OMA tests, with different mass or stiffness configurations, see for example [1–4];
2. methods based on knowing the mass matrix of the structure, expand the OMA mode shapes to the size of the mass matrix, and scale the mode shapes using the weighted mode vector orthogonality property, see [5];
3. methods based on exciting the structure by a known force, and use this force for scaling, usually referred to as *OMAX*, see for example [6, 7].

Of the methods above, the last method has the advantage that it uses an actual measurement of the force, and is thus, in some sense, scaling the modal model to some calibrated force value. On the other hand, it is generally difficult to excite large structures with broadband force. The authors recently suggested to use harmonic forces for the excitation, since this requires less performance of the actuator used [8]. The method, called OMAH, was extended with a global formulation in

---

A. Brandt (✉)

Department of Technology and Innovation, University of Southern Denmark, Odense M, Denmark  
e-mail: [abra@iti.sdu.dk](mailto:abra@iti.sdu.dk)

M. Berardengo · M. Vanali

Department of Engineering and Architecture, Università degli Studi di Parma, Parma, Italy

S. Manzoni · A. Cigada

Department of Mechanical Engineering, Politecnico di Milano, Milan, Italy

[9], allowing to use multiple degrees of freedom (DOFs) for force as well as response locations. The global OMAH method is therefore capable of scaling mode shapes also in cases where there is no single DOF to be chosen for excitation of all modes. Furthermore, using several response points for the scaling reduces the variance in the estimates of the modal mass of the structure.

Using harmonic force to scale OMA mode shapes has the advantage that it puts little demand on the actuator, as the actuator only needs to produce a narrowband excitation. Relatively inexpensive actuators can readily be designed for harmonic excitation – even for exciting large structures at low frequencies with relatively high force levels. Furthermore, the estimation of the harmonic signal, hidden in random noise from wind, traffic, and other possible sources, can be achieved under poor signal-to-noise ratios (SNRs), with well-known signal processing methods (mainly the so-called three-parameter sine fit method), see Sect. 1.2.2.

## 1.2 Theory

The theory of the global formulation of the OMAH method is presented in this section. First, in Sect. 1.2.1 by laying out the method for scaling, based on estimates of the frequency response of the structure at a number of frequencies. Secondly, in Sect. 1.2.2 the method to accurately determine the harmonic force and responses at a particular frequency, is discussed.

### 1.2.1 OMAH Mode Shape Scaling

Scaling mode shapes is identical to determining the modal mass of each mode. We start by assuming a frequency response function (FRF) in receptance format (displacement over force) between excitation in DOF  $q$  and response in DOF  $p$ , which can be written as a function of angular frequency,  $\omega$ , as

$$H_{p,q}(j\omega) = \sum_{r=1}^N \frac{\psi_r^q \psi_r^p}{m_r(j\omega - s_r)(j\omega - s_r^*)} \quad (1.1)$$

where  $m_r$  denotes the modal mass of mode  $r$ , and  $*$  denotes complex conjugate. Moreover,  $\psi_r^p$  and  $\psi_r^q$  are the eigenvector coefficients (from the OMA) for mode  $r$  at DOFs  $p$  and  $q$ , respectively. The poles,  $s_r$ , are defined by the undamped natural frequencies (in rad/s),  $\omega_r$ , and the relative damping ratios,  $\zeta_r$ , as

$$s_r = -\zeta_r \omega_r + j\omega_r \sqrt{1 - \zeta_r^2}. \quad (1.2)$$

Finally,  $j$  is the imaginary unit.

After OMA parameter extraction all factors on the right-hand side are known, except the modal mass, and scaling the modal model thus requires to determine the modal mass of each mode.

The OMAH method relies on first making an OMA test, whereafter a number of frequency responses,  $H_{p,q}(j\omega)$ , are estimated at a number of response DOFs  $p = p_1, p_2, \dots, p_m$  and one or more excitation DOFs  $q = q_1, q_2, \dots, q_v$ . Then, an equation system is set up to estimate the modal masses and, potentially, residual terms accounting for out-of-band modes. In the simplest of cases, however, Eq. (1.1) can be used directly employing a single FRF estimate, assuming a single-DOF approximation and no effects of surrounding modes.

For the general case, we define a global scaling method by first assuming we wish to scale a number,  $g$ , modes, from mode number  $h$  to  $h + g - 1$ , using the set of measured FRFs. We also define constant residual terms  $C_{pq}$  (for modes below the modes of interest) and  $D_{pq}$  (for modes above the modes of interest) by approximating the FRF by

$$H_{p,q}(j\omega) \approx \sum_{r=h}^{h+g-1} \frac{\psi_r^p \psi_r^q}{m_r(j\omega - s_r)(j\omega - s_r^*)} + \frac{C_{pq}}{\omega^2} + D_{pq}. \quad (1.3)$$

Next, we define the FRF column vector  $\{H\}_1$ , containing measured FRFs, by

$$\begin{aligned} \{H\}_1 = & \begin{bmatrix} H_{p_1,q_1}(j\omega_{\text{ex},1}) & H_{p_1,q_1}(j\omega_{\text{ex},2}) & \dots & H_{p_2,q_1}(j\omega_{\text{ex},1}) & H_{p_2,q_1}(j\omega_{\text{ex},2}) & \dots \\ H_{p_m,q_1}(j\omega_{\text{ex},1}) & H_{p_m,q_1}(j\omega_{\text{ex},2}) & \dots & H_{p_1,q_2}(j\omega_{\text{ex},1}) & H_{p_1,q_2}(j\omega_{\text{ex},2}) & \dots \\ H_{p_m,q_v}(j\omega_{\text{ex},1}) & H_{p_m,q_v}(j\omega_{\text{ex},2}) & \dots \end{bmatrix}^T \end{aligned} \quad (1.4)$$

where the superscript  $[\ ]^T$  denotes vector transpose. Furthermore, we define the column vector  $\{x\}_1$  with the unknown modal masses and residual terms, by

$$\{x\}_1 = \begin{bmatrix} 1 & 1 & \dots \\ m_h & m_{h+g-1} & \dots \\ C_{p_1q_1} & D_{p_1q_1} & C_{p_2q_1} & D_{p_2q_1} & \dots \\ C_{p_mq_1} & D_{p_mq_1} & C_{p_1q_2} & D_{p_1q_2} & \dots \\ C_{p_mq_v} & D_{p_mq_v} \end{bmatrix}^T. \quad (1.5)$$

We now introduce the function  $\Gamma(p, q, r, \omega_{\text{ex}})$ , defined by:

$$\Gamma(p, q, r, \omega_{\text{ex}}) = \frac{\psi_r^p \psi_r^q}{(j\omega_{\text{ex}} - s_r)(j\omega_{\text{ex}} - s_r^*)} \quad (1.6)$$

at one of the experimental frequencies  $\omega_{\text{ex}}$  where the FRF is measured. Finally we build a matrix  $[A]_1$ , defined by

$$[A]_1 = \begin{bmatrix} \Gamma(1,1,h,\omega_{\text{ex},1}) & \Gamma(1,1,h+1,\omega_{\text{ex},1}) & \dots & \Gamma(1,1,h+g-1,\omega_{\text{ex},1}) & 1/\omega_{\text{ex},1}^2 & 1 & 0 & 0 & \dots \\ \Gamma(1,1,h,\omega_{\text{ex},2}) & \Gamma(1,1,h+1,\omega_{\text{ex},2}) & \dots & \Gamma(1,1,h+g-1,\omega_{\text{ex},2}) & 1/\omega_{\text{ex},2}^2 & 1 & 0 & 0 & \dots \\ \vdots & \vdots & \vdots & \vdots & \vdots & \vdots & \vdots & \vdots & \vdots \\ \Gamma(2,1,h,\omega_{\text{ex},1}) & \Gamma(2,1,h+1,\omega_{\text{ex},1}) & \dots & \Gamma(2,1,h+g-1,\omega_{\text{ex},1}) & 0 & 0 & 1/\omega_{\text{ex},1}^2 & 1 & \dots \\ \Gamma(2,1,h,\omega_{\text{ex},2}) & \Gamma(2,1,h+1,\omega_{\text{ex},2}) & \dots & \Gamma(2,1,h+g-1,\omega_{\text{ex},2}) & 0 & 0 & 1/\omega_{\text{ex},2}^2 & 1 & \dots \\ \vdots & \vdots & \vdots & \vdots & \vdots & \vdots & \vdots & \vdots & \vdots \\ \Gamma(p_m,1,h,\omega_{\text{ex},1}) & \Gamma(p_m,1,h+1,\omega_{\text{ex},1}) & \dots & \Gamma(p_m,1,h+g-1,\omega_{\text{ex},1}) & \dots & \dots & \dots & \dots & \dots \\ \Gamma(p_m,1,h,\omega_{\text{ex},2}) & \Gamma(p_m,1,h+1,\omega_{\text{ex},2}) & \dots & \Gamma(p_m,1,h+g-1,\omega_{\text{ex},2}) & \dots & \dots & \dots & \dots & \dots \\ \vdots & \vdots & \vdots & \vdots & \vdots & \vdots & \vdots & \vdots & \vdots \\ \Gamma(1,2,h,\omega_{\text{ex},1}) & \Gamma(1,2,h+1,\omega_{\text{ex},1}) & \dots & \Gamma(1,2,h+g-1,\omega_{\text{ex},1}) & \dots & \dots & \dots & \dots & \dots \\ \Gamma(1,2,h,\omega_{\text{ex},2}) & \Gamma(1,2,h+1,\omega_{\text{ex},2}) & \dots & \Gamma(1,2,h+g-1,\omega_{\text{ex},2}) & \dots & \dots & \dots & \dots & \dots \\ \vdots & \vdots & \vdots & \vdots & \vdots & \vdots & \vdots & \vdots & \vdots \\ \Gamma(p_m,q_v,h,\omega_{\text{ex},1}) & \Gamma(p_m,q_v,h+1,\omega_{\text{ex},1}) & \dots & \Gamma(p_m,q_v,h+g-1,\omega_{\text{ex},1}) & \dots & \dots & \dots & \dots & \dots \\ \Gamma(p_m,q_v,h,\omega_{\text{ex},2}) & \Gamma(p_m,q_v,h+1,\omega_{\text{ex},2}) & \dots & \Gamma(p_m,q_v,h+g-1,\omega_{\text{ex},2}) & \dots & \dots & \dots & \dots & \dots \\ \vdots & \vdots & \vdots & \vdots & \vdots & \vdots & \vdots & \vdots & \vdots \end{bmatrix} \quad (1.7)$$

at various frequencies  $\omega_{\text{ex},k}$  for some integers  $k$ .

Using the vectors and matrices thus defined, we can form an equation system

$$[H]_1 = [A]_1 \{x\}_1 \quad (1.8)$$

which can be solved for the vector  $\{x\}_1$  by a least squares solution or a pseudo inverse.

It is important to note that the frequencies in each line of the matrix  $[A]_1$ , although for simplicity denoted  $\omega_{\text{ex},1}, \omega_{\text{ex},2}, \dots$ , may actually be arbitrary frequencies, albeit in most cases it will be practical to calculate many of the FRFs from simultaneous measurements of several responses.

Next, it is important to consider which requirements apply in order to make the matrix  $[A]_1$  well conditioned. First, we need to ensure that we have more rows in the equation system than the number of unknowns (i.e. modal masses plus residual terms). If we have measured  $M$  unique FRF locations  $(p, q)$ , then it is sufficient that the number of lines in the equation system,  $L > g + 2M$ . In most cases this will be fulfilled without any extra thought, if the recommendations in Sect. 1.2.3 are followed.

Next, we note that each function  $\Gamma(p, q, r, \omega_{\text{ex},k})$  in the matrix  $[A]_1$ , belongs to the FRF value  $H_{p,q}(j\omega_{\text{ex},k})$  due to mode  $r$ , at frequency  $\omega_{\text{ex},k}$ . The natural way to ensure that  $[A]_1$  is well conditioned, is to excite the structure at frequencies close to the eigenfrequencies and including all the modes to be scaled. Also it should be ensured that the excitation DOF in each case, is at a point of the structure where the mode in question is well excited (i.e. has a large mode shape coefficient). This will ensure that each line in  $[A]_1$  has at least one large function  $\Gamma(p, q, r, \omega_{\text{ex},k})$ .

### 1.2.2 Estimating Harmonics in Noise

One of the strengths with the OMAH method, is that harmonics hidden in noise can be accurately and efficiently estimated even in cases with very low SNRs. The method therefore does not rely on large excitation forces. Furthermore, as will be shown in the present section, the measurement time does not have to be very long even in cases with poor SNRs.

The method we recommend for estimating the complex amplitudes of the force and response signals  $F_q(j\omega_{ex})$  and  $U_p(j\omega_{ex})$  is the so-called *three-parameter sine fit* method [10]. The name implies that the DC value as well as two Fourier coefficients  $a$  and  $b$  are unknown, whereas in our case the DC does not apply since we remove the mean of the signals prior to estimating the harmonics. Regardless, the method is usually referred to as the three-parameter sine fit.

For simplicity, in the following we assume that we are exciting the structure at a frequency  $\omega$  (corresponding to one of the frequencies previously denoted  $\omega_{ex,k}$ ). We furthermore assume we have measured  $N$  samples of the signal  $y(t)$  at  $y(n) = y(n \cdot \Delta t)$  ( $y(t)$  being a force or a response signal) using a sampling frequency  $f_s = 1/\Delta t$ . The measured signal will then conform to the model

$$y(t) = a \cos(\omega t) + b \sin(\omega t) + e(t) \quad (1.9)$$

where the Fourier coefficients  $a$  and  $b$  are the desired unknowns, and  $e(t)$  contains the random part of the signal, due to wind, traffic, and other random contributions, and possibly higher (and undesired) harmonics of the excitation frequency. To calculate the complex FRF values, we calculate the amplitude and phase of  $y(n)$  as  $\sqrt{a^2 + b^2} \cdot \exp(j \arctan(b/a))$ .

Based on the measurements of  $y(n)$ , we can define the matrix  $B$

$$[B] = \begin{bmatrix} \cos(\omega \cdot 0\Delta t) & \sin(\omega \cdot 0\Delta t) \\ \cos(\omega \cdot 1\Delta t) & \sin(\omega \cdot 1\Delta t) \\ \cos(\omega \cdot 2\Delta t) & \sin(\omega \cdot 2\Delta t) \\ \vdots & \vdots \\ \cos(\omega \cdot (N-1)\Delta t) & \sin(\omega \cdot (N-1)\Delta t) \end{bmatrix} \quad (1.10)$$

and the unknown coefficient vector  $\{x\} = [a \ b]^T$ , and the measurement vector

$$\{y\} = \begin{bmatrix} y(0) \\ y(1) \\ y(2) \\ \vdots \\ y(N-1) \end{bmatrix}. \quad (1.11)$$

The model in Eq. (1.9), can now be written as:

$$[B]\{x\} = \{y\} + \{e\} \quad (1.12)$$

which we can solve for the estimate  $\hat{x}$  of  $x$  in Eq. (1.12), by a least squares solution. Furthermore, having solved for the estimate  $\hat{x}$ , the remaining signal  $\hat{e}$  may be calculated by

$$\{\hat{e}\} = \{y\} - \{B\}\{\hat{x}\}. \quad (1.13)$$

after which we can estimate the variance of the remaining signal  $\hat{e}$  by

$$\sigma_{\hat{e}}^2 = \frac{\{\hat{e}\}^T \{\hat{e}\}}{N}. \quad (1.14)$$

Since the power of the unknown harmonic is  $(\hat{a}^2 + \hat{b}^2)/2$  the SNR can be calculated as

$$\text{SNR} = \frac{\hat{a}^2 + \hat{b}^2}{2\sigma_{\hat{e}}^2} = \frac{\hat{x}^T \hat{x}}{2\sigma_{\hat{e}}^2}. \quad (1.15)$$

When the coefficients in  $\{\hat{x}\}$  are computed, the absolute value of  $\hat{F}_q$  that we need for the FRF estimates, may be computed by

$$\left| \hat{F}_q(j\omega) \right| = \sqrt{\hat{x}^T \hat{x}} \quad (1.16)$$

In [10] it is shown that the mean square error (MSE) of  $\left| \hat{F}_q(j\omega) \right|$  in Eq. (1.16) is approximately

$$\text{MSE}[\hat{F}_q] \approx \frac{2\sigma_e^2}{N} \quad (1.17)$$

which is a conservative error.

The result in Eq. (1.17) is a very important result. It shows, that at any SNR (i.e. any level of variance of the random part of the response, independent of the harmonic amplitude), the relative error in the amplitude can be made arbitrarily small, by increasing the number of samples,  $N$ . Furthermore, it is important to realize that *this number of samples can be recorded in a short time*, by increasing the sampling frequency without increasing the bandwidth of the measurement system, since this will not affect the SNR, but will result in more samples in a given time. In most modern measurement systems, this will not be allowed because the cutoff frequency is chosen as a factor of the selected sampling frequency. But a higher performance can be achieved by sampling at a high frequency, and then bandpass filtering the data after the data acquisition is finished (which will improve the SNR as well as create more samples).

If we want to have a particular maximum uncertainty on the estimate of the FRF value, we can allow half that uncertainty on each of the force and response values. Furthermore, since the MSE includes both random and bias errors, a conservative measure may be to use three times the square root of the MSE as the maximum deviation from the measured values. Say, for example, that we may allow 5% inaccuracy on the FRF estimate. For the force (and similar for the response) measurements, we then need to assure that,

$$100 \frac{3 \cdot \sqrt{\text{MSE}[\hat{F}_q]}}{\left| \hat{F}_q \right|} \leq 2.5 \quad (1.18)$$

### 1.2.3 Guidelines for Applying OMAH

Using the results in Sects. 1.2.1 and 1.2.2, we will now present some guide lines for the design of a test for scaling mode shapes from an OMA test. The following procedure can thus be used.

1. Complete the OMA measurements. This is usually done by measuring batches of channels, keeping some references. Keep all the sensors in place after the last batch measurement. If all DOFs can be measured simultaneously, the better.
2. Complete the OMA parameter estimation, resulting in poles and unscaled mode shapes.
3. Study the mode shapes, and choose a DOF with large mode shape coefficients for some (if possible most) modes. Attach the actuator in this DOF. (In many cases where the mode shapes are, at least approximately, known beforehand, this actuator position can be determined prior to performing the OMA test.)
4. Add an accelerometer on the mass of the actuator, for measuring the force. If there is no available channel, replace one of the response channels with the accelerometer for measuring the force.
5. Investigate a proper force amplitude, by measuring an arbitrary amount of time, and estimate the signals  $F_q(t)$  and  $U_p(t)$ , where  $p$  denotes all the DOFs in the last measured batch. Furthermore,  $U_q$  must be included in the set of  $U_p$ . This requires estimating the MSE using Eq. (1.17), and to calculate an appropriate relative error. If necessary, increase the sampling frequency and follow up by lowpass filtering the signals prior to estimating the amplitudes and phases, to ensure the measurement time is kept appropriately short. This step may also involve changing the moving mass of the actuator, to produce an appropriate force.
6. For each frequency,  $\omega_{\text{ex},k}$ , compute the amplitudes and phases of the force and all responses, and compute the FRF values  $H_{p,q}(j\omega_{\text{ex},k})$  and store these FRF values.
7. Make consecutive measurements of frequencies near all modes which are well excited by the DOF  $q$  where the actuator is located. This means that data for creating a relatively large number of rows for the matrix  $[A]_1$  in Eq. (1.7) will be acquired.

8. For the mode or modes *not well excited* by the first chosen excitation DOF, move the actuator to a DOF where one or more of these modes will be well excited. Excite the mode or modes near their natural frequency (frequencies), measure the force and all response channels, produce the new FRF values, and store these. In most cases, each of these modes needs to be excited only at a single frequency near the natural frequency of the mode in question in order to be able to solve Eq. (1.8). However, exciting more frequencies, as long as they are close to a mode that is well excited by the DOF  $q$ , can result in higher accuracy of the estimated modal masses. Repeat this step until all modes have been well excited at least at one frequency.
9. Now build the measurement vector  $\{H\}_1$  and the matrix  $[A]_1$  by Eqs. (1.4) and (1.7), respectively, and solve for the unknown modal masses and residual terms by solving Eq. (1.8).

### 1.3 Discussion

To see how an OMAH test may be conducted, we assume we would scale the first 8 vertical modes of the Little Belt Bridge, see [11]. The information about the modes is found in Table 1.1. We also assume that we have an eight-channel measurement system, and that we use seven accelerometers for the response measurements for scaling, including the reference (in the same DOF as the force). The final channel is used to measure the acceleration of the moving mass of the actuator, so we can compute the excitation force. Using the information in Table 1.1 and information about the mode shapes (that are essentially the shapes of a pinned narrow plate), we define three excitation points, in order to be able to excite all modes well:

1. vertically on one side, at 1/4 from one end, to excite modes 1, 2, 5, 7, 8
2. vertically on one side, at 1/3 from one end, to excite modes 4, and 6
3. vertically on one side, at 1/2 from one end, to excite mode 3

Note that these may not be optimal points, but are given as an example.

We thus start the test by positioning the actuator in position 1, and set the frequency close to 0.155 Hz. Since mode 1 has a damping value of 1.5%, we need to wait approximately 500 s for the structure to reach its steady-state condition. After this time, we acquire a number of samples, for example corresponding to five periods of the harmonic, i.e. 32.3 s. After calculating the complex sines of the force and the 7 responses, we check that Eq. (1.18) is fulfilled, and if not, we may set the sampling frequency higher, acquire data again, and BP filter data to a narrow bandwidth around the frequency of interest, and then recompute the complex amplitudes and using them to produce seven estimates of the FRFs.

After this, we tune the frequencies of modes 2, 5, 7, and 8, in turn, and for each of them wait for steady state, acquire data, and check the accuracy. When the accuracy is adequate, we compute the complex amplitudes, and then the FRF values. Once this is accomplished, the shaker is moved to position 2, the frequency tuned to the frequencies of modes 4 and 6 and the procedure is repeated. Finally, the same is done for position 3 for mode 3.

When all this is done, we have acquired 7 FRFs times 5 frequencies from position 1, 7 FRFs times 2 frequencies from position 2 and finally 7 FRFs times 1 frequency for position 3. This thus produces 56 rows in the matrix  $[A]_1$  in Eq. (1.7). The number of unknowns we have are eight modal masses, plus 2 residuals times 7 response DOFs times 3 excitation DOFs, which equals 50 unknowns. We can thus solve the equation system. It would be advantageous, however, if time allows, to measure a few more frequencies to obtain a more overdetermined system of equations. This could easily be achieved by adding those frequencies, in each position of the actuator, for which there is a reasonably large mode shape coefficient in the forcing DOF.

**Table 1.1** First 8 modes of the Little Belt Bridge, used as an example for a mode shape scaling case

Mode #	Frequency [Hz]	Damping [%]	Description
1	0.155	1.49	First vertical bending
2	0.171	11.41	Second vertical bending
3	0.258	0.69	Third vertical bending
4	0.402	0.75	Fourth vertical bending
5	0.524	0.65	First torsion
6	0.572	0.45	Fifth vertical bending
7	0.769	0.71	Sixth bending
8	0.807	0.72	Second torsion

**Table 1.2** Values of settling times (time until the response is steady-state, defined by less than 1% change in RMS level from 5 periods to next 5 periods), and measurement times (5 periods) for the entire test. See text for details. The total time in columns 5 and 6 adds up to 2595 s, or approx. 45 min

Meas. #	Exc. pos.	Mode #	Frequency [Hz]	Settling time [s]	Measurement time [s]
1	1	1	0.155	500	32.3
2	1	2	0.171	75	29.2
3	1	5	0.524	300	9.5
4	1	7	0.769	220	6.5
5	1	8	0.807	200	6.2
6	2	4	0.402	300	12.4
7	2	6	0.572	400	8.7
8	3	3	0.258	600	19.4

So, how long would this whole test take? In Table 1.2 we present all measurements with the settling time and the time taken for measuring five periods of each frequency of excitation. We have defined steady-state conditions as the time when the RMS of the response from one block of data containing five periods to the next five periods, does not change more than 1%. As can be seen in the table, the total time of data acquisition is approximately 45 min, of which the major time is spent waiting for the system to reach steady-state conditions. The time to move the actuator is not taken into account in this example. Also note, that the measurement time is independent of the SNR used. So the actuator can, for example, be set to generate 10% of the RMS of the random response. This example shows that even on a relatively low-frequency structure like this, the OMAH method does not require very long measurement times.

A further advantage with the OMAH technique is that, once the modes are scaled, the accuracy of the scaling can be investigated. This was demonstrated in the previous papers presenting the method, see [8, 9]. It is done by comparing the measured harmonic response amplitudes in the response DOFs, with the computed responses using the synthesized FRF (using the scaled modal model) times the excitation force.

Finally, it should also be mentioned that an advantage of the OMAH method is that the response of the structure to changes in the amplitude of the force can easily be included in the measurements. Thus, the linearity of the structure may be investigated. This is not easily done with most other methods for scaling OMA mode shapes.

## 1.4 Conclusions

In this paper we have described the theory of global OMAH scaling of mode shapes, using harmonic excitation. The method depends on exciting the structure in one or more DOFs, and, although not strictly necessary, we recommend exciting at frequencies close to the eigenfrequencies of the structure. The least squares global solution method described in the paper can handle structures with closely coupled modes. Furthermore, it gives modal masses for all the modes taken into account as well as residual terms for all the pairs of measuring and forcing points.

It has been shown that the technique offers several attractive properties:

- It puts low demands on the actuator, as the force level can be low relative to ambient response.
- The accuracy of the method may be increased by using more response measurements.
- The method can handle closely coupled modes.
- The sine hidden in noise can be accurately determined without needing long measurement times.
- The method allows to investigate the accuracy of the mode shape scaling, by comparing the measured responses with those from synthesized frequency response multiplied by the harmonic force applied.
- The method allows to easily investigate the linearity, by observing the response for several different force levels.

An example of how to scale the first eight modes of a bridge with eigenfrequencies from approx. 0.15 to 0.8 Hz was shown to require approximately 45 min of total measurement time, exciting the structure in three DOFs, at a total of eight frequencies.

## References

1. Parloo, E., Verboven, P., Guillaume, P., Van Overmeire, M.: Sensitivity-based operational mode shape normalisation. *Mech. Syst. Signal Process.* **16**(5), 757–767 (2002)
2. Bernal, D.: Modal scaling from known mass perturbations. *J. Eng. Mech.* **130**(9), 1083–1088 (2004)
3. Coppotelli, G.: On the estimate of the FRFs from operational data. *Mech. Syst. Signal Process.* **23**, 288–299 (2009)
4. Aenlle, M.L., Fernandez, P., Brincker, R., Fernandez-Canteli, A.: Scaling-factor estimation using an optimized mass-change strategy. *Mech. Syst. Signal Process.* **24**(5), 1260–1273 (2010)
5. Aenlle, M.L., Brincker, R.: Modal scaling in operational modal analysis using a finite element model. *Int. J. Mech. Sci.* **76**, 86–101 (2013)
6. Reynders, E., Degrauwe, D., De Roeck, G., Magalhães, F., Caetano, E.: Combined experimental-operational modal testing of footbridges. *J. Eng. Mech.* **136**(6), 687–696 (2010)
7. Cara, J.: Computing the modal mass from the state space model in combined experimental operational modal analysis. *J. Sound Vib.* **370**, 94–110 May (2016)
8. Brandt, A., Berardengo, M., Manzoni, S., Cigada, A.: Scaling of mode shapes from operational modal analysis using harmonic forces. *J. Sound Vib.* **407**, 128–143 Oct (2017)
9. Brandt, A., Berardengo, M., Manzoni, S., Vanali, M., Cigada, A.: Global scaling of OMA modes shapes with the OMAH Method. In: *Proceedings of International Conference on Structural Engineering Dynamics (ICEDyn)*, Ericeira, Portugal (2017)
10. Händel, P.: Amplitude estimation using IEEE-STD-1057 three-parameter sine wave fit: statistical distribution, bias and variance. *Measurement* **43**, 766–770 (2010)
11. Christensen, S.S., Andersen, M.S., Brandt, A.: Dynamic characterization of the little belt suspension bridge by operational modal analysis. In: *Proceedings of the 36th international modal analysis conference (IMAC)*, Orlando (2018)





# Chapter 2

## Delamination Identification of Laminated Composite Plates Using a Continuously Scanning Laser Doppler Vibrometer System

Da-Ming Chen, Y. F. Xu, and W. D. Zhu

**Abstract** Delamination frequently occurs in a laminated composite structure and can cause prominent local anomalies in curvature vibration shapes associated with vibration shapes of the composite structure. Spatially dense vibration shapes of a structure can be rapidly obtained by use of a continuously scanning laser Doppler vibrometer (CSLDV) system, which sweeps its laser spot over a vibrating surface of the structure. This paper extends two damage identification methods for beams to identify delamination in laminated composite plates using a CSLDV system. One method is based on the technique that a curvature vibration shape from a polynomial that fits a vibration shape of a damaged beam can well approximate an associated curvature vibration shape of an undamaged beam and local anomalies caused by structural damage can be identified by comparing the two curvature vibration shapes, and the other is based on the technique that a continuous wavelet transform can directly identify local anomalies in a curvature vibration shape caused by structural damage. In an experimental investigation, delamination identification results from the two methods were compared with that from a C-scan image of a composite plate with delamination.

**Keywords** Delamination identification · Composite plate · Continuously scanning laser Doppler vibrometer system · Polynomial fit · Wavelet transform

### 2.1 Introduction

Among various types of structural damage, delamination is one that frequently occurs in laminated composite structures. Since delamination is usually hidden from external view, it can be difficult to identify. When delamination occurs, local stiffness of a laminated composite structure in neighborhoods of the delamination can change and modal parameters of the structure, including natural frequencies, modal damping ratios and mode shapes, can subsequently change [1–3]. Effects of delamination on modal parameters of composite structures have been studied with their analytical, semi-analytical and finite element models [4–6]. Specifically, vibration shapes, such as mode shapes and operating deflection shapes, have been widely used for structural damage identification since spatial derivatives of vibration shapes, such as curvature vibration shapes [7] and slope vibration shapes [8], better manifest local anomalies caused by the damage, and identification methods that use curvature vibration shapes of laminated composite structures have been developed [3, 9, 10]. A polynomial-based method was proposed in Ref. [7], where curvature mode shapes of damaged and undamaged beams are compared and damage can be identified in neighborhoods with large differences between them. In the polynomial-based method, a curvature vibration shape of an undamaged beam is not needed as it is obtained from a polynomial that fits a vibration shape of a damaged beam; the method was extended to identify damage in plates using vibration shapes measured in a point-by-point manner by a scanning laser Doppler vibrometer [11]. A wavelet-based method was proposed in Ref. [8], where slope vibration shapes of damaged beams are wavelet-transformed and damage can be identified in neighborhoods with large wavelet-transform coefficients. The polynomial- and wavelet-based methods inspect smoothness of vibration shapes of beams by isolating prominent local anomalies in curvature and slope vibration shapes caused by damage, and they can be extended to identify delamination in laminated composite plates, since delamination can also cause local anomalies in curvature vibration shapes of plates.

---

D.-M. Chen · W. D. Zhu (✉)

Department of Mechanical Engineering, University of Maryland, Baltimore County, Baltimore, MD, USA  
e-mail: [damingc1@umbc.edu](mailto:damingc1@umbc.edu); [wzhu@umbc.edu](mailto:wzhu@umbc.edu)

Y. F. Xu

Department of Mechanical and Materials Engineering, University of Cincinnati, Cincinnati, OH, USA  
e-mail: [xu2yf@uc.edu](mailto:xu2yf@uc.edu)

A laser Doppler vibrometer is capable of accurate, non-contact surface vibration measurement thanks to Doppler shifts between the incident light from and scattered light back to the vibrometer [12]. A laser Doppler vibrometer becomes a scanning laser Doppler vibrometer when equipped with a scanner that consists of a pair of orthogonal scan mirrors and its laser beam can be directed to any positions visible to the scanner. However, point-by-point acquisition of a vibration shape of a large-sized structure with a dense measurement grid can be time-consuming even though it can be achieved in an automatic and well-controlled manner. The idea of continuous scanning was first proposed in Refs. [13, 14], where a scanning laser Doppler vibrometer continuously sweeps its laser over a surface of a structure under sinusoidal excitation to obtain its vibration shapes that are approximated by Chebysev series. Two vibration shape measurement methods for continuous scanning, including demodulation and polynomial methods, were later proposed in Refs. [15–17]. The demodulation method was extended for structures under impact and multi-sine excitation in Refs. [18] and [19], respectively. A lifting method was proposed to obtain mode shapes of a structure under impact excitation by treating its free response measured by a CSLDV system as that of a linear time-periodic system [20]. The demodulation and polynomial methods were synthesized to identify damage in beams, where damage behind an intact surface of a beam could be identified by use of a CSLDV system that scanned the intact surface [21]. A type of vibration shapes called free-response shapes was developed and a corresponding damage identification method was proposed to identify damage in beams undergoing free vibration [22]. Damage indices associated with multiple elastic modes of beams can be obtained in one measurement by a CSLDV system and damage can be identified near neighborhoods with consistently high damage index values.

In this work, the polynomial- and wavelet-based identification methods are extended from beam damage identification to laminated composite plate delamination identification using a CSLDV system. A vibration shape of a plate is formed by vibration shapes along multiple straight scan paths spanning a scan area assigned on the plate. Damage indices on each scan path from the two methods constitute corresponding damage indices of a whole plate and edges of delamination areas can be identified near neighborhoods with high damage index values. A composite plate with delamination was manufactured to experimentally investigate effectiveness of the two methods and experimental delamination identification results were compared with that of a C-scan image of the plate.

## 2.2 Methodology

### 2.2.1 Damage Identification Using Curvature Vibration Shapes

A curvature vibration shape of a beam is the second-order spatial derivative of a vibration shape  $z$  along the direction of its length  $x'$ , and it can be calculated using a central finite difference scheme:

$$z_{x'x'}(x') = \frac{z(x' - h) - 2z(x') + z(x' + h)}{h^2} \quad (2.1)$$

where  $h$  is the distance between two neighboring measurement points of  $z$  along  $x'$ . Structural damage can cause local changes of bending stiffness of a beam  $EI$ . Since the relationship between  $z_{x'x'}$  and  $EI$  can be expressed by [8]

$$z_{x'x'}(x') = \frac{M(x')}{EI(x')} \quad (2.2)$$

with  $M$  denoting the bending moment of the beam, prominent local anomalies can be observed in  $z_{x'x'}$  in neighborhoods of the damage, and the damage can be identified by inspecting  $z_{x'x'}$  for anomalies.

A similar relationship between bending stiffness of a plate  $\frac{Eh^3}{12(\nu^2-1)}$  and its curvatures along an arbitrary scan path of a CSLDV system, with  $x$  and  $y$  denoting its tangential and normal directions, respectively, can be expressed by [23]

$$\begin{bmatrix} M_{xx} \\ M_{yy} \end{bmatrix} = \frac{Eh^3}{12(\nu^2-1)} \begin{bmatrix} 1 & \nu \\ \nu & 1 \end{bmatrix} \begin{bmatrix} z_{xx} \\ z_{yy} \end{bmatrix} \quad (2.3)$$

where  $z_{xx}$  and  $z_{yy}$  denote curvatures of the plate along  $x$  and  $y$ , respectively;  $M_{xx}$ ,  $M_{yy}$  and  $\nu$  denote bending moments along  $x$  and  $y$  and Poisson's ratio of the plate, respectively. As structural damage can cause changes to  $\frac{Eh^3}{12(\nu^2-1)}$ , prominent local anomalies can be observed in neighborhoods of the damage, and the damage can be identified by inspecting  $z_{xx}$  and/or  $z_{yy}$ . Straight scan paths are assigned on a plate and its vibration shapes are formed by those along assigned straight scan paths on the plate. The central finite difference scheme in Eq. (2.1) can be applied to calculate  $z_{xx}$ , and it can be expressed by

$$z_{xx}(x) = \frac{z(x+h) - 2z(x) + z(x-h)}{h^2} \quad (2.4)$$

By assuming that measurement points on a straight scan path are equally spaced, the smaller  $h$  in Eq. (2.4) the more accurate the resulting  $z_{xx}$ , which is true when  $z$  is free of measurement noise. When  $z$  is contaminated by measurement noise, it can be expressed by

$$z(x) = z^{\text{NF}}(x) + \sigma(x) \quad (2.5)$$

where  $z^{\text{NF}}$  and  $\sigma$  denote a noise-free vibration shape and measurement noise, respectively. Substituting Eq. (2.5) into Eq. (2.7) yields

$$\begin{aligned} z_{xx}(x) &= \frac{z^{\text{NF}}(x+h) + \sigma(x+h) - 2z^{\text{NF}}(x) - 2\sigma(x) + z^{\text{NF}}(x-h) + \sigma(x-h)}{h^2} \\ &= \frac{z^{\text{NF}}(x+h) - 2z^{\text{NF}}(x) + z^{\text{NF}}(x-h)}{h^2} + \frac{\sigma(x+h) - 2\sigma(x) + \sigma(x-h)}{h^2} \end{aligned} \quad (2.6)$$

When  $h$  is small, adverse effects of  $\sigma$  can be drastically amplified in the resulting  $z_{xx}$  due to the term  $\frac{\sigma(x+h) - 2\sigma(x) + \sigma(x-h)}{h^2}$  in Eq. (2.6). One can modify Eq. (2.4) by introducing a resolution parameter  $n$ :

$$z_{xx}(x) = \frac{z(x+nh) - 2z(x) + z(x-nh)}{(nh)^2} \quad (2.7)$$

Substituting Eq. (2.5) into Eq. (2.7) yields

$$\begin{aligned} z_{xx}(x) &= \frac{z^{\text{NF}}(x+nh) + \sigma(x+nh) - 2z^{\text{NF}}(x) - 2\sigma(x) + z^{\text{NF}}(x-nh) + \sigma(x-nh)}{(nh)^2} \\ &= \frac{z^{\text{NF}}(x+nh) - 2z^{\text{NF}}(x) + z^{\text{NF}}(x-nh)}{(nh)^2} + \frac{\sigma(x+nh) - 2\sigma(x) + \sigma(x-nh)}{(nh)^2} \end{aligned} \quad (2.8)$$

By comparing the term  $\frac{\sigma(x+h) - 2\sigma(x) + \sigma(x-h)}{h^2}$  in Eq. (2.6) and the term  $\frac{\sigma(x+nh) - 2\sigma(x) + \sigma(x-nh)}{(nh)^2}$  in Eq. (2.8), one can see that adverse effects of measurement noise on  $z_{xx}$  can be alleviated in the latter by  $n^2$  times due to the introduction of  $n$ . A suitable value of  $n$  is the least one with which  $z_{xx}$  seems free of adverse effects of measurement noise and one can obtain such a value by increasing  $n$  from a small value and observing resulting  $z_{xx}$ . When  $x$  in Eq. (2.4) is close to a boundary of  $z$ , either  $z(x+h)$  or  $z(x-h)$  may not exist and the central finite difference scheme can fail. A mode shape extension technique was proposed in Ref. [7] to append virtual mode shape extensions to boundaries of a mode shape so that both  $z(x+h)$  and  $z(x-h)$  become available even when  $x$  in Eq. (2.4) is close to a boundary of  $z$ . The mode shape extension technique is applicable to a vibration shape.

### 2.2.2 Demodulation Method

Application of the demodulation method for obtaining a vibration shape along a straight scan path using a CSLDV system is summarized below. Steady-state response of a structure under sinusoidal excitation with a frequency  $f$  measured by a CSLDV system can be expressed by

$$r(t) = z(x(t)) \cos(2\pi ft - \alpha - \theta) \quad (2.9)$$

where  $x(t)$  denotes the spatial position of the laser spot from the CSLDV system on the structure,  $\alpha$  is the difference between a phase determined by initial conditions of the structure and that determined by a mirror feedback signal, and  $\theta$  is a phase variable that controls amplitudes of in-phase and quadrature components of  $z$ , which can be expressed by

$$z_I(x) = z(x) \cos(\alpha + \theta) \quad (2.10)$$

and

$$z_Q(x) = z(x) \sin(\alpha + \theta) \quad (2.11)$$

respectively [21]. Each obtained vibration shape from the demodulation method corresponds to a half-scan period. A half-scan period starts when the laser spot of the CSLDV system arrives at one end of a scan path and ends when the laser spot arrives at the other end. The steady-state response  $r(t)$  in Eq. (2.9) can be further expressed by

$$r(t) = z_I(x(t)) \cos(2\pi ft) + z_Q(x(t)) \sin(2\pi ft) \quad (2.12)$$

Multiplying Eq. (2.12) by  $\cos(2\pi ft)$  and  $\sin(2\pi ft)$  yields

$$\begin{aligned} & r(t) \cos(2\pi ft) \\ &= z_I(x(t)) \cos^2(2\pi ft) + z_Q(x(t)) \sin(2\pi ft) \cos(2\pi ft) \\ &= \frac{1}{2}z_I(x(t)) + \frac{1}{2}z_I(x(t)) \cos(4\pi ft) + \frac{1}{2}z_Q(x(t)) \sin(4\pi ft) \end{aligned} \quad (2.13)$$

and

$$\begin{aligned} & r(t) \sin(2\pi ft) \\ &= z_Q(x(t)) \cos(2\pi ft) \sin(2\pi ft) + z_Q(x(t)) \sin^2(2\pi ft) \\ &= \frac{1}{2}z_Q(x(t)) - \frac{1}{2}z_Q(x(t)) \cos(4\pi ft) + \frac{1}{2}z_Q(x(t)) \sin(4\pi ft) \end{aligned} \quad (2.14)$$

respectively. A low-pass filter is applied to  $r(t) \cos(2\pi ft)$  and  $r(t) \sin(2\pi ft)$  to obtain  $\frac{1}{2}z_I$  and  $\frac{1}{2}z_Q$ , respectively, and terms corresponding to the frequency  $2f$  in Eqs. (2.13) and (2.14) can be removed. Further,  $z_I$  and  $z_Q$  can be obtained by multiplying the corresponding filtered response by two. The value of  $\theta$  in Eq. (2.11) can be optimized so that  $z_I$  and  $z_Q$  attain their maximum and minimum amplitudes, respectively. In what follows, all vibration shapes from the demodulation method are presented as their in-phase components with maximum amplitudes, which are denoted by  $z$  for convenience.

### 2.2.3 Polynomial-Based Damage Identification

As mentioned in Sect. 2.2.1, damage can cause prominent local anomalies in curvature vibration shapes and be identified by inspecting curvature vibration shapes. Such anomalies can be identified by comparing curvature vibration shapes of undamaged and damaged structures. However, vibration shapes and curvature vibration shapes of undamaged structures are usually unavailable in practice. It was shown in Ref. [7] that curvature vibration shapes of an undamaged beam can be well approximated by those from polynomials that fit vibration shapes of a damaged beam outside their boundary regions. Though vibration shapes from polynomial fits may not satisfy boundary conditions of damaged and undamaged beams, curvature vibration shapes associated with the vibration shapes can be used for damage identification purposes outside boundary regions. The mode shape extension technique in Ref. [7] can yield curvature mode shapes from polynomial fits that well approximate those of whole undamaged beams. However, this technique is inapplicable to vibration shapes of beams that are obtained using the demodulation method, as their curvature vibration shapes have inherent local distortions near boundaries of scan paths [21]. Due to the same reason, the mode shape extension technique mentioned in Ref. [7] is not applicable to vibration shapes of plates. A polynomial that fits  $z$  of a damaged plate along a straight scan path with order  $r$  can be expressed by

$$z^p(x) = \sum_{q=0}^r a_q x^q \quad (2.15)$$

where  $a_q$  are coefficients of the polynomial that can be obtained by solving a linear equation

$$\mathbf{U}\mathbf{a} = \mathbf{z} \quad (2.16)$$

in which  $\mathbf{U}$  is an  $M \times (r + 1)$  Vandermonde matrix with  $M$  being the number of measurement points of  $z$ :

$$\mathbf{U} = \begin{bmatrix} 1 & x_1 & x_1^2 & \cdots & x_1^r \\ 1 & x_2 & x_2^2 & \cdots & x_2^r \\ \vdots & \vdots & \vdots & \ddots & \vdots \\ 1 & x_M & x_M^2 & \cdots & x_M^r \end{bmatrix} \quad (2.17)$$

$\mathbf{a} = [a_0 \ a_1 \ \dots \ a_r]^T$  is an  $(r + 1)$ -dimensional coefficient vector, and  $\mathbf{z}$  is the vibration shape vector to be fit. To avoid ill-conditioning of  $\mathbf{U}$ , it is proposed that  $x$  in Eq. (2.15) be normalized using the ‘‘center and scale’’ technique [24] before formulating the linear equation in Eq. (2.15). The normalized coordinate  $\hat{x}$  can be expressed by

$$\hat{x} = \frac{2x - 2\bar{x}}{l} \quad (2.18)$$

where  $\bar{x}$  is the  $x$ -coordinate of the center point of a straight scan path and  $l$  is its length.

In order to determine the proper value of  $r$ , a fitting index fit and a convergence index con can be used. Fitting index fit at  $r$  can be expressed by

$$\text{fit}(r) = \frac{\text{RMS}(\mathbf{z})}{\text{RMS}(\mathbf{z}) + \text{RMS}(\mathbf{e})} \times 100\% \quad (2.19)$$

where  $\text{RMS}(\cdot)$  denotes the root-mean-square value of a vector and  $\mathbf{e} = \mathbf{U}\mathbf{a} - \mathbf{z}$  is an error vector. Convergence index con can be expressed by

$$\text{con}(r) = \text{fit}(r) - \text{fit}(r - 2) \quad (2.20)$$

where  $r \geq 3$ . When fit is close to 100%,  $z^p$  completely fits  $z$ ; the lower fit, the lower the level of fitting of  $z^p$  to  $z$ . When con is close to 0, increasing  $r$  cannot further improve how well  $z^p$  fits  $z$ ; the lower con, the higher the level of convergence of  $z^p$ . It is proposed in this work that the proper value of  $r$  be the minimum value of  $r$  with which con  $(r)$  is below 0.05%. When  $z^p$  is obtained from a polynomial with a proper order, a curvature damage index  $\rho$  can be defined along a straight scan path at  $x$  [7]:

$$\rho(x) = |z_{xx}(x) - z_{rxx}^p(x)|^2 \quad (2.21)$$

and the damage can be identified in neighborhoods with high  $\rho$ . When  $\rho$  associated with  $n$  different vibration shapes are available, an auxiliary curvature damage index  $\rho_a$  is proposed:

$$\rho_a(x, y) = \sum \bar{\rho}_k(x, y) \quad (2.22)$$

where  $\bar{\rho}_k$  is the normalized damage index associated with the  $k$ -th available vibration shape, whose maximum index value is one. Due to inherent local distortions in curvature vibration shapes near boundaries of scan paths, only  $\rho$  outside boundary regions are considered for delamination identification purposes here.

## 2.2.4 Wavelet-Based Damage Identification

A wavelet transformation can be defined by

$$W_\psi z(u, s) = \int_{-\infty}^{+\infty} z(x) \psi_{u,s}^*(x) dx \quad (2.23)$$

where  $W_\psi$  denotes a wavelet transformation operator with a wavelet function

$$\psi_{u,s}(x) = \frac{1}{\sqrt{s}} \psi\left(\frac{x-u}{s}\right) \quad (2.24)$$

in which  $u$  and  $s$  are spatial and scale parameters of  $\psi_{u,s}$ , respectively, and the superscript  $*$  denotes complex conjugation. In this work, a wavelet function is defined in the real domain and the superscript  $*$  in Eq. (2.23) can be dropped. The wavelet transformation in Eq. (2.23) can be expressed in the form of a convolution:

$$W_\psi z(u, s) = \frac{1}{\sqrt{s}} \int_{-\infty}^{+\infty} z(x) \bar{\psi}\left(\frac{u-x}{s}\right) dx = \frac{1}{\sqrt{s}} z \otimes \bar{\psi} \quad (2.25)$$

where an overbar denotes function reflection over the  $y$ -axis, i.e.,  $\bar{\psi}(x) = \psi(-x)$ , and  $\otimes$  denotes convolution.

The energy-normalized Gaussian function

$$g_0(x) = \left(\frac{2}{1}\right)^{\frac{1}{4}} e^{-x^2} \quad (2.26)$$

is used to generate Gaussian wavelet family for the wavelet transformation in this work due to its smoothness, differentiability, localization in the spatial domain and explicit mathematical expressions. The  $p$ -th-order Gaussian wavelet function can be expressed by

$$g_p(x) = (-1)^n \frac{d^p g_0(x)}{dx^p} \quad (2.27)$$

In order to inspect vibration shapes for local anomalies caused by structural damage,  $g_2$  is used in a wavelet transformation of  $z_{xx}(x)$  that is expressed by

$$W_{g_2 z_{xx}}(u, s) = \frac{1}{\sqrt{s}} z_{xx} \otimes \overline{g_2} \quad (2.28)$$

By the theorem of convolution differentiation [25],  $W_{g_2}$  in Eq. (2.28) can be further expressed by

$$W_{g_2 z_{xx}}(u, s) = \frac{1}{\sqrt{s}} z \otimes \frac{d^2 \overline{g_2}}{dx^2} = \frac{1}{s^{\frac{5}{2}}} z \otimes \overline{g_4} \quad (2.29)$$

A wavelet damage index  $\delta$  can be defined along a straight scan path at the location  $u$  with the scale  $s$ :

$$\delta(u, s) = |W_{g_2 z_{xx}}(u, s)|^2 = \left| \frac{1}{s^2} W_{g_4 z}(u, s) \right|^2 \quad (2.30)$$

and damage can be identified near neighborhoods with high  $\delta$ . When  $\delta$  associated with  $n$  different vibration shapes are available, an auxiliary wavelet damage index  $\delta_a$  is proposed:

$$\delta_a(x, y) = \sum_{k=1}^n \overline{\delta}_k(x, y) \quad (2.31)$$

where  $\overline{\delta}_k$  is the normalized wavelet damage index associated with the  $k$ -th available vibration shape, whose maximum index value is one.

## 2.3 Experimental Investigation

A composite laminated plate with delamination was manufactured using FS-A23 resin and FS-B412 hardener to experimentally investigate effectiveness of the two damage identification methods. In the composite plate, a teflon film was embedded between the third and fourth laminates of the composite plate during its manufacturing process to simulate the delamination. A strip area with the width of 2.54 cm adjacent to one boundary of the composite plate was clamped by two aluminum beams with the width of 2.54 cm that were clamped by a bench vice, as shown in Fig. 2.1a. Since the width of the bench vice jaw was smaller than the side length of the composite plate, the clamping force imposed on the clamped area of the composite plate was not evenly distributed along the length of the clamped area and the clamped boundary condition was imperfect. Since the two damage identification methods intend to identify local anomalies in vibration shapes caused by delamination in composite plates, they can be applicable to composite plates with any boundary conditions, such as the imperfectly clamped boundary in the experiment here, as well as those with nonlinearities.

The test setup of vibration shape measurement of the composite plate is shown in Fig. 2.1. A speaker was used to excite the composite plate and a Polytec PSV-500 scanning laser Doppler vibrometer was used to measure its velocity response, which was placed with a relatively long distance from the composite plate. The vibrometer has two key components of a

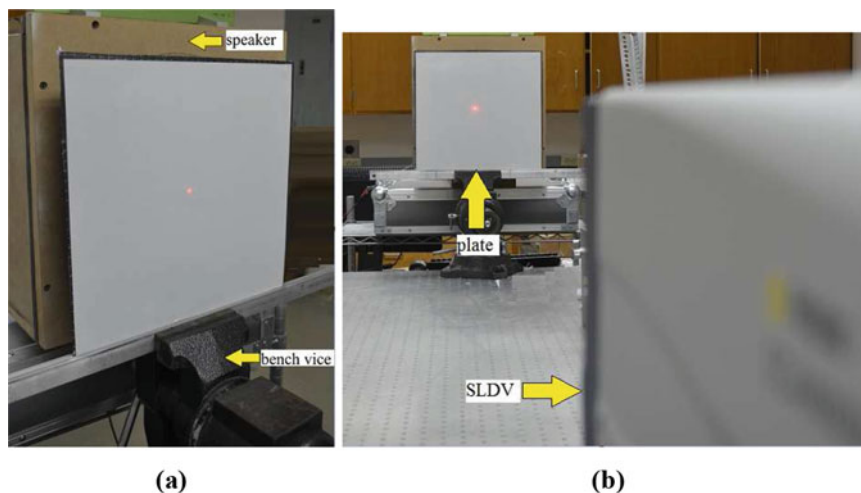


**Fig. 2.1** (a) Fixture of the composite plate with delamination and (b) the test setup for measurement of vibration shapes of the plate, where “SLDV” stands for scanning laser Doppler vibrometer

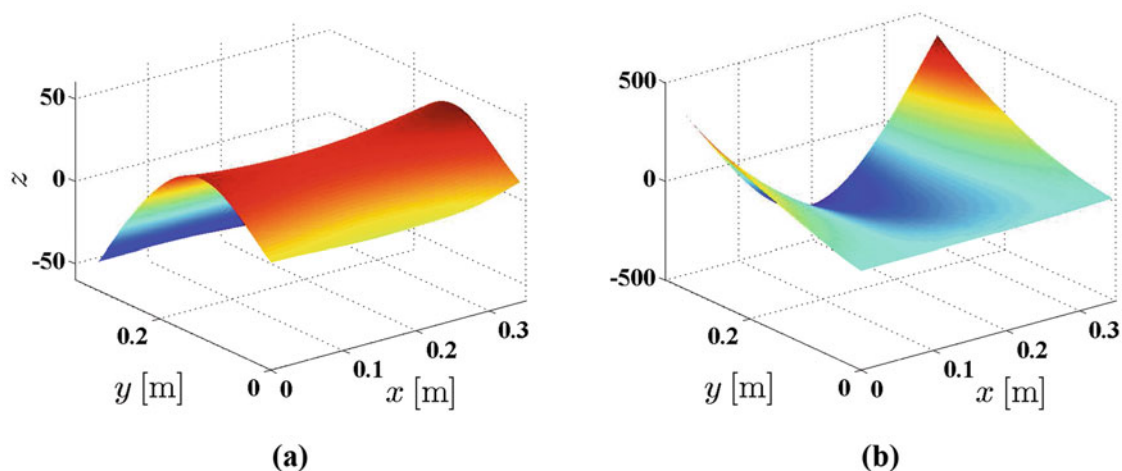


**Fig. 2.2** (a) Vibration shape of the composite plate at 89 Hz and (b) that of the plate at 150 Hz

CSLDV system, including a single-point laser vibrometer and a scanner. A dSPACE MicroLabBox was connected to the vibrometer to control X and Y mirrors of the scanner. Approximate frequency response functions of the composite plate were measured, with velocity response of the composite plate measured by the vibrometer and a burst chirp signal given to the speaker, which served as response and excitation signals, respectively. There were two peaks at 89 and 150 Hz in a measured frequency response function. Sinusoidal signals with frequencies of 89 and 150 Hz were then given to the speaker to generate acoustic excitation. Vertical and horizontal scan trajectories were assigned to the composite plate to measure its vibration shapes at 89 and 150 Hz, respectively. Vibration shapes at the two frequencies are shown in Fig. 2.2. Measured vibration shapes at 89 and 150 Hz correspond to the second and fourth modes of the composite plate in its finite element model.

In this experimental investigation,  $nh = 0.005$  m and  $s = 0.005$  m were used to calculate curvature vibration shapes and wavelet transforms of vibration shapes, respectively. Curvature damage indices associated with vibration shapes at 89 and 150 Hz are shown in Figs. 2.3a, b, respectively, and the associated auxiliary curvature damage index is shown in Fig. 2.3c. Wavelet damage indices associated with vibration shapes at 89 and 150 Hz are shown in Figs. 2.4a and b, respectively, and the associated auxiliary wavelet damage index is shown in Fig. 2.4c. It can be seen in Figs. 2.3a and 2.4a that upper and lower edges of the delamination area can be clearly identified; it can be seen in Figs. 2.4b and 2.3b that left and right edges of the delamination area can be clearly identified. In Figs. 2.3c and 2.4c, four edges of the delamination area can be clearly identified. Delamination identification results from the two methods also compared well with that of a C-scan image of the composite plate shown in Fig. 2.5. By comparing damage identification results from the polynomial-based and wavelet-

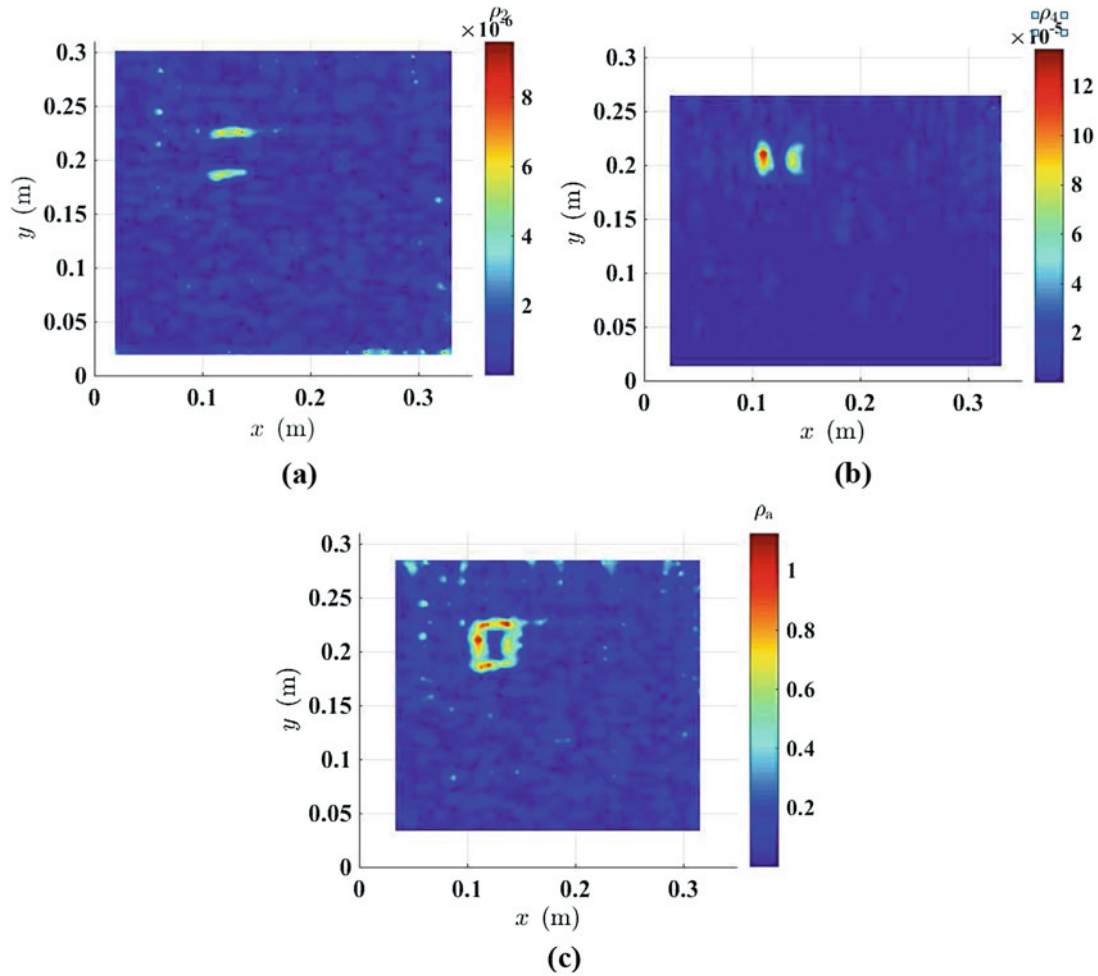


**Fig. 2.3** (a) Curvature damage index associated with the mode shape at 89 Hz, (b) the curvature damage index associated with the mode shape at 89 Hz and (c) the auxiliary curvature damage index associated with the two mode shapes;  $nh = 0.005$  m was used to calculate curvature vibration shapes

based methods in Figs. 2.3 and 2.4, respectively, one can see that the former has a larger identifiable area than the latter since wavelet transforms can incur severe boundary distortion in associated wavelet damage indices. More importantly, the former yielded the better auxiliary damage index than the latter as a lower level of noise is observed in Fig. 2.3c.

## 2.4 Conclusions

Two non-model-based methods are used to identify delamination in a composite laminated plate using a CSLDV system and their identification results are compared. One is a polynomial-based method that uses polynomial fits to approximate curvature vibration shapes of a corresponding undamaged composite plate and the other is a wavelet-based method that uses continuous wavelet transforms of vibration shapes. In the two methods, local anomalies caused by delamination in curvature vibration shapes are identified in neighborhoods with high damage index values. Auxiliary damage indices associated with curvature damage and wavelet damage indices are formulated, from which positions and lengths of delamination edges can be accurately and completely identified. Both methods do not require any a priori and baseline information of composite plates, such as dimensions, boundary conditions, material properties and vibration shapes of corresponding undamaged plates. Effectiveness of the two methods has been experimentally investigated to identify delamination in the composite plate. Experimental delamination identification results compare well with that from a C-scan image of the composite plate, and the position and dimensions of the delamination area were accurately and completely identified.



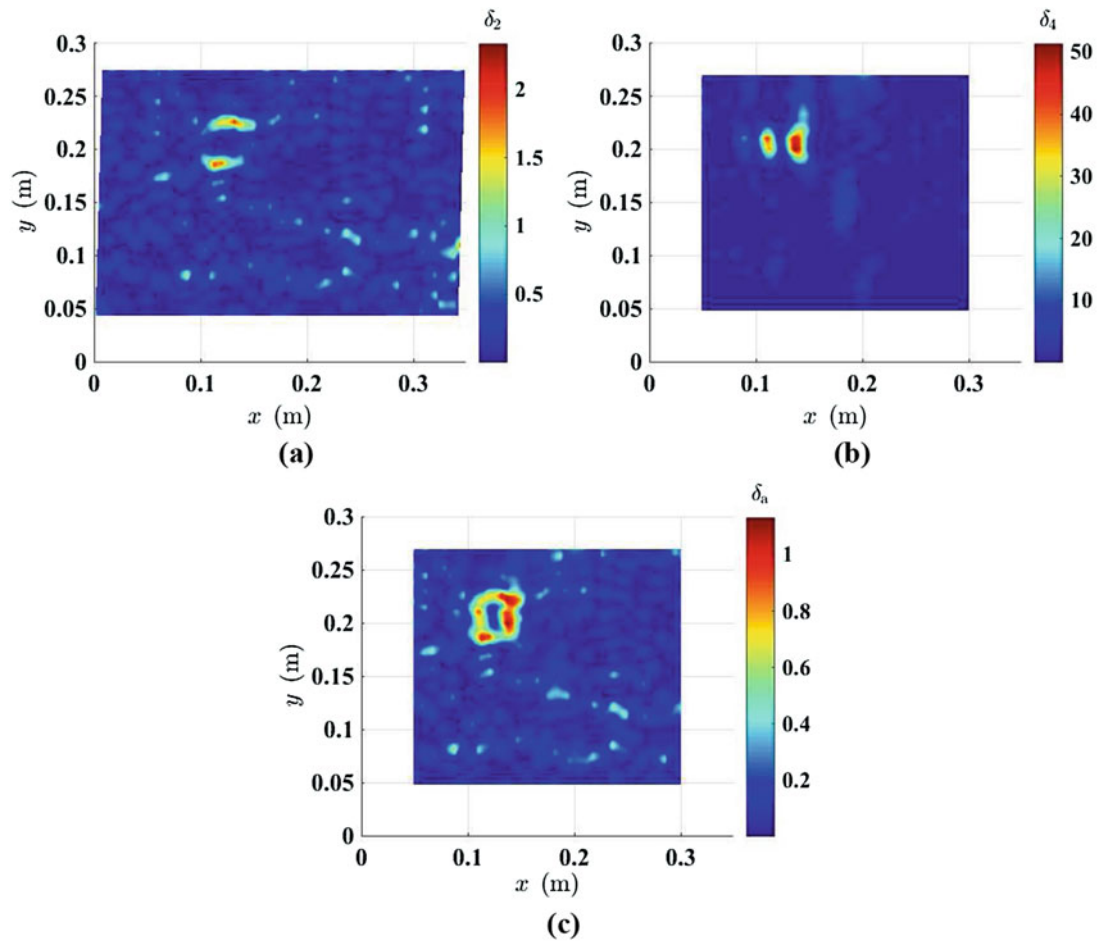
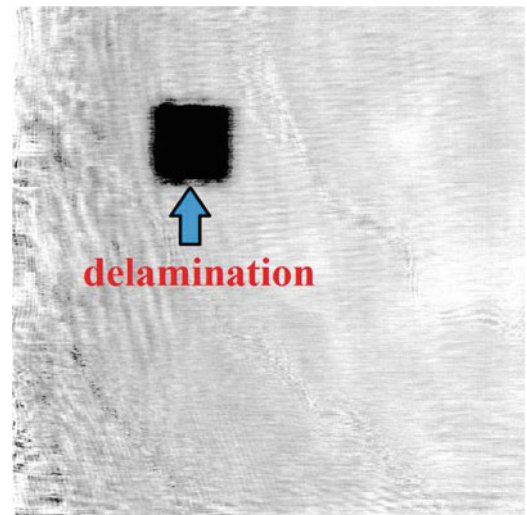


**Fig. 2.4** (a) Wavelet damage index associated with the vibration shape at 89Hz, (b) the wavelet damage index associated with the vibration shape at 150 Hz and (c) the auxiliary wavelet damage index associated with the two vibration shapes;  $s = 0.005$  m was used to calculate wavelet transforms of vibration shapes

**Fig. 2.5** C-scan image of the composite plate with delamination



**Acknowledgements** The authors are grateful for the financial support from the National Science Foundation under Grant Numbers CMMI-1229532 and CMMI-1335024 and the College of Engineering and Information Technology at the University of Maryland, Baltimore County through a Strategic Plan Implementation Grant. They would like thank Prof. Aditi Chattopadhyay and Guoyi Li for manufacturing the composite plate used in the experiment and performing a C-scan inspection on the plate.

## References

1. Valdes, S.D., Soutis, C.: Delamination detection in composite laminates from variations of their modal characteristics. *J. Sound Vib.* **228**(1), 1–9 (1999)
2. Zou, Y., Tong, L., Steven, G.P.: Vibration-based model-dependent damage (delamination) identification and health monitoring for composite structures—a review. *J. Sound Vib.* **230**(2), 357–378 (2000)
3. Qiao, P., Lu, K., Lestari, W., Wang, J.: Curvature mode shape-based damage detection in composite laminated plates. *Compos. Struct.* **80**(3), 409–428 (2007)
4. Jafari-Talookolaei, R.A., Abedi, M., Hajianmaleki, M.: Vibration characteristics of generally laminated composite curved beams with single through-the-width delamination. *Compos. Struct.* **138**, 172–183 (2016)
5. Castro, S.G., Donadon, M.V.: Assembly of semi-analytical models to address linear buckling and vibration of stiffened composite panels with debonding defect. *Compos. Struct.* **160**, 232–247 (2017)
6. Chakraborty, S., Mandal, B., Chowdhury, R., Chakrabarti, A.: Stochastic free vibration analysis of laminated composite plates using polynomial correlated function expansion. *Compos. Struct.* **135**, 236–249 (2016)
7. Xu, Y.F., Zhu, W.D., Liu, J., Shao, Y.: Identification of embedded horizontal cracks in beams using measured mode shapes. *J. Sound Vib.* **333**(23), 6273–6294 (2014)
8. Xu, W., Zhu, W.D., Smith, S.A., Cao, M.: Structural damage detection using slopes of longitudinal vibration shapes. *J. Vib. Acoust.* **138**(3), 034501 (2016)
9. Lestari, W., Qiao, P., Hanagud, S.: Curvature mode shape-based damage assessment of carbon/epoxy composite beams. *J. Intell. Mater. Syst. Struct.* **18**(3), 189–208 (2007)
10. Yang, Z.B., Radziński, M., Kudela, P., Ostachowicz, W.: Two-dimensional modal curvature estimation via fourier spectral method for damage detection. *Compos. Struct.* **148**, 155–167 (2016)
11. Xu, Y., Zhu, W., Smith, S.: Non-model-based damage identification of plates using principal, mean and gaussian curvature mode shapes. *J. Sound Vib.* **400**, 626–659 (2017)
12. Rothberg, S., Baker, J., Halliwell, N.A.: Laser vibrometry: pseudo-vibrations. *J. Sound Vib.* **135**(3), 516–522 (1989)
13. Sriram, P., Hanagud, S., Craig, J., Komerath, N.: Scanning laser doppler technique for velocity profile sensing on a moving surface. *Appl. Opt.* **29**(16), 2409–2417 (1990)
14. Sriram, P., Hanagud, S., Craig, J.: Mode shape measurement using a scanning laser doppler vibrometer. *Int. J. Anal. Exp. Modal Anal.* **5**(3), 169–178 (1992)
15. Stanbridge, A., Ewins, D.: Using a continuously-scanning laser doppler vibrometer for modal testing. In: 14th International Modal Analysis Conference (IMAC), Dearborn, pp. 816–822 (1996)
16. Stanbridge, A., Ewins, D.: Modal testing using a scanning laser doppler vibrometer. *Mech. Syst. Signal Process.* **13**(2), 255–270 (1999)
17. Stanbridge, A., Ewins, D., Khan, A.: Modal testing using impact excitation and a scanning LDV. *Shock Vib.* **7**(2), 91–100 (2000)
18. Stanbridge, A., Martarelli, M., Ewins, D.: The scanning laser doppler vibrometer applied to impact modal testing. In: SPIE Proceedings Series, Society of Photo-Optical Instrumentation Engineers, pp. 986–991 (1999)
19. Di Maio, D., Ewins, D.: Continuous scan, a method for performing modal testing using meaningful measurement parameters; Part I. *Mech. Syst. Signal Process.* **25**(8), 3027–3042 (2011)
20. Allen, M.S., Sracic, M.W.: A new method for processing impact excited continuous-scan laser doppler vibrometer measurements. *Mech. Syst. Signal Process.* **24**(3), 721–735 (2010)
21. Chen, D.M., Xu, Y.F., Zhu, W.D.: Damage identification of beams using a continuously scanning laser doppler vibrometer system. *J. Vib. Acoust.* **138**(5), 051011 (2016)
22. Xu, Y.F., Chen, D.M., Zhu, W.D.: Damage identification of beam structures using free response shapes obtained by use of a continuously scanning laser doppler vibrometer system. *Mech. Syst. Signal Process.* **92**, 226–247 (2017)
23. Timoshenko, S.P., Woinowsky-Krieger, S.: *Theory of Plates and Shells*. McGraw-Hill, New York (1959)
24. Cox, I., Gaudard, M.: *Discovering Partial Least Squares with JMP*. SAS Institute, Cary (2013)
25. Mallat, S.: *A Wavelet Tour of Signal Processing*. Academic, San Diego (1999)



# Chapter 3

## Rapid and Dense 3D Vibration Measurement by Three Continuously Scanning Laser Doppler Vibrometers

Da-Ming Chen and W. D. Zhu

**Abstract** This paper presents an investigation of rapid and dense three-dimensional (3D) vibration measurement by three continuously scanning laser Doppler vibrometers (CSLDVs) in a synchronously scanning mode, which means that three laser spots from three CSLDVs continuously move along the same scan trajectory and synchronously measure vibration of the same point on a surface. Three CSLDVs, i.e., Top, Left, and Right CSLDVs, are from a Polytec PSV-500-3D system and input signals to scan mirrors of each CSLDV are controlled by a dSPACE MicroLabBox control unit. The whole system is called a 3D-CSLDV system. Rotation angles of scan mirrors of Left and Right CSLDVs can be obtained from those of the Top CSLDV based on positional relations among three CSLDVs. With the proposed methodology, three laser spots from three CSLDVs can continuously move in a synchronously scanning mode. An experiment is conducted to obtain 3D operational deflecting shapes (ODSs) of a composite plate in a measurement coordinate system (MCS) by a 3D-CSLDV system. Results of 3D ODSs in the MCS are in good agreement with those from a PSV-500-3D system in a step scanning mode.

**Keywords** 3D vibration measurement · Continuously scanning laser Doppler vibrometer system · Synchronously scanning mode

### 3.1 Introduction

A scanning laser Doppler vibrometer (SLDV) is widely used in the vibration community because it provides non-contact and spatially dense vibration measurement. In a conventional measurement method, the surface of a structure is divided by a measurement grid, and the laser spot from a SLDV stays at one point long enough to acquire sufficient vibration data of this point and then moves to the next one. This step scanning measurement mode usually takes a long acquisition time, especially when the surface is large and the measurement grid is dense. An improved method is that the laser spot continuously moves over the surface of a structure [1]. Since the laser spot continuously moves instead of staying at one point, an operating deflection shape (ODS) in the laser line-of-sight direction can be obtained from velocity response measured by a continuously SLDV (CSLDV). Several methods to extract ODSs and modal characteristics from velocity response have been investigated [2–7]. Stanbridge and Ewins [2] developed two CSLDV measurement methods to obtain ODSs of a structure under sinusoidal excitation. One measurement method is the demodulation method, where velocity response is multiplied by sinusoidal signals at the excitation frequency and a low-pass filter is applied to obtain an ODS. The other one is the polynomial method, where an ODS is represented by a polynomial whose coefficients are obtained by processing the discrete Fourier transform of velocity response. Allen and Sracic [5] proposed a lifting method to treat velocity response of a structure measured by a CSLDV as free response of a linear time-periodic system and decomposed it into a set of frequency response functions, from which natural frequencies, mode shapes, and modal damping ratios of the structure can be obtained using conventional curve fitting methods. These methods are applied with different scan trajectories, such as line scans, circular scans, and area scans. Since rapid and spatially dense vibration measurement can be obtained by a CSLDV, Chen et al. [8, 9] and Xu et al. [10] investigated its feasibility in damage identification of beams by using curvatures of ODSs. All the investigations of continuously scanning in references mentioned above are done by a single CSLDV. Since a single SLDV cannot simultaneously measure in-plane and out-of-plane vibration, a 3D-SLDV system has been developed and commercialized (e.g., a Polytec PSV-400-3D or PSV-500-3D system), where three laser spots from three SLDVs are synchronously directed to a point to measure its vibration and then move to the next point. A lot of investigations have been conducted by using a 3D-SLDV system [11–15].

---

D.-M. Chen · W. D. Zhu (✉)

Department of Mechanical Engineering, University of Maryland, Baltimore County, Baltimore, MD, USA

e-mail: [damingc1@umbc.edu](mailto:damingc1@umbc.edu); [wzhu@umbc.edu](mailto:wzhu@umbc.edu)

Similar to a single SLDV, a 3D-SLDV system in a step scanning mode takes a long time to obtain spatially dense 3D ODSs of a structure. The aim of this work is to develop a 3D-CSLDV system that can rapidly obtain spatially dense 3D ODSs of a structure, which can provide more vibration information than an ODS obtained by a single CSLDV, and they can be further processed for damage identification in the future. This work addresses the main challenge of a 3D-CSLDV system that is to ensure that three laser spots from three CSLDVs continuously move along the same scan trajectory and synchronously measure vibration of the same point on a surface. Three CSLDVs, i.e., Top, Left, and Right CSLDVs, are from a Polytec PSV-500-3D system and input signals to scan mirrors of each CSLDV are controlled by a dSPACE MicroLabBox control unit. Rotation angles of scan mirrors of Left and Right CSLDVs can be obtained from those of the Top CSLDV based on positional relations among three CSLDVs. With the proposed methodology, three laser spots from three CSLDVs can continuously move in a synchronously scanning mode. An experiment is conducted to obtain 3D ODSs of a composite plate in a measurement coordinate system (MCS) by a 3D-CSLDV system. For a prescribed scan trajectory, two scan frequencies corresponding to different scan time are used and 3D ODSs of the composite plate are obtained from velocity response by the demodulation method. Results of 3D ODSs in the MCS corresponding to two different scan frequencies are in good agreement. Further, they are also in good agreement with those from a PSV-500-3D system in a step scanning mode. However, the scan time is much less and spatial resolutions of 3D ODSs are much denser when using the 3D-CSLDV system.

## 3.2 Methodology

### 3.2.1 Geometrical Model of a CSLDV

The laser spot from a CSLDV can be directed to any visible point on a surface by rotating two orthogonal scan mirrors called X and Y mirrors, which control horizontal and vertical movements of the laser spot, respectively. Rotations of scan mirrors are driven by corresponding stepper motors. To obtain 3D ODSs of a structure, a MCS  $o-xyz$  needs to be first defined. In this work, a Polytec PSV-A-450 reference object that has some points with known coordinates is used to define a MCS, as shown in Fig. 3.1a. In order to obtain the position of a CSLDV with respect to the MCS, the geometrical model of a CSLDV is built, as shown in Fig. 3.1b. Note that the layout of scan mirrors in Fig. 3.1a is different from the SLDV developed in Ref. [16] and the geometrical model of the CSLDV in this work is new. Another coordinate system  $o'-x'y'z'$ , which is fixed on the CSLDV and called a vibrometer coordinate system (VCS), is defined to describe the position of the CSLDV. The VCS  $o'-x'y'z'$  is specified as follows:  $x'$  and  $y'$  axes are along rotation axes of X and Y mirrors, respectively. Positive directions of  $x'$  and  $y'$  axes are directed to sides of corresponding stepper motors. The  $y'$  axis is parallel to the  $y''$  axis and has an intersection point  $o'$  with the  $x'$  axis. The  $z'$  axis is perpendicular to the plane formed by  $x'$  and  $y'$  axes; it goes through point  $o'$  and has an intersection point  $o''$  with the  $y''$  axis. The length of  $o'o''$ , denoted by  $d$ , is defined as the separation distance between two mirrors, which is equal to 29.2 mm for three CSLDVs used in this work. Variables  $\alpha$  and  $\beta$  are rotation angles of X and Y mirrors measured from their initial positions, respectively.

Coordinates of point  $P$  on the reference object in the MCS are  $\mathbf{P}_{MCS} = [x, y, z]^T$ . To direct the laser spot from the CSLDV to point  $P$ , rotation angles of X and Y mirrors are  $\alpha$  and  $\beta$ , respectively. Based on the geometrical model of the CSLDV in Fig. 3.1b, coordinates of point  $P$  in the VCS of the CSLDV can be expressed as

$$\mathbf{P}_{VCS} = [-d \tan(\beta) - r \sin(\beta), -r \cos(\alpha) \cos(\beta), -r \sin(\alpha) \cos(\beta)]^T \quad (3.1)$$

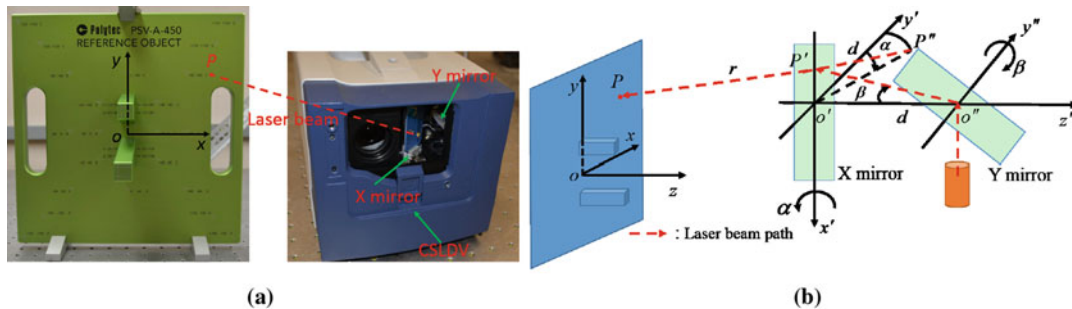


**Fig. 3.1** (a) Configuration of a CSLDV and a reference object to define a MCS and (b) the geometrical model of the CSLDV

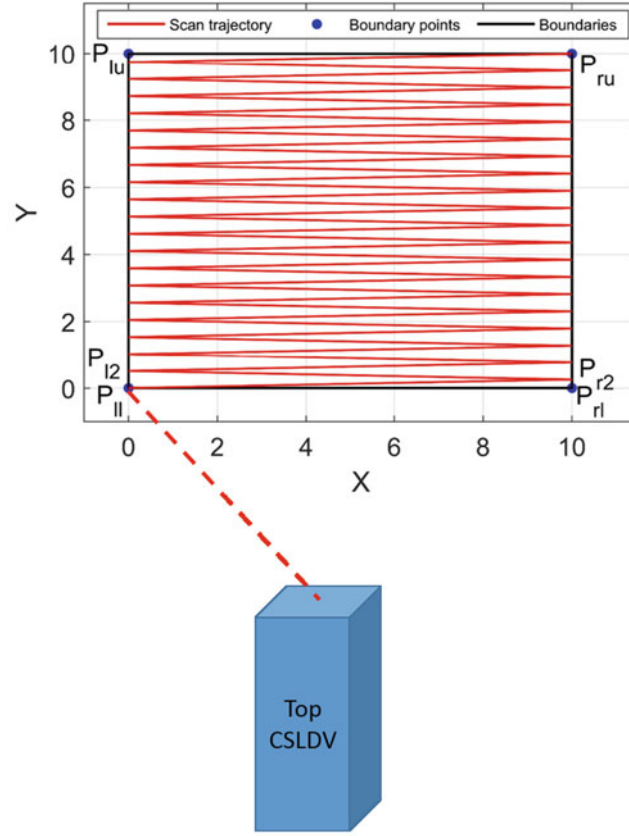


**Fig. 3.2** Prescribed scan trajectory for a structure by the Top CSLDV

where  $r$  is the distance from point  $P'$ , which is the incident point of the X mirror, to point  $P$ . The relation between  $\mathbf{P}_{MCS}$  and  $\mathbf{P}_{VCS}$  can be established by

$$\mathbf{P}_{MCS} = \mathbf{T} + \mathbf{R}\mathbf{P}_{VCS} = \begin{bmatrix} x_{o'} \\ y_{o'} \\ z_{o'} \end{bmatrix} + \begin{bmatrix} \cos(x, x') & \cos(x, y') & \cos(x, z') \\ \cos(y, x') & \cos(y, y') & \cos(y, z') \\ \cos(z, x') & \cos(z, y') & \cos(z, z') \end{bmatrix} \mathbf{P}_{VCS} \quad (3.2)$$

where  $\mathbf{T} = [x_{o'}, y_{o'}, z_{o'}]^T$  is a translation vector that specifies coordinates of origin  $o'$  in the MCS,  $\mathbf{R}$  is the direction cosine matrix from the VCS to the MCS. The translation vector  $\mathbf{T}$  together with the direction cosine matrix  $\mathbf{R}$  can determine the position of a CSLDV with respect to the MCS.  $\mathbf{T}$  and  $\mathbf{R}$  can be obtained by the method in Ref. [16].

### 3.2.2 Constant-Speed Scan for the Top CSLDV

In order to use the demodulation method to obtain an ODS of a structure from velocity response measured by a CSLDV, a constant-speed scan algorithm is proposed for a prescribed scan trajectory, as shown in Fig. 3.2. The shape of a surface is controlled by four boundary points  $P_{ll}$ ,  $P_{rl}$ ,  $P_{lu}$ , and  $P_{ru}$ , which are located at left lower, right lower, left upper, and right upper corners of the surface, respectively. Boundaries of the surface in Fig. 3.2 are four lines formed by four boundary points. The laser spot from the Top CSLDV starts at point  $P_{ll}$  and simultaneously moves in right and upward directions until reaching point  $P_{r2}$ , which completes a scan of line  $P_{ll}P_{r2}$ . If multiple scans for line  $P_{ll}P_{r2}$  are required, the laser spot moves back to point  $P_{ll}$  and repeats the same scan process between points  $P_{ll}$  and  $P_{r2}$  until multiple scans are completed. At the time when multiple scans are completed, the laser spot is at point  $P_{r2}$  and continues to simultaneously move in left and upward directions until reaching point  $P_{l2}$ . The laser spot repeats the above scan process and finally reaches point  $P_{ru}$  to complete the whole prescribed scan trajectory. Note that if multiple scans are applied to a scan line, the number of multiple scans should be odd to ensure that the laser spot is at the other end of the scan line that is different from the start point when multiple scans are completed.

After velocity response along the prescribed scan trajectory is measured by a CSLDV, an ODS in the laser line-of-sight direction can be obtained from velocity response by the demodulation method. Details of the demodulation method can be seen in Ref. [8].

Rotation angles of scan mirrors of the Top CSLDV to direct the laser spot to point  $P^k$  on the prescribed scan trajectory are obtained by the proposed algorithm in Sect. 3.2.2. The third variable  $r_{Top}^k$  in Eq. (3.1), which is the distance from point  $P'$  on the X mirror of the Top CSLDV to point  $P^k$ , can be calculated by

$$r_{Top}^k = \frac{r_{Top}^0}{\cos(\alpha_{Top}^k) \cos(\beta_{Top}^k)} \quad (3.3)$$

where  $r_{Top}^0$  is the distance from point  $P'$  to the point on the prescribed scan trajectory with  $\alpha_{Top} = 0$  and  $\beta_{Top} = 0$  and can be obtained by the geometrical scan unit of the Top CSLDV, and  $\alpha_{Top}^k$  and  $\beta_{Top}^k$  are corresponding rotation angles of X and Y mirrors of the Top CSLDV for point  $P^k$ , respectively. Hence, coordinates of point  $P^k$  in the VCS of the Top CSLDV can be obtained by Eq. (3.1). Since the position of the Top CSLDV with respect to the MCS is obtained by the method described in Sect. 3.2.1, coordinates of point  $P^k$  in the MCS can be obtained by

$$\mathbf{P}_{MCS}^k = \mathbf{T}_{Top} + \mathbf{R}_{Top} \mathbf{P}_{VCS(Top)}^k \quad (3.4)$$

where  $\mathbf{T}_{Top}$  and  $\mathbf{R}_{Top}$  are the translation vector and the direction cosine matrix of the Top CSLDV with respect to the MCS, respectively. Since coordinates of point  $P^k$  is constant in the MCS, in order to let laser spots from Left and Right CSLDVs direct to the same point  $P^k$ , positional relations among three CSLDVs for point  $P^k$  are established by

$$\mathbf{T}_{Top} + \mathbf{R}_{Top} \mathbf{P}_{VCS(Top)}^k = \mathbf{T}_{Left} + \mathbf{R}_{Left} \mathbf{P}_{VCS(Left)}^k = \mathbf{T}_{Right} + \mathbf{R}_{Right} \mathbf{P}_{VCS(Right)}^k \quad (3.5)$$

where  $\mathbf{T}_{Left}$  and  $\mathbf{R}_{Left}$  are the translation vector and the direction cosine matrix of the Left CSLDV with respect to the MCS, respectively, and  $\mathbf{T}_{Right}$  and  $\mathbf{R}_{Right}$  are the translation vector and the direction cosine matrix of the Right CSLDV with respect to the MCS, respectively. Hence, coordinates of point  $P^k$  in VCSs of Left and Right CSLDVs can be obtained by

$$\mathbf{P}_{VCS(Left)}^k = \mathbf{R}_{Left}^{-1} (\mathbf{T}_{Top} - \mathbf{T}_{Left}) + \mathbf{R}_{Left}^{-1} \mathbf{R}_{Top} \mathbf{P}_{VCS(Top)}^k \quad (3.6)$$

and

$$\mathbf{P}_{VCS(Right)}^k = \mathbf{R}_{Right}^{-1} (\mathbf{T}_{Top} - \mathbf{T}_{Right}) + \mathbf{R}_{Right}^{-1} \mathbf{R}_{Top} \mathbf{P}_{VCS(Top)}^k \quad (3.7)$$

respectively. Further, rotation angles of X and Y mirrors of Left and Right CSLDVs for point  $P^k$  can be obtained by

$$\alpha_{Left}^k = \arctan(z_{VCS(Left)}^k / y_{VCS(Left)}^k), \beta_{Left}^k = \arctan(x_{VCS(Left)}^k / (y_{VCS(Left)}^k / \cos(\alpha_{Left}^k) - d)) \quad (3.8)$$

and

$$\alpha_{Right}^k = \arctan(z_{VCS(Right)}^k / y_{VCS(Right)}^k), \beta_{Right}^k = \arctan(x_{VCS(Right)}^k / (y_{VCS(Right)}^k / \cos(\alpha_{Right}^k) - d)) \quad (3.9)$$

respectively.

With the proposed methodology described above, three laser spots from three CSLDVs can synchronously scan the same point on the prescribed scan trajectory. After velocity response of point  $P^k$  is measured by three CSLDVs, vibration information of point  $P^k$  in three laser line-of-sight directions can be obtained by the demodulation method. Then vibration information of point  $P^k$  in the MCS can be obtained by

$$[V_x^k, V_y^k, V_z^k]^T = [[\mathbf{R}_{Top} \mathbf{e}_{Top}^k, \mathbf{R}_{Left} \mathbf{e}_{Left}^k, \mathbf{R}_{Right} \mathbf{e}_{Right}^k]^T]^{-1} [V_{Top}^k, V_{Left}^k, V_{Right}^k]^T \quad (3.10)$$

where  $\mathbf{e}_X^k = [\sin(\beta_X^k), -\cos(\alpha_X^k) \cos(\beta_X^k), -\sin(\alpha_X^k) \cos(\beta_X^k)]^T$ , in which  $X = Top, Left, \text{ and } Right$ , is a unit vector of the laser beam direction in the VCS of each CSLDV when the laser spot is directed to point  $P^k$ . The process described above is repeated for each point on the prescribed scan trajectory. Finally, 3D ODSs of the structure in the MCS can be obtained by a 3D-CSLDV system.

### 3.3 Experimental Investigation

In order to obtain 3D ODSs of a structure in a MCS by a 3D-CSLDV system with the proposed methodology, an experiment is conducted to measure velocity response of a six-laminate composite plate by three CSLDV in a synchronously scanning mode, as shown in Fig. 3.3a. The composite plate is manufactured using FS-A23 resin and FS-B412 hardener. A strip area with the width of 25.4 mm adjacent to the lower boundary of the plate, which is in the vertical plane, is clamped by two aluminum beams with the width of 25.4 mm that are clamped by a bench vice, as shown in Fig. 3.3b. A speaker located at the back side of the plate is used to excite the plate in a non-contact manner. The reference object PSV-A-450 in Fig. 3.3b is mounted on a tripod with an arbitrary angle to define a MCS. A scan trajectory is defined to cover the whole surface of the plate and dimensions of the scan area are shown in Fig. 3.3b. A 3M removable reflection graphic film is attached on the front side of the plate to enhance laser reflection. Three CSLDV, i.e., Top, Left, and Right CSLDVs, are from a Polytec PSV-500-3D system. Since the PSV-500-3D system is used in a step scanning mode and cannot be directly applied for continuously scanning, an external control system is developed to control scan mirrors of three CSLDVs by a dSPACE MicroLabBox control unit, as shown in Fig. 3.3c. There is an external control interface on the back side of each CSLDV and input signals to scan mirrors of three CSLDVs are transmitted by six BNC cables.

#### 3.3.1 3D ODSs in the MCS by the 3D-CSLDV System

In order to investigate rapid and dense characteristics of 3D ODSs obtained by the 3D-CSLDV system, two different scan frequencies, i.e., 0.1 and 1 Hz, are used to scan the same prescribed trajectory in Fig. 3.3b obtained with  $N = 20$  and  $M = 3$ . The total scan time corresponding to scan frequencies of 0.1 and 1 Hz is  $(2 * 20 - 1) * 3/2/0.1 = 585$  s and  $(2 * 20 - 1) * 3/2/1 = 58.5$  s, respectively. The sampling frequency of the 3D-CSLDV system is 10,000 Hz. Rotation angles of scan mirrors of the Top CSLDV are obtained to scan the prescribed scan trajectory. Rotation angles of scan mirrors of Left and Right CSLDVs are then obtained from those of the Top CSLDV based on positional relations among three CSLDVs. All the input signals are generated in MATLAB and controlled by the MicroLabBox control unit via the software dSPACE ControlDesk and the SignalEditor module.

The plate is sinusoidally excited by the speaker at an excitation frequency of 148 Hz, which is close to a natural frequency of the plate. Three laser spots from three CSLDVs continuously move along the same prescribed scan trajectory in a synchronously scanning mode, which means that only one laser spot with larger light intensity than that of a single laser spot is seen on the plate during the whole scan time. Velocity response measured by three CSLDVs in three laser line-of-sight directions corresponding to scan frequencies of 0.1 and 1 Hz are shown in Fig. 3.4a and b, respectively. Since three CSLDVs in a synchronously scanning mode always measure vibration of the same point during the whole scan time, one can see from Fig. 3.4a and b that the only differences among velocity response measured by three CSLDVs are velocity amplitudes. Since excitation is in the out-of-plane direction of the plate, velocity response measured by the Top CSLDV has larger amplitudes than those measured by Left and Right CSLDVs. Results of 3D ODSs in the MCS corresponding to the scan frequency of 0.1 Hz are calculated by Eq. (3.10), as shown in Fig. 3.5. One can see that velocity amplitudes of the ODS in the  $y$  direction are smaller than those in  $x$  and  $z$  directions, which matches with the definition of the MCS. Results of 3D ODSs in the MCS corresponding to the scan frequency of 1 Hz are shown in Fig. 3.6. One can see that 3D ODSs in the MCS obtained with two different scan frequencies agree well with each other.

#### 3.3.2 Comparison with Step Scanning

In order to validate accuracy of 3D ODSs obtained by the 3D-CSLDV system where three laser spots moves in a synchronously scanning mode, the PSV-500-3D system is used to measure 3D ODSs of the plate in the same MCS in a

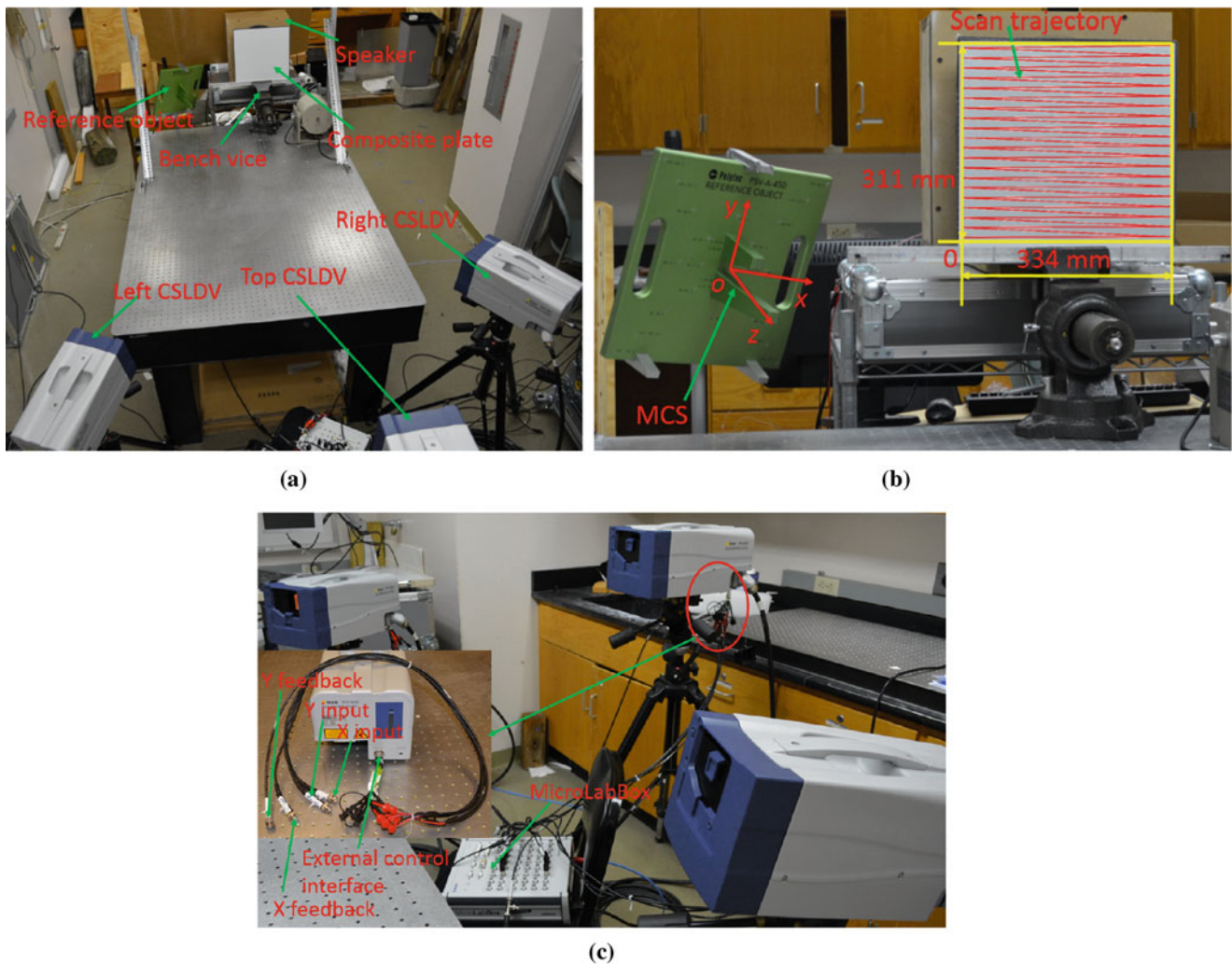


**Fig. 3.3** (a) Experimental setup to measure velocity response of a composite plate by a 3D-CSLDV system, (b) the MCS and the prescribed scan trajectory on the plate, and (c) the MicroLabBox control unit to control scan mirrors of three CSLDVs

step scanning mode at the same excitation frequency. The surface of the plate is divided by a  $39 \times 65$  measurement grid, as shown in Fig. 3.7; 39 is selected to correspond to the number of scan lines in the prescribed scan trajectory in Fig. 3.3b, and 65 is obtained based on the ratio between the width and height of the plate. The total time to complete the whole grid in a step scanning mode is 2516 s and results of 3D ODSs are shown in Fig. 3.8. Since excitation is in the out-of-plane direction of the plate and the  $y$  direction is almost perpendicular to the out-of-plane direction, vibration in the  $y$  direction is small and the signal-to-noise ratio of vibration in the  $y$  direction is not as high as that in  $x$  and  $z$  directions. There are several small peaks on the ODS in the  $y$  direction in Fig. 3.8b, which are caused by measurement noise. There are no small peaks on ODSs in the  $y$  direction in Figs. 3.5b and 3.6b because ODSs there are obtained by the demodulation method where a low-pass filter is applied to velocity response measured by the 3D-CSLDV system, which can filter high-frequency noise. One can see that 3D ODSs in the MCS obtained in a step scanning mode are in good agreement with those obtained by the 3D-CSLDV system in a synchronously scanning mode. Spatial resolutions and the total scan time in these two modes are compared in Table 3.1. One can see that the scan time is much less and spatial resolutions of 3D ODSs are much denser when using the 3D-CSLDV system. With a lower scan frequency, the spatial resolution is denser but it also needs more scan time. Note that the sampling frequency of a 3D-CSLDV system can also affect the density of the spatial resolution. A higher sampling frequency would yield more sample points during the same scan time and increase the density of the spatial resolution. However, in a step scanning mode, the sampling frequency would have no effect on the density of the spatial resolution.



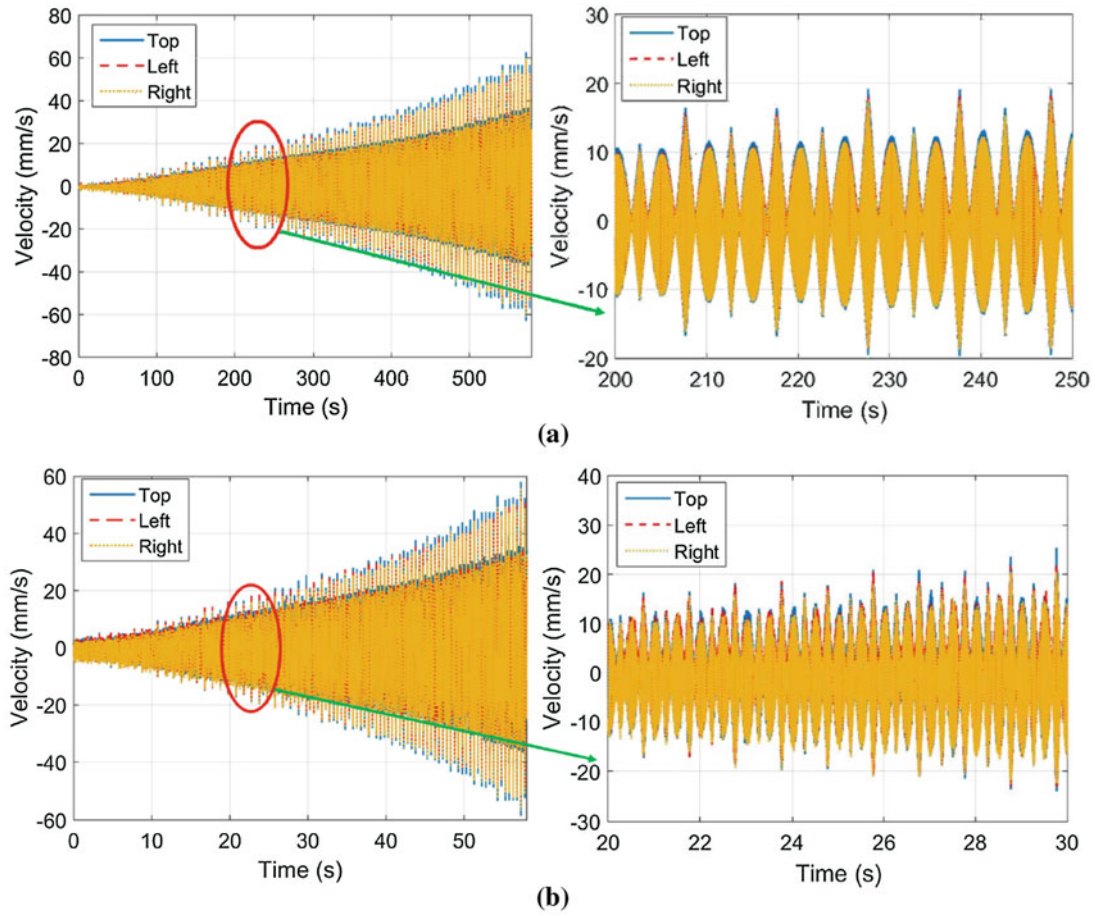


**Fig. 3.4** Velocity response of the plate measured by three CSLDVs in a synchronously scanning mode with scan frequencies of (a) 0.1 and (b) 1 Hz

### 3.4 Conclusions

An investigation of rapid and dense 3D vibration measurement by a 3D-CSLDV system in a synchronously scanning mode is presented in this work for the first time. To achieve this mode where three laser spots from three CSLDVs can always measure vibration of the same point during scanning, three steps are needed and summarized as follows: (1) A MCS is first defined and positions of three CSLDVs with respect to the MCS are obtained based on the geometrical model of a CSLDV. (2) A scan trajectory is defined based on the shape of a structure and rotation angles of the Top CSLDV is obtained. (3) Rotation angles of Left and Right CSLDVs are obtained from those of the Top CSLDV based on positional relations among three CSLDVs. Three ODSs in laser line-of-sight directions are obtained from velocity response by the demodulation method. Finally, 3D ODS in the MCS are obtained by applying Eq. (3.10) to each sample point on the prescribed scan trajectory. An experiment is conducted to obtain 3D ODSs of a composite plate in a MCS by a 3D-CSLDV system. Two scan frequencies corresponding to different scan time are used and results of 3D ODSs in the MCS by two scan frequencies are in good agreement with each other. Further, they are in good agreement with those from a PSV-500-3D system in a step scanning mode. However, the scan time is much less and spatial resolutions of 3D ODSs are much denser when using the 3D-CSLDV system.

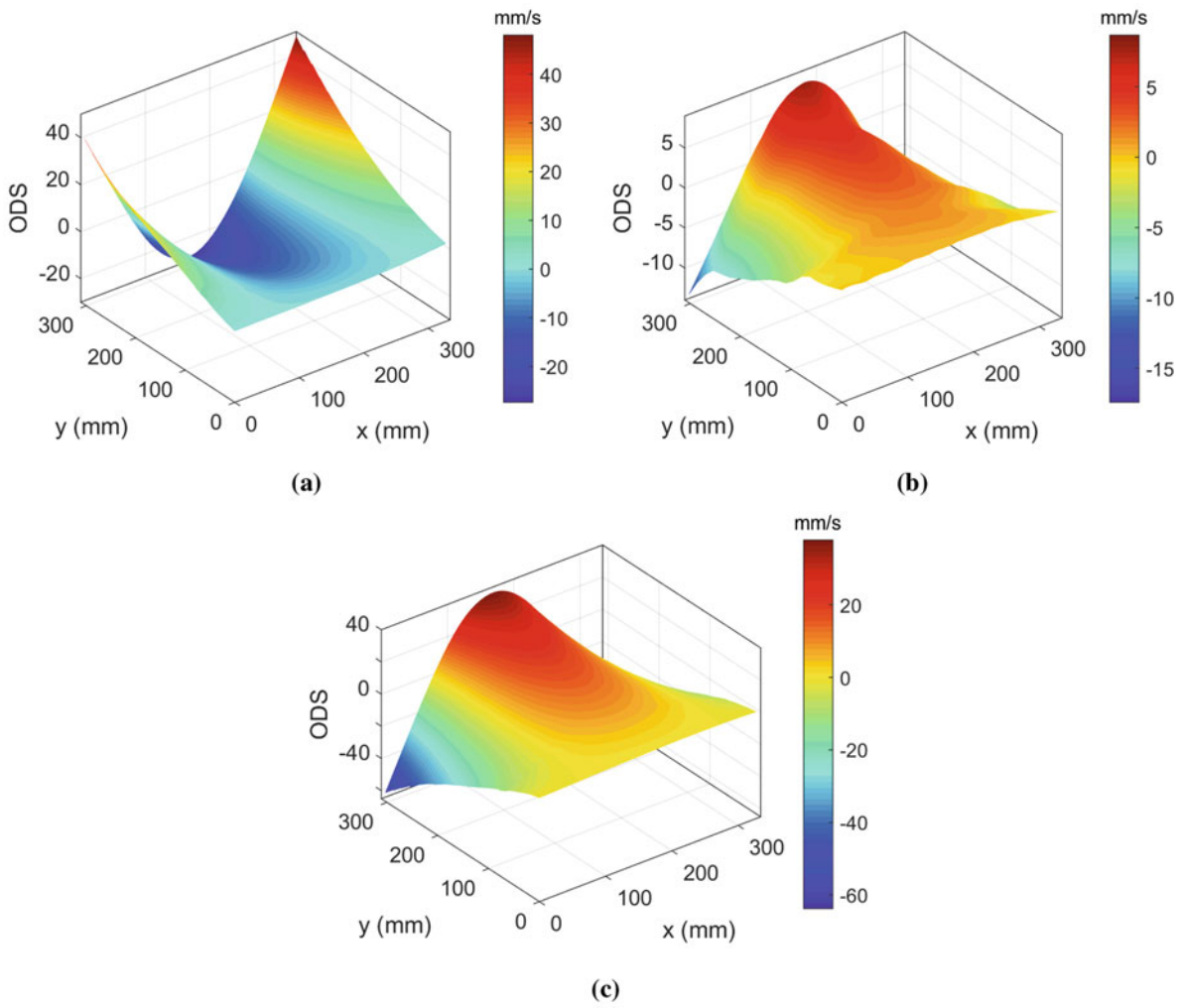


**Fig. 3.5** 3D ODSs of the plate in (a) x, (b) y, and (c) z directions of the MCS obtained by the 3D-CSLDV system with the scan frequency of 0.1 Hz

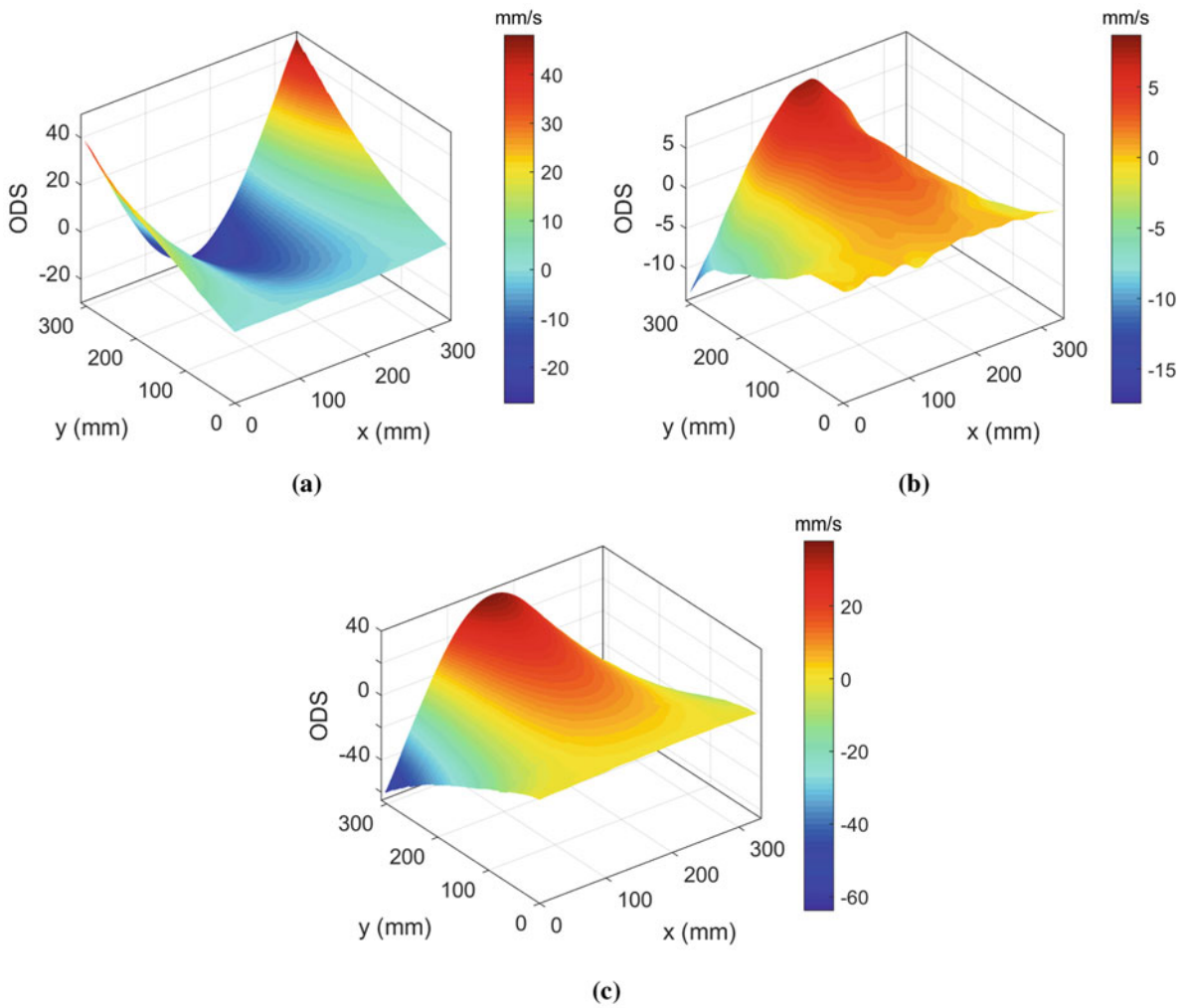


**Fig. 3.6** 3D ODSs of the plate in (a) x, (b) y, and (c) z directions of the MCS obtained by the 3D-CSLDV system with the scan frequency of 1 Hz

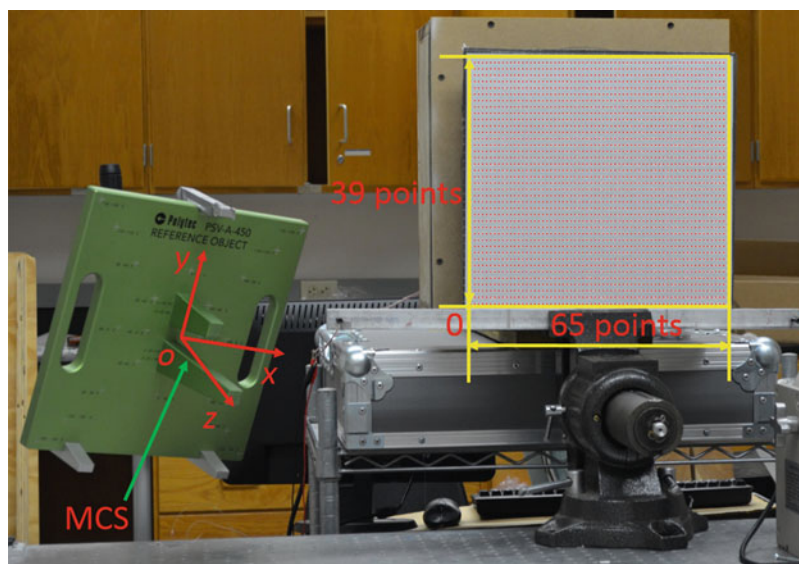


**Fig. 3.7** Step scanning of the plate by the PSV-500-3D system

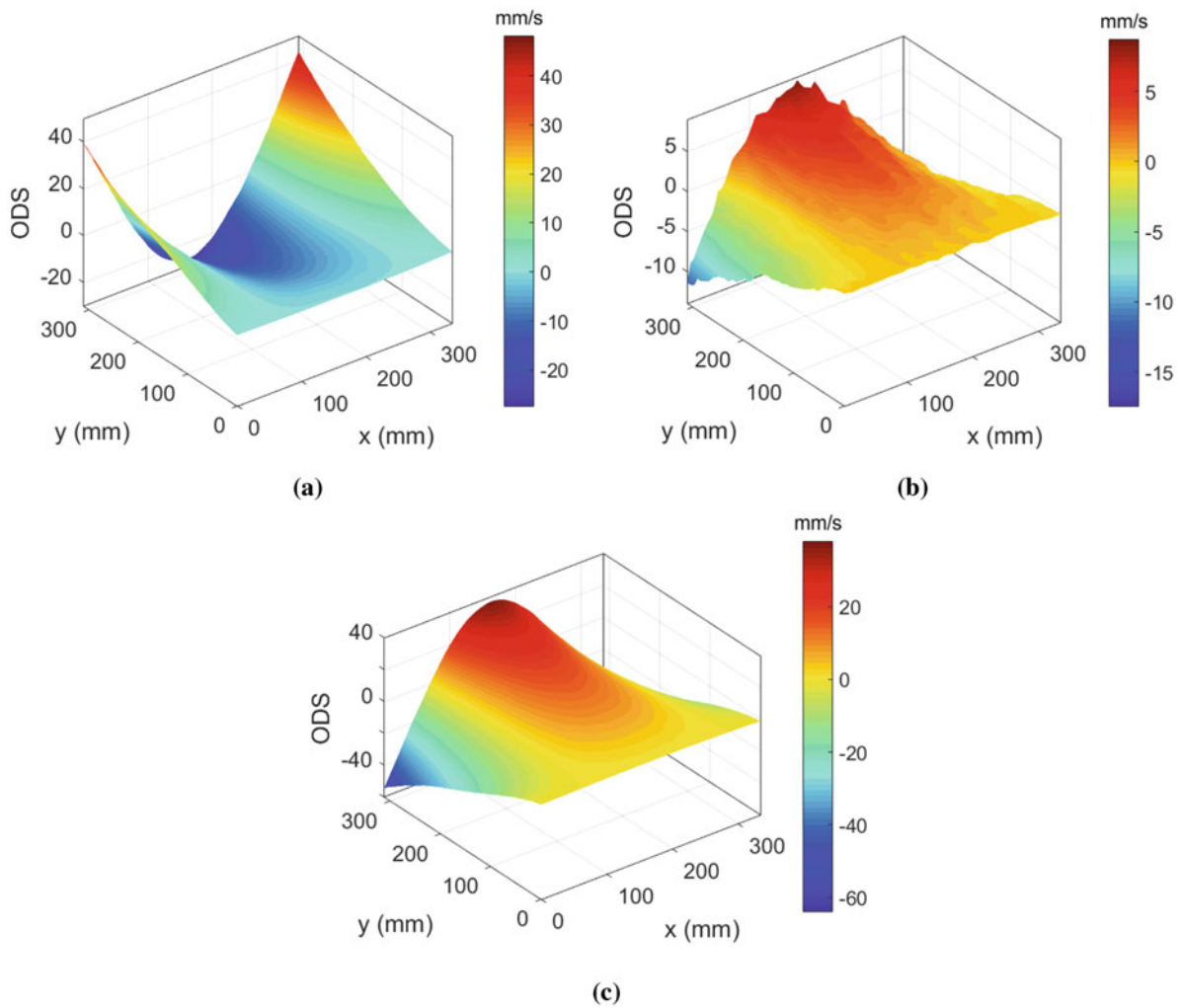


**Fig. 3.8** 3D ODSs of the plate in (a)  $x$ , (b)  $y$ , and (c)  $z$  directions of the MCS obtained by the PSV-500-3D in a step scanning mode

**Table 3.1** Comparison between synchronously and step scanning modes for the plate

	Scan frequency of 0.1 Hz	Scan frequency of 1 Hz	Step scanning
Spatial resolution	$39 \times 50,000$	$39 \times 5000$	$39 \times 65$
Scan time	585 s	58.5 s	2516 s

**Acknowledgements** The authors are grateful for the financial support from the National Science Foundation through Grant numbers CMMI-1229532 and CMMI-1335024 and the College of Engineering and Information Technology at the University of Maryland, Baltimore County through a Strategic Plan Implementation Grant.

## References

1. Sriram, P., Hanagud, S., Craig, J.: Mode shape measurement using a scanning laser doppler vibrometer. *Int. J. Anal. Exp. Modal Anal.* **7**(3), 169–178 (1992)
2. Stanbridge, A., Ewins, D.: Modal testing using a scanning laser doppler vibrometer. *Mech. Syst. Signal Process.* **13**(2), 255–270 (1999)
3. Stanbridge, A., Ewins, D., Khan, A.: Modal testing using impact excitation and a scanning LDV. *Shock Vib.* **7**(2), 91–100 (2000)
4. Di Maio, D., Ewins, D.: Continuous scan, a method for performing modal testing using meaningful measurement parameters; Part I. *Mech. Syst. Signal Process.* **25**(8), 3027–3042 (2011)

5. Allen, M.S., Sracic, M.W.: A new method for processing impact excited continuous-scan laser doppler vibrometer measurements. *Mech. Syst. Signal Process.* **24**(3), 721–735 (2010)
6. Yang, S., Allen, M.S.: Lifting approach to simplify output-only continuous-scan laser vibrometry. *Mech. Syst. Signal Process.* **45**(2), 267–282 (2014)
7. Ehrhardt, D.A., Allen, M.S., Yang, S., Beberniss, T.J.: Full-field linear and nonlinear measurements using continuous-scan laser doppler vibrometry and high speed three-dimensional digital image correlation. *Mech. Syst. Signal Process.* **86**, 82–97 (2017)
8. Chen, D.M., Xu, Y., Zhu, W.: Damage identification of beams using a continuously scanning laser doppler vibrometer system. *J. Vib. Acoust.* **138**(5), 051011 (2016)
9. Chen, D.M., Xu, Y., Zhu, W.: Experimental investigation of notch-type damage identification with a curvature-based method by using a continuously scanning laser doppler vibrometer system. *J. Nondestruct. Eval.* **36**(2), 38 (2017)
10. Xu, Y., Chen, D.M., Zhu, W.: Damage identification of beam structures using free response shapes obtained by use of a continuously scanning laser doppler vibrometer system. *Mech. Syst. Signal Process.* **92**, 226–247 (2017)
11. Vuye, C., Vanlanduit, S., Preseznik, F., Steenackers, G., Guillaume, P.: Optical measurement of the dynamic strain field of a fan blade using a 3D scanning vibrometer. *Opt. Lasers Eng.* **49**(7), 988–997 (2011)
12. Weisbecker, H., Cazzolato, B., Wildy, S., Marburg, S., Codrington, J., Kotousov, A.: Surface strain measurements using a 3D scanning laser vibrometer. *Exp. Mech.* **52**(7), 805–815 (2012)
13. Ihrle, S., Eiber, A., Eberhard, P.: Experimental investigation of the three dimensional vibration of a small lightweight object. *J. Sound Vib.* **334**, 108–119 (2015)
14. Staszewski, W., Lee, B., Traynor, R.: Fatigue crack detection in metallic structures with lamb waves and 3D laser vibrometry. *Meas. Sci. Tech.* **18**(3), 727 (2007)
15. Weekes, B., Ewins, D.: Multi-frequency, 3D ODS measurement by continuous scan laser doppler vibrometry. *Mech. Syst. Signal Process.* **58**, 325–339 (2015)
16. Chen, D.M., Zhu, W.: Investigation of three-dimensional vibration measurement by a single scanning laser doppler vibrometer. *J. Sound Vib.* **387**, 36–52 (2017)



# Chapter 4

## Modal Control of Magnetic Suspended Rotors

Marcus Vinicius Fernandes de Oliveira, Felipe Carmo Carvalho, Adriano Borges Silva, Aldemir Ap Cavalini Jr., and Valder Steffen Jr.

**Abstract** The present work is devoted to the conception of a Systematic Approach for the Robust Design of an Active Modal Controller applied to Supercritical Rotors supported by Magnetic Bearings. For this purpose, all the steps involved in the design of a robust controller based on the multimodel eigenstructure assignment technique is discussed. The first step is the development of a numeric/computer model in MATLAB/SIMULINK environment, based on the specifications of the test rig used in the experimental part of this work (which are provided by the test rig manufacturer). The first stage of the controller synthesis has to do with the specification of all design requirements. Then, all the phases involved in the process of the multimodel eigenstructure assignment are addressed in detail, starting from the determination of the plant dominant poles, so that, finally, the model based analysis of the system stability and performance are studied. The performance of the controller was evaluated through the analysis of its closed loop Transfer Functions and by investigating the unbalance response of the rotating system. It is worth mentioning that for all presented investigations, comparisons between two architectures of the controller, namely, the modal controller and the PI controller were performed, accordingly. The following natural step is the analysis of the correlation of theoretical and experimental results for validation purposes, which will be presented in a further contribution.

**Keywords** Rotor Dynamics · Magnetic Bearing · Modeling · Control · PID

### 4.1 Introduction

The first studies about magnetic levitation were presented by [1, 2] and a few years later [3] proposed the first industrial application of Active Magnetic Bearings (AMB) for aerospace momentum wheels [4]. In the last three decades, Active Magnetic Bearings (AMB) have been the subject of significant efforts to disseminate their potential and to make them more viable for industrial application [5, 6]. Nowadays, Active Magnetic Bearings (AMB) technology has achieved a considerable level of maturity and is regarded as one of the most promising solutions for several applications of rotating machinery [6, 7]. In such devices, the rotating shaft literally levitates suspended by magnetic forces, thus preventing any wear due to mechanical contact between the bearings and the bearings. In addition, this technology allows abolishing the need for lubricants, reaching very high rotation speeds without any relevant heating. According to [4], the AMB's can be classified as a mechatronic product, since they are composed by a combination of mechanic and electronic devices, controlled by a dedicated software. Besides, the inherent AMB's capabilities of sensing, data processing and actuation assure them a prominent position as a fundamental component for innovative design of smart rotating machines, opening new possibilities for incorporating Active Vibration Control techniques as well as Structural Health Monitoring methodologies.

Active Vibration Control (AVC) is considered as the most sophisticated vibration attenuation strategy. This technique is based on the application of dynamic forces for the control the undesired system vibration [8]. In a simplified way, an AVC system is composed by sensors, actuators and a control unit. The sensors are responsible for providing information about the controlled variables. The control unit possesses the function of processing the information from the sensors and determining the command signals, calculated according to the control algorithms. Finally, the actuators convert the command signals, provided by the control unit, into effective actions upon the system. As an example of application of AVC, we can mention the work presented in [9], where a hybrid bearing, based on electromagnetic actuators, is employed to attenuate vibrations in rotating systems using different control strategies.

---

M. V. F. de Oliveira (✉) · F. C. Carvalho · A. B. Silva · A. A. Cavalini Jr. · V. Steffen Jr.

LMEst – Laboratory of Mechanics and Structures, INCT (EIE) – National Institute of Science and Technology, Federal University of Uberlandia, School of Mechanical Engineering, Uberlandia, MG, Brazil

Due to its inherent instability, for any system supported by AMB's a mandatory requirement is to reach stable levitation along the operation range, which is only possible with the employment of a controller (such as a PID controller). Therefore, a very important step is the investigation of the main characteristics of the system in order to obtain representative computational models, which are necessary for the analysis and synthesis of the most advanced control design methods. In this context, several authors have addressed AMB's system identification. Among them, it is worth mentioning the work presented by [10], where the authors propose strategies for auditing systems with AMB's, discuss their main requirements and also perform a brief review about the main architecture options and show guidelines for modeling the system components. Another important study was presented in [11] where the author performed the identification of a rotating system supported AMB's and proposed an automated technique for robust controller design. In this context, [12] modelled and characterized an AMB test rig for the design of robust controllers by using model based techniques with the objective of investigating rotordynamics instability in the presence of uncertainties.

The present work is dedicated to the analysis and synthesis of a Robust Modal Controller through the attribution of auto-structure, using the technique of Multiple Models. In this sense, the first task is the clear and objective specification of the design requirements to be fulfilled by the closed-loop system. Next, the main sources of uncertainty found in rotating systems supported by MMA's are discussed in a concise manner, as well as some means of incorporating them adequately into the nominal model of the plant for the synthesis of the controller. Afterwards, these are the main concepts that support the attribution of self-structure through the Multiple Models technique. After that, the entire design phase of the robust modal controller is presented, from the definition of the uncertainties to be considered until the stability and performance analysis of the closed-loop system. In this sense, comparisons are made between the results obtained with both the modal controller and the original PI controller (provided by the manufacturer).

## 4.2 Modal Robust Control

Rotating systems supported by magnetic bearings are intrinsically unstable. Therefore, the primary objective of any controller to be developed is to ensure the robust stability of the system over the entire operating range [4]. According to [13], this means that the system must be robust both in relation to parametric uncertainties and dynamic uncertainties. In this sense, it is possible to use simpler analyzes, such as those suggested by ISO 14839-3 (based on the Sensitivity Functions) [14], as well as more elaborate tools, such as the analysis of singular structured values, recommended for more complex systems [13].

The robust design strategy adopted in this work is mostly based on the works of [15–19]. In these references, Multiple Models techniques are employed to design robust controllers through the assignment of the self-structure. In the Multiple Models technique there are two main approaches. The first is based on the elaboration of a dynamic compensator in the form of an array of transfer functions. The second technique is to obtain a controller based on a structure in which the original plant is extended through the use of state observers. In this work, the first approach will be used, i.e., the one based on transfer functions, since it offers greater freedom of design [16].

The design of robust controllers in relation to uncertainties on real parameters is a subject that still has great potential to be explored, especially in applications related to multivariate systems. In general, uncertainties are modeled using the Fractional Linear Transformation (TLF) representation, also known as formulation  $\mathbf{M} - \Delta$ , which is much more efficient for analysis than for controller synthesis. From there, it is possible to identify the most critical cases and evaluate the robustness of the system through the use of several tools, such as poles/zeros maps and time responses.

In this work the analysis  $\mu$  will also be used, since by calculating the upper and lower limits of  $\mu$ , it is possible to identify the most critical cases from the stability point of view. Then, through the use of the Multiple Models Technique, a robust low-order controller is designed by contemplating a set of the worst cases identified in the previous phase. This cycle is repeated until a controller capable of satisfying the design criteria is obtained. It should be noted that although the synthesis is performed based on a limited number of models, the resulting design is valid throughout the continuous set represented by the formulation  $\mathbf{M} - \Delta$ , allowing a significant reduction of the computational effort [16]. This project cycle is known as “ $\mu$ iteration”, since it alternates the  $\mu$  analysis with the multimodel project. The required steps are given below:

**Step 0:** Design an initial controller based, for example, on the nominal model;

**Step 1:** Carry out the stability analysis and the robust performance of the closed loop system. This task can be accomplished using  $\mu$  analysis, time response analysis, and/or pole map. If the design is satisfactory with respect to the design requirements for all relevant values, terminate the process. Otherwise, identify the worst cases and go to step 2;

**Step 2:** Insert the worst cases in the optimization process in order to meet the design requirements for all models handled in the previous iteration. Then, return to step 1.

It is important to mention that at step 0, the initial controller does not need to be based on the modal approach [17] employed as a starting point an initial controller designed on the basis of the  $H_\infty$  approach. In step 1, which is dedicated to identifying the worst cases, the use of the  $\mu$  analysis technique is quite attractive for the evaluation of robust stability due to the presence of structured uncertainties.

### 4.3 Model and Numerical Results

The test rig presented in Fig. 4.1 is composed by three main parts: the flexible rotor supported by radial AMB's, the controller and the external interface MBResearch™. It consists of a demonstration kit manufactured by SKF and is delivered with a control architecture based on a SISO PID controller, connected in series with a bank of filters. The shaft is supported by two identical radial AMB's to provide a maximum load capacity of 283 N. Such components are energized by a bias current of 1.0 A, and are capable of supporting a maximum current of 3.0 A. The shaft is driven by an electric motor of 500 W, operating in the range of 0 to 12,000 rpm. The kit is also equipped with two conventional backup ball bearings, located at both ends of the shaft, devoted to support the rotor in the case of any failure in the magnetic levitation. The nominal clearance between the surface of the shaft and the inner ring of the backup bearings is approximately 0.1 mm. Table 4.1 presents the main parameters of the system.

The first step was to develop individual computational models for each main component of the system (showed in Fig. 4.2) based on the design specification provided by the manufacturer. The following step was the assembling of those component models into a global one.

Once the AMB's stiffness parameters were determined, it was necessary to consider the subsystem represented by the rotor itself. In this case, the model was also based on the Finite Element method. For this aim, a proprietary software specially designed for handling rotordynamics problems was used, as developed in MATLAB environment. In order to properly represent this subsystem, the rotor was discretized into 51 Timoshenko beam elements, considering 4 dofs per

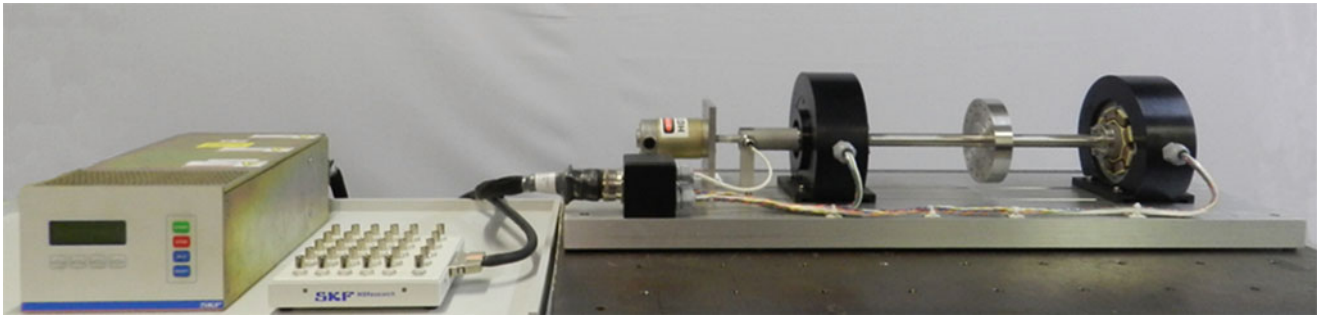


**Fig. 4.1** Experimental Test Rig

**Table 4.1** System parameters

Parameter description		Unit
Number of turns per coil, $N$	276	–
Air gap, $g_0$	0.364	mm
Pole cross sectional area, $A_g$	430.74	mm <sup>2</sup>
Maximum voltage	10	V
Bias current, $i_b$	1	A
Current stiffness, $k_i$	143.76	N/A
Position stiffness, $k_s$	0.395	N/m
AMB load capacity	283	N
Shaft length	645	mm
Disc mass	5.89	kg
Motor power	500	W
Operation range	0–12,000	rpm



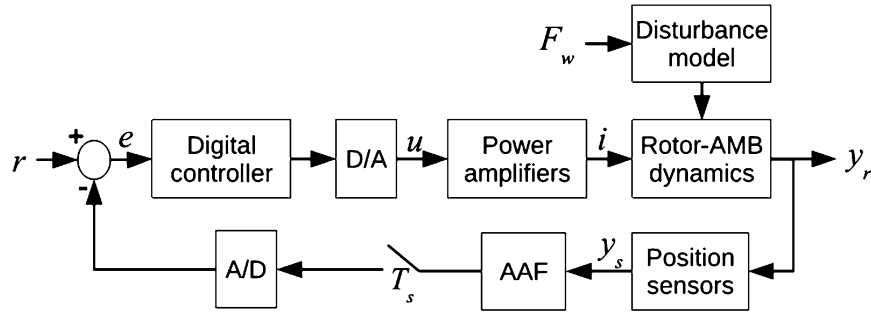


Fig. 4.2 Main components of an AMB system

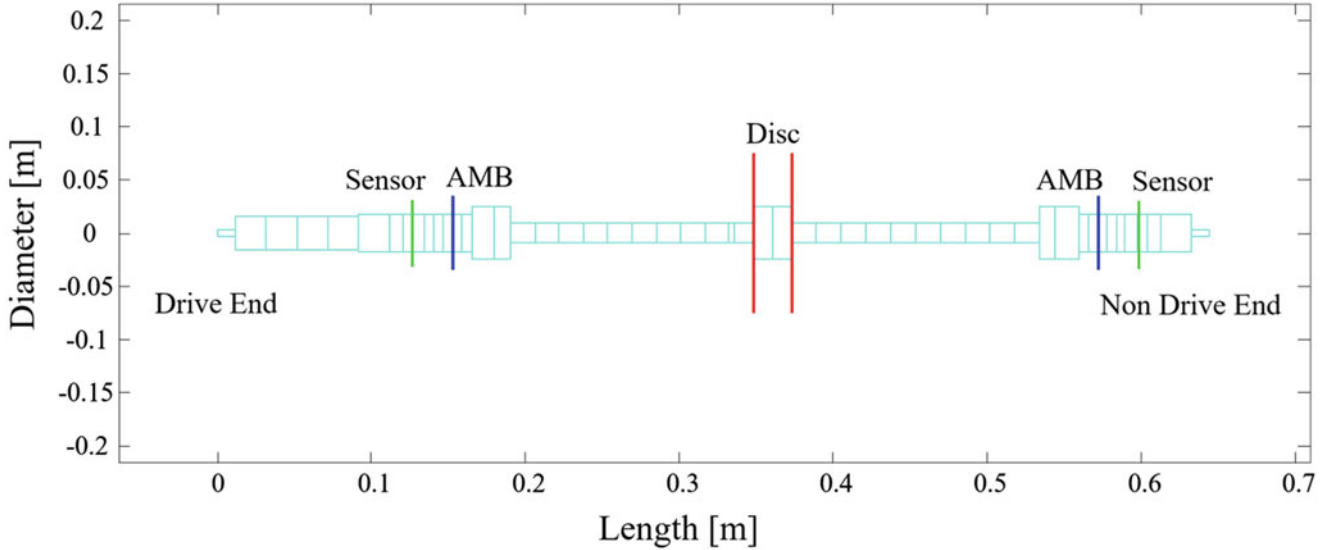


Fig. 4.3 Rotor finite element model

node, two displacements and two rotations along the  $x$  and  $y$  directions. Figure 4.3 presents the rotor model, where the axial positions of the sensors and AMB's are also indicated. Due to the size of this model, the pseudo modal method [18] was used to reduce the system, thus keeping only the first 10 rotor mode shapes, which were identified as relevant for the dynamic behavior of the system as pointed out by Hankel singular value analysis.

According to [20], the dynamic behavior of power amplifiers can be accurately modeled by a first order transfer function, as given by Eq. (4.1):

$$G_{amp} = K_{amp} \frac{1}{\frac{1}{\omega_{camp}}s + 1} \quad (4.1)$$

where  $G_{amp}$  is the power amplifier transfer function,  $K_{amp}$  is the system gain and  $\omega_{camp}$  is the amplifier frequency bandwidth. According to the manufacturer:  $K_{amp} \cong 1.0\text{A/V}$ ;  $\omega_{camp} \cong 1000\text{Hz}$ . We are interested on the the frequency corresponding to an amplitude reduction of 3 dB (frequency bandwidth) (Fig. 4.4).

The time delay of the AMB system is mostly due to the process of conversions A/D and D/A. In the literature [13, 20], this phenomenon is usually modeled by a second order Padé approximation, as presented in Eq. (4.2). This approach considers that the time delay is given by  $1.5T_s$ , where  $T_s$  is the inverse of the acquisition rate. In this case,  $T_s = 1/10000\text{ s}$  and  $n = 20$ .

$$e^{-T_s s} \approx \left(1 - \frac{T_s s}{2n}\right)^n / \left(1 + \frac{T_s s}{2n}\right)^n \quad (4.2)$$

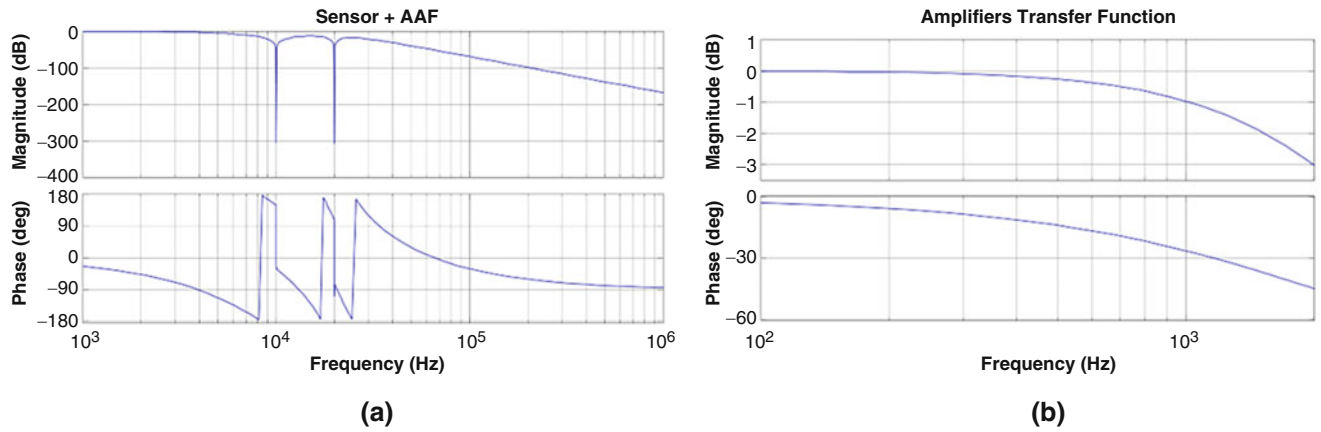


**Fig. 4.4** Transfer functions: (a) position sensor and (b) amplifier

**Table 4.2** Parameters of the PID controller

Parameter	AMB	
	DE	NDE
$K_T$	0.0062	0.0046
$K_P$	1.0	1.0
$K_D$	0.0	0.0
$K_I$	46.0	35.0

The PID controller is the most widely used in the industry due to its simplicity and efficiency. Therefore, it is also commonly found in applications involving AMB's. However, this element alone is not capable of guaranteeing the required performance and stability under certain circumstances. Equation (4.3) describes the standard transfer function for a PID controller.

$$PID = \frac{K_T (K_D s^2 + K_P s + K_I)}{s} \quad (4.3)$$

where  $K_T$  represents a total gain that multiplies all the other gains; and  $K_P$ ,  $K_I$  and  $K_D$  are the proportional, integral and derivative gains, respectively. Table 4.2 presents the values employed for each bearing DE and NDE.

After all individual models related to the main components of the system have been modeled, next step is to assemble them together in order to obtain the global open loop plant. All the operations required for the design and analysis of the robust modal compensator were performed in MATLAB. First, the uncertainties to be accounted for in the design are defined. Next, we present the process of synthesis of the controller itself, based on the technique of Multiple Models. Finally, the stability and performance of both the controllers, modal and PI, are analyzed for comparison purposes (Fig. 4.4).

Li [14] has shown in his work that the parameters whose uncertainties have the most critical effects on the dynamic behavior of rotating systems supported by MMA's are the natural rotor frequencies, gyroscopic effect, natural frequencies of the bearing base/support and the cross stiffness. The approach used in this work is the same as the one proposed by [12], which takes into account uncertainties in the natural frequencies of the system due to the gyroscopic effect and, additionally, small variations that occurred during the manufacturing process.

The Campbell diagram, Fig. 4.5, shows that the flexible modes Nc3, Nc4 and Nc5 exhibit separation between the forward and inverse precession modes due to the gyroscopic effect. The Nc3 mode has a variation in the operating range due to the gyroscopic effect of  $\pm 2.96\%$  around the nominal value, which is 111.4 Hz (levitated rotor at rest). Therefore, in order to assimilate both the separation between direct and inverse precession modes and small variations in manufacturing tolerances, an uncertainty of  $\pm 5.0\%$  is considered. The mode Nc4 has a much more pronounced influence of the gyroscopic effect:  $-11.7\%$  to  $+12.14\%$  in relation to the nominal value of 399.0 Hz (levitated rotor at rest). Analogously to the Nc3 mode, a slightly greater uncertainty will be considered to also accommodate small variations related to manufacturing processes:  $\pm 15.0\%$ . In contrast, since the Nc5 mode is located outside the frequency band of the controller whose upper limit is approximately 650.0 Hz, its stabilization will occur by roll-off, which consists of the attenuation of gains above the cutoff frequency of the filter. In Fig. 4.6 the open-loop system transfer function is presented considering the uncertainties in the natural frequencies according to the methodology used.

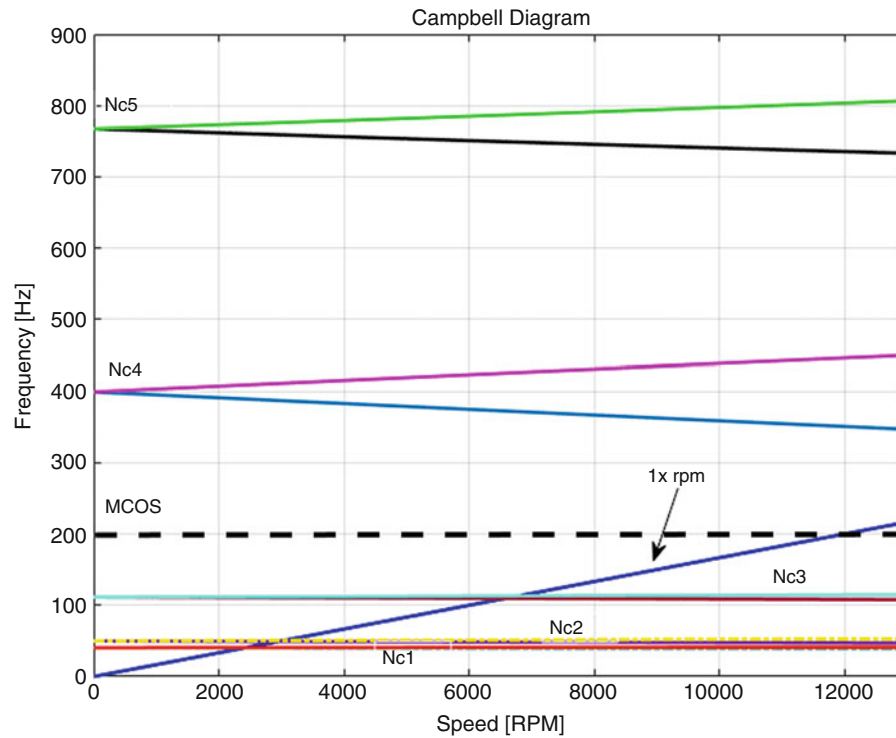


Fig. 4.5 Campbell diagram

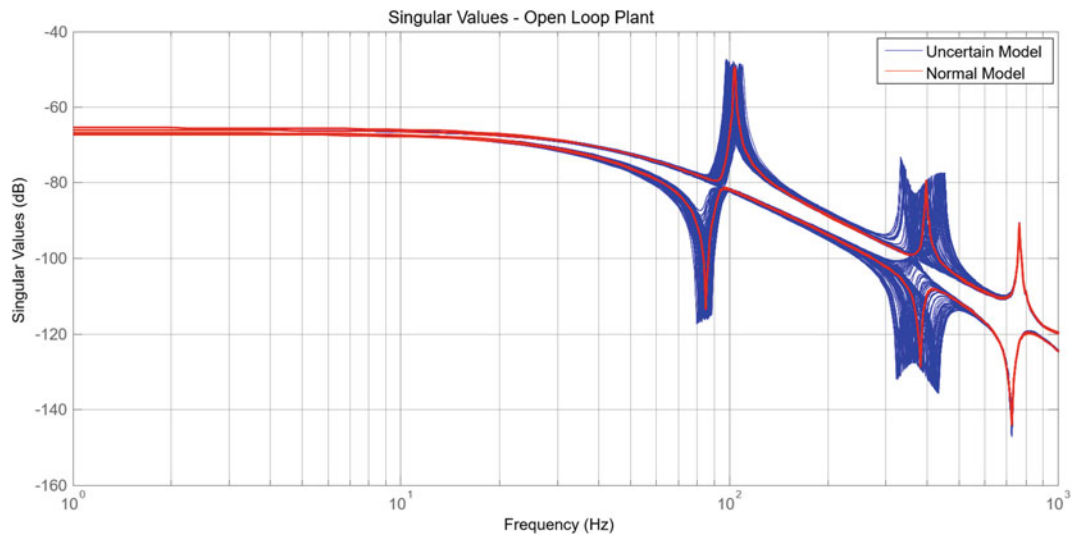
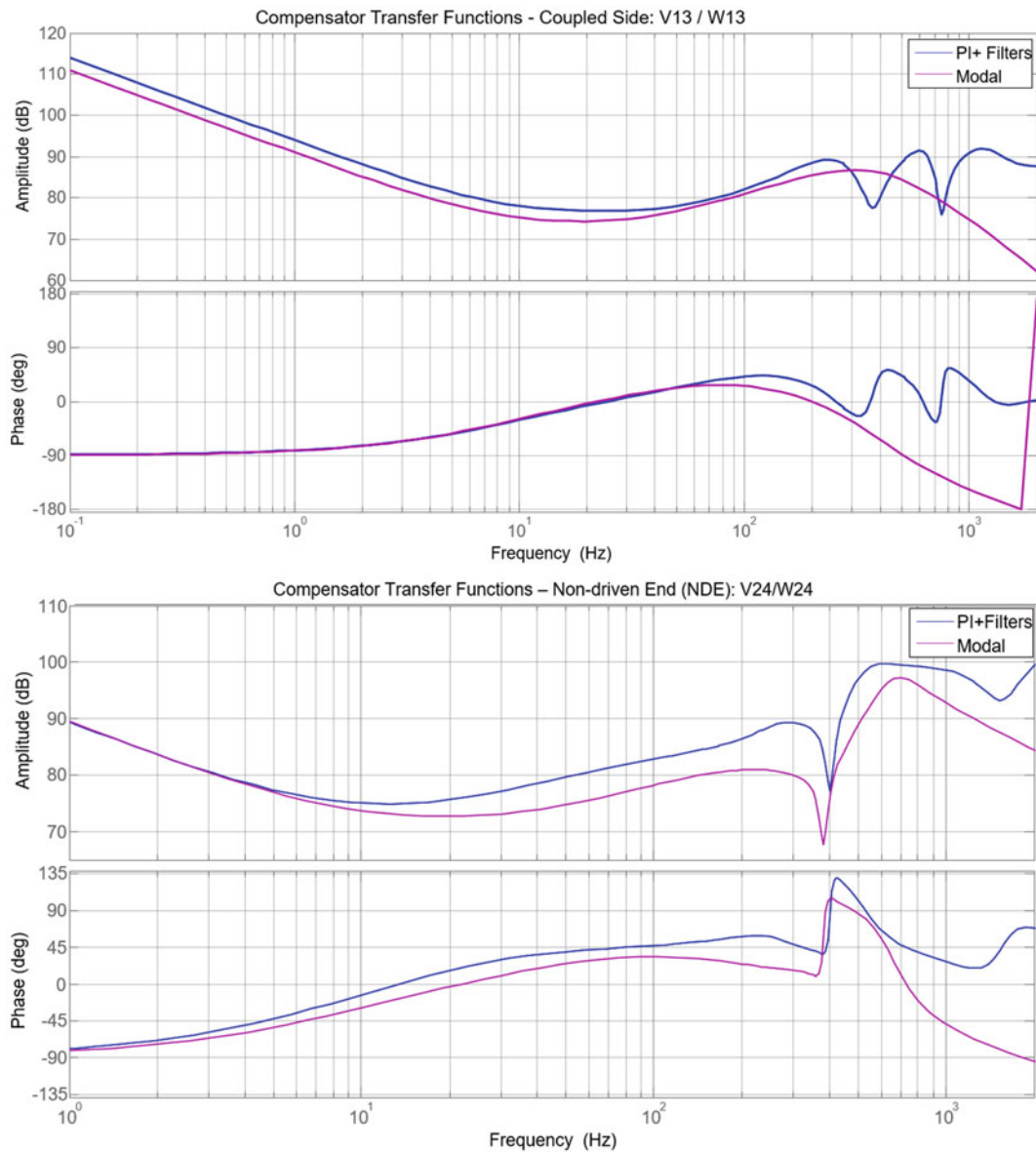


Fig. 4.6 Diagram of the singular values of the open-loop plant, considering the uncertainties in the Nc3 and Nc4 modes

Due to controllability problems of Nc4 mode, some additional precautions are necessary to ensure its stability during operation. In this sense, the same resource used by the manufacturer of the system was used, that is, the use of generic filters of second order, which are discussed in [21]. The filters are not necessary to the MMA on the coupled side due to their ability to deal adequately with the Nc4 mode, which has good controllability at this position. In addition to this feature, it was also necessary to limit the controller's action at higher frequencies to avoid spillover and noise contamination difficulties. This was done with the help of four first-order Butterworth low-pass filters. For each channel of the coupled side a filter with a cut-off frequency was used at 2450.4 rad/s (390 Hz). On the free-side channels, a cut-off frequency of 2513.3 rad/s (400 Hz) was used. In Fig. 4.7 a comparison is made between the modal controller to be implemented and the controller provided by the manufacturer (PI + filters).



**Fig. 4.7** Comparison of Transfer functions: PI controller × Modal controller

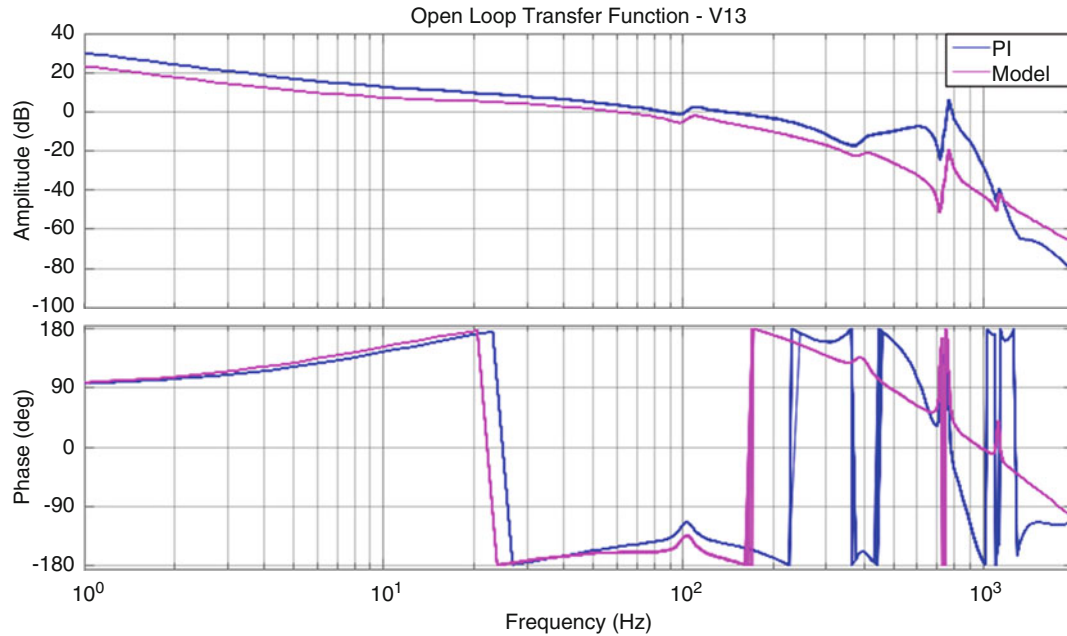
The evaluation of the performance and stability of the closed loop plant was performed through the main transfer functions of the system, which will be classified according to the recommendations of ISO 14839. In addition, comparisons will be made between the results obtained with the use of the modal controller and the original PI controller. In this way, it is intended to investigate the potentialities and drawbacks of the technique of attribution of self-structure using Multiple Models technique.

According to [10, 14], the method of assessing the stability margin proposed by ISO 14839–3 is well suited to deal with a number of uncertainties inherent to rotational systems supported by MMA's, such as variations on gains and phases of sensors and amplifiers/actuators. However, the fact that peak transfer functions are located in the zones A and B does not guarantee that the system is robust with respect to other events common to rotating machines such as cross-streaming and, apparently, small variations on the natural frequencies of the rotor due to assembling/disassembling for maintenance. In addition, there may be cases involving controllers sensitive to the gyroscopic effect, whose sensitivity functions do not present high peaks. In view of these points, it can be stated that the specifications of ISO 14839–3 are necessary requirements to ensure an acceptable stability margin, but alone are not sufficient to handle several applications found in the industry. In these cases, more detailed analyses are recommended as suggested by [10, 14].

**Table 4.3** Results of robust stability analysis – ISO 14839–3/analysis  $\mu$ 

Controller	Controller order	Uncertainties		ISO 14839-3	
		Adopted variations [%]	Max. limit. <sup>a</sup> analysis $\mu$ [%]	$S_{max}$	Stability zone
PI+ Filters	40	$\pm 5.0\%$ (Nc3)	10.7%	10.8 dB	B
		$\pm 15.0\%$ (Nc4)	39.2%		
Modal	27	$\pm 5.0\%$ (Nc3)	$\pm 13.1\%$	9.1 dB	A
		$\pm 15.0\%$ (Nc4)	$\pm 38.0\%$		

<sup>a</sup>Combination of limiting uncertainties to destabilize the system

**Fig. 4.8** Comparison of Open Loop Transfer Functions: PI Controller  $\times$  Modal Controller – DE (V13)

In this context, the  $\mu$  analysis was used to evaluate the stability of the system with respect to the uncertainties inserted in the model. As previously, an uncertainty of  $\pm 5.0\%$  and a  $\pm 15.0\%$  was considered in order to evaluate the robust stability of the system due to the gyroscopic effect and variations in the modes Nc3 and Nc4, respectively. The results of the robust stability analysis are presented in Table 4.3.

In Table 4.3, the difference between the controllers complexity can be observed. The modal controller has only 27 states, whereas the original PI controller has 40 states. This can be seen as a considerable advantage as a smaller controller is easier to implement in practical applications. In addition, the results of the  $\mu$  analysis show that, although simpler, the modal controller is able to handle uncertainties in the mode Nc3 approximately 22% larger than the PI controller, without significant loss of its tolerance to uncertainties in the mode Nc4. In this way, it can be seen that from the point of view of ISO 14839–3 and from the  $\mu$  analysis, the modal controller is able to assure a more adequate stability margin than the original PI controller. Based on the results obtained, it can be considered that the modal controller obtained from the multiple models technique was successful regarding the robust stabilization of the plant.

The dynamic behavior of dynamic systems can be evaluated both on the basis of time domain and frequency domain response analyses. In this work, the second option was taken due to its practicality, since by observing the transfer functions of a system it is possible to have a broad view regarding its behavior for the entire frequency band of interest. Moreover, most of the works found in the literature use this method to present their results [6, 10, 14]. In Figs. 4.8 and 4.9 we present comparisons between the Open Loop Transfer Functions obtained with the modal controller and the original PI controller.

It is observed in Figs. 4.8 and 4.9 that the Open Loop Transfer Functions obtained from both the controllers have a higher gain at low frequencies in order to reject external disturbances in this region, besides stabilizing the system. It is also possible to note that there is no additional peak due to the control system or to electronic components, such as amplifiers and sensors. Finally, it is worth mentioning that, as the amplitudes of the curves obtained for the modal controller are always lower than their counterparts from the original PI controller, especially in the priority region (8500 rpm at 12000 rpm), the control effort is also lower, thus indicating energy saving since it requires smaller control currents.

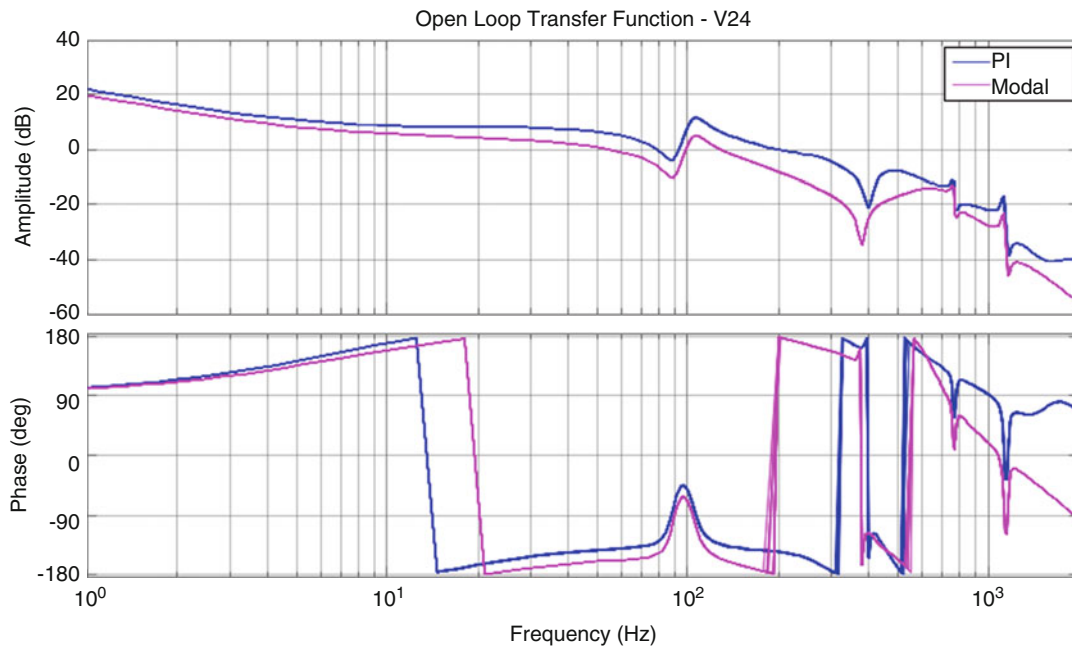


**Fig. 4.9** Comparison of Open Loop Transfer Functions: PI Controller  $\times$  Modal Controller – NDE (V24)

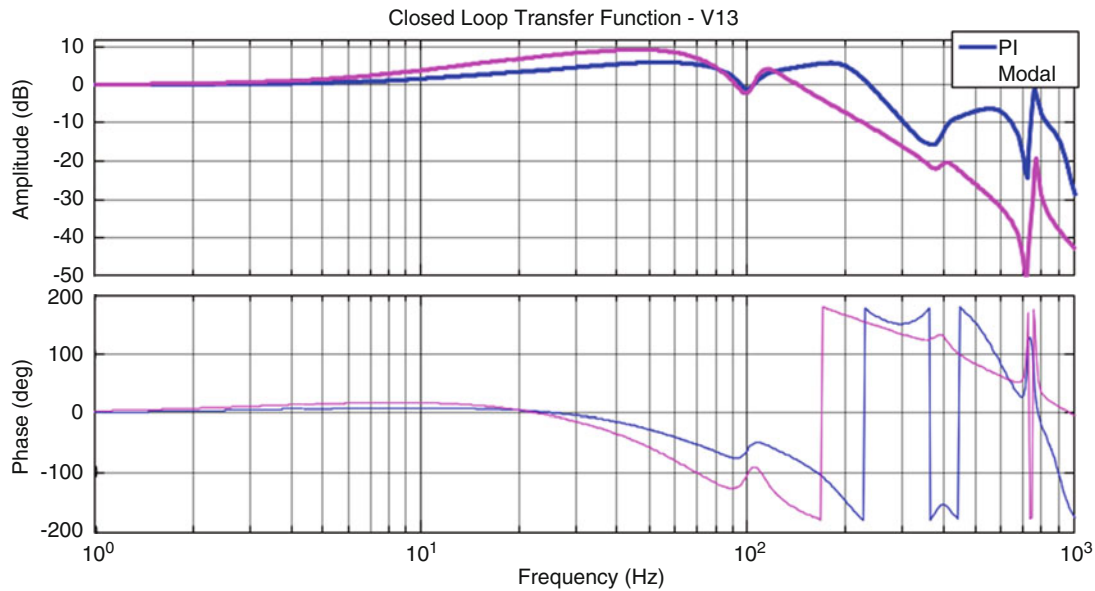


**Fig. 4.10** Comparison of the Transfer Functions in Closed Loop: PI Controller  $\times$  Modal Controller – DE (V13)

The Closed Loop Transfer Functions using the original PI controller are compared to their counterparts obtained with the modal controller in Figs. 4.10 and 4.11.

Analyzing Figs. 4.10 and 4.11, it is noticed that there is no high magnification factor for the cases evaluated, which indicates that both controllers were able to properly handle the eigen modes of the system. In these figures, it is also verified that both controllers give the plant a similar dynamic behavior for frequencies below 10 Hz. However, for the frequency range located between 10 and 75 Hz, the PI controller provides a lower amplification factor than the one obtained with the modal controller. For the operating range defined as priority, that is, between 8500 rpm (143 Hz) and 12,000 rpm (200 Hz), the modal controller is able to provide a considerably greater attenuation than the one obtained for the original PI controller of the system in closed loop. It should be mentioned that this better performance derives from another interesting advantage, which is the use of significantly lower control currents (Figs. 4.10 and 4.11) by the modal controller.

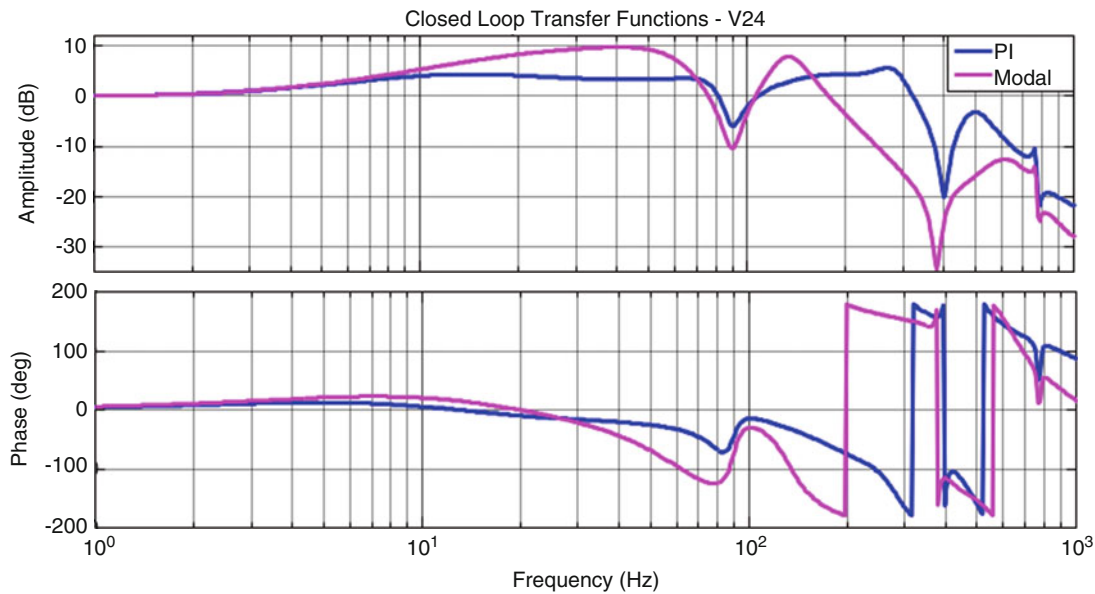


**Fig. 4.11** Comparison of the Transfer Functions in Closed Loop: PI Controller  $\times$  Modal Controller – NDE (V24)

From the analysis of the system performance based on the Closed Loop Transfer Functions of the model it was verified that both controllers were able to adequately attenuate all modes located in their frequency band of interest. In addition, it was possible to conclude that, although the modal controller allows for a higher vibration level than the PI for operating speeds below 8500 rpm, its performance is similar and even surpasses it in some cases for higher operating speeds. On the other hand, since the control effort exerted by the modal controller was always inferior to the one exerted by the PI controller, mainly for speeds above 8500 rpm, it is expected that the control currents follow this same trend, which would represent a considerable power saving. It is recalled that the ecologically compatible machines have as one of their requirements the lowest possible energy consumption.

## 4.4 Conclusion

The present paper is dedicated to the systematization of the Robust Design of Modal Active Control Systems of Supercritical Rotors supported by Magnetic Bearings. Other equally important contributions should be mentioned, namely: the development of representative models of rotary systems for application in active controlled plants, determination and implementation of active control architectures aiming at real world applications in the industry, development of experimental techniques for magnetically supported supercritical rotors, design and characterization of active controllers for magnetic bearings focusing on modal controllers.

**Acknowledgments** The authors are thankful to the Brazilian Research Agencies FAPEMIG, CNPq, and CAPES for the financial support provided for this research effort through the INCT-EIE.

## References

1. Earnshaw, S.: On the nature of the molecular forces which regulate the constitution of the lumiferous ether. *Trans. Camb. Phil. Soc.* **7**(Part I), 97–112 (1842)
2. Braunbek, W.: Frei schwebende Körper im elektrischen und magnetischen Feld. *Z. Phys.* **112**, 753–763 (1939)
3. Habermann, H., Liard, G.: Le palier magnetique active: un principe revolutionaire. *SKF Rev. Roulements* Nr. 192 (1977)
4. Schweitzer, G., Maslen, E.H.: *Magnetic Bearings: Theory, Design, and Application to Rotating Machinery*, 535p. Springer, Berlin (2009)
5. Steffen, V. Jr., Lepore, N.F.P.: A control force to reduce magnetically excited rotor vibrations. *Mécanique, Matériaux, Electricité.* **65**(404), 90–93 (1984)

6. Yoon, S.Y., Lin, Z., Allaire, P.E.: Control of Surge in Centrifugal Compressors by Active Magnetic Bearings: Theory and Implementation (Advances in Industrial Control), 275p. Springer, London (2013)
7. Chiba, A., Fukao, T., Ichikawa, O., Oshima, M., Takemoto, M., Dorrel, D.: Magnetic Bearings and Bearingless Drives, 400 p. Newnes, Oxford (2005)
8. Tammi, K.: Active control of radial rotor vibrations: identification, feedback, feedforward, and repetitive control methods. PhD Thesis, Helsinki University of Technology, Espoo (2007)
9. Koroishi, E.H., Borges, A.S., Cavalini Jr, A.A., Steffen Jr, V.: Numerical and experimental modal control of flexible rotor using electromagnetic actuator. *Math. Probl. Eng.* **2014**, ID 361418. <https://doi.org/10.1155/2014/361418>, p. 14 (2014)
10. Swanson, E., Maslen, E.H., Li, G., Cloud, C.H.: Rotordynamic design audit of AMB supported machinery. In: Proceedings of the Thirty-Seventh Turbomachinery Symposium, pp. 133–158 (2008)
11. Löschi, F.: Identification and automated controller design for active magnetic bearing systems. ETH Zürich. 239p. (2002)
12. Mushi, S.E.: Robust control of rotordynamic instability in rotating machinery supported by active magnetic bearings. PhD thesis, University of Virginia (2012)
13. ISO Standard 14839. Mechanical Vibrations – Vibrations of rotating machinery equipped with active magnetic bearings – Part 1: Vocabulary, Part 2: Evaluation of vibration, Part 3: valuation of stability margin, Part 4: Technical guidelines, system design (Draft) (2002/2006)
14. Li, G.: Robust stabilization of rotor-active magnetic bearing systems. PhD thesis, University of Virginia (2007)
15. Magni, J.: Robust Modal Control with a Toolbox for Use with MATLAB®. Kluwer Academic/Plenum Publishers, New York (2002)
16. Magni, J., Le Gorrec, Y., Chiappa, C.: A multi-model approach to robust self-scheduled control design. In: Proceedings of 37th IEEE conference on decision, & control, pp. 3009–3014. Tampa (1998)
17. Chiappa, C.; Magni, J.; Le Gorrec, Y.; Kubica, F.; Döll, C.: Flexible structure control by modal multi-model approach: application to a flexible aircraft. In: 21st ICAS Congress – International Council of the Aeronautical Sciences, Melbourne (1998)
18. Le Gorrec, Y., Magni, J., Doll, C., Chiappa, C.: Modal control design approach applied to aircraft autopilot design. *J. Guid. Control. Dyn.* **21**(1), 77–83 (1998)
19. Le Gorrec, Y., Magni, J., Chiappa, C.: Flexible transmission system controlled by modal dynamic feedback. In: Proceedings of European Control Conference, pp. 1179–1784. Brussels (1997)
20. Sanadgol, D.: Active control of surge in centrifugal compressors using magnetic thrust bearing actuation. PhD thesis, University of Virginia (2006)
21. Oliveira, M.V.F., Carvalho, F.C., Borges, A.S., Cavalini, A.A., Steffen Jr., V.: Modeling and Characterization of a Flexible Rotor Supported by Active Magnetic Bearings. *ICEDyn, Ericeria* (2017)



# Chapter 5

## On the Implementation of Metastructures in Rotordynamics



Carlo Rosso, Elvio Bonisoli, and Fabio Bruzzone

**Abstract** This paper presents the possibility to apply distributed vibration absorbers to reduce the vibration amplitude in axially symmetric components. The kind of metastructures here presented does not require complicated and expensive production processes such as additive manufacturing, but can be manufactured with more conventional means, for example with wire electrical discharge machining (EDM). Flexible rotating structures have a lot of natural frequencies in the operative range and the geometry changing approach is often not sufficient to improve the dynamic behavior. Using structural damping becomes fundamental to increase the transmitted power and the system life. In the present paper, the authors investigate the possibility to apply different geometrical configurations, each designed and tuned to suppress a particular mode shape, by means of the metastructure concept applied to flexible rotating devices. Their performances are analyzed with and without a balanced mistuning added to the metastructure. A number of distributed absorbers is set in order to act on each mode to be damped. Their vibration amplitude is firstly compared by keeping the total mass constant with respect to the original component, but also cases with higher and lower mass are analyzed. The frequency response of the proposed configurations is obtained from three-dimensional (3D) finite element models and some interesting results are evinced.

**Keywords** Vibration suppression · Metastructure · Passive damping

### 5.1 Introduction

In [1] a detail analysis of the state of the art about metastructures is reported. The principal aspect underlined in this paper is that metastructures are used in several physical field trying to use the combination of different structures for changing the response of the system. Usage of metastructures starts with structures with local absorbers [2] or lead spheres coated with rubber inserted into an epoxy matrix [3]. Other metastructures are referred to a periodic lattice structure able to affect the wave propagation into the material, realizing a structure with distributed vibration absorber [4].

The principle that makes the metastructures working was investigated in [5, 6], and it is formalized that this mechanism is the same of the tuned mass dampers. A wide literature on tuned mass damper is present and this kind of devices is widely used in machines in order to reduce dynamic response, the most famous example in the mechanical field is the mass damper used in the suppression of a torsional mode in crank mechanism. This example is also important for the goal of this paper, because it is a device that rotates with the element it has to damp.

Combining the idea exposed in [1] and the usage of mass damper in torsional mode suppression, the authors have imaged to apply the metastructure idea to a rotating gear. In aerospace field, gears have thin web and very light cross section, so they have the possibility to have dangerous mode shapes in the operative range. Nowadays damping effect in this occurrence is performed using a ring damper [7], so mass is added to the gear and deep wear effects are present. In order to avoid the increase of mass and wear problem, the authors thought to applied the metastructure concept to the web of a gear. In the present paper, the feasibility of this approach is investigated.

---

C. Rosso (✉) · E. Bonisoli · F. Bruzzone

Department of Mechanical and Aerospace Engineering, Politecnico di Torino, Torino, Italy

e-mail: [carlo.rosso@polito.it](mailto:carlo.rosso@polito.it)

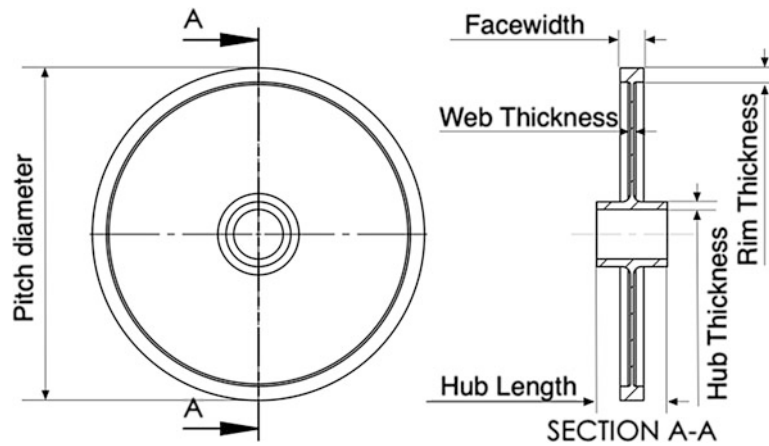


Fig. 5.1 Gear shape used for testing the metastructure concept

### 5.1.1 Metastructure Definition

Two directions are followed in order to increment the efficiency of the gearboxes, on a side the speed increment and on the other side the mass reduction. Both these actions act on the gears design in the same way, they increase the frequency of excitation and in the same time the structure stiffness and mass are reduced as much as possible for lightweighting the gears. The mass reduction means also material removal from points where stresses are low. If this is not a problem for static analysis, it becomes dangerous for the dynamic behaviour of the gear, in fact the material removal means a reduction of the structure stiffness and, combined with the increase of speed, it can happen that dangerous normal modes fall into the operative range. As a consequence, the material reduction increases the overall level of stress (if the same power is transmitted) and the addition of dynamic stresses due to the gear dynamic behaviour can easily bring gear to a failure. In order to reduce gear vibration a way can be the usage of a ring damper that adds a little mass contribution and helps to dissipate energy by friction. The ring damper is an easy and effective solution, but the wear due to fretting can reduce the efficiency, create oil contamination and contribute to the degradation of the gearbox performance.

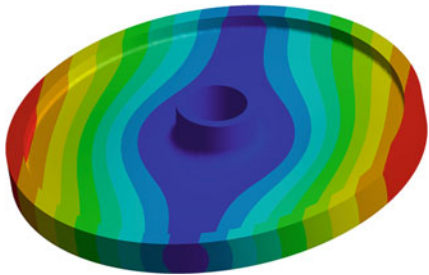
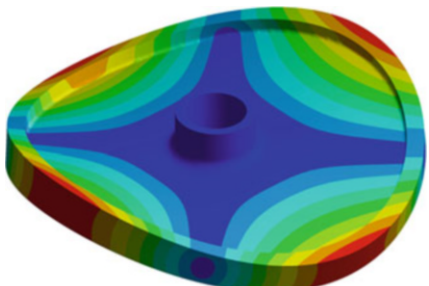
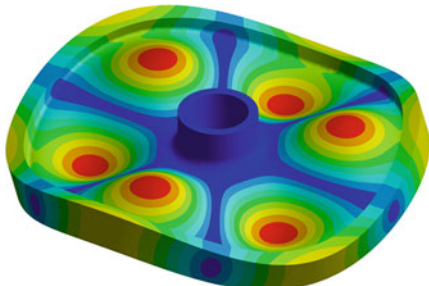
For these reason, the authors in the present paper investigate the possibility to use metastructure concept in a gear. Usually 2D, 3D and 4D out of plane modes of the gear body are the main responsible of gear damage, so the authors investigate a thin webbed gear for understanding the possibility to damp the effects of 2D and 3D out of plane modes. The gear shape can be seen in Fig. 5.1. It can be notice the thin web with respect to the hub and the rim.

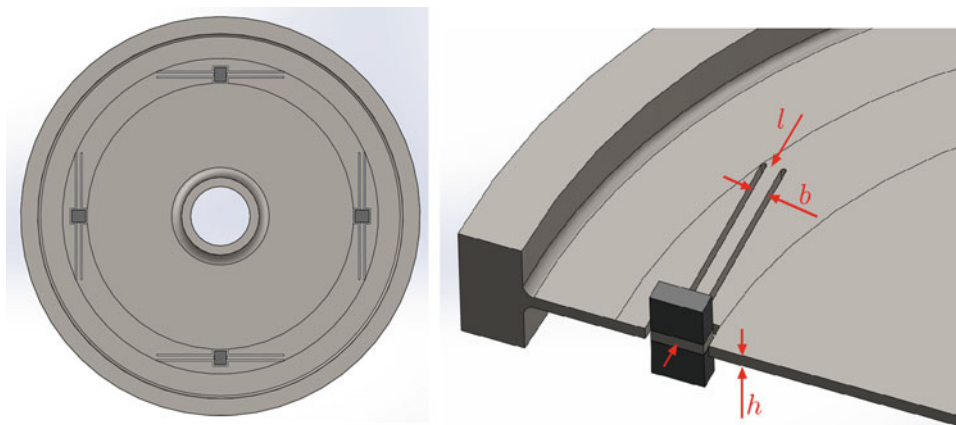
As expected, this kind of gear has the modes summarized in Table 5.1. The most interesting are modes with low frequency because they can be easily excited by the meshing. As a matter of fact, the excitation frequency of this kind of gear is the number of teeth times the spin speed, so the frequency of the excitation can be very high. As an example, a gear with 100 teeth and a spin speed of 6000 rpm can be excited by a meshing frequency of 10 kHz. The computed modes range from 97 Hz to 1900 Hz, so if the spin speed runs from 0 to 6000 rpm, many harmonics of the spin speed can excite those frequencies. In order to reduce the vibration level a damping solution as to be implemented. In this case the authors decided to implement the metastructure approach. In such a gear, a very thin web is present, and it usually presents a series of lightweighting holes. The studied modes, that have to be damped, are out of plane modes, so the authors have imaged that the web can be laser cut in order to generate a series of springs with concentrated masses that can move in the axial direction of the gear. The concept is expressed in Fig. 5.2. A sort of leaf spring is cut into the web and an additional mass is applied to this spring. For balancing and rotordynamic issues a number of 4 elements is necessary, so the elements are cut with a 90° pattern. In the frequency response, a mode multiplicity of 4 is expected.

The leaf spring cross section is selected in order to uncouple the two bending planes and placing the first bending mode in the axial direction of the gear. The dimension of the leaf spring can be estimated considering the tuned frequency  $f$  (650 Hz in this particular case) and an initial mass  $m$  of 1/100 of the overall body mass. In that way, the leaf spring stiffness can be computed as:

$$k = m(2\pi f)^2 \quad (5.1)$$

**Table 5.1** First three mode shapes of the gear

Mode name	Frequency (Hz)	Mode shape
1D	97	
2D	645	
3D	1888	

**Fig. 5.2** Metastructure concept applied to a gear

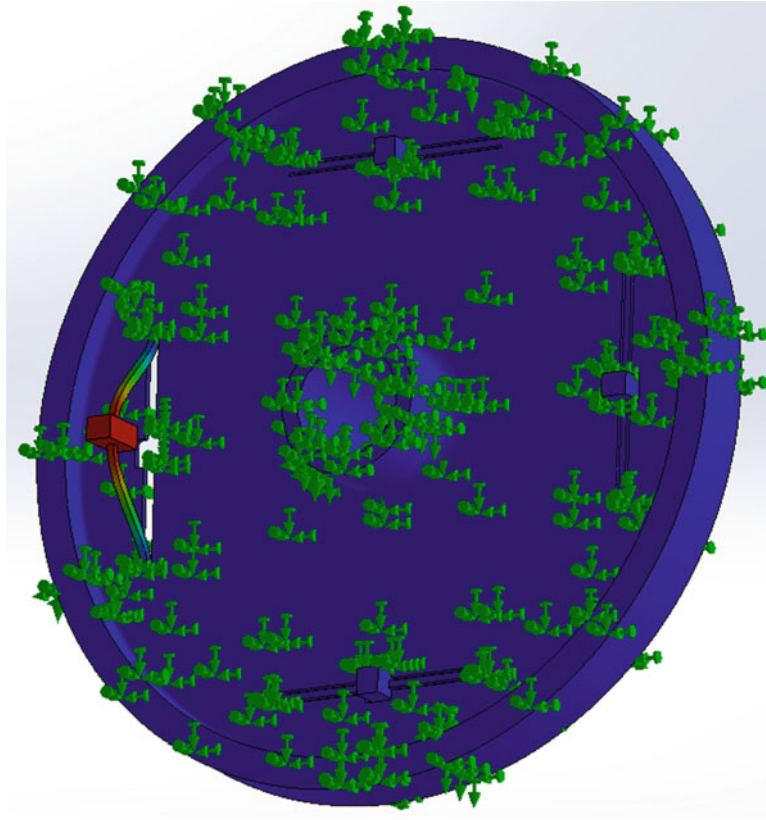


**Fig. 5.3** Tuning of the metastructure

The cross-section dimensions are set considering the thickness of the web  $h$  (2.54 mm in this particular case) and a quantity a little bit greater for  $b$  (2.7 mm in this case) in order to enable the first bending mode in the axial direction. The length of the leaf spring is set considering the equation

$$l = \left( \frac{Ebh^3}{8k} \right)^{\frac{1}{3}} = \left( \frac{Ebh^3}{8m(2\pi f)^2} \right)^{\frac{1}{3}} \quad (5.2)$$

It has to be noted that the mass is considered just one time in the calculation, even if the applied are 2.

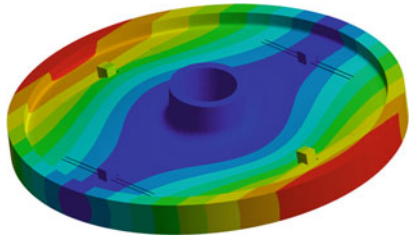
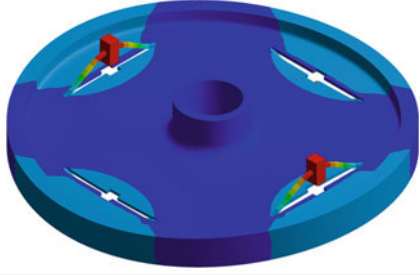
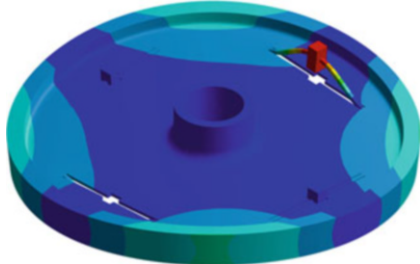
### 5.1.2 Element Tuning

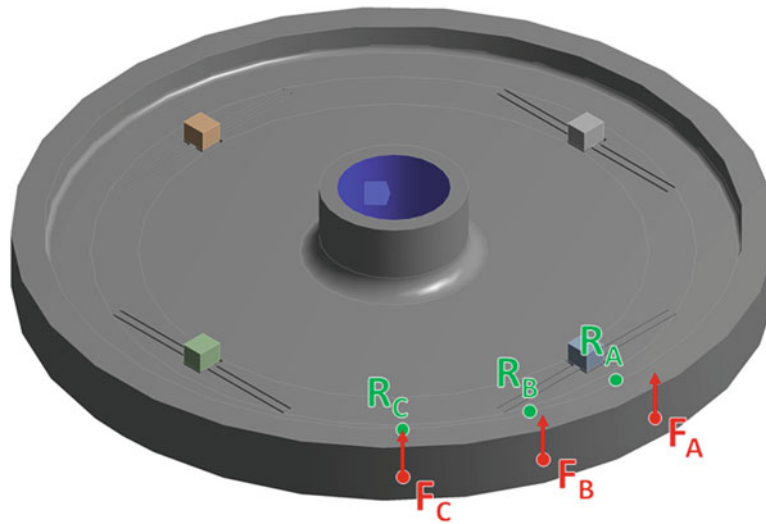
In order to correctly tune the proposed elements, the finite element model is modified. All the nodes of the gears are fixed except the nodes of the leaf spring and the mass. In that way, by performing a computational modal analysis, it is possible to evaluate the natural frequencies of the leaf spring. Having to tune a low frequency (650 Hz), the spring has to be thin and long, and mass important, because the mode the authors considered to tune is the first bending mode of the leaf spring.

In Fig. 5.3 it is possible to see the finite element model and the first bending mode used. Once the proper mass is obtained, a fine tuning is performed considering the gears just constrained in the hub.

After the fine tuning process, the mode shapes of the gear with metastructure appear as in Table 5.2.

**Table 5.2** First two mode shapes of the damped gear

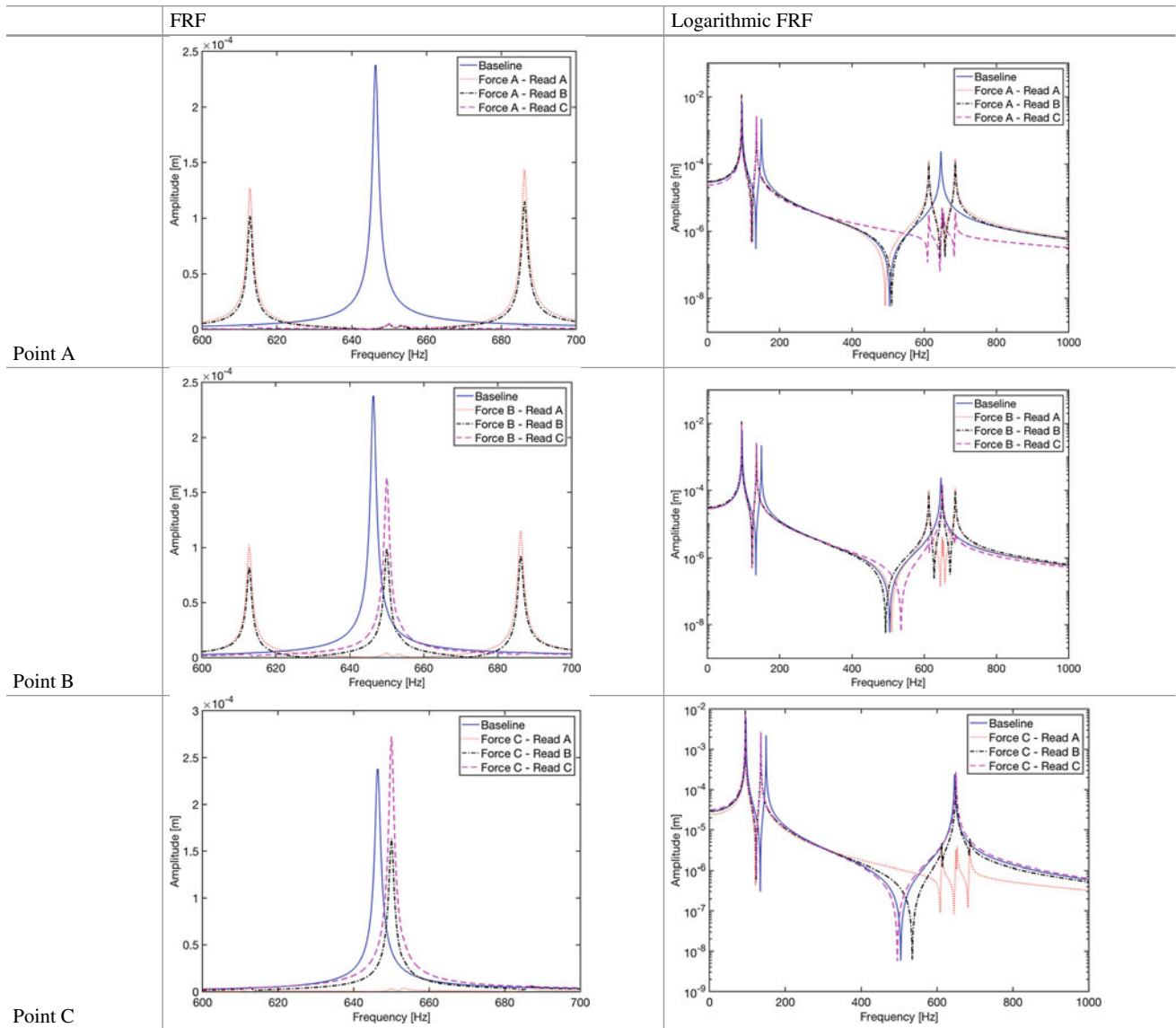
Mode name	Frequency (Hz)	Mode shape
1D	94	
Damped 2D	613	
Damped 2D	650	

**Fig. 5.4** Points where FRF is evaluated, in red the excitation points, in green the reading points

### 5.1.3 Dynamic Response Estimation

In order to evaluate the effect of metastructure on the gear dynamics, a FRF analysis is performed by considering an exciting force axially oriented and applied at the pitch diameter of the gear, see Fig. 5.4.

Three points are considered for evaluating the FRF, as depicted in Fig. 5.4 at  $0^\circ$ ,  $22.5^\circ$  and  $45^\circ$  with respect to the centre of the added mass. This is due to the necessity of having a proper reconstruction of the dynamic behaviour. Results are

**Table 5.3** Dynamic response of the metastructure both in linear and in logarithmic scale

resumed in Table 5.3. It can be noticed that the metastructure effect is appreciable and the displacement of the pitch diameter is reduced of almost a half. This correspond in halving the stress, increasing the life of the component.

By inserting the metastructure, the leaf springs become possible sources of vibration and failures. So, it is necessary to verify the dynamic behaviour of such elements. The most relevant dynamic problem of such design is represented by the torsional mode of the leaf spring. As depicted in Fig. 5.5, this occurs at a low frequency, so a design review is needed.

The idea proves to be effective, so in the design review the authors decide to damp also the 3D mode, by inserting 6 elements, with a different geometry. In order to increase the torsional modes of the damping elements, a spider configuration is chosen, and the process of tuning is performed for both of the target modes.

### 5.1.4 Geometry Optimization

In Fig. 5.6, the new design is presented and in Table 5.4 the FRF results are exposed. As expected, the proposed geometry modifies the dynamic behaviour of the gear and reduce the oscillation of gear pitch. The three points where the data are collected are for the 2D the same of Fig. 5.4 and for the 3D they are angularly spaced by  $15^\circ$ , so  $0^\circ$ ,  $15^\circ$  and  $30^\circ$  with respect to the centre of the added mass. In that way, it is possible to check the behaviour of an elementary sector.

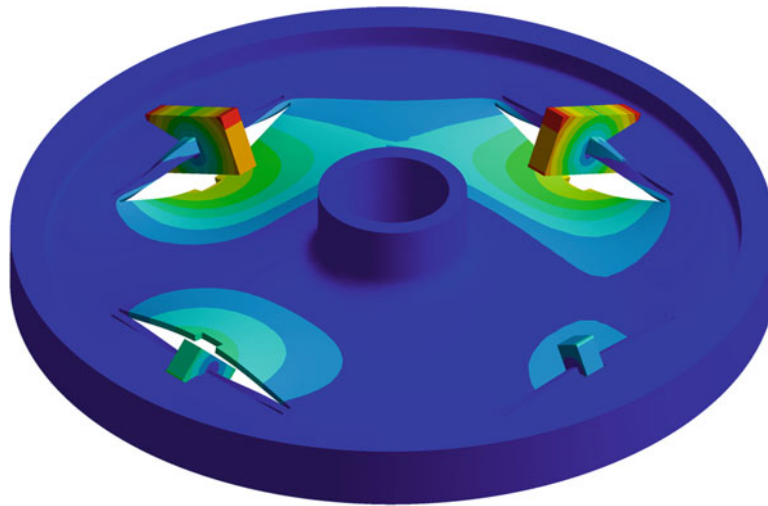


**Fig. 5.5** Torsional mode of the leaf springs: it appears at around 1000 Hz

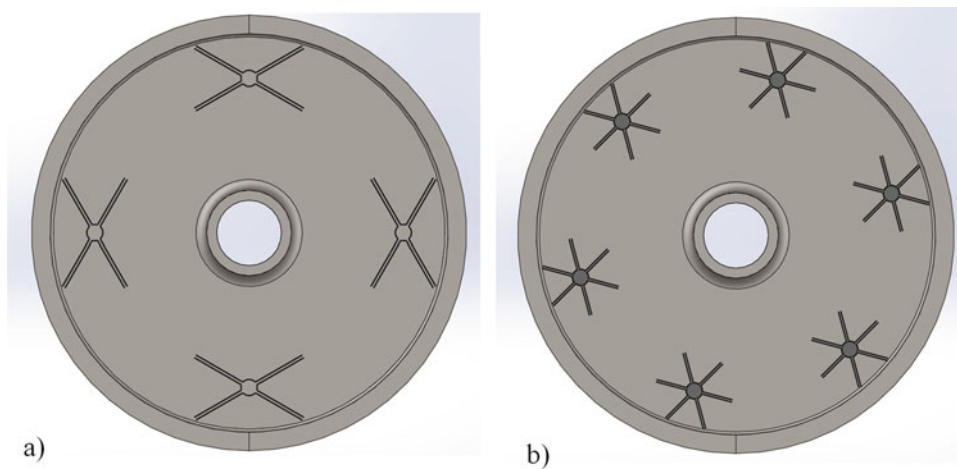


**Fig. 5.6** Metastructure design for damping 2D (a) and 3D (b) out of plane normal modes

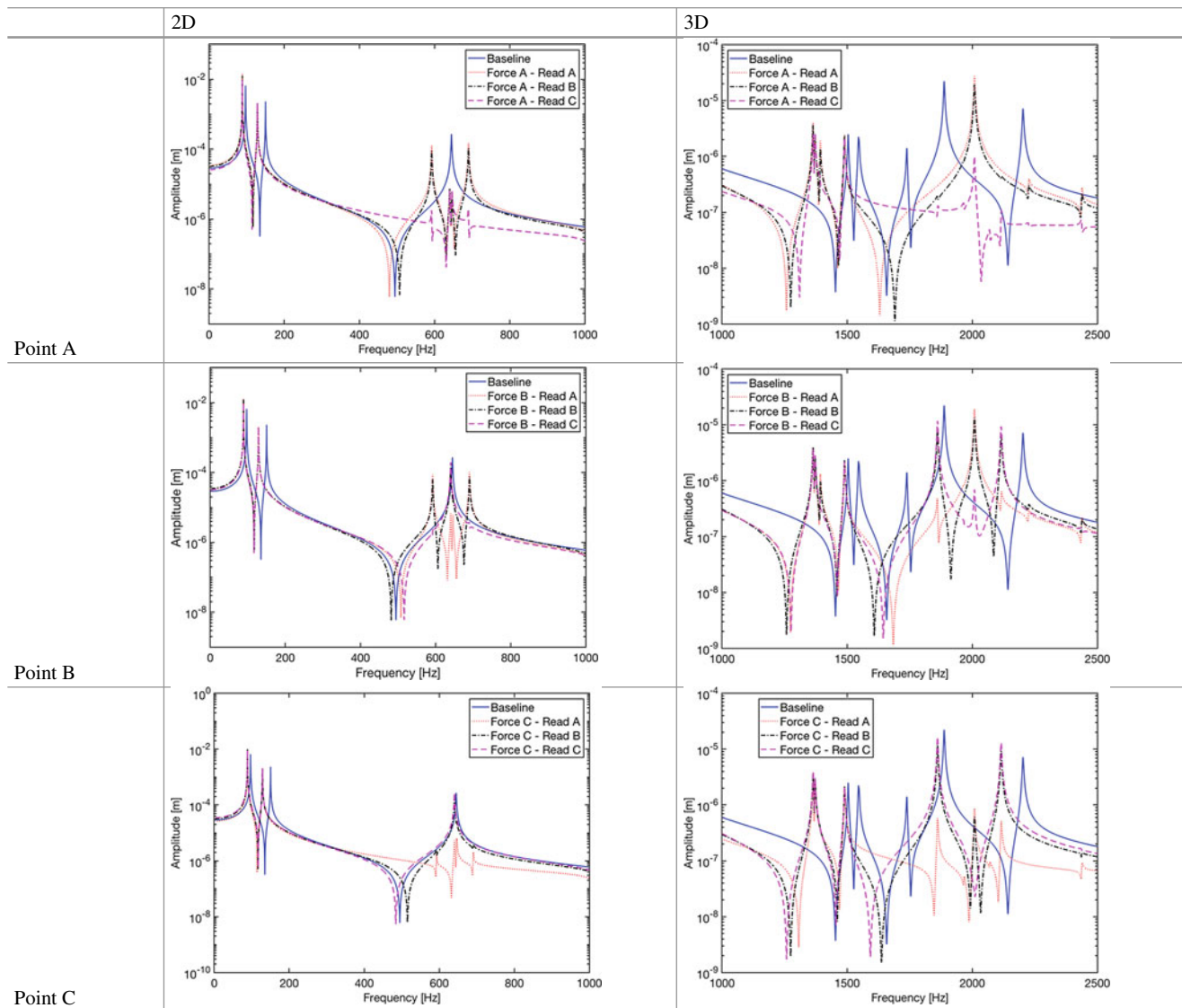
By observing Table 5.4, it is possible to see how the metastructure works in an appreciable way on the 2D mode, as a matter of fact the displacement of the rim is reduced for most of the points where the data are collected. As far as the 3D mode is concerned, a lower effect can be appreciated. This can be due to a greater difficulty in tuning the correct value of the masses.

Some considerations have to be done:

1. No spin speed is considered, so the gyroscopic effects are not yet considered;
2. The geometry of the gear can be optimised in order to create a more integrated design;
3. The results have to be considered in a rotating frame, in order to understand if the fatigue cycles are reduced or not;
4. An experimental test has to be conducted in order to verify the assumption.

## 5.2 Conclusions

The present paper wants to demonstrate the applicability of metastructure philosophy to an axisymmetric component. The results prove that metastructure can be applied to gears in order to damp the effects of some dangerous modes. In this preliminary study, some considerations can be drawn:

**Table 5.4** FRF of the gear with metastructure for damping 2D and 3D out of plane normal modes

1. The design of damping elements has to be performed in order to shift at high frequency all the modes that can be dangerous for the integrity of damping elements;
2. The number of added masses depends on the mode to be damped, for 2D the needed masses are 4 for the 3D the needed masses are 6;
3. In the particular case of a gear, that can run at a very high spin speed, gyroscopic effects have to be considered, because they affect the dynamic response of the gear and also of the small masses;
4. A fatigue analysis has to be performed in order to assess the lasting of all the elements, in particular under the torsional effects due to torque. In a first analysis, authors verified that the root fillet of each springs can be potentially dangerous;
5. The overall mass is a little bit increased, less than 3%, so this solution is comparable to the ring damper in terms of weight increase, but no friction and fretting phenomena are expected, so oil debris can be significantly reduced.

## References

1. Reichl, K.K., Inman, D.J.: Lumped mass model of a 1D metastructure for vibration suppression with no additional mass. *J. Sound Vib.* **403**, 75–89 (2017.) <https://doi.org/10.1016/j.jsv.2017.05.026>
2. Milton, G.W., Willis, J.R.: On modifications of Newton's second law and linear continuum elastodynamics. *Proc. R. Soc. A Math. Phys. Eng. Sci.* **463**, 855–880 (2007.) <https://doi.org/10.1098/rspa.2006.1795>



3. Liu, Z., Zhang, X., Mao, Y., Zhu, Y.Y., Yang, Z., Chan, C.T., Sheng, P.: Locally resonant sonic. *Mater. Sci.* **289**, 1734–1736 (2000.) <https://doi.org/10.1126/science.289.5485.1734>
4. Saxena, K.K., Das, R., Calius, E.P.: Three decades of auxetics research materials with negative Poisson's ratio: a review. *Adv. Eng. Mater.* **18**, 1847–1870 (2016.) <https://doi.org/10.1002/adem.201600053>
5. Sun, H., Du, X., Pai, P.F.: Theory of metamaterial beams for broadband vibration absorption. *J. Intell. Mater. Syst. Struct.* **21**, 1085–1101 (2010.) <https://doi.org/10.1177/1045389X10375637>
6. Pai, P.F.: Metamaterial-based broadband elastic wave absorber. *J. Intell. Mater. Syst. Struct.* **21**, 517–528 (2010.) <https://doi.org/10.1177/1045389X09359436>
7. Firrone, C.M., Zucca, S.: Passive control of vibration of thin-walled gears: advanced modelling of ring dampers. *Nonlinear Dyn.* **76**(1), 263–280 (2014)

# Chapter 6

## Analysis of the Dynamic Response of Coupled Coaxial Rotors



Alexander H. Haslam, Christoph W. Schwingshackl, and Andrew I. J. Rix

**Abstract** The fundamental dynamics of a single rotor are very well understood, and extensively covered in the literature. However, many rotating machines such as aircraft engines consist of multiple shafts, which are often directly coupled by inter-shaft bearings. This paper aims to provide better insight into the underlying dynamics of such systems by analysing a simple but representative model of a rigid dual-rotor system. The modes and natural frequencies were computed numerically and it was found that the different modes could be classified by the following criteria: (i) relative phase of the motion of each rotor, (ii) whirl direction of the rotors, and (iii) presence of rotational or translational motion. The high-speed mode shapes could also be classified into (i) “static” modes with very low frequencies, (ii) “flat” modes which tend towards constant frequencies, and (iii) “precessional” modes which have a frequency which linearly increases with speed. A parameter study was performed in order to obtain a better understanding of the sensitivity of the modal properties. It was found that increasing the inter-shaft bearing stiffness can raise the natural frequencies of the modes at low speeds as well as the critical speeds, but has less influence at high speeds. The speed ratio influences the whirl direction of the modes and hence plays a crucial role in determining how each mode varies with speed. Since the speed ratio also controls the frequency of excitation from unbalances, it has a particularly profound effect on the critical speeds, and extra ones can arise. The importance of considering the dynamics of the complete system in the design of turbomachinery with multiple-shafts was highlighted.

**Keywords** Dual-rotor · Mode shape · Critical speed · Bearing stiffness · Speed ratio

### Nomenclature

$\eta$	Speed ratio between rotor 2 and rotor 1
$\mathbf{G}$	Skew-symmetric gyroscopic matrix
$\mathbf{M}, \mathbf{C}, \mathbf{K}$	Mass, damping and stiffness matrices
$\mathbf{R}, \mathbf{S}$	State-space matrices
$\mathbf{x}$	Rotor position vector
$\mathbf{z}$	State-space vector
$\Omega$	Speed of rotor 1
$k_c$	Inter-shaft bearing stiffness
FE	Finite Element
FW, BW	Forwards, Backwards
IP, OP	In-phase, Out-of-phase
TM	Transfer Matrix

---

A. H. Haslam (✉) · C. W. Schwingshackl  
Imperial College London, London, England, UK  
e-mail: [a.haslam16@imperial.ac.uk](mailto:a.haslam16@imperial.ac.uk)

A. I. J. Rix  
Rolls-Royce plc., Bristol, UK

## 6.1 Introduction

The dynamics of a single rotor are well understood and there are many textbooks on the topic [1, 2]. The angular velocity of the rotor leads to centrifugal loading, so any slight asymmetry leads to a net rotating load on the rotor known as an unbalance. Additionally, the rotor will feel gyroscopic moments as it rotates out-of-plane, which causes each mode to bifurcate into a pair of modes: one mode in which the rotor “whirls” in the same direction as its own rotation, and another where it whirls in the opposite direction. These are termed forwards (FW) and backwards (BW) modes respectively [2]. The natural frequencies of these modes also become speed dependent; the FW modes tend to increase in frequency with speed and the BW ones tend to decrease.

Dual-rotor systems can be more complex to analyse. The two shafts may rotate at different speeds, which has two main effects: (i) the gyroscopic moments felt by each rotor will be scaled by their relative speeds, (ii) and the unbalances on each rotor will lead to excitations at different frequencies. In addition to these inertial effects, the rotors are often directly connected by an inter-shaft bearing for packaging reasons, which means the dynamics can be heavily coupled.

Many of the techniques used to analyse single rotors have been extended to dual-rotor systems. One of the first was Childs who computed natural frequencies and mode shapes of 2 flexible rotors, including gyroscopic effects [3]. Glasgow and Nelson applied Component Mode Synthesis, which is a form of modal reduction, to a dual-rotor system and demonstrated it provided accurate results in a more computationally efficient way [4]. The Transfer Matrix (TM) method [5, 6] and the Finite Element (FE) method [7], have both been extended to dual-rotor systems. It was shown to be possible to use these methods to compute the mode shapes, natural frequencies and critical speeds of complex rotor models representative of industrial turbomachinery.

Limited effort appears to have been put into investigating the dynamics of dual-rotor systems. Ferraris et al. carried out an in-depth theoretical study on a heavily simplified model of a dual-rotor system, and it was found that the sense of whirl was greatly affected by the direction of rotation of each shaft [8]. Gupta et al. analysed a more realistic coaxial arrangement using the TM method to study the effects of gyroscopic moments and found that the effect was more significant for the larger inner rotor, and the results were validated on a test rig [9]. However, only a limited range of rotation speeds were considered. Chiang et al. modelled a jet engine using the FE method, and outlined how to compute the mode shapes and natural frequencies. They also demonstrated how to compute the critical speeds for both synchronous and asynchronous operation [7]. However, what is missing from the literature is a detailed physical explanation of the fundamental dynamics of dual-rotor systems. This paper aims to fill this gap by performing a thorough analysis on a more general rotor model to establish how the modal properties can be characterised and the mechanisms at play. The sensitivity to key parameters will also be investigated in a more systematic way than has been carried out so far.

## 6.2 Theory

### 6.2.1 Model of Interest

A multi-shaft arrangement with 2 rotors was chosen as the system of interest, as depicted in Fig. 6.1. The focus of the analysis will be on the low frequency behaviour, so both rotors were assumed to be rigid. This has the additional advantage that it reduces the number of degrees of freedom. The rotors were also assumed to be axisymmetric, which is a good approximation for most rotating machinery, and means the inertia tensor does not vary in the inertial frame [1]. The bearings were assumed to be identical at the front and rear of each rotor, as well as isotropic so that the orbits would be circular. The damping from the bearings was assumed to be negligible, since it is normally small in real systems and has little effect on the modes when the bearings are isotropic [1]. The centre of mass of each rotor was offset from the centre of the bearings, so that there would be cross-coupling between the translational and rotational degrees of freedom, and therefore all modes would display gyroscopic effects.

An arrangement where both rotors were connected to ground was chosen, so that the stiffness of the inter-shaft bearings could be varied in order to control the coupling between the rotors, without altering the natural frequency of each rotor in isolation. The ratio between the two shaft speeds was denoted by  $\eta$ . This parameter can be positive or negative, corresponding to co-rotation and counter-rotation respectively.

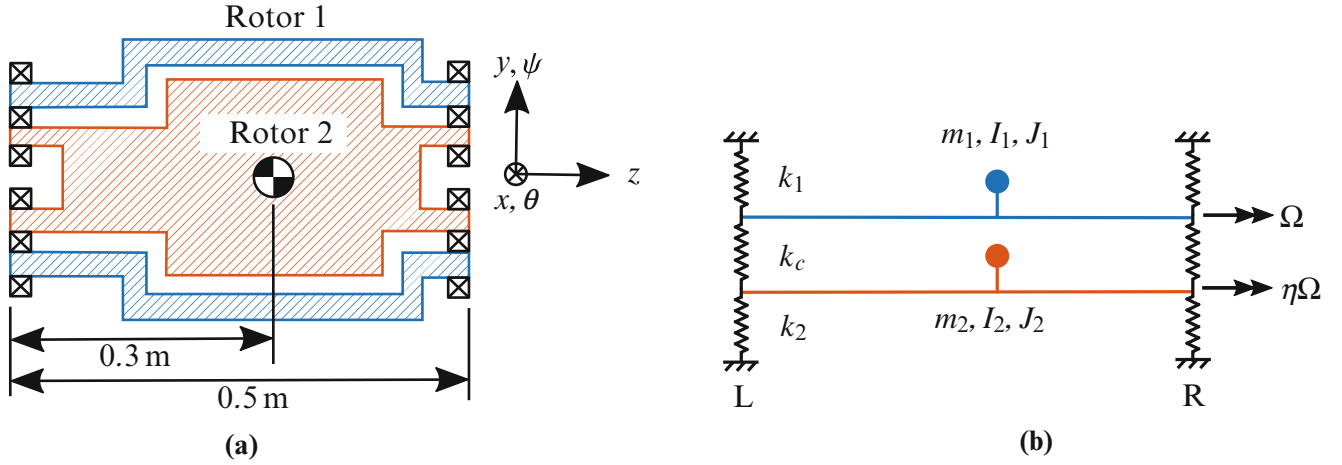


Fig. 6.1 Dual-rotor model. (a) Physical system. (b) Schematic

### 6.2.2 Equations of Motion

The position vector of each rotor will be denoted by  $\mathbf{x}_i = [x_i, y_i, \theta_i, \psi_i]^T$ . Using the combined position vector  $\mathbf{x} = [\mathbf{x}_1^T, \mathbf{x}_2^T]^T$ , the equations of motion of this system can be expressed in the following form:

$$\mathbf{M}\ddot{\mathbf{x}} + (\Omega\mathbf{G} + \mathbf{C})\dot{\mathbf{x}} + \mathbf{K}\mathbf{x} = \mathbf{f}_e \quad (6.1)$$

where  $\mathbf{M}$ ,  $\mathbf{C}$  and  $\mathbf{K}$  are the conventional mass, damping and stiffness matrices respectively and  $\mathbf{f}_e$  is the vector of excitation forces. For flexible rotors, it is possible for the stiffness matrix  $\mathbf{K}$  to vary with speed due to centrifugal stiffening. However, for systems consisting of rigid discs mounted on shafts, this effect can be neglected so  $\mathbf{K}$  is constant. Since the damping was assumed negligible,  $\mathbf{C} = \mathbf{0}$ .

The matrix  $\mathbf{G}$  is the skew-symmetric gyroscopic matrix [1]. The non-zero elements of this matrix are associated with the polar moment of inertia and rotation speed of each rotor. This will have the following block-diagonal form:

$$\begin{bmatrix} \mathbf{G}_1 & \mathbf{0} \\ \mathbf{0} & \eta\mathbf{G}_2 \end{bmatrix} \quad (6.2)$$

where  $\mathbf{G}_1$  and  $\mathbf{G}_2$  are the gyroscopic matrices of each rotor, and the speed ratio  $\eta$  has been introduced to account for the fact that rotor 2 spins at a different speed compared to rotor 1. Equation 6.1 can be expressed in the following state-space form [10]:

$$\mathbf{S}\dot{\mathbf{z}} + \mathbf{R}\mathbf{z} = \mathbf{u} \quad (6.3)$$

where  $\mathbf{z} = [\dot{\mathbf{x}}, \mathbf{x}]^T$ ,  $\mathbf{u} = [\mathbf{f}_e, \mathbf{0}]^T$  and the matrices  $\mathbf{S}$  and  $\mathbf{R}$  are given by

$$\mathbf{S} = \begin{bmatrix} \mathbf{M} & \Omega\mathbf{G} \\ \mathbf{0} & \mathbf{I} \end{bmatrix} \quad (6.4)$$

$$\mathbf{R} = \begin{bmatrix} \mathbf{C} & \mathbf{K} \\ \mathbf{I} & \mathbf{0} \end{bmatrix} \quad (6.5)$$

This state-space representation has reduced Eq. 6.1 to a first-order ODE, which allows standard eigenvalue analysis tools to be used to compute the natural frequencies and critical speeds. This is discussed further in Sects. 6.2.3 and 6.2.4.

### 6.2.3 Natural Frequencies and Mode Shapes

The natural frequencies can be found by setting  $\mathbf{u}$  to zero and assuming a response of the form  $\mathbf{z} = \mathbf{z}_0 e^{st}$ :

$$(s\mathbf{S} + \mathbf{R}) \mathbf{z}_0 = \mathbf{0} \quad (6.6)$$

This is a generalised eigenvalue problem and can be solved using the `eig` command in MATLAB. In this undamped case, the eigenvalues will come in pairs of the form  $s = \pm j\omega$ , and the corresponding eigenvectors  $\mathbf{z}_0$  will also come in complex conjugate pairs. Each pair corresponds to a different mode. This equation can be solved for multiple values of a parameter, updating the  $\mathbf{S}$  and  $\mathbf{R}$  matrices each time, in order to ascertain how the modal properties vary. However, the function `eigenshuffle` was used instead of `eig` in this case, since this utilises a continuation algorithm to correctly match the modes from one solution to the next [11].

Once the mode shapes have been found, the whirl direction at a certain axial location can be determined by comparing the  $x$  and  $y$  displacements of the given mode. For a rotor spinning around the positive  $z$  axis, there is FW whirl if the  $y$  component lags the  $x$  component by  $90^\circ$ , and BW whirl if it leads by  $90^\circ$ . The opposite rule applies if the rotor is spinning about the negative  $z$  axis. For the rotor considered here, all axial locations along each rotor will whirl in the same direction because the bearings are isotropic, but this would not apply for anisotropic bearings [1].

### 6.2.4 Critical Speeds

An unbalance on one of the rotors will lead to an excitation of the form  $\mathbf{f}_e = \mathbf{f}_0 e^{jn\Omega t}$ , where  $n = 1$  for an unbalance on rotor 1, and  $n = \eta$  for an unbalance on rotor 2. If the damping is small, a harmonic response of the form  $\mathbf{x} = \mathbf{x}_0 e^{jn\Omega t}$  can be assumed. Substituting this into Eq. 6.1 equating coefficients yields:

$$\left( -n^2 \Omega^2 \left[ \mathbf{M} - \frac{j}{n} \mathbf{G} \right] + jn\Omega \mathbf{C} + \mathbf{K} \right) \mathbf{x}_0 = \mathbf{f}_0 \quad (6.7)$$

This can again be expressed in state-space form by making the substitutions  $\mathbf{z}_0 = [j\Omega \mathbf{x}_0, \mathbf{x}_0]^T$  and  $\mathbf{u}_0 = [\mathbf{f}_0, \mathbf{0}]^T$ :

$$\left( j\Omega \begin{bmatrix} n^2 \mathbf{M} - jn\mathbf{G} & \mathbf{0} \\ \mathbf{0} & \mathbf{I} \end{bmatrix} + \begin{bmatrix} n\mathbf{C} & \mathbf{K} \\ \mathbf{I} & \mathbf{0} \end{bmatrix} \right) \mathbf{z}_0 = \mathbf{u}_0 \quad (6.8)$$

At resonance, the matrix on the left must be near singular [1]. This leads to another generalised eigenvalue problem, where the eigenvalues directly yield the critical speeds and the eigenvectors are the shape of the response. Since an unbalance on a given rotor will rotate FW by definition, it can be shown that this excitation pattern is orthogonal to the modes where the corresponding rotor whirls BW. This means only modes where the unbalanced rotor whirls FW can be excited, so only these critical speeds need to be retained. However, in the more general case of anisotropic bearings, it is possible for unbalances to also excite BW modes so all critical speeds would have to be considered.

### 6.2.5 Summary

It has been shown how the mode shapes and natural frequencies of a dual-rotor system can be computed by solving a first-order generalised eigenvalue problem. This method can also be extended to directly compute the critical speeds for unbalance excitations on either rotor.

## 6.3 Modal Analysis of the Baseline System

The parameters for the baseline system are shown in Table 6.1. The rotors were assumed to have identical properties, and connected to ground by bearings with identical stiffnesses. The value of the inter-shaft stiffness  $k_c$  was set to be the same value as the other bearings, so the coupling between the rotors would be strong. It was arbitrarily assumed rotor 2 spins faster so that  $|\eta| = 2$ , which is representative of real turbomachinery which often have compressors spinning at different speeds. Both positive and negative values were considered, allowing both co-rotation and counter-rotation to be investigated.

**Table 6.1** Baseline parameters used for the dual-rotor model

Parameter	Description	Value	Units
$k_1, k_2$	Bearing stiffness to ground	1	MN m <sup>-1</sup>
$k_c$	Inter-shaft bearing stiffness	1	MN m <sup>-1</sup>
$m_1, m_2$	Rotor mass	100	kg
$I_1, I_2$	Rotor diametral moment of inertia	1.08	kg m <sup>2</sup>
$J_1, J_2$	Rotor polar moment of inertia	2	kg m <sup>2</sup>
$ \eta $	Speed ratio	2	–

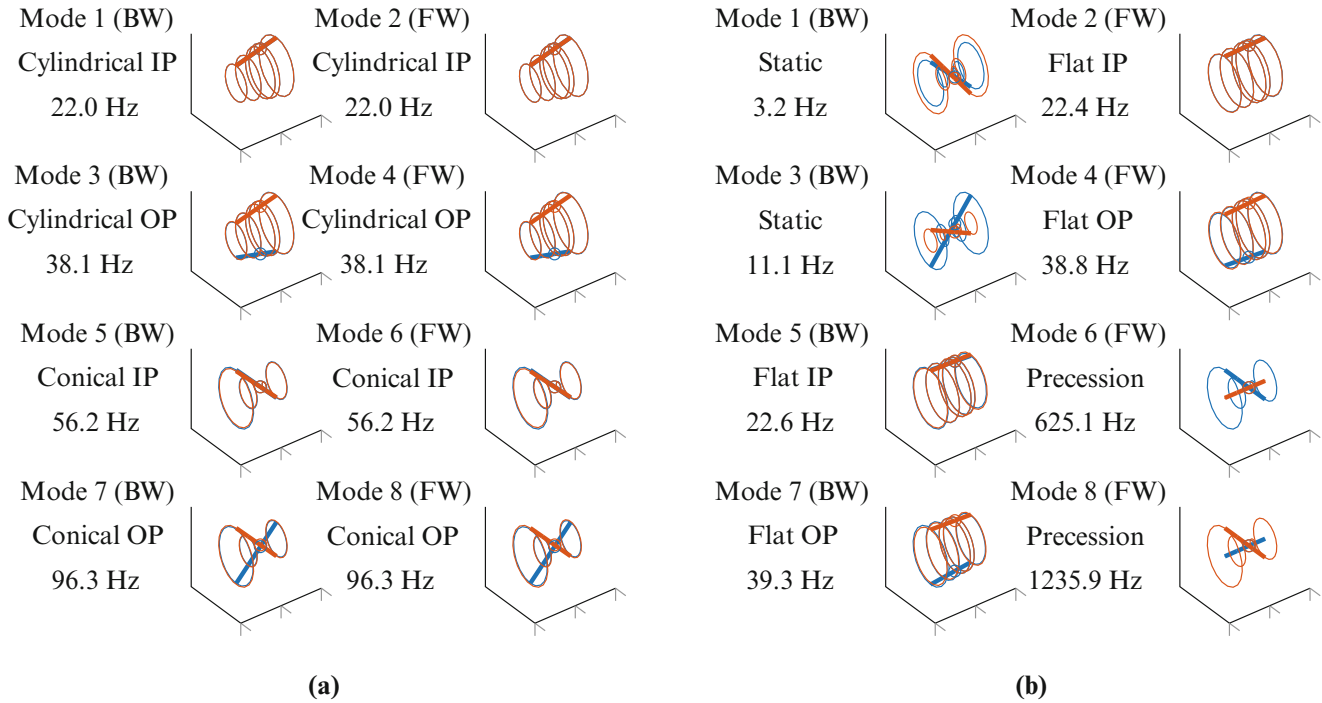


**Fig. 6.2** Mode shapes of the co-rotating dual-rotor system: rotor 1 (—), rotor 2 (—). (a) Mode shapes @ 0 rpm. (b) Mode shapes @ 20,000 rpm

Note that in all of the following plots, the modes have been placed in ascending order based on their frequency at 0 rpm. The numbering system has been maintained as the modes were tracked. This means that mode 3 for example will have the 3rd lowest frequency at 0 rpm, but may *not* have the 3rd lowest frequency at 20,000 rpm. This also means a given mode may also change shape with speed.

### 6.3.1 Co-rotating Rotors

It was first assumed that the rotors were rotating in the same direction, so that  $\eta = +2$ . It can be seen from the mode shapes in Fig. 6.2a that there are 4 “cylindrical” modes, and 4 “conical” modes; the conical modes have higher frequencies in this case because the rotor diametral moment of inertia is very low compared to its mass. Unlike for a single rotor, each type can further be split into a lower-frequency mode where the 2 shafts move in-phase (IP) with each other, and another higher-frequency out-of-phase (OP) mode. Finally, each subtype can be further split into a forward (FW) and backward (BW) mode. If the rotors were compliant, there would be many more varieties of each of these types of mode, which could be further categorised by the shaft deflection shape.

From the Campbell diagram in Fig. 6.3, it can be seen that there are 4 pairs of modes starting at 4 different frequencies @ 0 rpm. In each pair there is a FW and BW mode. As the rotation speed increases, the FW modes increase in frequency and the BW ones decrease. It can also be noted that none of the FW modes cross each other at higher rotation speeds, and similarly

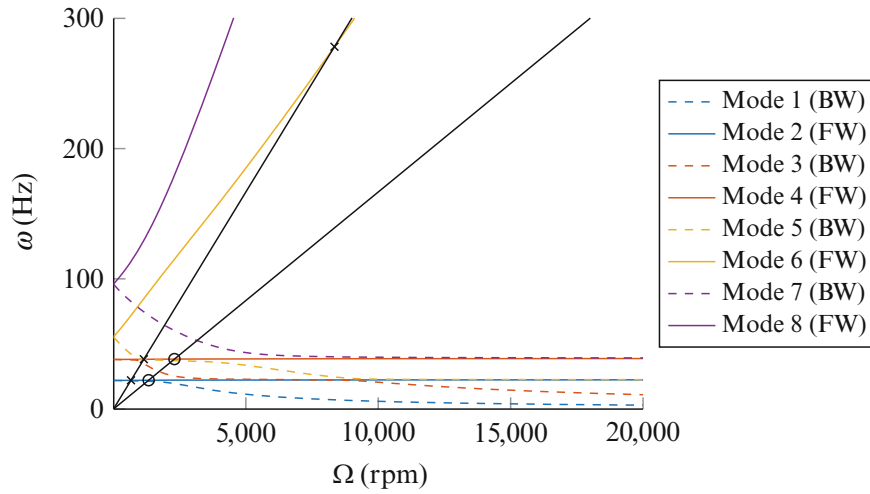


**Fig. 6.3** Campbell Diagram of the co-rotating dual-rotor system: FW modes (—) and BW modes (- - -); critical speeds from unbalances on rotor 1 ( $\circ$ ) and rotor 2 ( $\times$ )

none of the BW ones. This is an example of curve veering, which is a very common phenomenon in rotating machinery [12]. It is more likely to occur in dual-rotor systems as there are more modes. Curve veering has the consequence that a given mode can change its characteristic with speed; for example modes 5 and 7 effectively “swap” behaviour @  $\Omega \approx 5000$  rpm rather than crossing.

It can also be noted that as the rotation speed increases, the mode shapes change quite significantly, as shown in Fig. 6.2b. The 2 highest frequency FW modes (modes 6 & 8) tend to linear asymptotes, which are gyroscopic “precessional” modes, where the inertial and gyroscopic moments balance. Since the elastic loads are small, very similar modes would be observed if the rotors were compliant. The 2 lowest frequency BW modes (modes 1 & 3) asymptote towards (but never reaching) 0 Hz, and these will be termed “static” modes. It can be shown that these are BW modes where the elastic and gyroscopic loads balance. For a system with compliant rotors, similar modes would be observed except the shaft would bow slightly. The natural frequencies of the remaining modes settle to constant values, which is because the rotors only deflect translationally so there are no gyroscopic effects. These will be termed “flat” modes. There are 2 IP modes (modes 2 & 5) which tend towards a lower-frequency IP “flat” mode, and another 2 OP modes (modes 4 & 7) which tend towards a higher-frequency OP “flat” mode. For a system with compliant rotors, the shaft would have to bow in modes like this due to inertial loading; since the rotor would have rotated out-of-plane, gyroscopic moments would be present. This means it is likely the natural frequency would vary with speed, but this depends on the specific rotor configuration.

The frequency of unbalance excitations will scale linearly with the rotation speed  $\Omega$ , and these have also been plotted in Fig. 6.3. Where these lines cross one of the natural frequency lines, this corresponds to a critical speed, and these have been marked with a cross or circle depending on which rotor has the unbalance. Since there are 2 unbalance lines for this dual-rotor system, there are more critical speeds than for a single-rotor system. There are more critical speeds for rotor 2 unbalances since it is rotating faster and is able to excite higher order modes, such as mode 6 @  $\Omega \approx 8000$  rpm.

### 6.3.2 Counter-rotating Rotors

It was now assumed that the rotors were rotating in opposing directions so that  $\eta = -2$ . Note that the direction of whirl quoted in Figs. 6.4 and 6.5 has been specified w.r.t the direction of rotor 1; this means that in a FW mode, rotor 1 is whirling FW and rotor 2 is whirling BW, and vice versa. As a consequence, unbalances on rotor 1 will excite FW modes, and unbalances on rotor 2 will excite BW modes. The engine order line for rotor 2 on Fig. 6.5 is dashed to emphasise this.

It can be seen from the mode shapes in Fig. 6.4a that as with the co-rotating case, the modes can be categorised into cylindrical/conical, in-phase/out-of-phase and FW/BW modes. However, the BW modes now increase in frequency and the FW modes decrease in frequency as shown in the Campbell diagram in Fig. 6.5. This is because the angular momentum of rotor 2 is always greater in magnitude than that of rotor 1 due to its higher speed, so the direction of whirl of rotor 2 in a given mode determines whether it increases or decreases in frequency with speed. It can be shown that for this system, the speed

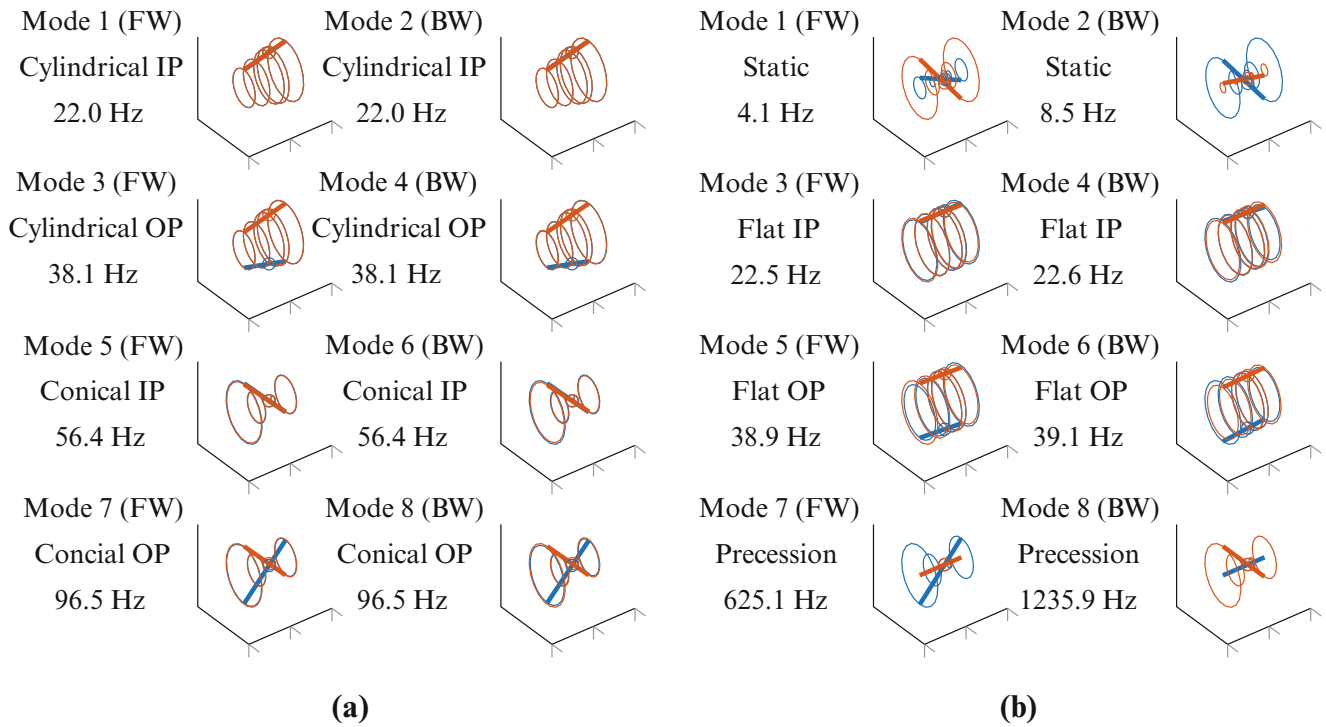


**Fig. 6.4** Mode shapes of the counter-rotating dual-rotor system: rotor 1 (—), rotor 2 (—). (a) Mode shapes @ 0 rpm. (b) Mode shapes @ 20,000 rpm

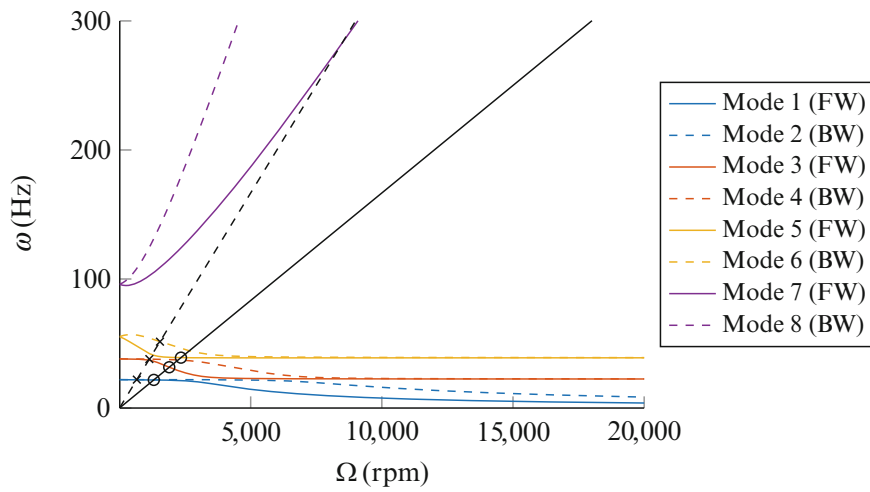


**Fig. 6.5** Campbell Diagram of the counter-rotating dual-rotor system: FW modes (—) and BW modes (- - -); critical speeds from unbalances on rotor 1 (—○—) and rotor 2 (- -x -)



ratio at which this transition from FW modes increasing with speed to BW modes increasing with speed is at  $\eta = -1$ . Note that for this counter-rotating system, in all the modes one of the rotors is whirling FW compared to its own spin direction, so it will be possible for more of the modes to be strongly excited by unbalances.

The high speed mode shapes are plotted in Fig. 6.4b, and the same three types from the co-rotating case are observed. However, some of the low-speed modes now tend to different types of high-speed mode, when compared to the co-rotating case. The 2 highest frequency modes (modes 7 & 8, compared to modes 6 & 8 before) now tend to “precessional” mode shapes. This is because modes 7 & 8 are now the highest frequency modes where rotor 1 and 2 are whirling FW w.r.t their own direction of rotation respectively. The 2 lowest frequency modes (now modes 1 & 2, compared to modes 1 & 3 before) now tend to “static” mode shapes. This is because modes 1 & 2 are now the lowest frequency modes where rotor 2 and 1 are whirling BW w.r.t their own direction of rotation respectively. These are now both IP. The remaining modes become “flat” modes, but it is no longer the case that IP modes must tend towards IP “flat” modes and similarly for OP modes. For example, modes 3 & 4 start out as OP cylindrical modes @ 0 rpm, but tend towards IP ‘flat’ modes at high speeds.

There is a greater density of critical speeds at lower speeds than for the co-rotating system, as shown in Fig. 6.5. There are now 3 critical speeds for rotor 1 unbalances compared to only 2 before, as there is now an additional FW mode in the bottom half of the Campbell diagram. Rotor 2 unbalances now excite BW modes so the precessional mode cannot be excited @ 8000 rpm. However, there are still 3 critical speeds as before, because the engine order line crosses 3 BW modes in the bottom half of the Campbell diagram.

### 6.3.3 Summary

It has been shown that the modes at low-speeds of the dual-rotor system can be classified based on the following 3 criteria:

- **Shape:** Whether the mode appears “cylindrical” involving primarily translational motion, or “conical” involving primarily rotational motion
- **Whirl:** Whether there is forwards or backward whirl
- **Phase:** Whether the rotors move in-phase or out-of-phase with each other

The first two criteria apply to single-rotor systems as well, but the third criterion is unique to dual-rotor systems. For co-rotating arrangements, the FW modes always increase in frequency with speed as with a single rotor. However, for counter-rotation the BW modes can instead increase with frequency depending on the speed ratio. Although not shown here, the specific rotor configuration will also have an influence. At high speeds, the modes tend towards 3 types of mode shape:

- **“Static”:** Purely conical modes which tend towards very low frequencies.
- **“Precessional”:** Modes where one rotor precesses around the other, and the natural frequency increases linearly with speed.
- **“Flat”:** Purely cylindrical modes which tend towards constant non-zero natural frequencies. There are both in-phase and out-of-phase varieties.

The same types of high-speed modes arise in both co- or counter-rotating systems. However, each type of low-speed mode can asymptote towards a different type of high-speed mode, depending on the speed ratio.

## 6.4 Parameter Study

The focus then moved onto understanding how the dynamics of the system vary with certain key parameters. The mode shape and natural frequencies were computed at 0 rpm and 20,000 rpm, as well as the critical speeds. Unlike the rotor properties, there is often more design freedom in the choice of the inter-shaft bearing for rotating machinery, so the stiffness of this bearing  $k_c$  was chosen as the first parameter to be varied. The relative rotation speed of the two rotors can often vary during operation of turbomachinery, so the speed ratio  $\eta$  was chosen as the second parameter.

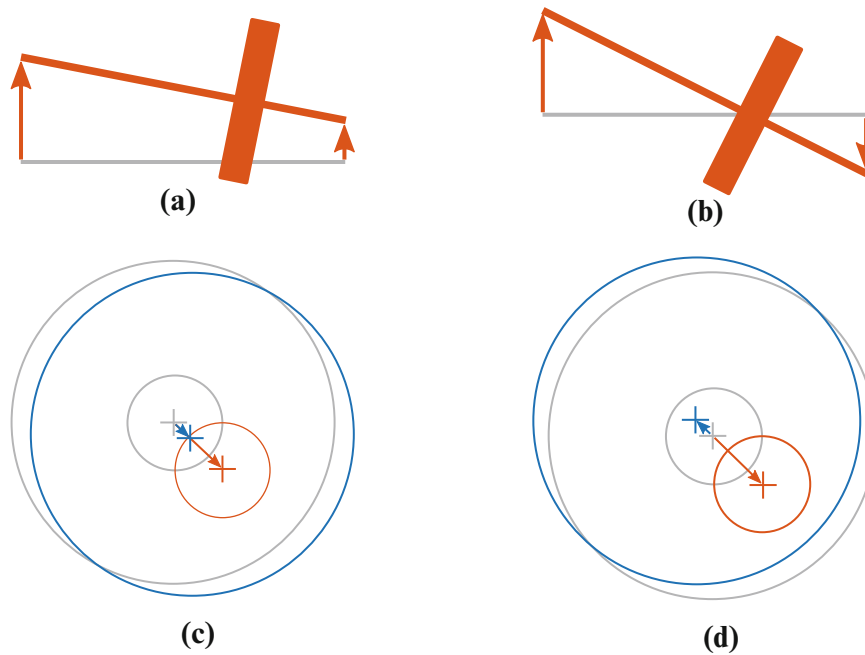


**Fig. 6.6** Diagram showing orbit radii for different types of mode shape. (a) Cylindrical (b) Conical (c) In-phase (d) Out-of-phase

### 6.4.1 Inter-shaft Bearing Stiffness

The stiffness of the inter-shaft bearing  $k_c$  was now varied around its nominal value. The speed ratio was kept at  $\eta = 2$ , corresponding to the co-rotating rotor arrangement, which is more common for turbomachinery. Note that modes have been ordered based on their natural frequencies at 0 rpm for  $k_c = 1 \text{ MN m}^{-1}$ , so they can be compared with Figs. 6.2 and 6.3 for the baseline co-rotating case.

#### 6.4.1.1 Natural Frequencies and Mode Shapes

The mode shapes and natural frequencies at low and high speeds have been plotted in Fig. 6.7. There are 8 pairs of axes (one for each mode), where the  $x$  axis is the bearing stiffness  $k_c$ . The (signed) orbit radius of each rotor has been plotted in using the left axis and the natural frequency using the right axis. Each rotor is denoted by a different colour, and the orbit radius at each end (L & R) is denoted with a solid and dotted line. A given mode shape is conical if the two ends of each rotor have orbits with different signs (shown in Fig. 6.6b). For example, see mode 7 @ 0 rpm in Fig. 6.7a. It will be cylindrical if they are of the same sign (shown in Fig. 6.6a). For example, see mode 1 @ 0 rpm in Fig. 6.7a. A mode is IP if the orbits at one end of both rotors have the same sign (shown in Fig. 6.6c), and OP if they have a different sign (shown in Fig. 6.6d). For example in mode 7 in Fig. 6.7a, the solid blue and solid orange lines are on opposite sides of the  $x$ -axis, so this is an OP mode.

At low speeds, the IP modes will be unaffected by the inter-shaft bearing stiffness due to the symmetry of the system, whilst the OP modes increase in frequency with  $k_c$ . Modes 1 & 2 always correspond to the IP cylindrical modes and remain independent of  $k_c$ , and modes 7 & 8 always correspond to the OP conical modes and monotonically increase in frequency. However, modes 3–6 display sharp changes in behaviour at  $k_c = 2.6 \text{ MN m}^{-1}$ , which is when the OP cylindrical modes overtake the IP conical modes in frequency. Modes 5 & 6 correspond to the IP conical modes for  $k_c < 2.6 \text{ MN m}^{-1}$  so the frequency is constant in this region. However, at this critical value, they transform into the OP cylindrical mode, so their frequencies start to increase with  $k_c$ . Modes 3 & 4 display the opposite transition.

At high speeds, it can be seen that bearing stiffness generally has less influence over the mode shapes and frequencies compared to at low speeds. The frequencies of the “precessional” modes (modes 6 & 8) are only slightly increased by the bearing stiffness, because the gyroscopic and inertial forces dominate in these modes. For the IP “static” mode (mode 1) the natural frequency increases slightly with  $k_c$  because the decay towards 0 Hz is slowed. For the “flat” modes, the IP types vary very little in frequency (mode 2) whereas the OP modes increase significantly (modes 4 & 7). Modes 3 & 5 swap behaviour at  $k_c = 2.6 \text{ MN m}^{-1}$ , as was found to occur at 0 rpm in Fig. 6.7a. Mode 3 is the OP “static” mode for  $k_c < 2.6 \text{ MN m}^{-1}$

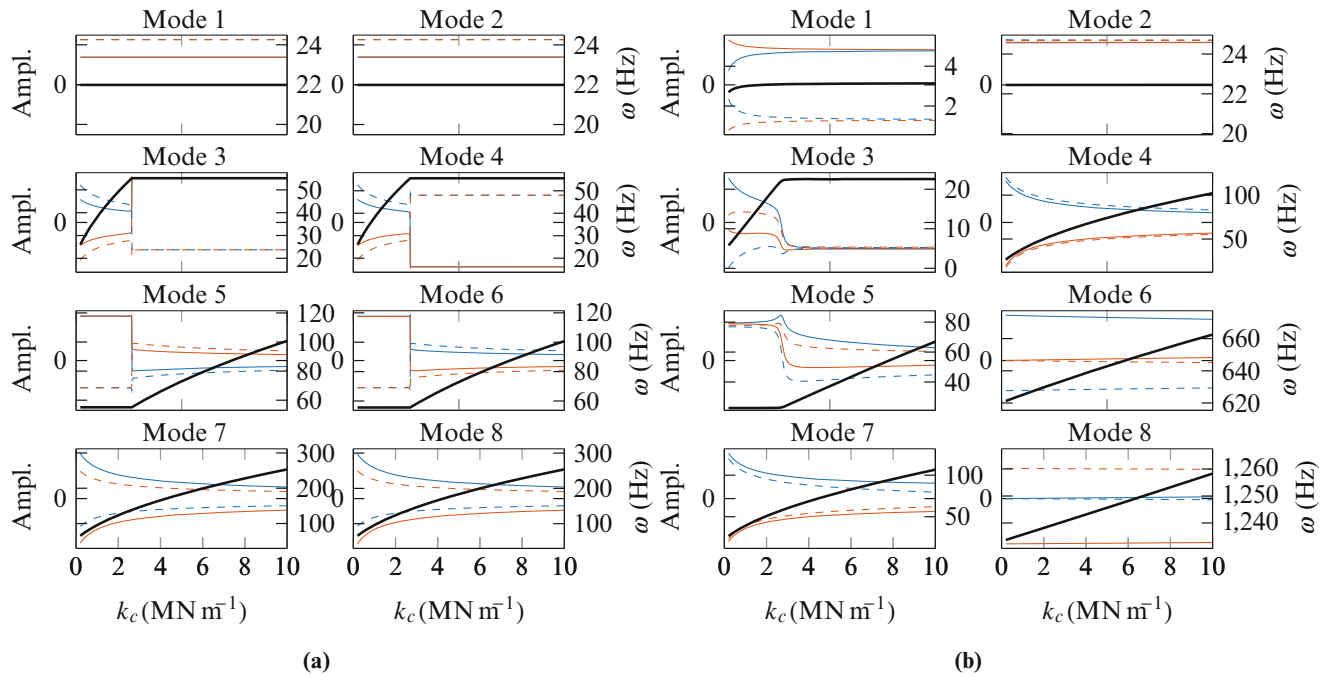


**Fig. 6.7** Variation of the mode shapes of the dual-rotor system with inter-shaft bearing stiffness  $k_c$ : rotor 1 L (---), R (—); rotor 2 L (-.-.), R (—); natural frequency (—). (a) Mode shapes @ 0 rpm. (b) Mode shapes @ 20,000 rpm

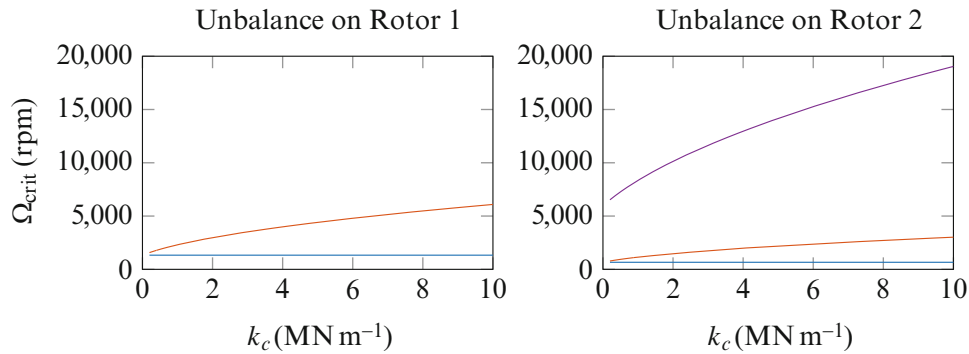


**Fig. 6.8** Variation of the critical speeds of the dual-rotor system with inter-shaft bearing stiffness  $k_c$

so increases in frequency with  $k_c$ , leaving mode 5 to be an IP “flat” mode independent of  $k_c$ . The opposite applies for  $k_c > 2.6 \text{ MN m}^{-1}$ . This transition is again associated with the OP cylindrical mode overtaking the IP conical mode in terms of frequency.

### 6.4.1.2 Critical Speeds

The critical speeds were also computed for the same range of bearing stiffnesses by solving Eq. 6.8. The variation of the critical speeds with  $k_c$  has been plotted in Fig. 6.8. There are two axes, one showing the critical speeds for unbalances on rotor 1, and another for unbalances on rotor 2.

There are only 2 critical speeds for unbalances on rotor 1, whereas there are 3 for rotor 2 because it is rotating more quickly so can excite higher order modes. The first critical speeds in both cases are unaffected by the bearing stiffness, because these correspond to the IP cylindrical modes. However, the other critical speeds do increase with  $k_c$  as these are all OP modes. The increase is most significant for the highest critical speed for rotor 2 unbalances; in Fig. 6.3, this corresponds to the critical speed at around 8000 rpm, where mode 6 is excited @  $\Omega \approx 8000 \text{ rpm}$ . Since the natural frequency line crosses the excitation line at an oblique angle, the rotation speed where the lines cross is very sensitive to any increases in natural frequency due to  $k_c$ .

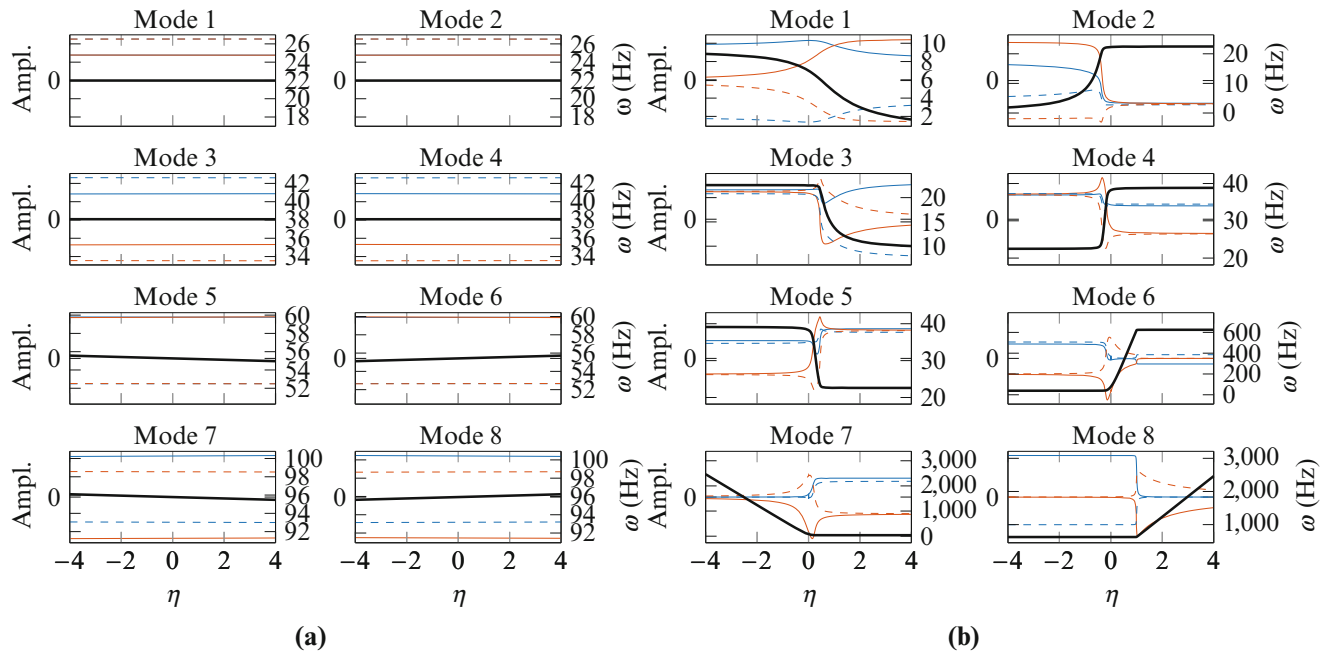


**Fig. 6.9** Variation of the mode shapes of the dual-rotor system with speed ratio  $\eta$ : rotor 1 L (---), R (—); rotor 2 L (---), R (—); natural frequency (—). (a) Mode shapes @ 0 rpm. (b) Mode shapes @ 20,000 rpm

For all the critical speeds which do vary with  $k_c$ , the sensitivity to stiffness eventually decreases. This is because the elastic forces start to dominate when the stiffness is very large, so that the natural frequency  $\omega \sim \sqrt{k_c}$ . The critical speeds will therefore tend towards a similar power law.

## 6.4.2 Rotor Speed Ratio

The relative speed of the inner rotor was now varied by changing the speed ratio  $\eta$ . The inter-shaft bearing stiffness was reset to its initial value  $k_c = 1 \text{ MN m}^{-1}$ . Note that all modes have been numbered based on their frequencies at  $\eta = 2$  so that they agree with Figs. 6.2 and 6.3 for the baseline co-rotating case.

### 6.4.2.1 Natural Frequencies and Mode Shapes

The natural frequencies have been plotted in Fig. 6.9, in the same way as for the bearing stiffness. The mode shapes and natural frequencies are entirely unaffected by the value of  $\eta$  for low rotation speeds as shown in Fig. 6.9a, because gyroscopic loads are not significant in this regime. However, the high speed behaviour is significantly affected as shown in Fig. 6.9b, and all of the modes have different behaviour for positive and negative values of  $\eta$ . Mode 1 is always a “static” mode as discussed in Sect. 6.3.2, but rotor 1 has a larger displacement for  $\eta < 0$  and rotor 2 for  $\eta > 0$ . The frequency of this mode decay towards 0 Hz more slowly when  $\eta < 0$  because the gyroscopic moments of the 2 rotors partially cancel out. Mode 8 is always a “precessional” mode as discussed in Sect. 6.3.2, but rotor 1 precesses for  $\eta > 1$  and rotor 2 precesses for  $\eta < 1$ . This is because  $\eta$  changes which rotor has the highest angular momentum and therefore the highest precession frequency. The frequency increases rapidly with  $\eta$  when  $\eta > 1$ , because  $\eta$  scales the rotor 2 precession frequency.

The type of asymptotic behaviour of the other modes changes with the sign of  $\eta$ . Modes 6 & 7 switch between different “flat” modes with lower frequencies and “precessional” modes with considerably higher frequencies. Modes 2 & 3 similarly switch between “static” modes and “flat” modes. These changes arise because the whirl direction of each mode is affected by the value  $\eta$ ; however it must remain the case that the 2 highest modes where each rotor whirls FW must tend towards “precessional” modes; and the 2 lowest modes where each rotor whirls BW must tend towards “static” modes, as discussed in Sect. 6.3.2. Modes 4 & 5 remain “flat” modes, because these modes are never the highest FW or BW modes, but they do swap between the IP and OP varieties.

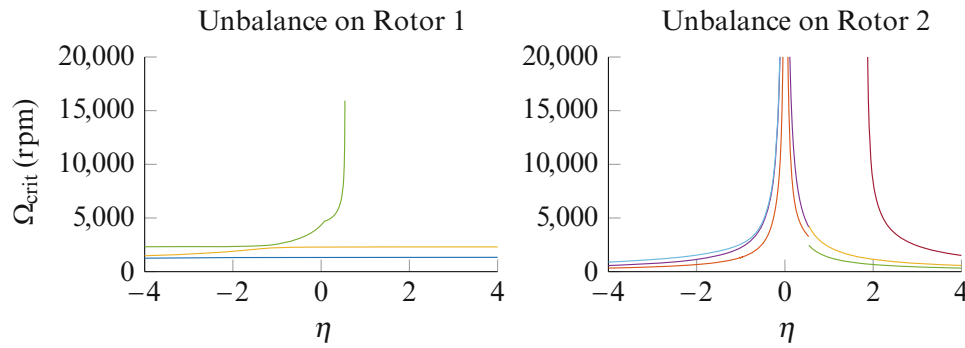


**Fig. 6.10** Variation of the critical speeds of the dual-rotor system with speed ratio  $\eta$

A final point of note is while modes 6 remain a “precessional” mode for  $\eta > 0$ , it is always the rotor with the lowest speed which precesses in this mode. Therefore this is a rotor 2 precessional mode for  $0 < \eta < 1$  and the frequency increases with  $\eta$ . For  $\eta > 1$  it is rotor 1 which precesses, so the frequency becomes independent of  $\eta$  again.

#### 6.4.2.2 Critical Speeds

The critical speeds have been plotted in the same way as before in Fig. 6.10. They vary with  $\eta$  in a much more complex way compared to the inter-shaft bearing stiffness. For rotor 1 unbalances, the first two critical speeds vary very little with  $\eta$ , because the gyroscopic moments are not significant at these speeds, so  $\eta$  has little effect. However, when  $\eta < 0.5$ , a third critical speed can arise, when it becomes possible to excite the lower frequency precessional mode. There is a kink in this critical speed at  $\eta = 0$  (shown in green), because the nature of the mode being excited changes at this point.

For rotor 2 unbalances, there are more critical speeds, but they all vary in a similar way. When the rotors are co-rotating corresponding to  $\eta > 0$ , there are 2 critical speeds, but a third arises when  $\eta > 2$ . This is because the gradient of the  $\eta$ -order line on the Campbell diagram has increased, so the lower precessional mode can be excited. For example, in the case  $\eta = 2$  shown in Fig. 6.3, this corresponds to where mode 6. When the rotors are counter-rotating corresponding to  $\eta < 0$ , there are 3 critical speeds. This is because one of the precessional modes initially decreases in frequency before eventually increasing rapidly, therefore becoming easier to excite; for example, for the case  $\eta = -2$ , see mode 7 shown in Fig. 6.5.

Around  $\eta = 0$ , which corresponds to the case rotor 2 is non-rotating but rotor 1 is still rotating, all of the critical speeds for rotor 2 unbalances increase rapidly. This is because the  $\eta$  engine order line becomes very flat on the Campbell diagram. Physically this means that the natural frequencies are increasing at a much faster rate with rotation speed than the excitation frequency is increasing, so the system remains far from resonance. One final feature of note is the jump in critical speeds around  $\eta \approx 0.5$ . This is because the value of  $\eta$  can change at what speed curve veering occurs, so the mode being excited by an unbalance can suddenly change.

#### 6.4.3 Summary

It has been shown that increasing the inter-shaft bearing stiffness can increase the frequencies of the OP modes, which can reorder the low-speed modes. However, the inter-shaft bearing stiffness only affects the frequency of the OP “flat” modes at high speeds, since gyroscopic forces generally have a larger influence than elastic forces in this regime. Increasing this stiffness can raise some of the higher critical speeds, but there are diminishing returns.

The rotor speed ratio has no influence at low speeds since the gyroscopic moments are small. It does however play a crucial role in determining how they vary with speed, and can increase the frequency of the precessional modes. The speed ratio also controls the excitation frequency from rotor unbalances, and therefore has an even stronger influence on the critical speeds. It was found that there were more critical speeds in a counter-rotating arrangement, and increasing the speed ratio to a very high value can introduce extra critical speeds when they co-rotate.

## 6.5 Conclusions

In this paper a simple but representative model of a dual-rotor system has been analysed, and it has been shown that the behaviour is highly coupled. It was demonstrated that the modes of such a system can be categorised by 3 criteria: (i) relative phase of the motion of each rotor; (ii) whirl direction of the rotors, and (iii) presence of primarily rotational or translational motion. Whether the backwards or forwards modes increase or decrease in frequency was found to depend on whether the rotors are co- or counter-rotating.

It has been shown that the mode shapes can change significantly with speed. The high speed modes can be classified into 3 groups: (i) purely rotational “static” modes which tend towards 0 Hz, (ii) “precessional” modes whose frequencies rise linearly with speed, and finally (iii) purely translational “flat” modes which tend towards constant frequencies. Each low-speed mode may tend towards a different type of high-speed mode depending on the rotor configuration.

A parameter study was carried out and it was found that the inter-shaft bearing stiffness can reorder the modes at low speeds, but has less influence on the high speed behaviour. Increasing this stiffness can raise the higher critical speeds but that there are diminishing returns. The speed ratio has no influence at low speeds, but plays a crucial role in determining how each mode varies with speed. It has an even stronger influence on the critical speeds; it was found that there were more critical speeds in a counter-rotating arrangement, and increasing the speed ratio can introduce extra critical speeds in a co-rotating arrangement, since higher order modes can be excited.

The analysis presented in this paper could be repeated for the more general situation that the rotors have different inertial properties. It would be interesting to extend the analysis to the case of flexible rotors using the techniques discussed in Sect. 6.1, and it would be expected that this would introduce further sub-classes of modes. The assumption that the rotors operate synchronously could also be relaxed, as this is not always the case in industrial applications. When the rotors operate asynchronously, the modal properties and critical speeds will become functions of the rotation speeds of both rotors.

**Acknowledgements** The authors gratefully acknowledge EPSRC and Rolls-Royce plc. for funding this work and granting permission for its publication.

## References

1. Friswell, M.I., Penny, J.E.T., Garvey, S.D., Lees, A.W.: Dynamics of Rotating Machines, 1st edn. Cambridge University Press, Cambridge (2010)
2. Muszynska, A.: Rotordynamics, 1st edn. CRC Press, Boca Raton (2005)
3. Childs, D.W.: A modal transient rotordynamic model for dual-rotor jet engine systems. *J. Eng. Ind.* **98**, 876 (1976)
4. Glasgow, D.A., Nelson, H.D.: Stability analysis of rotor-bearing systems using component mode synthesis. *J. Mech. Design* **102**, 352 (1980)
5. Gupta, K., Gupta, K.D., Athre, K.: Unbalance response of a dual rotor system: theory and experiment. *J. Vib. Acoust.* **115**(4), 427 (1993)
6. Fang, H., Yang, B.: Modelling, synthesis and dynamic analysis of complex flexible rotor systems. *J. Sound Vib.* **211**, 571–592 (1998)
7. Chiang, H.W.D., Hsu, C.N., Jeng, W., Tu, S.H., Li, W.C.: Turbomachinery dual rotor-bearing system analysis. In: Turbo Expo 2002, Parts A and B. ASME, vol. 4, pp. 803–810 (2002)
8. Ferraris, G., Maisonneuve, V., Lalanne, M.: Prediction of the dynamic behavior of non-symmetrical coaxial co- or counter-rotating rotors. *J. Sound Vib.* **195**, 649–666 (1996)
9. Gupta, K., Kumar, R., Tiwari, M., Prakash, O.: Effect of rotary inertia and gyroscopic moments on dynamics of two spool aeroengine rotor. In: ASME 1993 International Gas Turbine and Aeroengine Congress and Exposition, Cincinnati, p. V002T12A010 (1993)
10. Ginsberg, J.H.: Mechanical and Structural Vibrations: Theory and Applications, 1st edn. Wiley, New York (2001)
11. D’Errico, J.: Consistently Sorted Eigenvalue and Eigenvector Sequences. <http://uk.mathworks.com/matlabcentral/fileexchange/22885-eigenshuffle>. [Online; Accessed: 19 Sept 2017]
12. Jei, Y.G., Lee, C.W.: Does curve veering occur in the eigenvalue problem of rotors? *J. Vib. Acoust.* **114**, 32 (1992)

# Chapter 7

## Operational Modal Analysis of Rotating Machinery



S. Gres, P. Andersen, and L. Damkilde

**Abstract** Harmonic excitation of structures caused by rotating equipment is a problem faced by many engineers in the field of Operational Modal Analysis (OMA). Several methods to discard the influence of harmonic inputs over systems natural responses has been proposed in the literature and implemented in various software solutions. This paper recalls some of the most used techniques and uses a new time domain method for removing harmonics from measurements. Deployed method does not rely on filtering, statistical detection nor on non-linear fitting. Instead, it predicts the harmonic part of the time series and deploys an orthogonal projection of the latter onto the raw measurements to remove the harmonic part of the signal. The new technique is a part of an semi-automated framework for OMA of structures contaminated with harmonics, whose flow is presented in this paper. The merit of the framework is discussed in the context of OMA of a full scale operating ship with rotating machinery on-board.

**Keywords** Operational modal analysis · Rotating machinery · Harmonic removal · Harmonic detection · Stochastic subspace identification

### 7.1 Introduction

In the context of OMA of rotating machinery, that is estimation of natural frequencies, damping ratios and mode shapes of structures subjected to both harmonic and random excitations based only on the response measurements, a couple of schemes has been proposed. As such, each strategy that deals with harmonic disturbances in OMA consists of a common triad: harmonic detection, harmonic removal and system parameter computation.

In that context Peeters et al. [1] presented a scheme of time-synchronous-averaging (TSA) and polyreference least-squares complex frequency-domain method (PolyMAX) that was used for OMA of an steady-flight helicopter and an operating diesel engine. Deployed duo enabled OMA of harmonic-affected signals by removing the harmonic peaks from an auto spectral densities of the measurement channels what improved clarity of the estimated stabilization diagrams. For a non-stationary harmonics the TSA required an tachometer measurements from rotating components for angular resampling, which is most often not recorded in real-life application; that was attempted to overcome by Combet and Gelman [2].

An alternative strategy for OMA of rotating machinery is based on cepstral methods. Cepstrum is an inverse Fourier transform of the logarithm of the spectrum which real part is deployed in the recent studies by Randall and Smith [3] and Randall et al. [4] to remove both stationary and varying harmonics from the time signals. Cepstral techniques can coincide with OMA by computing the pole and zero part of system transfer function by curve-fitting the liftered response measurements, what can also lead to estimation of frequency response functions, shown in [4]. Otherwise, cepstrally edited measurements can be used with a standard system identification methods for modal parameter computation.

The trio for a semi-automated OMA of rotating machinery proposed in this paper comprise of harmonic detection using a measure of signals kurtosis, harmonic reduction with orthogonal projections of a harmonic realizations of the signal onto the raw signals and estimation of modal parameters of the system with their statistical uncertainties propagated from the measurements. The paper is organized as follows: the next section recalls the methods, subsequently the results are presented in the Sects. 7.3 and 7.4 contains concluding remarks.

---

S. Gres · L. Damkilde

Department of Civil and Structural Engineering, Aalborg University, Aalborg, Denmark

P. Andersen (✉)

Structural Vibration Solutions A/S, NOVI Science Park, Aalborg, Denmark

e-mail: [pa@svibs.com](mailto:pa@svibs.com)

## 7.2 Framework for OMA with Harmonic Disturbances

Proposed framework for OMA of rotating machinery contains well-known methods and the concepts familiar to OMA community in general. Following section recalls their main assumptions and provides a brief description of the novel harmonic reduction technique. Examples illustrating the concepts listed in this section are from an experimental setup of a rectangular aluminum plate subjected to both random and harmonic excitations. More description about the experimental data can be found in [5].

### 7.2.1 Harmonic Detection

Since a distribution of a response of a structural system subjected to a random input is asymptotically Gaussian, the presence of deterministic (harmonic) components in the random inputs can be detected by examining its moments. The fourth moment, namely kurtosis  $\gamma$  (7.1), is a measure of the heaviness of the tail of the distribution and yields  $\gamma = 3$  for a normally distributed samples  $x$  with zero mean  $\mu$  and a unit variance  $\sigma$ ,

$$\gamma(x|\mu, \sigma) = \frac{E[(x - \mu)^4]}{\sigma^4} \quad (7.1)$$

where  $E(\cdot)$  is an expectation operator. An illustration of the probability density function from the modal response from an experimental plate subjected to both random and harmonic loads is depicted on Fig. 7.1.

The fact that  $\gamma \approx 1.5$  for a sinusoidal signals with  $\mu = 0$  and  $\sigma = 1$  is deployed by Jacobsen et al. [5] in an extended kurtosis check, which is based on extensive calculation of kurtosis of a signal  $y_i$  that is bandpass filtered around each examined frequency  $f_i$ . Frequencies  $f_i$  for which the kurtosis differs from the median computed up to Nyquist frequency are denoted as harmonics. A similar, yet less exhaustive test was proposed by Andersen et al. [6] where only the  $f_i$  that exhibits an abrupt change in corresponding singular values (SVs) of power spectral densities (PSDs) of measured channels are tested. The computation of the abrupt change of the SVs is based on a logarithmic metric between current and a median of windowed SVs.

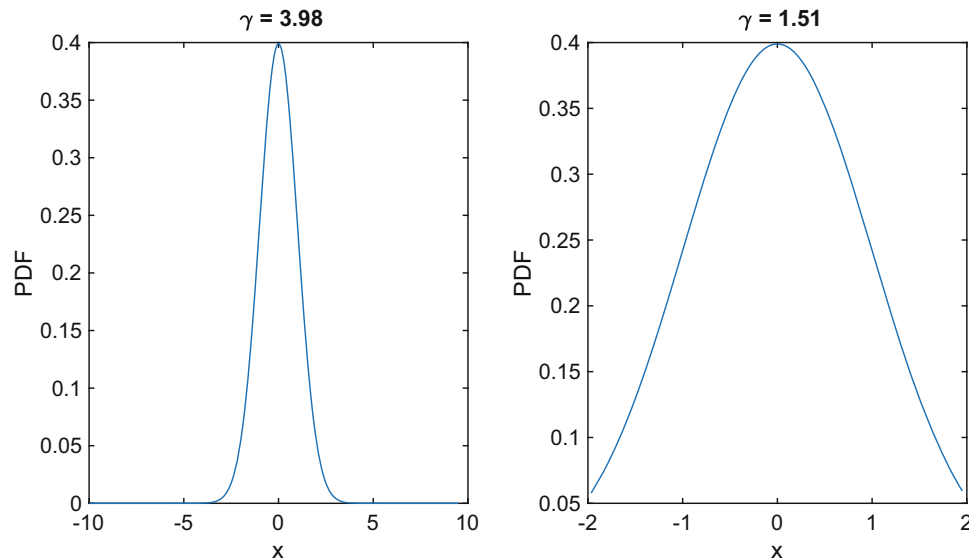


**Fig. 7.1** PDF of a predicted structural mode response (left) and a predicted harmonic mode response (right)



### 7.2.2 Harmonic Reduction

An application of the orthogonal projection-based algorithm to harmonic reduction was described by Gres et al. [7]. The method follows three steps, namely: a similarity transform of the innovation state space to a modal state space, a prediction of modes that correspond to the harmonic frequencies and an orthogonal projection of raw time series onto the harmonic realization of the output. The algorithm exploits the fact that given a state space system that is completely controllable and observable the subspace-based methods identify all the harmonics as lightly damped modes that can be well predicted and removed by an orthogonal projection onto the subspace spanned by the raw measurements.

The algorithm begins with a similarity transform of the innovation state space model to a modal state space that writes (7.2a),

$$\hat{z}_{t+1} = (A_0 - K_0 C_0) \hat{z}_t + K_0 y_t \quad (7.2a)$$

$$\hat{y}_t = C_0 I_m \hat{z}_t \quad (7.2b)$$

where  $A_0$ ,  $C_0$  and  $K_0$  are the state, observation and Kalman gain matrices in a modal form,  $\hat{z}_t$  are the modal states and  $y_t$  denotes raw time series. The prediction of the modal state space model  $\hat{y}_t$  is given by (7.2b) where  $I_m$  is the diagonal selection matrix with ones on a diagonal entries corresponding to harmonic modes. The projection itself is given by (7.3),

$$E(y_t | \hat{y}_{har}) = y_t - E(y_t \hat{y}_{har}^T) E(\hat{y}_{har} \hat{y}_{har}^T)^{-1} \hat{y}_{har} \quad (7.3)$$

where  $\hat{y}_{har}$  is the predicted harmonic response. The projection yields the reduced, harmonic-free response  $y_{red}$  (7.4),

$$y_{red} = E(y_t | \hat{y}_{har}) \quad (7.4)$$

To illustrate the concept behind the algorithm, we selected the harmonic frequencies from the experimental plate measurements, namely 374, 748, and 1496 Hz, for which the prediction of an optimally selected state space model and the projection onto raw measurements were computed, see Fig. 7.2.

The SVs of the PSDs from the predicted harmonic modes (blue line) match well with the harmonic peaks in the raw measurements, as depicted on Fig. 7.2. The SVs from the data after projection do not contain any artifacts from the orthogonally projected harmonics, hence concluded as harmonic-free.

In general, the principal given by (7.3) and (7.4) can be extended not only to harmonic reduction but also to removal of any arbitrary mode from the measurements. That is illustrated based on the same experimental data set from a plate on Fig. 7.3.

The top subplot of Fig. 7.3 illustrates the SVs of the PSDs from the plate measurements reduced by mode 4 at 868 Hz, and mode 8 at 1660 Hz. The realization of the modes at 868 and 1660 Hz is depicted on the bottom part of Fig. 7.3 (thick black lines), along with the complete modal decomposition of the structural modes from the plate measurements. That suggests that any mode can be selected to be reduced in a similar manner.

### 7.2.3 Modal Parameters Computation

The identification of the system matrices of a state space model using both data and covariance driven stochastic subspace identification (SSI-data, SSI-cov) algorithms is subjected to variance errors due to e.g. a finite number of data samples used to calculate the Hankel matrix, unmeasured inputs, measurement noise. A scheme to propagate the sample covariances through all the steps of modal parameter computation for the SSI-cov was proposed by Reynders et al. [8] and Döhler and Mevel [9]. That was extended with SSI-data and input-output algorithms in Mellinger et al. [10].

A method to compute the (co)variance of the modal parameters of the global model order with a data-driven Unweighted Principal Component (UPC) algorithm was developed by Döhler et al. [11]. Method deploys the fast uncertainty computation from [9] and involves computation of the modal parameters of the global mode as a weighted mean of different model orders where the (co)variance of the global model is computed subsequently as a covariance of the weighted mean. The

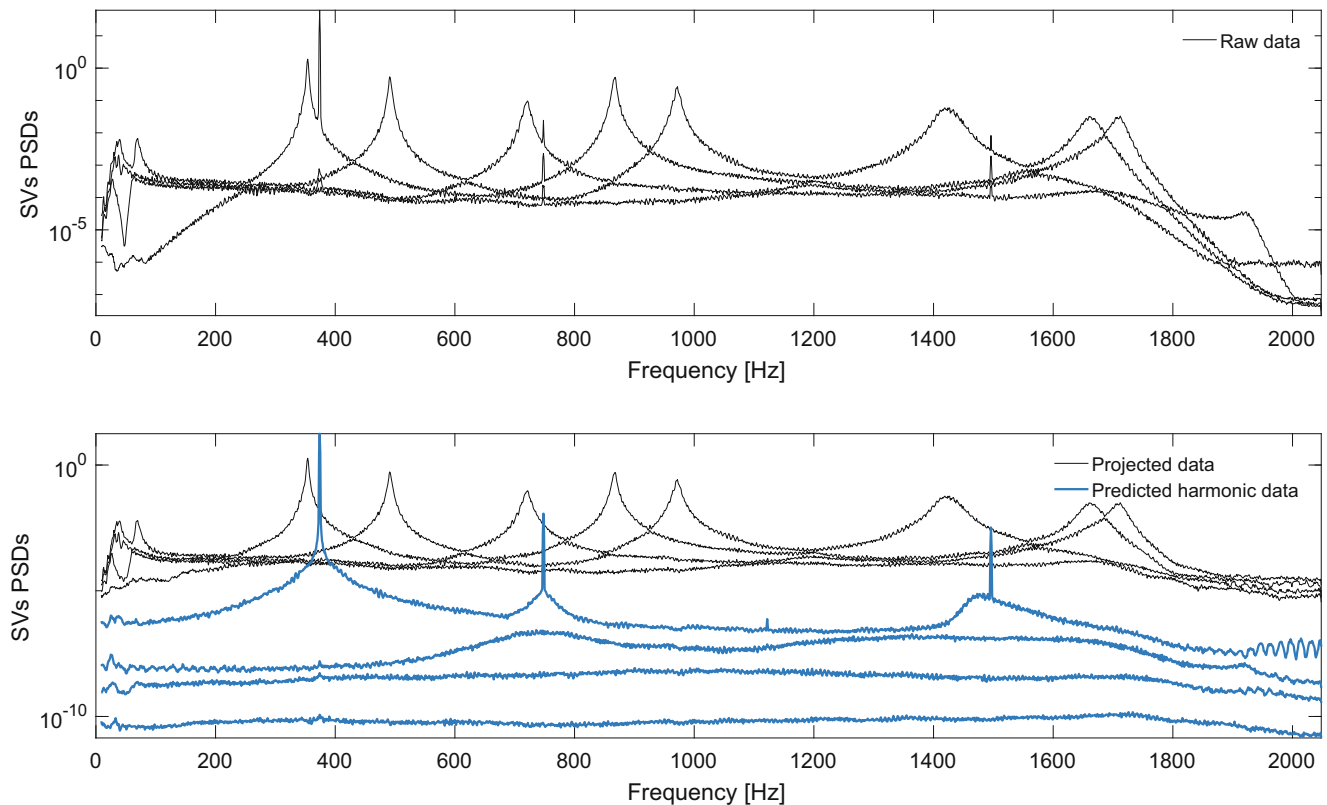


**Fig. 7.2** SVs of PSDs from raw, predicted harmonic and projected harmonics-free measurements

implementation of this algorithm, denoted as SSI with Extended Unweighted Principal Component (UPCX), is used here for the computation of modal parameters and corresponding uncertainties.

### 7.3 Results

In the following, we apply presented framework for dealing with harmonics in OMA to an experimental measurements of a full scale ferry during its operation. The analysis is conducted in semi-automatic chain and is illustrated based on the results from a commercial software *ARTeMIS Modal Pro 5.2* [12].

The ferry with its geometrical and mechanical data is presented on Fig. 7.4.

The dynamic tests are conducted under operational conditions where the response measurements are recorded with piezoelectric accelerometers using a 16-channel B&K Dyn-X acquisition system. The ferry is excited by a combination of a random environmental (wind and waves) and harmonic (operating engine and propeller) loads. The response is measured over a period of 90 min and sampled with 128 Hz. The measurements were carried out by Dr. Sven-Erik Rosenow, Santiago Uhlenbrock and Prof. Günter Schlottmann from University of Rostock in Germany and made available to analysis by Structural Vibration Solutions A/S from Aalborg, Denmark. The same data set was analyzed in [13] and [14] with respect to harmonic detection and in [7] for harmonic reduction.

Prior to harmonic detection the measurements are detrended, normalized by the standard deviation of each channel and decimated to 21.33 Hz. The families of the harmonic frequencies caused by the engine operating at the frequency of 2.05 Hz and the propeller blade at 8.2 Hz are identified with fast kurtosis check, what is illustrated on the Figs. 7.5 and 7.6.

In total five frequencies with the kurtosis below 2.65 are denoted as harmonics, see Fig. 7.5, what is in good agreement with the sharp peaks of SVs depicted on Fig. 7.6. Selected frequencies are one of the input parameters for the orthogonal projection-based harmonic reduction. Besides that, user defined settings boil down to setting a number of block rows of the data Hankel matrix and a maximum damping ratio of the modes to reduce. Selected parameters navigate the method in

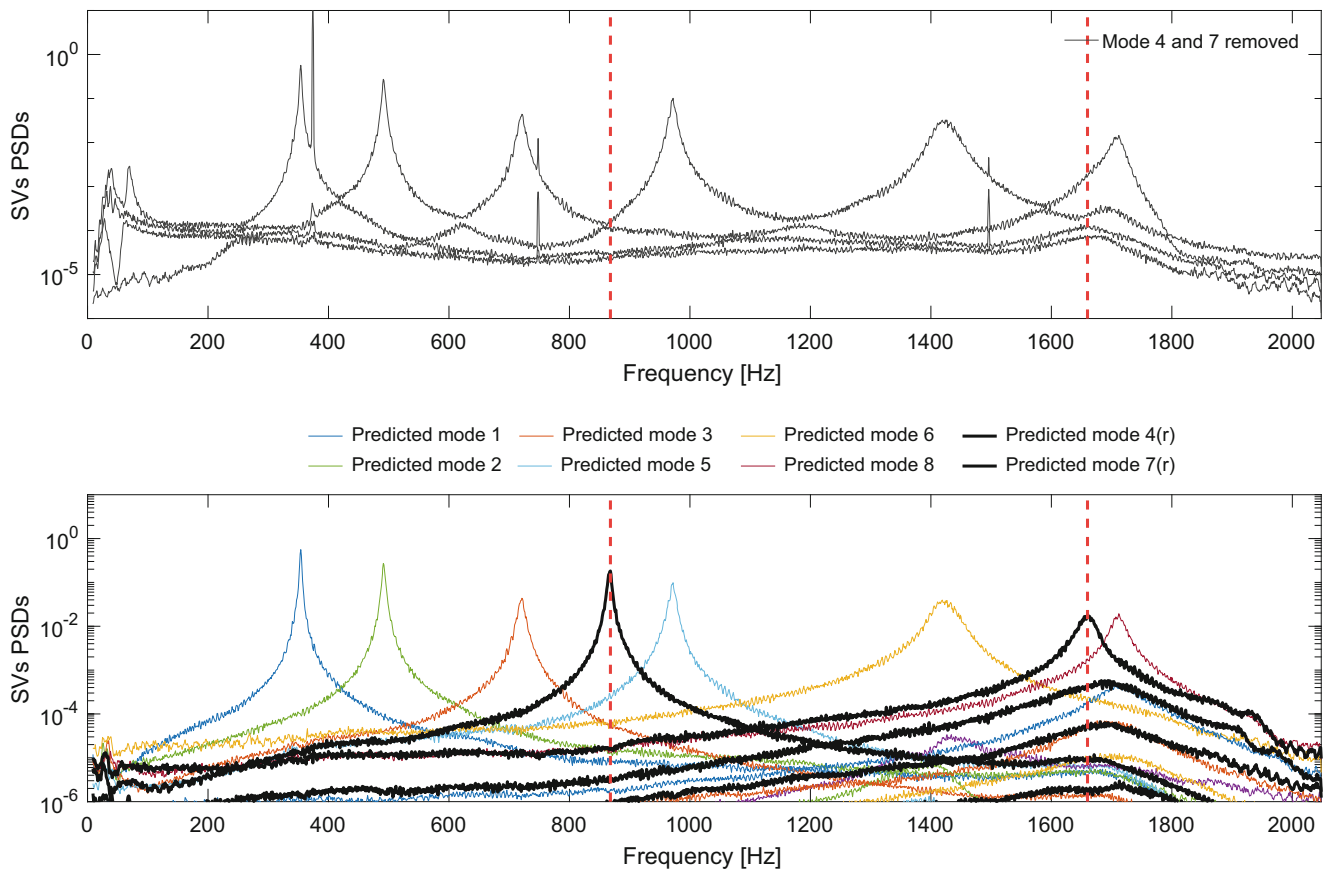


Fig. 7.3 SVs of PSDs from the projected response with mode 4 and 8 removed and predicted responses from each structural mode

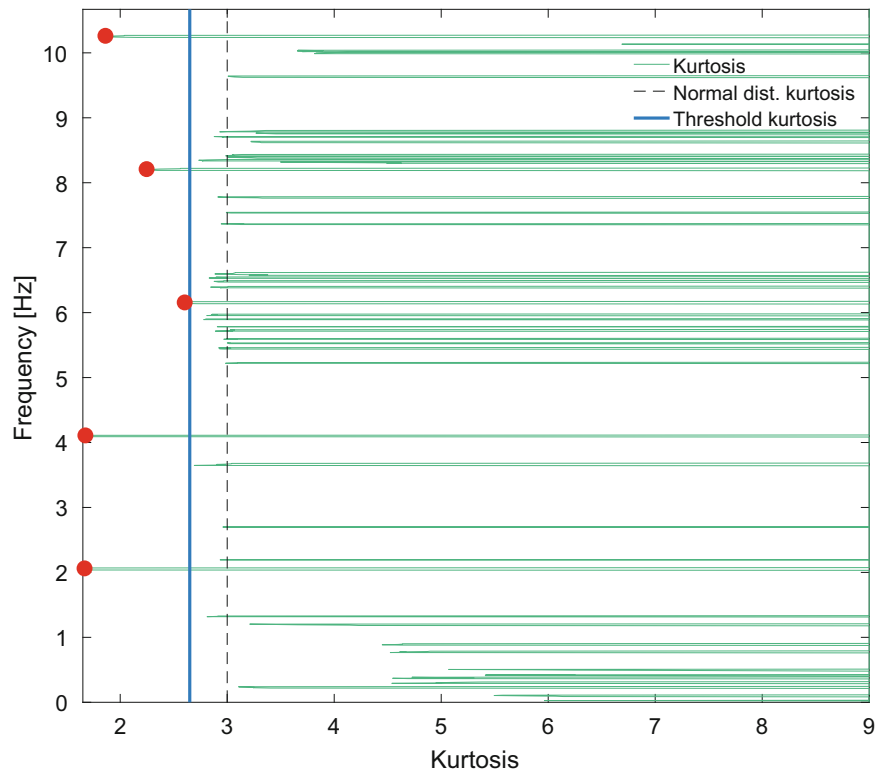


Fig. 7.4 Full-scale ship docking at Flensburg shipyard

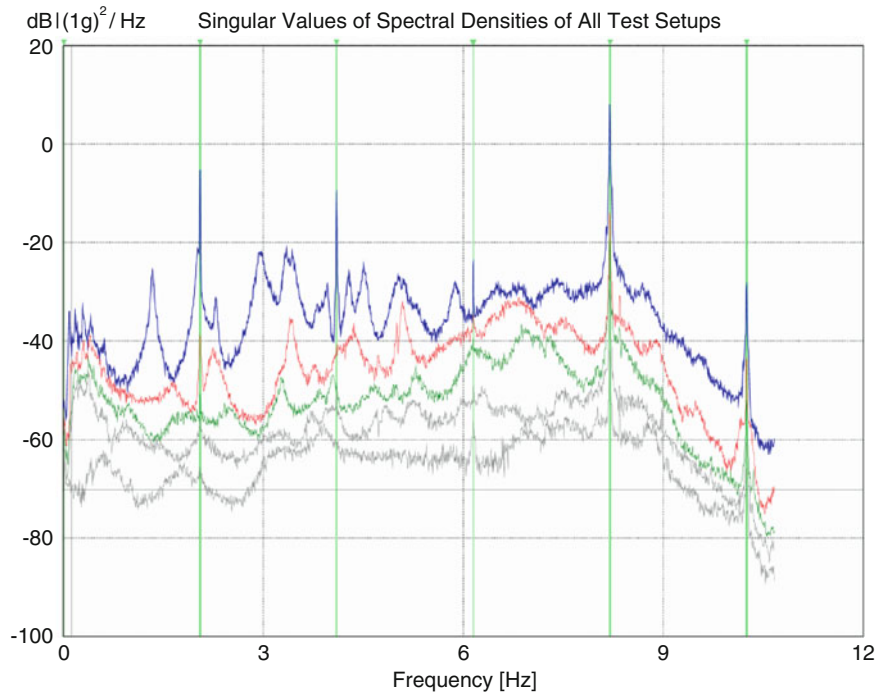
finding the optimal state space model to predict the harmonic responses. The input settings with the SVs of PSDs of the measurements before and after the reduction are illustrated on Fig. 7.7.

Figure 7.7 illustrates that the harmonic peaks at 2.05, 4.1 and 6.15 Hz are removed completely. The first SV shows a remanence of the propeller mode at 8.2 Hz and the engine mode at 10.2 Hz, however both are marginal and not identified during system identification, see Fig. 7.10. The harmonic removal uncovered a mode at 8.14 Hz, which being reasonably damped, 1.62%, and with a low complexity, 7.19%, indicates a structural mode close to a resonance with the propeller frequency.

To prove the merit of removing the harmonics prior to system identification we conducted a OMA of two data sets before and after harmonic reduction. That is illustrated by the results of the 95% confidence ellipsoids of the 1st mode frequency and damping ratios and the modal assurance criteria (MAC) between the identified sets of mode shapes, see Figs. 7.8 and 7.9



**Fig. 7.5** Kurtosis of the signal calculated for the selected frequencies



**Fig. 7.6** SVs of PSDs with harmonic indicators computed with the fast kurtosis check

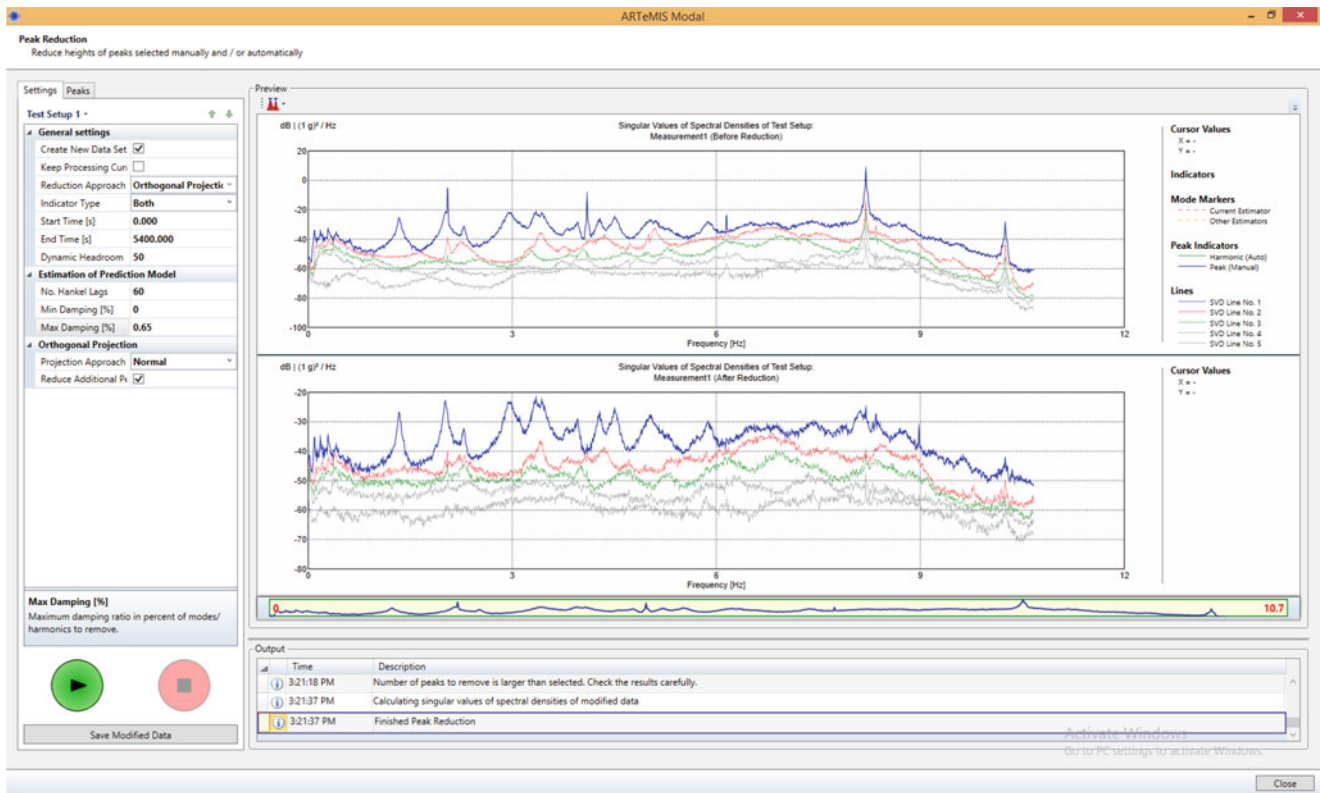


Fig. 7.7 Removal of harmonics at 2.05, 4.1, 6.15, 8.2 and 10.2 Hz

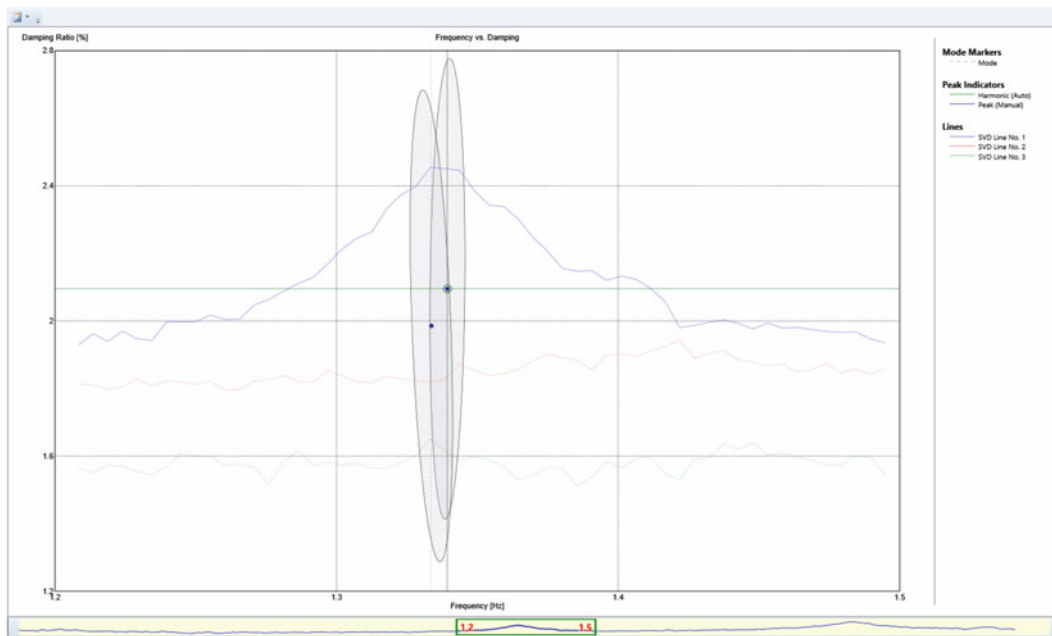
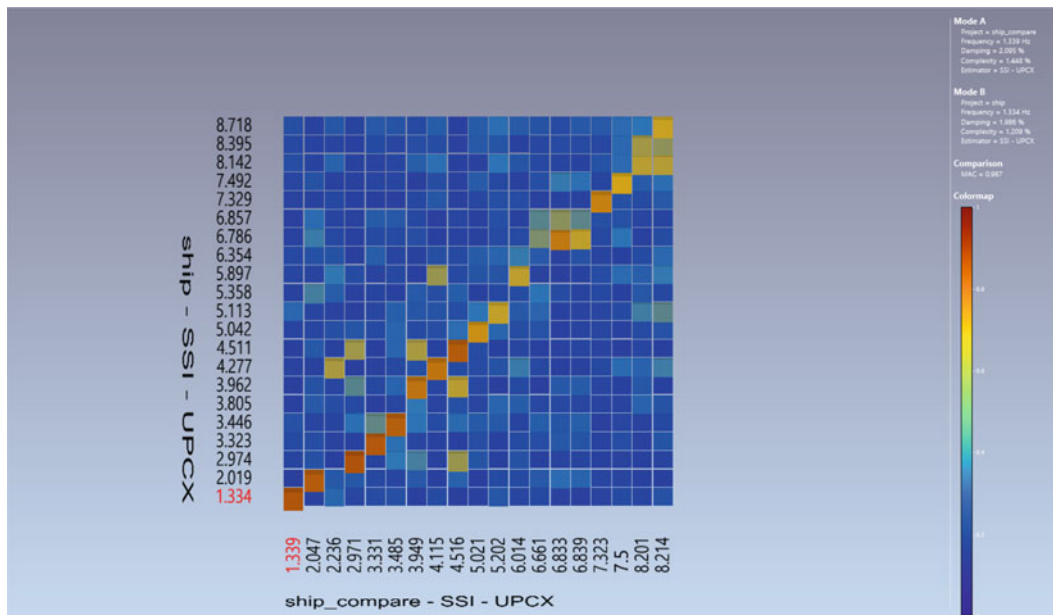


Fig. 7.8 95% confidence ellipsoids for 1st mode frequency and damping before and after harmonic reduction



**Fig. 7.9** MAC diagram obtained from mode shapes of the system before and after harmonic reduction

respectively. The modal parameters from both sets are computed with SSI-UPCX with max. model order of 140 and 38 eigenvalues in the state matrix.

For the global mode estimate, the pairs of the natural frequency and the damping ratio of the 1st mode (unaffected by the harmonics) yields 1.33 Hz with 1.99% and 1.34 Hz with 2.02%, respectively for the measurements before and after the harmonic reduction. After examining the uncertainty ellipsoids depicted on Fig. 7.8 it becomes apparent that the difference between the modal properties of two modes described above is acceptable hence the mean values from both test are encapsulated within a common uncertainty interval. The diagonal MAC values illustrated on Fig. 7.9 are varying in between 0.75 and 0.99 suggesting that the modes with similar shapes are computed in both data sets. The modes at 3.8, 5.35, 6.35, 6.86, 8.4 and 8.7 Hz were not identified before harmonic reduction, see Fig. 7.9. For the completeness of the results a stabilization diagram with corresponding natural frequencies estimated after the harmonic removal is presented on Fig. 7.10.

Figure 7.10 illustrates multiple stable modes for all the model orders up to 140. One can notice a mode present at 2.29 Hz which is denoted as a noise mode- that is a result of a high coefficient of variation of the frequency of the corresponding mode, namely 0.015. Otherwise, the remaining modes present in the measurements exhibit low uncertainties for both the frequency and damping ratio below the threshold being 0.01 and 1 respectively. The harmonic modes previously present in the recorded data are not detected.

## 7.4 Conclusion

In this paper we presented a semi-automated framework for OMA of rotating machinery. Proposed strategy combines the well-known methods for harmonic detection and modal parameters computation with a novel harmonic reduction technique. Deployed methods operate in time domain, do not require additional inputs for reduction of non-stationary harmonics such as a tachometer measurements and estimate the variance of a global modal parameters, which provides more precise identification of the modal properties in case of realistic applications.

## References

1. Peeters, B., Cornelis, B., Janssens, K., Van der Auweraer, H.: Removing disturbing harmonics in operational modal analysis. In: Proceedings of the International Operational Modal Analysis Conference (2007)
2. Combet, F., Gelman, L.: An automated methodology for performing time synchronous averaging of a gearbox signal without speed sensor. *Mech. Syst. Signal Process.* **21**(6), 2590–2606 (2007)
3. Randall, R., Smith, W.: New cepstral techniques for operational modal analysis. In: Proceedings of the First World Congress on Condition Monitoring (2017)

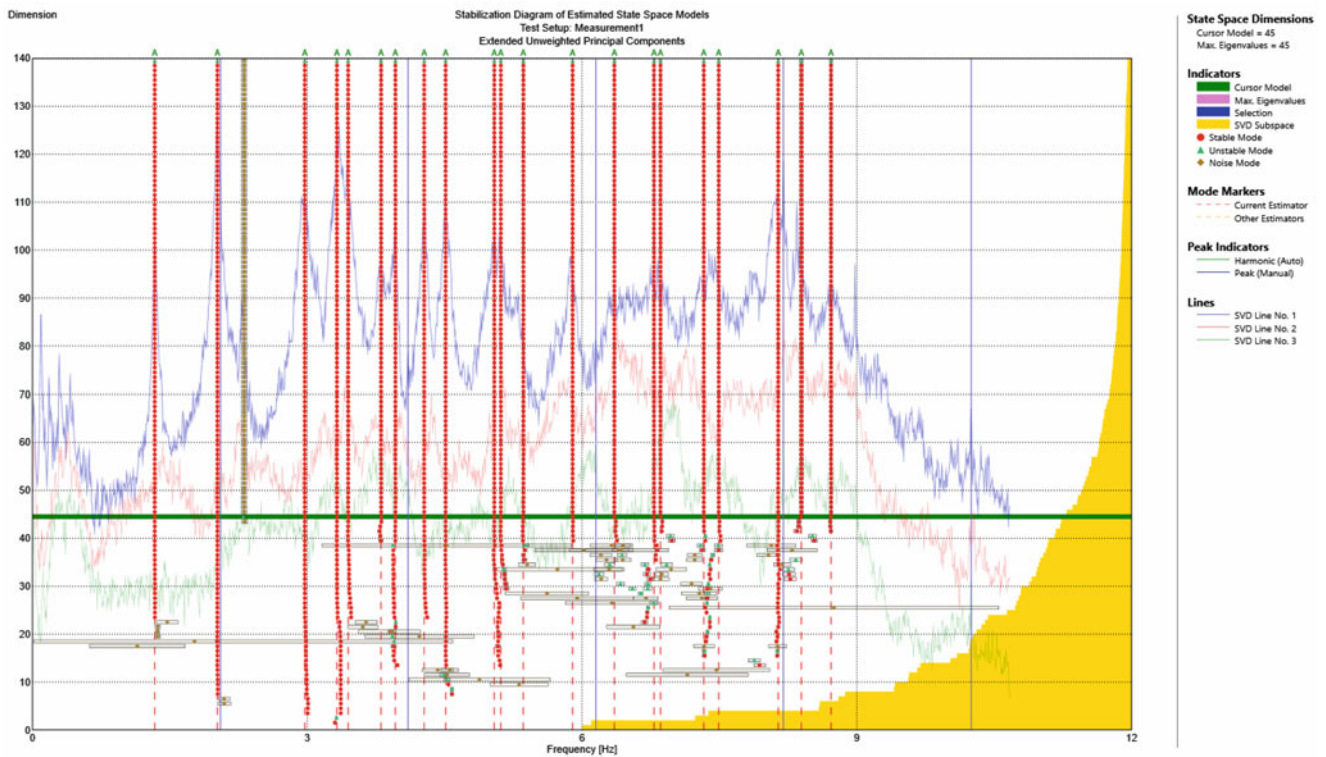


Fig. 7.10 Stabilization diagram of models obtained from data after the harmonic reduction. SSI-UPCX

4. Randall, R., Coats, M., Smith, W.: Repressing the effects of variable speed harmonic orders in operational modal analysis. *Mech. Syst. Signal Process.* **79**(Supplement C), 3–15 (2016). Special Issue from ICEDyn 2015
5. Jacobsen, N.J., Andersen, P., Brincker, R.: Using enhanced frequency domain decomposition as a robust technique to harmonic excitation in operational modal analysis. In: *Proceedings of the International Operational Modal Analysis Conference (IOMAC 2007)*, vol. 4 (2007)
6. Andersen, P., Brincker, R., Ventura, C., Cantieni, R.: Estimating modal parameters of civil engineering structures subject to ambient and harmonic excitation. In: *EVACES – 7th International Conference of Experimental Vibration Analysis for Civil Engineering Structures*, Porto (2007)
7. Gres, S., Andersen, P., Hoen, C., Damkilde, L.: Orthogonal projection-based harmonic signal removal for operational modal analysis. In: *IMAC – XXXVI International Modal Analysis Conference*, Orlando (2018)
8. Reynders, E., Pintelon, R., Roeck, G. D.: Uncertainty bounds on modal parameters obtained from stochastic subspace identification. *Mech. Syst. Signal Process.* **22**(4), 948–969 (2008). Special issue: Crack effects in rotordynamics
9. Döhler, M., Mevel, L.: Fast multi-order computation of system matrices in subspace-based system identification. *Control Eng. Pract.* **20**(9), 882–894 (2012)
10. Mellinger, P., Döhler, M., Mevel, L.: Variance estimation of modal parameters from output-only and input/output subspace-based system identification. *J. Sound Vib.* **379**(Supplement C), 1–27 (2016)
11. Döhler, M., Andersen, P., Mevel, L.: Variance computation of modal parameter estimates from UPC subspace identification. In: *IOMAC – 7th International Operational Modal Analysis Conference*, Ingolstadt (2017)
12. Structural-Vibration-Solutions, ARTEMIS Modal Pro 5.2 (2017)
13. Jacobsen, N.-J., Andersen, P.: Operational modal analysis on structures with rotating parts. In: *Proceedings of the International Conference on Noise and Vibration Engineering*, KU Leuven (2008)
14. Rosenow, S.-E., Uhlenbrock, S., Schlottmann, G.: Parameter extraction of ship structures in presence of stochastic and harmonic excitations. In: *Proceedings of the International Operational Modal Analysis Conference (IOMAC 2007)*, vol. 4 (2007)

# Chapter 8

## Characterization of Torsional Vibrations: Torsional-Order Based Modal Analysis



Emilio Di Lorenzo, C. Colantoni, F. Bianciardi, S. Manzato, K. Janssens, and B. Peeters

**Abstract** Torsional vibrations are angular vibrations of a rotating machine, typically a shaft along its axis of rotation. When these vibrations are amplified, they could lead to comfort, efficiency, noise or coupling wear problems. Torsional vibrations are important in cases in which the power needs to be transmitted using a rotating shaft or couplings, such as in the case of automotive, truck and bus drivelines, marine drivelines or power-generation turbines. Their characterization both in terms of frequency and damping ratios is quite difficult since they are influenced by several parameters such as material properties and operating conditions (temperature, load, rpm, etc). New powertrain designs, such as start-stop systems, downsized engines and lighter powertrains, increase the importance of developing an in-depth understanding of torsional vibrations. These are the main reasons behind the development of the so-called Torsional-Order Based Modal Analysis (T-OBMA) technique. As its name suggests, this technique is based upon the Order-Based Modal Analysis (OBMA) technique that showed to be very powerful for identifying the modal parameters in operational conditions in case of rotating machines during transient operations. The classical OBMA is performed by measuring both the rotational speed (by means of zebra tapes or digital encoders) and some other quantities in several points on the structure itself (accelerations, deformations, etc.). On the other hand, T-OBMA is focused on the identification of the torsional modal parameters by measuring only the rotational speed in two or more points along a driveline. The technique has been validated both in a simulation environment and in a real test scenario. In this paper the main outcomes of the simulations will be explained and the guidelines to apply it in a rotating machinery context for torsional vibrations identification will be listed.

**Keywords** Order-based modal analysis · Torsional vibrations · Order tracking · Operational modal analysis · Rotating machines · Powertrain analysis

### 8.1 Introduction

An important subject of current research is the reduction of vehicle weight which helps to improve its performance and to reduce fuel consumption. However, these improvements cause a negative effect in terms of noise and vibration. In fact, systems which have been optimized for weight and efficiency tend to be highly sensitive to excitation. A major source of noise and vibration in a vehicle is the driveline system which is defined as the assembly of all the subcomponents from the engine to the contact between the tires and the road. These vibrations could be transmitted to the chassis causing a deterioration in the passenger comfort. One of the most important vibrational phenomena is connected with the natural frequencies of the driveline which should not coincide with the engine torque harmonics or other excitation sources. Among the others, the torsional resonances are very critical as well known in the automotive industry. Many researchers have looked into the torsional vibrations problem for different kind of systems such as trucks, tractors and cars drivelines. The so-called torsional dampers have been incorporated in the drivelines in order to improve their torsional behavior.

Due to the complexity of the powertrain system, many studies have aimed to understand very specific problems. Several publications [1, 2] have modeled the automotive driveline systems as a set of inertia discs representing rotating masses linked by linear springs simulating the torsional stiffness of the rotating shafts. The driveline system is highly nonlinear, lightly damped and excited by both engine and road inputs [3]. The exclusions of nonlinearities could lead to erroneous results [4]. In large engines, such as those used in marine applications, the torsional natural frequency of the crankshaft is

---

E. Di Lorenzo (✉) · F. Bianciardi · S. Manzato · K. Janssens · B. Peeters  
Siemens Industry Software NV, Leuven, Belgium  
e-mail: [emilio.dilorenzo@siemens.com](mailto:emilio.dilorenzo@siemens.com)

C. Colantoni  
Department of Mechanical and Aerospace Engineering, University of Rome “La Sapienza”, Rome, Italy



so low that even lower order critical speeds could fall within the operating speed range. On the other hand for small engines like the ones used in automotive applications, the torsional natural frequency of the crankshaft is comparatively higher and, as consequence, only higher orders critical speeds are a problem. If the engine has a higher number of cylinders (e.g. high performance luxury cars), the torsional natural frequency could lead to comfort issues [5].

The aim of this paper is the dynamic characterization of torsional vibrations of rotating machines in operating conditions by means of modal analysis techniques. In fact the modal analysis is an efficient tool to describe in depth the structural dynamic behavior of a system through the estimation of the modal parameters as natural frequencies, damping ratios and mode shapes. Two different techniques have been used: Operational Modal Analysis (OMA) and Order-Based Modal Analysis (OBMA). The advantages and drawbacks of both techniques will be underlined in a simulation environment. OMA has several limitations in case of rotating machines and, for this reason, the OBMA technique has been chosen to be extended to torsional measurements. This technique allows the identification of torsional modes of a shaft. The first step consists in the orders estimation from the rpm (revolutions-per-minute) measured trace. In other words, instead of analyzing acoustics or vibration channels, the Torsional-Order Based Modal Analysis (T-OBMA) takes into account only the measured tachometer signals. If these are measured with a good accuracy, the torsional modes can be identified in terms of natural frequencies and damping ratios.

## 8.2 Operational Analysis Techniques

The dynamic characterization of structures in operating conditions is a challenging step. The purpose of this section is to introduce the analysis techniques which allow to characterize the dynamic behavior of systems in operational conditions. Operational Deflection Shapes (ODS) are widely used in the industrial domain to visualize the deformation of the structure at certain critical frequencies. This technique is not able to identify the modal parameters and for this reason Operational Modal Analysis (OMA) is often used for the dynamic characterization of big and complex structures [6]. It is also known as output-only modal analysis because it is based only on measurements of the response of the system without the need of measuring the forces acting on it. In previous works, the limitations of using OMA in a rotating machine context have been highlighted [7]. This is the motivation behind the formulation of Order-Based Modal Analysis (OBMA) technique which was further developed in next works [8]. This technique is based on the hypothesis that the most dominant source of excitation is a rotating force. It has been demonstrated that this technique is able to characterize the dynamic behavior of rotating machines [9]. In this paper this technique will be extended to torsional measurements and, from here, the name of Torsional-Order Based Modal Analysis (T-OBMA).

### 8.2.1 Operational Deflection Shapes

Traditionally, an Operational Deflection Shape (ODS) is defined as the deflection of a structure at a particular frequency of excitation. In general, an ODS can be defined as any motion of two or more points on a structure produced by a certain excitation. It contains both forced and natural vibration components. This is the main difference between a deformation pattern obtained with ODS and a mode shape that is an inherent characteristic of the structure and contains only natural (resonant) vibration components. The basis equation for ODS studies is the forced response which is expressed in Eq. (8.1).

$$\{U(\omega)\} = [H(\omega)] \{F(\omega)\} \quad (8.1)$$

In this equation the displacement vector  $\{U(\omega)\}$  is obtained as a multiplication in the frequency domain between the forces  $\{F(\omega)\}$  which are considered being unknown and the frequency response matrix  $[H(\omega)]$ . The most important thing to be noticed is that the frequency response function acts as a filter on the input force which results in some output response. If the excitation contains all the frequencies, all the modes will be activated and the response can be seen as a linear superposition of all these modes. In case of ODS, the excitation does not contain all frequencies, but only excites a single frequency line. In any case all the modes contribute to the ODS.

### 8.2.2 Operational Modal Analysis

Although ODS represents a powerful tool for understanding the dynamic behavior of a system, it cannot be used for troubleshooting and root-cause analysis. In fact it becomes quite complicated to understand if the measured response is caused by the presence of a structural resonance or if it is due to the excitation or again to a combination of the two. For this reason, in order to determine the modal characteristics of a structure, Operational Modal Analysis was developed. In its first development, it was used for civil engineering structures like buildings, bridges and wind turbines. Today it is a well-established technique which is widely used for the dynamic identification of all kind of structures such as aircraft, helicopters, vehicles, ships, stadiums, bridges and any kind of industrial machinery. OMA replaces the classical experimental modal analysis for an accurate modal identification under operating conditions and when it is very difficult to artificially excite the structure. In general, we can state that the identification methods used for OMA are very similar to those for input-output modal analysis. The main difference lies in the fact that they are based on auto- and cross correlations in the time domain and on auto- and cross spectra in the frequency domain. On the other hand, the methods developed for classical modal analysis are based on the impulse and frequency responses respectively [10]. Under the assumption of white noise input, the output spectra can be modelled in a very similar way as Frequency Response Functions (FRFs). The FRF matrix  $H(\omega)$  is expressed in Eq. (8.2) as a function of the modal parameters.

$$[H(\omega)] = \sum_{i=1}^n \frac{\{v_i\} \langle l_i^T \rangle}{j\omega - \lambda_i} + \frac{\{v_i^*\} \langle l_i^H \rangle}{j\omega - \lambda_i^*} \quad (8.2)$$

$n$  is the number of complex conjugated mode pairs,  $*$  is the complex conjugate of a matrix,  $^H$  is the complex conjugate transpose (Hermitian) of a matrix,  $v_i$  are the mode shapes and  $l_i$  are the modal participation factors.  $\lambda_i$  are the poles which are related to the eigenfrequencies  $\omega_i$  and damping ratios  $\xi_i$  as shown in Eq. (8.3).

$$\lambda_i, \lambda_i^* = -\xi_i \omega_i \pm i \sqrt{1 - \xi_i^2} \omega_i \quad (8.3)$$

For stationary stochastic processes, the auto- and cross power spectral density matrix between the outputs  $S_{yy}$  is given in Eq. (8.4).

$$[S_{yy}(\omega)] = [H(\omega)][S_{uu}][H(\omega)]^H \quad (8.4)$$

$S_{uu}$  is the auto- and cross power spectral density matrix between the input forces. In case of operational data, the output spectra are the only available information and some hypothesis regarding the input forces need to be made. In fact, under the assumption of white noise inputs, the input matrix is not frequency dependent and equals a constant matrix. By combining Eqs. (8.2) and (8.4), the auto- and cross power spectral density matrix between the outputs can be decomposed in modal components, as shown in Eq. (8.5).

$$[S_{yy}(\omega)] = \sum_{i=1}^n \frac{\{v_i\} \langle g_i \rangle}{j\omega - \lambda_i} + \frac{\{v_i^*\} \langle g_i^* \rangle}{j\omega - \lambda_i^*} + \frac{\{g_i\} \langle v_i \rangle}{-j\omega - \lambda_i} + \frac{\{g_i^*\} \langle v_i^* \rangle}{-j\omega - \lambda_i^*} \quad (8.5)$$

$g_i$  are the so-called operational reference factors which are the corresponding of the modal participation factors in case of OMA. It is quite difficult to interpret their physical meaning because they are a function of the modal parameters of the system and the constant input spectrum matrix. The last equation is the basis for most of the frequency domain operational modal identification techniques. In all cases, the unknown input is assumed to be represented by white noise.

### 8.2.3 Order Based Modal Analysis

Both ODS and OMA have some limitations when the objective is the characterization of the dynamic behavior of rotating machines. Some of the peaks in the overall spectrum are originated from order components that suddenly stop at the maximum rpm. These components are identified as poles, while they are not physically present in the system. They have been named “end-of-order” related poles. Order Based Modal Analysis (OBMA) estimates the modal parameters of a structure

during a run-up or a run-down test by applying the curve fitting algorithms to the extracted orders instead than to the overall spectra. It can be assumed that the measured responses are mainly caused by the rotational excitation. Run-up and run-down can be assimilated to multi-sine sweep excitation in the frequency band of interest. Several observations need to be taken into account for applying the same OMA algorithms to the orders:

1. Displacement orders are proportional to the squared rotation speed and acceleration orders are proportional to the fourth power of the same rotation speed. The main difference is that in the classical modal analysis the acceleration FRFs are proportional to the squared frequency axis.
2. Complex upper and lower residuals, while in classical modal analysis they are real.
3. Complex participation factor both in classical modal analysis and in order based modal analysis.

Methods such as Operational Polymax are robust again these observations and they can be employed for estimating the modal parameters in case of rotating machineries by looking at the orders rather than at the spectra. Compared to other applications of order tracking, OBMA requires that the orders are calculated with respect to a reference signal  $\Theta_m(t)$  which is synchronous with the excitation coming from the rotating source. This signal has been chosen as a sine sweep with frequency equal to the instantaneous rotational speed  $\omega(t)$  of the machine multiplied by the order  $o_m$  which is being extracted, as shown in Eq. (8.6).

$$\Theta_m(\tau) = \cos\left(\int_0^\tau o_m \omega(t) dt\right) \quad (8.6)$$

In all cases, the following steps need to be taken for applying with success the OBMA technique [11]:

- Measure the tachometer signal during run-up or run-down conditions:  
Several alternatives are possible. The sensors to be used are depending from both the application and the objective of the study. For this reason, several sensors can be found in the market with a huge variety of costs and performances. The best sensor can then be selected for each individual application based on the type of analysis, the accessibility of the shaft, the ease of instrumentation and the required accuracy or level of detail. Some example of sensors are the magnetic pickups, zebra tapes, laser interferometers, low and high resolution encoders.
- Select the measurement points and the measurement sensors to be put on the structure:  
Several alternatives also in terms of sensors are available in the market. The most used ones are the accelerometers, but also velocity or displacement sensors or strain gauges could be used for modal analysis purposes.
- Use order tracking techniques for extracting the orders and select the proper phase reference channel:  
The best compromise in terms of resolution and noise has to be found. Both phase and amplitude are important. A very good phase reference channel synchronous with the rotational speed is needed.
- Use Operational Polymax to estimate the modal parameters:  
An estimation of natural frequencies, damping ratios and mode shapes can be obtained by using as input functions the orders instead than the spectra. Inputs remain unknown and the main assumption is that the input force is mainly due to the rotation.

In order to perform the third step, several order tracking techniques could be used. Previous works have shown that in some cases a technique could perform much better than another. In this work two different techniques have been used:

- Time domain sampling based Fast Fourier Transform order tracking (FS)
- Resampling based order tracking (AD)

### 8.2.3.1 Time Domain Sampling Based Fast Fourier Transform Order Tracking (FS)

The time domain sampling based Fourier transform order tracking requires time domain data sampled with constant time intervals. As its name suggests, it is based upon standard Discrete Fourier Transform (DFT) implementation on time domain data. This is the simplest and commonly applied digital order tracking technique. Since the Fast Fourier Transform (FFT) is the most computationally efficient algorithm to perform DFT, the signal is divided into a number of blocks with power of two blocksize. FFT is performed for each block and the results are displayed as FFT waterfall or spectrogram plot. The waterfall plot is a 3D plot in which the FFT spectra are displayed in cascaded form. It is quite useful for detecting the resonances while the machine speed sweeps through a certain frequency range. Another way to show the same kind of data is the so-called spectrogram. It is a 2D plot in which the horizontal axis represents the frequency and the vertical one the time or rotational speed. The amplitudes of the FFT are color coded. Figure 8.1 shows an example of both plots for the same case.

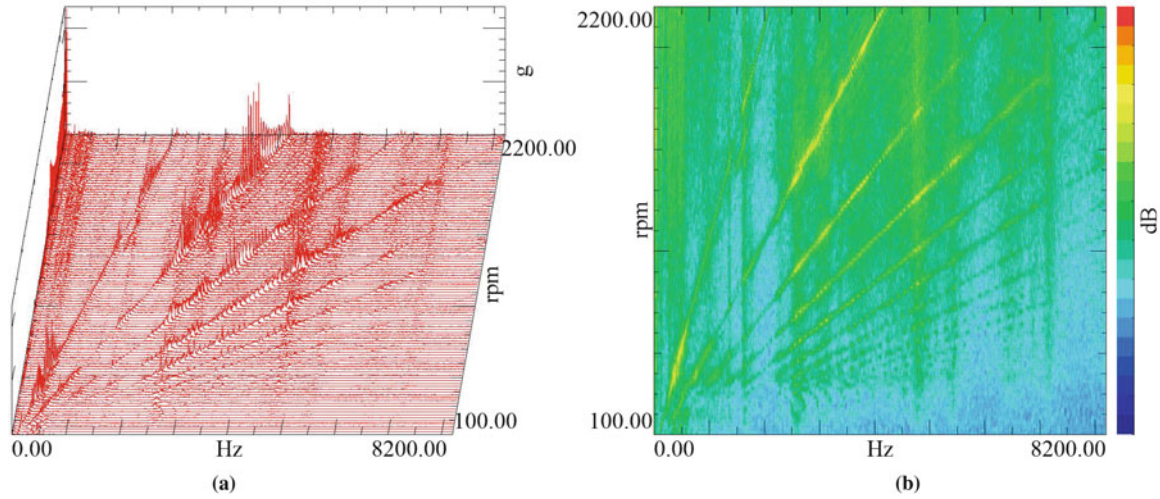


**Fig. 8.1** Fixed Sampling order tracking processing. (a) Waterfall plot. (b) Colormap plot

Each of the FFT is calculated by considering an average rpm value over the selected block. The FFTs appear to be horizontal lines in both the colormap and waterfall plot. The rpm step defines the rpm interval between two consecutive FFTs. Of course, Finally, the order, in terms of amplitude and phase, can be extracted from the FFT spectra. The FFT kernel is given in Eq. (8.7).

$$\begin{aligned}
 a_m &= \frac{1}{N} \sum_{n=1}^N x(n\Delta t) \cos(2\pi \frac{k}{p} n\Delta t) \\
 b_m &= \frac{1}{N} \sum_{n=1}^N x(n\Delta t) \sin(2\pi \frac{k}{p} n\Delta t)
 \end{aligned} \tag{8.7}$$

$N$  is the number of time blocks and  $n\Delta t$  represents the  $n$ th time interval. The extracted orders do not normally fall on a single spectral lines. For this reason, often multiple spectral lines are summed together. The main advantage of this method is its computational efficiency. Several drawbacks could be listed. First of all, the blocksize (time interval) is not related to the rpm of the machine. This cause problems both at low and high rotational speed. In fact, at low speeds, the interval is too short to capture the low orders resulting in power leakage (smearing) between closely-spaced orders. At high speeds, the interval is too long to capture rapid variations and spikes in the signal. For minimizing the smearing problem, a Hanning window is typically applied.

### 8.2.3.2 Resampling Based Order Tracking (AD)

The time domain sampling based FFT order tracking (FS) has several drawbacks. Some of these can be solved by resampling from time to angle domain before applying the FFT to the acceleration signals. Assuming that the blocksize remains constant, the resampling implies that the signal is now sampled at a constant  $\Delta\theta$  rather than at a constant  $\Delta t$ . The resampling process requires some computational time and it includes two main steps: oversampling and then interpolating in order to get the required  $\Delta\theta$ -spaced samples. As the technique is based on the angle information, a very accurate tachometer signal is needed in this case. In fact, the resampling intervals are calculated by integrating the speed signal. After the resampling step, the variable-frequency order components are converted into regular sinusoidal signals. The DFT (or FFT) can then be used to process the resampled data and to obtain the order components as spectral lines since the transformation is based on angle domain data rather than time domain data. The kernels of the FFT are reformulated from Eq. (8.7) and they are reported in Eq. (8.8).

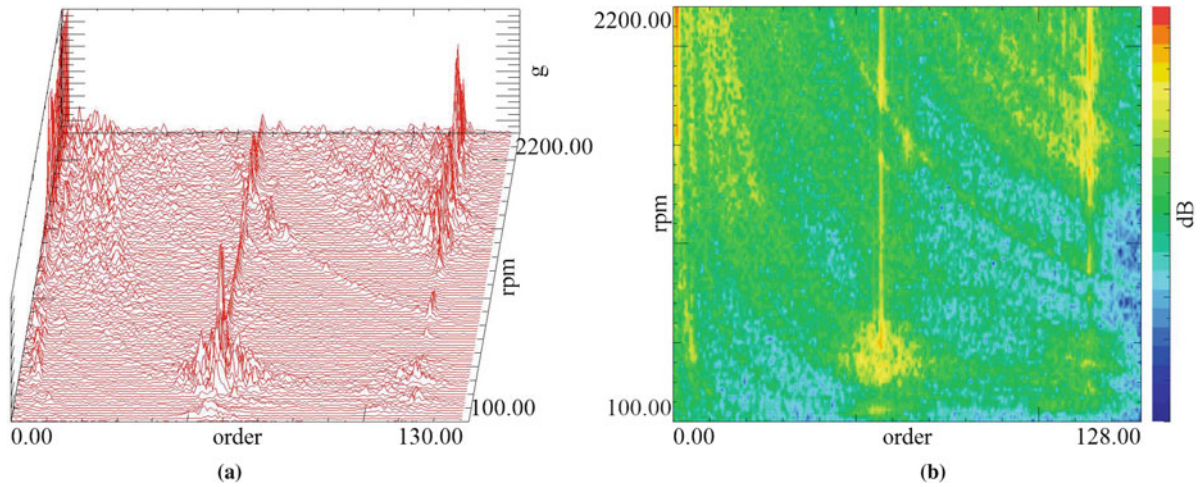


**Fig. 8.2** Resampled order tracking processing. (a) Waterfall plot. (b) Colormap plot

$$a_m = \frac{1}{N} \sum_{n=1}^N x(n\Delta\theta) \cos(2\pi \frac{k}{p} n\Delta\theta) \quad (8.8)$$

$$b_m = \frac{1}{N} \sum_{n=1}^N x(n\Delta\theta) \sin(2\pi \frac{k}{p} n\Delta\theta)$$

In this case,  $n\Delta\theta$  represents the  $n$ th angular interval. The order resolution  $\Delta o$  can be found in a similar way to the frequency resolution  $\Delta f$  as the reciprocal of the total angle of rotation of the machine (Eq. 8.9).

$$\Delta o = \frac{1}{N\Delta\theta} \quad (8.9)$$

An equivalent Nyquist-Shannon sampling theorem can be stated in the order domain (Eq. 8.10).

$$o_{Nyq} = o_s = \frac{1}{2\Delta\theta} \quad (8.10)$$

$o_s$  is the angular sampling rate and  $o_{Nyq}$  stands for the angular Nyquist rate which corresponds to the maximum order which can be processed. It must be noticed that by choosing  $N$  such that an integer number of revolutions is described, then the smearing problem is minimized even without using any window. On the other hand, if non-harmonic components are present, then a smoothing window is required. For FFT algorithm that needs a power of 2 as blocksize, the zero-padding can be used in order to provide extra samples beyond the integer number of revolutions. Figure 8.2 shows a waterfall and a colormap for the same case analyzed in Fig. 8.1 for the FS case.

The key property of angle domain data is that an order during run-up or coast-down conditions becomes constant in frequency relative to the sample rate. In other words, the order now falls on a single spectral line for all time values. Several drawbacks are still present. In fact, orders can only be tracked with reference to one rotating shaft and it is quite complicated to distinguish among crossing orders. Another limitation is due to the finite order resolution which makes the analysis of orders which do not fall on a spectral line very difficult. Furthermore, the resampling step can be quite time consuming in some cases.

### 8.3 Torsional-Order Based Modal Analysis

The classical Order Based Modal Analysis (OBMA) is performed by measuring both accelerations acquired on the structure by means of accelerometers and the rotational speed. The measurement of the rotational speed can be done by using several types of sensors (e.g. zebra tapes, encoders). The Torsional-Order Based Modal Analysis (T-OBMA) has the objective

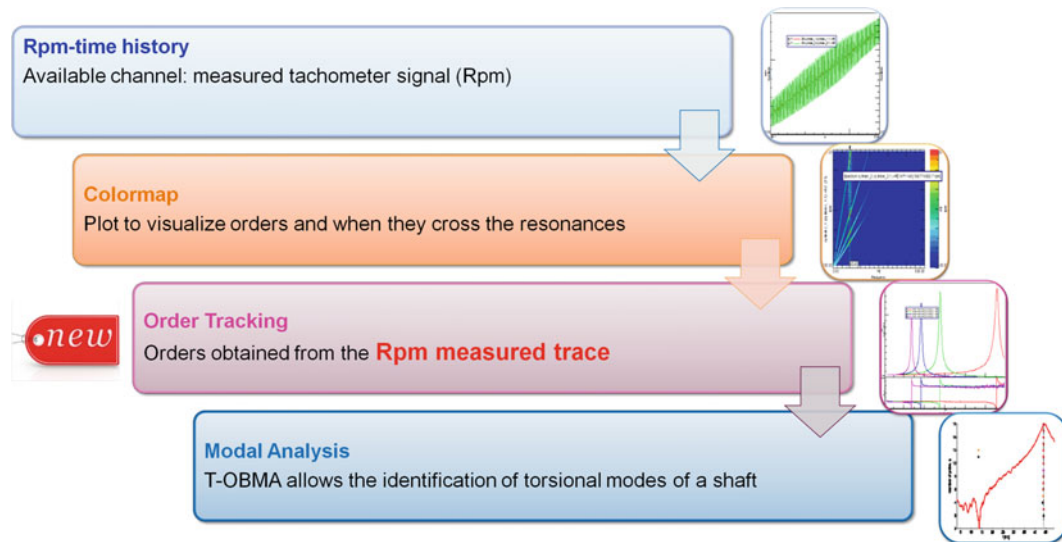


**Fig. 8.3** Torsional – order based modal analysis flow chart

to identify the torsional modal parameters by measuring only the rotational speed. This means that the only available measurement channels for this kind of analysis are the tachometer signals. The flowchart of the T-OBMA technique is shown in Fig. 8.3.

The first step consists in the measurement of the rpm signal from which the so-called colormaps can be calculated to visualize the main orders to be extracted. These orders have an amplification in correspondence of the natural frequencies. Order tracking algorithms can then be applied to extract these orders which are then used in the modal analysis step. Operational Polymax is applied on the orders for estimating the modal properties such as natural frequencies, damping ratios and mode shapes. The final step consists in the validation of the obtained modal parameters with respect to the measured data. Since the OBMA technique does not suffer of the so-called “end-of-order” effect and its main hypothesis is that the dominant excitation source is the rotational one, then it becomes obviously the best candidate to be used in case of torsional vibrations analysis.

### 8.3.1 Multi-orders Algorithm

There are two different ways to perform the analysis. The first and simplest way applies the technique order by order. This could be the case of very well separated orders like in case of gears in which the main orders are related to the number of teeth. If a gear has 57 teeth, then the main orders will be order 57, 114 and so on. This is not the case of engine orders. In fact in this case the main orders are quite low and very close to each other (e.g. order 2, 4, 8 and so on are the most excited ones). In case of experimental data, performing an order by order analysis leads to a resonance frequency shift due to the fact that each order “sweeps” with a different sweep rate through the frequencies. This case can be compared to the case in which different sine sweeps are applied to a structure by means of a shaker. Sweeping too fast through the frequencies will cause a shift of the peaks due to the fact that the system does not have the time to stabilize at a certain frequency. It is then quite difficult to state which order is the most reliable one for describing the torsional behavior of the system under test. The phase shift will not allow to perform a simple sum of the orders. For this reason the so-called “Multi-orders algorithm” has been formulated. The algorithm is based on four main steps:

1. Select the frequency band of interest (the torsional resonance should be included in the selected range).
2. Resample the orders which are fully included in this range such that each of them has the same number of samples.
3. Create an order matrix considering all the orders included in the band of interest and all the measurement points.
4. Apply Order-based Polymax to identify natural frequency and damping ratio of the torsional resonance.

It is better to do not consider orders which are ending within the selected frequency band to avoid issues in the modal parameter estimation step. The orders will be placed along the columns of the so-called order matrix. The number of columns

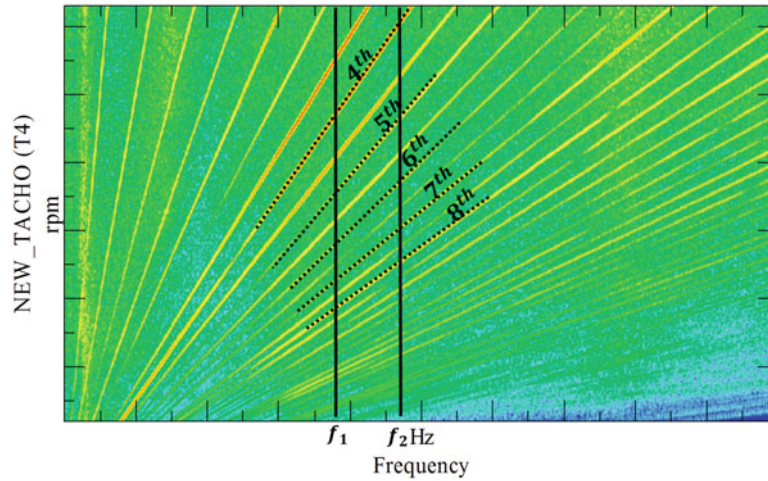


**Fig. 8.4** Multi-orders algorithm colormap

$n_{col}$  will be equal to the number of measurement points  $n_{dof}$  multiplied by the number of orders  $n_{ord}$  lying in the frequency band of interest, as shown in Eq. (8.11).

$$n_{col} = n_{dof} * n_{ord} \quad (8.11)$$

Figure 8.4 shows the colormap during an experimental measurement campaign in which five orders included in the selected frequency band  $[f_1 - f_2]$  are considered and then resampled to identify the torsional resonance by means of T-OBMA.

It has been proven both numerically and experimentally that this algorithm gives much more reliable results than the T-OBMA applied to a single order because of the added information coming from different orders at the same time.

## 8.4 Application Cases

### 8.4.1 Simulated Example

One of the most common approaches to model a rotating machine consists in using lumped parameter models. Lumped-mass models are idealized systems composed of rigid masses connected by massless springs and dampers. These kind of models allow to perform faster simulation studies if compared with distributed-mass models. In this section the results of virtual tests performed on simulation models will be illustrated. Orders have been introduced in the lumped parameters models by means of an unbalance systems and a mathematical increasing function, as shown in Fig. 8.5.

As first step, a 1 Degree-Of-Freedom (DOF) system has been modeled using LMS Virtual.Lab in a Motion environment. The lumped system is composed of two cylinders supported by radial bush elements (similar to bearings), which have stiffness and damping values in each direction ( $x, y, z$  for the translations and  $R_x, R_y, R_z$  for the rotations). In addition they have been linked by a radial bush element with high torsional stiffness value, to simulate a torsional spring, as shown in Fig. 8.6.

This first simple step serves as evaluation step for establishing the procedure to follow for characterizing the torsional behavior of rotating structures in the experimental world. Both order tracking techniques have been applied and modal parameters have been extracted by using Operational Polymax. In Fig. 8.7, the red curve shows the input signal which simulates the run-up applied to the driving shaft's edge. On the other hand, the green curve shows the driven shaft response. Amplified oscillations are clearly visible in correspondence of the resonance frequency zone. The colormap shows the four excited orders and their amplification when crossing the natural frequency, identified by the vertical line. In this specific case the rpm function goes from 0 to 6000 rpm in 1980s.

Figure 8.8 shows the extracted orders by means of AD technique. Finally Table 8.1 summarizes the results in terms of natural frequency and damping ratio for each technique and by using an order by order post-processing. These modal

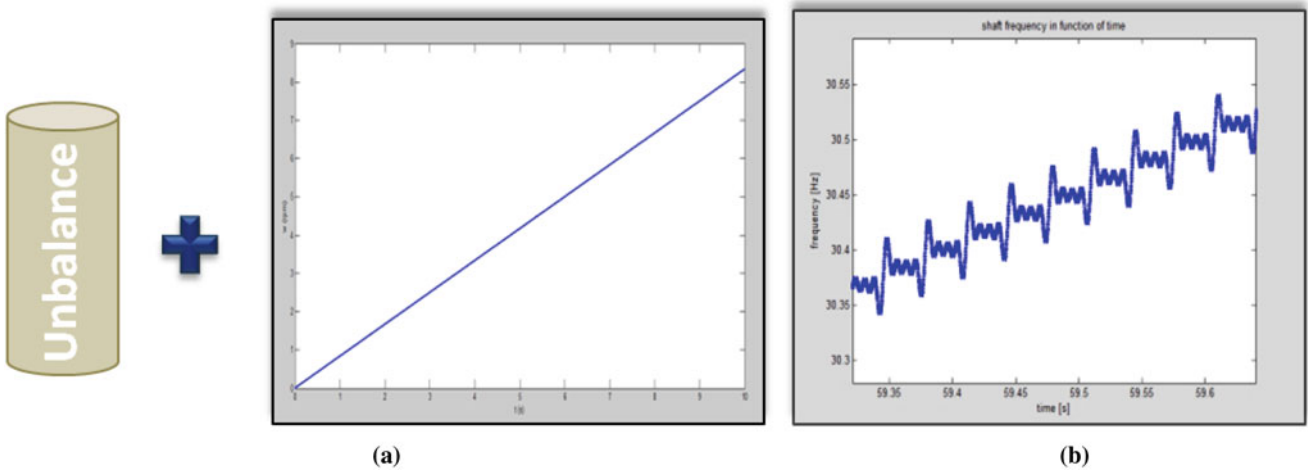


Fig. 8.5 Methods to generate simulated orders. (a) Unbalance and increasing function. (b) Mathematical increasing function with 4 orders

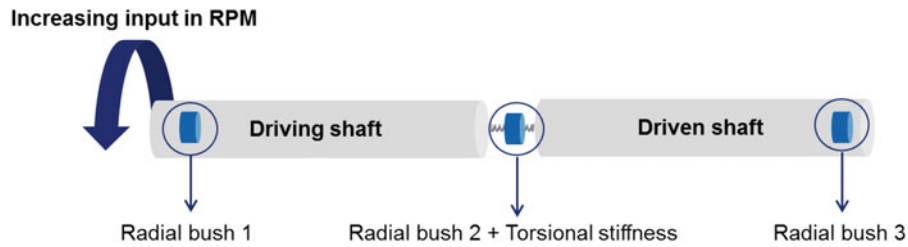


Fig. 8.6 Lumped system

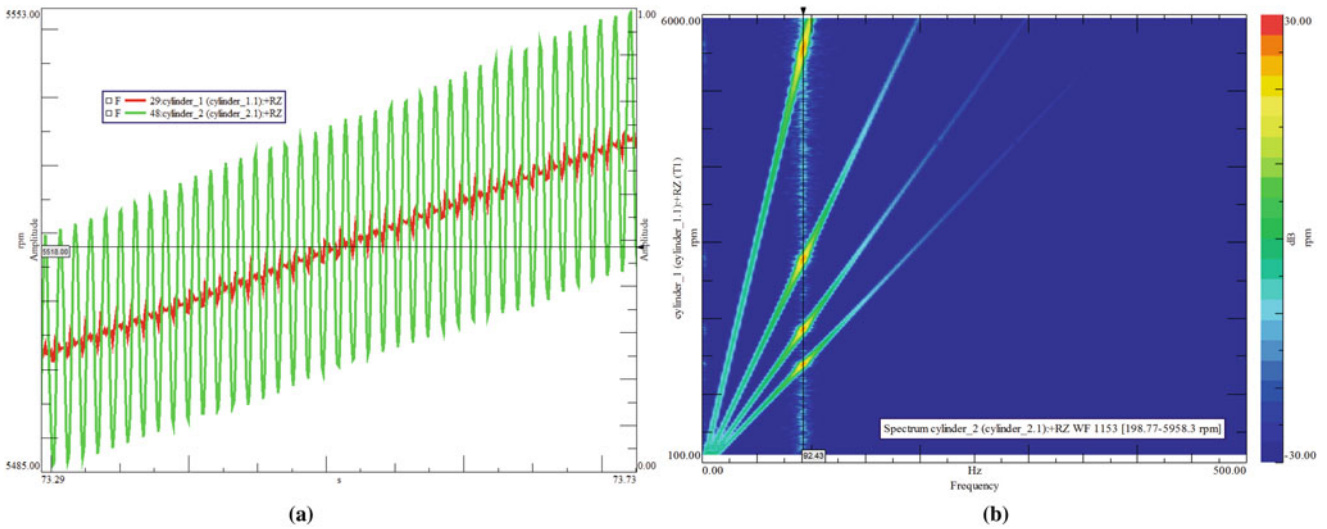


Fig. 8.7 Response of the system at the torsional resonance. (a) Time history at resonance zone. (b) Colormap

parameters are compared with the simulation model natural frequency and damping ratios. A very good match has been found in this case which means that the T-OBMA technique allows identifying the torsional modal parameters of the lumped system.

In order to increase the complexity of the model, a 4 DOF system has been built by using LMS Virtual.Lab. Four lumped masses are linked by bush elements with the torsional stiffnesses. The colormaps in Fig. 8.9 show the 4 orders by considering the three measurement channels (three driven shafts responses). This figure shows clearly that a single channel (rpm measurement point) is enough for identifying all the torsional natural frequencies of the system.



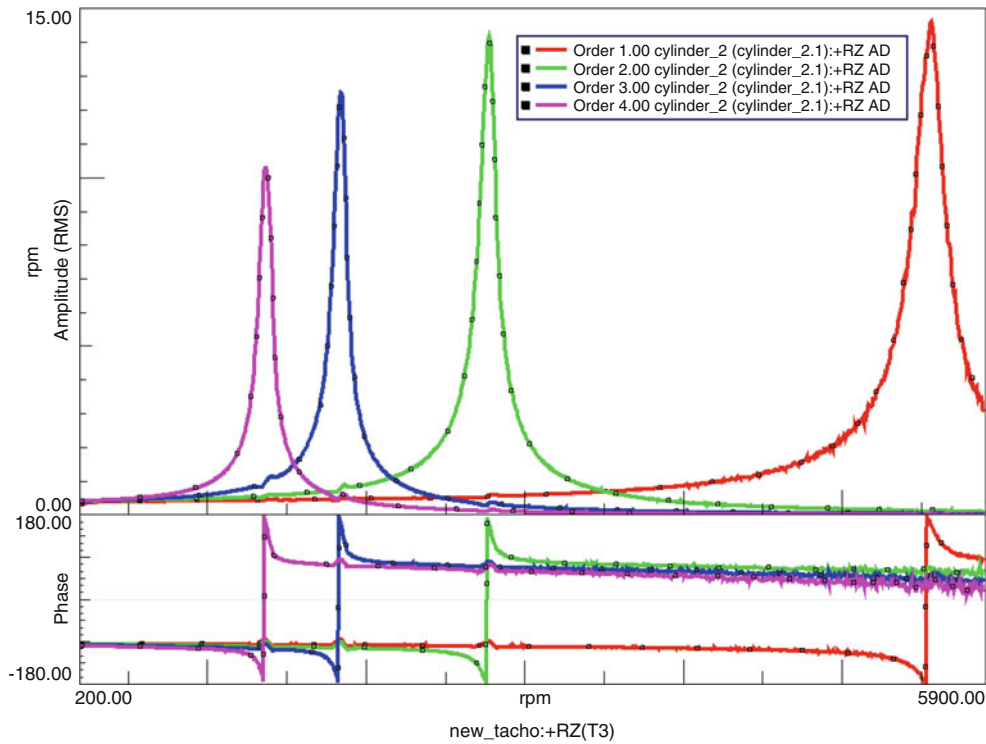


Fig. 8.8 Angle domain orders for a 1 DOF system

Table 8.1 Comparison of modal parameters: AD, FS and LMS virtual.lab

	Angle domain		Fixed sampling		LMS virtual.lab	
	Natural frequency	Damping ratio	Natural frequency	Damping ratio	Natural frequency	Damping ratio
Order 1	92.52 Hz	1.32 %	92.45 Hz	1.41%	92.44 Hz	1.59 %
Order 2	92.20 Hz	1.40 %	92.51 Hz	1.47%		
Order 3	91.82 Hz	1.53 %	92.57 Hz	1.49%		
Order 4	91.27 Hz	1.91 %	92.60 Hz	1.56%		

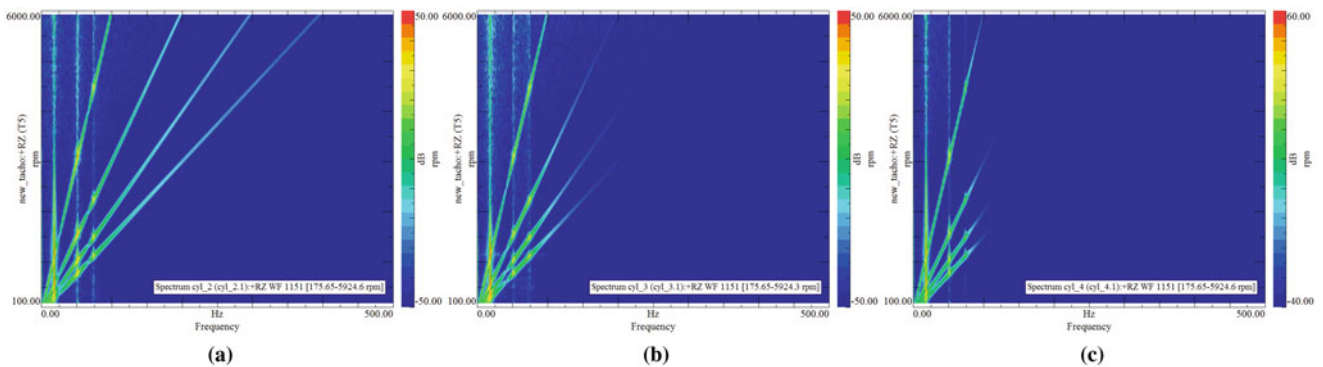
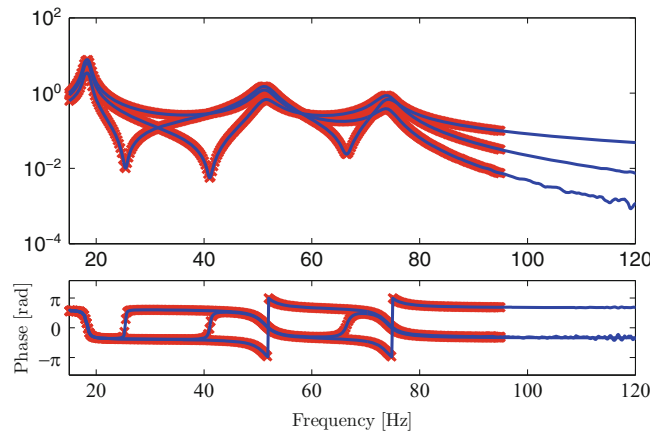


Fig. 8.9 4 DOF system: colormap for each cylinder. (a) Cylinder 2. (b) Cylinder 3. (c) Cylinder 4

In fact, each channel shows three clear peaks for each order in correspondence of the three expected resonances. Since the results of FS and AD techniques were coinciding for the 1 DOF case, for this case only the result of FS are compared with the LMS Virtual.Lab natural frequencies and damping ratios. Also in this case T-OBMA allows to obtain the true modal parameters, as shown in Table 8.2.

**Table 8.2** Comparison of modal parameters: FS and LMS virtual.lab

	Fixed sampling		LMS virtual.lab	
	Natural frequency	Damping ratio	Natural frequency	Damping ratio
Order 1	18.32 Hz	1.90 %	18.27 Hz	1.64 %
	51.26 Hz	3.36 %	51.23 Hz	3.36 %
	74.00 Hz	2.28 %	74.04 Hz	2.30 %
Order 2	18.28 Hz	1.91 %		
	51.28 Hz	3.35 %		
	73.99 Hz	2.30 %		
Order 3	18.00 Hz	1.97 %		
	51.21 Hz	3.30 %		
	73.94 Hz	2.28 %		



**Fig. 8.10** Multi-orders algorithm: comparison between measured and resampled orders

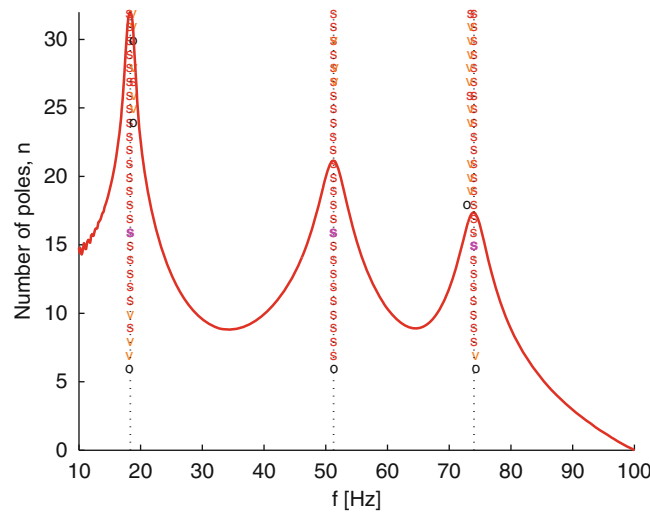


**Fig. 8.11** Multi-orders algorithm: stabilization diagram

This example can be used for validating the Multi-orders algorithm. Figure 8.10 shows the same order for different measurement channels before and after the resampling step. It confirms that the resampling step has been performed in the correct manner. Figure 8.11 shows the stabilization diagram obtained after having applied the multi-orders algorithm. The three main resonances are very well identified with a perfect match with the LMS Virtual.Lab natural frequencies and damping ratios, as shown in Table 8.3.

**Table 8.3** Comparison of modal parameters: Multi-orders and LMS virtual.lab

Multi-orders		LMS virtual.lab	
Natural frequency	Damping ratio	Natural frequency	Damping ratio
18.34 Hz	1.78 %	18.27 Hz	1.64%
51.26 Hz	3.39 %	51.23 Hz	3.36 %
73.99 Hz	2.30 %	74.04 Hz	2.30 %

**Fig. 8.12** Torsional mode in the experimental case



#### 8.4.2 Experimental Case

A first experimental validation of the Torsional-Order Based Modal Analysis has already been performed on a car engine on a test bench during run-up tests. The rotational speed has been measured at the two edges of the crankshaft (Rear and Front). Data have been analyzed by using the Multi-orders algorithm. The first torsional resonance has been identified together with the damping ratio by a very clear stabilization diagram obtained by applying the Order-based Polymax algorithm. The presence of a torsional damper (mass-spring-damper system that allows to split the high resonant peak into two different peaks at a lower amplitude) could be underlined by the high value of the damping for this mode. Finally the mode shape was plotted by using the so-called disk visualization. This clearly shows that the identified mode is related to a torsional mode. In fact the mode components related to the measurement points (Front and Rear) are out-of-phase as shown in Fig. 8.12, which is what typically happens for a torsional mode.

Figure 8.12 shows also the fact that the analyzed system is not fully symmetric between the Front and Rear part. This is due to the presence of a flywheel located close to the Rear part which moves the node of the first torsional resonance (which is theoretically placed in the middle of the shaft) close to the rear side of the shaft. This causes the difference in terms of amplitude between shafts edges. This flywheel is a counterweight and is a requirement to reduce torsional vibrations.

## 8.5 Conclusions

The challenge of this work is the extension of the OBMA to torsional vibrations problems (e.g. car engine). For this reason, the Torsional Order Based Modal Analysis (T-OBMA) technique has been developed. It allows the identification of torsional modes of a shaft by applying OBMA to orders obtained from the rpm measured traces. It takes into account only the measured tachometer signals. If these are measured with a good accuracy, the torsional modes identification in terms of natural frequencies and damping ratios can be performed. This tool will be helpful in the automotive domain, where the problem of torsional vibrations is quite important. The main objective is to fully understand and propose solutions (Multi-orders algorithm) to the limitations occurring when trying to apply Order Based Modal Analysis (OBMA) to rpm measurements. There are several parameters and considerations which must be taken into account when choosing the order tracking technique to apply to the acquired data. It is important to know which is the reason why an order tracking step is going to be performed. For instance, if the aim is the dynamic analysis of the rotating system by means of T-OBMA technique, then a particular care need to be reserved to the phase of the orders. In fact this is an essential part of the measurement function especially when curve-fitting methods are used afterwards (like in modal analysis). If the main scope is to analyze only at which frequencies orders are facing a resonance or at which frequency the highest order amplitude is obtained, then most of the techniques will be able to give these kind of information. Further steps to be performed in the future involve the validation of the approach on a FE simulation model and the validation in an experimental case in which the rpms are measured at several locations along the shaft (and not only at the edges of the shaft).

## References

1. Wu, H.L., Shao, C., Feng, Z.D.: A study of the torsional vibration of automotive power trains. In: Proceedings of 2nd International Pacific Conference on Automotive Engineering, Tokyo (1983)
2. Reik W.: Torsional vibrations in the drive train of motor vehicles. In: Proceedings of 4th LuK International Symposium, Baden-Baden (1990)
3. Centea, D., Rahnejat, H., Munday, M.T.: Non-linear multi-body dynamic analysis for the study of clutch torsional vibrations. *Appl. Math. Model.* **25**(3), 177–192 (2001)
4. Kushwaha, M., Gupta, S., Kelly, P., Rahnejat H.: Elasto-multi-body dynamics of a multicylinder internal combustion engine. In: Proceedings of the Institution of Mechanical Engineers (2002)
5. Rajendran, S., Narasimhan, M.V.: Effect of inertia variation due to reciprocating parts and connecting rod on coupled vibration of crankshaft. *J. Eng. Gas Turbines Power* **119**, 257–264 (1997)
6. Peeters, B., Van der Auweraer, H., Vanhollebeke, F., Guillaume, P.: Operational modal analysis for estimating the dynamic properties of a stadium during a football game. *Shock Vib.* **11**, 395–409 (2004)
7. Janssens, K., Kollar, Z., Peeters, B., Pauwels, S., Van der Auweraer, H.: Order-based resonance identification using operational polymax. In: Proceedings of 24th International Modal Analysis Conference (IMAC), Saint Louis (2006)
8. Di Lorenzo, E., Manzato, S., Vanhollebeke, F., Goris, S., Peeters, B., Desmet, W., Marulo, F.: Dynamic characterization of wind turbine gearboxes using order-based modal analysis. In: Proceedings of 26th International Conference on Noise and Vibration Engineering (ISMA), Leuven (2014)
9. Di Lorenzo, E., Manzato, S., Peeters, B., Marulo, F., Desmet, W.: Best practices for using order-based modal analysis for industrial applications. In: Proceedings of 35th International Modal Analysis Conference (IMAC), Los Angeles (2017)
10. Heylen, W., Lammens, S., Sas, P.: Modal Analysis Theory and Testing. KU Leuven, Department Werktuigkunde, Leuven (2007)
11. Di Lorenzo, E.: Operational Modal Analysis for rotating machines: challenges and solutions. Ph.D. thesis, KU Leuven, Leuven, Belgium and University of Naples “Federico II”, Naples (2017)



# Chapter 9

## Long-Term Automatic Tracking of the Modal Parameters of an Offshore Wind Turbine Drivetrain System in Standstill Condition

Mahmoud El-Kafafy, Nicoletta Gioia, Patrick Guillaume, and Jan Helsen

**Abstract** Modal behavior of a wind turbine is an important design aspect for tackling noise, vibration, and harshness (NVH) issues and validating complex simulation models. This paper focusses long-term modal analysis on an offshore wind turbine (OWT) in stand still conditions. It presents the results of an automated procedure to track the variation of the modal parameters of the drivetrain system of the OWT. The tracking focuses on the continuous monitoring of the resonant frequencies and damping values of the most dominant modes of the drivetrain unit during more than half a day of stand still. The long-term tracking of the natural frequencies and modal damping of the drivetrain vibration modes under distinct ambient conditions allows to better understand the dynamics of the drivetrain by gaining confidence in modal parameters estimated over multiple measurement blocks and helps in gaining understanding in the dynamics of the OWT. The used automatic tracking procedure is based on the well-known parametric operational modal analysis algorithm, pLSCF estimator. The experimental data used in this paper has been obtained during a long-term measurement campaign lasting 6 months on an offshore wind turbine with instrumentation directly mounted on the drivetrain. Both eigenfrequencies and damping values are of particular interest.

**Keywords** Modal parameters · Offshore wind turbine · Drivetrain · Operational modal analysis · Automatic mode tracking

### 9.1 Introduction

Wind power is the renewable energy that has seen the largest and most successful deployment over the last two decades, achieving 486.8 GW of global cumulative capacity at the end of 2016 [1]. More than 54 GW of clean renewable wind power was installed across the global market in 2016, which now comprises more than 90 countries. To reduce the cost of wind energy, the size of the offshore wind turbines has been increased in the last decades going from 5 kW rated power machines to the current 9.5 MW turbines. The bigger wind turbines have the advantage that they can harvest wind at higher altitudes, resulting in bigger wind speeds and allow the turbine to be equipped with bigger blades. Moreover, it is assumed that by decreasing the number of machines per Mega-watt the operations and maintenance costs of the wind park will decrease. On the other hand, bigger wind turbines and corresponding blades impose higher loads on the wind turbine components, amongst others on the drivetrain. Moreover, these loads cannot be assumed to be quasi-static as in most industrial applications. Wind turbine loading includes aerodynamic loads at variable wind speeds, gravitational loads and corresponding bending moments, inertial loads due to acceleration, centrifugal and gyroscopic effects, operational loads such as generator torque and loads induced by certain control actions like blade pitching, starting up, emergency braking or yawing [2–5]. These dynamic loads are significantly influencing the fatigue life of the wind turbine structural components. In addition to the tower and blades also the drivetrain has several structural components for which the design is fatigue driven, such as for example the torque arms of the gearbox. In addition to turbine reliability also noise and vibration (N&V) behavior is becoming increasingly important for onshore turbines [6]. Since aerodynamic noise is decreasing by means of improved blade designs, the problem

---

M. El-Kafafy (✉)  
Helwan University, Cairo, Egypt

Vrije Universiteit Brussel (VUB), Brussel, Belgium  
e-mail: [mahmoud.el-kafafy@vub.be](mailto:mahmoud.el-kafafy@vub.be)

N. Gioia · P. Guillaume · J. Helsen  
Vrije Universiteit Brussel (VUB), Brussel, Belgium

is shifting towards drivetrain tonalities. Accurate insights in the dynamic behavior are necessary to avoid these tonalities. This is because bigger turbines imply that the resonance frequencies of the drivetrain are decreasing towards the excitations coming from the wind turbine rotor and gears of the gearbox [5]. Therefore, the flexibility of the structural components of the drivetrain is becoming increasingly of influence on the dynamic design of the drivetrain [7]. Accurate knowledge about the resonance behavior of the drivetrain is as such essential for improved design both for fatigue and reliability as for noise. If resonances are coinciding with harmonic excitation frequencies, there is potential for increased fatigue life consumption and tonal excitation.

In general, one can say that an accurate prediction of the dynamic behavior of the bigger wind turbines is something mandatory since their components are becoming structurally more flexible to limit the weight, thus they can be resonated easily. Moreover, with the fact that the inspection and maintenance for the offshore installations are much more cumbersome and expensive than for onshore turbines, a remote monitoring application with the ability to track the structural changes/dynamic behavior in the different components of the offshore wind turbine can help to reduce O&M costs and assess the lifetime of these structures. For a certain component, the structural changes can be tracked by tracking the changes in so-called modal parameters (resonance frequencies, damping ratios, and mode shapes) of the fundamental vibration modes of that component. Those parameters are directly related to the physical/structural properties of the component under test. A continuous monitoring of the modal parameters of the fundamental vibration modes of the drivetrain's structures will allow us to verify the existing design assumptions and understand its dynamic behavior.

Normally, the identification of the modal parameters is done by means of the classical experimental modal analysis methods, but these methods cannot be applied to a structure like a wind turbine because the input force owing to the wind, waves, and the dynamic interaction between the different components cannot be measured. For this reason, operational modal analysis (OMA) methods were developed to identify the modal parameters from the response of a mechanical structure in operation to unknown random inputs [8–11]. OMA has proven its' use in aerospace and automotive and is increasingly used nowadays in the wind energy domain. OMA techniques work under the assumption that the system is linear time invariant and the input excitation has a white noise spectrum within the frequency band of interest. Owing to the presence of rotating components and their corresponding harmonic force contributions that do not comply with the operational modal analysis assumptions the identification process becomes difficult or impossible. The analysis in this paper is focused on a wind turbine in idling or parked conditions (not producing energy). This means that the risk of having some harmonic components in the frequency band of interest resulting from the rotating equipments is very low. Therefore, the white noise assumption in parked conditions is valid and operational modal analysis (OMA) is applicable. Also, this specific operating condition will have an impact on the modal behavior observed in the drivetrain, since the teeth can be out of contact during these conditions; whereas this is necessarily the case for nominal power production [12]. Moreover, the damping properties of the wind turbine will change according to the operating conditions [13].

There are different frequency ranges of interest for the wind turbine. The lower frequency range contains the more global modes of the wind turbine, such as the blade modes and the tower modes. The higher frequency ranges contain more localized modes for the drivetrain's components (e. g., the gearbox and generator). The analysis done in this paper is focusing on the higher frequency range that contains drivetrain modes. The results of a long-term automatic tracking of the fundamental vibration modes of an offshore wind turbine drivetrain system will be presented. The tracking is performed in terms of the resonance frequency, the damping ratio, and the mode shape for each mode.

## 9.2 Offshore Measurements

A long-term measurement campaign with duration of 6 months was performed on an offshore wind turbine with the instrumentation was limited to the drivetrain. The structure of the instrumented wind turbine and the locations of the sensors on the drivetrain system are represented in Fig. 9.1. In total 17 accelerometer channels were acquired. Fourteen channels were originating from accelerometers on the gearbox.

This consisted of 4 tri-axial sensors and 2 uni-axial sensors. One tri-axial accelerometer was placed on the generator unit. All accelerometers used were ICP accelerometers with a sensitivity of 100 mV/g. Three accelerometers had a high sensitive frequency range between 2 and 5000 Hz, whereas the other sensors were tailored for a range between 0.5 and 5080 Hz. It can therefore be stated that the measurement set-up was tailored towards the higher frequency range identification. In addition to detailed acceleration measurements, the speed of the wind turbine rotor is measured by means of an encoder at the low speed shaft with 128 pulses per revolution. The data-acquisition system measures continuously and sends data every 10 min with a sampling rate of 5120 Hz.

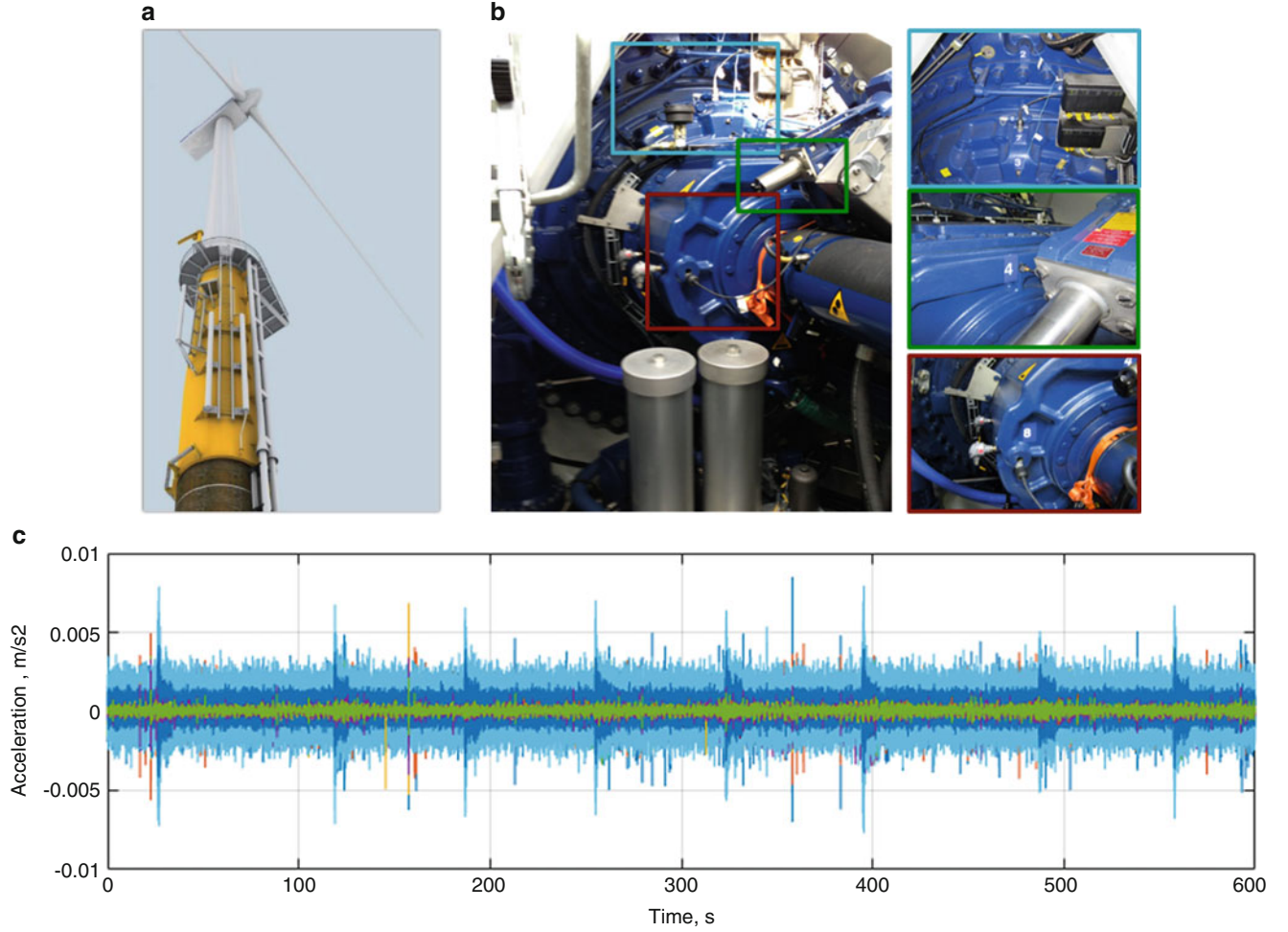


**Fig. 9.1** (a) The structure of the instrumented wind turbine; (b) Locations of the accelerometers on the drivetrain unit; (c) A typical measured acceleration signals

### 9.3 The Automatic Tracking Approach of the Drivetrain's Modal Behavior

In [14], a short-term automatic tracking of some of the drivetrain modes in a frequency band of 2–15 Hz was introduced, and it was shown that there are 10 physical vibration modes can be found in that frequency band. Therefore, in this paper and by means of the automatic mode tracking approach introduced in [14], those 10 physical modes of the drivetrain system will be tracked but over a longer period. The 3 steps of the used automatic mode tracking are illustrated in Fig. 9.2. In the first step, the time-domain data is loaded and transformed to the frequency-domain by calculating the power spectrum using the Periodogram approach [15, 16]. In the Periodogram approach, the time-domain data is divided into some overlapped blocks, and for each block the discrete Fourier transform (DFT) is calculated to obtain the spectrum. To reduce the leakage effects when applying the DFT, a Hanning window can be applied to each time-data block before the calculation of the DFT. The final power spectrum is taken as the average spectrum over the different processed time blocks as follows:

$$\widehat{S}_{\mathbb{Y}_o \mathbb{Y}_o}(\omega_k) = \frac{1}{N_b} \sum_{b=1}^{N_b} \mathbb{Y}_{ob}^w(\omega_k) \mathbb{Y}_{ob}^{w*}(\omega_k) \in \mathbb{R} \quad (9.1)$$

$$\widehat{S}_{\mathbb{Y}_o \mathbb{Y}_{ref}}(\omega_k) = \frac{1}{N_b} \sum_{b=1}^{N_b} \mathbb{Y}_{ob}^w(\omega_k) \mathbb{Y}_{Refb}^{w*}(\omega_k) \in \mathbb{C} \quad (9.2)$$

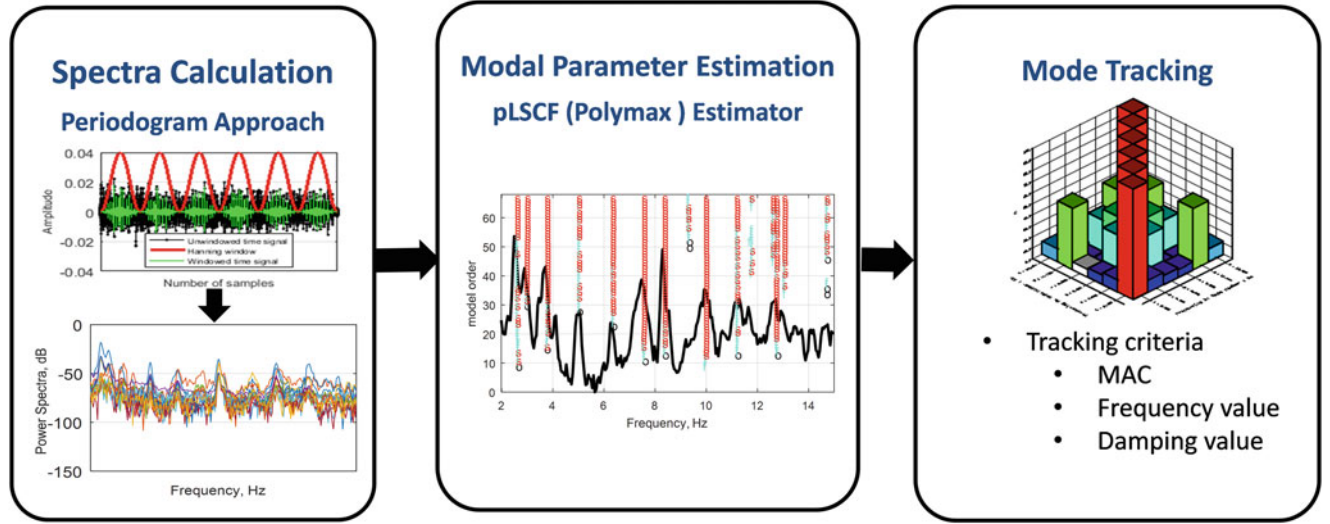


Fig. 9.2 The different steps of the automatic tracking procedure of the drivetrain modes [14]

with  $\widehat{S}_{Y_o Y_o}(\omega_k)$  the auto power spectra,  $\widehat{S}_{Y_o Y_{ref}}(\omega_k)$  the cross-power spectra calculated between the different channels and the channels taken as references,  $\omega_k$  the circular frequency in  $r/s$  at frequency line  $k$ ,  $N_b$  the number of the overlapped blocks,  $Y_{o_b}^w(\omega_k)$  the DFT of the  $b^{th}$  windowed time-domain data block of the  $o^{th}$  channel, and  $Y_{Ref_b}^w(\omega_k)$  the DFT of the  $b^{th}$  windowed time-domain data block of reference channel.

In the second step, the well-known operational pLSCF (Polymax) modal parameter estimator [17, 18] is applied to the calculated power spectra matrix to estimate the resonance frequencies, the damping ratios, and the mode shapes of the different physical modes in the selected frequency band. In the operational pLSCF modal parameter estimator, the following so-called right matrix-fraction model is assumed to represent the measured power spectra matrix:

$$S_{YY}(\omega_k) = \sum_{r=0}^n \Omega_k^r [\beta_r] \left( \sum_{r=0}^n \Omega_k^r [\alpha_r] \right)^{-1} \in \mathbb{C}^{N_o \times N_{ref}} \quad (9.3)$$

where  $[\beta_r] \in \mathbb{R}^{N_o \times N_{ref}}$  are the numerator matrix polynomial coefficients,  $[\alpha_r] \in \mathbb{R}^{N_{ref} \times N_{ref}}$  are the denominator matrix polynomial coefficients,  $n$  is the polynomial order,  $N_o$  is the number of measured outputs, and  $N_{ref}$  is the number of the channels taken as reference signals. The operational pLSCF (Polymax) estimator uses a discrete time frequency domain model (i.e. z-domain model) with  $\Omega_k = e^{-j\omega_k T_s}$  ( $\omega_k$  is the circular frequency in  $r/s$  and  $T_s$  is the sampling time). Equation (9.3) can be written for all the values of the frequency axis of the power spectra data. The unknown model coefficients  $[\beta_r]$  and  $[\alpha_r]$  are then found as the least-squares solution of these equations. Once the denominator coefficients  $[\alpha_r]$  are determined, the poles  $\lambda_i$  and the right eigenvectors  $V_i \in \mathbb{C}^{N_{ref} \times 1}$  are retrieved from these coefficients as the eigenvalues and the eigenvectors of their companion matrix. An  $n^{th}$  order right matrix-fraction model yields  $nN_{ref}$  poles. For a displacement output quantity, the full power spectrum can be written as a function of the modal parameters as follows [8, 18]:

$$\widehat{S}_{YY}(\omega_k) = \sum_{i=1}^{N_m} \frac{\psi_i g_i^T}{j\omega_k - \lambda_i} + \frac{\psi_i^* g_i^H}{j\omega_k - \lambda_i^*} + \frac{g_i \psi_i^T}{-j\omega_k - \lambda_i} + \frac{g_i^* \psi_i^H}{-j\omega_k - \lambda_i^*} \quad (9.4)$$

with  $g_i \in \mathbb{C}^{1 \times N_o}$  are the so-called operational reference factors, which replace the modal participation factors in case of output-only data,  $\psi_i \in \mathbb{C}^{N_o \times 1}$  the mode shapes, and  $N_m$  the number of the estimated modes. The operational reference factors  $g_i$  is a complex function of the spectral density matrix  $\widehat{S}_{YY}(\omega_k)$  of the random input force and the modal parameters of the structure under test, and they are simply the right eigenvectors  $V_i$  that are obtained from the companion matrix of the denominator coefficients  $[\alpha_r]$ . After getting the poles and the right eigenvectors from the denominator coefficients, the mode shapes can be calculated from Eq. (9.4) by solving a linear least-squares problem. When the number of the reference channels  $N_{ref}$  is not equal to the number of the outputs  $N_o$  a special implementation of Eq. (9.4) is needed to obtain the mode shapes.



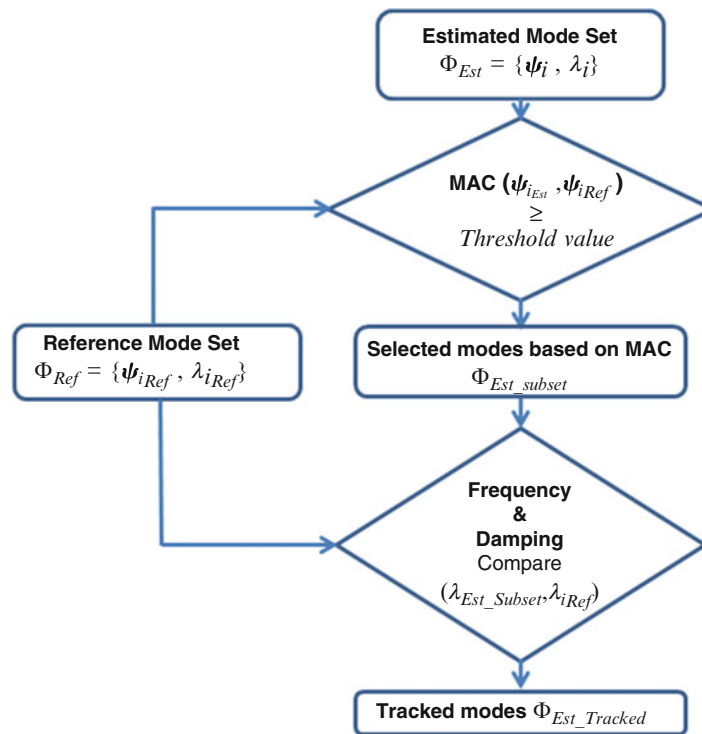


Fig. 9.3 Mode tracking criteria [14]

In the third step and after estimating the different modes by the operational pLSCF (Polymax) estimator, the 10 most dominant drivetrain's modes are tracked by comparing the modal parameters (frequencies, damping ratios, and mode shapes) of all estimated modes to the ones of the reference modes set. First, the Modal Assurance Criterion (MAC) is calculated between the estimated modes set and the reference modes set. The MAC value measures how coherent is the estimated mode with respect to the reference one in terms of the mode shapes. It has a value between 0 and 100% (zero value means not correlated modes at all while 100% means fully correlated modes). The estimated modes are filtered according to a user defined threshold value of the MAC (e.g. 50%). Then, the mode shapes-based selected subset of modes is compared to the reference modes in terms of the pole's value, which measures how coherent is the estimated mode with respect to the reference one in terms of the resonance frequency and damping ratio. The closest mode to the reference one in terms of resonance frequency and modal damping values is selected. Figure 9.3 shows a flow chart that represents the criteria that have been used in the tracking of the drivetrain's modal behavior.

## 9.4 Results and Discussions

A long-measured data record of a duration of 13.67 h, where the turbine was not producing power, has been processed using the tracking approach presented in Sect. 9.3. The full record is divided into 82 sub-records of 10 min each. All the sub-records are processed consecutively to track the modal parameters of the 10 most dominant vibration modes of the instrumented drivetrain unit. The reason behind the selection of those 10 modes amongst the other modes in the frequency band of interest was explained in [14]. For each 10-min data record the power spectra matrix is calculated, the Operational pLSCF (Polymax) estimator is applied to the calculated power spectra matrix with the aim to estimate the modal parameters of the drivetrain's vibration modes in the frequency band of interest, and the 10 most dominate modes are tracked by following the procedure shown in Fig. 9.3. Since the spatial resolution of the measured data is not that high due to the limited number of sensors, the modal assurance criterion (MAC) threshold value is relaxed (set to zero) in the tracking process.

The results of the continuous tracking for the selected 10 modes are shown in Fig. 9.4 in terms of the evolution of the resonance frequencies and damping ratios over the tracking period. One can see from Fig. 9.4 that the tracked modes are highly consistent in terms of the resonance frequency while their modal damping ratios show a high scatter behavior

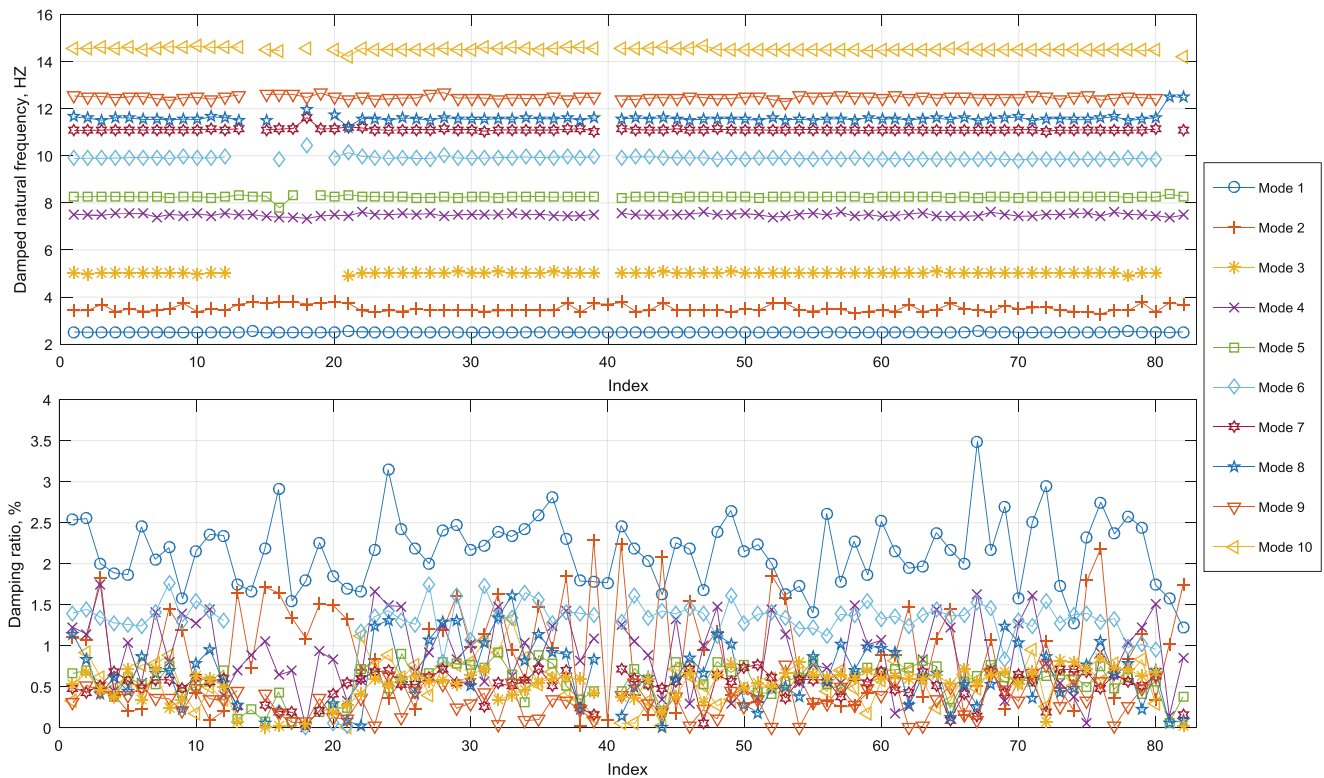


**Fig. 9.4** Evolution of the resonance frequencies (top) and damping ratios (bottom) of the 10 most dominant drivetrain modes during the tracking period

obviously for modes 1,2,4, and 8. This scatter behavior of the modal damping ratios could be explained by two facts. The first fact is that the wind turbine is a multi-physical machine with significant interaction between its subcomponents, and for the instrumented wind turbine the rotor is directly connected to the gearbox. This means that any change in the ambient conditions (e. g. wind speed) will affect the damping characteristics of the rotor and hence the same will happen for the drivetrain unit that is directly connected to the rotor. Therefore, the change in the ambient conditions plays a role in the variation pattern of the modal damping over the tracking period. The second fact that could help in understanding the scatter behavior of the tracked modal damping is that most of the identified modes are closely spaced modes. This can be seen in Fig. 9.5 that shows a typical stabilization chart constructed by the Operational pLSCF (Polymax) estimator when applied to one data record in the frequency band of interest. Identifying two closely spaced modes always increases the uncertainty, especially on the damping values.

A statistical analysis on the results obtained during the continuous monitoring is shown in Fig. 9.6, which illustrates one box and whisker plot per frequency and damping value of each tracked mode. These statistical results confirm the results shown in Fig. 9.4 where it can be seen from Fig. 9.6 that the frequency estimates are indeed more consistent than the modal damping estimates. In terms of the median value of the damping estimates, the results presented in Fig. 9.6 show a good agreement with the ones published in [14] that were obtained based on a short-term tracking. For the modal damping ratios, it can be seen from Fig. 9.6 that for most of the identified modes the distribution is symmetric around the median and the length of the tails is about the same length as the box. This gives indication that the damping estimates have a normal distribution over the tracking period.

Figure 9.7 shows the boxplot for the MAC value calculated with respect to the reference modes set per identified mode. The MAC evaluates the degree of correlation between the identified mode shape and the reference one. All the modes, except modes 2,4, and 8, show a high correlation with the reference mode shapes with a median value of MAC higher than 70%. The low MAC value of those 3 modes (i.e. 2,4, and 8) agrees with their results in terms of the damping estimates where they showed the highest scatter as it was shown previously in Fig. 9.6.

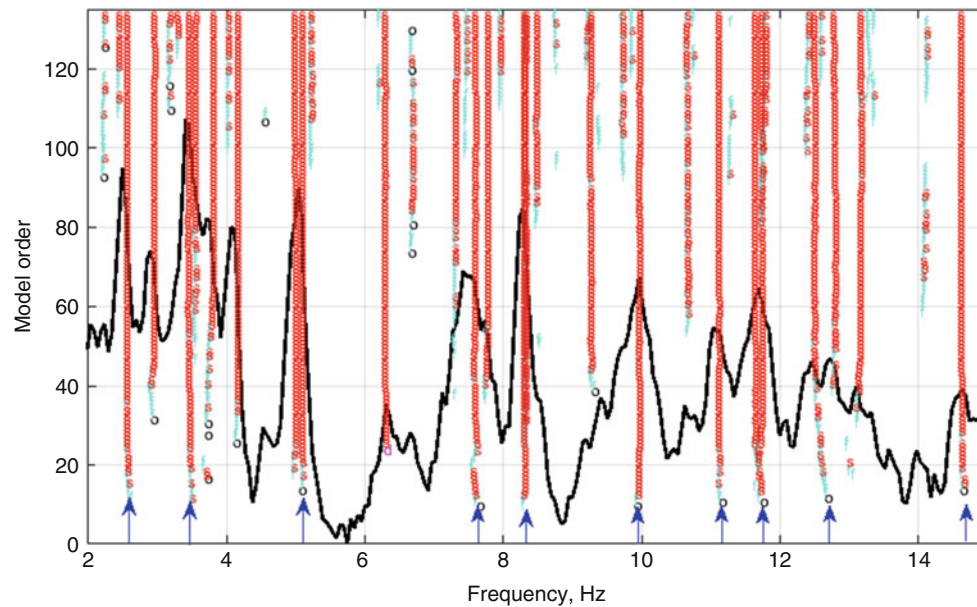


**Fig. 9.5** A typical stabilization chart constructed by the Operational pLSCF (Polymax) modal parameter estimator when applied to the calculated power spectra matrix of one data record (Blues arrows point to the tracked modes)

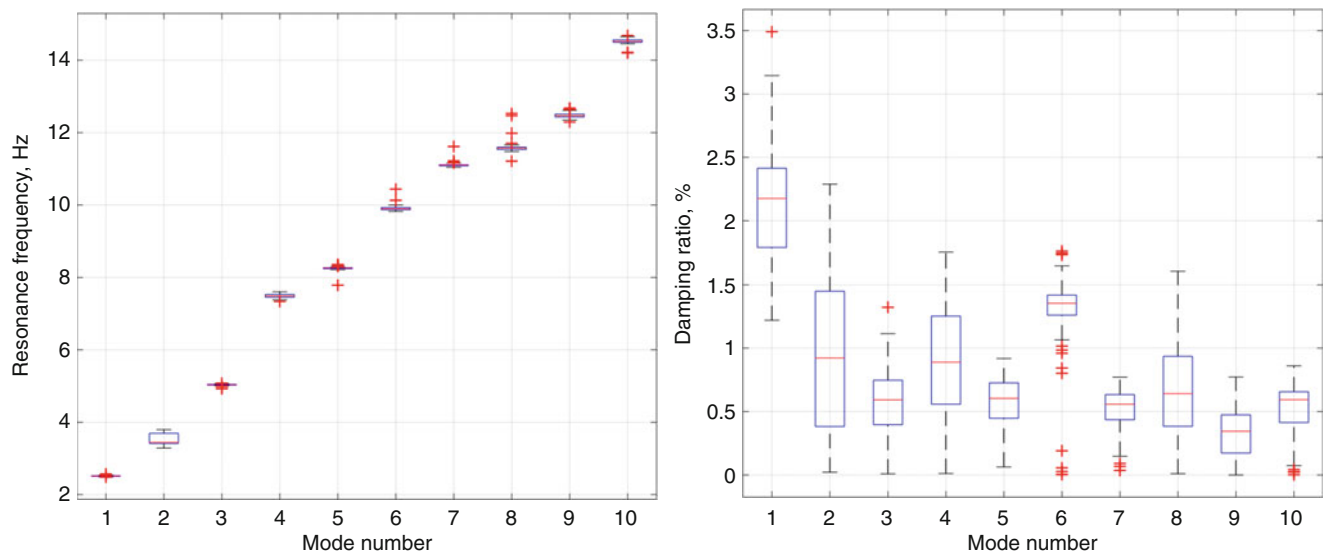


**Fig. 9.6** Boxplots of the resonance frequencies (left) and damping values (right) of the 10 most dominant modes of the drivetrain system during the tracking period. On each box, the central mark is the median, the edges of the box are the 25th and 75th percentiles, the whiskers extend to the most extreme values that were not considered as outliers and the outliers are plotted individually using the ‘+’ symbol

## 9.5 Conclusions

The modal behavior of a drivetrain unit of an offshore wind turbine is investigated while the wind turbine was not producing power. Seventeen acceleration signals acquired from 5 tri-axial and 2 uni-axial accelerometers mounted on the drivetrain system are processed by means of OMA technique, which combines the pre-processing Periodogram approach and the operational pLSCF (Polymax) estimator, to estimate the modal parameters of the 10 most dominant modes of the drivetrain system in a frequency band goes from 2 Hz till 15 Hz. The identified 10 modes are continuously and automatically tracked over a period that lasts 13.67 h. The tracking is done by continuously monitoring the resonance frequencies, damping ratios, and mode shapes of those 10 drivetrain’s modes. The statistical analysis of the results of this long-term tracking showed that the tracked resonance frequencies are more consistent over the tracking period in comparison with the damping ratios that

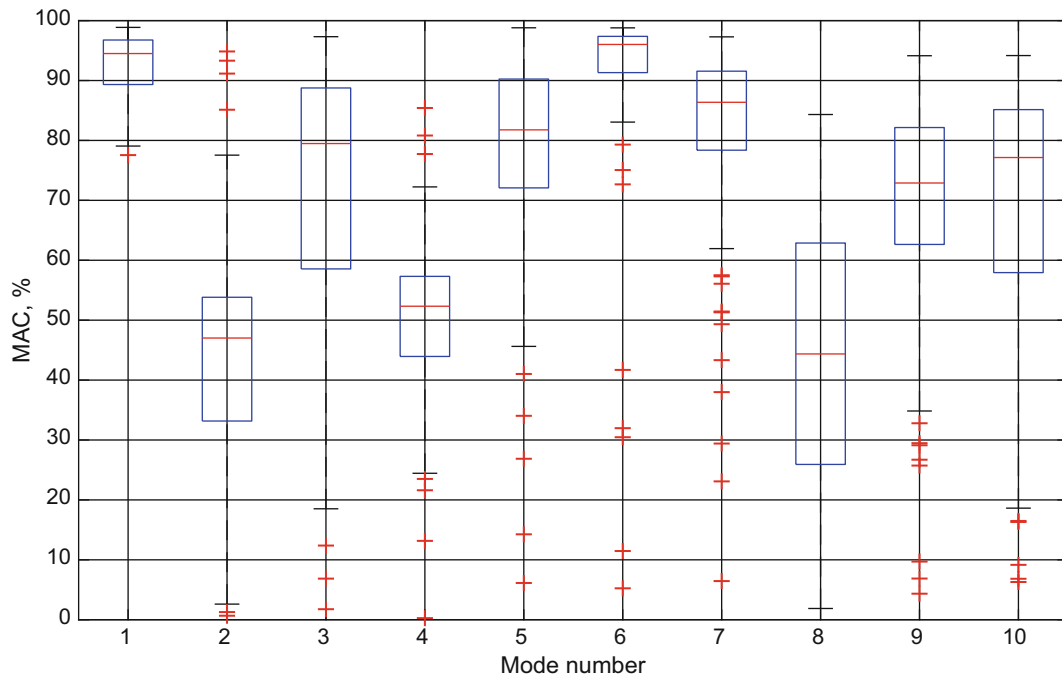


**Fig. 9.7** Boxplots of the Modal Assurance Criterion (MAC) calculated between the mode shapes of the estimated 10 dominant modes of the drivetrain system during the tracking period and the corresponding reference mode shapes. On each box, the central mark is the median, the edges of the box are the 25th and 75th percentiles, the whiskers extend to the most extreme values that were not considered as outliers and the outliers are plotted individually using the ‘+’ symbol

show a high scatter behavior for some modes. However the scatter behavior the damping estimates have over the tracking period, their boxplot showed that they have a normal distribution around the median value over the tracking period. In addition, the results showed a good agreement with the published ones that were obtained based on a short-term tracking. This confirms the repeatability of the analysis and gives more confidence on the obtained modal parameters of the drivetrain system. These standstill condition -based identified modal parameters of the drivetrain will help us in better understating and tackling the modal behavior of the drivetrain system while the OWT is in operational conditions.

**Acknowledgments** The authors would like to acknowledge the VLAIO SBO HYMOP and Proteus Project, as well as the farm owner and the original equipment manufacturer OEM for facilitating the measurement campaign.

## References

1. Global Wind Energy Council (GWEC): Global wind statistics. Available at: <http://files.gwec.net/register?file=/files/GWR2016.pdf> (2017). Accessed 12.10.2017
2. Veers, P.S.: Three-Dimensional Wind Simulation; SAND-88-0152C, CONF-890102-9-ON: DE89003171; Sandia: Albuquerque, New Mexico 87185; Livermore, CA, USA (1988)
3. Mann, J.: Wind field simulation. *Probab. Eng. Mech.* **13**, 269–282 (1998)
4. Peeters, J.: Simulation of dynamic drive train loads in a wind turbine. PhD thesis, Leuven (Heverlee), Belgium: Katholieke Universiteit Leuven, Department of Mechanical Engineering, Division PMA. Available online: <http://hdl.handle.net/1979/344> (2006)
5. Peeters, J., Vandepitte, D., Sas, P.: Analysis of internal drive train dynamics in a wind turbine. *Wind Energy J.* **9**, 141e61 (2006)
6. Goris, S., Ribbentrop, A., et al.: A validated virtual prototyping approach for avoiding wind turbine tonality. In: 5th International Conference on Wind Turbine Noise Denver
7. Helsen, J.: The dynamics of high power density gearboxes with special focus on the wind turbine application. PhD thesis, Leuven (Heverlee), Belgium: Katholieke Universiteit Leuven, Department of Mechanical Engineering, Division PMA (2012)
8. Guillaume, P., Hermans, L., Van der Auweraer, H.: Maximum likelihood identification of modal parameters from operational data. In: Proceedings of the 17th International Modal Analysis Conference (IMAC), Kissimmee, FL (1999)
9. Hermans, L., Van der Auweraer, H.: Modal testing and analysis of structures under operational conditions: Industrial Applications. *Mech. Syst. Signal Process.* **13**(2), 193–216 (1999)

10. Reynders, E.: System identification methods for (operational) modal analysis: review and comparison. *Arch. Comput. Meth. Eng.* **19**(1), 51–124 (2012)
11. El-Kafafy, M., Devriendt, C., Weijtjens, W., De Sitter, G., Guillaume, P.: In: Catbas, F.N. (ed.) *Evaluating Different Automated Operational Modal Analysis Techniques for the Continuous Monitoring of Offshore Wind Turbines*, in *Dynamics of Civil Structures*, vol. 4, pp. 313–329. Springer International Publishing, Cham (2014)
12. Vanhollenbeke, F., Peeters, P., Helsen, J., Di Lorenzo, E., Manzato, S., Peeters, J., Vandepitte, D., Desmet, W.: Large scale validation of a flexible multibody wind turbine gearbox model. *J. Comput. Nonlinear Dyn.* **10**(4), 041006 (2015)
13. Weijtjens, W., Shirzadeh, R., De Sitter, G., Devriendt, C.: Classifying resonant frequencies and damping values of an offshore wind turbine on a monopole foundation for different operational conditions. In: *Proceedings of EWEA, Copenhagen* (2014)
14. El-Kafafy, M., Devriendt, C., Guillaume, P., Helsen, J.: Automatic tracking of the modal parameters of an offshore wind turbine drivetrain system. *Energies*. **10**(4), 574 (2017)
15. Marple, S.L.: *Digital Spectral Analysis: With Applications*. Prentice-Hall, Inc., Upper Saddle River (1986)
16. Welch, P.D.: The use of fast Fourier transform for the estimation of power spectra: a method based on time averaging short modified periodograms. *IEEE Trans. Audio Electroacoust.* **15**, 70–73 (1967)
17. Guillaume, P., Verboven, P., Vanlanduit, S., Van der Auweraer, H., Peeters, B.: A poly-reference implementation of the least-squares complex frequency domain-estimator. In: *Proceedings of the 21th International Modal Analysis Conference (IMAC)*, Kissimmee, FL, USA, 3–6 February 2003
18. Peeters, B., Van der Auweraer, H., Vanhollenbeke, F., Guillaume, P.: Operational modal analysis for estimating the dynamic properties of a stadium structure during a football game. *Shock. Vib.* **14**, 283–303 (2007)



# Chapter 10

## Dynamic Modelling and Vibration Control of a Turbomolecular Pump with Magnetic Bearings in the Presence of Blade Flexibility

Alysson B. Barbosa Moreira and Fabrice Thouverez

**Abstract** This article presents the development of a tridimensional phenomenological model of a turbomolecular pump taking into account the blades dynamics as well as the gyroscopic effects, centrifugal stiffening and spin softening. Rotor and blades behavior is approximated by Euler-Bernoulli beams. Rayleigh-Ritz method is used to approximate continuous displacements and an energetic approach is used to obtain the equations of motion. The global dynamics of the system is analyzed by assuming linear bearings, whose stiffness is experimentally defined. Mistuning of the blades is experimentally identified and simulated so that its influence on blades modes organization could be studied. The obtained model has shown good correlation with experimental results.

**Keywords** turbomolecular pumps · dynamics · blade flexibility · mistuning · turbomachinery

### 10.1 Introduction

Turbomolecular pumps are vacuum pumps capable of generating very low levels of pressure, up to  $10^{-11}$  mbar for some models. The applications of such pumps are in constant demand of improvement of performance in terms of vibration levels. They are composed of a multi-stage turbine suspended by active contact-free magnetic bearings (AMB).

Active magnetic bearings are instable and non-linear. To operate correctly, such AMBs need a controller to stabilize the system and reject external perturbations. In the literature, control systems of this kind of machines are designed by taking into account the rigid body translation and tilting of the rotor and the first bending mode of the shaft, while blades are considered as rigid bodies [1–3]. However, it has been experimentally shown that local bending of the blades may have some influence on the controller performance.

A full tri-dimensional model of such system involving the control law is difficult to use because of the time simulations require. Therefore, the aim of this work is to propose a phenomenological model of a turbomolecular pump, which is capable to represent all the phenomena involved in turbomachinery, taking into account the flexibility of the blades. With such a model, quick time simulations could be made to develop a controller and assess its performance.

### 10.2 Mechanical Model

The aim of this section is to derive the equations of motion of the analytical model illustrated in Fig. 10.1a, inspired by the works of Refs. [4–6]. It is composed by (1) a flexible shaft, modelled as an Euler-Bernoulli rotating beam; (2) a rigid disk where blades are mounted and an axial bearing, that works as a thrust bearing; (3) eight stages of flexible blades modeled as rectangular, section variable Euler-Bernoulli beams, clamped to the rigid disk; and (4) an elastic element for the connection of the disk and the shaft whose stiffness is  $k_m$ . As the aim of this section is to assess the mechanical behavior of complete system, the bearings have been modeled as linear springs ( $k_p$ ). Their stiffness are experimentally identified from pumps in operation.

---

A. B. Barbosa Moreira · F. Thouverez (✉)  
École Centrale de Lyon, LTDS, CNRS UMR 5513,Écully, France  
e-mail: [bruno.moreira@doctorant.ec-lyon.fr](mailto:bruno.moreira@doctorant.ec-lyon.fr); [fabrice.thouverez@ec-lyon.fr](mailto:fabrice.thouverez@ec-lyon.fr)

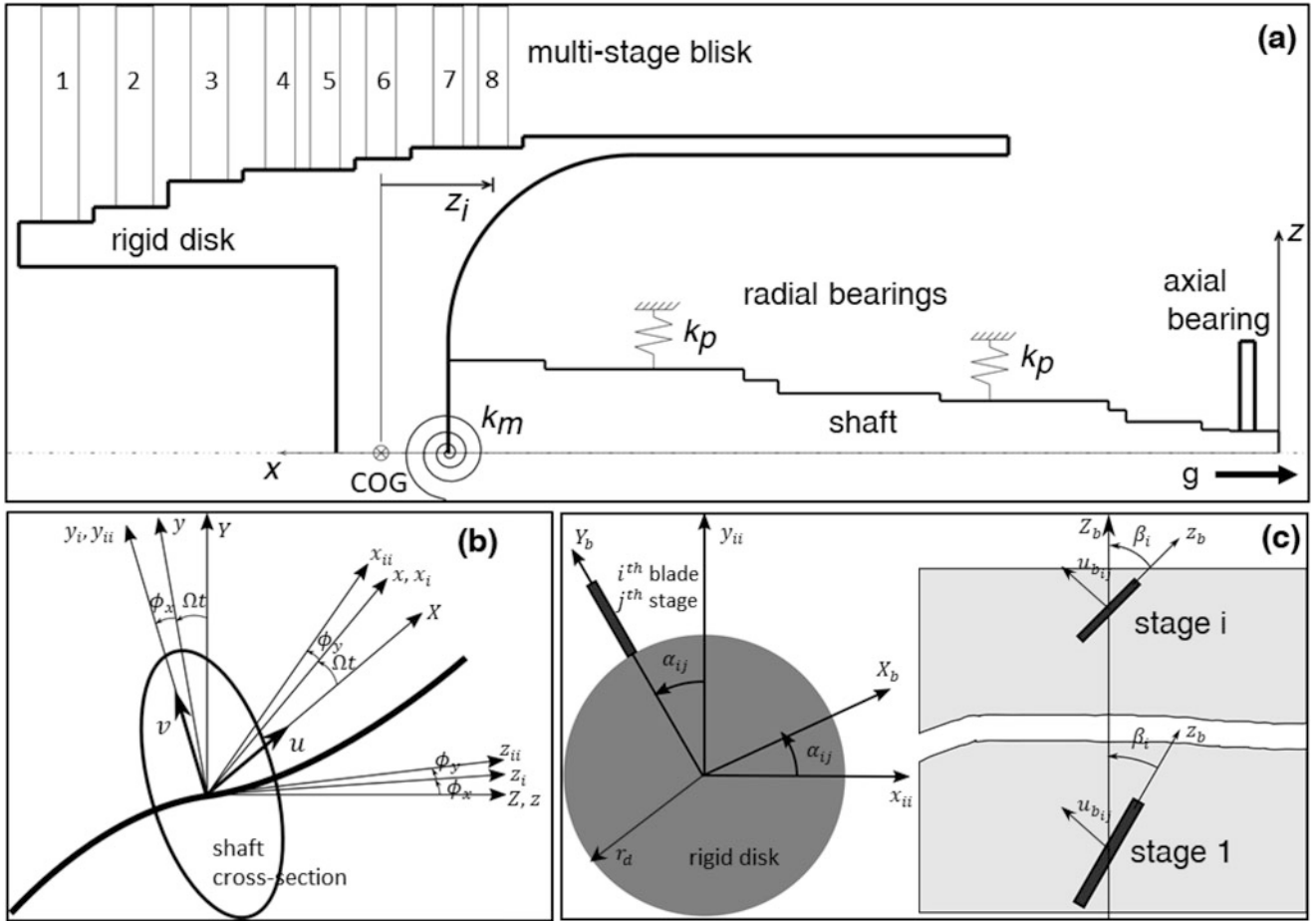


**Fig. 10.1** (a) Schematic drawing of the model (pump works in vertical position) (b) Euler angles of different frames in a shaft cross-section (c) blades frames

### 10.2.1 Energetic Approach and Rayleigh-Ritz Approximation

To avoid periodic terms in the equations of motion, the system is modeled in the rotating frame  $R(x, y, z)$ . This frame is defined by applying the transformation matrix  $\mathbf{R}(t)$ , from the inertial frame  $R_0(X, Y, Z)$ .

$$\mathbf{R}(t) = \begin{bmatrix} \cos(\Omega t) & \sin(\Omega t) \\ -\sin(\Omega t) & \cos(\Omega t) \end{bmatrix} \quad (10.1)$$

From the rotating frame, a cross-section of the shaft tilts by an amount  $\phi_x$  around x-axis, defining the frame  $R_i(x_i, y_i, z_i)$  and by  $\phi_y$  around y-axis, defining  $R_{ii}(x_{ii}, y_{ii}, z_{ii})$ , as shown in Fig. 10.1b. Thus, it is possible to define the translational and angular velocities, defined in the rotating frame:

$$\mathbf{V}_{R_0}^R = \begin{Bmatrix} \dot{u} - \Omega v_s \\ \dot{v}_s + \Omega u_s \\ 0 \end{Bmatrix} \quad (10.2)$$

$$\boldsymbol{\Omega}_{sR_0}^R = \begin{Bmatrix} \dot{\phi}_{x_s} \cos \phi_{y_s} - \Omega \cos \phi_{x_s} \sin \phi_{y_s} \\ \dot{\phi}_{y_s} + \Omega \sin \phi_{x_s} \\ \dot{\phi}_{x_s} \sin \phi_{y_s} + \Omega \cos \phi_{x_s} \cos \phi_{y_s} \end{Bmatrix} \quad (10.3)$$

For the definition of the blades velocities, two other frames are defined (Fig. 10.1c):  $R_{B_{ij}}$  ( $x_{B_{ij}}, y_{B_{ij}}, z_{B_{ij}}$ ), which sets the angular position of each blade  $j$  of a stage  $i$ , at  $z_i$  (see Fig. 10.1a);  $R_b$  ( $x_{b_i}, y_{b_i}, z_{b_i}$ ), which orientates the frame with respect to the pitch angle  $\beta_i$ ; and  $R_{\psi_{ij}}$  ( $x_{\psi_{ij}}, y_{\psi_{ij}}, z_{\psi_{ij}}$ ), which is the frame attached to the section of the blade in its flexural motion. Each of these frames are associated with a transformation matrix. The translational and angular velocities vectors for a given blade cross-section are:

$$\mathbf{V}_{b_{ijR_0}}^R(s, t) = \frac{d}{dt} \begin{Bmatrix} u_d(s, t) \\ v_d(s, t) \\ 0 \end{Bmatrix} + \frac{d}{dt} \left( \mathbf{P}_{\phi_{x_d}}^T \mathbf{P}_{\phi_{y_d}}^T \mathbf{P}_{\alpha_{ij}}^T \mathbf{P}_{\beta_i}^T \begin{Bmatrix} u_{bij}(s, t) \\ r_d + s \\ 0 \end{Bmatrix} + \begin{Bmatrix} 0 \\ 0 \\ z_i \end{Bmatrix} \right) \quad (10.4)$$

$$\mathbf{\Omega}_{b_{ijR_0}}^R(s, t) = \begin{Bmatrix} 0 \\ 0 \\ \dot{\psi}_{b_{ij}}(s, t) \end{Bmatrix} + \mathbf{P}_{\psi_{b_{ij}}} \mathbf{P}_{\beta_i} \mathbf{P}_{\alpha_{ij}} \begin{Bmatrix} 0 \\ \dot{\phi}_{y_d}(s, t) \\ 0 \end{Bmatrix} + \mathbf{P}_{\psi_{b_{ij}}} \mathbf{P}_{\beta_i} \mathbf{P}_{\alpha_{ij}} \mathbf{P}_{\phi_{y_d}} \begin{Bmatrix} \dot{\phi}_{x_d}(s, t) \\ 0 \\ 0 \end{Bmatrix} + \mathbf{P}_{\psi_{b_{ij}}} \mathbf{P}_{\beta_i} \mathbf{P}_{\alpha_{ij}} \mathbf{P}_{\phi_{y_d}} \mathbf{P}_{\phi_{x_d}} \begin{Bmatrix} 0 \\ 0 \\ \Omega \end{Bmatrix} \quad (10.5)$$

Where  $u_d$  and  $v_d$  are the disk displacements;  $\phi_{x_d}$  and  $\phi_{y_d}$  are the disks rotations;  $\mathbf{P}_{\phi_{x_d}}$ ,  $\mathbf{P}_{\phi_{y_d}}$ ,  $\mathbf{P}_{\alpha_{ij}}$ ,  $\mathbf{P}_{\beta_i}$ ,  $\mathbf{P}_{\psi_{ij}}$  are the transformation matrices associated to the frames described in Fig. 10.1;  $u_{bij}$  and  $\psi_{bij}$  are the blades cross-section displacements and rotations, respectively;  $\Omega$  is the spin speed of the shaft.

With these velocities, kinetic energies may be calculated with the following expression:

$$T_p = \frac{1}{2} \int_0^{L_p} \rho_p S_p \mathbf{V}_p^T(l, t) \mathbf{V}_p(l, t) dl + \frac{1}{2} \int_0^{L_p} \mathbf{\Omega}_p^T(l, t) \mathbf{I}_p \mathbf{\Omega}_p(l, t) dl \quad (10.6)$$

Where index  $p$  corresponds to the different organs,  $L_p$  is the length,  $\rho_p$  the density,  $S_p$  the cross-sectional area,  $\mathbf{V}_p$  the translational velocity vector,  $\mathbf{\Omega}_p$  the rotational velocity vector,  $\mathbf{I}_p$  the tensor of the moments of inertia.

Strain energies and dissipation functions are defined by:

$$U_p = \frac{1}{2} \int_0^{L_p} E_p I_p \left( \left( \frac{\partial^2 u_p(l, t)}{\partial l^2} \right)^2 + \left( \frac{\partial^2 v_p(l, t)}{\partial l^2} \right)^2 \right) dl \quad (10.7)$$

$$F_p = \frac{1}{2} \eta \int_0^{L_p} E_p I_p \left( \left( \frac{\partial^2 \dot{u}_p(l, t)}{\partial l^2} \right)^2 + \left( \frac{\partial^2 \dot{v}_p(l, t)}{\partial l^2} \right)^2 \right) dl \quad (10.8)$$

Where  $u_p$  and  $v_p$  are the displacements of the organ  $p$ ,  $E_p$  and  $I_p$  are the Young's modulus of the material and the second moment of area of the cross-section.

Centrifugal stiffening (only for the blades) is calculated by:

$$\mathbf{T}_{stiff} = \frac{1}{2} \Omega^2 \rho_b \int_0^{L_b} S_b \left( (r_d + L_b)^2 - (r_d + l)^2 \right) \left( \frac{\partial^2 u_{bij}(l, t)}{\partial l^2} \right)^2 dl \quad (10.9)$$

Where  $r_d$ ,  $L_b$  and are the blades inner radius and length.

The connection between shaft and disk is made by means of an angular spring. Therefore, the translation of the disk is the same as the translation of the shaft, but the angles are different. The strain energy of this spring is given by:

$$U_m = \frac{1}{2} k_m \left( (\phi_{x_d}(t) - \phi_{s_{x_d}}(t))^2 + (\phi_{y_d}(t) - \phi_{s_{y_d}}(t))^2 \right) \quad (10.10)$$

Where  $\phi_{s_{x_d}}$  and  $\phi_{s_{y_d}}$  are the rotations of the cross-section of the shaft where disk is clamped.

A base of functions that respect kinematic conditions approximates the shaft and blades displacements. These functions were already used by Refs. [4, 5, 7]. Polynomial functions express the displacement of the shaft as follows:

$$u_s(z, t) \approx u_s^h(z, t) = X_0(t) + \sum_{m=1}^{m_{tot}} W_m(z) X_m(t) \quad (10.11)$$



$$v_s(z, t) \approx v_s^h(z, t) = Y_0(t) + \sum_{m=1}^{m_{tot}} W_m(z) Y_m(t) \quad (10.12)$$

$$W_m(z) = \left( \frac{z}{L_s} \right)^m \quad (10.13)$$

Euler-Bernoulli's theory allows the following relations, which reduces the dimensions of the problem:

$$\begin{cases} \phi_{x_s}(z, t) = -\frac{dv}{dz} = -v'_s(z, t) \\ \phi_{y_s}(z, t) = \frac{du}{dz} = u'_s(z, t) \end{cases} \quad (10.14)$$

Equivalently, blades deformations are approximated by:

$$\begin{cases} u_{bij}(s, t) \approx u_{bij}^h = \sum_{n=1}^{n_{tot}} Y_n(s) X_{nij}^b(t) \\ \psi_{bij}(s, t) = -\frac{du_{bij}}{ds} = -u'_{bij}(s, t) \end{cases} \quad (10.15)$$

Where  $Y_n(s)$  are the approximating functions, defined by:

$$\begin{cases} Y_n(s) = \sin(a_n s) + b_n s + c_n s^2 \\ a_n = \frac{(2n-1)\pi}{2L_b}; b_n = -a_n; c_n = \frac{b_n^2}{2} \sin(b_n L_b) \end{cases} \quad (10.16)$$

The application of Lagrange's equations (10.4) results in the following equations of motion:

$$\mathbf{M}\ddot{\mathbf{q}} + (\mathbf{D} + \mathbf{G}(\Omega))\dot{\mathbf{q}} + (\mathbf{K} + \mathbf{N}(\Omega^2) + \mathbf{K}_{stiff}(\Omega^2))\mathbf{q} = \mathbf{0} \quad (10.17)$$

Where  $\mathbf{M}, \mathbf{D}, \mathbf{G}, \mathbf{K}, \mathbf{N}, \mathbf{K}_{stiff}$  are the mass, structural damping, gyroscopic, structural stiffness, spin softening and centrifugal stiffening effect matrices.  $\mathbf{q}$  is the vector of generalized coordinates:

$$\mathbf{q} = [X_1 \ \cdots \ X_{m_{tot}} \ Y_1 \ \cdots \ Y_{m_{tot}} \ X_{11}^b \ \cdots \ X_{ij}^b]^T \quad (10.18)$$

### 10.2.2 Modal Analysis and Rayleigh Quotient Applied to Rotating Structures

When  $\Omega = 0$  and for conservative systems, terms  $\mathbf{G}, \mathbf{D}, \mathbf{N}$  and  $\mathbf{K}_{stiff}$  of Equation (10.17) are zero. Therefore, it is possible to write the eigenvalues problem as follows:

$$(\mathbf{K} - \lambda_k \mathbf{M}) \mathbf{q}_k = \mathbf{0}; \lambda_k = \omega_k^2 \quad (10.19)$$

where  $\omega_k$  is the natural frequency of the  $k^{th}$  mode.

Rayleigh quotient of such system is defined by:

$$\mathcal{R}_k = \frac{\mathbf{q}_k^T \mathbf{K} \mathbf{q}_k}{\mathbf{q}_k^T \mathbf{M} \mathbf{q}_k} = \omega_k^2 \quad (10.20)$$

For a complex structure, composed of different organs, if one can identify mass and stiffness matrix for each organ, the participation of each one in the Rayleigh quotient can be defined. This is very useful when characterizing the sensitivity of different modes to design parameters.

For conservative rotating structures, the eigenvalues problem is defined in the state-space as follows:

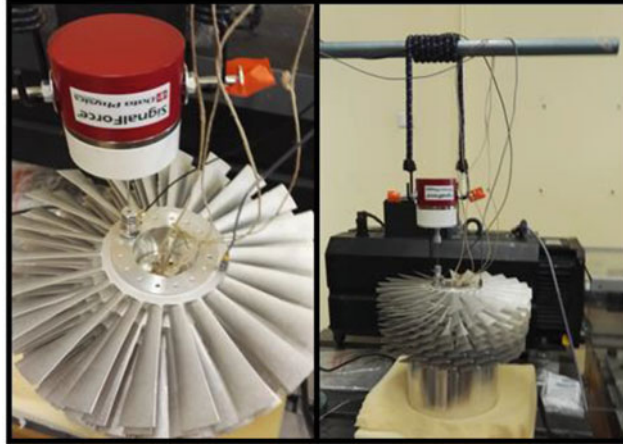


**Fig. 10.2** Experimental setup for modal testing of the turbine

$$\begin{aligned}
 (\mathbf{A} - \lambda_k \mathbf{B}) \mathbf{g}_k &= 0 \\
 \left( \begin{bmatrix} \mathbf{0} & \tilde{\mathbf{K}} \\ -\tilde{\mathbf{K}} & -\mathbf{G}(\Omega) \end{bmatrix} - \lambda_k \begin{bmatrix} \tilde{\mathbf{K}} & \mathbf{0} \\ \mathbf{0} & \mathbf{M} \end{bmatrix} \right) \begin{Bmatrix} \mathbf{q}_k \\ \lambda_k \mathbf{q}_k \end{Bmatrix} &= \mathbf{0}; \\
 \tilde{\mathbf{K}} &= \mathbf{K} + \mathbf{N}(\Omega^2) + \mathbf{K}_{\text{raid}}(\Omega^2)
 \end{aligned} \tag{10.21}$$

Rayleigh quotient of this system is defined by [8]:

$$\mathcal{R}_k = \frac{\mathbf{q}_k^T \mathbf{A} \mathbf{q}_k}{\mathbf{q}_k^T \mathbf{B} \mathbf{q}_k} = \lambda_k \tag{10.22}$$

If the eigenvector is written as  $\mathbf{g}_k = \begin{Bmatrix} \boldsymbol{\alpha}_k + i\boldsymbol{\beta}_k \\ \boldsymbol{\mu}_k + i\boldsymbol{\gamma}_k \end{Bmatrix}$ , equation (10.22) can be rewritten as follows:

$$\mathcal{R}_k = \frac{[2\boldsymbol{\alpha}_k^T(\mathbf{K} + \mathbf{N} + \mathbf{K}_{\text{raid}})\boldsymbol{\gamma}_k - 2\boldsymbol{\mu}_k^T(\mathbf{K} + \mathbf{N} + \mathbf{K}_{\text{raid}})\boldsymbol{\beta}_k - 2\boldsymbol{\beta}_k^T \mathbf{G} \boldsymbol{\gamma}_k]j}{\boldsymbol{\alpha}_k^T(\mathbf{K} + \mathbf{N} + \mathbf{K}_{\text{raid}})\boldsymbol{\alpha}_k + \boldsymbol{\mu}_k^T(\mathbf{K} + \mathbf{N} + \mathbf{K}_{\text{raid}})\boldsymbol{\mu}_k + (\boldsymbol{\beta}_k^T \mathbf{M} \boldsymbol{\beta}_k + \boldsymbol{\gamma}_k^T \mathbf{M} \boldsymbol{\gamma}_k)} = \lambda_k \tag{10.23}$$

## 10.3 Results and Model Updating

### 10.3.1 Experimental Modal Identification

To define the model with realistic parameters, modal tests were carried out. The aim of these tests was to identify (1) the frequency and damping ratio of the first bending mode of the shaft mounted to the turbine and (2) the frequency range of the first bending modes of the blades, stage by stage, in order to estimate the mistuning and the mean damping ratio of the blades.

For the experiments, the turbine, with its shaft, lays down over a very soft foam, so that the free-free boundary conditions are simulated (see Fig. 10.2). The ensemble is excited by an electrodynamic shaker with a swept sine and the response of the system is collected by an accelerometer. The frequency response is then calculated, and the modal identification is made by interpolating the experimental resonances. First, one test where all of the blades are free to vibrate was carried out. Then stage by stage identification is achieved by interposing a damping material between the blades of the stages that are not being measured, so that only one stage is free to respond at a time. Table 10.1 summarizes the experimental results. All of the values are scaled so that the experimental frequency of the first bending mode of the shaft, herein called  $\omega_{\text{shaft}}^e$ , is set to 1.

**Table 10.1** Results of the modal identification at rest

Organ	Frequency range	Mean frequency	Damping ratio
All stages' blades	$[0,686 \ 0,795]\omega_{shaft}^e$	–	0.025%
1st stage blades	$[0,685 \ 0,711]\omega_{shaft}^e$	$0,698\omega_{shaft}^e$	<sup>a</sup>
2nd stage blades	$[0,730 \ 0,761]\omega_{shaft}^e$	$0,746\omega_{shaft}^e$	<sup>a</sup>
3rd stage blades	$[0,723 \ 0,765]\omega_{shaft}^e$	$0,744\omega_{shaft}^e$	<sup>a</sup>
4th stage blades	$[0,708 \ 0,765]\omega_{shaft}^e$	$0,731\omega_{shaft}^e$	<sup>a</sup>
5th stage blades	$[0,705 \ 0,745]\omega_{shaft}^e$	$0,725\omega_{shaft}^e$	<sup>a</sup>
6th, 7th and 8th stage blades	$[0,743 \ 0,779]\omega_{shaft}^e$	$0,761\omega_{shaft}^e$	<sup>a</sup>
Shaft	$1\omega_{shaft}^e$	-	0.5%

<sup>a</sup>Blades damping ratio are estimated during tests where all blades can respond. See first line of the table

**Table 10.2** Comparison of natural frequencies of the blades before and after adjustments

Organ	Before update		After update		Relative error <sup>a</sup> (%)
	$b_p$ (mm)	Calculated frequency	$b_p$ (mm)	Calculated frequency	
1st stage blades	$b_{p_1}$	$0.935 \omega_{shaft}^e$	$0.77 b_{p_1}$	$0.699 \omega_{shaft}^e$	0.034
2nd stage blades	$b_{p_2}$	$0.945 \omega_{shaft}^e$	$0.80 b_{p_2}$	$0.725 \omega_{shaft}^e$	2.734
3rd stage blades	$b_{p_3}$	$1.009 \omega_{shaft}^e$	$0.76 b_{p_3}$	$0.733 \omega_{shaft}^e$	1.466
4th stage blades	$b_{p_4}$	$0.934 \omega_{shaft}^e$	$0.80 b_{p_4}$	$0.744 \omega_{shaft}^e$	1.750
5th stage blades	$b_{p_5}$	$0.935 \omega_{shaft}^e$	$0.77 b_{p_5}$	$0.746 \omega_{shaft}^e$	2.911
6th, 7th and 8th stage blades	$b_{p_6}$	$0.924 \omega_{shaft}^e$	$0.81 b_{p_6}$	$0.761 \omega_{shaft}^e$	0.047

<sup>a</sup>Between tests and calculations

### 10.3.2 Results at Rest: Conservative System

The eigenvalues problem for the conservative, non-rotating system is solved according to equations (10.19). Table 10.2 summarizes the results of the calculations of the blade modes before and after parameters updating. The differences in blades frequencies before adjustment is due to the simplification of their complex geometry to a prismatic beam of variable thickness ( $b_p$  at blade root and  $b_t$  at blade tip). Variations in  $b_p$  have a large impact on the blade mode frequency because this parameter have significant influence on mass and stiffness matrices. So the adjustment of  $b_p$  is carried out to follow experimental data. The resulting frequencies, as well as the relative deviations between calculated and measured values, are also shown on Table 10.2. Variations in the estimation of  $b_p$  are from 20 to 24%, which is reasonable in view of the simplifications explained in the beginning of this paragraph.

The frequency of the first bending mode of the shaft is very sensitive to the parameter  $k_m$ , which is the stiffness of the connection element with the blisk. This stiffness has been calculated by means of a membrane model [9]. The thickness of this membrane ( $t_m$ ) is chosen as the control parameter of  $k_m$ . An initial value for  $t_m$  is set to the mean thickness of the real geometry ( $t_{m_1}$ ), which leads to a frequency of  $1.29\omega_{shaft}^e$ . By adjusting  $t_m$  to  $0.6 t_{m_1}$ , the frequency goes down to  $1.02 \omega_{shaft}^e$ . Such adjustment is justified by the complexity of the membrane section that is far from a membrane with a constant thickness.

Figure 10.3 shows the frequency evolution of the different modes (blue dots) and a color map of the participation in strain energy of different stages of blades to the modes, calculated by the numerator of equation (10.20). Each color represents the contribution of a different stage. One can see that the participation of the different stages are well separated. In order to take into account the mistuning effects, a random mistuning scheme is applied stage by stage, according to the frequency variations experimentally measured (Table 10.1). Figure 10.4 shows the same curve of Fig. 10.3, but this time including mistuning in the system. One can see that mistuning changes the evolution of the frequency, since there is no more constant distribution by stage, and the participations of the modes are no more ordered. This result shows that mistuning may influence the whole dynamics of the system. While for a tuned system excitations at a given frequency lead to the response of the corresponding stage, in a mistuned system multiple stages can respond at a time. Thus, the spreading of the mode/frequency curve indicates that the blades motions are probably not concentrated to one blade stage, but to a larger part of the structure.

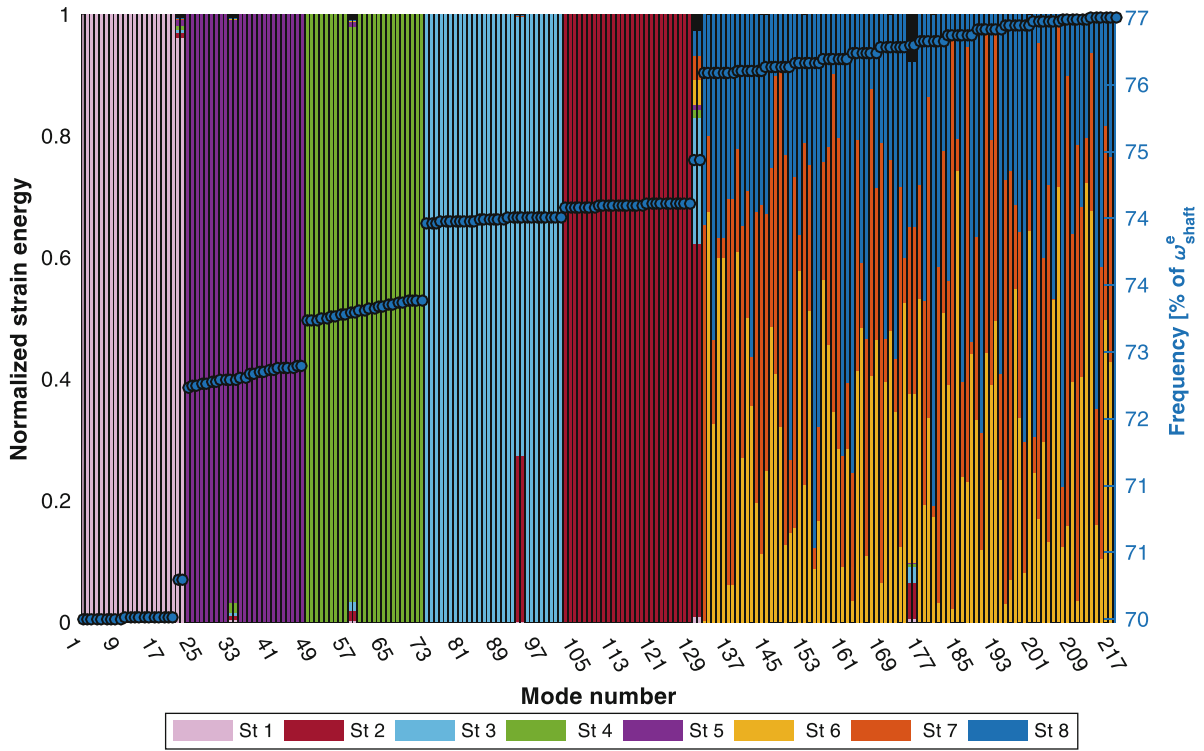


Fig. 10.3 Eigenfrequencies evolution and strain energy distribution stage by stage – tuned blades

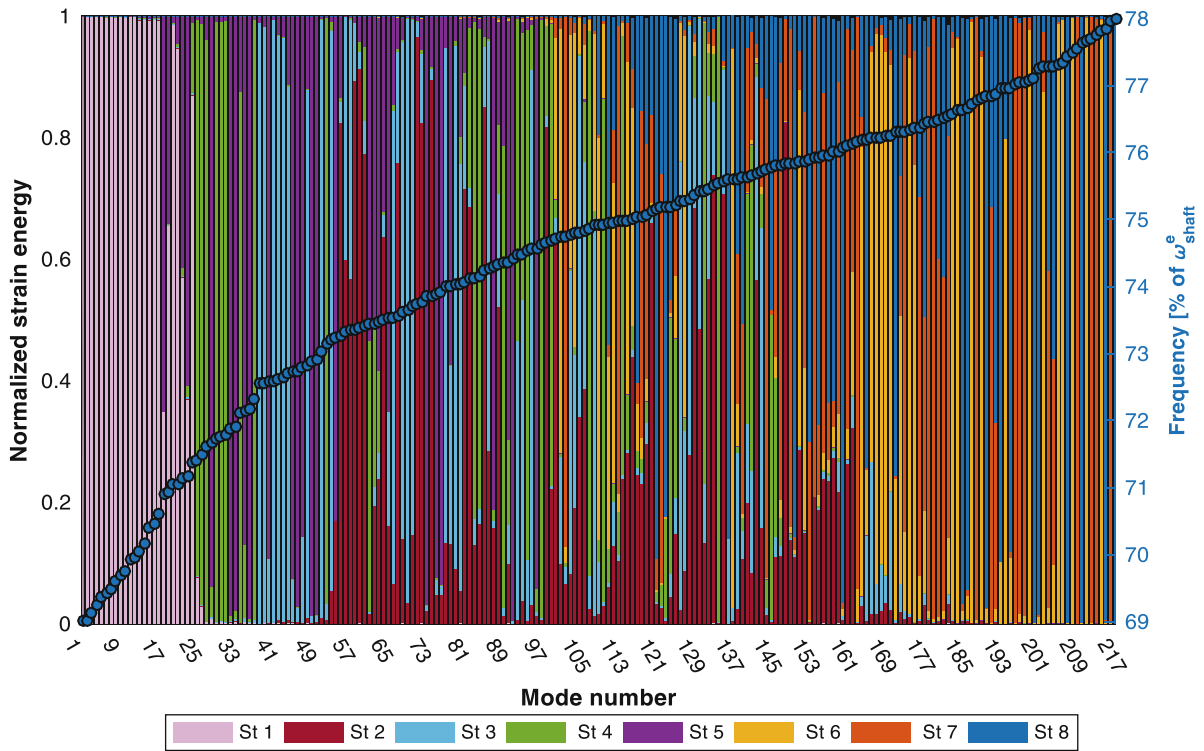


Fig. 10.4 Eigenfrequencies evolution and strain energy distribution stage by stage – mistuned blades

### 10.3.3 Spinning Results: Conservative System

When  $\Omega > 0$ , gyroscopic, spin softening and the centrifugal spin stiffening effects are taken into account. The eigenvalue problem is solved for different spin speeds, according to equation (10.21). This equation is defined in the rotating frame, and the eigenvalues of the problem is also estimated in this frame in order to avoid time dependence of the matrices. Nevertheless, experimental results of the operating pump are expressed in the inertial frame. Such data is measured from operational pumps.

In the inertial frame, one cannot define the eigenvalues problem as stated in equation (10.21), since matrices would contain periodic terms. In such cases, the Campbell diagram cannot be defined in the inertial frame. In order to know the frequency spectrum of the free response of the system in the inertial frame, a *pseudo-Campbell diagram* is defined, based on *pseudo-natural frequencies* [10].

Let  $\begin{Bmatrix} u_k^R \\ v_k^R \end{Bmatrix} e^{i\omega_k t}$  be the projection of the free response according to the  $k^{\text{th}}$  mode of the system onto the  $xy$ -axis of the rotating frame. When this vector is projected to the inertial frame by using equation (10.1), one obtains the free response of the system seen from the inertial frame:

$$\begin{Bmatrix} u_k^{R_0} \\ v_k^{R_0} \end{Bmatrix} = \begin{Bmatrix} \frac{1}{2} u_k^R (e^{i(\omega_k + \Omega)t} + e^{i(\omega_k - \Omega)t}) + \frac{1}{2i} v_k^R (e^{i(\omega_k + \Omega)t} - e^{i(\omega_k - \Omega)t}) \\ \frac{1}{2i} u_k^R (e^{i(\omega_k + \Omega)t} - e^{i(\omega_k - \Omega)t}) - \frac{1}{2} v_k^R (e^{i(\omega_k + \Omega)t} + e^{i(\omega_k - \Omega)t}) \end{Bmatrix} \quad (10.24)$$

It is clear from equation (10.24) that the free response (seen from the inertial frame) of the system is composed of the natural frequency  $\omega_k$  (calculated in the rotating frame) modulated by the spin speed  $\Omega$ ; which leads to *pseudo-natural frequencies*:  $\omega_k \pm \Omega$ .

When the structure is axisymmetric, forward and backward modes lead to relations between  $u_k$  and  $v_k$  [11] that eliminate one of the frequencies of equation (10.24). Such relations are given by equations (10.25) and (10.26). Forward modes are indicated by the exponent  $\blacksquare^+$ , and their natural frequencies are given by  $\omega_k^+$ . Backward modes are indicated by  $\blacksquare^-$ , and their natural frequencies are given by  $\omega_k^-$ .

$$u_k^+ = i v_k^+ \quad (10.25)$$

$$u_k^- = -i v_k^- \quad (10.26)$$

Substituting relations (10.25) and (10.26) in equation (10.24) results in:

$$\begin{aligned} \begin{Bmatrix} u_k^{R_0} \\ v_k^{R_0} \end{Bmatrix}^+ &= \begin{Bmatrix} u_k^R \\ v_k^R \end{Bmatrix}^+ e^{i(\omega_k^+ - \Omega)t}; \quad \text{for the forward mode} \\ \begin{Bmatrix} u_k^{R_0} \\ v_k^{R_0} \end{Bmatrix}^- &= \begin{Bmatrix} u_k^R \\ v_k^R \end{Bmatrix}^- e^{i(\omega_k^- + \Omega)t}; \quad \text{for the backward mode} \end{aligned} \quad (10.27)$$

Based on these results, Fig. 10.5a shows the Campbell diagram computed in the rotating frame. The spin speed is normalized by the nominal speed of the pump ( $\Omega_n$ ) and the modal frequencies are normalized by  $\omega_{shaft}^e$ . One can observe the evolution of the rigid body modes and the first bending modes of the shaft (S-1F<sup>+</sup> and S-1F<sup>-</sup>). The evolution of the modes with spin speed is controlled by the centrifugal stiffening. As for the diagram from Fig. 10.5b, the *pseudo-Campbell diagram*, the angle between the forward and backward shaft modes (flexible and rigid body) are smaller, as a result of relations (10.27). Blades modes are split in two groups associated to the frame change equation (10.24).

Figure 10.5c shows an experimental waterfall diagram. It is important to underline that these data correspond to a forced response of the system, which is different from a modal analysis (Campbell diagram). Therefore, it is natural that the response intensity, marked in Fig. 10.5c by the colors of the lines, cannot be compared to our computed values. This explains why the calculated results show more lines than the experimental ones

We can identify on both experimental and calculated diagrams that the first bending modes of the shaft (S-1F<sup>+</sup> and S-1F<sup>-</sup>) have the same behavior: their frequency at rest and the evolution with spin speed are similar. Blades modes evolution are similar on both curves, including the interaction with S-1F<sup>+</sup>. These modes influence each other's evolution as there is a *veering* phenomenon, explained later in this document. Comparisons of Fig. 10.5a and b show that the model is capable to

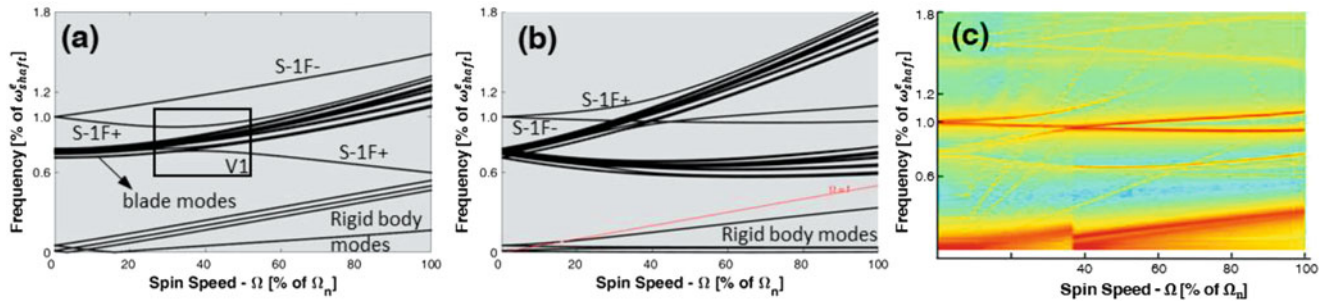


Fig. 10.5 (a) Campbell diagram of the system in the rotating frame after updating (b) pseudo-Campbell diagram of the system in the inertial frame after updating (c) experimental waterfall diagram

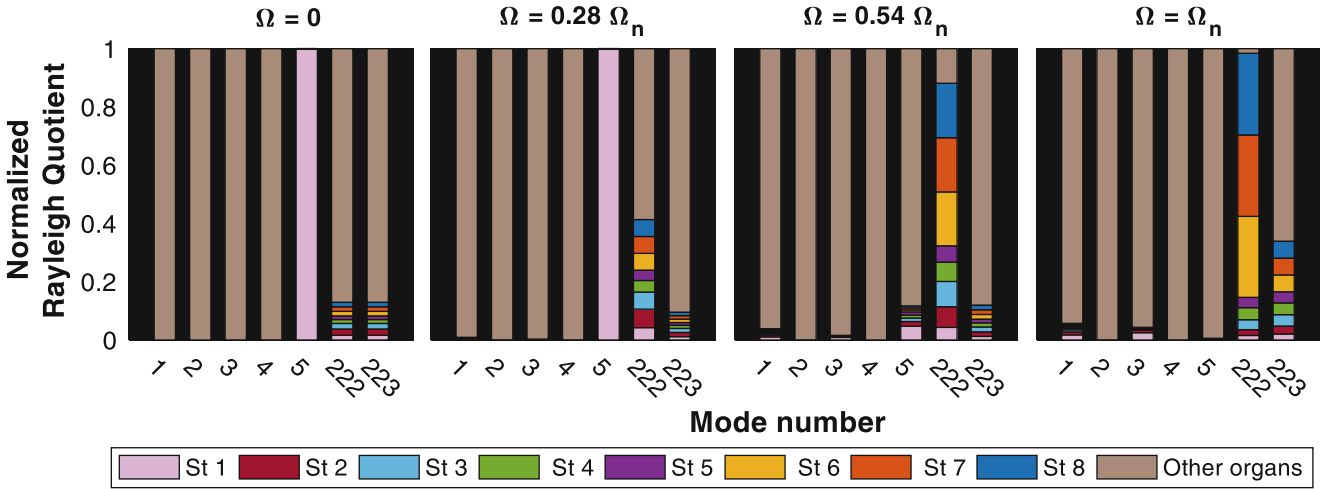


Fig. 10.6 Evolution of Rayleigh quotient of different parts during veering – tuned model (St = Stage)

reproduce the phenomena experimentally observed: the shaft flexible modes are situated on the same frequency range, and their evolution are the same; the blades dynamics are well represented and the interaction of blade modes with S-1F<sup>+</sup> is well reproduced.

In region V1 of the diagrams, one can observe the *veering* phenomenon, on both experimental and theoretical curves. This phenomenon, already studied by Pierre [12], consists of a mode shape exchange between blade mode and the direct mode of the shaft. The analysis of the participation of the different parts of the structure involved in the veering is carried out. For that, equation (10.23) is used to calculate the Rayleigh quotient of the different parts.

Figure 10.6 shows the results of this analysis for the tuned system. The diagrams show the participation of the different blade stages in the Rayleigh quotient for seven different modes and for four different spin speeds. The modes analysed are the rigid body modes (1 to 4), one blade mode where there is only the participation of the first stage (5), mode S-1F<sup>+</sup> of the shaft (222) and mode S-1F<sup>-</sup> (223). As spin speed increases, mode 5 becomes a shaft mode, and mode 222 becomes a mode where all of the stages of the blades participate, but without deflection of the shaft. In Fig. 10.7, this evolution is shown for the mistuned system. One observes exactly the same phenomenon, which indicates that mistuning do not influence this behaviour

### 10.4 Conclusions and Perspectives

In this paper the results of a phenomenological model of a turbomolecular pump are presented. The different organs of the system have been modeled, with the hypothesis of the Euler-Bernoulli beam theory through a simplified approach in order to carry out quick sensitivity analysis and also the organs participation in different modes. Model parameters have been updated based on experimental data, including mistuning effects.

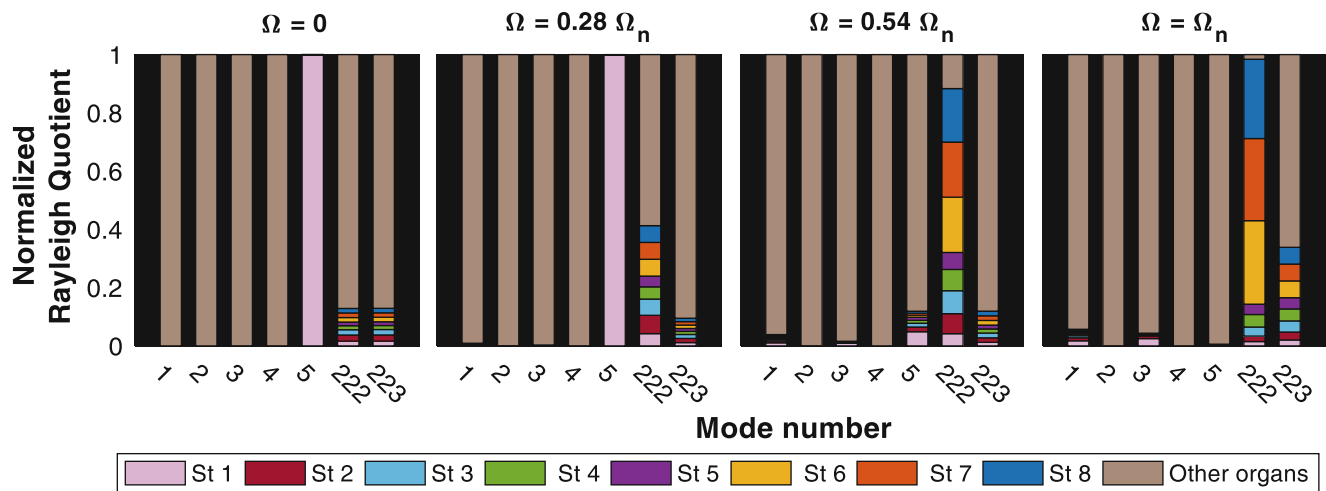


Fig. 10.7 Evolution of Rayleigh quotient of different parts during veering – mistuned model (St = Stage)

In the first instance, calculations were made by assuming a linear bearing, whose stiffness is measured during pump operation. Results show that the model is efficient to reproduce phenomena that were observed experimentally. Gyroscopic effect, spin softening, centrifugal stiffening are correctly taken into account and the veering phenomena has been reproduced. Mistuning has been added to the model and the analysis of its influence on the organization of the blade modes and on the veering phenomenon was carried out.

The small dimension of the model makes it suitable for the simulations of control laws taking into account the flexibility of the blades. In this scenario, the perspective of this work is to define the magnetic bearing model and a control law to study the impact of the blades motion on the controller performance.

## References

1. Defoy, B., Alban, T., Mahfoud, J.: Experimental assessment of a new fuzzy controller applied to a flexible rotor supported by Active Magnetic Bearings. In: Proceedings of the Tenth International Conference on Vibrations in Rotating Machinery, pp. 1–10 (2012)
2. De Lepine, X., Der Hargopian, J., Mahfoudh, J.: Contrôle modal à partir d'un modèle condensé équivalent réduit, application à un treillis. In: Vibrations. Chocs et bruits, Lyon (2006)
3. De Miras, J., Charara, A.: Unbalance cancellation with rotating reference control for a horizontal shaft. In: Proceedings of the Sixth International Symposium on Magnetic Bearings, pp. 673–672, MIT, Cambridge (1998)
4. Parent, M-O, Thouverez, F.: Whole Engine Interaction in a Bladed Rotor-to-Stator Contact. In: Proceedings of ASME Turbo Expo 2014: Turbine Technical Conference and Exposition (2014)
5. Gruin, M., Thouverez, F., Blanc, L., Jean, P.: Nonlinear dynamics of a bladed dual-shaft. *Eur. J. Comput. Mech.* **20**(1–4), 207–225 (2011)
6. Lesaffre, N., Sinou, J.-J., Thouverez, F.: Contact analysis of a flexible blades-rotor. *Eur. J. Mech. A/Solid.* **26**(3), 541–557 (2007)
7. Sinha, S.K.: Dynamic characteristics of a flexible bladed-rotor with Coulomb damping due to tip-rub. *J. Sound Vib.* **273**(4–5), 875–919 (2004)
8. Gmür, T.: *Dynamique des Structures: Analyse Modale Numérique*. Presse Polytechnique et Universitaires Romandes, Lausanne (1997)
9. Roark, R.J., Young, W.C., Budynas, R.G.: *Roark's Formulas for Stress and Strain*, vol. 2002. McGraw-Hill, New York (2002)
10. Friswell, M.: *Dynamics of Rotating Machines*. Cambridge University Press, Cambridge (2010)
11. Lalanne, M., Ferraris, G.: *Rotordynamics Prediction in Engineering*. Wiley, Chichester (1998)
12. Pierre, C.: Mode localization and eigenvalue loci veering phenomena in disordered structures. *J. Sound Vib.* **126**(3), 485–502 (1988)



# Chapter 11

## Pushing 3D Scanning Laser Doppler Vibrometry to Capture Time Varying Dynamic Characteristics

Bryan Witt and Brandon Zwink

**Abstract** 3D scanning laser Doppler vibrometry (LDV) systems are well known for modal testing of articles whose excited dynamic properties are time-invariant over the duration of all scans. However, several potential test situations can arise in which the modal parameters of a given article will change over the course of a typical LDV scan. One such instance is considered in this work, in which the internal state of a thermal battery changes at different rates over its activation lifetime. These changes substantially alter its dynamic properties as a function of time. Due to the extreme external temperatures of the battery, non-contact LDV was the preferred method of response measurement. However, scanning such an object is not optimal due to the non-simultaneous nature of the scanning LDV when capturing a full set of data. Nonetheless, by carefully considering the test configuration, hardware and software setup, as well as data acquisition and processing methods it was possible to utilize a scanning LDV system to collect sufficient information to provide a measure of the time varying dynamic characteristics of the test article. This work will demonstrate the techniques used, the acquired results and discuss the technical issues encountered.

**Keywords** 3D · Laser · Vibrometer · Experimental · Modal

### 11.1 Introduction

3D Scanning laser Doppler vibrometer systems are increasingly used to measure vibration data for extracting modal parameters of an impressive range of test articles. These test articles are typically time-invariant; their dynamic characteristics remain unchanged during the time it takes to complete a full scan, or even multiple scans to obtain all necessary data. Indeed, this is a general requirement for scanning LDV tests in order to ensure a consistent set of vibration data, such as frequency response functions (FRF), are being collected. However, many test articles do not necessarily satisfy this time-invariant stipulation, such as rotating machinery or systems with mass transfer or state changes. This work will focus on one such application, an activated thermal battery, which undergoes rapid thermal and internal state changes over time.

Modal properties of these batteries, which are used for finite element model (FEM) updating, were previously only extracted from tests conducted under ambient conditions (pre- or post-activation) due to the extreme temperatures they reach during activation. However, it is desired to develop a FEM that is representative of the batteries during activation. Since it was expected that the modal properties of the batteries change continuously over their activated lifetime, a test method was required which can capture and describe dynamic characteristics as a function of time. Such a test method must also be capable of handling extreme external temperatures of the test article and not mass load the relatively small object. For these reasons, the 3D SLDV still presented the best possibility of capturing the required data of all the methods available to the authors at the time.

---

Sandia National Laboratories is a multimission laboratory managed and operated by National Technology and Engineering Solutions of Sandia, LLC., a wholly owned subsidiary of Honeywell International, Inc., for the U.S. Department of Energy's National Nuclear Security Administration under contract DE-NA-0003525.

B. Witt (✉) · B. Zwink

Sandia National Laboratories, Albuquerque, NM, USA

e-mail: [blwitt@sandia.gov](mailto:blwitt@sandia.gov); [bzwink@sandia.gov](mailto:bzwink@sandia.gov)



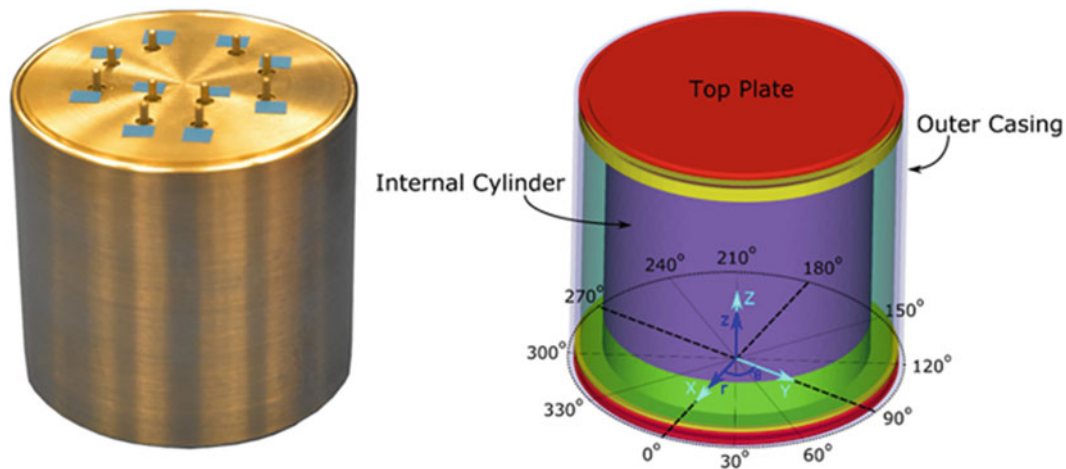


**Fig. 11.1** Test article and model representation

## 11.2 Test Article Description

The test article can be characterized as a sealed outer cylindrical casing with a solid cylindrical internal feature. The unit is approximately 6 cm tall, 6 cm in outer diameter, and has a mass of roughly 0.5 kg. The outer casing is metallic and the top and bottom plates are welded to the outer casing. The internal cylindrical feature is under a preload and supported within the casing by a non-homogeneous layer of insulation which contacts the internal surfaces. A pictorial representation of this generalized characterization is provided in Fig. 11.1. A global Cartesian coordinate system, denoted  $[X, Y, Z]$  was defined at the center of the outer casing bottom plate. A cylindrical coordinate system, denoted  $[r, \theta, z]$ , used to locate the measurement nodes, was defined at  $[0, 0, 0]$  in the global Cartesian system. The  $0^\circ$  azimuth was aligned directly the global  $X$  axis.

A discussion of the mechanics behind the internal state changes of an activated thermal battery are beyond the scope of this paper. Rather, a simple dynamic analogy is offered to help understand the time-varying nature of these batteries: the internal cylindrical feature can be thought of as a mass suspended by spring elements which drop to very low stiffness values once activated, then stiffening/relaxing as a function of temperature. Even with the internal insulation, the external surfaces of these units will reach very high temperature levels (hundreds of degrees Celsius).

## 11.3 Preliminary 3D SLDV Modal Survey

Prior to the activated testing which is the focus of this work, a modal survey was conducted on these thermal batteries [1]. This preliminary modal testing also utilized the 3D SLDV system to prevent mass loading the units. A summary of that testing is presented here for completeness.

A rigid, portable stand was constructed for the 3D SLDV system, which is shown in Fig. 11.2. The laser system was anchored in position and a 3D alignment procedure was performed. The battery was placed in the test bay on a stack of high temperature silicon sponge to approximate a free-free boundary condition. A small modal hammer attached to a linear actuator driven by a square wave function generator was used as an automatic impact hammer setup. The auto hammer assembly was attached to a linear positioning stage which allowed for precision adjustments of the hammer impact location in two degrees of freedom (up/down, left/right).

A high spatial density of measurement points (see Fig. 11.3) was achieved by using the 3D SLDV system versus a traditional roving hammer test technique (to keep from mass loading the unit). Testing conducted in [1] indicated that the capability to measure all three translational degrees of freedom (DOF) at each measurement location was critical to accurately characterizing the modes of the battery, particularly in inferring the motion of the internal cylindrical feature.

The preliminary modal survey identified five modes of interest for FEM updating and overall response characterization: two internal cylinder translation/rocking modes, a top/bottom plate drumming mode, and two internal cylinder axial translation/torsion modes. These shapes are shown in Fig. 11.4. In addition, there are two well excited internal cylinder rotation modes about  $X$  and  $Y$  that are higher in frequency than the FEM would attempt to correlate, which are not shown

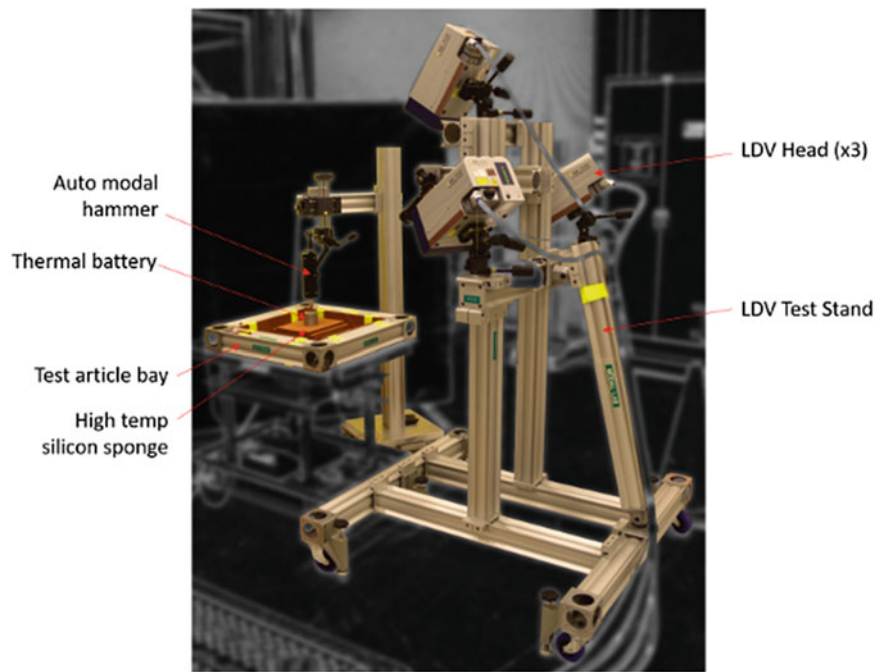


**Fig. 11.2** Preliminary (pre-activation) modal survey test setup

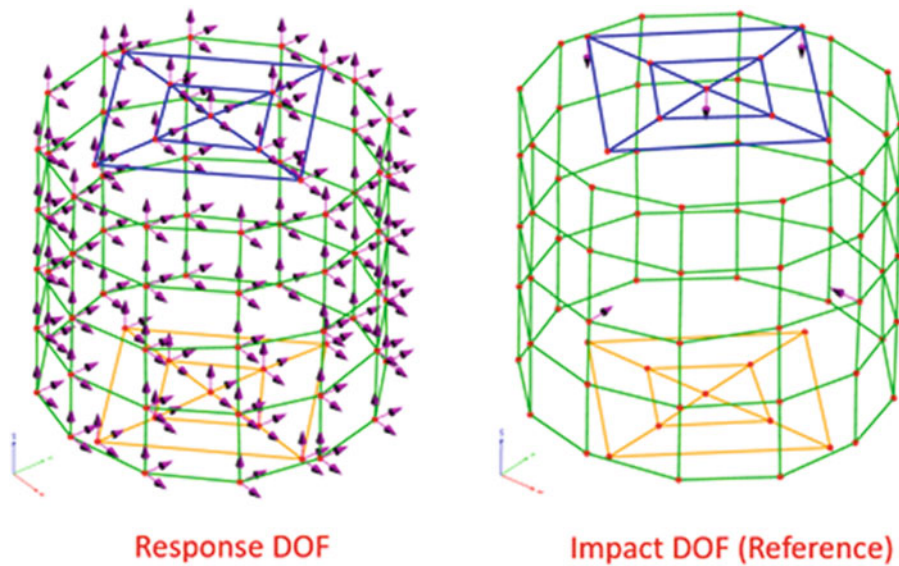


**Fig. 11.3** Measured DOF in preliminary 3D SLDV modal survey

in Fig. 11.4 but are noted for later analysis. The motion of the visibly inaccessible internal cylindrical feature is inferred from the external measurements of the LDV by considering the conservation of momentum. For example, the first mode (translation + rocking) appears nearly to be rigid body motion, although at frequencies much higher than the actual rigid body motion of the unit as tested. This indicates that the internal mass must be moving opposite of the external motions observed.

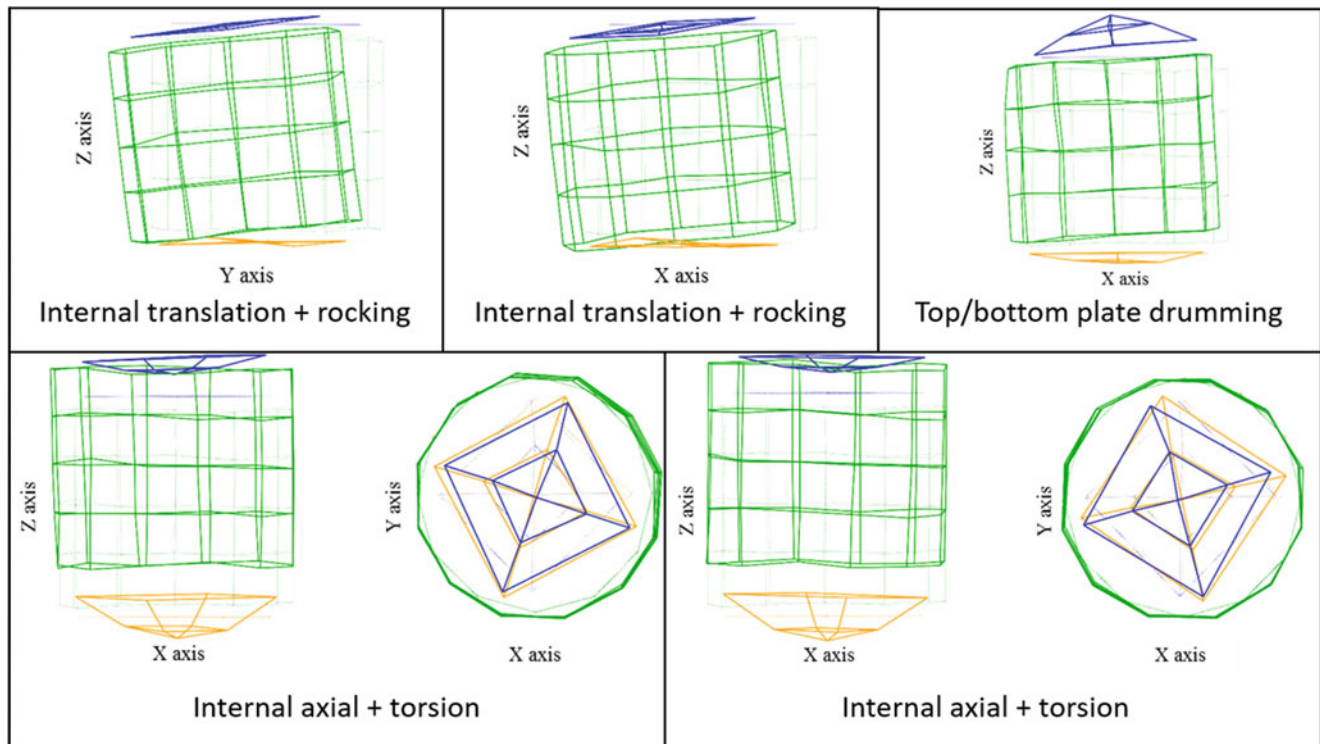


Fig. 11.4 Mode shapes from preliminary modal survey

## 11.4 Activated Test Setup

A representation of the overall test setup used to collect dynamic data during battery activation is shown in Fig. 11.5. The entire test setup shown is contained within a local exhaust ventilation (LEV) system (vent hood). The LEV sash window was closed during all testing and the exhaust system was continuously pulling air through the enclosed hood. The overarching goal of this test setup was to contain the battery in the event of an abnormal activation, mitigate the effects of heat on the load cells, and reduce the amount of time required to complete a “full” scan of the battery. The test setup needed to be robust and controlled remotely; no further adjustments could be made once the battery was activated as it was contained in the LEV for safety considerations.

The test article can be seen in the center of the primary figure (a) as well as the inset picture. The metallic surface of the battery was quite shiny, which untreated, resulted in very poor signal return to the laser system and a low signal to noise ratio. The surface of the battery to be scanned was covered with white high temperature paint, into which a layer of retroreflective glass beads was deposited (sprinkling with a measuring spoon) while still wet. The resulting increase in signal return to the laser was appreciable, however, the surface reflectivity was not uniform and demonstrated “low spots” in signal return due to the deposition method. This was easily dealt with by slightly moving final measurement points, but a more uniform surface treatment method could be established which would preclude the issue altogether. Other surface treatments were evaluated (developer spray, whiteout, silver permanent marker spots, silicon grease with retroreflective glass beads) but the high temperature paint with beads was found to provide the best combination of ability to withstand high temperatures without degrading and resistance to mechanical abuse (would not wipe off if touched accidentally during test setup).

It should be noted that the laser spots in the inset picture in Fig. 11.5 are not co-located because the LEV glass sash was up when the picture was taken; 2D and 3D alignments, 3D transformations and measurement point placement for the 3D SLDV system were performed with the glass sash down, since testing would be conducted in this configuration (i.e. when the glass sash is lowered, the three laser spots in the figure are co-located). The alignment through the sash window accounted for the refraction caused by the glass, thus removing the glass for the photograph resulted in the non-collocation of the laser spots.

A free-free boundary condition was desirable for this test and was approximated using insulative fiber sheets (b) and soft, high temperature rated silicon sponge material (c). Initially only one insulation sheet was placed between the test article and the sponge as shown in the primary figure. However, the coefficient of thermal expansion is very high for the sponge material and, in an initial trial run, it expanded enough to displace the battery up so much that the automatic hammer (f) load cells

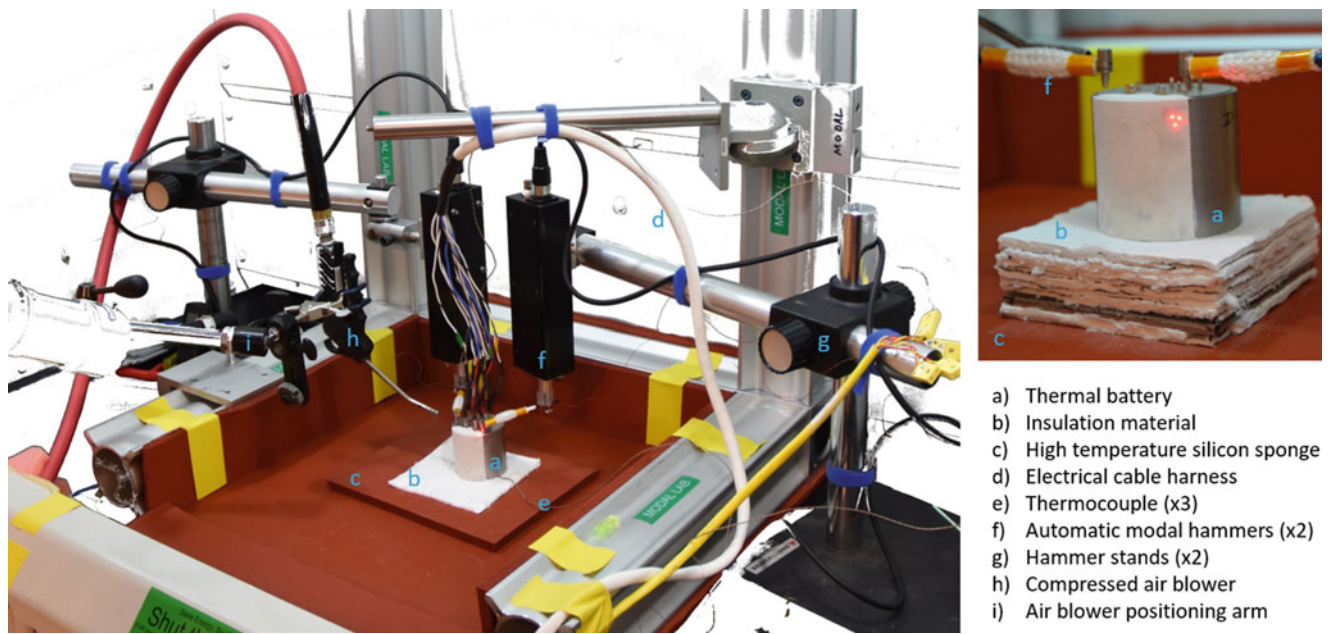


**Fig. 11.5** Overall test setup

were in contact with the top of the unit. To prevent the same issue during actual testing, several sheets of fiber insulation material and a steel plate were placed between the battery and sponge material. It was observed that the elastic modes of the test article were still sufficiently separated from the rigid body modes of the test article in this configuration to achieve an approximate free-free boundary condition.

Small instrumented modal hammers attached to linear actuators (f) were used to excite the batteries, impacting at two locations on the top plate determined by the results of the preliminary modal survey. The impact locations were chosen such that they were approximately  $90^\circ$  apart to better excite orthogonal mode pairs. It was also important that the laser system had line of sight to the hammer impact points, providing the ability to make drive point measurements.

The handles of the hammers were covered in a ceramic fiber braided shielding which was secured with a polyimide tape. This was done as a protective measure since it was unknown at the time how much heat loading the load cell and hammer handle would pick up from the extreme external temperatures of the battery. In addition to the shielding, a compressed air nozzle was positioned with an articulating arm (h, i) such that cool air was constantly blown directly over the hammer load cells. It was noted that the nozzle was positioned closer to the load cell on the left (hammer #1) and so its effectiveness for the right side (hammer #2) was expected to be diminished. Two single arm boom stands (microscope equipment) were used to hold and position the linear actuators/hammers over the test article.

## 11.5 Data Acquisition and Processing

Ideally, data would be collected at all measurement points simultaneously rather than scanning from point to point individually, as must be done with the 3D SLDV system. If this were achievable, each scan would represent a full and consistent representation of the test article's dynamic characteristics at the time the "instantaneous scan" occurred. This idealized "instantaneous scan" is not achievable with the SLDV system however, and the best approximation can only be to reduce two aspects of data collection: (1) the time between an individual scan set's start and finish, and (2) the time between successive scan sets. These two goals seek to minimize the changes in the battery dynamics during a scan set and to keep from missing temporal information due to a "picket fence effect" from having too much time between successive scan sets. Missing temporal information between sets was viewed as a secondary concern to the system dynamics changing during a scan set which embeds several issues into the data, particularly that the resulting FRF are not consistent (each scan point is technically of a different dynamic system) and modes will appear to be complex (due to phase shifts caused by measuring points successively).

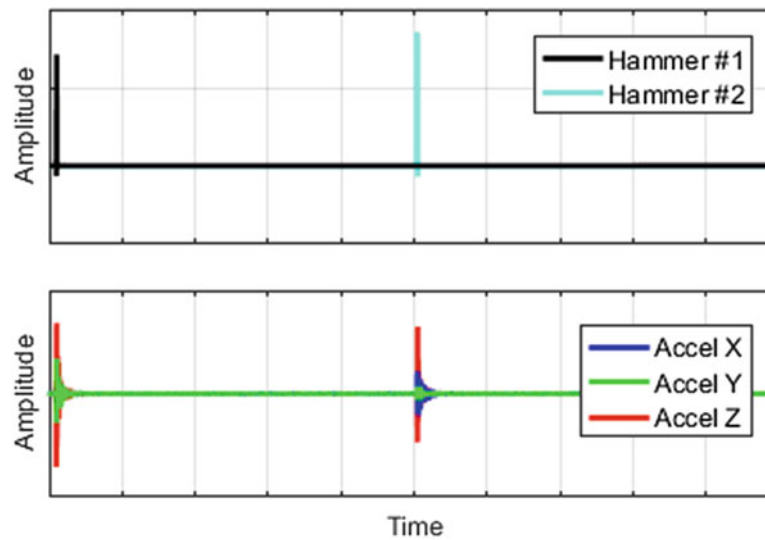


**Fig. 11.6** Representative time frame capture with alternating hammer impacts

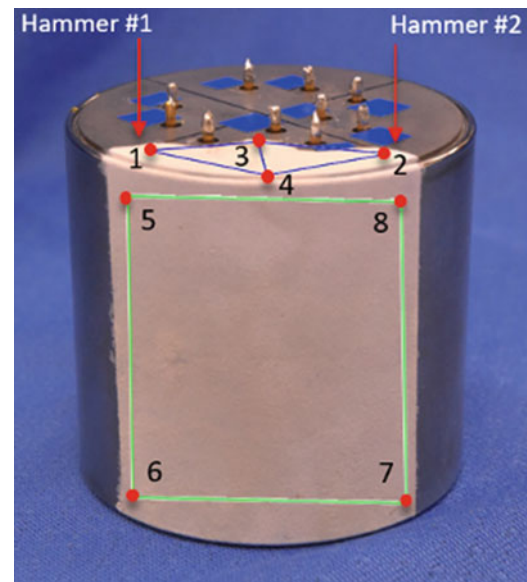
As discussed in Section 4, two impact locations on top of the battery spaced at an approximately  $90^\circ$  interval were identified as necessary to excite all modes of interest (Fig. 11.4). Hence, it was necessary to use two hammers functioning in parallel to collect a full scan set in as short of a time as possible. To accomplish this, two function generators were used to send square wave signals to the linear actuators which “swung” the hammers. The first generator signal (to hammer #1) had a frequency of 3.4 Hz with a 50% duty cycle, a burst period of 333 ms, and an internal trigger. The second generator signal used the same frequency, duty cycle and burst period but used the first signal as an external trigger reference. The phasing of the second signal relative to the first was then adjusted such that the time between hammer #1 and hammer #2 impacts was approximately 100 ms (on average this required approximately  $-120^\circ$  phase shift). The 100 ms time frame was selected as a sufficiently short period in which the acceleration response at all measurement points was completely observed (with margin in case modes of the activated battery had lighter damping, though not expected). Since the signals were completely observed in the time frame, no windows were applied to the response time histories to prevent spectral leakage. The peak force was maintained at the lightest level observed to provide adequate signal to noise, be repeatable with the linear actuators, and minimize response amplitude dependent nonlinear effects.

For activated testing, all data were collected in the time domain and post-processing was done in Matlab. Typically, each hammer impact and subsequent response measurement would be collected in a separate frame with the impact reference DOF specified explicitly in the SLDV software, making subsequent frequency response function (FRF) calculations easier. Using two alternating reference impact DOF complicated this practice, so both impacts and their corresponding response measurements were captured in one frame and then parsed out post-test in Matlab. This also set the time window of each scan point at 200 ms. A representative time frame before parsing into individual impacts is shown in Fig. 11.6.

The frequency bandwidth of interest was known from the preliminary modal survey. Accordingly, the data sample rate was set to 2.5 times the useful bandwidth to satisfy the Nyquist criterion. Fixing the sample rate and time frame dictated the final time resolution. SLDV velocity response data were differentiated to acceleration within the SLDV data acquisition system. Acceleration was used due to large, lightly damped rigid body velocity responses which took an extremely long time to decay which was not conducive to speeding up the data acquisition process. The vibrometer tracking filter was set to “slow” to help with speckle noise. Also, in the interest of taking the fastest measurements possible, averaging was turned off as was the option to automatically remeasure points with low signal to noise ratios (SNR).

The SLDV data acquisition graphical user interface (GUI) is designed to collect one scan set in time history mode, which is normal practice. However, for this application, it was desired to take sequential scan sets with as little time in between (picket fence effect) for an extended period (on the order of several hours). A Visual Basic macro that is included in the SLDV data acquisition software was utilized to perform exactly this task. To use the macro, a user enters the desired data acquisition settings in the GUI, launches the macro which has a separate GUI, and enters the desired number of sequential scan sets to take, as well as a base filename which will be automatically incremented. The macro then immediately launches a scan sequence, saves to disk the completed scan set as a separate record with an incremented filename, and launches the next scan. This process repeats until the desired number of scan sets have been taken or the user aborts the macro process.

**Fig. 11.7** Reduced set of measurement points for activated testing



The last technique used to reduce the scan time was to limit the number of response measurement points to the minimum necessary to be able to spatially resolve the modes of interest. A set of 8 nodes were selected (see Fig. 11.7): four on the casing and four on the top plate, two of which were drive points. These nodes were selected to allow visualization of top plate motion, as well as outer case lateral/axial translation and rocking. The scan order was set as shown, taking both drive points first (1,2).

Using these scan settings, measurement/impact points and the macro code to automate launching scan sets the total time to take and save to disk a complete set of 48 time histories (2 references  $\times$  8 nodes  $\times$  3 DOF) was approximately 6 s. Of the 6 s per scan set, approximately 3 s were taken up by writing the data to mechanical hard drive and launching the next scan.

Data processing started with reading the SLDV scan file into Matlab using a File Access Software server and extracting the raw data. Individual time frames were parsed into two separate time histories, one for either impact reference. All time histories were then trimmed to have an equal number of points. Time stamps were also collected from the scan file and used as the basis for determining the timing and synchronizing the vibration data with the external thermocouples attached during the test. FRFs were calculated for each measured DOF using the H1 estimator. Finally, complex mode indicator functions (CMIF) were generated for each scan set, which provide a “roll up summary” of all 48 FRFs.

## 11.6 Results

Each scan set was treated as though all measurement points had been collected simultaneously, even though the collection period was on average approximately 3 s. In doing so, the CMIF calculated for each scan set (or record) is now said to represent the battery’s dynamic characteristics at a given point in time. By stacking CMIFs from sequential records together, a spectrogram is formed that shows the time-varying dynamics of the thermal battery over its entire activation lifetime (see Fig. 11.8). Hence, *each vertical line in the CMIF spectrogram represents a complete transfer function matrix, from which modal properties can be extracted*. At  $t < 0$  (red line), the battery is in its initial state. At  $t = 0$  (red line), the battery is activated and the dynamic properties are observed to change dramatically as the external temperatures rapidly increase. The external (and internal) temperatures continue to rise, eventually peaking. Inflection points, or knees, in the response frequencies are observed to occur at different times following peak external temperature, which may correspond to internal temperature trends. Finally, at  $t \gg 0$  the battery has returned to ambient and is at its final state. One general observation is that in the moments following activation there appear to only be two well excited modes or groups of modes. Resonance peaks then begin to split off and form knees before relaxing in frequency again as the battery cools.

Clearly, there are drastic differences in the dynamic characteristics of the battery before, during and after activation. If only one DOF response had been collected and the spectrogram comprised only a single spectrum or FRF, it would be almost impossible to track where each mode shifted to in terms of frequency and damping, as well as to what extent each shape has changed. Since this data set contains an entire transfer function matrix at each “time step” we can use the spectrogram to

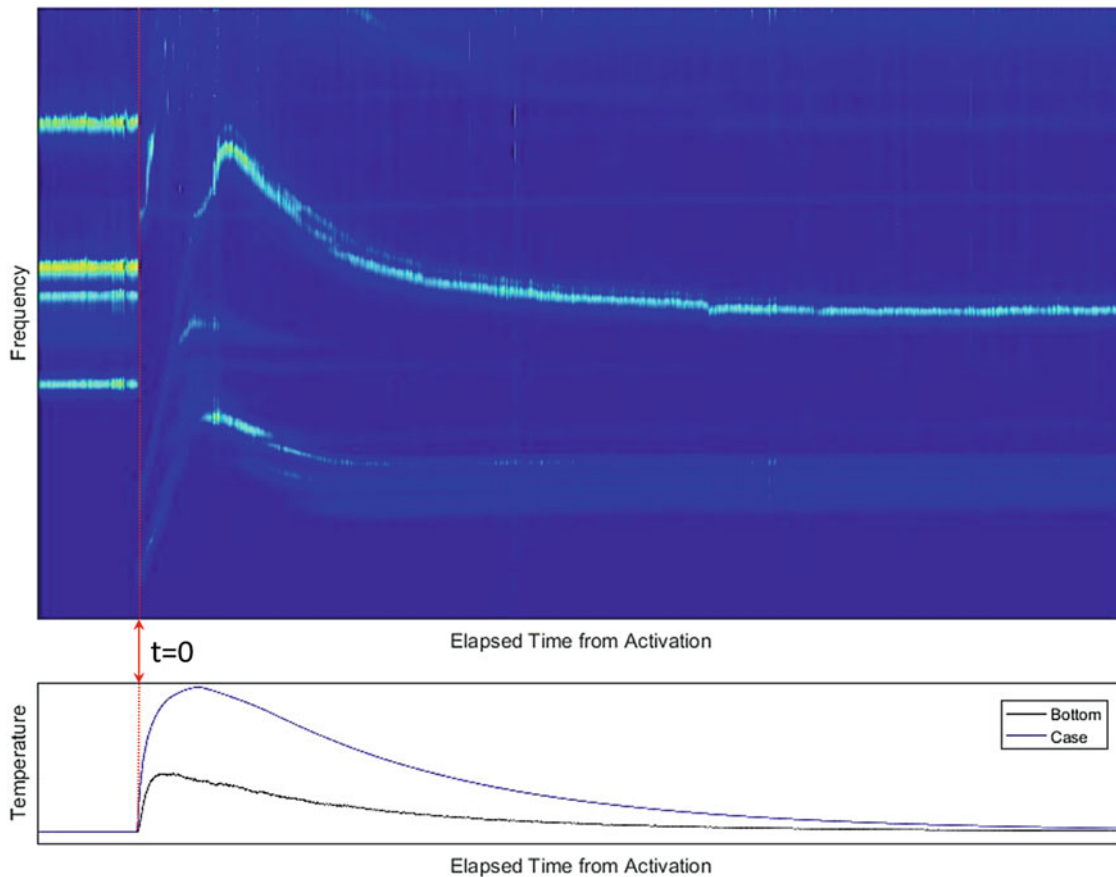


**Fig. 11.8** CMIF Spectrogram of battery activation lifetime

discern which “times,” or more accurately, scan sets are of most interest. These scan sets can then be analyzed separately to identify modal parameters at that point in time. Noise in the data was accepted at several steps (no averaging, no remeasuring) to gain data acquisition speed, and this trade-off makes fitting the modal parameters a difficult task, particularly given the reduced measurement point set. Even so, modes were extracted using the Synthesize Modes and Correlate (SMAC) algorithm [2] from four scan sets corresponding to (1) pre-activation, (2) activation, (3) near the peak case temperature and (4) final ambient state. Once modal parameters were extracted, efforts were made to track and map them to the CMIF spectrogram. Currently, tracking is done manually by visual comparison of mode shapes only (future work may investigate other methods of comparison such as the modal assurance criterion). This is shown in Figs. 11.9, 11.10, and 11.11 for selected internal cylinder modes: two translation/rocking modes, one axial/torsion mode, and two rotation modes (about X and Y). In these figures, the inset CMIF plots have colored borders corresponding to the arrows marking their position in the spectrogram.

These figures further illustrate the drastic changes in dynamic response at different stages of the battery’s lifetime. Table 11.1 contains the percent differences in frequency between the pre-activation and later stages of activation. Each mode drops 45–60% in frequency almost instantly. Except for the axial mode, each mode returned to within approximately 10% of its original frequency before stabilizing at 20–30% lower than it started. The mechanics of the internal state change have a greater and longer lasting effect on the axial mode(s). It is also noted that in all times following activation, the damping values are appreciably higher. In summary, the data clearly indicate that there are serious implications for using modes of the battery in either pre- or post-activation ambient states for FEM updating if the model is meant to represent an activated system.

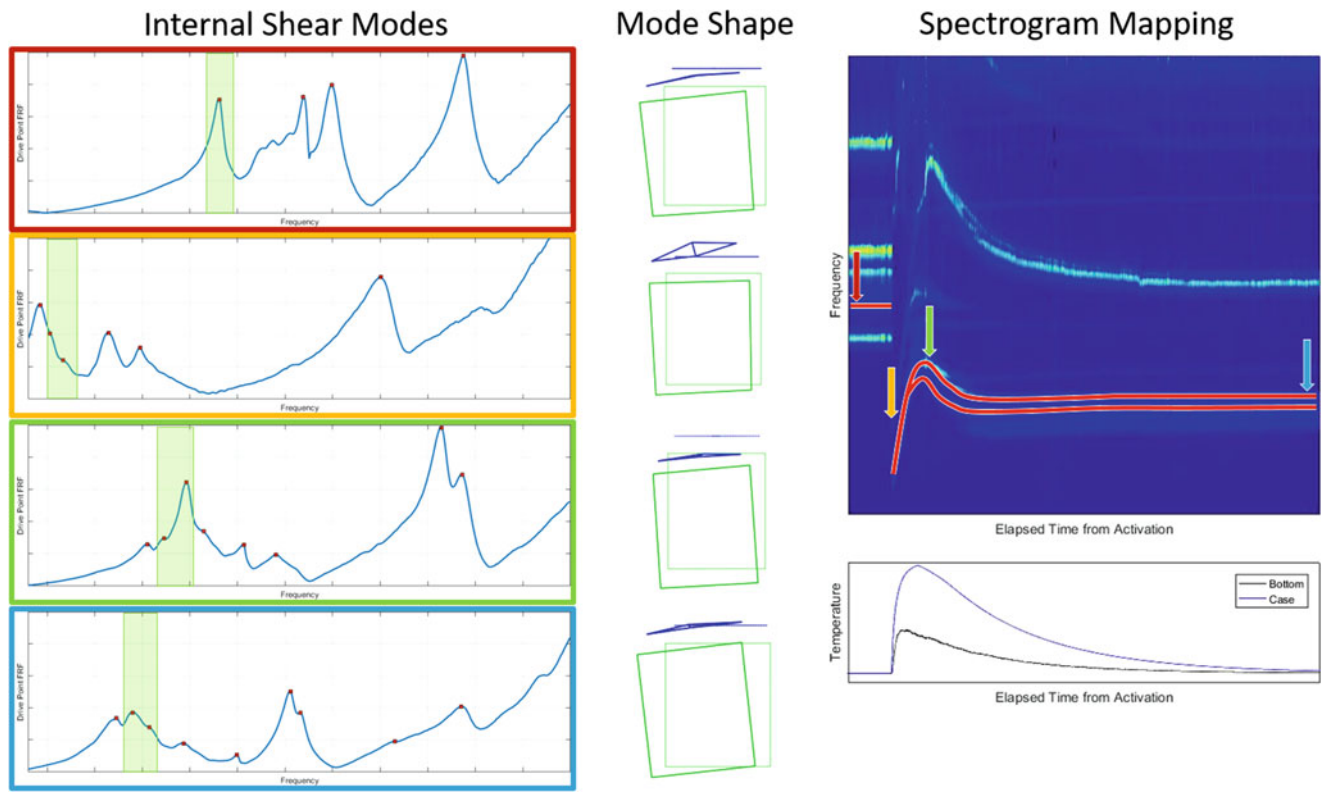


Fig. 11.9 Mode tracking for internal cylinder translation

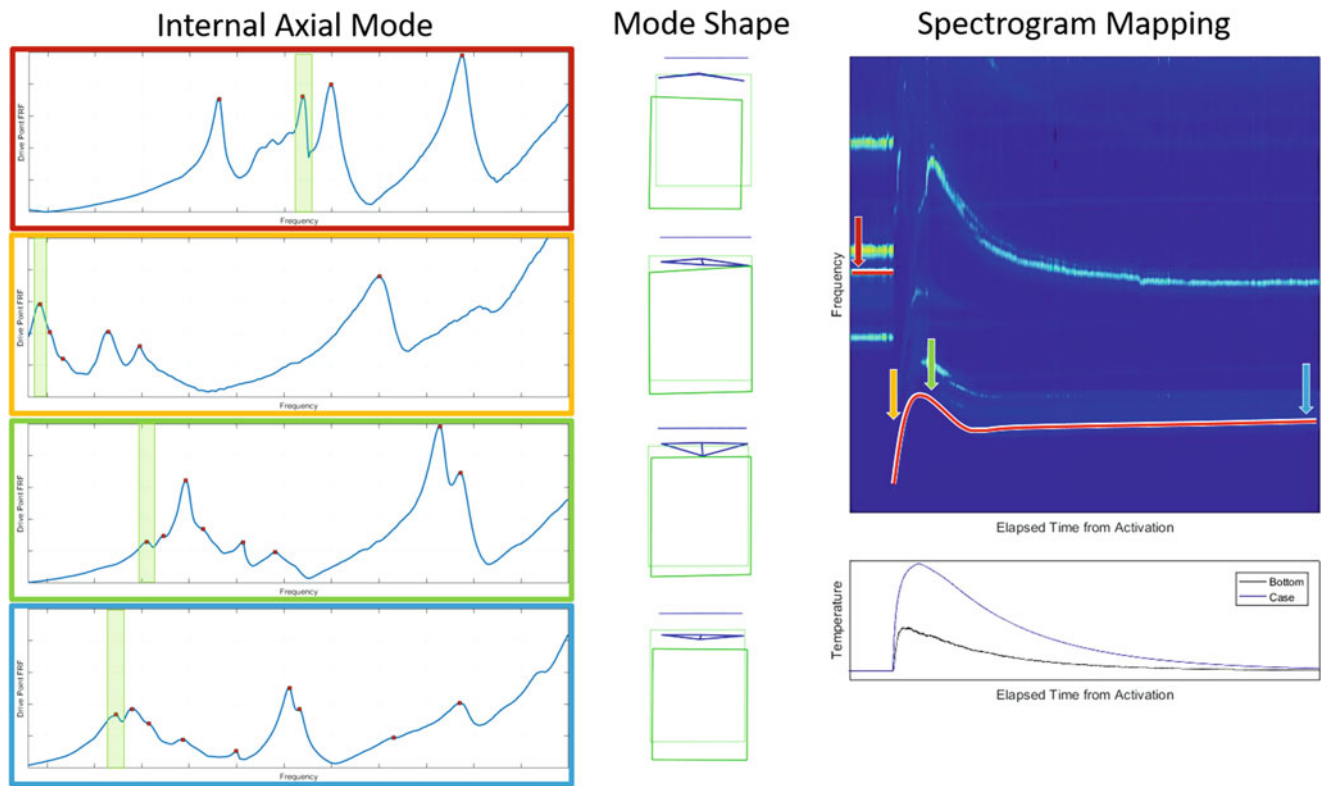
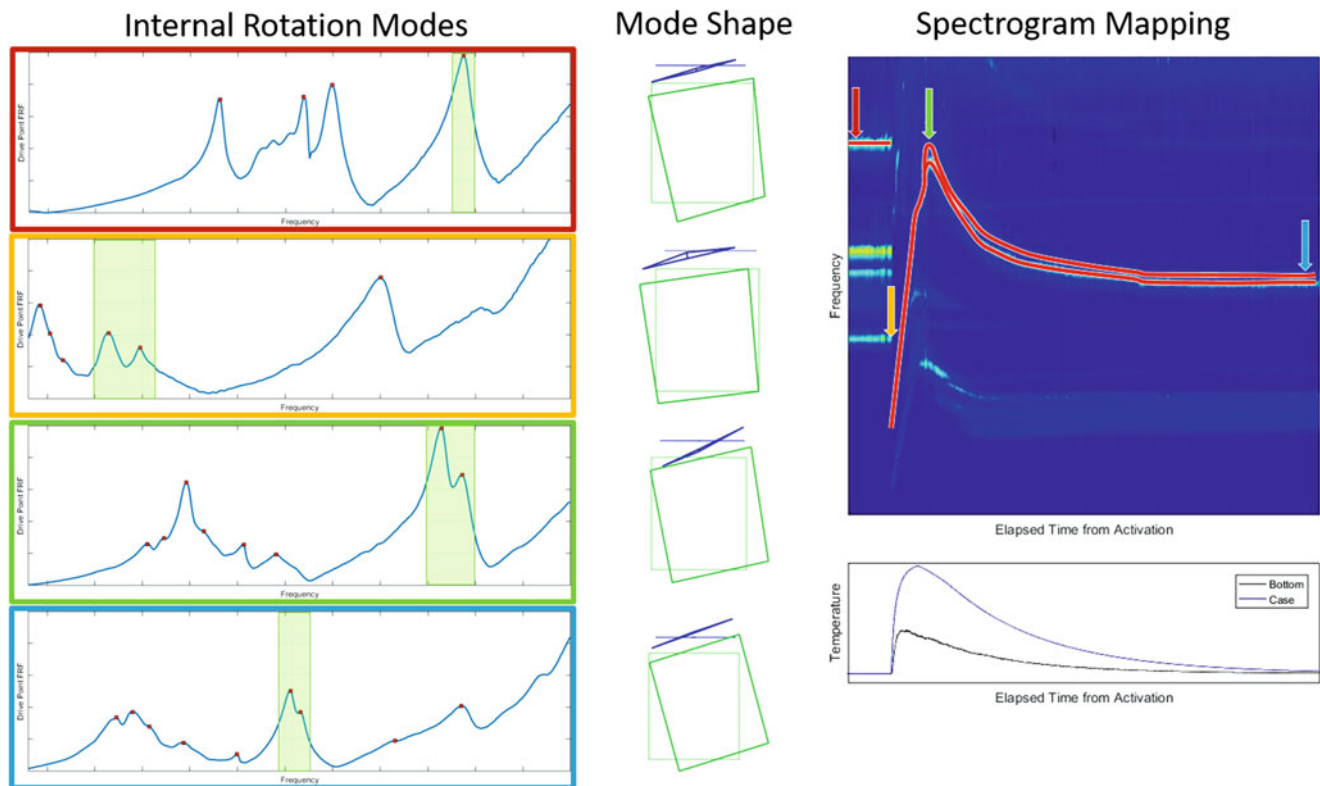


Fig. 11.10 Mode tracking for internal cylinder axial





**Fig. 11.11** Mode tracking for internal cylinder rotation

**Table 11.1** Frequency differences between pre-activation and later states

Internal cylinder mode	% Difference to pre-activation		
	Activated (%)	Peak external temp (%)	Post-activation (%)
Translation 1	-47	-10	-20
Translation 2	-44	-9	-20
Axial	-59	-34	-40
Rotational 1	-60	-4	-29
Rotational 2	-58	-1	-27

## 11.7 Technical Issues & Conclusions

Several technical issues were encountered during this test effort. Some were easily remedied by changing aspects of the test setup, such as using several sheets of insulation material as a base rather than a silicon sponge material with a high coefficient of thermal expansion (discussed in Sect. 11.4).

Free air temperature measurements near the load cells during testing indicated that the temperatures did not reach levels which would affect the sensor sensitivity. It is unknown if the compressed air blowing over the sensors was necessary, though it would likely be included again in future testing as a precaution.

As soon as the battery was activated, the noise levels in the measured response data became substantially more pronounced. Once temperatures began to recede, the noise dropped to pre-activation levels. No differences in the test setup were observed during the time when noise levels were elevated (e.g. LEV flow rates were stable, etc.). Accordingly, we conjecture that either the high temperatures affected the surface treatment (paint/glass beads) in a reversible manner, or thermal gradients around the battery induce changes in the refractive index of the air in the laser signal path, in turn leading to increased speckle noise. The latter is believed to be a more plausible scenario but is still being studied. It was also noted that the response measurement points on the top plate nearest the compressed air nozzle were less noisy than the others, further suggesting thermal gradient induced noise.

The most fundamental issue with this test is the use of a sequential scanning system to capture the dynamics of a time-varying system. Digital image correlation (DIC) may be explored, although the high damping levels observed during activation may lead to test data in the noise floor of current systems. Another potential future alternative is multipoint LDV systems, which are still in early stages of implementation. Both of these methods would suffer from thermal gradient effects however.

In conclusion, while not ideal, pushing the 3D SLDV did provide data for FEM updating which had not been practically obtainable before. The test configuration successfully captured a wide range of time-varying dynamic characteristics of the test article. The test data collected has also provided useful information which is being coupled with other physical tests and models to help understand the underlying physics of the battery during activation.

**Note** This manuscript has been authored by National Technology and Engineering Solutions of Sandia, LLC. under Contract No. DE-NA0003525 with the U.S. Department of Energy/National Nuclear Security Administration. The United States Government retains and the publisher, by accepting the article for publication, acknowledges that the United States Government retains a non-exclusive, paid-up, irrevocable, world-wide license to publish or reproduce the published form of this manuscript, or allow others to do so, for United States Government purposes.

## References

1. Witt, B., Zwink, B., Hopkins, R.: Applications of 3D scanning laser doppler vibrometry to an article with internal features. In: Rotating Machinery, Hybrid Test Methods, Vibroacoustics & Laser Vibrometry. Proceedings of the 35th International Modal Analysis Conference, Springer, NY, vol. 8, pp. 85–95 (2017)
2. Hensley, D., Mayes, R.: Extending SMAC to multiple references. In: Proceedings of the 24th International Modal Analysis Conference, The Printing House, Inc. Stoughton, WI, pp. 220–230 (2006)



# Chapter 12

## Dynamic Measurements on Miniature Springs for Flaw and Damage Detection

Daniel P. Rohe

**Abstract** Small components are becoming increasingly prevalent in today's society. Springs are a commonly found piece-part in many mechanisms, and as these components become smaller, so do the springs inside of them. Because of their size, small manufacturing defects or other damage to the spring may become significant: a tiny gouge might end up being a significant portion of the cross-sectional area of the wire. However, their small size also makes it difficult to detect such flaws and defects in an efficient manner. This work aims to investigate the effectiveness of using dynamic measurements to detect damage to a miniature spring. Due to their small size, traditional instrumentation cannot be used to take measurements on the spring. Instead, the non-contact Laser Doppler Vibrometry technique is investigated. Natural frequencies and operating shapes are measured for a number of springs. These results are compared against springs that have been intentionally flawed to determine if the change in dynamic properties is a reasonable metric for damage detection.

**Keywords** SLDV · Damage Detection · Modal

### 12.1 Introduction

Small parts find their way into a number of components, especially in today's world of miniaturization. If such parts are involved in a system critical application, they often undergo some form of acceptance testing in order to determine whether or not there has been any damage or manufacturing defect prior to being installed. The component of interest in this work is a small extension spring, shown in Fig. 12.1 laid on top of a penny for size reference. The spring itself is very small, a nick or gouge could easily penetrate a significant portion of the cross sectional area of the wire which could lead to decreased strength or fatigue life of the component. Unfortunately, the size and shape of the spring are not conducive to easy identification of such flaws. They would not be visible without the aid of magnifying optics, and the helical shape ensures that there are a number of hidden surfaces where such a flaw might be overlooked. Sandia National Laboratories has investigated many approaches to determining flaws in these objects including optical methods such as high-resolution microscopy, stiffness screening, digital radiography and computed tomography, electrical resistivity measurements, and thermal imaging during electrical conduction. None of these approaches yielded an efficient, robust way to identify damage to these parts.

It is well known that damage to a particular component can influence a part's dynamic properties [1], so this work aimed to investigate whether such techniques could be used for these small springs. These parts have many properties that could confound a damage detection scheme. As this spring is at the lower size limit of what the manufacturer can produce reliably, there is significant amount of unit-to-unit variability between springs even within the same lot. There is also uncertainty in the boundary conditions during dynamic tests as the spring hooks are not always in the same plane, which results in different contact areas on the mounting pins. Additionally, the size of the spring poses challenges for excitation and data acquisition which can lead to reduced data quality.

Due to their size, accelerometers could not be adhered to the springs without significantly altering its mass and stiffness, and this would certainly derail any attempt to detect damage in the spring. Instead, a scanning laser Doppler vibrometer

---

Sandia National Laboratories is a multimission laboratory managed and operated by National Technology and Engineering Solutions of Sandia LLC, a wholly owned subsidiary of Honeywell International Inc. for the U.S. Department of Energy's National Nuclear Security Administration under contract DE-NA0003525.

D. P. Rohe (✉)

Structural Dynamics Department, Sandia National Laboratories, Albuquerque, NM, USA

e-mail: [dprohe@sandia.gov](mailto:dprohe@sandia.gov)

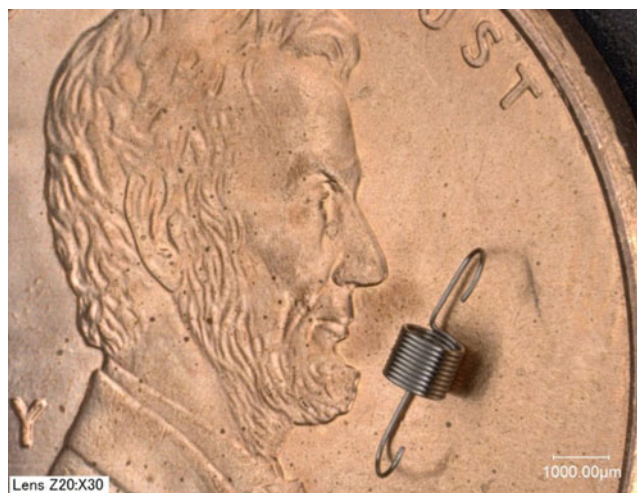


**Fig. 12.1** Small spring shown on an penny for size reference

(SLDV) was used to measure the response of the spring to vibration excitation. The SLDV has advantages over traditional mounted sensors in that it does not mass load the test article. In addition, its sensor footprint is very small, so it can measure the motion of individual coils of the spring resulting in better mode shape resolution [2]. The natural frequencies and deflection shapes of several modes were extracted using the SLDV.

## 12.2 Spring Dynamic Testing

The spring is much smaller than the objects usually tested in the modal laboratory at Sandia National Laboratories. The wire diameter of the spring was approximately  $75\ \mu\text{m}$ , and the stretched length of the spring was about 0.5 cm. The mass of the spring was approximately 2 mg. Given that the smallest accelerometer owned by the modal laboratory at Sandia National Laboratories was over 100 times as massive as the spring, and any fixture onto which the accelerometer could be mounted would likely be equally as massive, the approach of identifying spring natural frequencies by measuring on the fixture itself was discarded. Instead, the laser vibrometer system would be used to measure directly on the spring itself.

A simple fixture was designed to hold the spring during testing, as shown in Fig. 12.2. The fixture consisted of a rectangular base with two cylindrical pins. The fixture was excited using base excitation from a modal shaker (B + K Type 4809). In order to determine whether fixture modes would contaminate the spring data, preliminary finite element analysis of the fixture was performed, showing the first mode of the fixture above 100 kHz. This was well above the bandwidth of interest for the test so for this work the fixture was assumed to be rigid. Rather than trying to measure the force applied to the fixture by the shaker, a transmissibility approach was used instead. A reference accelerometer was mounted to the shaker alongside the fixture to serve as the input acceleration.

The SLDV was set up in 1D mode with a single laser head. A 3D measurement was initially considered to get the in-plane responses; however, it was unclear whether the laser system would be accurate enough to triangulate three laser points onto the thin wire of the spring. In the author's experience the typical alignment accuracy for the laser system is on the order of 0.1–0.5 mm, which is larger than the wire diameter. Additionally, only one set of close-up hardware (close-up module and lenses) were available to use at the time. Once testing started, it became clear that it would be useful to have an in-plane measurement to help identify the many modes in the bandwidth, but it was found that re-mounting the spring so the perpendicular face would be visible to the laser would result in changing natural frequencies. An alternative would be to move the laser head, but this would require re-aligning the laser to the part. Because a large number of springs were to be tested, this idea was discarded. Instead, a small piece of first-surface mirror was placed next to the spring on the shaker at a 45 degree angle allowing the laser system to measure two perpendicular sides of the spring. The final test setup can be seen in Fig. 12.3. A representative view from the laser system is shown in Fig. 12.4.

The SLDV was set up to measure 21 points on each face of the spring. This was supplemented by measurement points on the fixture to verify that it was in fact moving rigidly over the bandwidth of interest. For each test the transfer function between these fixture points and the reference accelerometer was verified to be close to 1. Because the spring is small and

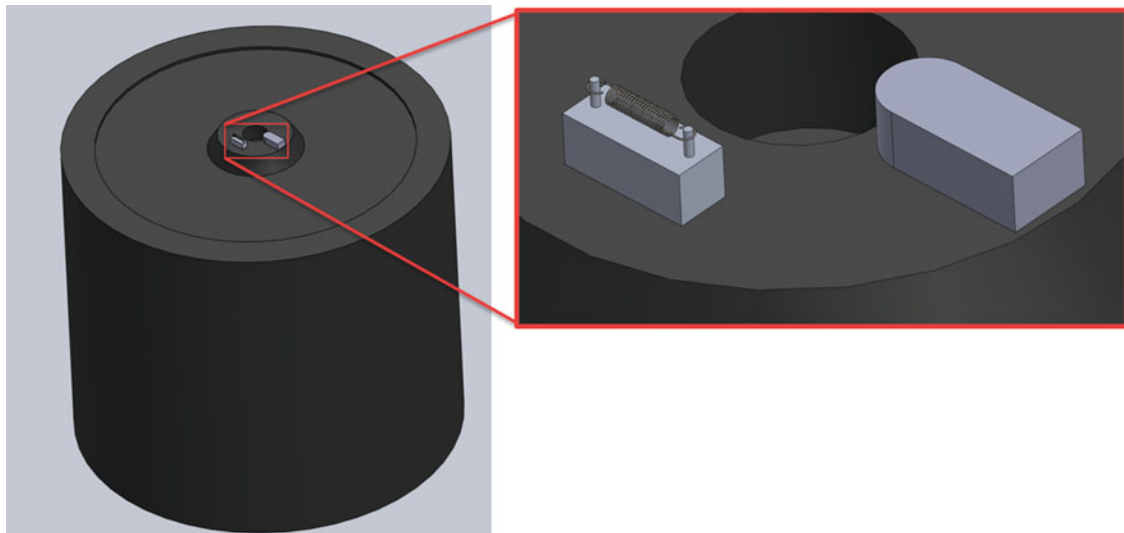


**Fig. 12.2** Schematic test setup showing the B&K Type 4809 shaker, spring fixture with spring, and a reference accelerometer

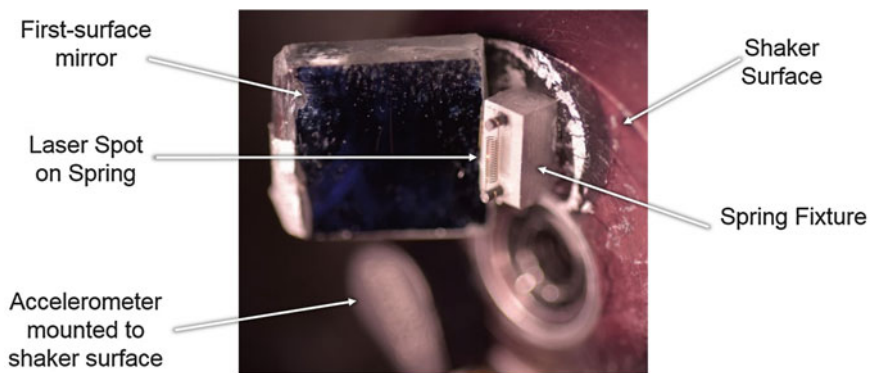


**Fig. 12.3** Close-up of test setup showing a spring mounted on the fixture alongside a first surface mirror that enables measurement of in-plane velocity

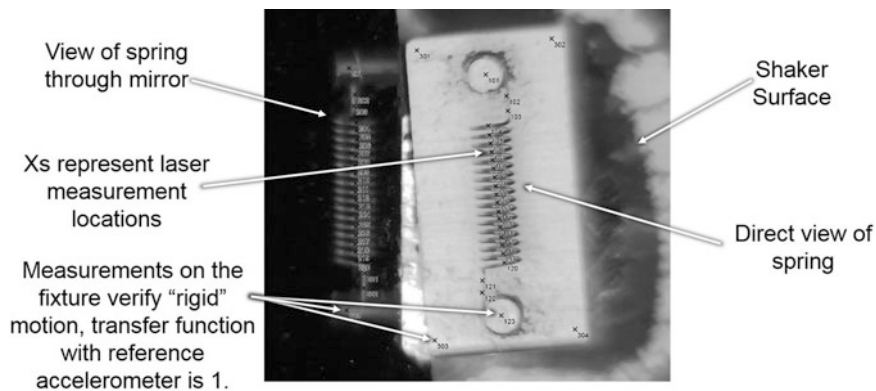


**Fig. 12.4** Representative view from the laser system; the spring can be seen directly on the right, but it can also be seen through the mirror on the left, which allows measuring the in-plane motions

the laser spot is relatively bright, it was difficult to determine exactly where the laser spot was on the spring. To aid in finding the laser spot, an external camera was used to view the spring close up, and the video was sent to a large monitor. A ring light was used to brighten the test setup, equalizing the video image exposure between the bright laser spot and the relatively dark surrounding image. This setup is shown in Fig. 12.5.

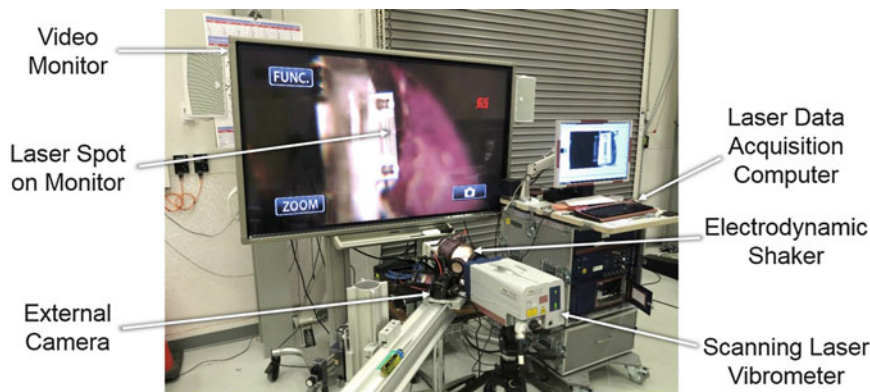


**Fig. 12.5** Overview of test setup showing the laser vibrometer, shaker, and video monitor used to find the laser spot

Flat pseudorandom vibration was applied to the shaker, and the laser vibrometer measured responses on the spring and fixture. Reasonable laser signal quality was obtained with no surface preparation, though small changes in the position of the laser spot could result in large differences in signal quality due to the cylindrical shape of the wire. The measured degrees of freedom allowed most modes of interest to be spatially distinguished, with torsion being the exception; the single line of measurement points along the centerline of the spring did not adequately capture torsional motion. The in-plane modes were excited less strongly due to being perpendicular to the motion of the shaker. In addition, the asymmetric (2nd and 4th) bending modes were not excited well since both pins are nominally moving in the same direction, although they were generally still visible above the noise floor of the measurement.

### 12.3 Natural Frequency Distributions

Since the goal of this effort was to determine the health of springs, a distribution of unflawed natural frequencies was desired against which potentially flawed springs could be compared. In order to generate these distributions, a statistically significant number of tests needed to be performed. Seven healthy springs were available to generate these distributions, and each spring was tested four times (removing it from the pins and remounting it between each test). Figure 12.6 shows a complex mode indicator function (CMIF) that highlights the spread in natural frequencies observed by mounting one spring four different times. This spread can be attributed primarily to the boundary conditions of the spring; the spring, while placed on the pins as accurately as the test engineer's dexterity would allow, could potentially have one hook slightly higher on the pin than the other, resulting in a slightly longer stretched length. Additionally, due to manufacturing variability, many springs did not have their hooks exactly in the same plane, and this could result in one or both hooks contacting the pin in more than one location. Figure 12.7 shows the CMIF for each test of all unflawed springs.

The prominent peaks in the CMIF in Fig. 12.7 were then grouped by shape. The modes never switched order from spring to spring, which made this process easier (i.e. the first peak was always first bending mode in the out-of-plane direction, second peak was always first bending in the in-plane direction, etc.). A normal distribution was fit to the natural frequencies of each mode. Figure 12.8 shows this analysis for the first bending mode of the spring. Table 12.1 shows the natural frequencies for each spring as well as the mean and standard deviation for each mode. Some modes were grouped fairly tightly, with a standard deviation of less than 20 Hz, while others showed a larger spread with a standard deviation of almost 200 Hz.

### 12.4 Flawed Spring Detection

In order to test whether or not the spring flaws could be detected by changes in natural frequency, a batch of healthy springs were deliberately flawed. A focused ion beam was used to create a cut in five springs approximately half the wire diameter deep in various locations. An additional spring was plastically yielded as a second form of damage to investigate. The six flawed springs were mixed with three healthy springs to perform a kind of "semi-blind" study to see if the flawed springs could be identified without *a priori* knowledge of which were flawed, which could bias the judgement of the technique. It

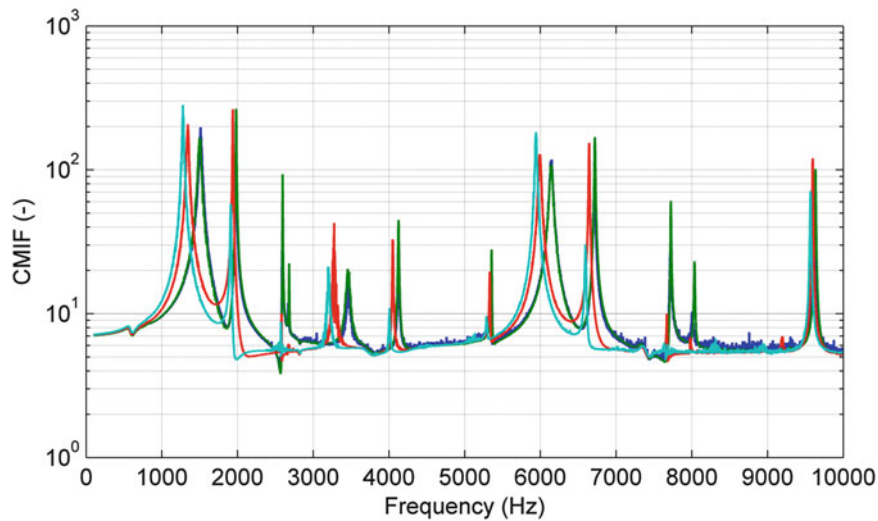


**Fig. 12.6** Spread in natural frequencies achieved by testing one spring four times

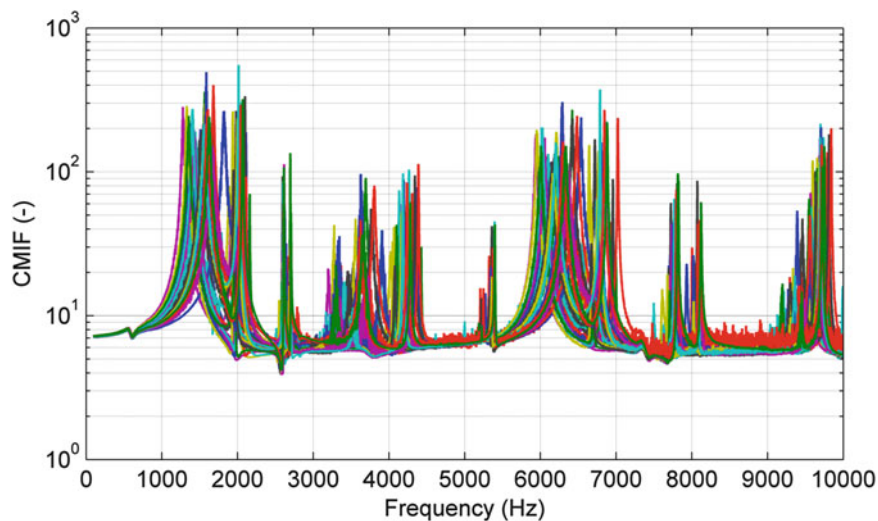


**Fig. 12.7** Spread in natural frequencies for all tests of all springs

should be noted that the author coordinated the flawing of the springs so he knew ahead of time how many flawed springs there were, but not which ones were flawed, which may bias the results.

To determine which springs were flawed, natural frequencies of this new batch were compared against the distributions from the unflawed baseline data in Table 12.1. Comparison of a measured natural frequency to its corresponding unflawed baseline distribution establishes the likelihood of that measurement if the spring were unflawed. If a natural frequency is unlikely to be found in the healthy distribution, it suggests the spring is in some way damaged. For each measured natural frequency, the percentage of the distribution that was farther from the mean than the given natural frequency was computed. Figures 12.10, 12.11, 12.12, 12.13, 12.14, 12.15, 12.16, 12.17, and 12.18 show the CMIFs from each of the blind test springs. The healthy natural frequency distributions are shown as vertical grey bands. Peaks corresponding to natural frequencies where the percentage of the distribution farther from the mean was less than 10% are annotated (Figs. 12.9, 12.11, 12.12, 12.13, 12.14, 12.15, 12.16, and 12.17).

Springs B, E, F, G, and H contain the most peaks highlighted by the 10% metric. Spring F showed the most severe deviations from the healthy distributions. Spring E broke halfway through the testing with only two of four tests completed (it turns out that a spring breaking as it is being mounted is a great indication that it had some kind of damage!). Springs A, C, D, and I had the fewest peaks highlighted by the 10% metric. Spring I had all of its peaks well within the healthy spring distributions. Although we knew prior to this analysis that we should have at most three healthy springs, four of them (A, C, D, or I) did not generate high damage metrics by our method, so all were guessed to be healthy. This was thought to be

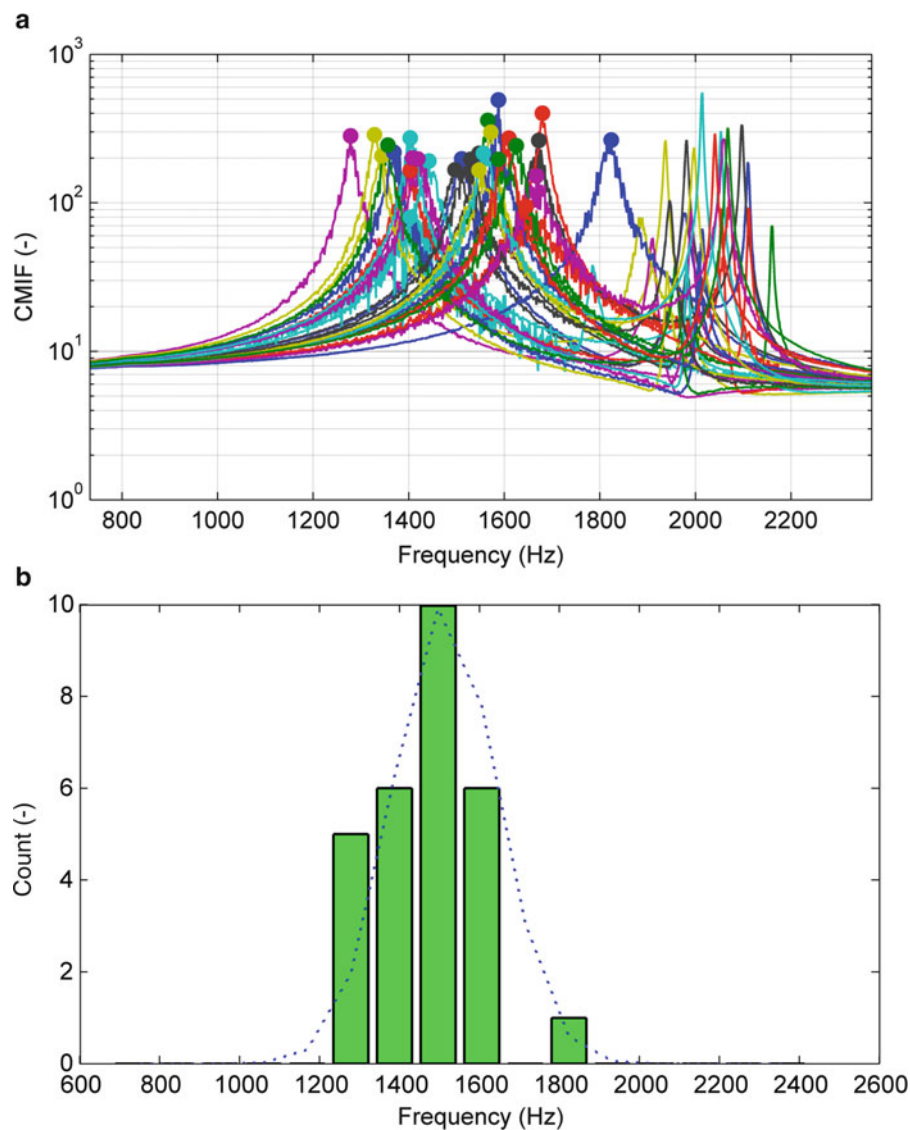


**Fig. 12.8** First mode peaks picked off CMIFs (a) and corresponding normal distribution (b)

fair as in practice an analyst would not have *a priori* knowledge of how many damaged springs they would have. Table 12.2 shows the blind predictions compared to the actual state of the springs. Three of nine assessed states were incorrect, which is not outstanding, especially considering two of the incorrect assessments are non-conservative in the sense that they would accept a flawed article.

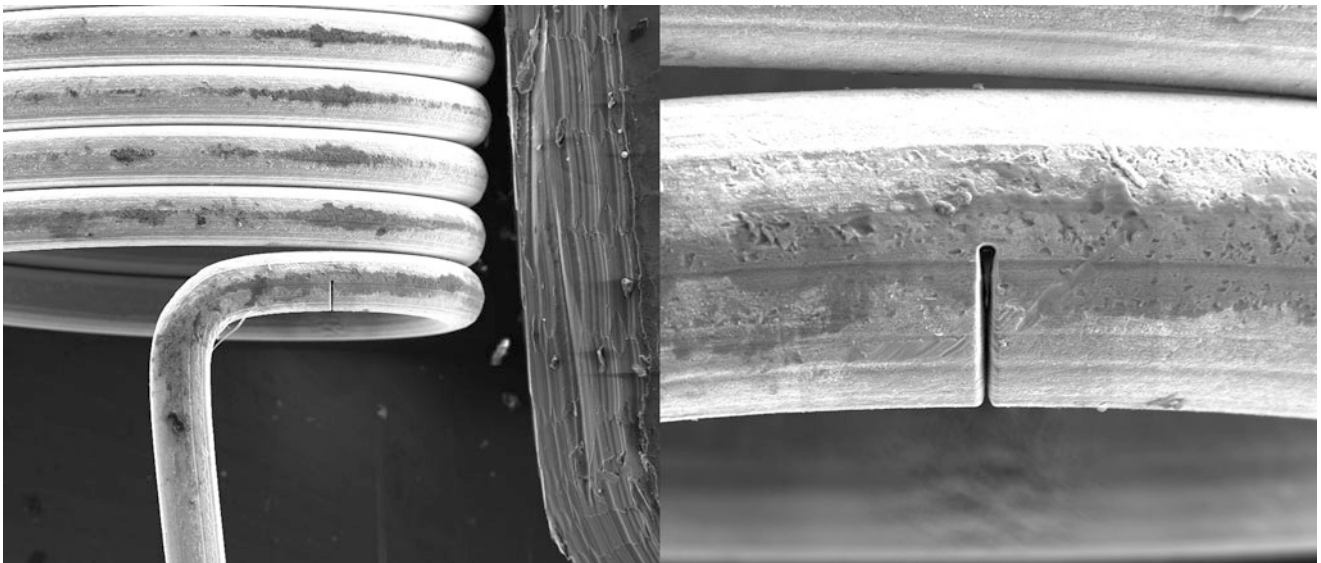
The data were re-examined (now with independent knowledge of which springs were actually healthy and which were flawed) to determine where potential oversights in the blind test occurred. On spring G (Fig. 12.16), it was noted that the majority of the unlikely natural frequencies were found in the fourth test, and this test seemed to have a large amount of noise as shown by the CMIF. In the author's experience with these springs, the increased noise could suggest that the spring was not seated quite right on the pins of the fixture, which could result in the spring sliding or banging on the pin, and might also result in changing natural frequencies. The discarding of a healthy spring is perhaps not as severe of an issue as the acceptance of a flawed spring, however. Spring A and D both show only one or two unlikely natural frequencies, so this metric may not be suitable.

The mean first natural frequency of both spring A and D are over one standard deviation away from the mean of the healthy distribution, so this was investigated next. Bias in the mean value of the natural frequency for a given spring was examined for each mode of each spring. Table 12.3 shows the number of standard deviations of the spring's mean natural frequency was from the mean of the healthy distributions. Figure 12.19 shows the same values in graphical form. A trend can



**Table 12.1** Healthy spring natural frequencies (– indicates mode not found in data)

	Mode 1	Mode 2	Mode 3	Mode 4	Mode 5	Mode 6	Mode 7	Mode 8	Mode 9	Mode 10	Mode 11	Mode 12	Mode 13
Spring 1 test 1	1511	1978	2592	2669	3467	4122	5334	6150	6713	7716	8006	9197	9613
Spring 1 test 2	1497	1981	2595	2680	3456	4125	5355	6141	6719	7722	8034	–	9633
Spring 1 test 3	1344	1938	2580	–	3277	4048	5330	5989	6644	7670	7983	9195	9595
Spring 1 test 4	1278	1909	2573	–	3195	4006	5288	5941	6595	7633	8316	–	9569
Spring 2 test 1	1403	–	–	–	3902	–	–	6088	6556	–	–	9203	9577
Spring 2 test 2	1403	2055	2600	2667	3364	4247	5323	6095	6838	7733	8003	9292	9695
Spring 2 test 3	1566	2159	2617	2695	3694	4425	5380	6419	6997	7823	8122	9548	9756
Spring 2 test 4	1369	2014	2588	2641	3344	4192	5272	6075	6797	7695	7931	9272	9680
Spring 3 test 1	1547	1981	2589	–	3528	4138	5331	6188	6752	7698	8000	9328	9697
Spring 3 test 2	1572	1881	2588	–	3558	4023	–	6211	6653	7608	–	9336	9650
Spring 3 test 3	1408	1988	2592	2680	3331	4142	5345	6044	6748	7700	8008	9223	9684
Spring 3 test 4	1442	2053	2608	2691	3408	4264	5378	6103	6873	7766	8088	9261	9739
Spring 4 test 1	1645	2070	2614	2683	3747	4305	5353	6372	6920	7788	8066	9431	9791
Spring 4 test 2	1588	2000	2602	2684	3586	4197	5352	6234	6813	7742	8025	9316	9750
Spring 4 test 3	1823	2109	2622	2684	3909	4363	5358	6538	6969	7814	8072	9548	9811
Spring 4 test 4	1672	2097	2617	2686	3761	4342	5359	6423	6956	7805	8072	9459	9811
Spring 5 test 1	1328	1941	2594	2663	3252	4067	5295	5950	6673	7678	7923	9153	9656
Spring 5 test 2	1419	1991	2613	–	3355	4145	5350	6058	6745	7733	8013	9245	9692
Spring 5 test 3	1403	1981	2606	–	3333	4134	5345	6017	6741	7714	–	9213	9700
Spring 5 test 4	1680	2113	2636	2698	3806	4388	5372	6484	7022	7850	8080	9559	9841
Spring 6 test 1	1356	1958	2583	2663	3300	4098	5330	6005	6705	7708	–	9197	9655
Spring 6 test 2	1588	2008	2598	2672	3628	4192	5342	6289	6803	7755	8019	9391	9706
Spring 6 test 3	1530	1945	2583	2663	3484	4077	5325	6150	6673	–	–	9303	9638
Spring 6 test 4	1547	1997	2594	2680	3513	4169	5358	6163	6767	7744	8022	9314	9683
Spring 7 test 1	1667	2059	2614	2708	3683	4261	5400	6356	6847	7814	8108	9494	9686
Spring 7 test 2	1556	2014	2603	2705	3523	4184	5395	6203	6788	7767	8089	9363	9697
Spring 7 test 3	1609	2041	2609	2700	3625	4238	5386	6297	6845	7795	8100	9420	9714
Spring 7 test 4	1625	2067	2613	2706	3675	4283	5398	6339	6881	7816	8122	9450	9723
Mean value	1513	2012	2601	2682	3525	4192	5348	6190	6787	7742	8052	9335	9694
Standard deviation	130	66	15	17	198	111	32	165	119	61	79	122	69

**Fig. 12.9** Flawed spring with a focused ion beam cut

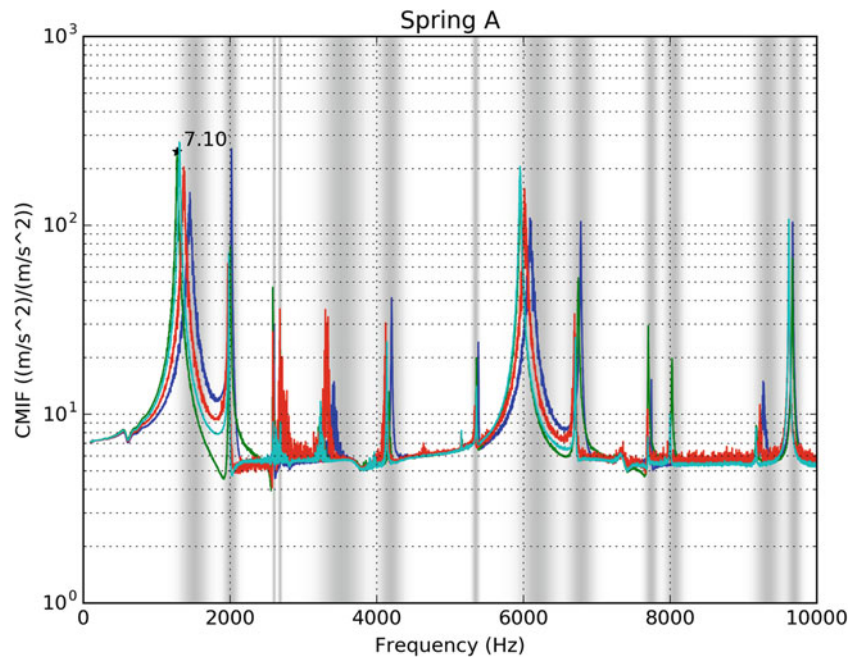


Fig. 12.10 Spring A CMIFs

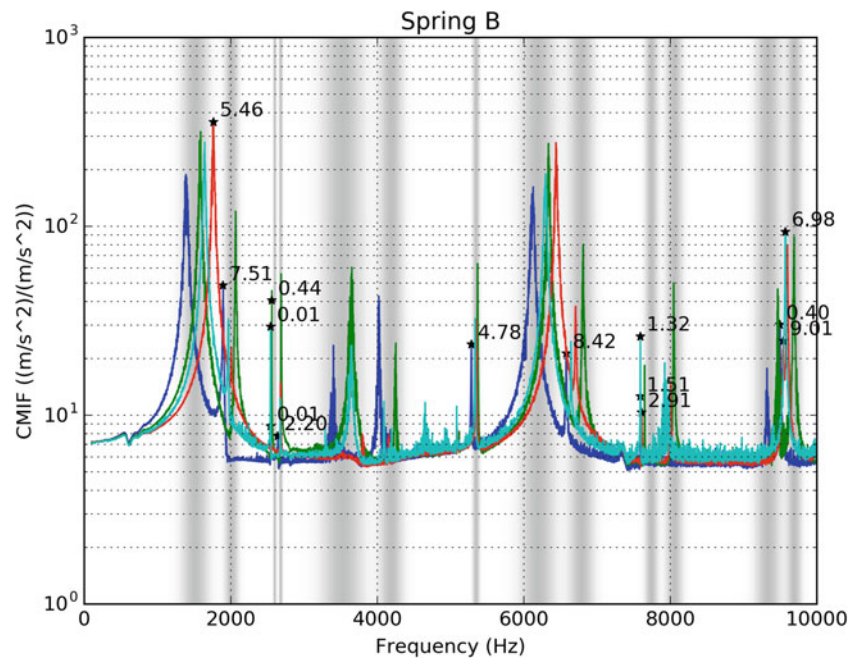


Fig. 12.11 Spring B CMIFs

be observed where many of the flawed springs have mean natural frequencies lower than the healthy springs, and this is to be expected as all of the imposed flaws would tend to decrease stiffness and lower natural frequencies. However, there are clear exceptions to this rule. Spring B, for example, which is a flawed spring, has mean 1st, 8th, and 12th natural frequencies well over half a standard deviation higher than the healthy spring mean natural frequencies. If an analyst were rejecting springs simply on the basis of seeing a drop in natural frequency, spring B would be accepted while a healthy spring like spring G would be discarded as it has a number of mean natural frequencies that are well below the accepted healthy spring mean.

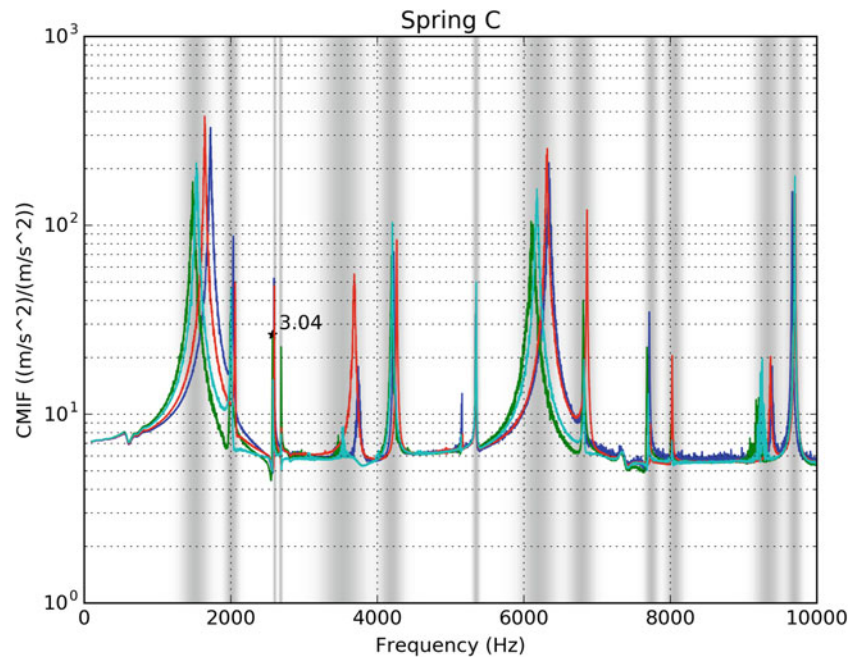


Fig. 12.12 Spring C CMIFs

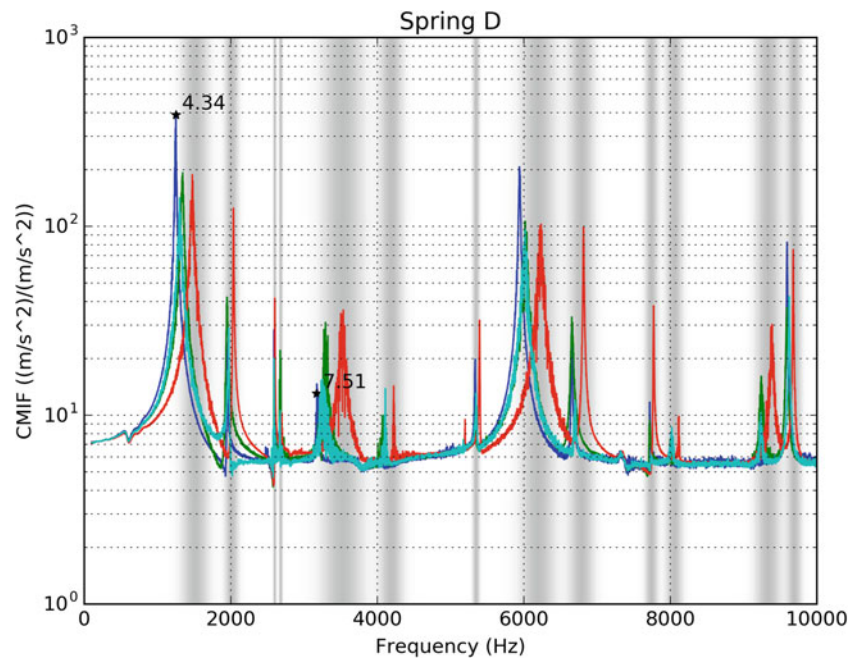


Fig. 12.13 Spring D CMIFs

## 12.5 Discussion

No definitive metric was found that correlated natural frequency to spring damage with 100% accuracy for the sample population of springs tested. Trends exist where the natural frequencies of damaged springs tend to be lower than those of healthy springs, but there are clear exceptions to this rule. The outlier frequency metric was able to correctly identify four of six flawed springs, but also identified one healthy spring as flawed. The metric seemed to be more sensitive to damage due to yielding the springs (spring F) than those from nicks or cuts on the wire (which were fairly egregious reductions in the cross-sectional area of the springs).

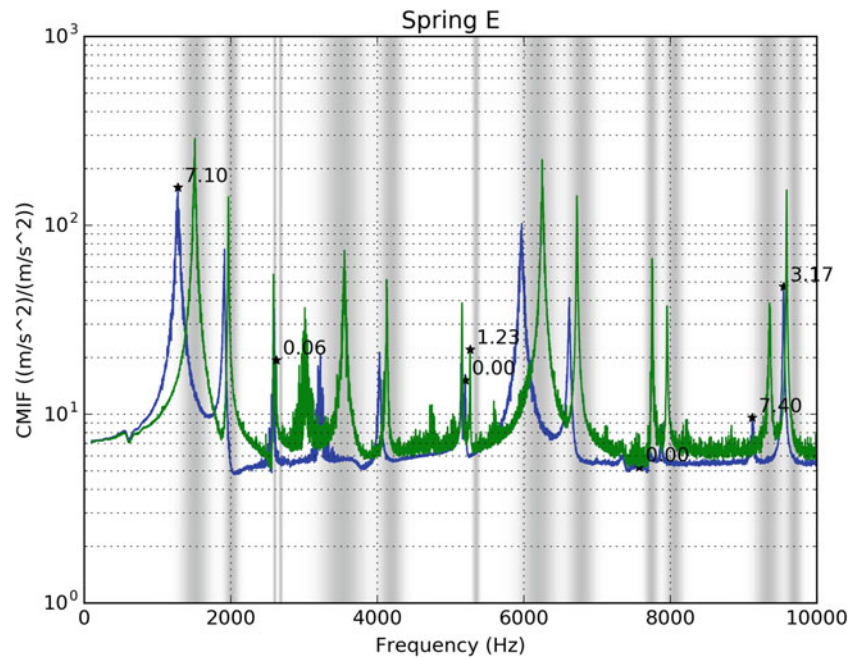


Fig. 12.14 Spring E CMIFs

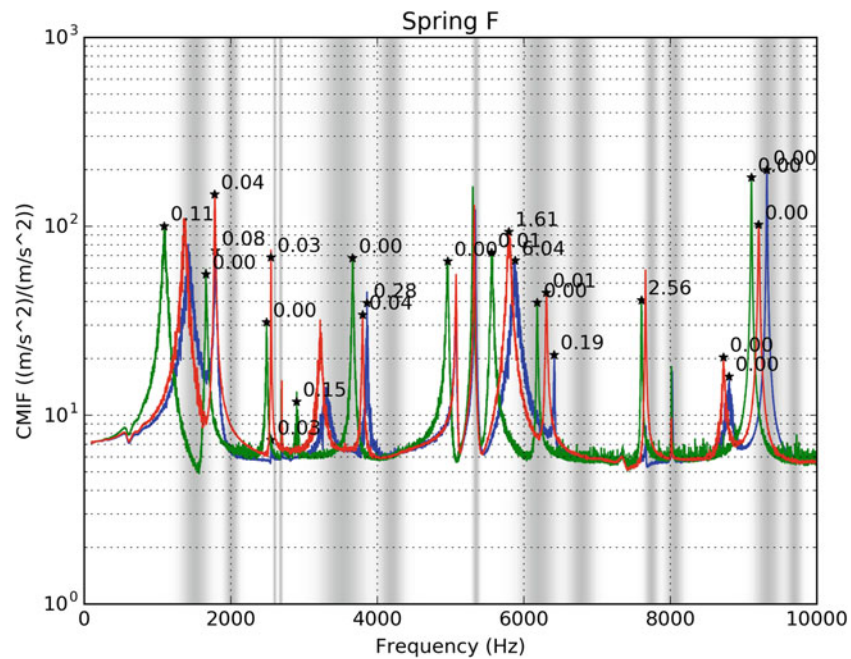


Fig. 12.15 Spring F CMIFs

One issue that is perhaps reducing the effectiveness of the technique is the spread of natural frequencies obtained. A large spread was found even when the same spring was tested multiple times, likely due to the boundary conditions of the spring, and this does not yet account for the significant manufacturing variability between different springs. The fixture could be improved so that there is a narrower range of positions that a spring could end up, perhaps by notching the pins rather than having them be smooth. More advanced tooling could also be created to aid the test engineer in placing the spring on the pins so the reliance on the engineer's manual dexterity to manipulate the very small objects could be reduced. It is thought that these improvements would potentially reduce the variability of the test setup and therefore allow the variability that is due to spring flaws to become more apparent.

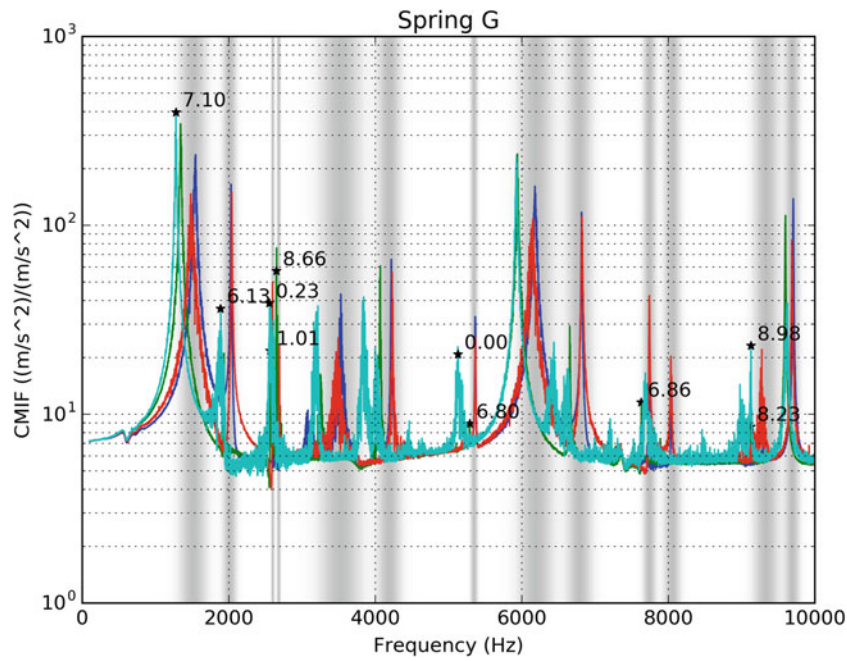


Fig. 12.16 Spring G CMIFs

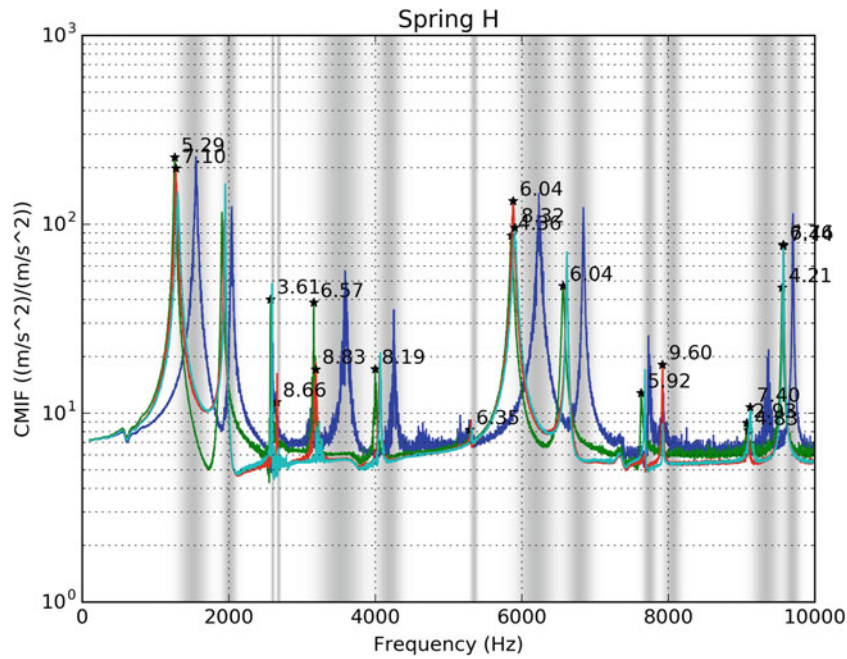


Fig. 12.17 Spring H CMIFs

A larger variety of flaws and higher population count to improve the baseline distributions could also be investigated. From the limited set, it is not clear whether a simple normal distribution or a more complex distribution is appropriate. Springs A, B, D, and E all had their flaws in approximately the same location on the spring. If local stiffness changes in this region do not result in natural frequency changes in the spring, then this effort may not have given the technique a fair trial.

Finally, a more sophisticated damage identification technique could be utilized that included shape information. The shapes achieved by this test were fairly noisy due to poor laser signal return at some points on the spring, so it was difficult to conclude whether a particular non-smooth part of the shape was due to a flaw or due to noise in the measurement. Photogrammetry/Digital Image Correlation is an alternative full-field technique that could be used to measure the motion of

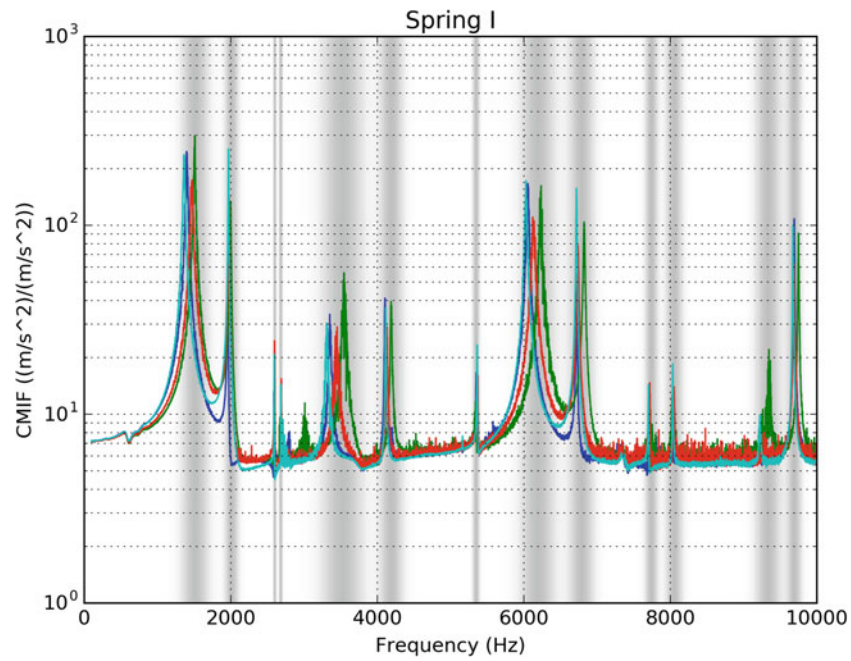


Fig. 12.18 Spring I CMIFs

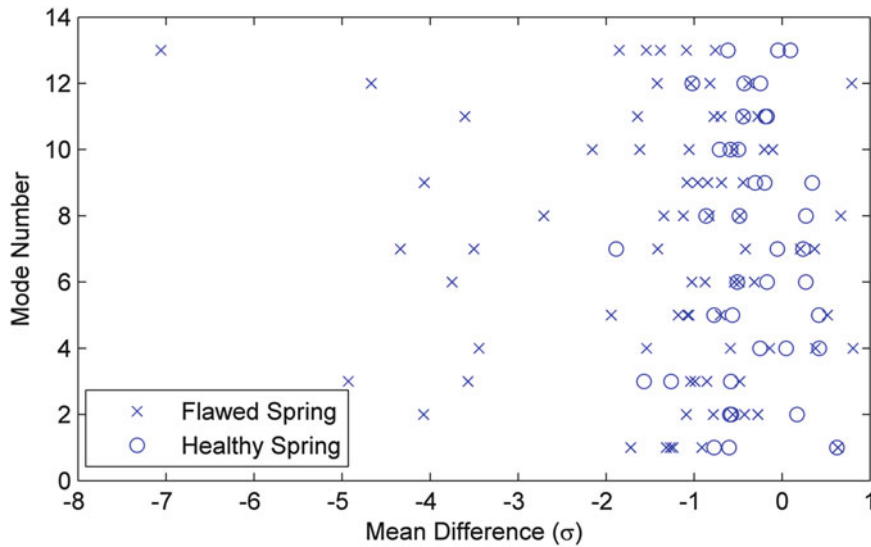


Fig. 12.19 Number of standard deviations of the spring mean from the healthy distribution mean

the spring with enough resolution to be able to identify local effects such as damage. The spring is likely too small to speckle appropriately for digital image correlation, but new techniques such as motion magnification [3, 4] have shown promise in providing deflection shapes in applications similar to the one described here. Future work aims to investigate these techniques for determining flaws in these springs.

**Table 12.2** Results of blind identification of flaws based on outlier natural frequencies

Spring Letter	Our Guess?	Actual Flaw
<b>A</b>	<b>Healthy</b>	<b>FIB cut, 5 coils from hook, out of hook plane</b>
B	Flaw	FIB cut, 6 coils from hook, out of hook plane
C	Healthy	Healthy
<b>D</b>	<b>Healthy</b>	<b>FIB cut, 6 coils from hook, out of hook plane</b>
E	Flaw	FIB cut, 6 coils from hook, in hook plane
F	Flaw	Yielded Spring
<b>G</b>	<b>Flaw</b>	<b>Healthy</b>
H	Flaw	FIB cut, End coil next to hook
I	Healthy	Healthy

**Table 12.3** Number of standard deviations of the spring mean from the healthy distribution mean. Flawed springs are shaded in grey

	Mode 1	Mode 2	Mode 3	Mode 4	Mode 5	Mode 6	Mode 7	Mode 8	Mode 9	Mode 10	Mode 11	Mode 12	Mode 13
Spring A	-1.24	-0.28	-0.85	0.38	-1.06	-0.32	0.37	-1.12	-0.44	-0.55	-0.69	-1.04	-0.76
Spring B	0.63	-0.43	-3.57	-0.59	0.52	-0.54	-0.42	0.67	-0.85	-2.16	-0.77	0.79	-1.54
Spring C	0.62	0.17	-1.26	0.42	0.42	0.27	-0.05	0.27	0.34	-0.59	-0.44	-0.25	-0.05
Spring D	-1.32	-0.56	-0.48	-0.14	-1.08	-0.49	0.21	-0.83	-0.69	-0.11	-0.28	-0.38	-1.09
Spring E	-0.91	-1.09	-1.04	-3.44	-0.7	-1.03	-3.5	-0.48	-0.96	-0.2	-3.6	-0.82	-1.85
Spring F	-1.72	-4.07	-4.93	0.81	-1.94	-3.75	-4.34	-2.71	-4.07	-1.62	-0.43	-4.67	-7.06
Spring G	-0.77	-0.59	-1.57	-0.25	-0.77	-0.17	-1.89	-0.86	-0.2	-0.71	-0.19	-1.02	-0.62
Spring H	-1.27	-0.78	-0.99	-1.54	-1.18	-0.88	-1.41	-1.34	-1.08	-1.06	-1.64	-1.42	-1.38
Spring I	-0.6	-0.58	-0.58	0.05	-0.57	-0.51	0.24	-0.48	-0.31	-0.5	-0.17	-0.43	0.09

## References

1. Doebling, S., Farrar, C., Prime, M., and Shevitz, D.: Damage identification and health monitoring of structural and mechanical systems from changes in their vibration characteristics: a literature review. Los Alamos National Laboratory Report LA-13070-MS (1996)
2. Castellini, P., Martarelli, M., Tomasini, E.P.: Laser Doppler Vibrometry: development of advanced solutions answering to technology's needs. *Mech. Syst. Signal Process.* **20**(6), 1265–1285 (2006)
3. Dorn, C.J., et al.: Automated extraction of mode shapes using motion magnified video and blind source separation. In: *Topics in Modal Analysis & Testing*, Volume 10, pp. 355–360. Springer, Cham (2016)
4. Yang, Y., et al.: Reference-free detection of minute, non-visible, damage using full-field, high-resolution mode shapes output-only identified from digital videos of structures. *Struct. Health Monit.* 1475921717704385 (2017)

# Chapter 13

## Using High-Resolution Measurements to Update Finite Element Substructure Models



Daniel P. Rohe

**Abstract** Many methods have been proposed for updating finite element matrices using experimentally derived modal parameters. By using these methods, a finite element model can be made to exactly match the experiment. These techniques have not achieved widespread use in finite element modeling because they introduce non-physical matrices. Recently, Scanning Laser Doppler Vibrometry (SLDV) has enabled finer measurement point resolution and more accurate measurement point placement with no mass loading compared to traditional accelerometer or roving hammer tests. Therefore, it is worth reinvestigating these updating procedures with high-resolution data inputs to determine if they are able to produce finite element models that are suitable for substructuring. A rough finite element model of an Ampair Wind Turbine Blade was created, and a SLDV measurement was performed that measured three-dimensional data at every node on one surface of the blade. This data was used to update the finite element model so that it exactly matched test data. A simple substructuring example of fixing the base of the blade was performed and compared to previously measured fixed-base data.

**Keywords** 3D · SLDV · Model Updating · Modal

### 13.1 Introduction

The model updating problem has been well-visited through the history of experimental structural dynamics. Many techniques have been proposed in which finite element matrices can be directly updated to exactly match test data, for example [1–3]. Such “direct” updating techniques have not achieved widespread acceptance at Sandia National Laboratories. Issues with these techniques include non-physical mass and stiffness matrices which leads to modes not in the updated set becoming spurious. This can result in erroneous results, especially in substructuring applications where a change in boundary conditions of the test article often requires a number of higher frequency modes for a good approximation of a fixed-base shape.

Scanning Laser Doppler Vibrometry (SLDV) has been shown to have advantages over traditional mounted sensors [4]. For example, it allows for non-contact measurements which do not mass-load the test article. Additionally, a finer measurement point resolution can often be achieved through the use of scanning mirrors in the laser heads which are much more precise than a roving hammer or roving accelerometer test. SLDV therefore has the potential to supply a finite element model (FEM) a larger volume of data at more precisely located measurement points. 3D SLDV can also provide three-dimensional data at each measurement point. This work investigates the use of 3D SLDV to provide data to update a rough finite element model for use in substructuring applications through a case study on a Ampair 600 Wind Turbine Blade [5, 6].

---

Sandia National Laboratories is a multimission laboratory managed and operated by National Technology and Engineering Solutions of Sandia LLC, a wholly owned subsidiary of Honeywell International Inc. for the U.S. Department of Energy’s National Nuclear Security Administration under contract DE-NA0003525.

D. P. Rohe (✉)

Structural Dynamics Department, Sandia National Laboratories, Albuquerque, NM, USA

e-mail: [dprohe@sandia.gov](mailto:dprohe@sandia.gov)



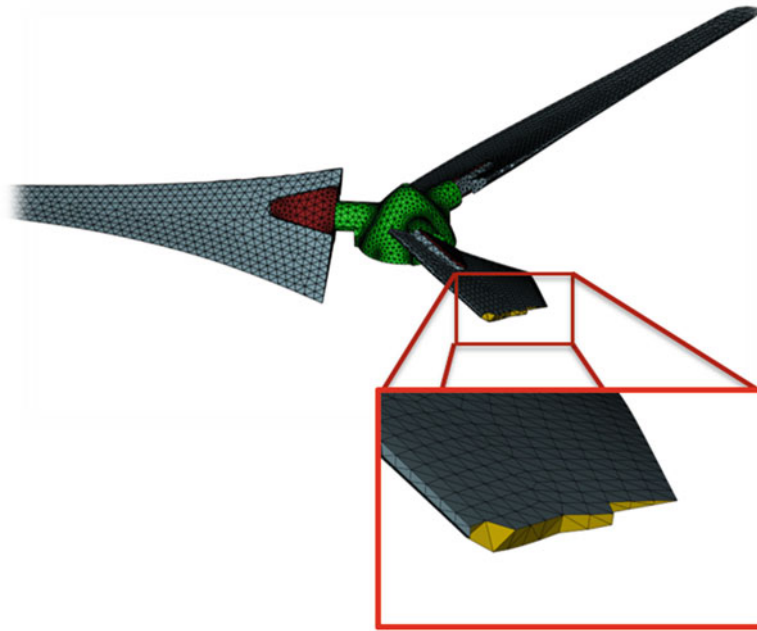


**Fig. 13.1** Rough finite element model for use in this investigation with one blade shown cut away to reveal element sparsity through the thickness

## 13.2 Preliminary Finite Element Model

A rough finite element model was created from the solid geometry provided by Nurbhai and Macknelly [7]. To facilitate efficient investigation into model updating approaches, the FEM was created such that it would run on a typical desktop computer in a reasonable amount of time. While a FEM of the entire blade and hub assembly was created, only a single blade was investigated here. The single blade FEM consisted of two element blocks, the solid “core” of the blade, consisting of 4681 tetrahedral elements and a thin “skin” consisting of 2570 triangular shell elements. The model contained 1504 nodes, of which the skin nodes had six degrees of freedom each whereas the nodes found only in the core contained only three degrees of freedom. Figure 13.1 shows the finite element model. With only one or two elements through the thickness of the blade core, the model was almost certainly not converged. The initial material properties were not known a priori, so these were updated after the experimental data was taken.

## 13.3 Experimental Modal Test and Analysis

Rather than needing to deal with some interpolation scheme between the experimental data and the FEM, it was decided to place the measurement points on the blade at the locations of the nodes in the FEM. The nodes to scan were chosen from the set of nodes on one side of the finite element model at least 1.27 cm (0.5 in) from the edge of the blade with an angle of incidence of less than 60 degrees to the axis of rotation of the hub.

### 13.3.1 Laser Alignment

Before the measurement points could be placed on the blade, the laser system had to be aligned with the part. Unfortunately, due to their popularity as a test bed structure, the blades had seen a lot of use and abuse in the structural dynamics laboratory. All of the sharp corners on the blade that would have been useful for alignment were damaged, so some other datum would be necessary to align the blade.

Alignment points were drawn over each blade as well as the hub. The entire blade-hub assembly was used for this portion of the alignment because it was thought that if the alignment was performed over a larger area, the alignment error could be

minimized. Approximately 30 points were spread over each blade (Fig. 13.3), but at this point the locations of these points in the blade coordinate system were not known, and due to the blade geometry they could not be easily measured using standard tools such as a ruler or compass and protractor. Instead, the 3D SLDV was used in a slightly nonstandard way to determine the locations of the points. The 3D SLDV system was aligned to an arbitrary coordinate system using the provided reference object. The blade-hub assembly was then placed in the coordinate system and the alignment points were triangulated using the laser vibrometer system. The  $(x, y, z)$  coordinates of the alignment points in this arbitrary coordinate system could then be extracted from the laser system. However, these coordinates were not yet aligned with the FEM coordinate system (Fig. 13.5).

To align the arbitrary alignment point coordinate system with the FEM coordinate system, the alignment points were exported into MATLAB for analysis. The goal of this analysis was to determine a transformation matrix  $\mathbf{T}$  that would transform the alignment point coordinates into the finite element model coordinates. More precisely, the goal was to determine the transformation  $\mathbf{T}$  that would result in the minimum sum-squared distance of the alignment points to the surface of the FEM (see Fig. 13.4). The alignment points were initially rotated and translated compared to the finite element model (Fig. 13.5), so any type of algorithmic optimization of the transformation matrix at this point would likely result in an incorrect local optimum rather than the global optimum. To give the search algorithm a better chance at locating the true minimum, the alignment points were transformed using a trial-and-error process to get the alignment points close to the surface (Fig. 13.6).

$$cost = \sum_{i=1}^{n_{points}} \|\mathbf{x}_i - \mathbf{x}_{i,closest}\|^2$$

With the initial conditions close to the optimal conditions, the FEM and Alignment point geometry could be passed into a cost function that could be optimized, with the additional parameters of three rotations and three translations to be optimized. This cost function computes the distance from each alignment point to the closest point on the structure. The problem of finding the closest point on a triangle to a different point in space is a straightforward geometric problem; however searching all triangles to determine which is the closest point is inefficient. To increase efficiency, the finite element model was culled to consist of only those elements that were close to an alignment point (Fig. 13.7). The cost function was then passed to the nonlinear optimization function `fminsearch` in MATLAB which determined the rotations and translations that resulted in the minimum distance of the alignment points from the FEM surface. This transformation was then applied to



**Fig. 13.2** Blade scan points shown on the finite element model

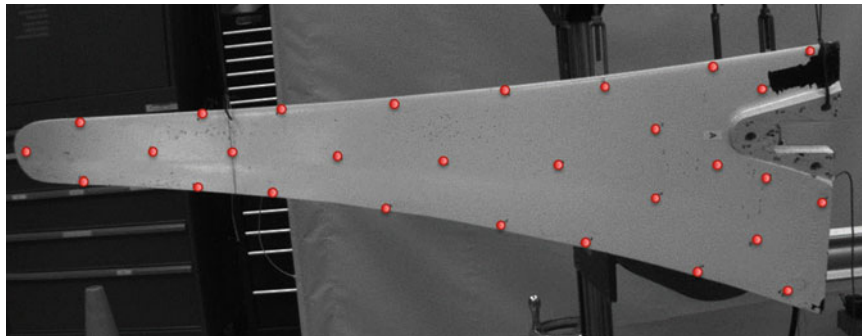


**Fig. 13.3** Alignment point locations on the blade

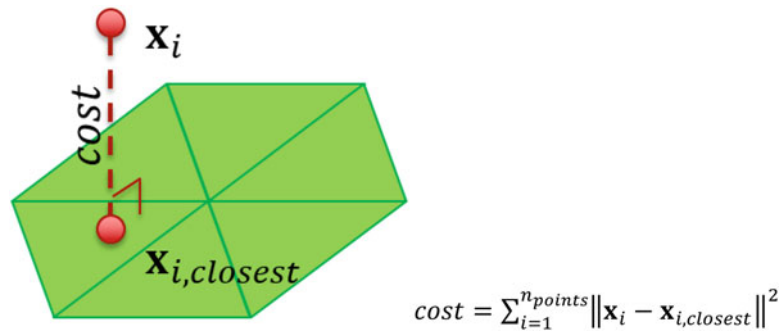


**Fig. 13.4** Schematic showing the cost function to be minimized, where the cost relates to the distance of the point  $x_i$  to the closest point on the FEM surface  $x_{i,closest}$

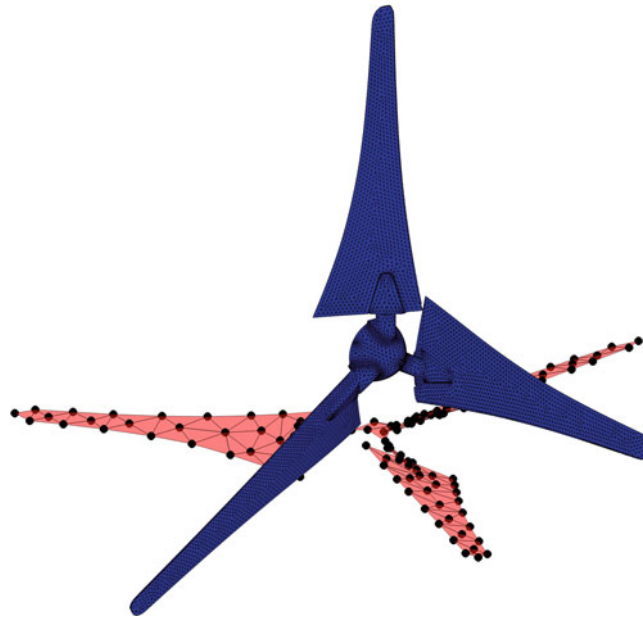


**Fig. 13.5** Initial alignment point locations compared to FEM model

the alignment point coordinates, which resulted in the alignment point coordinates in the FEM coordinate system. With the updated coordinates, these alignment points could be used as the alignment data for the 3D SLDV system. With the laser system aligned to the FEM coordinate system, the FEM nodal coordinates shown in Fig. 13.2 could be directly imported into the laser software to serve as the measurement points, shown in Fig. 13.8.

### 13.3.2 Blade Testing and Preliminary FEM Updating

A shaker and drive point accelerometer were attached to a single Ampair blade on the opposite side of the scan points, and pseudorandom excitation was applied to the part. 359 points were measured on the blade. 10 elastic modes were extracted from the blade below 800 Hz using the Synthesize Modes and Correlate (SMAC) algorithm [8]. A Complex Mode Indicator Function (CMIF) showing the experimental data and analytical fits is shown in Fig. 13.9.

This preliminary modal data was used to tune the material parameters of the rough FEM discussed in Sect. 13.2. A Poisson's ratio of 0.3 was assumed. The density of the core and skin material was assigned using the system of equations relating total mass and lengthwise center of gravity. The Young's modulus of each material was assigned via another nonlinear optimization using the `fminsearch` function. Here the cost function was set up so that with each iteration of the optimization, the Young's modulus of each material was passed as a parameter to the function and an eigenvalue finite element analysis was performed that solved for the first 10 elastic natural frequencies of the blade. The cost was defined as

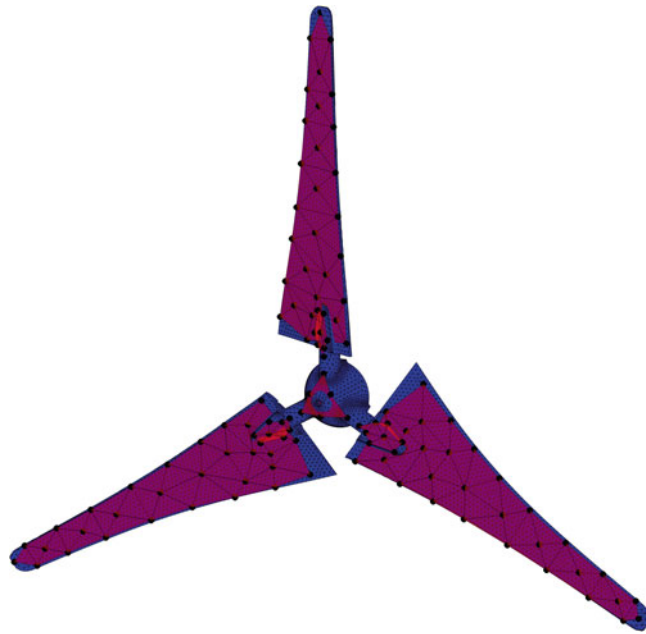


**Fig. 13.6** Closer alignment point locations compared to FEM model

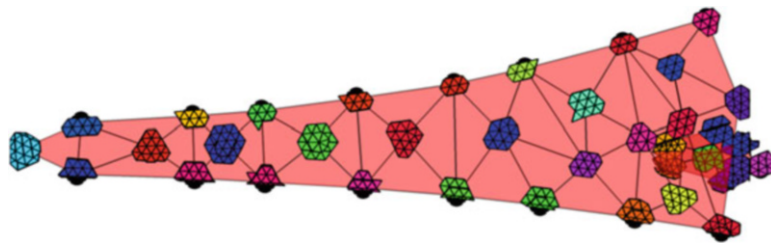


**Fig. 13.7** Reduced set of triangles for computing the closest distance

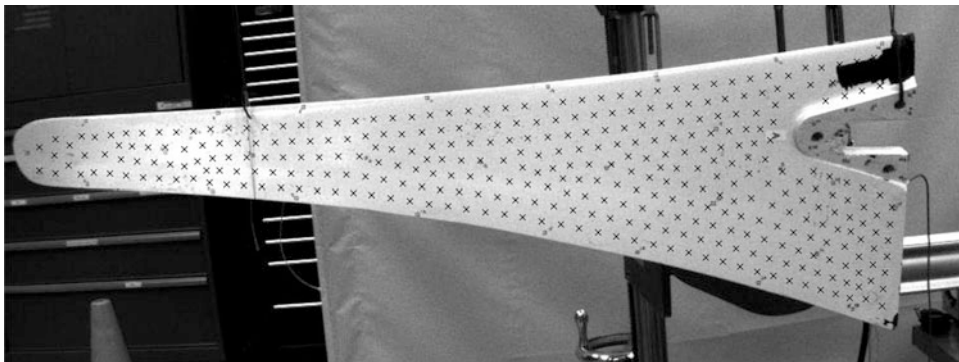


**Fig. 13.8** Measurement points on the blade marked with  $\times$  symbols

the sum squared percent error in natural frequencies. Note that no shape-based correlation of natural frequencies was used to pair corresponding shapes; if modes were out of order, then the natural frequencies would be miscorrelated. This can be seen in the flipping of the 3rd bending and torsion modes of the FEM and experimental data. Experimental and Preliminary FEM modal parameters are summarized in Table 13.1. The modal assurance criterion (MAC) matrix is shown in Fig. 13.10. The first two elastic shapes show good correlation between test and FEM, but higher modes show a lower degree of correlation.

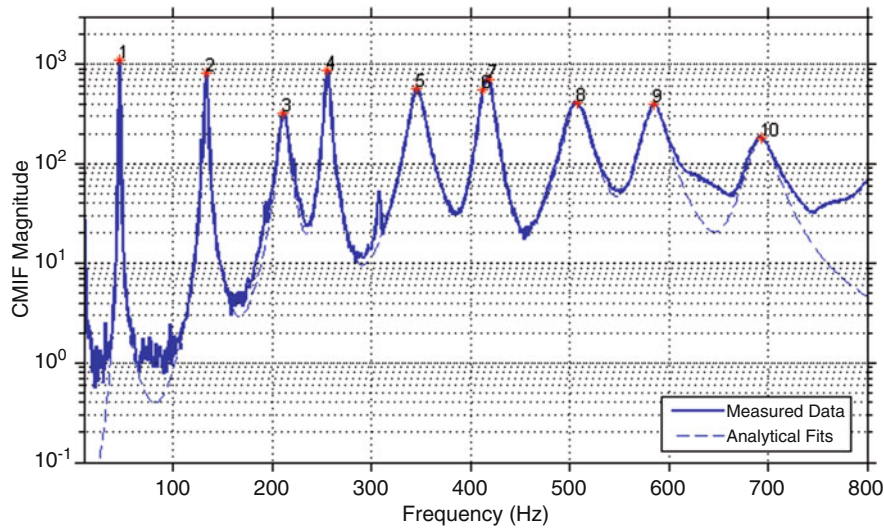


**Fig. 13.9** Analytical modal fits compared to experimental data

**Table 13.1** Summary of experimental and finite element modal parameters

Exp mode	Exp frequency	Prelim FEM mode	Prelim FEM freq
1st bending	46.0 Hz	1st bending	46.0 Hz
2nd bending	133 Hz	2nd bending	127 Hz
1st torsion	211 Hz	3rd bending	240 Hz
3rd bending	255 Hz	1st torsion	247 Hz
2nd torsion	346 Hz	1st Edgwise	346 Hz
4th bending	418 Hz	4th bending	381 Hz

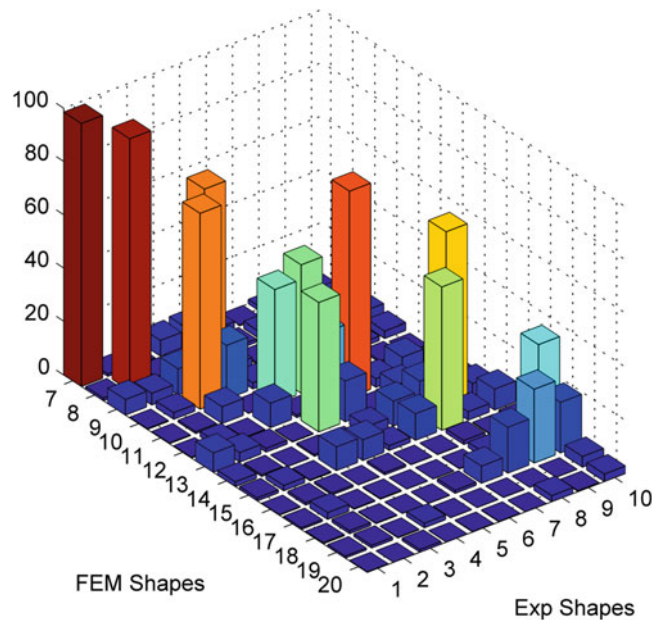


**Fig. 13.10** Modal assurance criterion matrix

### 13.4 Finite Element Model Updating

Three model updating techniques were investigated for this case study. The first was the Berman and Nagy approach [2] and the second was the Analytical Model Improvement (AMI) method of O’Callahan [3]. The final approach utilized the Variability Improvement of Key Inaccurate Node Groups (VIKING) [9] technique and was the same process used in [10].

The end goal is to be able to use the updated finite element model in substructuring applications. For this case study, that will consist of fixing the base of the blade to approximate the fixed-base modes of the structure.

The model updating is performed using MATLAB to modify the finite element matrices, which were exported from the finite element code. It is important to fully understand which degrees of freedom correspond to which rows and columns of the matrices, as well as to understand how the matrices are populated. For example, in the Sierra/Structural Dynamics code that was used for this effort, the degrees of freedom were sorted numerically by node number. A confounding aspect, however, was that the nodes have a variable number of degrees of freedom. In order to map the experimental degrees of freedom to the FEM degrees of freedom, the nodes first had to be binned by whether they were contained in shell elements (triangular elements on the skin) or not. These shell elements would have rotational degrees of freedom and therefore have six rows and columns in the matrix per node rather than only three. A good practice that was employed during this effort was to compute the eigenvectors (mode shapes) of the mass and stiffness matrices in MATLAB for one or two modes (even with large matrices this is not terribly computationally intensive because the eigenvalues were already known from the FEM eigensolution). Then, if the eigenvectors appeared correct when plotted, one could have a good deal of confidence that the book-keeping of the FEM matrices was performed correctly.

### 13.4.1 Berman-Nagy Approach

As a first attempt at updating a finite element model to match test data, the Berman Nagy Approach was used. This approach directly modifies the mass and stiffness matrices of the finite element model per the following equations:

$$\mathbf{M} = \mathbf{M}_A + \mathbf{M}_A \Phi m_A^{-1} (\mathbf{I} - m_A) m_A^{-1} \Phi^T \mathbf{M}_A \quad (13.1)$$

$$\mathbf{K} = \mathbf{K}_A + (\Delta + \Delta^T) \quad (13.2)$$

$$\Delta = \frac{1}{2} \mathbf{M} \Phi (\Phi^T \mathbf{K}_A \Phi + \Omega^2) \Phi^T \mathbf{M} - \mathbf{K}_A \Phi \Phi^T \mathbf{M} \quad (13.3)$$

where  $\Phi$  is the experimental mode shape matrix, expanded to the full finite element degrees of freedom,  $\mathbf{M}_A$  is the FEM mass matrix,  $\mathbf{K}_A$  is the FEM stiffness matrix,  $\Omega^2 = \begin{bmatrix} \cdot & \cdot & \cdot \\ \cdot & \omega^2 & \cdot \\ \cdot & \cdot & \cdot \end{bmatrix}$  is the diagonal experimental eigenvalue matrix,  $m_A = \Phi^T \mathbf{M}_A \Phi$  is the normalized generalized mass matrix, and  $\mathbf{I}$  is the identity matrix.

In order to apply equations (13.1) and (13.3), the experimental mode shape matrix must first be expanded to the full finite element degrees of freedom. This was done using Guyan expansion:

$$\mathbf{K}_A = \begin{bmatrix} \mathbf{K}_{aa} & \mathbf{K}_{ad} \\ \mathbf{K}_{da} & \mathbf{K}_{dd} \end{bmatrix} \quad (13.4)$$

$$\mathbf{T}_s = \begin{bmatrix} \mathbf{I} \\ -\mathbf{K}_{dd}^{-1} \mathbf{K}_{da} \end{bmatrix} \quad (13.5)$$

$$\Phi = \mathbf{T}_s \Phi_a \quad (13.6)$$

where  $a$  represents the degrees of freedom present in the measurement,  $d$  represents the degrees of freedom not present in the measurement, and  $\Phi_a$  are the mode shapes from the experiment.

As is the case with any experimental data, and perhaps especially with laser vibrometer data where optical issues such as signal dropout or speckle noise can occur, measurement error can contaminate the results. To smooth out some of the noise, the experimental shapes were projected to the space spanned by the first 100 finite element shapes as shown in (13.7).

$$\tilde{\Phi}_a = \Phi_{a,fem} \Phi_{a,fem}^+ \Phi_a \quad (13.7)$$

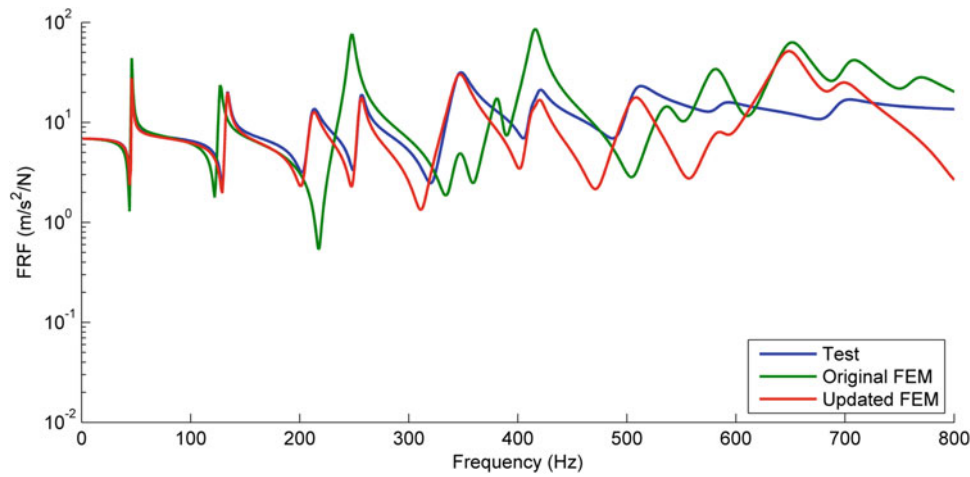


**Fig. 13.11** Representative frequency response function for the updated FEM via the Berman-Nagy approach with FEM rigid body modes included as target modes

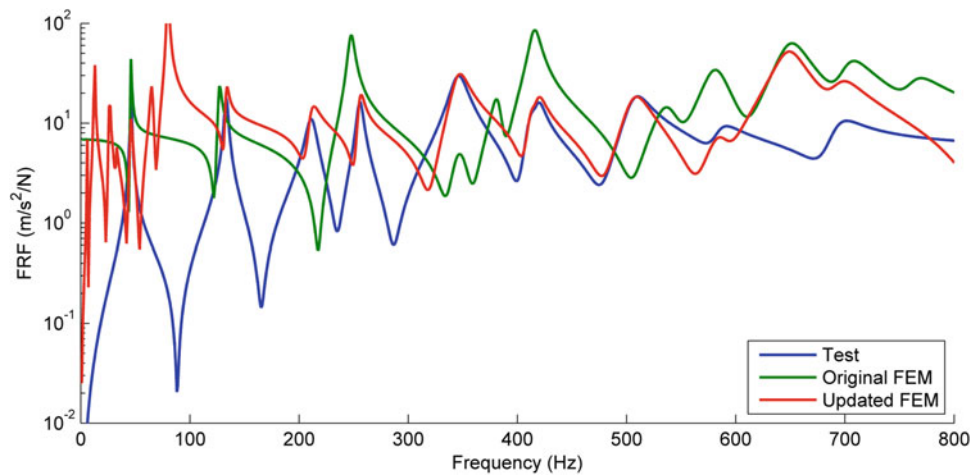


**Fig. 13.12** Representative frequency response function for the updated FEM via the Berman-Nagy approach. Note the rigid body natural frequencies up to nearly 100 Hz and the spurious mode near 650 Hz

The smoothed finite element shapes  $\tilde{\Phi}_a$  were then used in (13.6) to expand to the full set of degrees of freedom. The mass and stiffness matrices were then updated per (13.1) and (13.3). To verify that the updating process was performed correctly, the eigenvalue problem was solved for the elastic modes of the system corresponding to the experimental modes. The eigenvalue problem is more computationally intensive now that the  $\mathbf{M}$  and  $\mathbf{K}$  matrices are full from the updating process. It was found that though the FEM system contained eigenvalues and eigenvectors that exactly matched the experimental values, other eigenvalues of the system were now unphysical. For example, the rigid body modes, which are nominally at 0 Hz, now had non-zero stiffness. Other spurious modes also appeared in the bandwidth of interest. Figure 13.11 shows a representative frequency response function of the free-free FEM.

Clearly, as the rigid body modes play a large role in the substructuring calculations especially for low frequency modes [11], matching fixed base results with such a model seemed unlikely. The updating procedure was performed a second time, where the expanded experimental modes  $\tilde{\Phi}_a$  were supplemented with the FEM rigid body modes. In this case, the rigid body mode shapes and natural frequencies would be forced to be reasonable by the updating procedure. A representative frequency response function is shown in Fig. 13.12.

With the updated mass and stiffness matrices, the base of the blade was constrained to make a fixed base structure. The natural frequencies were compared to those in [6] using a fixed base configuration. To judge the effectiveness of the technique in improving the fixed base prediction, the results were compared against the fixed base prediction using only the non-updated finite element model. These results are shown in Table 13.2.

**Table 13.2** Fixed base FEM predictions using the Berman-Nagy updating approach. The truth column contains the average of the natural frequencies found in [6]

Mode	Truth	Non-updated FEM	Updated FEM only experiment	Updated FEM Exp + RBM
1	20.1 Hz	19.3 Hz	41.5 Hz	31.5 Hz
2	70.2 Hz	70.7 Hz	76.7 Hz	74.5 Hz
3	131 Hz	141 Hz	165 Hz	161 Hz

The coarse and poorly-correlated FEM still did reasonably well at predicting the fixed base natural frequencies. When the Berman-Nagy approach was used without including the analytical FEM rigid body modes, the predicted fixed base natural frequencies were terrible with over 100% error on the first natural frequency. The predictions improved drastically when the rigid body modes were included in the updating procedure; however, the results were still not as good as the non-updated FEM.

### 13.4.2 Analytical Model Improvement Approach

The same updating procedure was attempted using the AMI approach. This approach directly modifies the mass and stiffness matrices of the finite element model using the following equations:

$$\mathbf{M} = \mathbf{M}_A + \mathbf{V}^T (\mathbf{I} - \overline{\mathbf{M}}_A) \mathbf{V} \quad (13.8)$$

$$\mathbf{K} = \mathbf{K}_A + \mathbf{V} (\Omega^2 + \overline{\mathbf{K}}_A) \mathbf{V} - ((\mathbf{K}_A \Phi \mathbf{V}) - (\mathbf{K}_A \Phi \mathbf{V})^T) \quad (13.9)$$

$$\mathbf{V} = (\Phi^T \mathbf{M}_A \Phi)^{-1} \Phi^T \mathbf{M}_A \quad (13.10)$$

The new variables  $\overline{\mathbf{K}}_A$  and  $\overline{\mathbf{M}}_A$  are defined as  $\Phi^T \mathbf{K}_A \Phi$  and  $\Phi^T \mathbf{M}_A \Phi$ , respectively. Once again, the experimental shapes must be expanded to the full finite element degrees of freedom. In this case study, the SEREP technique is used to perform the expansion.

$$\mathbf{T}_{SEREP} = \Phi_{fem} \Phi_{a,fem}^+ \quad (13.11)$$

$$\Phi = \mathbf{T}_{SEREP} \Phi_a \quad (13.12)$$

Where  $\Phi_{fem}$  is the first 100 mode shapes of the FEM at the full set of degrees of freedom and  $\Phi_{a,fem}$  represents the same matrix partitioned to only the measurement set of degrees of freedom. Note that the SEREP updating also performs smoothing of the experimental data, so no additional smoothing step was performed here. Using the lesson learned from the previous approach, the FEM rigid body modes were used along with the experimental shapes in the updating procedure.

As in the first approach, the eigenvalue problem was solved with the updated mass and stiffness matrix to verify that the natural frequencies and mode shapes exactly matched the test data. Figure 13.13 shows a representative frequency response function.

Again base of the blade was fixed and the natural frequencies of this new system were found. The first three are shown in Table 13.3.

The results from using the SEREP expansion and AMI updating technique are worse than the Berman-Nagy approach using Guyan expansion, and again significantly worse than the preliminary FEM.



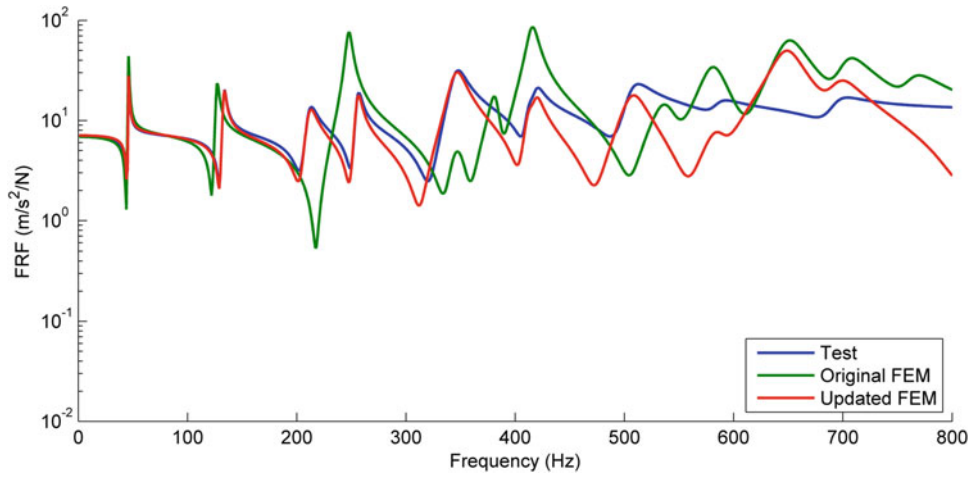


**Fig. 13.13** Representative frequency response function for the updated FEM via the AMI approach

**Table 13.3** Fixed-base FEM predictions using the AMI approach. The truth column contains the average of the natural frequencies found in [6]

Mode	Truth	Non-updated FEM	Updated FEM
1	20.1 Hz	19.3 Hz	40.0 Hz
2	70.2 Hz	70.7 Hz	78.2 Hz
3	131 Hz	141 Hz	169.9 Hz

### 13.4.3 Variability Improvement of Key Inaccurate Node Groups

The previous approaches utilized the full FEM matrix with updating, and additionally used the entire (smoothed) experimental shape to perform the updating. However, all of these approaches seemed to give poor results when the resulting FEM matrices were assembled to a different structure. The VIKING technique uses a different approach, noting that some degrees of freedom will be measured less accurately than others in any given mode, and instead uses only the best measured degrees of freedom to smooth the variation observed in measured data [10].

For each mode shape the degrees of freedom that are determined to be accurately measured are used in the expansion process. The degrees of freedom are judged by their contribution to the unit value on the diagonal of (13.13). The degrees of freedom with the largest contribution towards the unit diagonal are kept, up to 99%, resulting in approximately 400–600 of the 1100 experimental degrees of freedom being kept, referred to in this paper as the  $\nu$  set. Note that the  $\nu$  degrees of freedom vary from mode to mode. Figure 13.14 shows a representative curve showing degree of freedom contributions with the 99% cutoff marked.

$$\mathbf{I} = \Phi_a^+ \Phi_a \quad (13.13)$$

Once the degrees of freedom have been selected for each mode, the SEREP expansion procedure (13.11) is used, except instead of performing the expansion using the entire  $a$  set of degrees of freedom, only the  $\nu$  subset is used for each mode.

$$\phi = \Phi_{fem} \Phi_{\nu, fem}^+ \phi_\nu \quad (13.14)$$

where  $\phi$  represents a single modal vector (because the  $\nu$  set changes with each mode). Equation (13.14) is performed for each experimental mode using 25 FEM mode shapes as the filter. These then are the finite element mode shapes  $\Phi$  that are used in the AMI procedure (13.8)–(13.10). The mass and stiffness matrices were updated and the eigenvalue problem was solved to verify that the natural frequencies exactly matched test data. A representative frequency response function is shown in Fig. 13.15. One other noteworthy aspect is that it appears that the mass line of the FRF has changed. The substructuring exercise was repeated and results are shown in Table 13.4. It is clear from these results that the VIKING approach significantly improves the substructure model of the turbine blade; however, it is still a bit poorer than if the model had had no updating at all. A brief investigation was performed to see whether or not these results could be improved by tuning the VIKING analysis parameters.

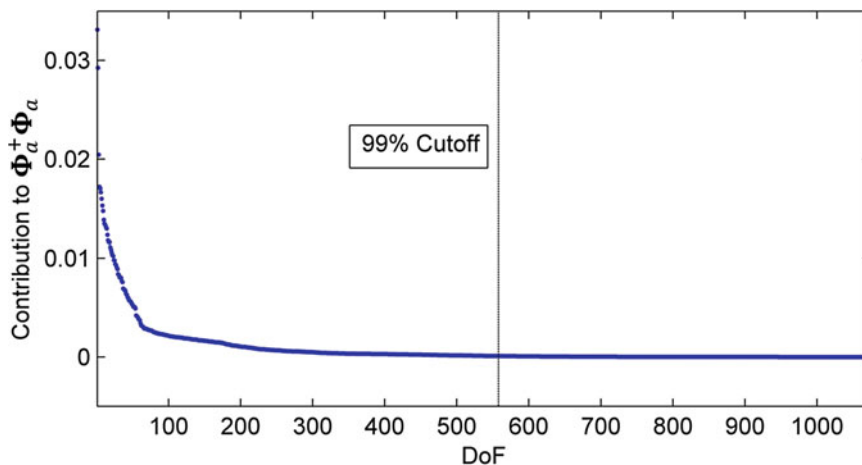


Fig. 13.14 Degree of freedom contribution to (13.13)

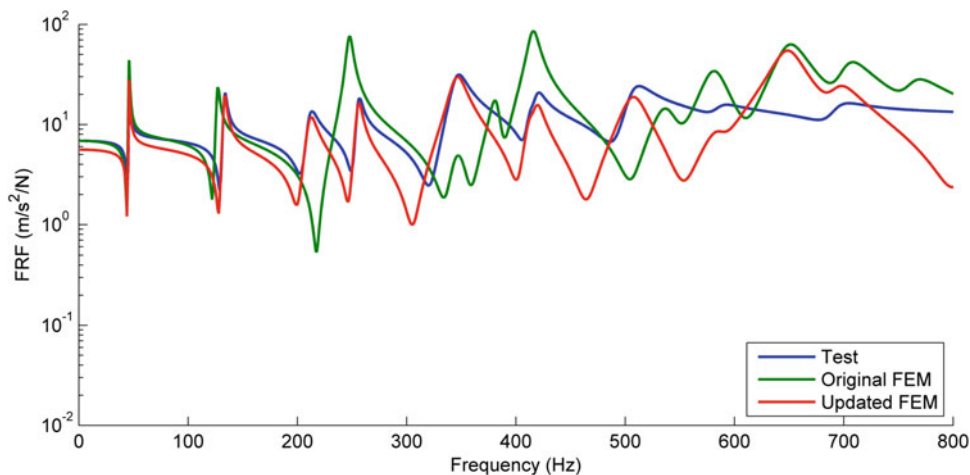


Fig. 13.15 Representative frequency response function for the updated FEM using the VIKING approach

Table 13.4 Fixed-base FEM predictions using the VIKING-AMI approach. The truth column contains the average of the natural frequencies found in [6]

Mode	Truth	Non-updated FEM	Updated FEM
1	20.1 Hz	19.3 Hz	22.3 Hz
2	70.2 Hz	70.7 Hz	73.7 Hz
3	131 Hz	141 Hz	149.2 Hz

### 13.5 VIKING Discussion

The VIKING and SEREP approaches have some parameters that need to be specified by the analyst performing the model updating, namely the degrees of freedom to keep in the  $\nu$  set (or proportion of the contribution to the unit diagonal that should be kept), and the number of finite element modes to use in the SEREP updating in (13.14). Additionally, the finite element model matrix could be reduced prior to updating as has been typically done with the VIKING technique [9, 10]. A handful of cases were run that varied these parameters.

In one example, the number of modes used in the SEREP expansion was increased to 50, while the number of degrees of freedom kept remained constant at 99% of the contribution to the diagonal of  $\Phi_a^+ \Phi_a$ . The degradation of the results was immediately visible in the MAC comparison between the experiment and the VIKING shapes: the first diagonal term was reduced to 77%. The first predicted fixed base mode using the updated model jumped to 34 Hz, a much poorer prediction.

The number of degrees of freedom were then increased to 99.99% of the contribution to the diagonal of  $\Phi_a^+ \Phi_a$  to see if this could compensate for the increased number of modes kept in the SEREP filter. The MAC correlation between the experiment and VIKING shapes improved such that the minimum diagonal value was now 97%. The prediction of the first fixed-base mode improved to 23.0 Hz. This is still not quite as good of a prediction as the parameters discussed in Sect. 13.4.3, which suggests including too many modes can degrade the results.

Keeping more degrees of freedom than necessary also degraded the results, as these non-accurate degrees of freedom only serve to confuse the updating procedure. If degrees of freedom corresponding to 99.99% of the contributions to the diagonal of  $\Phi_a^+ \Phi_a$  were kept, but only 25 modes were used in the SEREP expansion, the updated prediction of the first fixed base natural frequency remained 23.0 Hz. If 100% of the contributions to the diagonal of  $\Phi_a^+ \Phi_a$  (i.e. all of the degrees of freedom) were used, then the case becomes identical to that in Sect. 13.4.2, and the results are more severely degraded.

Finally, two sets of reduced order models were run using Guyan reduction to reduce to a smaller set of degrees of freedom in the finite element model, as was done in [10], where good results were obtained in a similar substructuring example. The first reduction simply reduced out the rotational degrees of freedom from the shell elements in the FEM. Using the same parameters as in Sect. 13.4.3, the reduced FEM predicted similar fixed base natural frequencies as that approach. A more severe reduction was performed, reducing the FEM down to only the experimental measurement nodes as well as 17 nodes scattered around the clamped section of the blade to provide degrees of freedom to constrain for the fixed base approach. This approach actually obtained the best results with predicted fixed base natural frequencies of 21.6, 69.1, and 133.5 Hz. This was the only approach that improved upon the preliminary FEM in terms of predicting fixed base natural frequencies.

## 13.6 Summary

Three case studies were performed using model updating techniques on an Ampair 600 Wind Turbine Blade with the goal of updating the finite element model to more closely match test data. The preliminary model matched test data reasonably well after tuning the elastic moduli of the materials, though it did not exactly match test data. Test data could be exactly matched after all three updating procedures; however very different results were obtained when the finite element model was fixed at the base and the modes of that configuration were solved for. The Berman-Nagy updating approach with Guyan expansion and AMI approach with SEREP expansion both resulted in models that predicted wildly inaccurate fixed base modes. Only when the VIKING technique was utilized were more reasonable results obtained. However, as judged by the metric in this paper, the preliminary model still performed the best in predicting the fixed base natural frequencies.

## References

1. Baruch, M.: Optimal correction of mass and stiffness matrices using measured modes. *AIAA J.* **20**(11), 1623–1626 (1982)
2. Berman, A., Nagy, E.J.: Improvement of a large analytical model using test data. *AIAA J.* **21**(8), 1168–1173 (1983)
3. O’Callahan, J., Leung, R.: Optimization of mass and stiffness matrices using a generalized inverse technique on the measured modes. In: *Proceedings of the 3rd International Modal Analysis Conference*, pp. 75–79, Orlando, FL (1985)
4. Castellini, P., Martarelli, M., Tomasini, E.P.: Laser Doppler Vibrometry: development of advanced solutions answering to technology’s needs. *Mech. Syst. Signal Process.* **20**(6), 1265–1285 (2006)
5. Mayes, R.L.: An introduction to the SEM substructures focus group test bed – The Ampair 600 wind turbine. In: *Proceedings of the 30th International Modal Analysis Conference*, pp. 61–71 (2012)
6. Harvie, J., Avitabile, P.: Comparison of some wind turbine blade tests in various configurations. In: *Proceedings of the 30th International Modal Analysis Conference*, pp. 71–72 (2012)
7. Nurbhai, M.S., Macknelly, D.J.: Modal assessment of wind turbine blade in preparation of experimental substructuring. In: *Proceedings of the 30th International Modal Analysis Conference*, pp. 73–79 (2012)
8. Hensley, D.P., Mayes, R.L.: Extending SMAC to multiple references. In: *Proceedings of the 24th International Modal Analysis Conference*, pp. 220–230 (February 2006)
9. Thibault, L., Butland, A., Avitabile, P.: Variability Improvement of Key Inaccurate Node Groups – VIKING. In: *Proceedings of the 30th International Modal Analysis Conference* (2012)
10. Butland, A., Avitabile, P.: Component mode synthesis using reduced order, test verified components. In: *Proceedings of the 27th International Modal Analysis Conference* (2009)
11. Allen, M.S., Kammer, D.C., Mayes, R.L.: Uncertainty in experimental/analytical substructuring predictions: a review with illustrative examples. In: *Proceedings of the International Conference on Noise and Vibration Engineering*. Leuven, Belgium (2010)



# Chapter 14

## Determination of Representative Offshore Wind Turbine Locations for Fatigue Load Monitoring by Means of Hierarchical Clustering

Andreas Ehrmann, Cristian Guillermo Gebhardt, and Raimund Rolfes

**Abstract** A fundamental issue during the planning of offshore wind farms is to determine representative locations for fatigue load monitoring, which can be used to reduce maintenance costs. The contribution of this work is an integrated concept based on geometry variations of the jacket substructure. A hierarchical clustering algorithm, using distance measures between these variations, aims to group turbines according to similar fatigue behavior under consideration of local environmental conditions such as wind speed, water depth, and foundation stiffness. Based on this procedure, common jacket designs for each cluster are determined. Next, one location for each cluster is identified to be most suitable for monitoring. At last, uncertainties in fatigue lifetime for other locations in the cluster are given.

**Keywords** Offshore wind farm · Jacket substructure · Environmental and operational conditions (EOC) · Hierarchical cluster algorithm (HCA) · Fatigue load monitoring

### 14.1 Introduction

For water depths between 40 and 60 meters, bottom-fixed jacket substructures are a promising technology for offshore wind turbines. Large offshore wind farms require significant effort for lifetime monitoring to minimize risk of failure and lower maintenance costs. Up to now, there is no holistic concept during wind farm planning to determine appropriate locations for sensor equipment, having a reliable significance for those locations not being monitored. In this work, a cluster design concept is proposed, that assigns turbine locations of a wind farm with different environmental and related operational conditions (EOC) to clusters, based on similar structural response (fatigue damage) of the jacket substructure. Thereby, jacket geometries are varied to find a valid common design with minimum total jacket weight for each cluster. However, the optimal solution for the cluster may not be an optimal solution for each specific location. One location of each cluster is identified to be monitored (“master location”), having a maximum transferability of fatigue results to the other locations (“blind locations”), see Fig. 14.1. Finally, the range of lifetime is calculated for each cluster.

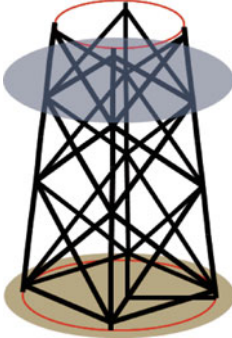
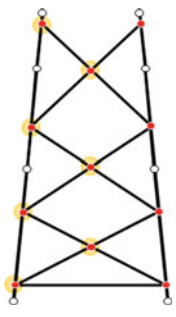
### 14.2 Model and Load Assumptions

In this study, transient simulations are carried out with FAST v8 [1], considering the NREL offshore 5-MW baseline wind turbine [2]. Due to a high computing time, only 600 s of DLC 1.2 (design load case for fatigue), according to IEC 61400–3 [3], are simulated, and only 2 load directions ( $0^\circ$  and  $45^\circ$ ) are considered for each variation of substructure geometry (100 samples) and site condition (15 generic locations). Then, damage due to fatigue stress is extrapolated to a reference lifetime of 20 years and a reference number of  $2 \cdot 10^6$  load cycles using S-N curves from DNVGL [4], following MINER’s Rule. The parameterized jacket model is based on [5]. It is limited to a 4-leg jacket with 3 bracing levels and a constant height. The overall 10 design parameters are uniformly scattered within well-chosen bounds (Table 14.1) using a Latin hypercube sampling Scheme [6]. Fatigue stress results are evaluated for 7 regions of tubular joints. The distribution of site conditions is taken into account using realistic assumptions [7]. Mean wind speed is taken from [3] and the related distribution is according

---

A. Ehrmann (✉) · C. G. Gebhardt · R. Rolfes  
Institute of Structural Analysis, Leibniz Universität Hannover, Hannover, Germany  
e-mail: [a.ehrmann@isd.uni-hannover.de](mailto:a.ehrmann@isd.uni-hannover.de)

**Table 14.1** Overview of chosen bounds for the parameterized jacket substructure with constant height according to [3] and illustration with 7 different tubular joint regions for fatigue assessment (highlighted in yellow on the right)

	Geometry assumptions <sup>a</sup>	Lower bound	Upper bound	
	foot radius head radius height ratio of bracing levels leg diameters (various) <sup>b</sup> leg thickness (various) <sup>b</sup> bracing diameters (various) <sup>b</sup> bracing thickness (various) <sup>b</sup>	12.500 m 4.250 m 0.666 0.800 m 0.025 m 0.400 m 0.015 m	25.000 m 8.500 m 1.500 2.000 m 0.060 m 1.000 m 0.040 m	
<sup>a</sup> See [3] for more information		<sup>b</sup> Complying with the geometry relations of DNVGL [4]		

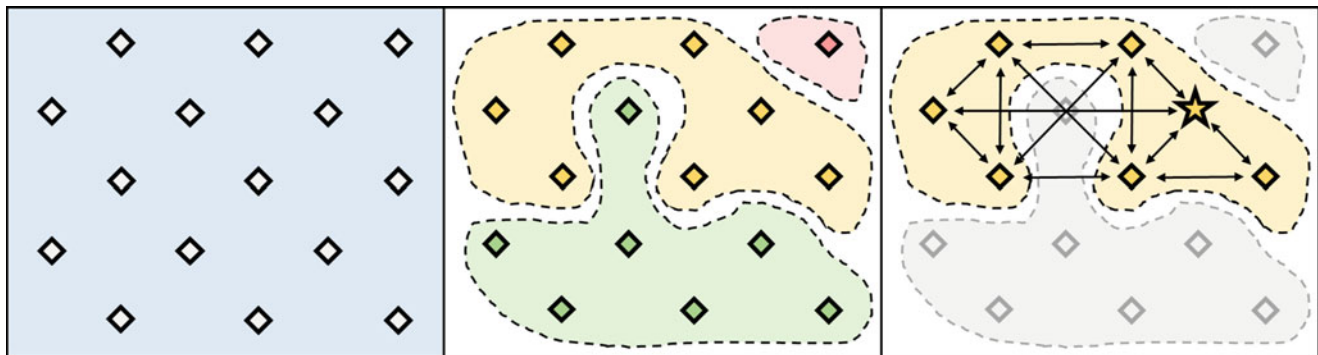


**Fig. 14.1** Schematic representation for the assignment of a given number of wind turbines (left) to clusters with a common substructure design (middle), and determination of representative “master locations” for fatigue load monitoring (right)

to the observations in [8]. The variation of water depth is randomly chosen, applying a truncated Gaussian distribution with a water depth between 37.5 m and 42.5 m. Different water depths are compensated by a varying pile stick-up to keep the jacket height constant. The pile structure is simplified as a uniform geometry and initial soil stiffness [9], which translates to a linearization of the nonlinear p-y- and t-z-curves for the adapted head condition. API methods [10] are applied for the axial and lateral stiffness, and subsequently, a finite element model of the embedded pile is built and condensed to a reduced stiffness matrix with six degrees of freedom at seabed level by using a static condensation [9]. The variation of foundation stiffness over the single sites is realized by a variation of mechanical soil parameters [11].

### 14.3 Clustering Procedure

The variation of geometric parameters from a fully parameterized jacket model provides relations to the resulting accumulated fatigue damage. When simulations are repeated with the same design configurations under different environmental conditions, distribution of fatigue damage over the structure changes. Based on these simulations, a hierarchical cluster algorithm (HCA) [12] quantifies similarities in fatigue results by applying Euclidean distance measures [13] over all jacket designs and regions for structural assessment. It results in a distance matrix [14] of crosswise comparisons, as depicted in Fig. 14.2 (left). The agglomerative HCA strategy starts with each location in its own cluster and merges pairs of clusters, as one moves up the hierarchy. To determine the best number of clusters, the silhouette value [15] measures the similarity of a result to its own cluster center compared to other clusters and gives a hint, when to terminate merging pairs of clusters, see the visualization with a dendrogram in Fig. 14.2 (right). Subsequently, jacket designs with minimum weight from the scope of geometry, complying with the fatigue verifications, are assigned to the clusters. The location, having the least cumulated difference in fatigue stress to all other locations within a cluster, is designated to be equipped with sensors as a “master location”. A range of fatigue lifetime for all locations in a cluster is summarized in Table 14.2, including all non-equipped “blind locations”.

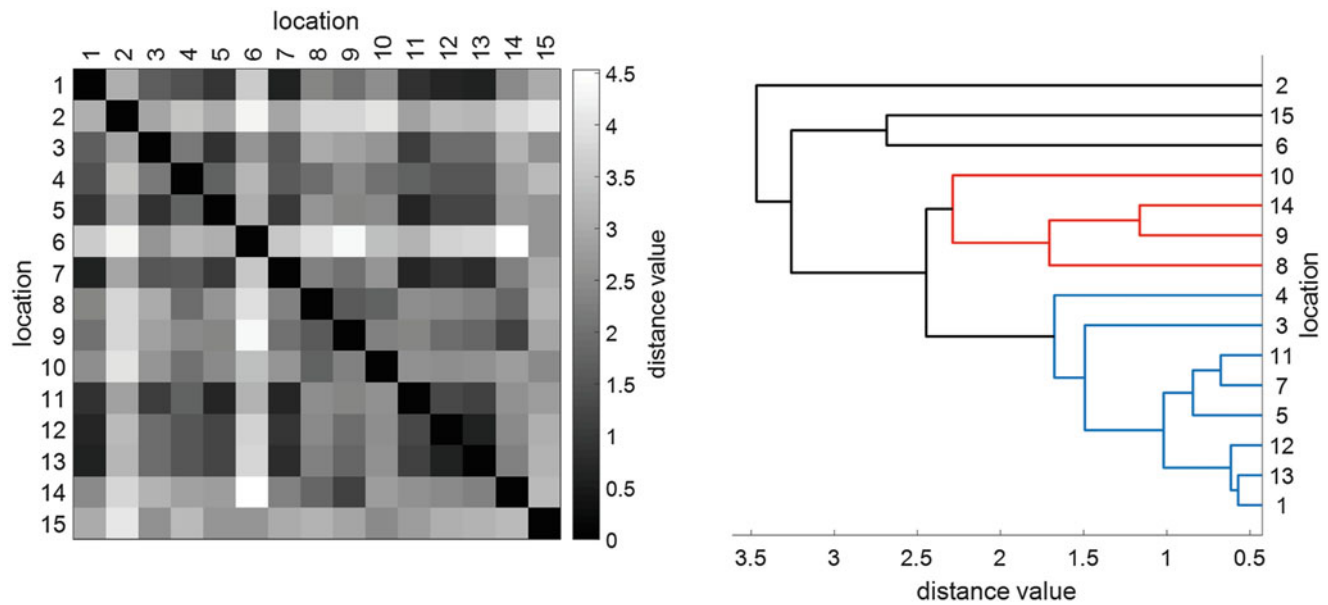


**Fig. 14.2** Distance matrix of all locations with cumulated distance measures (left) and related dendrogram of hierarchical clustering (right), resulting in 2 main clusters plus 3 single locations

**Table 14.2** Results for cluster assignment in terms of jacket design and monitoring (“master locations”)

Cluster	Location (no.)	Jacket design (weight)	Clustering option I (5 clusters)		Clustering Option II (2 clusters)	
			Master location (no.)	Uncertainty in lifetime <sup>a</sup> (years)	Master location (no.)	Uncertainty in lifetime <sup>a</sup> (years)
A.1	1 - 3 - 4 - 5 - 7 - 11 - 12 - 13	A (383.9 t)	4	15.3 to 22.1	11	13.7 to 28.1
A.2	2		2	-		
A.3	6		6	-		
A.4	15		15	-		
B	8 - 9 - 10 - 14	B (455.7 t)	8	16.8 to 20.7	8	16.8 to 20.7

<sup>a</sup>Related to 20 years reference lifetime

## 14.4 Results

The 15 turbine locations are appointed to 5 clusters in total – 2 clusters (A.1 and B) with 8 and 4 locations respectively, and 3 single locations (A.2, A.3, A.4). By assigning the valid jacket designs with minimum weight to the clusters, it is striking that the same jacket design is assigned to the single locations as to the cluster with 8 locations (A.1). So actually, only 2 design clusters, A and B, remain (see Table 14.2).

In case of choosing 5 clusters for monitoring (cluster option I), as determined by the silhouette value, the uncertainties in maximum lifetime are in a range from 15.3 to 22.1 years for Cluster A.1 and from 16.8 to 20.7 years for Cluster B (related to a targeted lifetime of 20 years). When aggregating Cluster A.1 with the single locations A.2, A.3, and A.4, as obtained before for the jacket design (clustering option II), the uncertainties in maximum lifetime increase significantly for Cluster A (from 13.7 to 28.1 years), which makes it adverse for monitoring.

**Acknowledgements** We gratefully acknowledge the financial support of the German Federal Ministry for Economic Affairs and Energy (research project DEUTSCHE FORSCHUNGSPLATTFORM FÜR WINDENERGIE under FKZ 0325936E) and the Lower Saxony Ministry of Science and Culture (research project VENTUS EFFICIENS under FKZ ZN3024).

## References

1. Jonkman, B., Jonkman, J.: FAST v8.16.00a–bjj, Guide from the National Renewable Energy Laboratory (NREL) (2016)
2. Jonkman, J., Butterfield, S., Musial, W., Scott, G.: Definition of a 5-MW Reference Wind Turbine for Offshore System Development, Technical Report from the National Renewable Energy Laboratory (NREL), NREL/TP-500-38060 (2009)
3. International Electrotechnical Commission, IEC 61400–3: Design Requirements for Offshore Wind Turbines (2009)
4. DNVGL: Recommended practice – Fatigue Design of Offshore Steel Structures, DNVGL-RP-C203 (2016)
5. Häfele, J., Rolfes, R.: Approaching the ideal design of jacket substructures for offshore wind turbines with a particle swarm optimization algorithm. In: 26th International Offshore and Polar Engineering Conference, Rhodes, pp. 1–8 (2016)
6. Ehrmann, A., Hübler, C., Gebhardt, C.G., Rolfes, R.: Identification of Significant Parameters of Offshore Support Structures by Means of a Hierarchical Multi-Step Global Sensitivity Analysis, Applied Ocean Research, Under Review
7. Hübler, C., Gebhardt, C.G., Rolfes, R.: Development of a Comprehensive Data Basis of Scattering Environmental Conditions and Simulation Constraints for Offshore Wind Turbines. *Wind Energy Science* **2**, 491–505 (2017)
8. Hasager, C.B., Astrup, P., Christiansen, M.B., Nielsen, M., Barthelmie, R.: Wind Resources and Wind Farm Wake Effects Offshore Observed from Satellite, European Wind Energy Conference, Athens (2006)
9. Hübler, C., Häfele, J., Gebhardt, C.G., Rolfes, R.: Experimentally supported consideration of operating point dependent soil properties in coupled dynamics of offshore wind turbines. *Mar. Struct.* **57**, 18–37 (2018)
10. American Petroleum Institute (API): Recommended Practice for Planning, Designing and Constructing Fixed Offshore Platforms – Working Stress Design, 22nd edn, Recommended Practice RP 2A–WSD (2014)
11. Zaijjer, M.: Foundation modelling to assess dynamic behaviour of offshore wind turbines. *Appl. Ocean Res.* **28**, 45–57 (2006)
12. Maimon, O., Rokach, L.: Data Mining and Knowledge Discovery Handbook, 2nd edn. Springer, New York (2010)
13. Bryant, V.: Metric Spaces: Iteration and Application. Cambridge University Press, Cambridge (1985)
14. Szekely, G.J., Rizzo, M.L.: Hierarchical clustering via joint between-within distances: extending Ward’s minimum variance method. *J. Classif.* **22**, 151–183 (2005)
15. Rousseeuw, P.J.: Silhouettes a graphical aid to the interpretation and validation of cluster analysis. *J. Comput. Appl. Math.* **20**, 53–65 (1987)



# Chapter 15

## Effect of Friction-Induced Nonlinearity on OMA-Identified Dynamic Characteristics of Offshore Platform Models

Tobias Friis, Antonios Orfanos, Evangelos Katsanos, Sandro Amador, and Rune Brincker

**Abstract** The identification of the modal characteristics of engineering systems under operational conditions is commonly conducted with the use of the Operational Modal Analysis (OMA), being a class of useful tools employed within various fields of structural, mechanical as well as marine and naval engineering. The current OMA methods have been advanced on the basis of two fundamental, though, restrictive assumptions: (i) linearity and (ii) stationarity. Nevertheless, there are several applications that are inherently related to various nonlinear mechanisms, which, in turn, violate the two cornerstones of OMA and hence, question its robustness and efficiency. Along these lines, the current study addresses the effect of friction-induced nonlinearity on OMA-identified dynamic characteristics of an experimental set up consisting of a pair of reduced scale offshore platform models that are connected through a friction-based mechanism. Both time-domain and frequency-domain methods were employed to assess the effect of the varying friction-induced nonlinearity on the OMA-identified modal characteristics. The findings of this study reveal that OMA-based methods provide reasonable identification results implying that nonlinear and nonstationary systems can be described by underlying linear systems, even though, in principles, the basic assumptions of linearity and stationarity are violated.

**Keywords** Friction damping · Random vibrations · Operational modal analysis · Nonlinear systems · Experimental testing

### 15.1 Introduction

The modal properties of engineering systems under operational conditions or ambient vibrations can be readily identified with the use of Operational Modal Analysis (OMA), being a robust framework associated with a class of useful tools employed already within various fields of engineering [1]. Since the 1960s, when the OMA was initially introduced, several advancements have been achieved and sophisticated OMA-based methods have refined the estimation of the modal characteristics and dynamic properties of structures with varying size, geometry, complexity and importance. A pair of fundamental principles regarding the (i) linearity and (ii) stationarity serves the theoretical basis for OMA [1, 2], and therefore, its employment provides reliable identification results for structural systems experiencing stationary response in the linear regime. Nevertheless, plenty of cases can be found, in which, for example, the nonlinear performance of structural systems violates the aforementioned principles of OMA and hence, the reliability of its application is rather questionable. More specifically, the use of friction dampers, which can be quite efficient to mitigate excessive structural vibrations, introduces nonlinearity that may cause the structural system to deviate from its linear response. It is, therefore, rather challenging to investigate the application of contemporary OMA-based methods on frictionally-damped systems and address the effect of the friction-induced nonlinearity on linear invariant systems on the basis of their OMA-identified dynamic characteristics.

To the best knowledge of the authors, limited research effort has been already spent to assess the application of OMA for nonlinear systems. Along these lines, Zhang et al. [3] undertook a detailed study to evaluate the identification performance of several OMA methods for a prototype system in the presence of both stiffness- and damping-related nonlinearities. Based on their simulation and experimental study, it was concluded that the linear dynamic characteristics could be extracted from such nonlinear systems. However, the issue of friction-induced nonlinearity needs to be investigated, since this kind of nonlinearity has different characteristics compared to the aforementioned ones.

---

T. Friis (✉) · A. Orfanos · E. Katsanos · S. Amador · R. Brincker  
Technical University of Denmark, Kgs. Lyngby, Denmark  
e-mail: [tofri@byg.dtu.dk](mailto:tofri@byg.dtu.dk); [vakat@byg.dtu.dk](mailto:vakat@byg.dtu.dk); [sdio@byg.dtu.dk](mailto:sdio@byg.dtu.dk); [runeb@byg.dtu.dk](mailto:runeb@byg.dtu.dk)



**Table 15.1** Settings of intensity levels

Intensity levels	Distance [m]	Nozzle diameter [m]
Low	0.2	0.0010
High	0.08	0.0035

Based on the discussion made above and the rather few resources found already to address the controversial coupling between OMA and nonlinearities, the study presented herein elucidates the effects of friction-induced nonlinearity on OMA-identified dynamic characteristics of a structural system. Particularly, experimental investigation was conducted by the use of two simplified and small scale models representing offshore platforms connected each other with a bridge model through a friction mechanism. The main objective of the current study is to investigate if OMA methods can identify the underlying linear systems of the friction-induced nonlinear and nonstationary system. It is notable that the present study is a part of a research project, in which the effect of friction-induced nonlinearity is also studied for OMA-based estimation of stresses [4, 5]. The damping estimation of friction systems subjected to random vibrations is also under investigation by the same research group [6].

## 15.2 Description of the Experimental Set-Up

The experimental set-up used herein includes two simplified, small scale one-story steel models, being representative of offshore platforms widely used in the Oil and Gas industry (Figs. 15.1 and 15.2). The platform models consist of 0.005 m thick steel plates, which are supported by four steel columns placed 0.05 m from each platform's corner. The steel plates are square with a side length of 0.3 and 0.4 m, respectively, by which the models will be hereafter referred to as the small and large platform. The columns, being clamped to the steel plates on the top and to a stiff wooden box at the bottom, have square cross section of 0.008 m and their height is equal to 0.6 m. The two platforms are connected by a  $0.7 \times 0.1 \times 0.005$  m wooden bridge, which is supported by three short cylindrical pieces, made of steel and loosely placed on top of the platforms in steel fixtures. When the platforms are oscillating, the bridge (along with the three supporting pieces) behaves like a friction mechanism. In the following, the experimental set-up without the bridge will be referred to as the linear system while the nonlinear system is assumed hereafter to include additionally the bridge model the related friction mechanism.

Each platform is approximated herein by adopting three degrees of freedom (DOF), as can be seen in Fig. 15.1; hence, two translational modes and a rotational one are considered to describe sufficiently the dynamic performance, which is measured by three accelerometers appropriately placed at each platform to capture the vibration corresponding to the three modes. The accelerations are recorded using a multiple-channel acquisition system that converts the data from analogue to digital format employing a sampling frequency of 1651.67 Hz. The platform models are randomly excited in six different positions by a pneumatic actuator and the related valves, see Figs. 15.1 and 15.2. The frequency content of the excitation is defined through an algorithm that controls each valve independently, ensuring a flat-like spectral density ranging from 2 up to 20 Hz. Furthermore, the duration of each random vibration test is set to 1200 s, being longer compared to what is commonly prescribed for OMA applications, in order to have estimates of a slightly increased precision compared to normal practise [1]. Nonetheless, tests were also carried out with varying durations and no indication has been observed to the requirement of extending the time duration because of the friction-induced nonlinearity and nonstationarity.

Conceptually, friction damping is a mechanism consisting of two motion states: (i) the stick state and (ii) the slip state. When the former is valid for a friction mechanism, the total stiffness of the system is increased by adding the separate stiffness contributions of the connected structures (or structural parts). On the other hand, if the external tangential force on the interacting surfaces exceeds the static friction force (i.e., the slip force), then motion occurs and damping is added to the entire system while the added stiffness vanishes [7]. The two states, corresponding to the aforementioned friction-induced motion states, are expected to affect significantly the dynamic performance of the frictionally connected systems. Thus, it is chosen herein to vary the intensity of the excitation in order to trigger the development of the two motion states and in turn, to identify potentially different modes, being dependent on whether the bridge sticks to the platforms or slips on them. Especially, the steel platforms connected by the bridge were subjected to broad band excitation with two different levels of intensity, i.e., the low and the high one respectively, achieved by varying the nozzle diameter of the output of the excitation and the distance between their position and the platform's deck (Table 15.1). In the case of the high intensity excitation, the slip state is expected to govern the friction mechanism adding, in such a way, nonlinear damping to the system. On the contrary, the low intensity vibration level is going to induce both motion states of the friction mechanism with dominance, most probably, of the stick state.

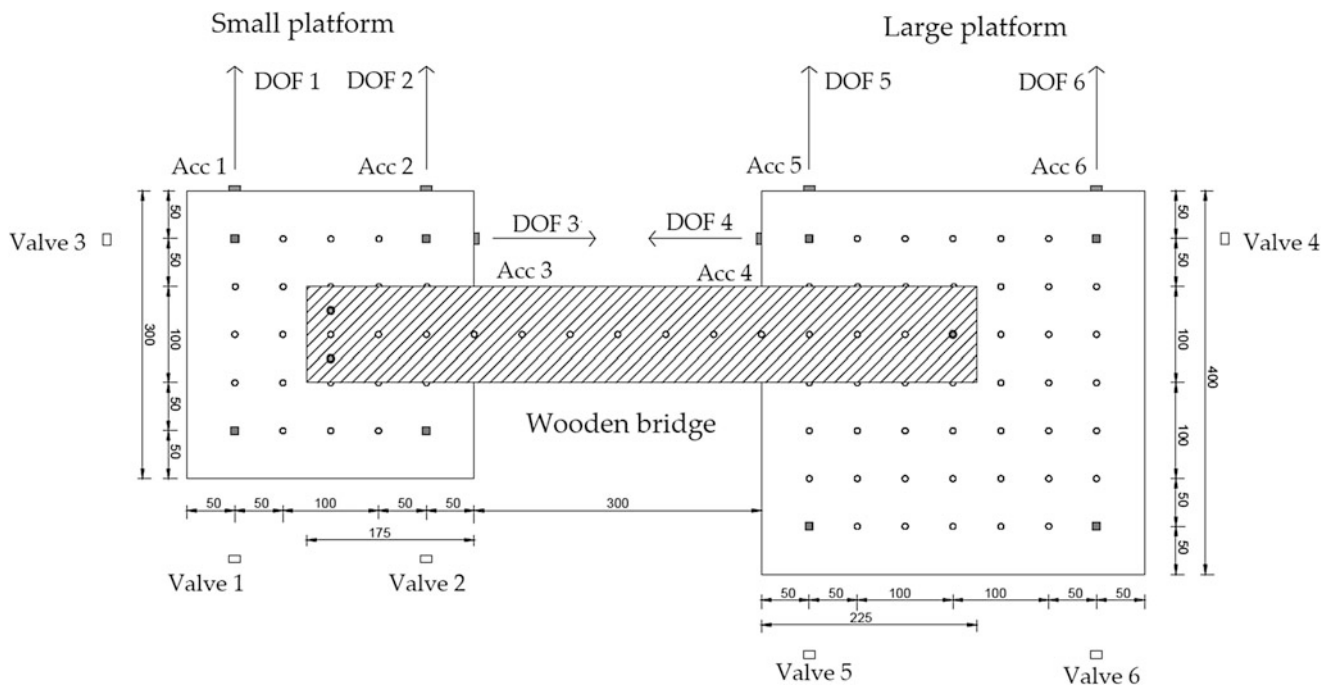


**Fig. 15.1** Sketch of experimental set-up

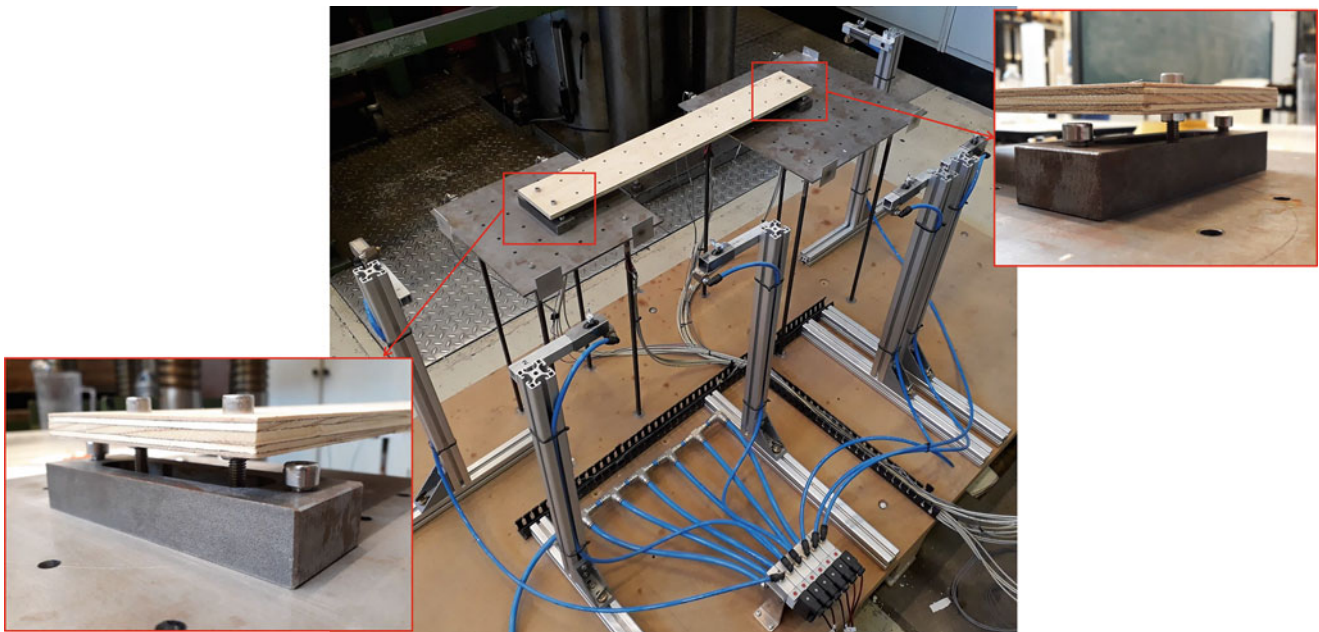


**Fig. 15.2** Photo of experimental set-up with close-up of the friction interface between the bridge and the platforms

To safeguard that the experimental set-up will favour both the linear and nonlinear performance of the scaled platform models, the random excitation system (i.e., the pneumatic actuator and the related valves), tuned in the high intensity level, was used to vibrate randomly both the friction-based, nonlinear system and the linear one, i.e., the steel platforms with and without the bridge connection respectively. The measured response, in terms of accelerations, for both systems were then statistically processed to derive probability densities and normal probability plots respectively, in which the concentration of the response around zero (Fig. 15.3a) and the extremes are more profound in the nonlinear case (Fig. 15.3b). These observations fit well to the typical behaviour of a friction damped system. Especially, response of lower magnitude is observed, when the friction interface is not slipping, and at higher response amplitudes the applied friction damping is

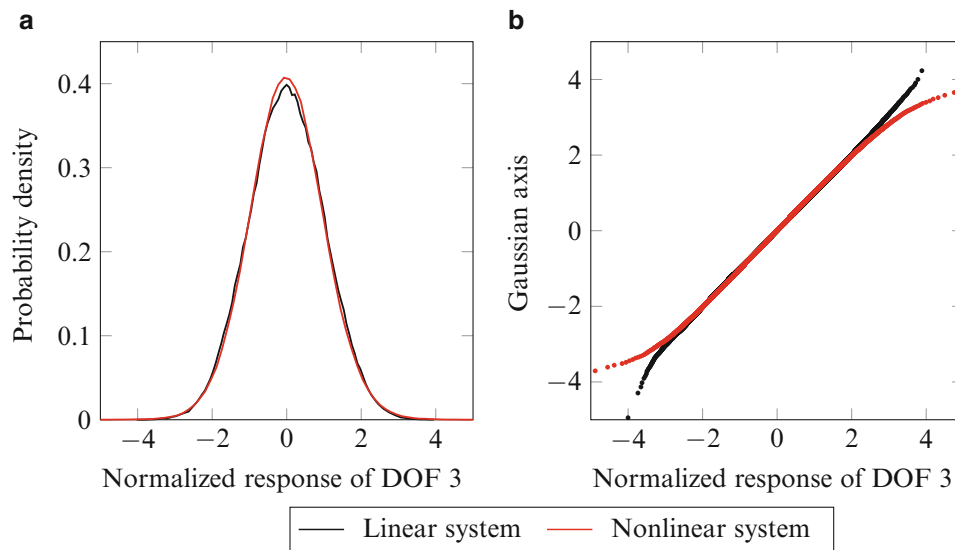


**Fig. 15.3** Estimated probability density (a), and normal probability plot (b), of the linear and nonlinear system based on the measured acceleration of the third DOF

expected to be lower resulting in more outliers. The change in bell shape is also quantified and the kurtosis is calculated equal to 3.3 in the nonlinear case compared to 3.0 found for the linear case (exact normal distribution). Based on the observations made above, the system is considered to experience nonlinear performance when the scaled models of platforms are connected through the bridge and the associated friction mechanism is activated.

### 15.3 Methodology

State-of-the-art OMA methods are utilized herein that are defined both in the time and the frequency domain respectively. For the former case, the estimates of modal characteristics are based on correlation functions while, for frequency domain methods, the modal characteristics are estimated from spectral densities. Especially, the Auto Regressive – Poly Reference method (AR-PR), performed in the time domain, is chosen to identify the modal characteristics of both the linear and nonlinear systems, while similar identification is conducted in the frequency domain by the use of Frequency Domain Decomposition method (FDD) and the Poly Reference Least Squares Complex Frequency-domain method (pLSCF). The detailed description of the aforementioned OMA methods is considered out of the scope of the current article, and hence, only a short overview is provided next along with relevant references.

Stemming from the time domain AR-PR method, a matrix of polynomial coefficients of the AR models is initially calculated on the basis of estimated correlation function by solving an overdetermined problem with the use of least squares regression or singular value decomposition. The modal characteristics are then estimated by forming the companion matrix of the polynomial coefficients and performing the eigenvalue decomposition. More details about the AR-PR method can be found elsewhere see [1, 8–13]. As for the AR-PR method, polynomial functions constitute the basis for the pLSCF method implemented, though, into the frequency domain. More specifically, the companion matrix is computed by forming and solving an overdetermined problem with the use of least squares regression techniques and then, the eigenvalue decomposition is adopted to estimate the modal characteristics [2, 14, 15]. Unlike the time domain AR-PR method, in which the polynomials of the AR models are based on correlation functions, the half spectrum is considered for the pLSCF method. Finally, the FDD method, introduced by Brincker et al. [1, 16–18], is based on the singular value decomposition of the spectral density matrix and provides qualitative presentation of the physical content of the measured signals in the frequency domain. It has been shown that the obtained singular values can be interpreted as auto spectral densities of the modal coordinates while the singular vectors represent the mode shapes.

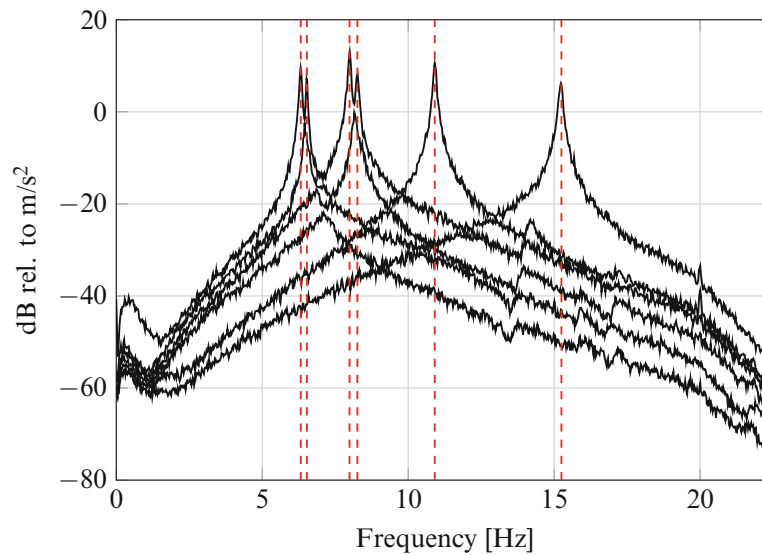


**Fig. 15.4** Singular values of spectral matrix of the linear case. Red lines indicate modes

## 15.4 Experimental Results

The experimental schedule followed herein accounts for both the linear system and nonlinear one (i.e., the scaled platform models without and with the bridge connection) while two intensity levels (i.e., low and high) were tested for the random excitation. In total, three experimental cases were considered: (i) the linear system exposed to random excitation of high intensity, and (ii–iii) the nonlinear system subjected to both high and low intensity random excitation respectively. The platform's horizontal accelerations, measured for each experimental case, are used as the basis to apply the aforementioned OMA methods (i.e., FDD, AR-PR and pLSCF) and to identify the modal characteristics, presented in the form of: (i) a plot of the singular values of the spectral density matrix, (ii) listed values of frequencies and damping ratios and (iii) a plot of the estimated mode shapes. It is notable that the spectral density matrix is estimated using the Welch averaging approach with 50% overlap while a Hanning window is adopted.

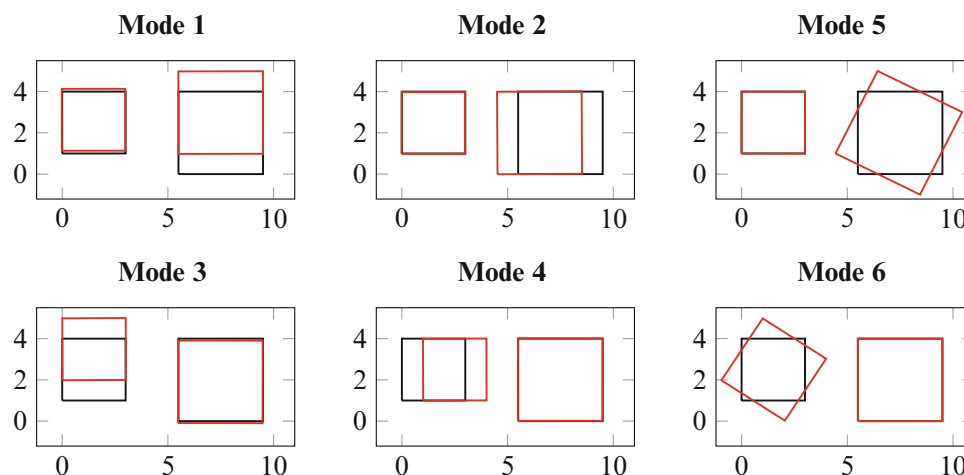
### 15.4.1 Linear Case

From the singular values of the spectral matrix plotted in Fig. 15.4, six modes are clearly observed and especially, the two closely-spaced modes with the lowest frequencies (at 6.32 and 6.53 Hz) represent the two translational modes of the large platform while the following set of closely-spaced modes (at 7.99 and 8.26 Hz) corresponds to the translational modes of the small platform. Furthermore, the two well-separated peaks at 10.9 and 15.2 Hz are related to the rotational modes of the large and small platform respectively. As expected for the linear case, each mode of the two platforms are well represented and transparently identified.

Additionally, Table 15.2 lists the results from the identification of the modal characteristics implemented on the basis of the three OMA methods considered herein. Almost identical results have been derived both for the eigenfrequencies and the damping ratios highlighting, in such a way, that the modal parameters identification for randomly excited linear systems is independent on the OMA method used. It is also notable that the dynamic performance of the linear system is mildly damped since the highest damping ratio identified herein was found equal to 0.54%. Moreover, the six mode shapes of the two platforms are found to be well defined and estimated (Fig. 15.5). More specifically, each of the two sets of closely-spaced modes represents a subspace, thus, the direction of the modes is chosen arbitrarily. It is notable that the mode shapes have been projected on planes parallel to the sides of the platforms in order to refine the illustration.

**Table 15.2** Analysis results of the linear case.

Mode	FDD	AR-PR		pLSCF	
	Frequency [Hz]	Frequency [Hz]	Damping ratio [%]	Frequency [Hz]	Damping ratio [%]
1	6.32	6.32	0.51	6.32	0.50
2	6.53	6.53	0.34	6.53	0.35
3	7.99	7.99	0.50	7.99	0.53
4	8.26	8.26	0.54	8.26	0.50
5	10.9	10.9	0.40	10.9	0.41
6	15.2	15.2	0.41	15.2	0.45

**Fig. 15.5** Mode shapes of the platform models estimated for the linear case

### 15.4.2 Nonlinear Case: High Intensity

The experimental results associated with the nonlinear system and the high intensity random excitation served the basis to calculate the singular values of the spectral density matrix (Fig. 15.6), the latter being quite similar to the singular values estimated for the linear case (Sect. 15.4.1). Additionally, the same six modes are identified as for linear case. Considering the estimation of the nonlinear system's eigenfrequencies (Table 15.3), they are found to be quite similar with the ones derived from the linear analysis case and this observation is independent on the OMA method used herein. On the other hand, the damping ratios have been amplified for all the translational modes and especially, the highest increase (260–370%) is found for the translational modes oscillating parallel to the bridge (modes 2 and 4), since this is the direction, in which the friction mechanism is mainly activated. Significantly increased (70–120%) damping ratios, compared to the linear case, are also identified for the translational modes being perpendicular to the bridge (mode 1 and 3). For the rotational mode of the large platform (mode 5), the damping ratio is approximately the same, while a slight increase of the damping ratio is found for the rotational mode of the small platform (mode 6). Furthermore, a rather limited decrease in frequency is found for the four translational modes (mode 1–4), however, this decrease is considered to be an effect of the significantly increased damping ratios.

Regarding the identified mode shapes, the ones calculated for the nonlinear system and the high intensity level for the random vibration (Fig. 15.7) are almost identical to the mode shapes related to the linear case discussed above (Sect. 15.4.1). Together with the results presented above regarding the present case (nonlinear – high intensity), it is considered that the modal characteristics can be reliably estimated in the case of friction damping equitably with the linear case. The latter is based on the fact that the limited decrease in frequency for the translational modes and the increase in damping ratios both correspond to the changes applied to the system. Nonetheless, the methods adopted herein estimate a linear approximation of the modal damping. The equivalence of the linear approximation of the modal damping with the nonlinear damping is, however, not further investigated in the present paper. Furthermore, it can be established that the friction mechanism has been primarily in the slip state during the test, since the system only exhibits the described changes.

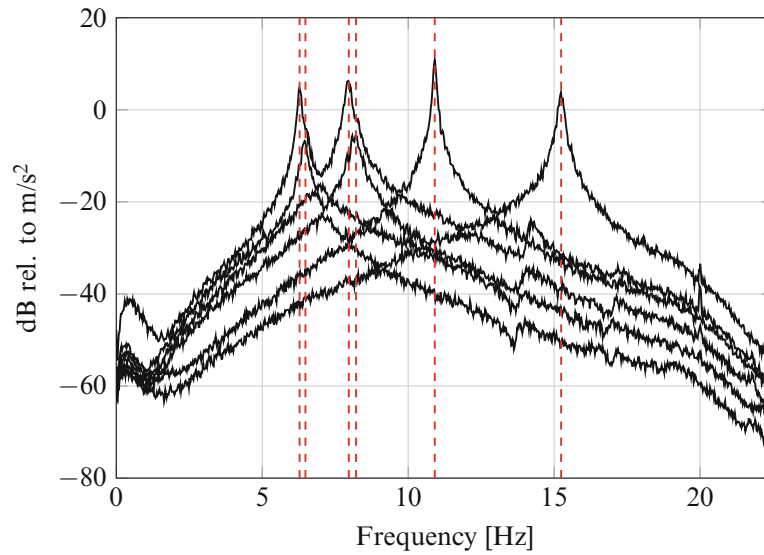


Fig. 15.6 Singular values of spectral matrix of the nonlinear case with high intensity. Red lines indicate modes

Table 15.3 Analysis results of the nonlinear case with high intensity

Mode	FDD	AR-PR		pLSCF	
	Frequency [Hz]	Frequency [Hz]	Damping ratio [%]	Frequency [Hz]	Damping ratio [%]
1	6.28	6.28	0.88	6.28	0.85
2	6.48	6.49	1.7	6.49	1.6
3	7.97	7.95	1.1	7.95	1.1
4	8.21	8.23	1.8	8.23	1.9
5	10.9	10.9	0.37	10.9	0.38
6	15.2	15.2	0.57	15.2	0.59

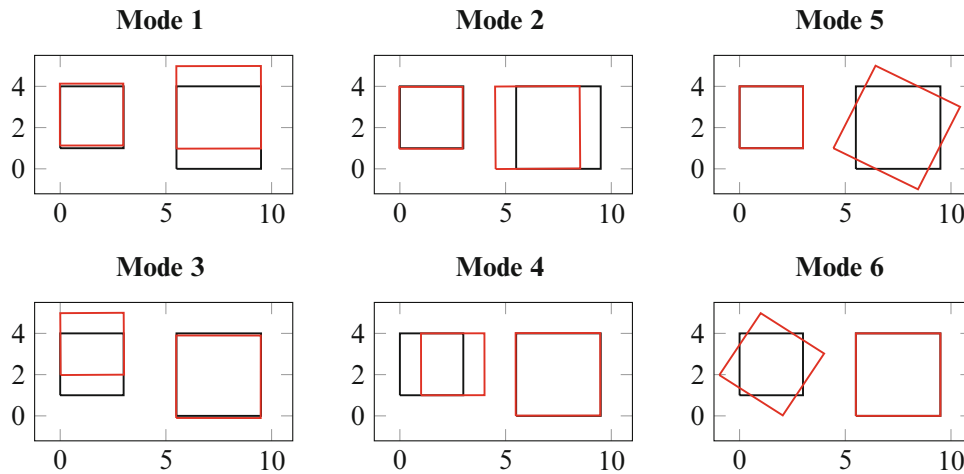
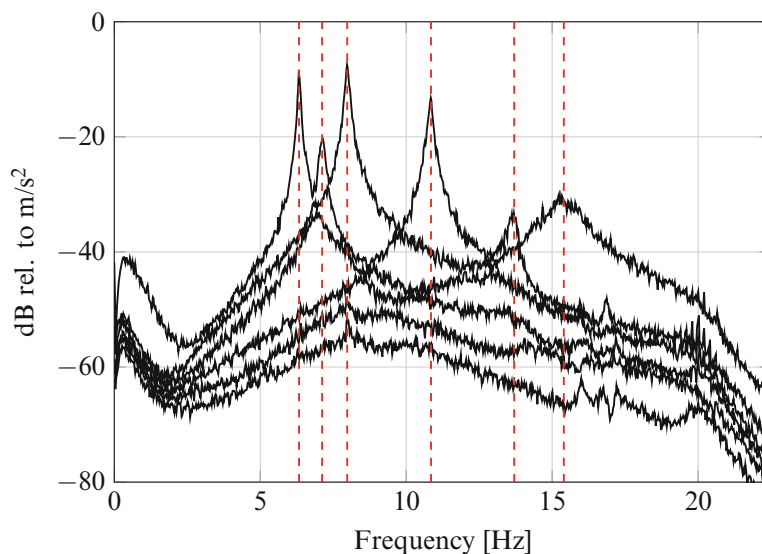


Fig. 15.7 Mode shapes of the platform models estimated for the nonlinear case with high intensity

### 15.4.3 Nonlinear Case: Low Intensity

The measured response of the scaled platforms models, being connected with the bridge and excited with the low intensity random vibration, enables calculating the singular values of the spectral density matrix (Fig. 15.8), found to deviate from the singular values that correspond to the two former cases (Figs. 15.4 and 15.6). Particularly, the second peak in Fig. 15.8 represents a “coupled mode” that merges the two translational modes oscillating in the direction of the bridge (i.e., mode 2



**Fig. 15.8** Singular values of spectral matrix of the nonlinear case with low intensity. Red lines indicate modes

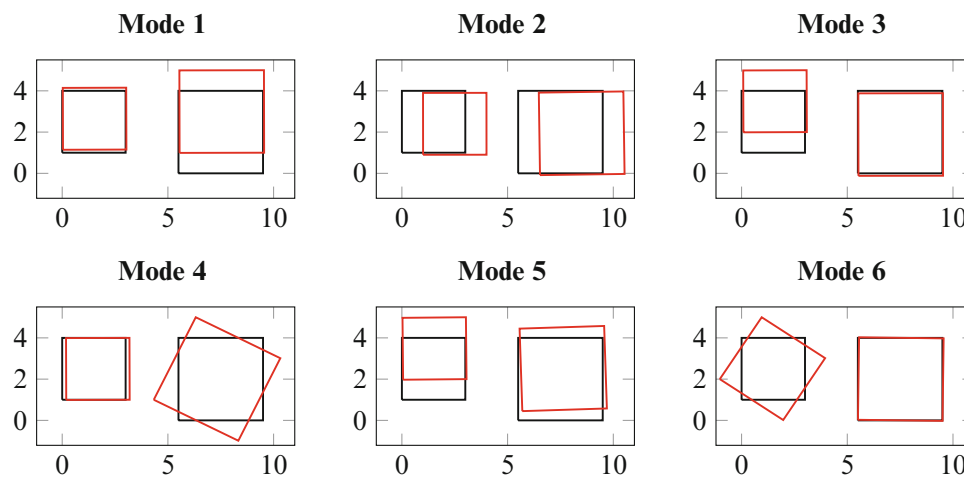


**Fig. 15.9** Mode shapes of the platform models estimated for the nonlinear case with low intensity

and 4 identified for the two aforementioned cases). The reason for detecting this “coupled mode” is related to the fact that the random vibrations with the lower intensity results in the slip state (i.e., sliding between the bridge and the platforms) occurring less frequently during the test. Hence, the two platforms experience mainly a coupled vibration (i.e., they move together) that corresponds to the common mode identified herein. Comparing with the singular values plotted in Figs. 15.4 and 15.6 for the two aforementioned cases, the rotational mode of the small platform (mode 6) is related to significantly higher damping while an additional mode, associated though with a small peak, has also emerged with frequency equal to 13.6–13.7 Hz. This mode is the result of coupling the rotational mode of the small platform (mode 6, Sects. 15.4.1 and 15.4.2) and the translational mode of the large platform (mode 1, Sects. 15.4.1 and 15.4.2) oscillating perpendicular to the bridge. The frequency of the second “coupled mode” is close to the frequency of the small platform’s rotational mode, revealing its dominance over the translational mode of the large platform. From this observation, the test results indicate that it is the ratio of the internal forces of the corresponding modes (and not just a simple average of eigenfrequencies) that determines the resulting eigenfrequency of the emerged “coupled mode”.

The observations discussed above for the current case are substantiated by the results listed in Table 15.3 in terms of the estimated eigenfrequencies and damping ratios. Comparing with the linear case, the dynamic performance of the current nonlinear system is found to be more damped and especially, the damping ratios corresponding to the “coupled modes” 2 and 5 as well the rotational mode of the small platform (mode 6) experience the increase (200–880%). Accounting for the modified modes and the higher damping found for the latter case, it is believed that the current nonlinear system subjected to

**Table 15.4** Analysis results of the nonlinear case with low intensity

Mode	FDD	AR-PR		pLSCF	
	Frequency [Hz]	Frequency [Hz]	Damping ratio [%]	Frequency [Hz]	Damping ratio [%]
1	6.33	6.33	0.62	6.33	0.63
2	7.12	7.12	1.3	7.13	1.3
3	7.98	7.98	0.78	7.98	0.78
4	10.8	10.8	0.76	10.9	0.90
5	13.7	13.7	1.6	13.6	1.3
6	15.4	15.4	4.1	15.4	4.33

random vibration of low intensity represents a nonstationary case, within which two different systems, corresponding to the stick and slip state respectively of the friction mechanism, emerge during the execution of the test. However, the stick state is the governing one since the related modes dominate the dynamic response. Finally, the “coupled modes” can be visualized by Fig. 15.9, where the six mode shapes of the specific nonlinear system are depicted.

## 15.5 Conclusion

The purpose of this study was to assess the identification performance of contemporary OMA-based methods on structural systems experiencing both nonlinearity and nonstationarity, being contradictory to the fundamental assumptions of OMA. A friction mechanism, appropriately introduced by connecting the scaled platform models through a wooden bridge, induced nonlinear damping while alternated the system’s modes depending on the intensity of the broad band random excitation and the corresponding motion states (i.e., slip and stick state of the friction element). The identification results mainly revealed:

- increased damping ratios and corresponding slightly decreased eigenfrequencies when the friction mechanism was introduced and the system was subjected to random excitation of high intensity.
- the low intensity excitation of the friction-based system affected its modes since coupled ones emerged as a result of the friction stick state occurring, though, not constantly during the entire duration of the test.

According to the aforementioned findings, it seems that the OMA-based methods provide reasonable identification results implying that even nonlinear and nonstationary systems can be described by underlying linear systems, for which the basic OMA assumptions are valid. Additional research should be spent to investigate the suitability of using OMA in order to perform intensity-independent identification of a nonstationary system, being composed by linear invariant systems.

**Acknowledgements** The authors acknowledge the funding received from Centre for Oil and Gas – DTU/Danish Hydrocarbon Research and Technology Centre (DHRTC).

## References

- Brincker, R., Ventura, C.: Introduction to Operational Modal Analysis. Wiley, New York (2015)
- Rainieri, C., Fabbrocino, G.: Operational Modal Analysis of Civil Engineering Structures. Springer, New York (2014)
- Zhang, E., Pintelon, R., Guillaume, P.: Modal identification using OMA techniques: nonlinearity effect. Shock Vib. vol. 2015, 12 pages (2015)
- Tarpø, M., Nabuco, B., Skafte, A., Kristoffersen, J., Vestermark, J., Amador, S., Brincker, R.: Operational modal analysis based prediction of actual stress in an offshore structural model. Procedia Eng. **199**(Supplement C), 2262–2267 (2017)
- Tarpø, M., Friis, T., Nabuco, B., Amador, S., Katsanos, E., Brincker, R.: Operational modal analysis based stress estimation in friction systems. In: Proceedings of the 36th International Modal Analysis Conference (2018)
- Friis, T., Katsanos, E., Amador, S., Brincker, R.: Damping estimation of friction systems in random vibrations. In: Proceedings of the 36th International Modal Analysis Conference (2018)
- Soong, T.T., Dargush, G.F.: Passive Energy Dissipation Systems in Structural Engineering. Wiley, Chichester (1997)
- Vold, H., Kundrat, J., Thomas Rocklin, G., Russell, R.: A multi-input modal estimation algorithm for mini-computers. SAE Technical Paper (1982)
- Vold, H.: The numerical implementation of a multi-input modal estimation method for mini-computers. In: Proceedings of 1st International Modal Analysis Conference (1982)
- Ljung, L.: System Identification: Theory for the User. Prentice-Hall, Upper Saddle (1987)



11. Harvey, A.C.: Time Series Models. Philip Allan Publishers Ltd., New York (1981)
12. Pandit, S.M., Wu, S.M.: Time Series and System Analysis with Applications. Wiley, New York (1983)
13. Norton, J.P.: An Introduction to Identification. Academic, London (1986)
14. Zhang, L., Kanda, H., Brown, D.L., Allemang, R.I.J.: Polyreference Frequency Domain Method for Modal Parameter Identification. American Society of Mechanical Engineers (1985)
15. Guillaume, P., Verboven, P., Vanlanduit, S., Van der Auweraer, H., Peeters, B.: A poly-reference implementation of the least-squares complex frequency domain-estimator. In: Proceedings of the 21st International Modal Analysis Conference (2003)
16. Brincker, R., Zhang, L., Andersen, P.: Modal identification of output-only systems using frequency domain decomposition. In: Proceedings of the European Cost F3 Conference on System Identification, pp. 273–282 (2000)
17. Brincker, R., Ventura, C.E., Andersen, P.: Damping estimation by frequency domain decomposition. In: Proceedings of the International Modal Analysis Conference – IMAC, vol. 1, pp. 698–703 (2001)
18. Brincker, R., Zhang, L., Andersen, P.: Modal identification from ambient responses using frequency domain decomposition. In: Proceedings of the International Modal Analysis Conference – IMAC, vol. 1, pp. 625–630 (2000)

# Chapter 16

## Remote Damage Detection of Rotating Machinery



Peter H. Fickenwirth, Charles H. Liang, Tyrel C. Rupp, Eric B. Flynn, and Adam J. Wachtor

**Abstract** Condition-based monitoring (CBM) is a method of damage detection that actively monitors continuously operating machines to identify the earliest signs of deteriorating performance. There are many accepted methods of CBM, however this paper focuses on remote sensing of the vibration signatures of rotating machinery, e.g. an AC motor. Traditionally, vibration-based CBM requires accelerometers to be mounted directly on the machinery of interest; however, certain operating conditions may prevent such direct accelerometer access. This research aims to understand how to improve upon existing CBM methods by developing a transfer function which accounts for the propagation environment between the machinery of interest and an accelerometer placed some distance away, and then use this transfer function to perform damage detection. By taking baseline measurements at the start of the life on an AC motor as well as a spatially separated location, a transfer function between the two measurements can be developed in a similar fashion to a frequency response function. Using the developed transfer function and spectral analysis, remote measurements can then be used to reconstruct the vibration signatures at the motor. Furthermore, it will be shown that using this transfer function improves performance of a damage detector using a matched filter. These methods were tested using a motor mounted to a plate that is mounted on a wooden table as well as with a characterization motor loosely mounted on compliant padding. Also discussed are the damage detection results, as evidenced by the improvement in the receiver operating characteristic (ROC) curves of four damage modes, showing that capturing the propagation environment through the transfer function improves remote damage detection performance.

**Keywords** Condition-based monitoring · Remote sensing · Vibration signatures · Frequency response function · Spectral analysis

### 16.1 Introduction

Condition-based monitoring (CBM) has gained tremendous interest in the past two decades, since it is both low-cost and detects damage when the earliest signatures are present. Traditionally, CBM has been most commonly applied to continuously rotating machinery such as induction motors and the implements to which they are attached. Despite being well characterized, the vast majority of industrial CBM methods require machine-mounted accelerometers or access to the supply current signature of the induction motor involved.

---

Peter H. Fickenwirth, Charles H. Liang, and Tyrel C. Rupp are contributed equally to this work.

P. H. Fickenwirth  
UMass Lowell, Lowell, MA, USA  
e-mail: [petefickenwirth@gmail.com](mailto:petefickenwirth@gmail.com)

C. H. Liang  
Columbia University, New York, NY, USA  
e-mail: [charles.liang@columbia.edu](mailto:charles.liang@columbia.edu)

T. C. Rupp  
University of Utah, Salt Lake City, UT, USA  
e-mail: [tyrel.rupp@gmail.com](mailto:tyrel.rupp@gmail.com)

E. B. Flynn · A. J. Wachtor (✉)  
Los Alamos National Laboratory, Los Alamos, NM, USA  
e-mail: [eflynn@lanl.gov](mailto:eflynn@lanl.gov); [ajw@lanl.gov](mailto:ajw@lanl.gov)

This limitation in the current state of CBM prevents its application to a number of extreme environmental situations. Examples include rotating equipment located in radioactive environments in which *in vivo* instrumentation might not be an option or in turbine engines where high temperatures, speed, and sizing constraints prevent instrumentation from being placed on the mechanism of interest, such as the shaft of bearings, or even the blades of the turbine itself. Furthermore, direct sensor mounting prevents simplified instrumentation through remote, centralized measurements. The goal of this study was to explore a method of vibration-based CBM that can be performed with an accelerometer located remotely to a machine which otherwise could not be instrumented and characterized locally.

Typically for linear systems, propagation environments are characterized using frequency response functions (FRFs), which require both an input and output. In a remote case where local measurements cannot be obtained, this traditional method is not feasible and an alternative must be explored. This posed problem has many potential solutions, however the objective of this research was to identify if a surrogate input signal similar to the actual input signal, could be used with actual remote signals to sufficiently account for a propagation environment and allow for damage detection.

## 16.2 Background

The health of rotating machinery is critical to many engineering and industrial processes. As such, CBM helps ensure the health of the machinery, preventing cost and time lost due to unexpected machine failure by identifying the signatures of damage as soon as they arise [1, 2].

Currently, the health of many industrial machines is maintained through either a periodic inspection-based approach, or a reaction-based approach, in which machinery is only repaired when it is broken. Both of the above approaches have drawbacks; a periodic inspection-based approach results in unnecessary inspections when the machines are healthy and may not detect damage when the earliest signatures of damage arise. A reaction-based approach detects faults when already significant damage has occurred, leading to significant downtime and repair of the machines. In many health monitoring systems, individual sensors are used to monitor the health of the machines, such as motors and turbines. However, the increased cost in data acquisition, installation, and maintenance of many sensors may make such distributed health monitoring systems economically unviable [2].

In contrast, CBM monitors machines in a low-cost and safe manner [3]. In most cases, CBM methods are used to detect damage in rotating machinery, such as turbines and motors [1]. The process of CBM is as follows: (1) collect dynamic response data, (2) extract features, i.e. signatures of damage, from the data using signal processing, and (3) utilize statistical methods to determine the presence of damage, i.e. machine in healthy or damaged state [2].

In terms of actual monitoring techniques, CBM conceivably could operate by monitoring acoustic, radio frequency, vibrational, electrical current or other physical phenomenon of systems. However, in terms of practical application, CBM most commonly monitors the output from motor current signature analysis (MCSA) and/or mechanical vibration analysis (MVA) to determine the operational status of induction based motor systems [4].

### 16.2.1 Motor Current Signature Analysis (MCSA)

MCSA is one of the dominant methods of CBM, and uses the current draw of an induction motor (often three-phase) while in operation to detect damage. MCSA can be used to identify a number of electrical problems within an induction motor, most commonly detecting broken rotor bars, air gap eccentricity, and shorted stator winding turns. The signatures of such damage modes have been well characterized and can be easily seen in the current spectrum of the motor in question [5]. MCSA lends itself well to the problem of indirect access to a motor as a current transformer need only be attached to one of the electrical supply lines of the motor. Thanks to the electromechanical nature of induction motors, current and vibration analysis can be used together to detect and determine the causes of damage in a motor [6]. Each analysis method has drawbacks which can be overcome by using them together. For example, MCSA can fail to identify a broken rotor bar when operating with no load [7].

### 16.2.2 Motor Vibrational Analysis (MVA)

With the advent of microfabricated piezoelectric accelerometers, non-invasively characterizing and monitoring the vibrational characteristics of induction motors has become relatively simple and much more convenient [8]. In the simplest terms, MVA-based CBM operates in the following fashion: First, a motor or system is fitted with one or more accelerometers usually detecting vibrations radial to the motor housing. Next, a fast-Fourier transform (FFT) is performed to convert the time series signal into the frequency domain. For healthy systems, the spectrum created by the FFT should, at a minimum, show a peak at the operating rotational frequency. For systems with degraded performance, a variety of changes to the vibration spectrum, including at the harmonics, can be witnessed. As a whole, the process of MVA and the corresponding damage libraries have been well researched [7, 9].

Instrumenting and diagnosing systems can be done periodically or continuously with the aid of CBM software, or simply by manually interpreting spectrogram data.

The background in performing MVA-based CBM remotely poses the question: what constitutes “remotely located?” Fundamentally, one could argue that any accelerometer attached to a bearing housing or motor housing is remote to the actual revolving machinery. For the sake of this research, however, we will define remote as in any position that an undesired propagation environment augments the input signal in such a way to add undesirable dynamic features to the output.

Research on remote MVA-based damage detection is sparse; in 2013, Walker showed that specific flywheel imbalances and bearing faults in a machine could be identified by using a single accelerometer located on the machine’s metal mounting platform, but testing at a farther distances was not performed. The actual identification of faults was done primarily by using an artificial neural network to identify and learn unexpected non-linearities in the accelerometer data. Furthermore, all training and testing data was acquired on the same machine, with the sensors used located in the same relative positions [10].

### 16.2.3 Signal Processing Techniques

To analyze the vibrations of the motor, signal processing techniques played a key role in identifying damage. In the literature, researchers performed diagnostics and then spectral analysis of the bearing/shaft assembly vibration [4, 10, 11]. Similar to the literature, initial baseline measurements of the motor were taken using an accelerometer. The motor has an operational frequency of 30 Hz, so the dominant peaks in the spectrum were at 30 Hz and its harmonics. The baseline accelerometer measurements show that the optical board, on which the motor is mounted, has resonant frequencies at approximately 75 Hz, 140 Hz, and 190 Hz.

The frequency response function,  $H$ , characterizes the vibrational response of the propagation environment from input to output. In the absence of noise on the input,  $H$ , is estimated using the  $H1$  estimator:

$$H1 = \frac{G_{xy}}{G_{xx}} \quad (16.1)$$

This equation is the ratio of the crosspower to the autopower spectrum of the input signal [12]. When there is no noise on the output, the  $H$  can be estimated using the  $H2$  estimator:

$$H2 = \frac{G_{yy}}{G_{yx}} \quad (16.2)$$

This equation is the ratio of the autopower spectrum of the output signal and the crosspower. Because of the presence of noise in the environment and thus noise in the input and output, the  $Hv$  frequency response function estimator was used to reduce error on both the input and output. In Eq. (16.3), the  $Hv$  estimator is the total least squares solution [13].

$$\{S_y\} - \{S_m\} = [Hv] \{\{S_x - S_n\}\} \quad (16.3)$$

In Eq. (16.3),  $S$  represents the linear Fourier spectra of the associated variable,  $y$  represents the output,  $x$  represents the input, and  $m$  &  $n$  are noise associated with the output and input, respectively. As the  $Hv$  estimator is the total least squares solution, it can be thought as the estimator that minimizes the perpendicular distance in an output (acceleration in g) vs. input (Hz) plot.

In CBM, machine learning is also a common technique, in which a pattern recognition algorithm is used to extract features from the combined data acquired from each sensor [14]. However, in this study, the rotating machine is first characterized by the manufacturer (as will be discussed in the following section on the experimental setup), so from a remote location, only training data of the motor in a healthy state is available. As a result, the machine learning approach is not useful, because there is no remote data of the motor in a damaged state available for training.

## 16.3 Experimental Setup

In order to account for the propagation environment, a function representing the input-output relationship of the environment needed to be developed. Traditionally, an FRF is created in order to understand how a structure responds to a forced input. By developing the FRF of a structure, the output from the structure can be found for any given input, assuming the system is linear. This FRF is usually developed through a modal tap test, giving a broad-band frequency input using a modal hammer, which has a force transducer inside in order to record the impact. Then, an accelerometer at a desired monitoring location is used to measure the vibrational response of the structure. Using this input and output, an FRF can be developed.

The problem statement of this work places a number of limitations on the way in which the propagation environment of a facility can be characterized. An ideal situation would allow for direct instrumentation of the machinery in question, or at the very least temporary access to perform tap tests, synchronous data collection, or some other means of traditional FRF development. However, barring these situations, a new approach has to be developed. A hypothesis to working within these limitations is to substitute the input excitation of a real-time measurement with a previously characterized signal. Instead of the FRF being developed by inputs and outputs that are collected simultaneously, the time series data from the characterization and remote accelerometers, which are collected separately on two different motors, are used to create what will be referred to as a asynchronous frequency response function (AFRF). Here the term “asynchronous” refers to the fact that the signals are captured at different times, which prevents this FRF from containing any phasal information. As no local access to the motor is available, the only excitation useable for AFRF development comes from the motors themselves. The goal of this development method was to encourage manufacturers of rotating machinery to test and develop the “characterization” data in a laboratory setting, and then distribute this data to industrial customers. This characterization data would include healthy vibration signatures as well as those from common failure modes. When customers receive their machinery and begin running it, they can then setup a CBM location and create the AFRF associated with their particular environment while they know the motor is still new and healthy. From then on, they would be able to use traditional CBM methods to monitor their machinery remotely.

To accomplish this study’s goal of finding a novel method of remote CBM, an experiment (see Figs. 16.1, 16.2, 16.3, and 16.4) was designed to assess the feasibility of utilizing characterization data from an accessible motor to measure the performance of a different, but same model, motor using remote instrumentation. The following sections describe the approach that was taken.

### 16.3.1 Instrumentation and Data Acquisition

In order to monitor motor performance (both remotely and locally), an accelerometer-based data acquisition system (DAQ) was designed. Accelerometers were considered and implemented since vibrations can be measured remotely. In particular, PCB 355B04 single-axis accelerometers were used with an operating range of 1 Hz–8 kHz, a sensitivity of 1000 mV/g ( $g$  = acceleration due to gravity) and a range of  $\pm 5$  g.

To excite and record the output of said accelerometers, a 4-channel NI USB-4431 DAQ and the MATLAB Data Acquisition Toolbox were used. Although capable of 100 kS/sampling, the DAQ was set to 10 kS/s, which was still 20 times the Nyquist frequency in our frequency range of interest (1–250 Hz). This rate remained consistent across all experiments.

### 16.3.2 General Motor Vibration Signal Acquisition

The first step in determining the AFRF was to characterize the vibration signature of a loaded industrial AC motor. It was desired to do so in a fashion that would be comparable to what a manufacturer might feasibly perform. As such, a Century

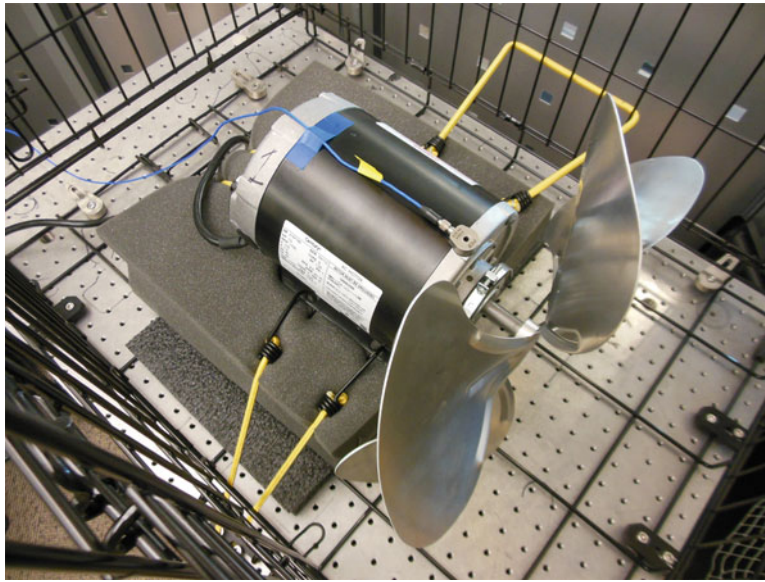


**Fig. 16.1** Characterization motor setup with undamaged blade and accelerometer

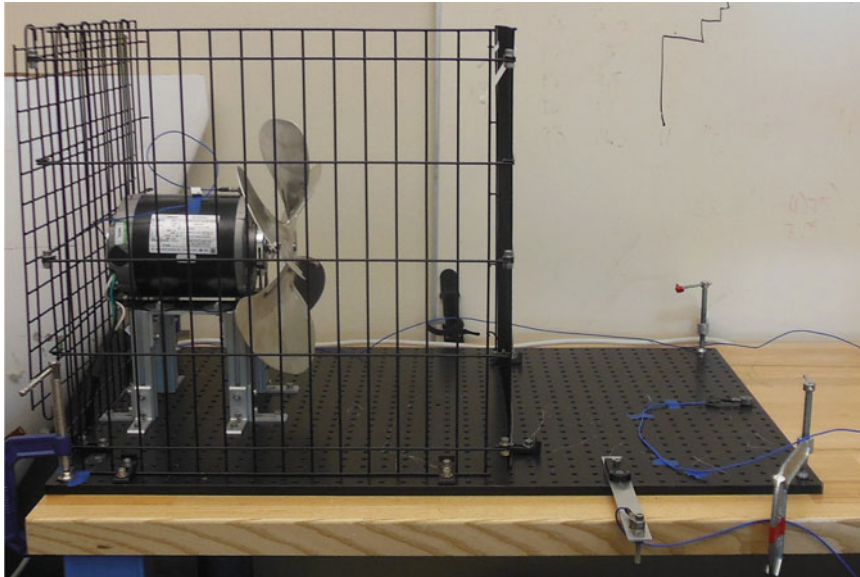


**Fig. 16.2** Application environment setup with local, original remote, and resonator remote accelerometers



**Fig. 16.3** Resonator assembly attached to breadboard

3016P760, split-phase AC,  $\frac{1}{2}$  hp, blower motor was chosen. This motor was loaded using a 35.6 cm (14") 5-blade aluminum fan rated at 1725 rpm (30 Hz) and a 0.27 hp load. The motor was then placed on a compliant foam base to approximate a "free-free" condition. In doing so, the vibration signatures measured on the motor were isolated from the response of the mounting environment. The last step in the setup was to instrument the motor with an accelerometer mounted radially to the motor shaft and parallel to the normal of the table to which the foam and motor were mounted. This configuration can be

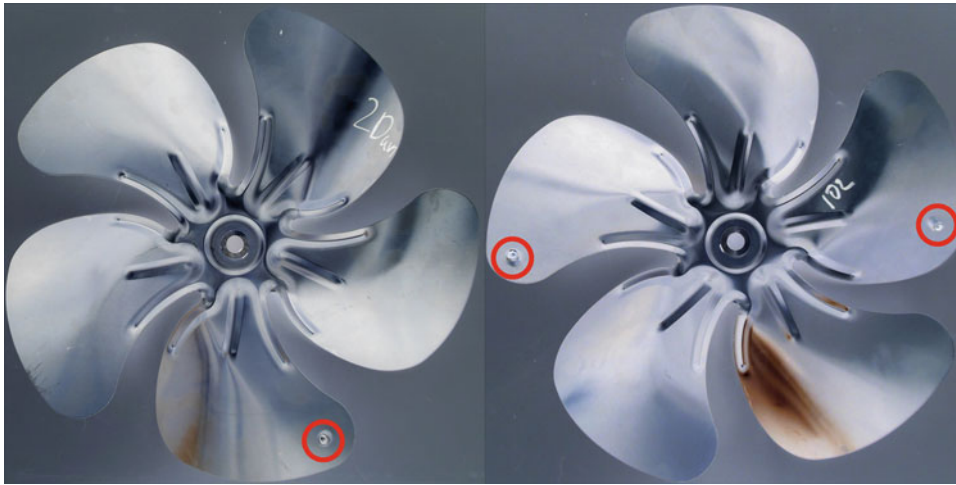


**Fig. 16.4** Single bolt damage (left) and two bolt damage (right) blades shown

seen in Fig. 16.1. After powering up the motor and allowing it to reach steady-state, time series vibration data were collected for what will be referred to as the “characterization” accelerometer.

### 16.3.3 Application Environment Motor Vibration Signal Acquisition

In parallel to the general motor characterization, an identical Century motor-fan setup was mounted onto a frame. The frame in turn was mounted to one end of a simulated foundation consisting of a 610 mm by 914 mm aluminum optical breadboard. An accelerometer was also mounted to the aluminum foundation on the opposite end of the breadboard (about 760 mm away). Again, after powering up the motor and allowing it to reach steady state, vibrational time series data was collected for both the “remote” and “local” accelerometers. This entire setup can be seen in Fig. 16.2.

In later developments, it was found that the environment between the fan and the remote accelerometer was not complex enough to make the developed environment-based damage detector more viable than a detector that simply did not account for the propagation environment. As such, complexity was added to the remote signal by placing the remote accelerometer at the tip of a cantilever resonator. The resonator itself consisted of a 3.2 mm × 25.4 mm × 229 mm aluminum bar bolted to the breadboard, making a 152 mm cantilever as seen in Fig. 16.3. At the tip, in addition to the accelerometer, a 27-gram mass was added to tune the resonator to have two wide band resonances at 46 Hz and 93 Hz.

### 16.3.4 Damaged Vibration Signal Acquisition

Utilizing the systems and acquisition method described above, damaged signals of both the general motor (characterization signal) and application environment (local and remote signals) were obtained. To simulate motor damage, fans were damaged in 4 ways, all of which ultimately yielded typical motor imbalance signatures. For the first damage method, a 6.5 mm ( $\frac{1}{4}$ ”) through hole was drilled approximately 12.7 mm in from the tip one of the fan blades (314 grams). Then, a 6.4 mm ( $\frac{1}{4}$ ”)-20 nut and 15.9 mm ( $\frac{5}{8}$ ”) SHC bolt with a 6.5 mm ( $\frac{1}{4}$ ”) washer were mounted through the hole. The nut-washer-bolt combination weighed 9.6 grams. The second damage mode was similar to the first however this time, in addition to the first hole at the tip of the blade, another hole, co-linear with axis of rotation and the first hole, was drilled at an equal radial distance to the first on the opposite side of the fan. Again bolts were added to the holes, however, washers were neglected and the bolts were only 9.5 mm ( $\frac{3}{8}$ ”) long – this combination weighed 7.5 grams each.

The other two damage techniques were much less severe and consisted of running the single bolt and two bolt blades with the nut, bolt, and washer removed leaving simply the through holes. Despite being a less than 0.1% weight reduction to the fans, these 6.4 mm ( $\frac{1}{4}$ ”) holes induced aerodynamic imbalances to the fan blade that caused a change in vibration outside of the fundamental and harmonic frequencies that the motor. The first two damage techniques and locations of the through

holes can be seen below in Fig. 16.4. Restricting damage to only the fan blades made it a simple matter to swap out healthy and damaged blades as needed on either motor setup.

## 16.4 Frequency Response Function (FRF) Development and Comparison

### 16.4.1 Asynchronous Frequency Response Function (AFRF) Development

To create the AFRF, the power spectral densities (PSDs) and the cross-power spectral density (CPSDs) of the time series data from both the characterization and remote accelerometers were calculated using Welch's method. From there, the three PSDs were used to create an  $Hv$  estimation of the asynchronous frequency response function. The  $Hv$  estimator uses a total least squares regression in order to account for error on both the input and the output, which is a condition faced in this experiment due to the nature of both measurement setups. Since only a single-input, single-output system is being used, the  $Hv$  estimator, Eq. (16.3), can be calculated as a geometric mean of the  $H1$  and  $H2$  estimators, Eqs. (16.1) and (16.2), at each frequency line. As the two signals used to create the AFRF were not synchronized, the phase information between them lost meaning. Thus the AFRF only looks at the magnitude of the two PSDs. While labelled an  $Hv$  estimator in this work, it is analogous to the uncommonly used  $H4$  estimator, which deals only with magnitudes.

$$Hv = \sqrt{H1 \cdot H2} = \sqrt{\frac{G_{yx}}{G_{xx}} \cdot \frac{G_{yy}}{G_{yx}}}$$

$$Hv = \sqrt{\frac{G_{yy}}{G_{xx}}} \quad (16.4)$$

Two sets of ten (twenty sets in total) time series data were collected for the healthy state of the motors. Of these sets, 3 sets were used for AFRF development. As this method is not affected by the time of collection between the two motors, these 3 data sets allowed for 6 different AFRFs to be calculated, which were then averaged to capture a strong model of the propagation environment.

Because the input to this AFRF was an acceleration measurement collected on the housing of the characterization motor, it was more of a transmissibility function than an FRF. This is because an FRF typically uses a forcing function as an input, as this is a true input into the system. The acceleration from the characterization motor is actually a response to the force from the motor, so it is not a true input. However, the aim of the function is to model the effect of the propagation environment in the frequency domain so that the output of any given input can be correctly predicted, just like an FRF.

### 16.4.2 Asynchronous Frequency Response Function Validation

Once the AFRF was developed, it had to be validated in order to justify its use for predicting damage signatures. To do so, the remaining sets of healthy time series data were used. The PSDs for these time series were calculated using Welch's method again. The AFRF was then used to transform the characterization data to predict the remote PSD. The accuracy of the prediction was then assessed visually and by two mathematical methods. The first mathematical method was the root mean square (RMS) error of the prediction, and the second method was the correlation of the prediction to the actual remote PSD. These values were then compared to the characterization data as a predictor. If the predicted PSD had a lower RMS error and a higher correlation compared to the untransformed one, it could be concluded that the AFRF was an adequate representation of the environment. This process was then also repeated using data from the damaged blades.

## 16.5 Damage Detector

Although applying the developed AFRF to the characterization PSD can predict what the remote PSD will look like, this method serves only to check the appropriateness of the AFRF and is not well suited to detect damage to the motor. Thus to



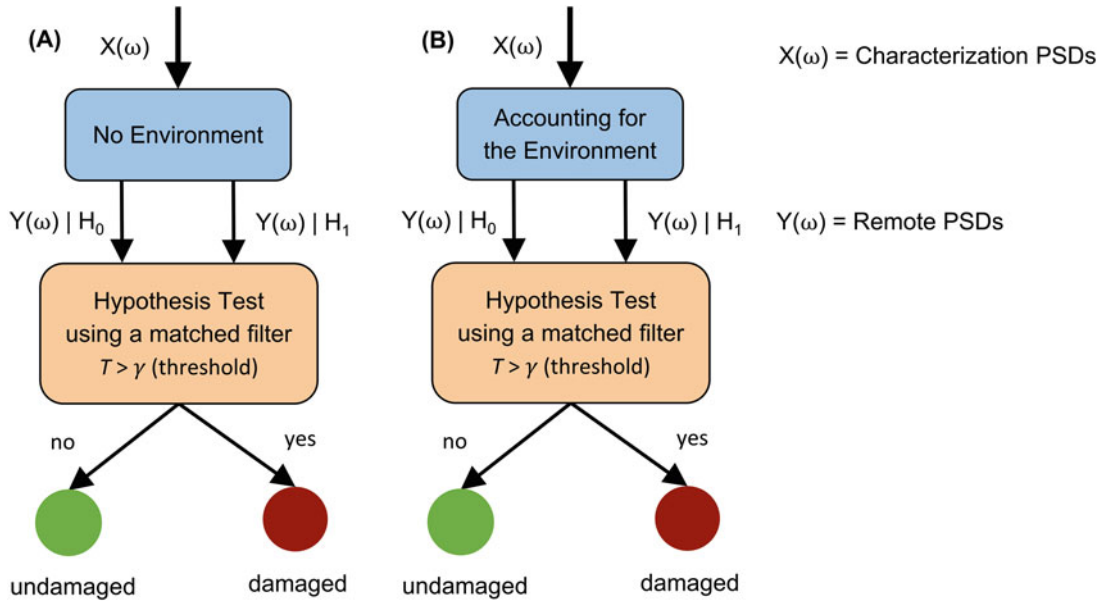


**Fig. 16.5** Comparison of the two damage detection models used to assess whether or not the motor was damaged

determine if the motor showed signs of damage, the collected PSD data was fed into a damage detector code in MATLAB. The detector used was a Generalized Matched Filter, because it is the optimal linear filter to detect a signal in the presence of random noise [15]. Similar to the detection method behind radar, this filter uses template matching to detect the presence of the known signal in the unknown one [16].

### 16.5.1 Damage Detection Model

In order to assess whether the AFRF developed to account for the propagation environment improved detection of damage, the performance of two damage detection models were tested: **(A) not accounting for the propagation environment** & **(B) accounting for the propagation environment**, as seen in Fig. 16.5.

### 16.5.2 Damage Detector Formulation

Hypothesis testing was carried out using a Matched Filter, with the null hypothesis  $H_0$  that the motor is undamaged, and the alternative hypothesis  $H_1$  that the the motor is damaged. All the following variables are a function of  $(\omega)$ , and for simplicity, the  $(\omega)$  will be omitted. The variable  $Y$  denotes the remote measured PSDs,  $G_{yy}$ ,  $G_{xx}$  signify the characterization PSDs of the healthy and damaged data that was fed into the detector. The term  $G_{xx_0}$  is the characterization PSD of a healthy motor as opposed to  $G_{xx_1}$  which is the characterization PSD of a damaged motor. Lastly,  $w$  refers to white Gaussian noise.

It was assumed that  $Y$  is a normal distribution with means  $\overline{G_{yy_0}}$  and  $H^2 * \overline{G_{xx_1}}$ , corresponding to healthy and damaged remote signals, respectively, where  $H^2$  is the transfer function and  $\sigma_{yy}^2$  is the variance of  $G_{yy_0}$ . **(A) not accounting for the propagation environment** is considered first, and then it is shown that **(B) accounting for the propagation environment** is a natural extension of (A) by using the transfer function to account for the propagation environment.

When **(A) not accounting for the environment** and under hypothesis testing,

$$Y = \overline{G_{yy_0}} + w \quad | H_0 \text{ (undamaged)}$$

$$Y = \overline{G_{xx_1}} + w \quad | H_1 \text{ (damaged)}$$

With the following predicted normal distributions,

$$Y \sim N(\overline{G_{yy_0}}, \sigma_{yy}^2) \quad | \quad H_0(\text{undamaged})$$

$$Y \sim N(\overline{G_{xx_1}}, \sigma_{yy}^2) \quad | \quad H_1(\text{damaged})$$

To cast the equations in a form to apply a matched filter, first let  $d$  stand for difference, and then let  $s_d = \overline{G_{xx_1}} - \overline{G_{yy_0}}$ . Then,

$$Y_d = w \quad | \quad H_0$$

$$Y_d = s_d + w \quad | \quad H_1$$

It is worth noting that  $H^2 * \overline{G_{xx_0}} = \overline{G_{yy_0}}$  could have been used for  $H_0$  in hypothesis testing, leading to  $Y | H_0 \sim N(H^2 * \overline{G_{xx_0}}, \sigma_{yy}^2)$  (*undamaged, accounting for propagation environment*). However, when not accounting for the propagation environment ( $H^2 = 1$ ), this would simplify to  $Y | H_0 \sim N(\overline{G_{xx_0}}, \sigma_{yy}^2)$  (*undamaged, not accounting for propagation environment*), but  $\sigma_{yy}^2$  is the variance of  $G_{yy_0}$  and not  $G_{xx_0}$ .

Now, the test statistic can be computed as [15]:

$$T_{\text{not accounting environment}} = Y_d^T C^{-1} s_d > \gamma \quad (16.5)$$

Where  $\gamma$  is the threshold chosen for damage detection and  $C$  is the covariance matrix. A reasonable assumption was that the noise was uncorrelated. Assuming uncorrelated noise, the noise has an independent basis and thus  $C$  can be represented by the diagonal matrix of the inverse of the variances  $1/\sigma_{yy}^2$ .

For a single parameter system, i.e.  $Y_d$ ,  $T$ , and  $s_d$  are simply column and row vectors, respectively, the test statistic simplifies to:

$$T_{\text{not accounting environment}} = \sum_{\omega} \frac{Y_d}{\sigma_{yy}^2} * s_d > \gamma \quad (16.6)$$

It can be noted that

$$\frac{Y - \overline{G_{yy_0}}}{\sigma_{yy}^2} = \frac{Y_d}{\sigma_{yy}^2}$$

is a zero mean, univariate distribution. Based on the literature, the signature of a damage detector is most evident in the difference between the damaged and healthy signal [7], which in this study is  $s_d$ , the difference between the damaged local PSDs and undamaged local PSDs.

Now, for **(B) accounting for the propagation environment**, the transfer function  $H^2$  is used to account for the propagation environment. Under hypothesis testing,

$$Y = \overline{G_{yy_0}} + w \quad | \quad H_0(\text{undamaged})$$

$$Y = H^2 * \overline{G_{xx_1}} + w \quad | \quad H_1(\text{damaged})$$

With the following predicted normal distributions,

$$Y \sim N(\overline{G_{yy_0}}, \sigma_{yy}^2) \quad | \quad H_0(\text{undamaged})$$

$$Y \sim N(H^2 * \overline{G_{xx_1}}, \sigma_{yy}^2) \quad | \quad H_1(\text{damaged})$$

**Table 16.1** Hypothesis testing decision matrix

	Undamaged state ( $H_0$ )	Damaged state ( $H_1$ )
Reject $H_0$	False alarm (Type I error)	True Detection
Fail to reject $H_0$	Correct decision	Fail to detect damage (Type II error)

The test statistic for **(B)** is computed similarly to the **(A)** **not accounting for the propagation environment** case by multiplying  $s_d$  by  $H^2$  in Eqs. (16.5) and (16.6) to account for the propagation environment:

$$T_{\text{accounting environment}} = Y_d^T C^{-1} (H^2 * s_d) > \gamma \quad (16.7)$$

Where as before,  $\gamma$  is the threshold chosen for damage detection and  $C$  is the covariance matrix. Then, the test statistic simplifies to:

$$T_{\text{accounting environment}} = \sum_{\omega} \frac{Y_d}{\sigma_{yy}^2} (H^2 * s_d) > \gamma \quad (16.8)$$

Table 16.1 below refers to the hypothesis testing decision matrix, which shows that reducing both false alarms (Type I error) and failure to detect damage (Type II error) is important and depends on the monitored machinery of interest. If the cost of shutting down the machine and servicing it is greater than the cost of minor damage to machine (the more damage, the more sensitive the detector), minimizing Type I error is more important.

## 16.6 Results and Analysis

### 16.6.1 Frequency Response Function Development and Validation Results

In total, 20 sets of healthy data were collected. Of these, 17 sets were used for testing the damage detector, and 3 for estimating the AFRF development and training the detector. This led to 6 different AFRFs which were then averaged together. Using the methods described in the Sect. 16.4.2, the AFRF was validated visually and quantitatively. Quantitatively, the RMS error was calculated (Eq. 16.9), where the error is the difference between the characterization data transformed via the AFRF, and the actual measured remote data. Figure 16.6 shows an example of this transformation of magnitude ( $g^2/\text{Hz}$  in dB) vs. Frequency (Hz), as well as the untransformed characterization data for this prediction. This process was carried out 17 times with the data that was not used for estimating the AFRF.

$$RMS \text{ Error} = \sqrt{\frac{\sum_{i=1}^n (\text{predicted}_i - \text{actual}_i)^2}{n}} \quad (16.9)$$

On average, using the AFRF yielded 60% less error (Table 16.2) than not using the transformation.

The same process as before was then repeated with sets of each damage mode. The results of each of these transformations are shown in Table 16.2. Once again, the AFRF reduced the prediction error by about 60% for most cases. However, it greatly reduced the error for the prediction of the 1 bolt and 2 hole damage modes. This stronger reduction is likely because the 1 bolt damage mode was the most extreme in terms of vibrational energy, which led to a larger amplitude vibrations transmitted through the propagation environment. While the two hole damage did not strongly increase the vibrational energy at the fundamental and harmonic frequencies of the motor's operation, it had a strong change in the resonances of the fan blades as their aerodynamic properties were changed. These changes were apparent through the loud whistling heard during testing. Moreover, these resonances are easily affected by the propagation environment, so their changes are lost without using the AFRF. The correlation coefficients of all the damage modes rested at about 0.95, regardless of the use of the AFRF.

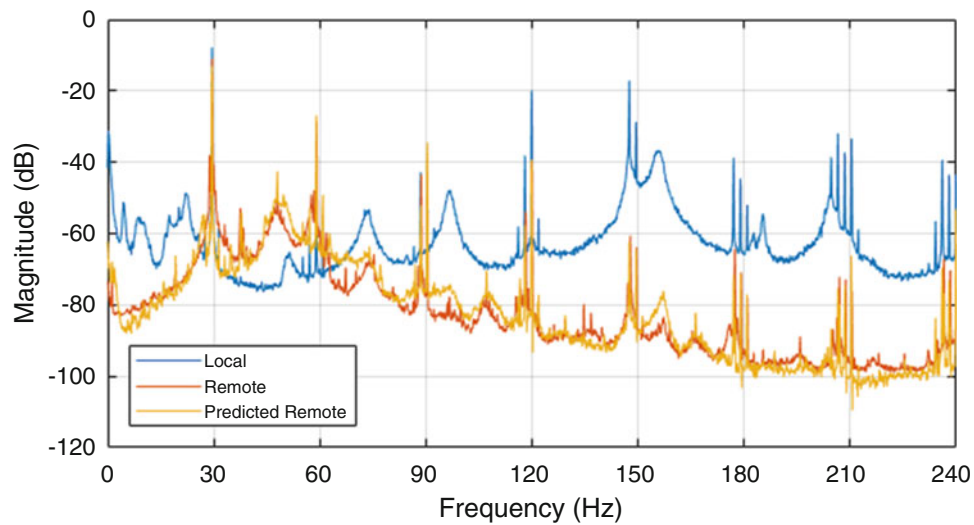


**Fig. 16.6** Healthy data is transformed to predict the output PSD and then compared with the untransformed data

**Table 16.2** Prediction errors for all damage modes

Damage mode	Non-AFRF prediction error ( $g^2/Hz$ )	AFRF prediction error ( $g^2/Hz$ )	Error reduction (%)
Healthy	$2.16 \cdot 10^{-3}$	$8.76 \cdot 10^{-4}$	59.4
1 Bolt	$4.58 \cdot 10^{-1}$	$9.26 \cdot 10^{-2}$	79.8
2 Bolts	$2.62 \cdot 10^{-3}$	$1.08 \cdot 10^{-3}$	58.8
1 Hole	$8.76 \cdot 10^{-4}$	$3.40 \cdot 10^{-4}$	60.5
2 Holes	$1.90 \cdot 10^{-3}$	$3.80 \cdot 10^{-4}$	80.0

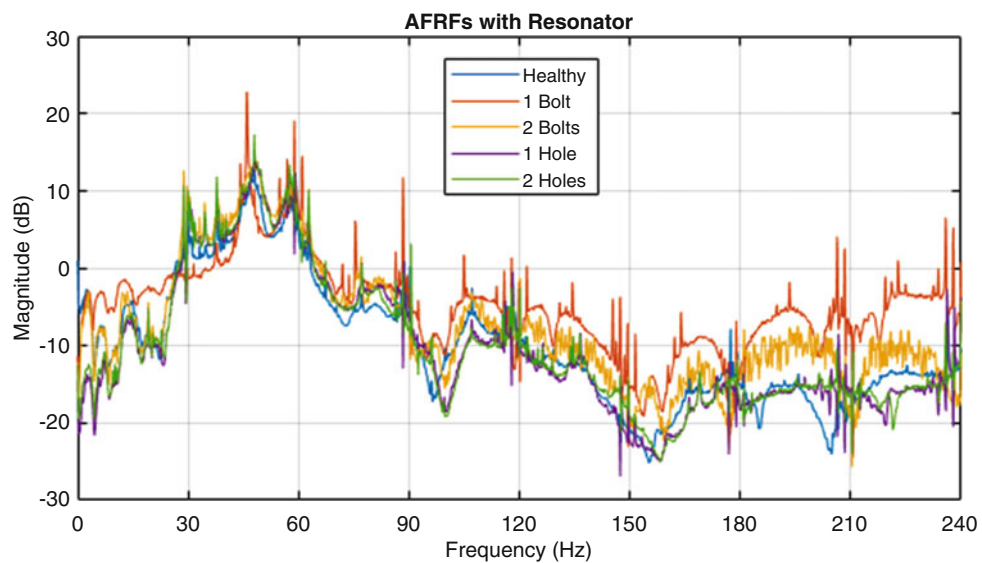


**Fig. 16.7** Asynchronous frequency response functions calculated under different health states

Another method of AFRF validation was a comparison between the functions made with healthy motor data and that of those made with damaged motor data. Figure 16.7 shows this comparison. It is expected that if the environment is being fully captured, the AFRF should not change with the type of data being used to make it. As can be seen in the plot, this is mostly true, however the various AFRFs do not match perfectly, especially beyond 150 Hz. The discrepancies beyond 150 Hz are not much cause for concern as the literature shows that damage is most evident in the fundamental frequency and first four harmonics, so the damage detector used only analyzes up to that point [7]. These variations would either indicate

**Table 16.3** Bhattacharyya distances for unaltered signals

Damage mode	Distance when accounting for the propagation environment	Distance when not accounting for the propagation environment	% Improvement when accounting for the propagation environment
1 Hole	0.566	0.425	33.2%
2 Holes	4.10	3.08	33.1%
1 Bolt	5.81	4.50	29.1%
2 Bolts	2.74	2.38	15.1%

that the environment is changing or that the forcing function of the motor is not being fully captured. Since the propagation environment is highly controlled, the latter is more likely. This begs the question of whether the AFRF should be called a transmissibility function.

### 16.6.2 Damage Detection Results

A receiver operating characteristic (ROC) curve was used to assess the performance of the detector. The ROC curve compares the true positive rate (TPR), i.e. probability of detection ( $P_D$ ) to the false positive rate (FPR), i.e. probability of false alarm ( $P_{FA}$ ) as the threshold  $\gamma$  is increased. After the test statistics were computed, a threshold  $\gamma$  of the computed test statistics was chosen, which was the cutoff value at which the detector decided if the motor was damaged or undamaged. Any test statistic value  $T$  greater than the threshold led to the decision that the motor was damaged; otherwise, the motor was decided to be undamaged. The ROC curves were expected to be close to a random guess when not accounting for the environment in subtle damage case, such as one and two holes damage.

The ROC curves seen in Fig. 16.7 show that the detector was better than a random guess for the one hole damage case when not accounting for the environment, but was significantly improved when accounting for the environment. For the other damage cases beyond the single hole the ROCs showed that the detector was near perfect, regardless of whether or not the environment was accounted for. This would indicate that the selected forms of damage were too significant. To compensate for this oversight, Bhattacharyya distances ( $BD$ ) were calculated (see Fig. 16.7) in addition to the ROCs to show the separation between  $P_{FA}$  and  $P_D$  for each scenario. The Bhattacharyya distance  $BD(p, q)$  between two different distributions,  $p$  and  $q$  is [17]:

$$BD(p, q) = \frac{1}{4} \ln \left( \frac{1}{4} \left( \frac{\sigma_p^2}{\sigma_q^2} + \frac{\sigma_q^2}{\sigma_p^2} + 2 \right) \right) + \frac{1}{4} \left( \frac{(\mu_p - \mu_q)^2}{\sigma_p^2 + \sigma_q^2} \right) \quad (16.10)$$

Using this method, it can be seen that for all damage cases the detector that incorporated knowledge of the propagation environment performs better than the alternative. The calculated BDs are shown in Table 16.3 (Fig. 16.8).

To examine the detector's performance more thoroughly, white Gaussian noise with an RMS value of  $2 \cdot 10^{-6} \text{g}^2/\text{Hz}$  was added to each of the PSDs to compensate for the overly aggressive damage cases. This results in a signal-to-noise ratio (SNR) of 50 dB for the healthy case, as well as all of the damage cases, except the 1 bolt. The SNR for the 1 bolt case was about 104 dB. However, these values do not include an estimate for the unknown noise already on the measured signal. By running these noisy PSDs through the same damage detection algorithm the results in Fig. 16.9 were generated. It becomes more apparent that accounting for the environment increased damage detection performance for all cases as seen in the ROC curves. The Bhattacharyya distances for these noisy cases can be found in Table 16.4. These distances also show that in all cases, knowledge of the environment improves the separation of the test distributions. In the one bolt damage case, the BD nearly doubled from 2.83 to 5.55.

## 16.7 Discussion

The ultimate goal of this research was to see if knowing the vibration propagation environment could improve damage detection rates for rotating machinery. From there the question of how to learn such propagation environments without

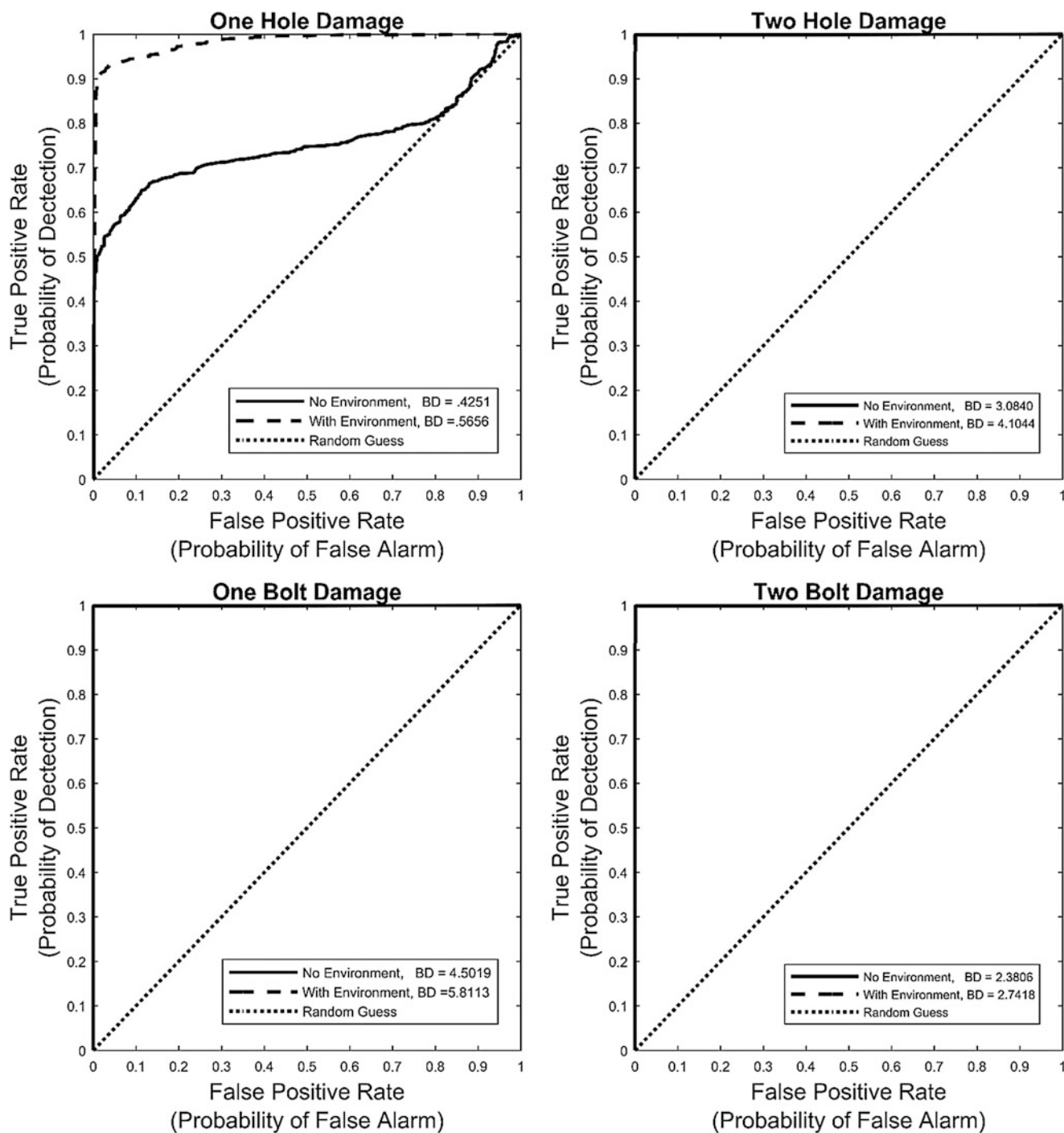


**Fig. 16.8** ROC curves & Bhattacharyya distances for various damage types of damage using unmodified data

being able to directly access the machinery was posed. Thus, the idea of an asynchronous frequency response function was conceived, developed, and tested. On a basic level these goals were achieved, but there remain many questions to answer and any possibilities to explore.

The first finding of this work was that it is possible to create an AFRF regardless of the time span between the two data sets used to calculate it. AFRFs were successfully calculated and validated from data sets that were collected seconds, minutes, and even days apart. Based on an average of 6 AFRFs, the resulting vibration signature predictions had very low RMS error for all 17 test data sets. While the AFRF is closer to a transmissibility function than a true frequency response function, the

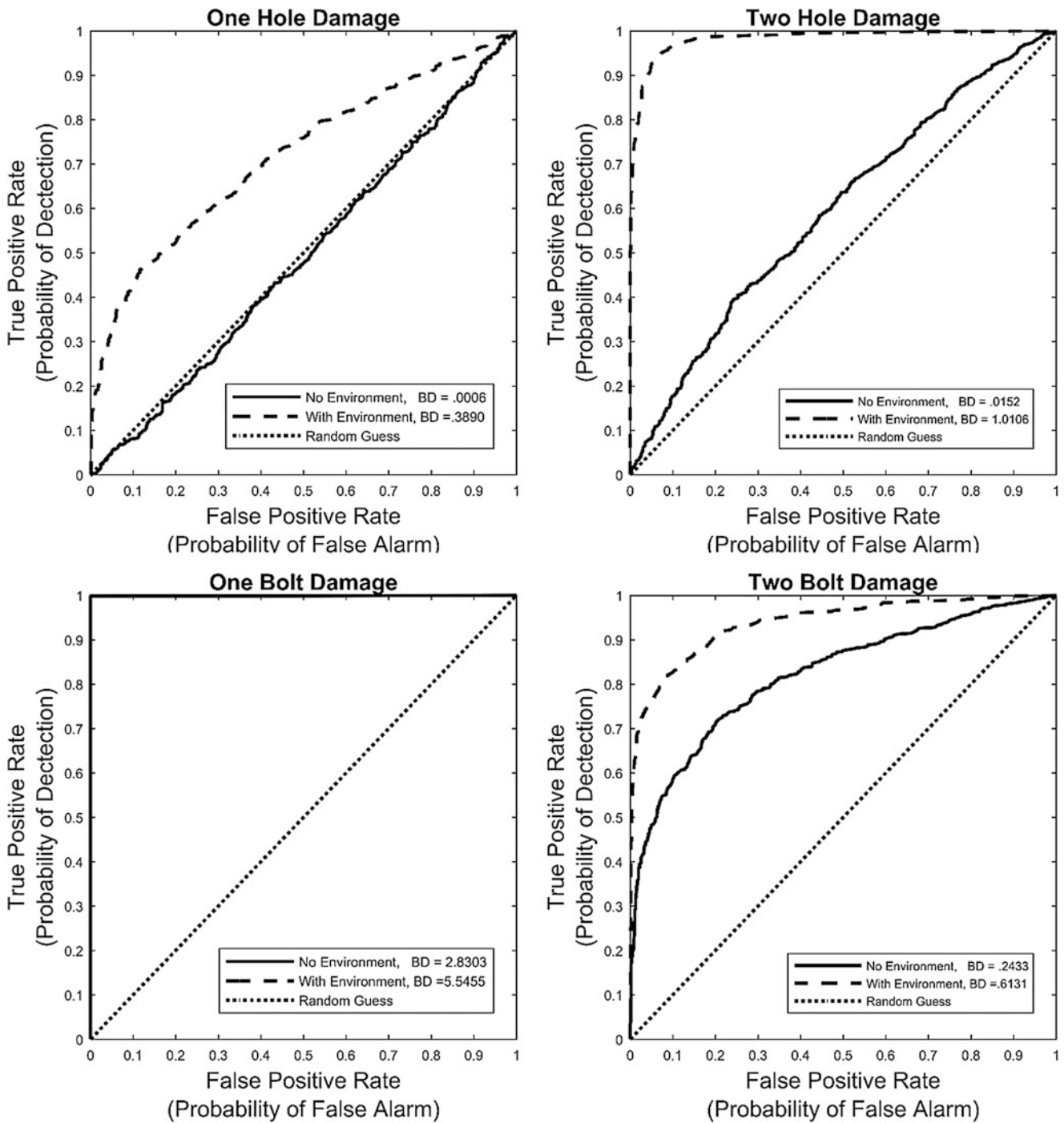


**Fig. 16.9** ROC curves & Bhattacharyya distances for various types of damage using noise-added data

AFRF correctly showed the resonance from the propagation environment at 46 Hz, as would be expected from a traditional frequency response function.

While it was understood that the areas lacking excitation, specifically areas between operating frequency harmonics, would not have high fidelity, not much was done to quantify the uncertainty in these regions beyond looking at the coherence. Another difficulty faced in the AFRF development was inconsistency in operating speeds ( $\approx 0.03$  Hz) between the two motors used in testing. The problem was alleviated by removing phase information from the AFRF and the PSDs used to calculate it because the phase information is irrelevant due to the lack of synchronization. Further problems will arise as discrepancies

**Table 16.4** Bhattacharyya distances for signals with added noise

Damage mode	Distance when accounting for propagation environment	Distance when not accounting for propagation environment
1 Hole	0.389	$6.20 \cdot 10^{-4}$
2 Holes	1.01	0.0152
1 Bolt	5.55	2.83
2 Bolts	0.613	0.243

in motor speeds increase, however this concern was not addressed in the scope of this research. The asynchronous frequency response function holds both many possibilities and difficulties that have yet to be explored.

The results of the experiment clearly show that knowledge of the propagation environment does in fact increase the rate of damage detection. It can even be seen that for this experiment, the damage detector was considered an ideal detector, especially when accounting for the environment. In these cases, the Bhattacharyya distance indicated that propagation environment compensation increased separation between damaged and healthy distributions. These results also indicate that the damage detection problem could be made more complex.

There are multiple solutions to this problem. The first would be to increase the amount of noise present in the environment. In a more realistic setting, it is likely that many different vibrations would be travelling through the propagation environment as well, all of which would be picked up by the remote sensor. This noise would make damage detection much more difficult. Since there was not time to simulate these conditions experimentally, white Gaussian noise was added to the input signals during post-processing. These results (Fig. 16.9) still demonstrated that knowledge of the environment improved damage detection, but it is no substitute for true experimentation.

A second solution to this problem would be to implement damage in more subtle ways. The scope of this research only included load imbalance, however using a machine fault simulator could further display the effectiveness of this method. Induction motors are very intricate electro-mechanical systems and have many common kinds of faults. It is important to be able to detect and identify each of the failure modes early in their progression in order for CBM to be worthwhile. Furthermore, some of these damage modes may be more difficult to detect; detectors that find and identify multiple types of damage are more difficult to develop. A detection problem of this kind would certainly support the concepts of this research if it also yielded positive results. Testing of all of these faults is not only necessary to further validate this remote detection concept, but also for the application of this research. In order for this remote sensing method to work, both the healthy and damaged signatures of a motor must first be characterized to detect damage.

Another solution would be to vary the actual remote distance of the detector in question. Although our current experiments do not explore the upper bound, it is highly conceivable that there would be limits to the distance such that the sensor is so remote, the damage so subtle, or the environment so noisy that the method of detection described would fail. Ultimately, the most rigorous approach to further validate this research would include a parametric study varying damage types, system noise, and remote distance to truly obtain a full understanding of this damage detection method.

## 16.8 Conclusion

It has been shown that in remote vibration-based monitoring of rotating machinery, accounting for the propagation environment increases damage detection performance. This improvement in performance occurred even if, when estimating the frequency response function of the environment, an asynchronously-collected surrogate measurement of the input is used in place of the true input. Future research on more subtle types of damage, such as smaller holes or cracks and small electrical damage should be tested to further evaluate the sensitivity of the presented damage detection method. In addition, more complex environments and greater remote detection distances should also be tested to simulate real industrial environments.

**Acknowledgements** The authors would like to thank the Los Alamos National Laboratory Engineering Institute for funding this research as well as the National Security Education Center for hosting such research activities. Also, the authors would like to express their gratitude to mentors Dr. Eric Flynn and Dr. Adam Wachtor for their guidance and support. The authors also thank Professor Peter Avitabile of UMass Lowell for his suggestions on the design and analysis of the experiment. Lastly, a large thank you is extended to Dr. Charles Farrar and entire staff of the Los Alamos Dynamics Summer School program for both technical and logistical support.



## References

1. Eisenmann Sr., R.C., Eisenmann Jr., R.C.: *Machinery Malfunction Diagnosis and Correction: Vibration Analysis and Troubleshooting for the Process Industries*. Prentice Hall, Upper Saddle River, NJ (1998)
2. Farrar, C.R., Worden, K.: *Structural Health Monitoring: A Machine Learning Perspective*. Wiley, Hoboken (2013)
3. Sohn, H., Farrar, C.R., Hemez, F.M., Shunk, D.D., Stinemates, D.W., Nadler, B.R., Czarnecki, J.J.: *A Review of Structural Health Monitoring Literature: 1996–2001*, Los Alamos National Laboratory Report (2004)
4. Lamim Filho, P.C.M., Brito, J.N., Silva, V.A.D., Pederiva, R.: Detection of electrical faults in induction motors using vibration analysis. *J. Qual. Maint. Eng.* **19**(4), 364–380 (2013)
5. Thomson, W.T., Gilmore, R.J.: Motor current signature analysis to detect faults in induction motor drives—fundamentals, data interpretation, and industrial case histories. In: *Proceedings of the thirty-Second Turbomachinery Symposium*, pp. 145–156 (2003)
6. Thomson, W.T., Orpin, P.: Current and vibration monitoring for fault diagnosis and root cause analysis of induction motor drives. In: *Proceedings of the thirty-First Turbomachinery Symposium*, pp. 61–67 (2002)
7. Finley, W.R., Hodowanec, M.M., and Holter, W.G.: An analytical approach to solving motor vibration problems. In: *Petroleum and chemical industry conference, 1999*. Industry applications society 46th annual, pp. 1467–1480, IEEE (1999)
8. Vishwanath, H., Maruthi, G.S.: Experimental investigation on detection of air gap eccentricity in induction motors by current and vibration signature analysis using non-invasive sensors. *Energy Procedia*. **14**, 1047–1052 (2012)
9. Mitchell, J.S.: *Introduction to Machinery Analysis and Monitoring*. PennWell Pub. Co. Tulsa (1993)
10. Walker, R.: *Localising imbalance faults in rotating machinery* (2013)
11. FRF – Siemens PLM Community.pdf. Siemens (2016)
12. Girod, B., Rudolf, R., Stenger, A.: *Signals and Systems*, 1st edn. Wiley, Chichester (2001)
13. Leuridan, J., De Vis, D., Van Der Auweraer, H., Lembregts, F.: A comparison of some frequency response function measurement techniques. In: *Proceedings of the Fourth International Modal Analysis Conference*, pp. 908–918 (1986)
14. Hall, D.L., Llinas, J.: An introduction to multisensor data fusion. In: *Proceedings of IEEE* **85**(1), 6–23 (1997)
15. Kay, S.M.: *Fundamentals of Statistical Signal Processing. Vol. II, Detection Theory*, Prentice Hall PTR (1993)
16. Woodward, P.: *Probability and Information Theory, with Applications to Radar*. Pergamon Press, London (1953)
17. Coleman, G.B., Andrews, H.C.: Image segmentation by clustering. In: *Proceedings of IEEE* **67**(5), 773–785 (1979)

# Chapter 17

## Experimental Demonstration of a Tunable Acoustoelastic System



Deborah Fowler, Garrett Lopp, Dhiraj Bansal, Ryan Schultz, Matthew Brake, and Micah Shepherd

**Abstract** Acoustoelastic coupling occurs when a hollow structure's in-vacuo mode aligns with an acoustic mode of the internal cavity. The impact of this coupling on the total dynamic response of the structure can be quite severe depending on the similarity of the modal frequencies and shapes. Typically, acoustoelastic coupling is not a design feature, but rather an unfortunate result that must be remedied as modal tests are often used to correlate or validate finite element models of the uncoupled structure. Here, however, a test structure is intentionally designed such that multiple structural and acoustic modes are well-aligned, resulting in a coupled system that allows for an experimental investigation. Coupling in the system is first identified using a measure termed the magnification factor and the structural-acoustic interaction for a target mode is then measured. Modifications to the system demonstrate the dependency of the coupling with respect to changes in the mode shape and frequency proximity. This includes an investigation of several practical techniques used to decouple the system by altering the internal acoustic cavity, as well as the structure itself. Furthermore, acoustic absorption material effectively decoupled the structure while structural modifications, in their current form, proved unsuccessful. The most effective acoustic absorption method consisted of randomly distributing typical household paper towels in the acoustic cavity; a method that introduces negligible mass to the structural system with the additional advantages of being inexpensive and readily available.

**Keywords** Structural-acoustic interaction · Coupled modes · Acoustic absorption · Acoustic modes · Modal testing

### 17.1 Introduction

Acoustoelasticity is the phenomena that describes the coupling between the modal responses of a structure and an enclosed acoustic volume, such as a fluid-filled cavity [1]. Such situations commonly arise in structures within the automotive and aerospace industries [2, 3]. If any modes of the structure and acoustic volume are similar in both shape and frequency, the modal responses can couple and behave similar to a vibration absorber [4]. This coupling leads to an increased number of resonance peaks in the structural response as compared to the structural response when neglecting the effects of the fluid. Furthermore, the structural mode shapes will be the same at these additional coupled peaks [5]. If the existence of this coupling is not known a priori, this can lead to confusion when analyzing the results of a structural modal test used for analytical model correlation. As the analytical models typically neglect the interaction with the surrounding fluid leading to the structure-only (in-vacuo) response, performing a modal test on a coupled structure will lead to discrepancies when compared to the model.

---

D. Fowler  
University of Massachusetts, Lowell, MA, USA

G. Lopp  
University of Central Florida, Orlando, FL, USA

D. Bansal  
University of Colorado Boulder, Boulder, CO, USA

R. Schultz (✉)  
Sandia National Laboratories, Albuquerque, NM, USA  
e-mail: [rschult@sandia.gov](mailto:rschult@sandia.gov)

M. Brake  
William Marsh Rice University, Houston, TX, USA

M. Shepherd  
The Pennsylvania State University, State College, PA, USA

One method of mitigating this issue is by including the fluid loading effects in the analytical model; however, this approach significantly increases model complexity and computational expense. Instead it is desirable if the issue can be mitigated in the experimental realm. In the automotive industry, structural modifications have shown success in reducing the structural-acoustic coupling by altering the structural mode shapes and frequencies and, consequently, reducing noise levels within the passenger compartment [2, 6–8]. Although these methods reduce sound levels, the coupling is not completely eliminated and undesirable peaks in the structural response may still persist. Instead, inclusion of an acoustic absorption material may be required to adequately damp out the acoustic response and fully eliminate this coupling, resulting in a decoupled structural response [2]. This paper seeks to build upon this knowledge by providing a more thorough experimental investigation to determine methods of both quickly identifying when acoustoelastic coupling occurs and measuring the associated structural-acoustic interaction. This paper also examines several methods of modifying either the acoustic volume, or the structure itself, to remove this coupling and achieve the decoupled structural response.

The remainder of the paper is composed as follows: Sect. 17.2 introduces the hollow, cylindrical shell deliberately designed to exhibit coupling that was used in this experimental study. Also provided is a schematic of the accelerometer and microphone locations used to determine the structural and acoustic mode shapes. Section 17.3 shows the results for a typical hammer test and the methods and procedures used to both identify and measure the structural-acoustic interaction. Section 17.4 shows the results of several mitigation strategies employed to decouple the structural response, including acoustic volume modifications and structural modifications.

## 17.2 Hardware and Test Set-up

The process for designing a hollow shell structure which exhibits acoustoelastic coupling began by looking up standard size, off the shelf, aluminum tubing. A relatively thick wall was desired, so shells with walls ranging from 6.35 to 12.7 mm were considered. Next, several finite element models were built with wall thickness and radius per the standard tubing sizes and several lengths were used for each radius and wall thickness combination. Modes were computed using these models and the low-order ovaling mode frequencies recorded in a table. Next, rigid walled acoustic modes were computed analytically for the interior dimensions of each of the shell finite element models; these acoustic mode frequencies were also recorded in a table. With the structure and acoustic mode frequencies for several modes for several geometries, the next step was to find the geometry which provided close matching between at least one pair of structure and acoustic modes (in terms of both shape and frequency). This was represented as a percent different in structure vs. acoustic mode frequency for ovaling modes of the same circumferential and axial orders. It was found that an aluminum shell with 12.7 mm wall thickness, 203 mm outer diameter and 610 mm length provided good matching at the 2,1 and 3,0 modes. The test hardware was then built with these specifications and did in fact exhibit acoustoelastic coupling. The cylinder was then suspended from two bungee cords to approximate a free-free boundary condition. Both end caps were connected to the cylinder using eight bolts torqued. Figure 17.1a shows the test with material properties and dimensions recorded in Table 17.1. Figure 17.1b shows one end cap with a small hole that enabled a rod holding the microphone array to move and rotate within the structure.

Figure 17.2 shows a schematic of the twenty-one uniaxial 10 mV/g accelerometers, at various locations on the cylinder surface, which were used to capture the structural modes of interest. Figure 17.3 shows the axial locations traversed by the array of 10 mV/Pa microphones used to capture the acoustic modes of interest of the internal air cavity, as well as the angular location of each microphone taken from the +X axis. The custom microphone holder held the microphones fixed with a separation angle of 45° between each microphone. Two measurements taken at each of the seven axial locations within the cavity, with the microphone holder and rotated 180° between measurements, captured the full acoustic mode shapes of the cavity with a total of 14 measurements.

## 17.3 Identification and Measurements of Acoustoelastic Coupling

This section introduces methods for both identifying and measuring the acoustoelastic coupling in the system. A modal impact hammer provided the excitation to excite both the structure and consequently, the coupled acoustic response of the internal cavity. The first part of this section covers repeatability tests that provided the uncertainty in the response from day-to-day testing. The second part introduces a method of identifying the frequency ranges where the system seems to exhibit acoustoelastic coupling when both microphone and accelerometer data is available. The third part measures this structural-acoustic interaction and discusses the procedure used to extract the coupled structural-acoustic mode shapes.

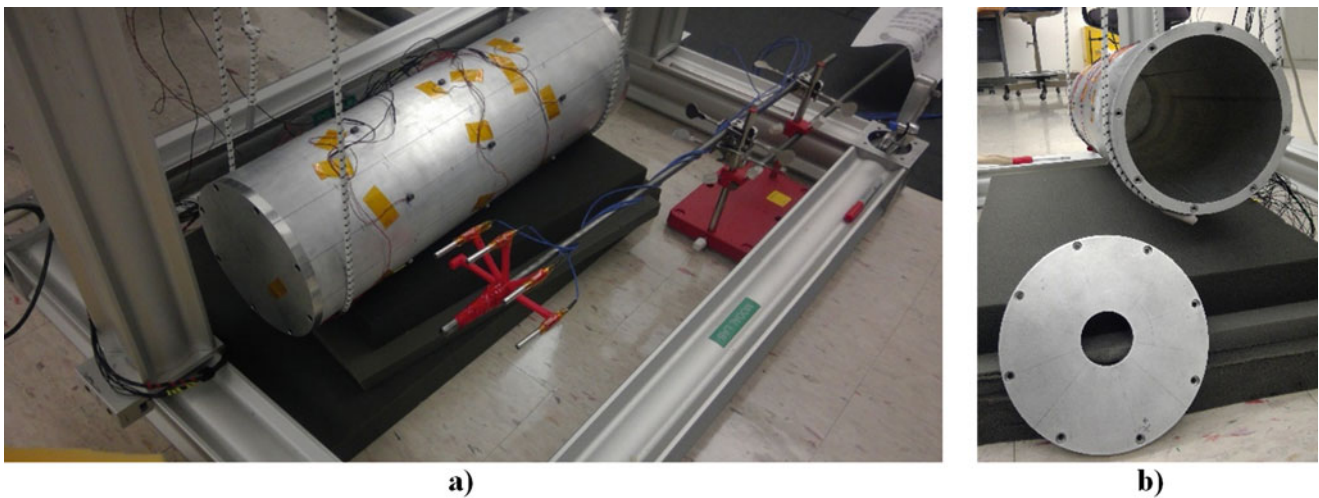


**Fig. 17.1** Experimental test setup. (a) Cylinder suspended from soft bungee cords with the accelerometers bonded on the outer surface, and the microphones distributed in an array. (b) Hollow cylinder cavity with end cap removed

**Table 17.1** Cylinder properties and dimensions

Material	Aluminum
Length	610 mm
Inner diameter	190 mm
Outer diameter	203 mm
Wall thickness	13 mm

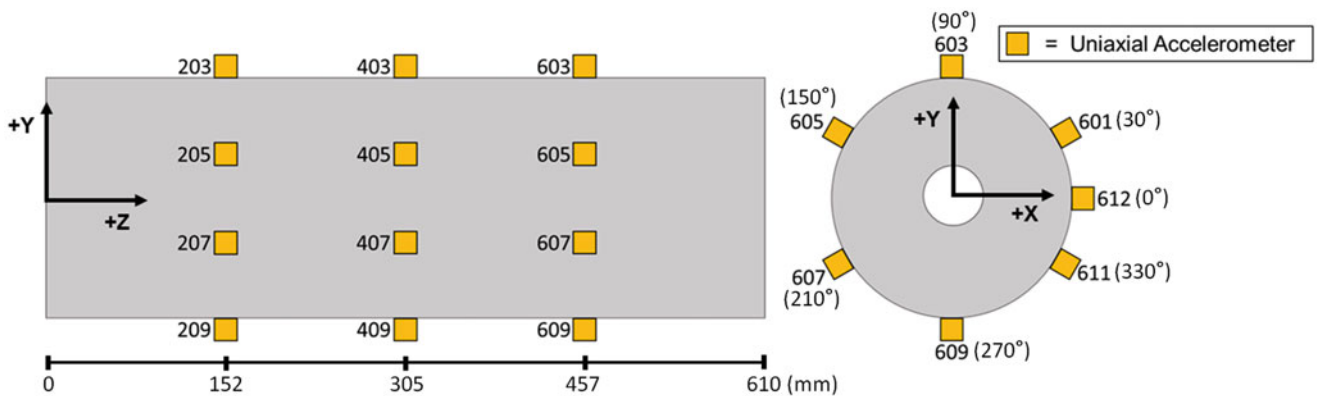


**Fig. 17.2** Accelerometer measurement locations

### 17.3.1 Repeatability Testing

Baseline tests with an empty internal cavity were recorded on different days and times throughout the 6 week testing period. Figure 17.4 shows the drive-point FRFs for location 603 for each of the baseline measurements. The baseline drive-point FRFs changed in magnitude and shifted in frequency across many of the peaks. Identified causes of these variations include slight changes in bungee cord tension and location, cylinder end cap removal and reattachment, and variations in the enclosed air properties such as temperature and pressure. Air properties had a significant effect on frequency shifts because it results in a change in the speed of sound and a corresponding shift in acoustic frequencies, affecting the acoustoelastic coupling interactions. In Fig. 17.4b, c, the close up of key frequency ranges show that the structural peak at 2700 Hz has very minimal frequency shifts between days, whereas the structural peak at 1790 Hz exhibits frequency shifts of the same magnitude of the coupled acoustic peaks. These large day-to-day variations show that it is important to only compare data from the same day to ensure differences observed are a result of test setup alterations and not changes from other factors.

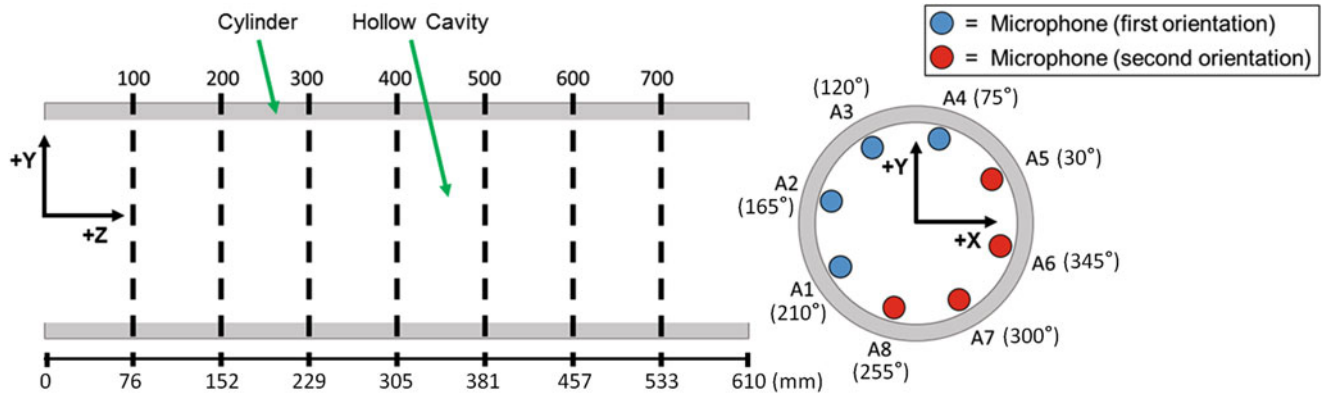


Fig. 17.3 Microphone measurement locations within the cylinder cavity

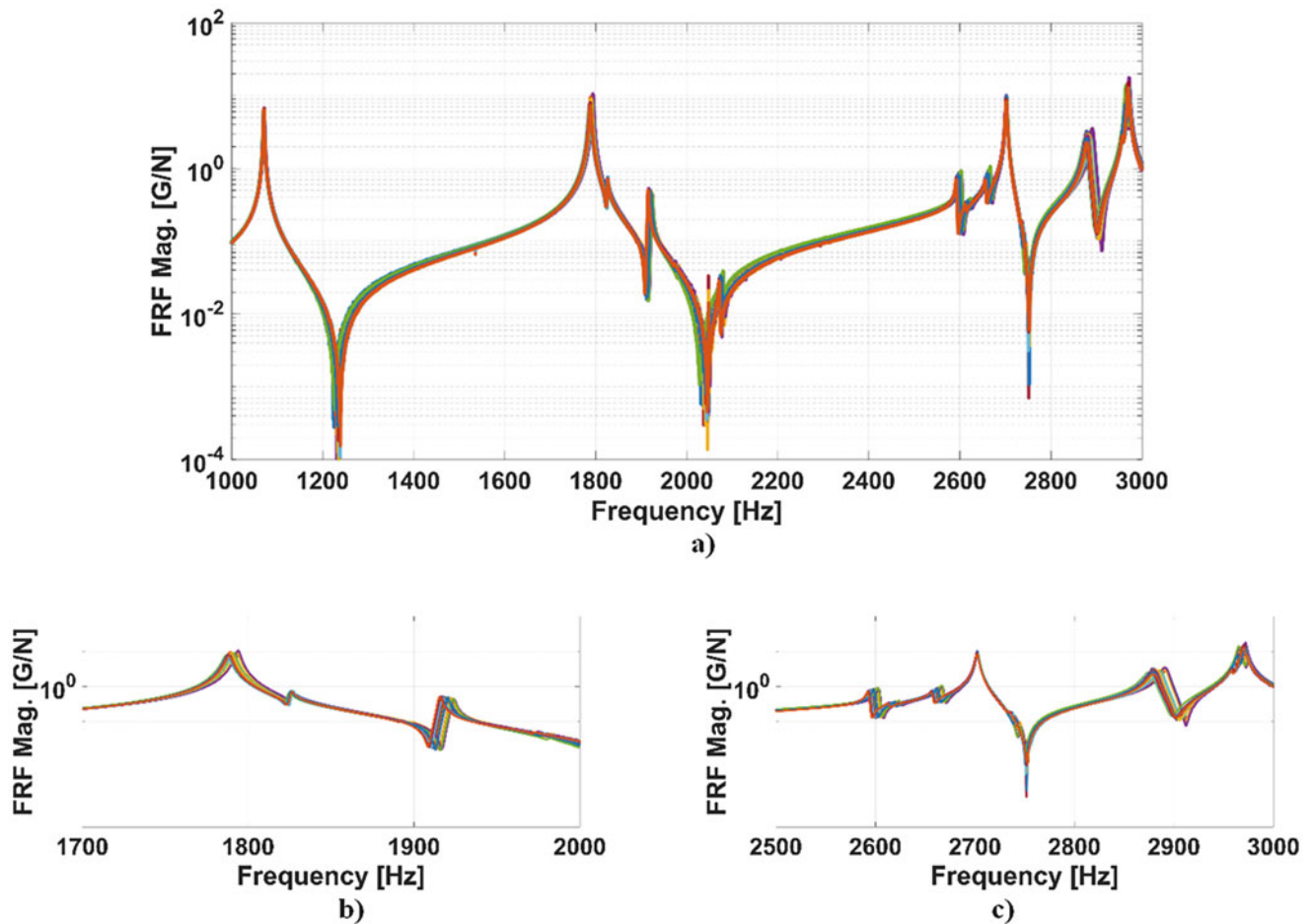
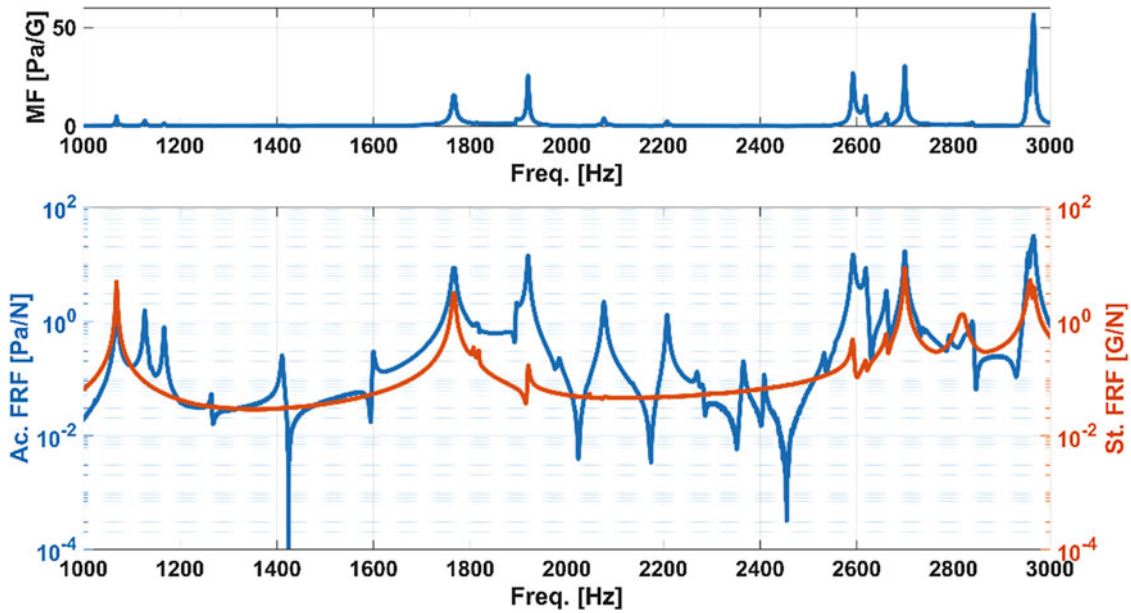


Fig. 17.4 Baseline test comparisons on different days and times. (a) FRF, 1000–3000 Hz. (b) Zoomed in FRF, 1700–2000 Hz. (c) Zoomed in FRF, 2500–3000 Hz

### 17.3.2 Coupling Identification

Coupling is identified through a simultaneous analysis of acoustic measurements and structural measurements. Figure 17.5 shows both the acoustic FRF from microphone A3 located at line 600. Also shown is the average structural FRF from all the accelerometer measurements. The hammer impact excites an increased number of acoustic modes compared to the structure; these additional acoustic peaks indicate that, although coupling does exist, it is not large enough to appreciably



**Fig. 17.5** Top: Magnification factor as a function of frequency. Bottom: Acoustic FRF for a single microphone location (left axis) and structural FRF averaged over all locations (right axis)

effect the structural response. In order to quickly identify when an appreciable amount of coupling exists to affect the structural response, a quantitative measure termed the magnification factor  $MF$  was developed:

$$MF = \left| \frac{H_{Ac}}{H_{St,RMS}} \right| \quad (17.1)$$

where  $H_{Ac}$  is the acoustic FRF at a point inside the cavity and  $H_{St,RMS}$  is the RMS value of the average structural FRF across the entire frequency range of interest. As the structure drives the air inside the cavity, this measure is in terms of pressure / acceleration. Figure 17.5 also shows the  $MF$  at every frequency line and the sharp peaks indicate large coupling. In this frequency range of interest, three frequency bands exhibit large coupling:  $f = 1700\text{--}2000$  Hz,  $f = 2550\text{--}2700$  Hz, and  $f = 2900\text{--}3000$  Hz.

### 17.3.3 Coupled Mode Shapes

This section outlines the procedure used to measure the coupled structural-acoustic modes. The cylindrical test article showed symmetry requiring two hammer impacts at locations 603 and 605 ( $60^\circ$  apart) to separate the repeated roots. An initial test provided the acceleration responses with the microphones removed from the cavity. To obtain the modal parameter estimates (frequencies, damping values, and mode shapes), we utilized the Polymax curve fitting routine built-in with the LMS Test.Lab software. The results presented here focus on the  $f = 1700\text{--}2000$  Hz frequency range where the first set of coupled modes exist, as indicated in Fig. 17.5. Figure 17.6 shows the structural drive-point FRF at location 603 over this range as well as the structural mode shapes shown with the hollow surface elements. The first peak near 1790 Hz is the location of two repeated (2,1) ovaling modes where the anti-node of the first mode was orientated with the +Y-axis of the cylinder and the second mode showed a  $45^\circ$  rotation; the second peak near 1820 Hz is two repeated bending modes but did not exhibit coupling with any acoustic modes; the third peak near 1920 Hz is the location of the coupled (2,1) ovaling modes.

Measuring the coupled acoustic mode shapes was not as straight forward. The microphones are not acoustically transparent so they add a perturbation to the acoustic cavity at each measurement location, and since the microphones were roved throughout the cavity, the boundary conditions are slightly different for each run. Additionally, the cap required an access hole for maneuvering the microphone array. Consequently, there was a slight frequency shift in the modes near 1920 Hz as the microphone array moved along the axial direction of the cavity. Such a shift required modal parameter estimations at each microphone location to obtain the local mode shapes which were then stitched together to produce the

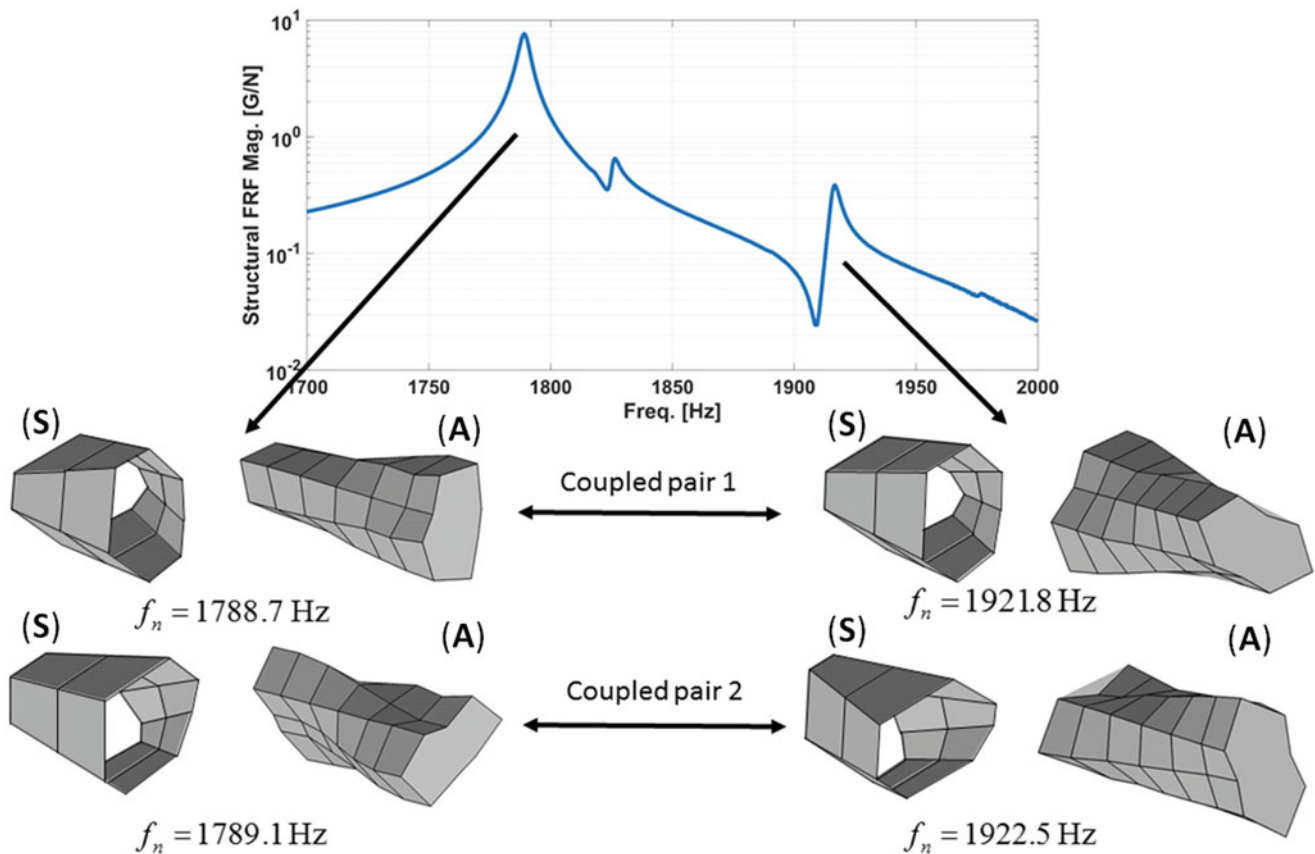


**Fig. 17.6** Structural drive-point FRF with the associated coupled structural-acoustic modes shown. Hollow surfaces represent structural modes (S), and filled volumes represent acoustic modes (A) (positive and negative displacements correspond to positive and negative pressures)

full cavity mode shape. Similar to the structural mode shapes, the acoustic mode shapes also showed repeated roots due to the symmetry of the internal cylindrical cavity. Figure 17.6 also shows the acoustic mode shapes for each mode of interest as filled volumes. Outward deflections indicate high pressure while inward deflections indicate low pressure. Furthermore, the first set of modes near 1790 Hz show that both the structural and acoustic modes oscillate in-phase, while the coupled pair near 1920 Hz show out-of-phase motion. These results are consistent with the findings in a previous numerical study that showed the lower frequency mode of a coupled pair exhibited this in-phase motion while the higher frequency mode exhibiting out-of-phase motion [5]. This result also makes sense when comparing this coupling behavior to a vibration absorber where the two coupled masses show in-phase motion at the lower modal frequency, and out-of-phase motion at the higher modal frequency [4].

## 17.4 Coupling Mitigation Strategies

This section details the strategies employed to mitigate the acoustoelastic coupling and is separated into two approach methodologies: acoustic cavity modifications and structural modifications. Although there are three frequency ranges that exhibit coupling, this analysis focuses on the 1700–2000 Hz frequency range for brevity, although similar results were seen for the coupled modes in the other frequency ranges.

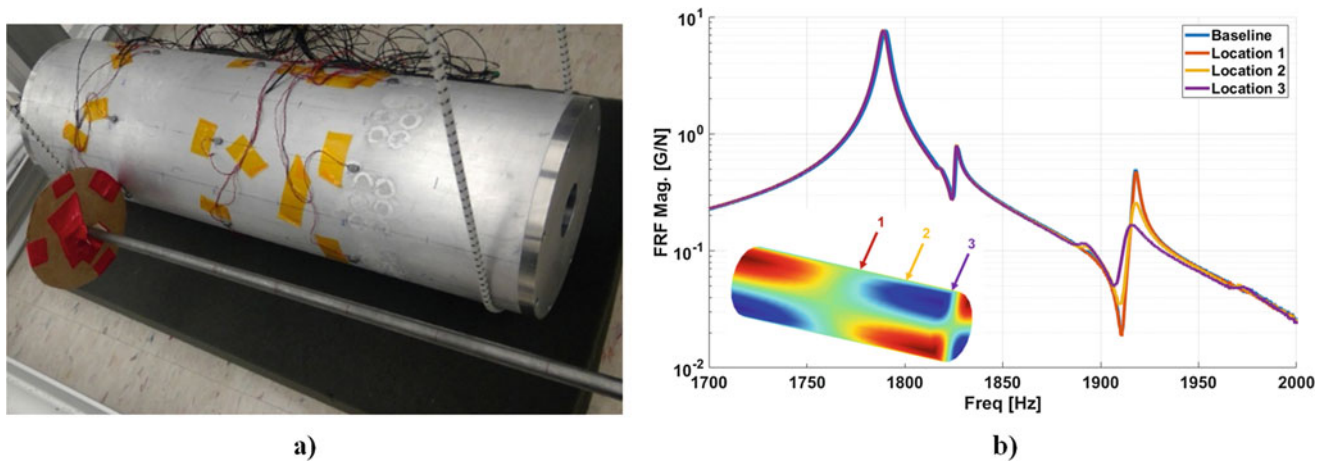


**Fig. 17.7** Inclusion of cardboard partition within cylinder cavity. (a) Cardboard disk partition connected to a rod to vary axial location. (b) FRF variation as a function of partition location

## 17.4.1 Acoustic Modifications

### 17.4.1.1 Partition Inclusion

As an initial attempt to disrupt the acoustic mode shapes and to reduce coupling, Fig. 17.7a shows a cardboard partition inserted into the cavity using a suspended rod to avoid contact with the structure. The partition is included to alter the boundary conditions and corresponding acoustic mode shapes and frequencies. Figure 17.7b shows the three axial locations of the partition as well as the target acoustic (2,1,1) mode, as well as the resulting effects on the structural drive-point FRF. With the partition placed at location 1, the axial node line of the acoustic shape, there was minimal effect on the coupling. As the partition travelled closer to the end of the cylinder where the pressure magnitudes increased, the coupling decreased, though did not completely disappear. This result is surprising as the expectation was that locating the partition closer to the edge would approximate an empty cylinder with no partition. The reason for this discrepancy may be that the partition was not fully rigid, and that there were air gaps around the periphery.

### 17.4.1.2 Foam Inclusion

Rather than disrupting the acoustic mode shapes, foam was inserted into the cavity to provide a source of acoustic damping to remove the acoustic energy from the system in a similar manner to [4]. Two different methods were utilized to insert the foam: Fig. 17.8a shows the first method with foam wrapped around the rod suspended in the cavity such that it was not contacting the structure and Fig. 17.8b shows the effects on the structural FRF. Filling the cavity with only 27% of foam resulted in complete removal of the coupled peak. For the structural peaks affected by the coupling behavior, there was a notable increase in damping as the foam increased in the cavity to a certain point corresponding to 66% of the cavity filled with foam. After which, further increases in foam decreased the damping for the structural peak as well as induced a slight frequency shift. This is a similar phenomenon seen with the vibration absorber model for the coupled system used in [4].

The second method involved incrementally inserting foam cubes, each with dimensions  $50 \times 50 \times 50 \text{ mm}^3$ , into the cavity. Figure 17.9a shows the foam cubes located within the cavity and Fig. 17.9b shows that for the same volume of foam, the foam cubes provided more acoustic damping and offers better reduction in coupling. One reason may be that wrapping the foam around the rod caused some compression in the foam, reducing the acoustic absorption potential. Although using foam cubes does require some contact with the structure, the mass-loading effect of the foam on the structure was negligible. Furthermore, inclusion of the foam eliminated the coupling from the 1.8 kHz and 2.7 kHz structural peaks with approximately 23% and 5% of the cavity filled with foam, respectively. The structural peaks at these frequencies also exhibited small shifts in frequency and decreases in damping after increasing the volume of foam past a certain point.



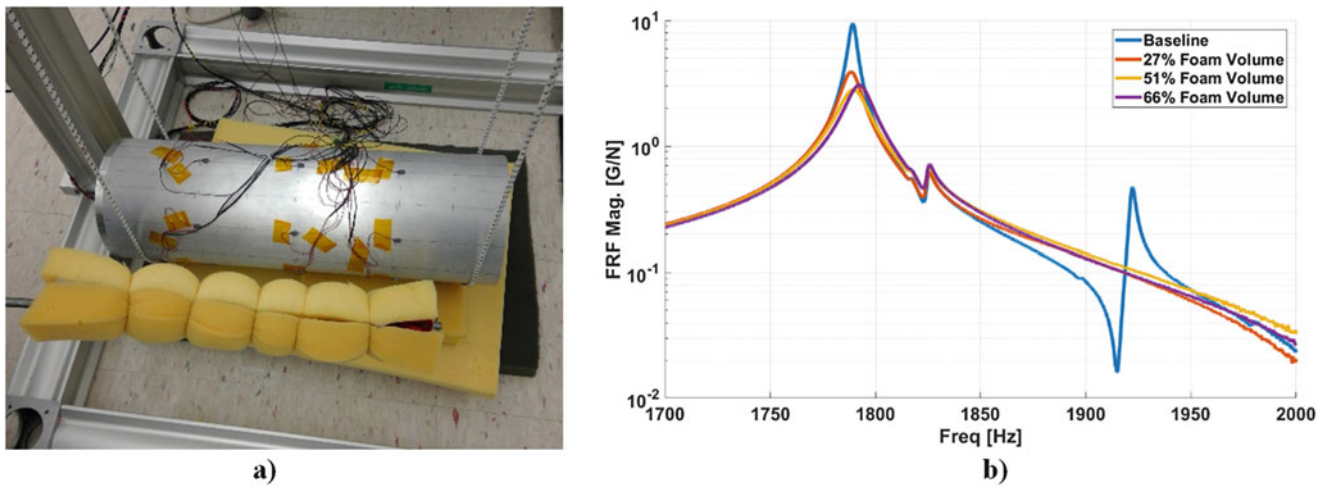


**Fig. 17.8** Inclusion of foam as an acoustic damper inside the cylinder cavity. (a) Foam wrapped around rod to suspend in cavity. (b) FRF variation with increasing foam volume

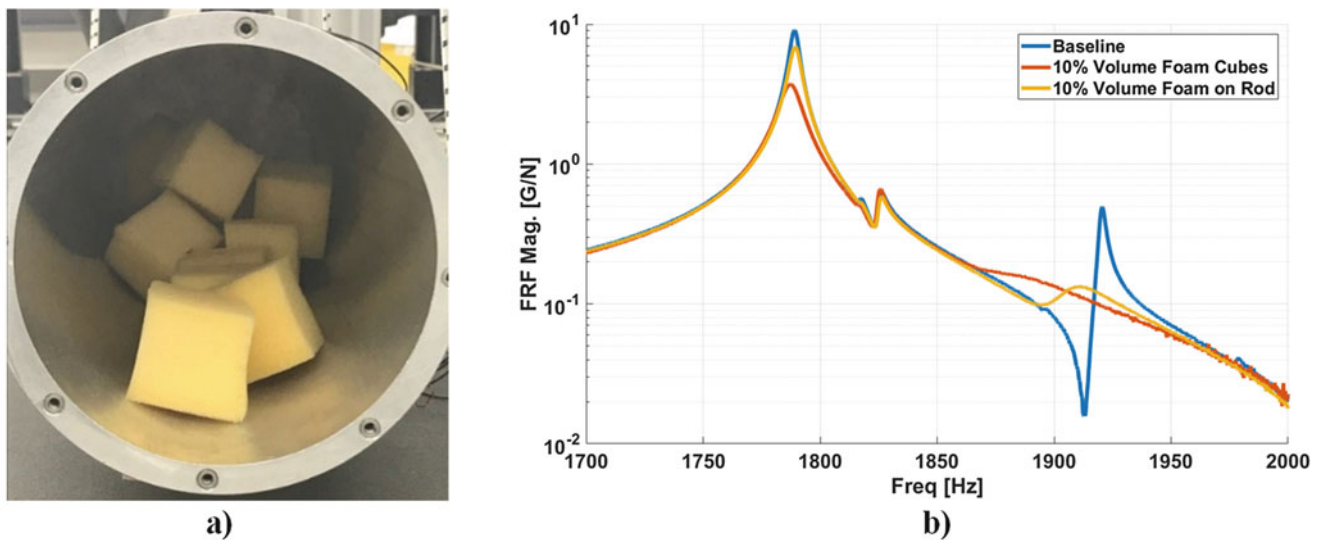


**Fig. 17.9** Comparison between the two foam approaches: foam placed within the cavity as cubes (contacting), and foam wrapped around rod suspended in cavity (non-contacting). (a) Foam cubes placed within cavity. (b) FRF showing the two foam approaches

### 17.4.1.3 Randomly Distributed Paper Towels

Other possibilities of introducing acoustic absorption while adding negligible mass to the system included randomly distributing common household paper towels within the cavity. Figure 17.10a shows the paper towels randomly distributed in the cavity and Fig. 17.10b compares the structural FRF from the best-case foam configuration with the paper towels. Surprisingly, including the paper towels resulted in the most effective removal of coupling, as evidenced by the slightly larger frequency shift and amplitude increase in the structural peak. Paper towels are the most advantageous approach by being more affordable, readily available, and quicker to implement than any of the previous mitigation strategies investigated. However, since the paper towel installation was random, it would not be easily repeatable or standardized.

Figure 17.11 shows the decoupling of the full frequency range tested using the paper towels. The extra peaks associated with the coupled acoustic modes are no longer present in the structural FRF, clearly indicating the effectiveness of this approach. As a second measure of the effectiveness of this approach, the sharp peaks present in the magnification factor corresponding with the coupled modes show a significant reduction.

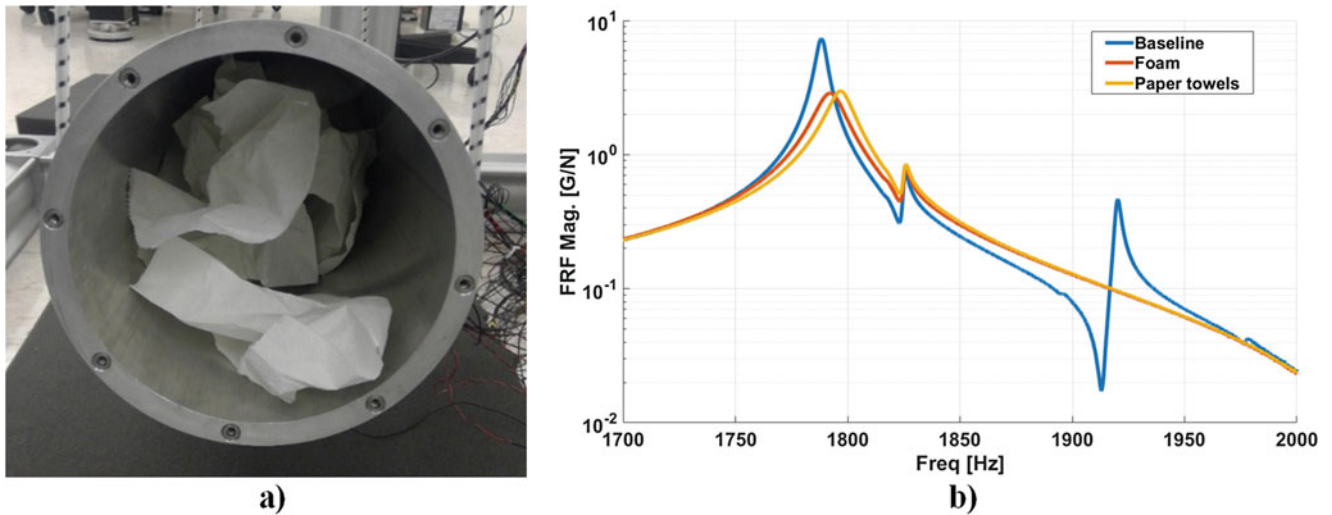


**Fig. 17.10** Randomly distributing house-hold paper towels within the cavity as an acoustic absorber. (a) Paper towels within the cavity. (b) FRF comparison between the best-case foam result and the paper towels

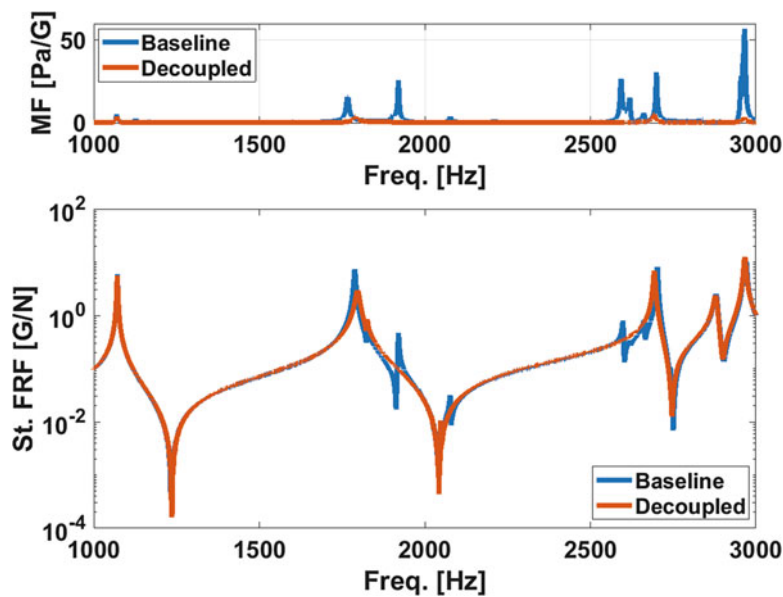


**Fig. 17.11** Comparison of the decoupled and coupled structural FRFs and magnification factor with the decoupled response obtained by including paper towels within the cavity

### 17.4.2 Structural Modifications

In some cases, the internal cavity of the system may not be accessible and the previously described acoustic modifications will not be available. Instead, the test structure was modified to shift the structural frequencies away from the acoustic frequencies and break up the similarity between the coupled mode shapes. Figure 17.12a shows the stainless steel nuts that provided the mass-loading on the structure. Bonding clusters of these masses at the antinodes of (2,1) structural mode with even spacing every  $45^\circ$  around the structure ensured adequate mass-loading for both of the repeated roots. Figure 17.12b shows that the largest applied mass induced over a 150 Hz frequency shift for the structural peak. A much smaller frequency shift occurred for the coupled peak with a corresponding reduction in the peak amplitude; the coupling, however, was not fully removed. Also, the added mass caused a second acoustic mode near  $f = 1895$  Hz to begin coupling with the structure, an unintended and seemingly unpredictable consequence caused by the shifting of the structural frequencies. Although not entirely effective in its current form, this method should be further explored by adding significantly more mass to induce more dramatic structural frequency shifts and mode shape perturbations. Structural dynamic modification techniques could then be used to computationally remove the added mass and calculate the structural response.

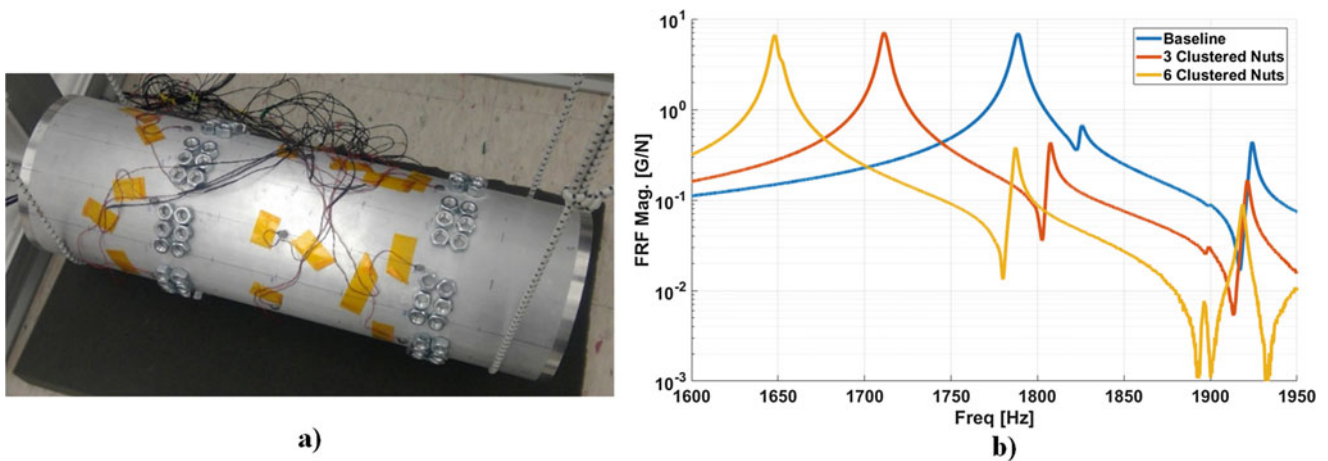


**Fig. 17.12** Mass added at anti-node locations of the target mode to shift structural frequencies. (a) Aluminum nuts clustered around cylinder to add mass. (b) FRF variation due to increasing mass

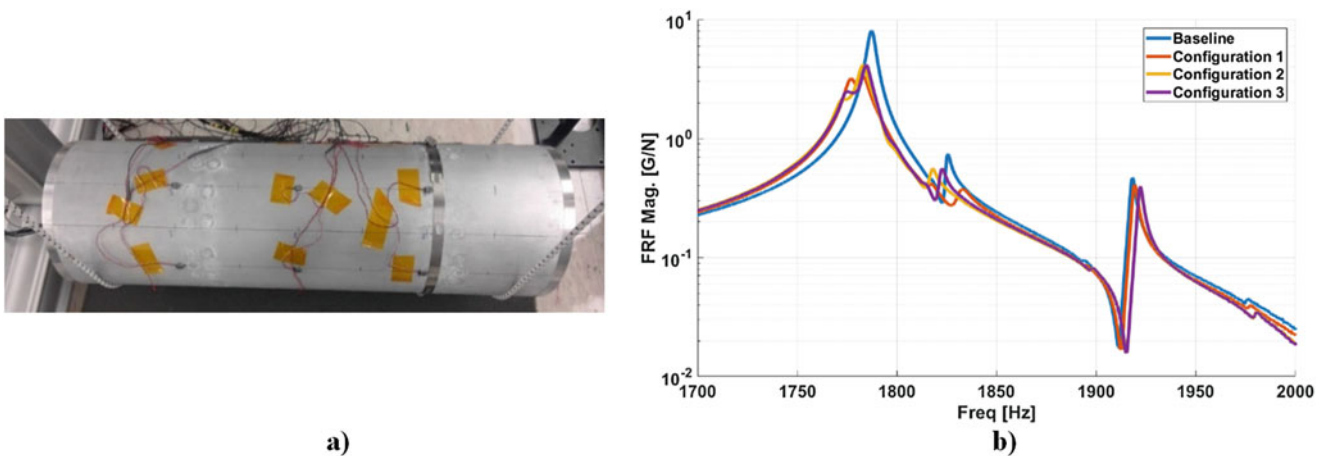


**Fig. 17.13** Hose clamps wrapped around cylinder to increase stiffness by restricting radial motion. (a) Hose clamp wrapped around cylinder. (b) FRF variation for various configurations

A second structural modification involved wrapping hose clamps around the cylinder in an attempt to restrict radial motion and add stiffness to the system. Figure 17.13a shows one configuration of the hose clamped wrapped around the cylinder; Fig. 17.13b shows that this approach was unsuccessful as there was no significant effect on reducing the magnitude of the coupled peak. In fact, the structural peak showed a slight downward shift in frequency indicating that this method provided more mass than stiffness, and induced a splitting of the repeated roots of the structural peak. However, only a small regime of possible stiffness modifications was tested and the effectiveness of other methods was not explored. It is also worth noting that had these approaches been successful at decoupling the structural response, the FRFs would represent the cylinder with the corresponding structural modifications, thus requiring a method to remove the effects of the added modifications. As such, modifying the structure with discrete masses are more preferable to stiffness modifications as their effects are easier to remove.

## 17.5 Conclusions and Future Work

This paper explored the phenomena of acoustoelastic coupling and developed ways of identifying, measuring, and mitigating the coupling effects. Typical structural impact tests on a hollow aluminum cylinder allowed for measurements of the coupled response FRFs. Development of a quantitative measure termed the magnification factor led to quick identification of the modes exhibiting large coupling. Measurement of the structural-acoustic interaction for one of the coupled modes revealed in-phase motion for the lower frequency coupled pair, and out-of-phase motion for the higher frequency.

Several mitigation strategies were also investigated. When the acoustic cavity is accessible, acoustic modifications showed the most promise in removing the coupling behavior. Selectively locating flexible partitions within the acoustic chamber did reduce, but not satisfactorily mitigate, the coupling behavior. However, including acoustic absorption material within the cavity successfully decoupled the structural response and typical house-hold paper towels proved to be the most effective mitigation method. For situations where the cavity may be inaccessible, the structural modifications employed so far have been unsuccessful.

Although some of the mitigation strategies outlined above provided a decoupled structural response, methods for determining whether this is the true in-vacuo response still require investigation. One method may be to include the structural-acoustic interaction in the analytical system model and tune the model parameters to match both the coupled numerical response to the experimental response; using the tuned structural parameters in a typical finite element model could then provide the decoupled response for comparison. A second method could be to isolate the acoustic modes by fixing or heavily damping the structure and then utilize a substructuring approach to remove their effects from the experimental response.

## References

1. Dowell, E.H., Gorman, G.F., Smith, D.A.: Acoustoelasticity: general theory, acoustic natural modes and forced response to sinusoidal excitation, including comparisons with experiment. *J. Sound Vib.* **52**(4), 519–542 (1977)
2. Jha, S.K.: Characteristics and sources of noise and vibration and their control in motor cars. *J. Sound Vib.* **47**(6), 543–558 (1976)
3. Davis, B.R., Joji, S. S., Parks, R. A., Brown, A. M.: Acoustic-structure interaction in rocket engines: validation testing. In: Conference Proceedings of the IMAC-XXVII. Orlando, FL (2009)
4. Schultz, R., Pacini, B.: Mitigation of structural-acoustic mode coupling in a modal test of a hollow structure. In: Conference Proceedings of the Society for Experimental Mechanics Series: Rotating Machinery, Hybrid Test Methods. *Vibro-Acoustics & Laser Vibrometry*, vol. 8, pp. 71–84 (2017)
5. Pacini, B., Tipton, G.: Structural-Acoustic Mode Coupling in a Bolted Aluminum Cylinder. In: Conference Proceedings of the Society for Experimental Mechanics Series: Topics in Modal Analysis & Testing. vol. 10, pp. 393–401 (2016)
6. Richards, T.L.: The reduction of structural acoustic coupling in car bodies, Ph.D. thesis, Cranfield Institute of Technology (1982)
7. Kim, S.H., Lee, J.M.: A practical method for noise reduction in a vehicle passenger compartment. *J. Vib. Acoust.* **120**(1), 199–205 (1993)
8. Kim, S.H., Lee, J.M., Sung, M.H.: Structural-acoustic modal coupling analysis and application to noise reduction in a vehicle passenger compartment. *J. Sound Vib.* **225**(5), 989–999 (1999)

# Chapter 18

## Numerical Modeling of an Enclosed Cylinder



Ryan Schultz and Micah Shepherd

**Abstract** Finite element models are regularly used in many disciplines to predict dynamic behavior of a structure under certain loads and subject to various boundary conditions, in particular when analytical models cannot be used due to geometric complexity. One such example is a structure with an entrained fluid cavity. To assist an experimental study of the acoustoelastic effect, numerical studies of an enclosed cylinder were performed to design the test hardware. With a system that demonstrates acoustoelastic coupling, it was then desired to make changes to decouple the structure from the fluid by making changes to either the fluid or the structure. In this paper, simulation is used to apply various changes and observe the effects on the structural response to choose an effective decoupling approach for the experimental study.

**Keywords** Acoustoelasticity · Structural acoustics · Finite element · Direct simulation · Design

### 18.1 Introduction

Acoustoelastic coupling can result in structural response different from the in-vacuo condition, even if structure is substantial and the internal fluid is air [1, 2]. For the coupling to be significant, the modes of the structure and internal fluid cavity need to be similar in both shape and frequency [3]. To support a recent test project in acoustoelasticity, a representative piece of hardware had to be designed with strong acoustoelastic coupling. Here, finite element (FE) simulation was utilized to design a shell structure with ovaling modes well aligned with internal acoustic modes. Then, simulations of the coupled structural-acoustic system were performed to assess how changes to the acoustic or structural component affect the structural response at frequencies near the coupled modes. Of particular interest was how to change the system to result in response similar to the in-vacuo structural response. Various changes were considered including adding mass to the structure, changing the fluid medium and adding damping to the internal fluid.

### 18.2 Designing an Acoustoelastic System Using Simulation

A research project was planned to study acoustoelastic response and methods to decouple the structural-acoustic system for modal testing [4]. To aid this project, a simulation-based study was conducted to design a simple shell with strong acoustoelastic coupling. Some of design objectives for the test hardware include (1) to have coupled ovaling modes below 4000 Hz to make modal testing easier, (2) to be less than 20 kg to be easy to handle, (3) to be inexpensive to build and easy to modify and (4) to be representative in size and wall thickness to structures of interest.

---

Sandia National Laboratories is a multimission laboratory managed and operated by National Technology and Engineering Solutions of Sandia, LLC., a wholly owned subsidiary of Honeywell International, Inc., for the U.S. Department of Energy's National Nuclear Security Administration under contract DE-NA0003525

R. Schultz (✉)

Structural Dynamics Department, Sandia National Laboratories, Albuquerque, NM, USA  
e-mail: [rschult@sandia.gov](mailto:rschult@sandia.gov)

M. Shepherd

Applied Research Laboratory, The Pennsylvania State University, State College, PA, USA  
e-mail: [mrs30@psu.edu](mailto:mrs30@psu.edu)

**Table 18.1** Shell geometries considered for the design, with shell and acoustic mode frequencies for various ovaling modes. Possible acoustoelastic modes are highlighted

O.D. [in.]	Wall [in.]	Length [in.]	Shell 2,0	Shell 2,1	Shell 3,0	Shell 3,1	Shell 4,0	Shell 4,1	Acs. 2,0	Acs. 2,1	Acs. 3,0	Acs. 3,1	Acs. 4,0	Acs. 4,1
6	0.50	10	2574	5316	5229	6868	9347	-	2622	2708	3611	3673	4574	4623
6	0.25	12	1525	3777	2512	3605	4530	5176	2384	2449	3282	3330	4158	4196
6	0.50	12	2264	4359	5085	6182	-	-	2622	2682	3611	3654	4574	4608
8	0.25	24	650	1586	1304	1620	2432	2596	1748	1771	2407	2424	3049	3062
8	0.50	20	1177	2292	2728	3196	5046	5381	1873	1903	2579	2601	3267	3284
8	0.50	24	1077	1857	2690	2988	-	-	1873	1894	2579	2594	3267	3279
10	0.25	24	618	1704	873	1348	1559	1780	1380	1408	1900	1921	2407	2424
10	0.50	24	824	1815	1730	2140	3191	3454	1457	1484	2006	2026	2541	2556

### 18.2.1 Parameterized Finite Element Shell Models

The geometry of the structure (a cylindrical shell) was chosen to match readily-available aluminum tubing from a metal supply catalog. A total of eight geometries were considered, shown in Table 18.1. To rapidly generate finite element models of the shell, a parameterized meshing script was developed which takes inputs of shell length, wall thickness and radius to build a 3D hex mesh. These models were small, around 150 k degrees of freedom (DOF) so computing modes for several shell geometries was tractable in the FE software Sierra/SD [5].

### 18.2.2 Analytical Acoustic Modes Model

As the interior cavity of the shell is a cylindrical, hard-walled volume, an analytical model was used to estimate the acoustic modes. For each shell geometry described above, acoustic modes were estimated using the expression below for rigid walled cylindrical cavities:

$$f_{l,m,n} = \frac{c_0}{2} \sqrt{\left(\frac{\alpha_{mn}}{\pi a}\right)^2 + \left(\frac{l}{h}\right)^2}, \quad (18.1)$$

where  $c_0$  is the sound speed,  $a$  is the radius,  $h$  is the length,  $\alpha_{mn}$  is the  $n$ -th zero of  $m$ -order Bessel function of the first kind, and  $l, m, n$  are the acoustic mode orders in the length, circumference, and radius, respectively. Only radial mode orders of  $n = 1$  were considered here, so the acoustic mode orders are listed in Table 18.1 as  $(m, l)$ . An acoustic mode with order  $(2,1)$  has two node lines around the circumference and one down the length and is the same shape as a  $(2,1)$  ovaling mode in the shell.

### 18.2.3 Final Design Selection

Table 18.1 shows the various shell geometries considered along with the FE-predicted shell mode frequencies and the analytically-predicted acoustic mode frequencies for compatible modes. Modes with shell and acoustic modes within 5% are highlighted. Of the various geometries, a shell with length 24 inches (61 cm), outer diameter 8 inches (20.3 cm) and 0.5 inch (1.2 cm) wall thickness proved to be the best match of acoustic modes to structural modes. Since both the  $(2,1)$  and  $(3,0)$  mode frequencies were within 5%, this geometry was selected. The actual hardware was designed with removable end caps, one of which has a hole in the end to allow for microphones and acoustic damping material to be added to the cavity. Fig. 18.1 shows the FE mesh and final hardware design.

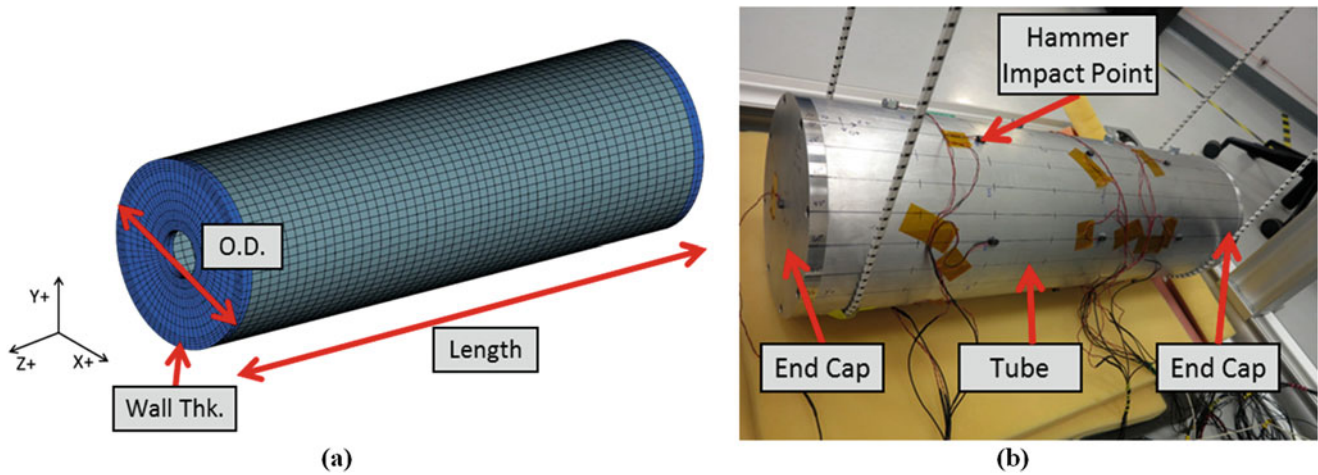


**Fig. 18.1** FE mesh of the shell structure (a) and final shell design in free-free test setup (b)

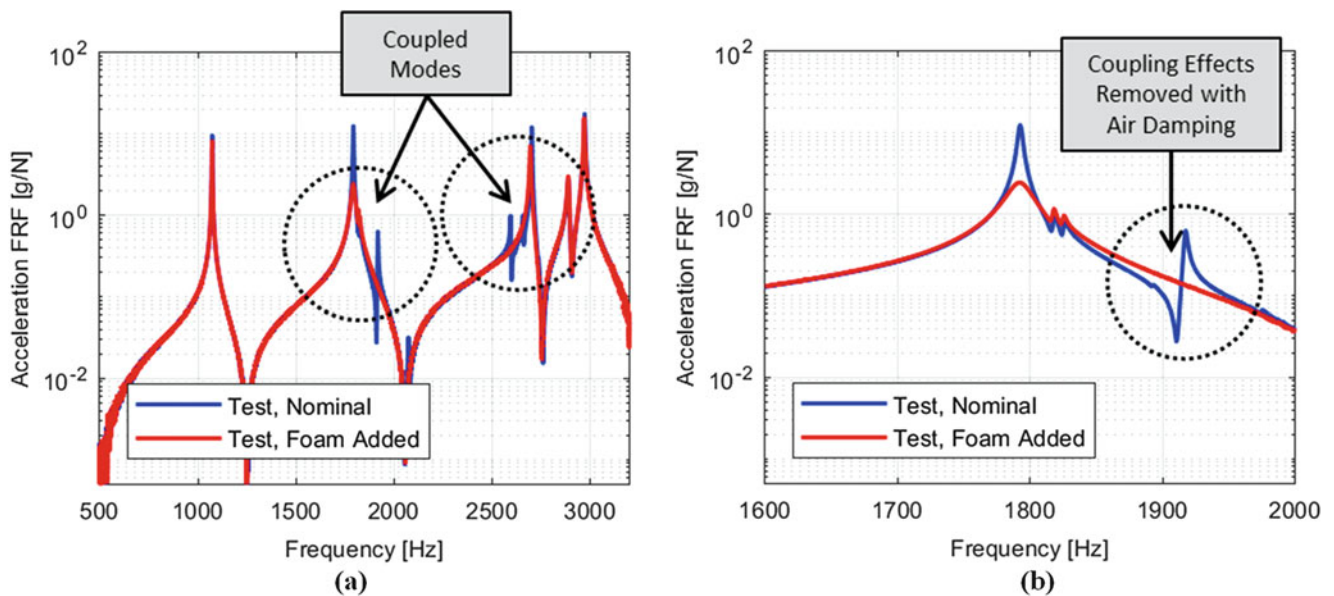


**Fig. 18.2** Experimental FRFs for the designed acoustoelastic system showing the effect on coupling of adding air damping, broadband (a) and zoomed in at the (2,1) mode (b)

#### 18.2.4 Example Test Data

An example modal hammer test frequency response function (FRF) is shown in Fig. 18.2. Here, a modal hammer impacts radially at the location shown in Fig. 18.1 and the response is measured by accelerometers at several locations. Included in this figure are drive point FRFs for two test configurations: the nominal, coupled structure and the structure with foam added to the cavity to damp out the acoustic modes, a technique previously demonstrated on a different coupled structure [2]. The two coupled modes can be seen around 1890 Hz and 2600 Hz, evidenced by an additional peak in the FRF which is removed when the air is damped with foam. A more detailed summary of the experimental examination of this hardware is found in [4]. If the structure and acoustic modes were very close in frequency, a split in the mode near 1800 Hz would be expected. As the coupling instead looks like an additional peak around 1890 Hz with little shift in frequency of the main peak, the hardware does not have perfectly aligned structure and acoustic modes.

### 18.3 Finite Element Simulations to Explore Changes to the Acoustoelastic System

To support the experimental study, a coupled structural-acoustic FE model was developed to explore how changes to the structure or acoustic components would affect the coupled system FRFs. This provides a simulation-based approach to evaluate decoupling techniques which could be used in modal tests of a structure. In this section, direct frequency response simulations near the first coupled mode are used to demonstrate the effect on structural FRFs of changes to air damping, sound speed of the air, and added mass to the shell. These mimic the system perturbations which could be employed in a test of an acoustoelastic system and signify which changes are most impactful to shift or eliminate the acoustoelastic coupling effects.

#### 18.3.1 Coupled Finite Element Fluid Mesh

An acoustic finite element mesh was built contiguous with the shell mesh at the wetted surface. A mesh size of around 1 cm was used in the acoustic mesh to give at least six elements per wavelength up to 4000 Hz. Direct frequency response simulation was used because it is the most accurate method for simulation of structural-acoustic systems with significant acoustic absorption. To mimic the test results shown above, a broadband unit input force was applied at the hammer impact location and the acceleration response output was computed at that drive point.

#### 18.3.2 Coupled Boundary Element Fluid Mesh

A separate approach was also considered to model the interior fluid using a lumped parameter boundary element approach [6]. In this approach, the structural mesh is used as the basis for the boundary mesh and the force to displacement transfer function due to the acoustic pressure field is computed and transformed to modal space. The interior and exterior acoustics can be captured with this approach which can lead to reduced meshing and solution time when compared to the finite element fluid mesh approach. However, losses in the fluid are not captured so that an investigation of the interior cavity damping cannot be completed. Thus, only the coupled FE model was used to simulate changes to the system.

#### 18.3.3 Simulating Changes to the Air Damping

As shown in the experimental results, increasing the damping in the air can change the acoustoelastic coupling effect. This was achieved in the model by changing the proportional damping terms of the air volume from a nominal level of 0.1% to 0.5, 1.0 and 2.0%, over the range 1000–4000 Hz. It is not immediately obvious how to correlate a damping ratio to the amount of foam or absorbing material needed in a test. However, the trends, shown in Fig. 18.3a, can also be observed experimentally [2]. Direct frequency response simulation appears to capture well the effects of adding damping to the air component.

#### 18.3.4 Simulating Changes to the Air Sound Speed

As an alternative method for changing the acoustoelastic coupling, the fluid medium or temperature could be changed such that the sound speed of the air is increased or decreased. To see how a change in sound speed affects the drive point FRF, the air properties were changed from nominal, room temperature sound speed of 343 m/s to cold (0 °C), 331 m/s and hot (40 °C), 355 m/s, temperatures. Figure 18.3b shows that changing sound speed does shift the acoustic mode frequency up and down as expected. Interestingly, for the 355 m/s case the acoustic mode is shifted further away from the structural mode, but the coupling effect remains largely intact. For the 331 m/s case, the modes are moved closer together and the split-peak effect is stronger, causing a shift down in frequency for the structure-dominant first peak.



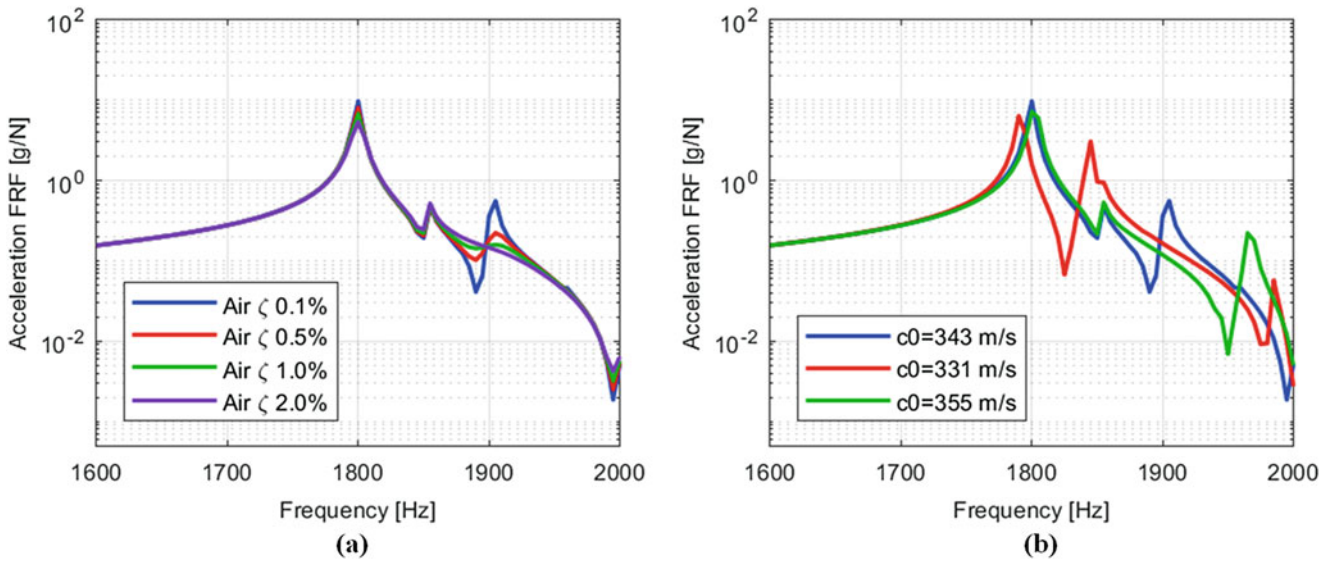


Fig. 18.3 Simulated drive point FRFs demonstrating the effects of adding air damping (a) and changing the air sound speed (b)

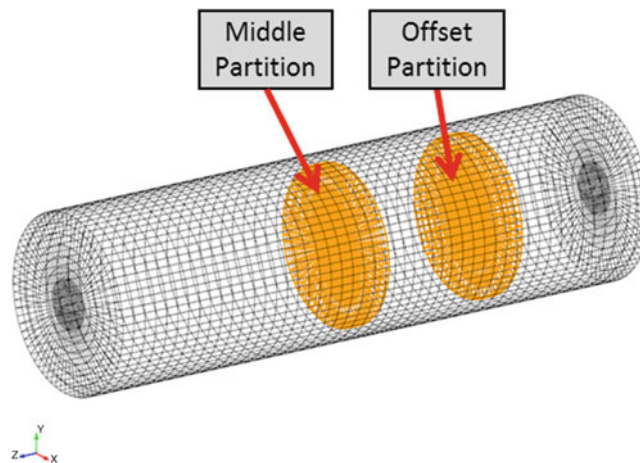


Fig. 18.4 Reflective partition locations in the acoustic mesh

### 18.3.5 Simulating Changes to the Geometry of the Air Cavity: Adding a Partition

The acoustic modes can also be altered by disrupting the air cavity with a non-structural wall or partition. Intuitively, the location of the partition relative to the acoustic mode shape will determine how effective the partition is at changing the acoustoelastic coupling. Two partition locations are considered and shown below in Fig. 18.4. These were employed by removing a disc of elements from the acoustic cavity from the mesh, thereby creating reflective boundary at the partition location. As the (2,1) mode is of interest here, the middle and offset partition locations should affect the acoustic modes and thereby the acoustoelastic coupling, in different ways. Figure 18.5a shows that the partitions do affect the coupled modes and the offset location seems to introduce an additional peak in the response. This is likely due to an additional acoustic mode with shifted frequency due to the different cavity lengths. Additionally, it would be difficult to completely seal off a partition to the shell wall in practice, so a partition with a circumferential gap was also simulated. Figure 18.5b shows that if the partition is not well sealed, the FRF is basically the same as if the partition is not there at all.

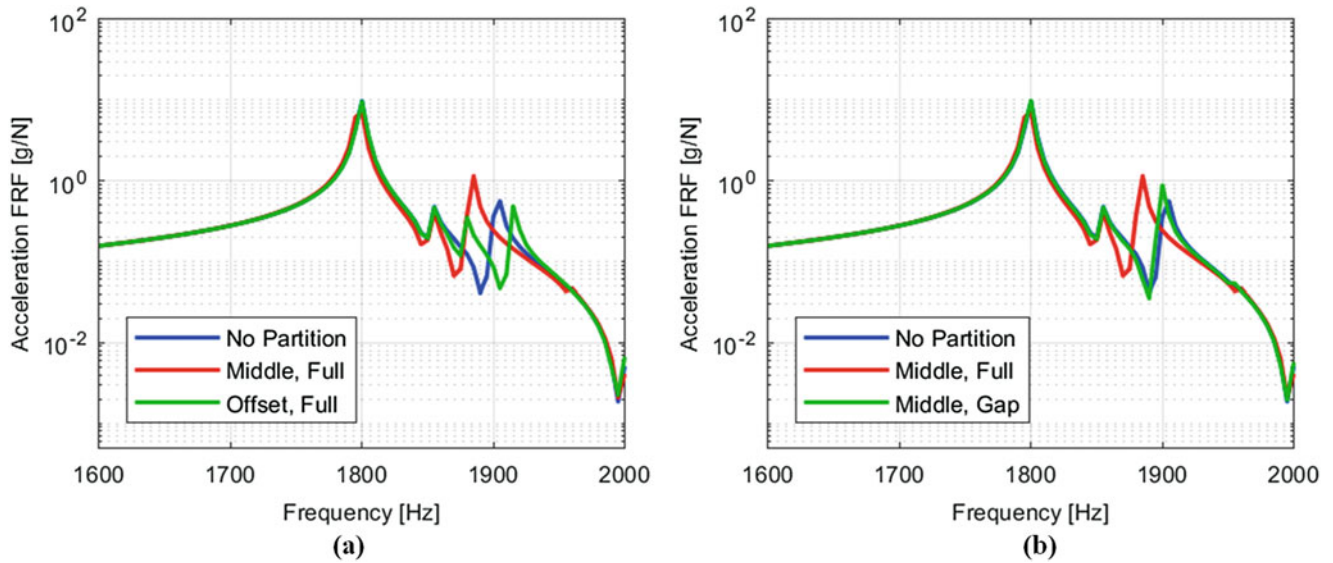


Fig. 18.5 Effects of partition axial location (a) and partition sealing to the shell wall (b)

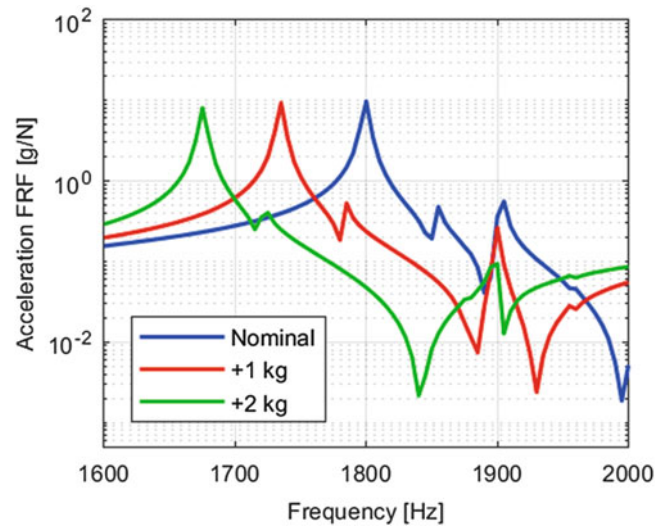


Fig. 18.6 Effects of added structural mass

### 18.3.6 Simulating Changes to the Structural Mass

The shell structure could also be modified to change the frequency proximity to the coupled acoustic mode. Simple changes, such as adding mass to the structure, could possibly be removed using a structural dynamic modification technique to result in the decoupled, un-altered structural response [7]. The effects of adding 1 and 2 kg of mass to the 12.5 kg shell structure is shown in Fig. 18.6. Though the modes are shifted, the coupling remains strong, perhaps indicating that for this coupled pair the shape similarity outweighs the frequency proximity effects [3].

### 18.3.7 Summary of Effects of System Changes

Here, a coupled system model was developed to explore how changes to the structure or acoustic volume would affect the structural response at a coupled mode. At this mode, the acoustic and structural mode shapes and frequencies are similar, causing the air inside the shell to change the response. It is desirable to understand if acoustoelastic coupling is occurring

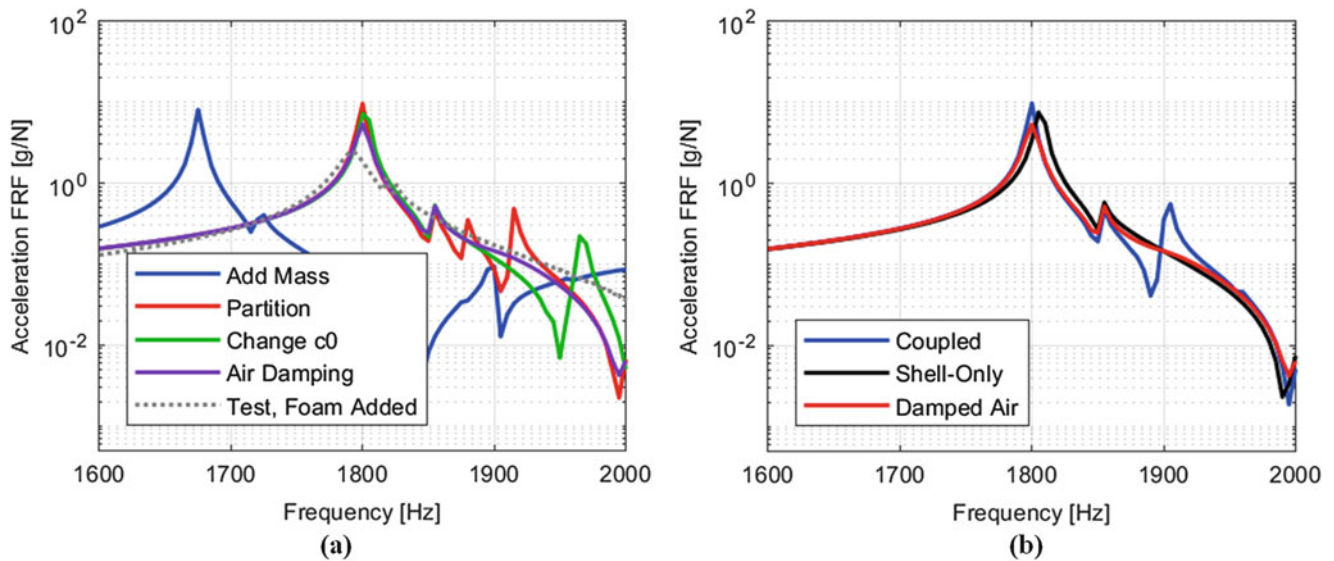


**Fig. 18.7** Comparison of all system change approaches (a) and a comparison of the coupled system, shell-only, and the coupled system with damped air volume (b)

in a test structure and to remove the coupling effects to result in structure-only response measurements. Simulations in this work show that changing the damping in the air volume is most effective at changing the coupling without drastic changes to the structural mode FRF, as seen in Fig. 18.7.

## 18.4 Conclusions

Simulation was used to design hardware to purposefully have coupled structural-acoustic modes. This was achieved by building several shell models using a parameterized meshing script and then comparing frequencies of the shell with acoustic mode frequencies for various ovaling mode orders. A shell geometry with good match to two acoustic modes was found and hardware built to use for experimental exploration of an acoustoelastic system.

Direct frequency response simulation was then used to explore the effects on the shell response of various decoupling methods including changing the air sound speed, adding mass the structure and increasing damping in the air. The simulation results match qualitatively with the experimental results for similar system changes employed in [4]. As such, simulation could be used to help design future tests of hollow structures or to diagnose coupling effects observed in tests.

## References

1. Davis, R.B.: Techniques to assess acoustic-structure interaction in liquid rocket engines. PhD Dissertation, Duke University (2008)
2. Schultz, R., Pacini, B.R.: Mitigation of structural-acoustic mode coupling in a modal test of a hollow structure. In: IMAC-XXXV International Modal Analysis Conference, Garden Grove, CA (2017)
3. Hambric, S.A., Sung, S.H., Nefske, D.J.: Engineering Vibroacoustic Analysis: Methods and Applications. Wiley, Chichester (2016)
4. Fowler, D., Lopp, G., Bansal, D., Schultz, R., Brake, M., Shepherd, M.: Experimental demonstration of a tunable acoustoelastic system. In: International Modal Analysis Conference XXXVI, Orlando, FL (2018)
5. Sierra Structural Dynamics Development Team: Sierra Structural Dynamics – User’s Notes, Sandia National Laboratories SAND Report (2015)
6. Koopmann, G.H., Fahnlne, J.B.: Designing Quiet Structures: A Sound Power Minimization Approach. Academic Press, San Diego (1997)
7. Avitabile, P.: Twenty years of structural dynamic modification – a review, sound and vibration magazine, pp. 14–25, January (2003)



# Chapter 19

## Exploiting Laser Doppler Vibrometry in Large Displacement Tests

E. Copertaro, P. Chiariotti, M. Martarelli, and P. Castellini

**Abstract** Large-displacement vibration testing has assumed increasing importance to answer the need of predicting damages for excessive real life vibration. Moreover, the need for reducing weight is pushing towards the use of non-contact methods in such tests. Discrete Scanning Laser Doppler Vibrometry (SLDV) has resulted to be an important tool for contactless measuring the dynamic behavior of structures. However, the method suffers when high displacements are reached because the laser spot continuously moves on the target surface with an associated uncertainty on the actual measurement point location that increases proportionally to the increase of the deformation of the structure. Such a condition causes the vibration signal to look alike the one recorded by a Continuous Scanning Laser Doppler Vibrometry (CSLDV) approach, with sidebands that are more pronounced the higher the structure deformation is.

This paper describes how SLDV can still be exploited for measuring on structures undergoing large displacements, with the further benefit of extracting information related to additional degrees of freedom deriving from the continuous scanning look-alike behavior of the measurement. This results in a better capability of the technique to extract incipient/potential damages on the structure under test. The concept is explored on simulated data representing a cantilever beam pushed to move at high displacements.

**Keywords** Laser Doppler Vibrometry · Large displacement · Dynamic Mechanical Measurements

### 19.1 Introduction

Laser Doppler Vibrometry (LDV) has established great importance in structural dynamic testing over the years. The main advantages it can carry are related to its optical non-contact nature, which avoids issues related to mass loading effects in lightweight structures, to hot surfaces, etc., and to the decrease in measurement testing time when adopting the scanning technology. Since its introduction in dynamic testing LDV has been exploited several application fields [1], ranging from vibroacoustics [2–5] to non-contact modal analysis chains [6] and even to Non-Destructive Testing [7, 8] or biomedical applications [9, 10].

However, despite very powerful, the LDV technology still suffers when the structure under test undergoes high displacements. This is clear if picturing that the laser spot no more stands still on the same measurement point during the vibration of the target structure, but continuously moves on the target surface with a location uncertainty increasing with the structure local deformation. This continuous movement of the laser spot makes the recorded vibration signal similar to the one that could be measured by the Continuous Scanning LDV (CSDLV) approach, i.e. an amplitude modulation directly related to the deformation characterizing the target structure on the trajectory of the laser spot. Even though this seems to make a LDV measurement invalid, it will be shown hereafter that this is not completely true once this phenomenon is known. Indeed, the knowledge of this CSLDV look-alike behavior makes correction of the measurement possible, with the further advantage of extracting additional information like rotational degrees of freedom and structure curvature from the same measurement. This concepts are illustrated, in the following, on simulated experiments.

---

E. Copertaro

Université du Luxembourg, Faculté des Sciences, de la Technologie et de la Communication, Esch-sur-Alzette, Luxembourg

P. Chiariotti (✉) · P. Castellini

Università Politecnica delle Marche, Ancona, Italy

e-mail: [P.chiariotti@univpm.it](mailto:P.chiariotti@univpm.it)

M. Martarelli

Università degli Studi e-Campus, Novedrate, Italy

## 19.2 Numerical Model

A numerical model of a cantilever beam has been developed with MATLAB, based on a 1D discretization. Geometrical parameters and material properties are the following: length 100 mm; width 10 mm; thickness 0.5 mm; mass density 7860 kg/m<sup>3</sup>; Young modulus 200 GPa.

Firstly, the model has been exploited for calculating natural bending modes. Subsequently, the first two modes ( $m_1$  and  $m_2$ , at the frequencies of  $f_1 = 40.7$  Hz and  $f_2 = 255.3$  Hz, respectively) have been combined into a Frequency Response Function (FRF), calculated for each element of the mesh. Participation factor of  $m_1$  has been set to one order of magnitude greater respect to the other, for reproducing a condition of large displacement at low frequency. Modal damping (loss factors set to  $3e-4$  and  $2e-4$  for  $m_1$  and  $m_2$ , respectively) has been introduced for avoiding singularities at the resonances. Nyquist frequency and frequency resolution have been set to 5000 Hz and 0.1 Hz, respectively.

The time-oscillation  $u_{y,i}(t)$  (being  $y$  the direction orthogonal to the axis of the beam) of each  $i$ -th element of the mesh has been obtained by calculating the inverse Fourier Transform (iFT) of the corresponding FRF.

The axial displacement  $u_x$  (being  $x$  the direction parallel to the axis of the beam) becomes relevant in a condition of large deflection and should be accounted for. The cinematic model from [12], which provides the expression for  $u_x$  reported in Eq. 19.1. Some manipulation leads to Eq. 19.2, where  $c_1$  and  $c_2$  are two constants.

$$u_{x,i} = u_{x,i-1} + \text{sqrt} \left[ dx^2 - (u_{y,i} - u_{y,i-1})^2 \right] \quad (19.1)$$

$$u_{x,i}(t) = c_1 \cdot \text{sqrt} \left[ 1 - c_2 \cdot u_{y,i}^2(t) \right] \quad (19.2)$$

$$v_x(t) = \frac{u_{x,s}(t) - u_{x,s}(t-1)}{dt} \quad (19.3)$$

$$v_y(t) = \frac{u_{y,s}(t) - u_{y,s}(t-1)}{dt} \quad (19.4)$$

$$\theta_R = \frac{2}{l} I_{f_{2+\Omega}} = -\frac{2}{l} I_{f_{2-\Omega}} \quad (19.5)$$

$$\theta_I = \frac{2}{l} R_{f_{2-\Omega}} = -\frac{2}{l} R_{f_{2+\Omega}} \quad (19.6)$$

Once  $u_x$  and  $u_y$  were determined, the instantaneous measurement spot  $s$  has been identified as the mesh element being closer to the laser at a certain time. The movement of the spot (i.e. the scanning area) has been obtained by iterating the tracking at each time step, as shown in Fig. 19.1. Finally, the instantaneous velocities at the measurement spot  $v_x(t)$  and  $v_y(t)$  have been calculated according to Eq. 19.3 and Eq. 19.4, respectively. The measured velocity  $v$  is the combination of  $v_x$  and  $v_y$  according to the angle of the laser.

## 19.3 Results

Subplot 2 of Fig. 19.2 shows the scanning area for different measurement points, which depends on both the angle of the laser respect to the vertical direction as shown in subplot 1 and the amplitude of the oscillation at the different points. Therefore, the scanning area goes to zero at mid length (points 18 and 19) because of the alignment of the laser with the  $y$ -oscillation, and close to the constraint (point 26) where oscillation is null. Consequently, the scanning effect is relevant only in the free-end side of the beam and the analysis of results has been limited to that part of the structure. Here the spacing of the measurement points has been reduced to 2.5 mm for a better spatial resolution.

Subplot 3 of Fig. 19.2 shows the FT of the displacement of the laser spot at the measurement point 2. Peaks at  $f_1$  and  $f_2$  ( $m_1$ - $y$  and  $m_2$ - $y$  in figure) are due to the  $y$ -displacement of  $m_1$  and  $m_2$ , respectively. Peak at 81.4 Hz ( $m_1$ - $x$  in figure) is due to the  $x$ -displacement of  $m_1$ . Indeed, consisting  $u_y$  of two contributions at  $f_1$  and  $f_2$ , it can be demonstrated from Eq. 19.2 that  $u_x$

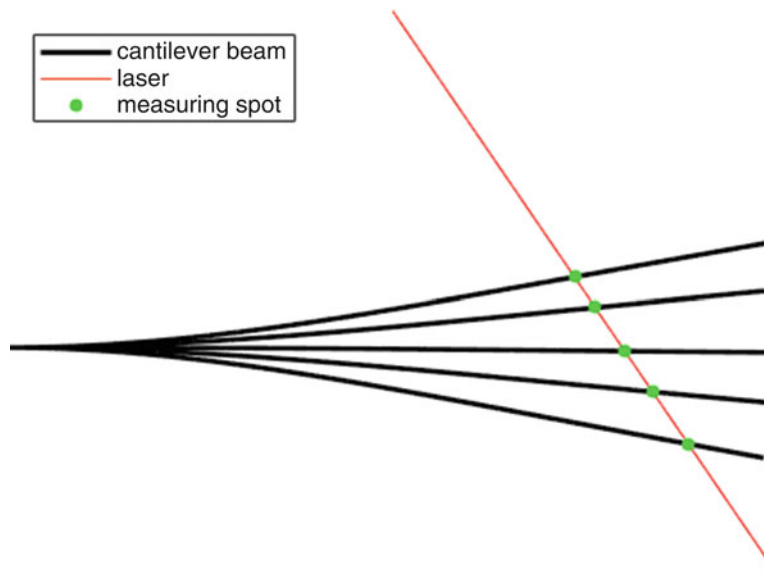


**Fig. 19.1** Cantilever beam under oscillation, laser and measuring spot

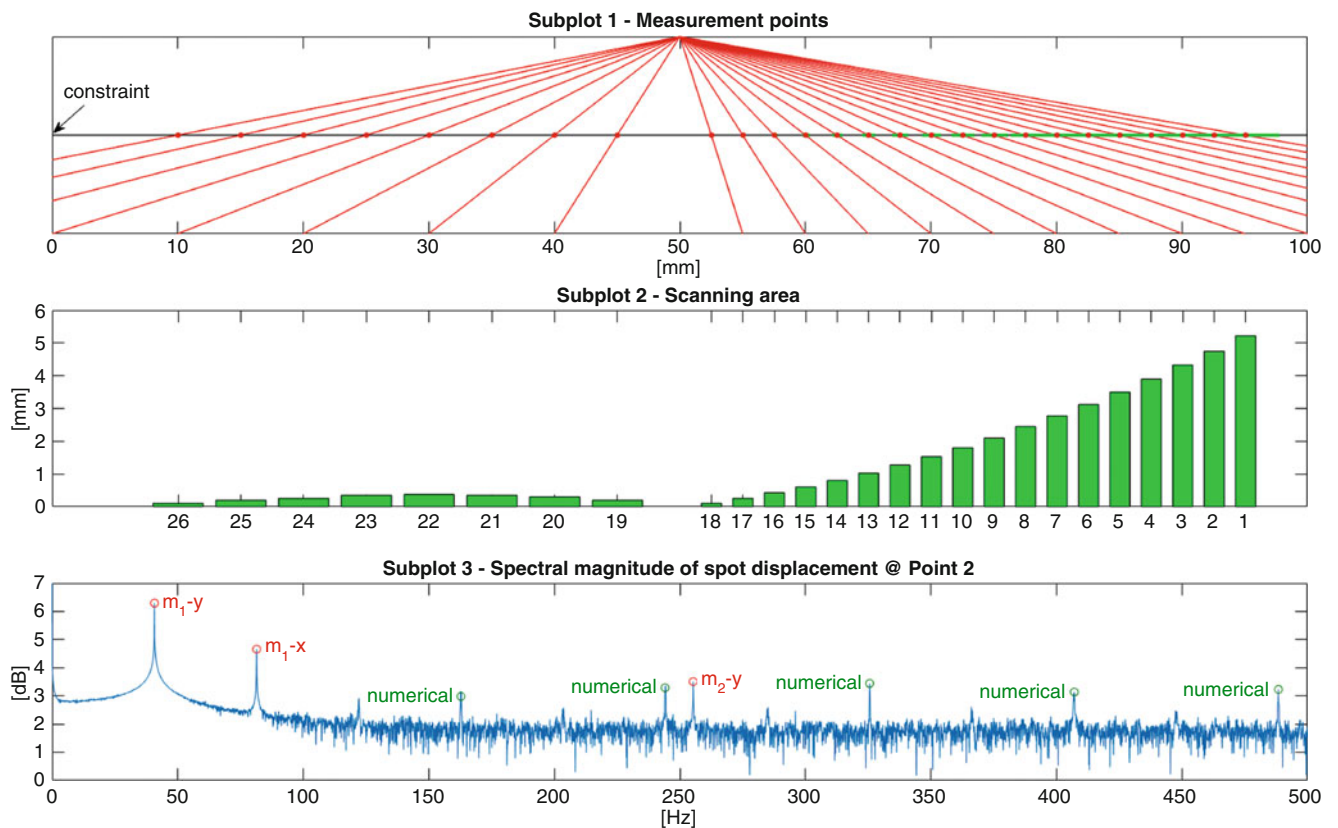


**Fig. 19.2** Measurement points, scanning area and FT of the displacement of the laser spot

has spectral contents at  $2f_1$  and  $2f_2$  plus a beat of  $f_1$  and  $f_2$ . Other peaks shown in subplot 3 are believed to be numerical errors introduced by the finite size of the mesh. However, they do not significantly affect the results as it has been demonstrated with a mesh sensitivity analysis that will be presented in the next. According to the previous considerations, a large oscillation can be effectively exploited in LDV as a kind of method for producing local, linear and harmonic scanings. Indeed, subplot 3

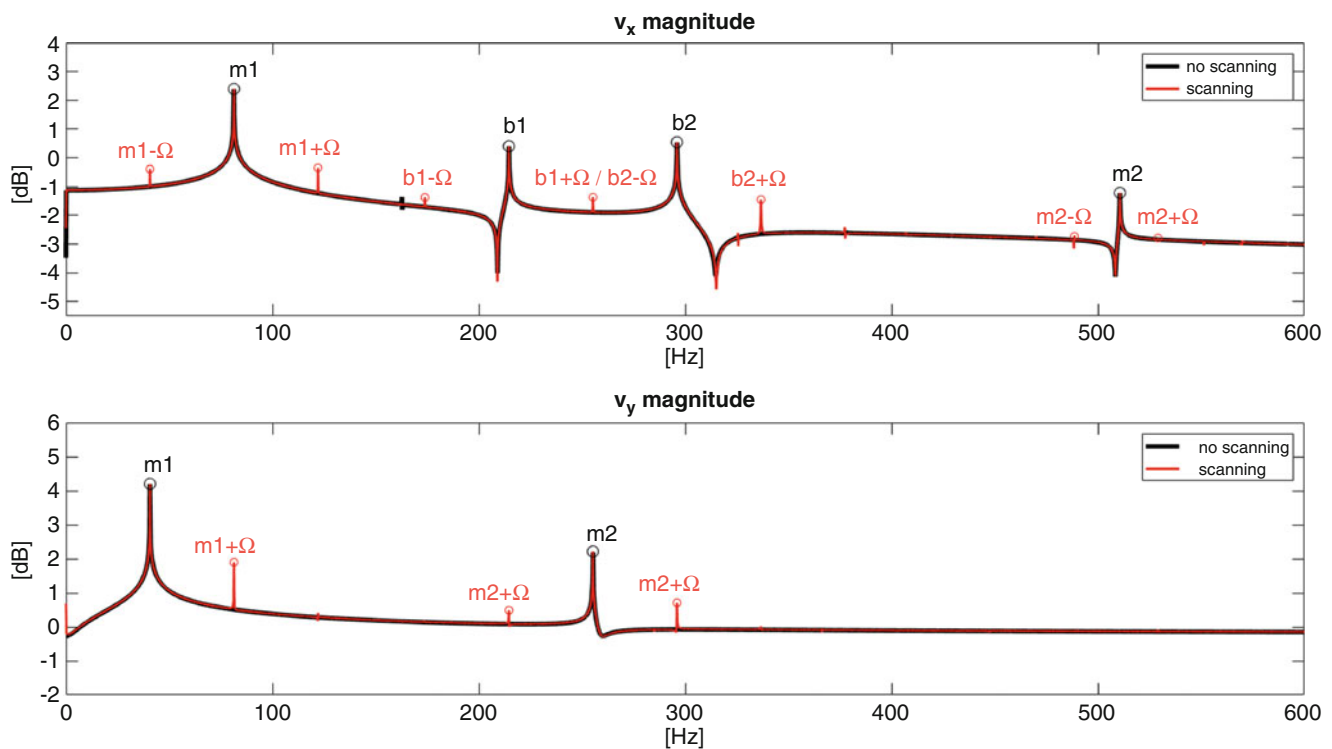


**Fig. 19.3** Velocity signal with and without scanning

demonstrates how the displacement of the laser spot is equivalent to the over-imposition of several harmonic scanings with the one at 40.7 Hz being prevalent respect to the others of about two orders of magnitude.

According to CSLDV theory [11] we shall look at a modulation of the velocity signal. Numerical results are consistent with that, as it can be seen in Fig. 19.3. Here the velocity signal at point 2 obtained including the scanning effect is superimposed to the correspondent signal without scanning, i.e. with the measurement spot fixed at the midpoint of the scanning area. The no-scanning signal provides the effective velocity contributions of the structure, with  $v_y$  having two peaks ( $m_1$  and  $m_2$  in the second subplot) at the modal frequencies and  $v_x$  at the correspondent doubles ( $m_1$  and  $m_2$  in the first subplot) plus one beat of  $f_1$  and  $f_2$  ( $b_1$  and  $b_2$  in the first subplot). In general, levels of  $v_x$  are sensibly lower than  $v_y$ , as expected. The only peak with comparable amplitude and that produces an appreciable scanning effect (as seen in subplot 3 of Fig. 19.2) is the one at 81.4 Hz, due to the large displacement of  $m_1$ . The scanning signal shows sidebands for each peak, spaced of 40.7 Hz ( $\Omega$  in figure).

A sensitivity analysis has been performed on the mesh in order to assess the numerical error due to its finite size. To the scope, the RMS values of  $v_y$  at peaks  $m_1$ ,  $m_2$ ,  $m_2 - \Omega$  and  $m_2 + \Omega$  have been compared for a number of mesh elements progressively increased. Results are reported in Fig. 19.4 for different measurement points (1, 6, 12 and 18). In particular, Fig. 19.4 shows the ratio between the RMS value obtained with a certain mesh size and that obtained with the finer mesh, and its progressive stabilization as the mesh becomes finer. As it can be seen,  $m_1$  and  $m_2$  show good stabilization already with the rawer mesh, because these peaks are not affected by the scanning. On the other hand, sidebands require a finer mesh since the element size affects the accuracy at which the movement of the laser spot is resolved. All the results presented in this paper have been obtained with the finer mesh of 4000 elements.

The information from peak  $m_2$  of  $v_y$  and its sidebands can be exploited for obtaining the rotational degree of freedom according to the method illustrated in [11] and reported in Eqs. 19.5 and 19.6, where  $I$  and  $R$  respectively denote the imaginary and real part of  $v_y$  at the subscript frequency and  $l$  is the length of the scanning area.

Applying the processing to the numerical data provides the results shown in subplot 3 of Fig. 19.5, calculated using both sidebands. These results have been compared with those obtained by using multi-point information as shown in subplot 1 and 2: in particular, the deflection shape has been calculated from the magnitude and phase of the central peak  $m_2$  at each measurement point, then bending has been obtained by differentiation. The comparison between the two sets of data indicates that bending can be assessed properly by using the left sideband. On the other hand, the right sideband does not provide adequate information. This is expected to happen because at that particular frequency ( $255.3 + 40.7$  Hz) the modulation of  $m_2$  by the displacement of  $m_1$  is super-imposed by the modulation of  $m_1$  by the displacement of  $m_2$ .

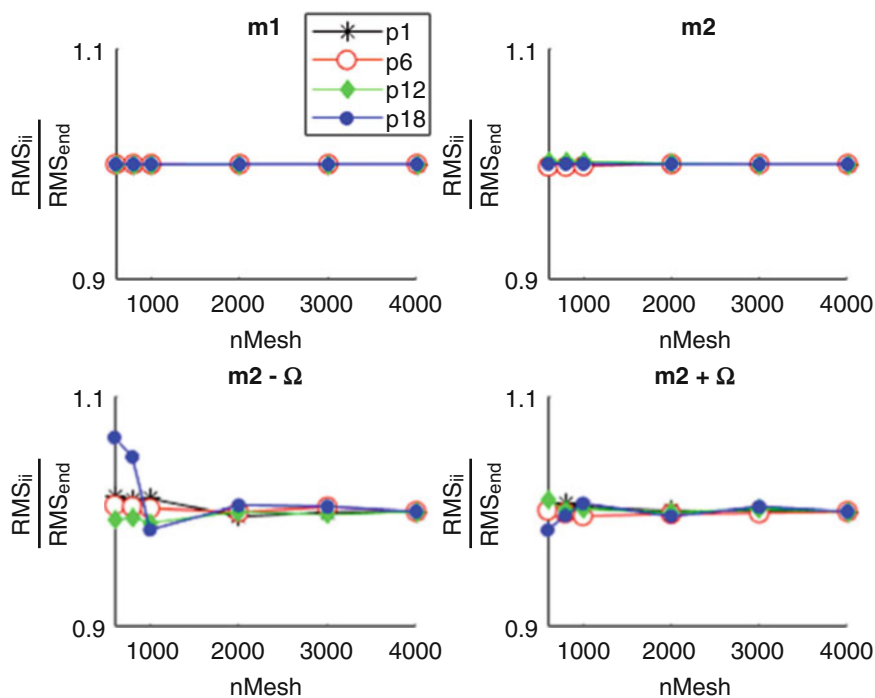


Fig. 19.4 Mesh sensitivity analysis

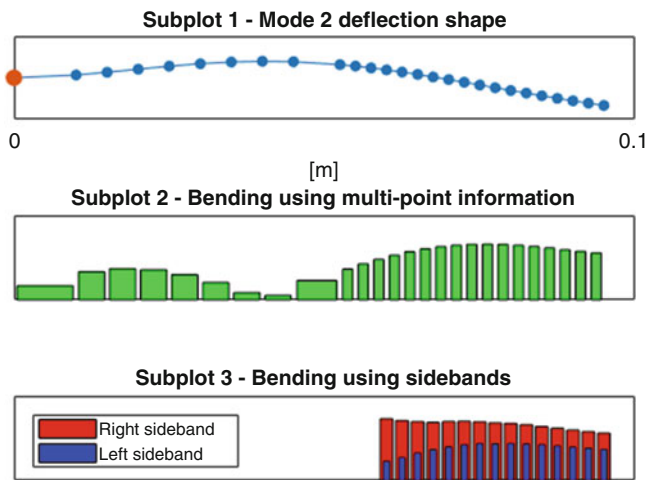


Fig. 19.5 Rotational degree of freedom

### 19.4 Estimation of Accuracy

In order to assess the accuracy of the method, it is fundamental to dispose of an exact reference for comparison. In a real-case scenario, the positioning of the laser spot is carried out with the structure at its neutral geometry i.e. before start vibrating and it identifies the expected measuring point. Therefore, the velocity signal obtained with the laser spot fixed there is the information expected and should be assumed as such reference.

The consequent comparison is very similar to the one depicted in Fig. 19.3. The only difference is the fixed point considered, since the position of the laser spot on the neutral geometry does not match the center of the scanning area. Such discrepancy introduces a leakage from the central peak, which increases as the displacement becomes larger. The sensitivity of such error respect to the amplitude of the displacement has been quantified through different simulations at point 5, with the participation factor of  $m_l$  progressively increased from 0 to  $1e4$ . Results are shown in Fig. 19.6 and they refer to the velocity signal  $v$ , which has been obtained by combining  $v_x$  and  $v_y$  according to the angle of the laser. In particular,



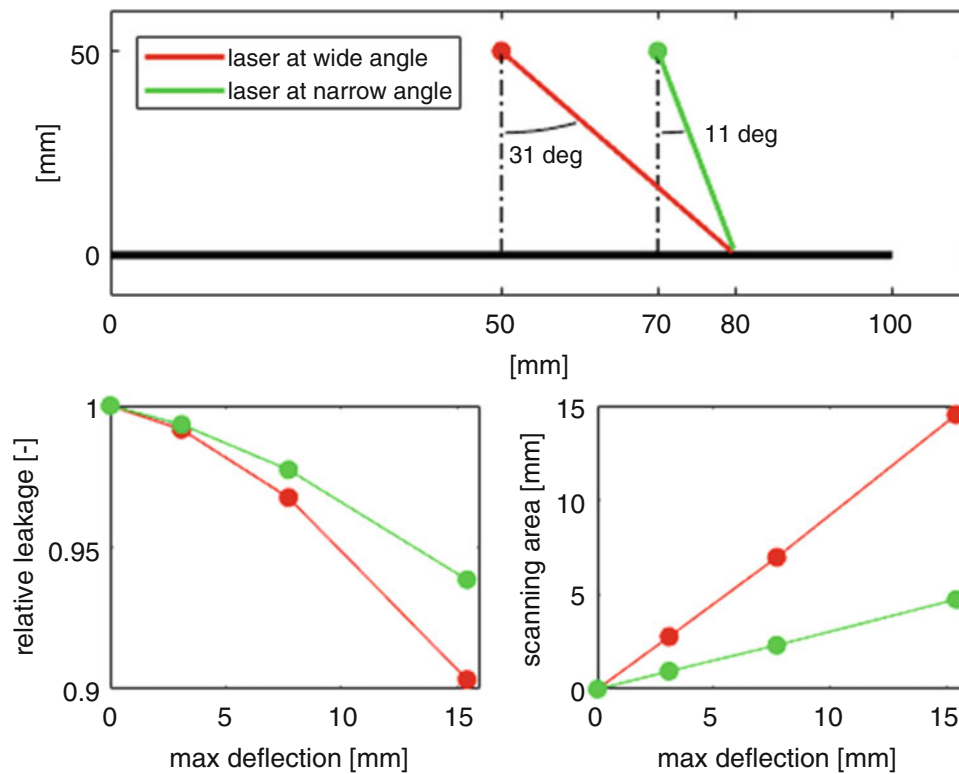


**Fig. 19.6** Wide- and narrow-angle laser geometry (top plot). Trends of relative leakage and scanning area (bottom plots)

Fig. 19.6 shows the relative variation of amplitude of  $m_2$  as the oscillation becomes larger, with a maximum deflection at the free-end point of 15 mm that corresponds to 15% of the total length of the beam. The trend of the correspondent scanning area is shown as well. As it can be observed, the amplitude of  $m_2$  can be assessed within an error of 10%.

Such uncertainty is relevant in many applications. Orientating the laser at a narrower angle respect to the  $y$ -direction could be effective in reducing it, with the further benefit of a greater sensitivity to that velocity component. However, it also produces a reduction of the scanning area, therefore a lower sensitivity to the rotational degree of freedom. Green curves in Fig. 19.6 refer to a second simulation with the laser positioned at a narrower angle. Using such measurement geometry results in a lower error, this at the cost of a smaller induced scanning area.

The previous results indicate that it is possible to optimize the angle of the laser in order to achieve the best compromise between sensitivity to rotation and accuracy in the location of the measurement point. However, it should be noted that in a real-case scenario the rotational degree of freedom can only be assessed qualitatively, since the value of  $l$  is unknown. These considerations limit the applicability of such technique in cases where the interest is not in the quantitative values, but in their trends. In upcoming work the method will be exploited in the setup for bending-fatigue tests depicted in Fig. 19.7, and it will concern the assessment of the different sensitivity of the sidebands and the central peak to the incipient damage of the specimen under test, as well as experimental validation.

## 19.5 Conclusions

A 1D numerical model of a cantilever beam was developed for simulating the scanning effect due to the large oscillation of the first bending mode, including a cinematic model for the axial displacement. The movement of the laser spot was found to be an over-imposition of local, harmonic linear scanings, with the one due to the  $y$ -displacement of the first mode being prevalent respect to the others. The consequent velocity signal showed left and right sidebands, which were used for calculating the rotational degree of freedom of the second mode according to CSLDV theory. The results were compared to those obtained using multi-point information and it was found that the left sideband can be effectively exploited for the purpose, whilst the right is affected by the super-imposition of more contributions. The discrepancy between the real

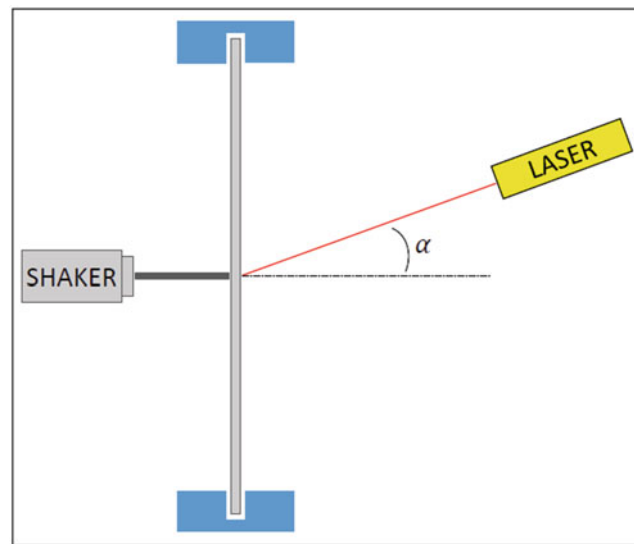


**Fig. 19.7** Setup for bending-fatigue tests

scanning center and the expected measurement point was found to be a cause of uncertainty and the problem will be analyzed with more focus in upcoming work. The new method is believed to present interesting applications in bending fatigue tests, since the progression of damage can be assessed with high sensitivity by monitoring the qualitative trend versus time of the rotational degree of freedom of the specimen, in the area close to the point of maximum stress.

**Acknowledgements** The results presented in this paper were obtained using the High Performance Computing (HPC) facilities of the University of Luxembourg [13] (see <http://hpc.uni.lu>).

## References

1. Castellini, P., Revel, G.M., Tomasini, E.P.: Laser Doppler vibrometry: a review of advances and applications. *ShockVib. Dig.* **30**(6), 443–456 (1998)
2. Di Sante, R., Revel, G.M., Rossi, G.L.: Measurement techniques for the acoustic analysis of synchronous belts. *Meas. Sci. Technol.* **11**(10), 1463–1472 (2000)
3. Revel, G.M., Martarelli, M., Chiariotti, P.: A new laser vibrometry-based 2D selective intensity method for source identification in reverberant fields: part I. Development of the technique and preliminary validation. *Meas. Sci. Technol.* **21**(7), 075107 (2010)
4. Revel, G.M., Martarelli, M., Chiariotti, P.: A new laser vibrometry-based 2D selective intensity method for source identification in reverberant fields: part II. Application to an aircraft cabin. *Meas. Sci. Technol.* **21**(7), 089803 (2010)
5. Chiariotti, P., Martarelli, M., Revel, G.M.: Exploiting continuous scanning laser Doppler vibrometry (CSLDV) in time domain correlation methods for noise source identification. *Meas. Sci. Technol.* **25**(7), 075204 (2014)
6. Castellini, P., Revel, G.M., Scalise, L., De Andrade, R.M.: Experimental and numerical investigation on structural effects of laser pulses for modal parameter measurement. *Opt. Lasers Eng.* **32**(6), 565–581 (2000)
7. Chiariotti, P., Revel, G.M., Martarelli, M.: Exploiting continuous scanning laser doppler vibrometry and wavelet processing for damage detection. In: *Conference Proceedings of the Society for Experimental Mechanics Series*, 2015, Orlando (USA).
8. Chiariotti, P., Martarelli, M., Revel, G.M.: Delamination detection by Multi-Level Wavelet Processing of Continuous Scanning Laser Doppler Vibrometry data. *Opt. Lasers Eng.* **99**, 66–79 (2017)
9. Marchionni, P., Scalise, L., Ercoli, I., Tomasini, E.P.: An optical measurement method for the simultaneous assessment of respiration and heart rates in preterm infants. *Rev. Sci. Instrum.* **84**, 121705 (2013)
10. Tabatabai, H., Oliver, D.E., Rohrbaugh, J.W., Papadopoulos, C.: Novel applications of laser Doppler vibration measurements to medical imaging. *Sens. Imaging.* **14**(1–2), 13–28 (2013). <https://doi.org/10.1007/s11220-013-0077-1>
11. Martarelli, M.: Exploiting the laser scanning facility for vibration measurements. Ph.D. Thesis, University of London (2001)
12. Hsieh, S.R., Shaw, S.V., Pierre, C.: Normal modes for large amplitude vibration of a cantilever beam. *Int. J. Solids Struct.* **31**, 1981–2014 (1994)
13. Varrette, S., Bouvry, P., Cartiaux, H., Feorgatos, F.: Management of an academic HPC cluster: The UL experience. In: *Proceedings of the 2014 International Conference on High Performance Computing & Simulation*, July 2014, pp. 959–967, Bologna (Italy).



# Chapter 20

## A Rational Basis for Determining Vibration Signature of Shaft/Coupling Misalignment in Rotating Machinery

Changrui Bai, Surendra (Suri) Ganeriwala, and Nader Sawalhi

**Abstract** Shaft misalignment is the most common fault in rotating machinery besides unbalance. A poorly aligned machine can cost a factory upward of 30–40% in machine down time, replacement parts, inventory, and energy consumption. Vibration analysis is prompted as a most common methodology for determining misalignment while a machine is in operation. Considering the importance of alignment, the vibration spectrum of misalignment lacks a consensus and is elusive. This work is an evolution from the research performed on a large body of the vibration data to determine a unique vibration signature for shaft/coupling misalignment while operating under varying conditions such as speed, type and level of misalignment, coupling types and machinery dynamic stiffness. The data is analyzed from tests conducted on different machinery fault simulators operated at several shaft speeds, types of couplings, shaft diameters, structural stiffnesses, and multiple misalignment configurations. The results indicate a confusing picture of misalignment vibration signature. In this paper we present the results of vibration data analysis and outline an approach for vibration analysis of the shaft/coupling misalignment of rotating machines. This includes uses of rotor frequency response function and physics based predictive model.

**Keywords** Misalignment · Vibration spectrum · Machinery dynamics stiffness · Misalignment forces · Rotor dynamics model · Diagnostics model · Machinery fault simulator

### 20.1 Introduction

When two misaligned shafts are joined together by a coupling, the machine structure is subjected to deformation (strain). The deformation will be different at each angle of rotation, depending on the type and level of misalignment. The corresponding stress will depend on the stiffness of the machine structure. The Fourier transform of the rotation angle dependent deformation (or stress) curve will contain several terms. When the machine starts turning, the varying stress will produce varying forces which lead to vibration at each of the Fourier components, assuming a linear relationship. The problem is complicated even further due to the inherent nonlinearities of the machine. Vibration signatures are widely promoted for studying machine malfunctions. However, the literature does not present a clear picture of signature characteristics uniquely attributable to misalignment [1–4]. One of the reasons for inconsistency is that a rotor exhibits several critical speeds over a range of frequencies used to characterize misalignment spectra. When fault frequencies fall near associated resonances their amplitude gets amplified and when they fall near anti-node the amplitudes are attenuated.

This is a report of a systematic series of experiments designed to determine the consistent features, if any, of vibration signatures for misaligned machinery. Operating and design parameters such as shaft speed, shaft diameter, type and level of misalignment and coupling types all have been reported to exhibit the effect on shaft misalignment. In this report we systematically varied coupling type or stiffness while all other parameters were held constant. The machine was fault-free with the exception of deliberate misalignment, which was also varied systematically. Baseline vibration data were recorded for each test condition.

The figures below pictorially depict the common two types, parallel and angular, shaft/coupling misalignment. Here a centrifugal pump driven by a motor is shown to be misaligned. One can easily see that under any of two conditions when motor starts driving the pump, there will be stresses on the entire structure. The level of stress will obviously depend on coupling type and structural stiffness. The results will show the effect (Fig. 20.1).

---

C. Bai · S. Ganeriwala (✉) · N. Sawalhi  
Spectra Quest, Inc., Richmond, VA, USA  
e-mail: [suri@spectraquest.com](mailto:suri@spectraquest.com)

■ The center lines of two shafts do no coincide.

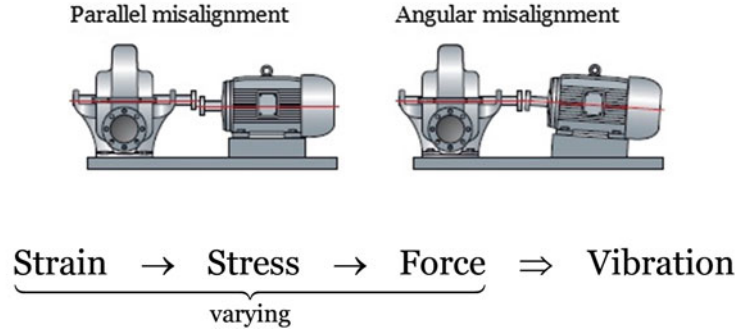


Fig. 20.1 Parallel and angular exhibit misalignment between the motor shaft and the pump shaft

The measured vibrations include the effects of both the forcing function and the structural transmission path. Theoretically, knowing the coupling stiffness as a function of rotation angle, and the frequency response function (FRF) between the coupling (location of the forcing function) and the measurement location, the misalignment of the machine could be determined from the recorded vibrations. However, this approach faces practical issues, since most of the time neither the coupling stiffness, nor the FRF is known or can be determined without shutting down the machine, which is not cost effective; therefore it is rarely allowed by the factory. It is possible and very useful to obtain all this information during machine setup for future diagnosis, but it seldom happens in real life. Relying on the vibration signature only, the problem is elusive, because the vibration signals lack consistency [1]. Analyzing the harmonics of the shaft speed shows a confusing picture, and it will be investigated in this paper. Special attention is paid to axial vibrations, because they may be able to distinguish misalignment from unbalance and other machine faults which cause radial vibrations. Unbalance, for example, generates a radial centrifugal force without producing any significant vibration in the axial direction. Figure 20.2a shows a force transmission model and the Fig. 20.2b depicts a typical FRF of a rotor over a range of frequency [4].

Figure 20.2 is a frequency response function exhibiting first three critical speeds or modes. Note that two nearby minor peaks are resonances on the other perpendicular direction due the coupling effect.

## 20.2 Basic Concept

The measured vibrations consist of two main components: the forcing function (FF) and the structural transmission path which is characterized by the frequency response function (FRF) between the location of the forcing function and the measurement or sensor location. In the frequency domain, assuming linearity, the vibration (V) is equal to the product of the forcing function and the frequency response function:

$$V = FF \times FRF. \quad (20.1)$$

The forcing function is the product of the coupling stiffness (CS) and the misalignment (M). For parallel misalignment the coupling's transverse stiffness, for angular misalignment the coupling's flexural stiffness is required. Therefore, the forcing function can be written as:

$$FF = CS \times M. \quad (20.2)$$

Putting (20.1) and (20.2) together, the measured vibration becomes

$$V = CS \times M \times FRF. \quad (20.3)$$

Equation (20.3) also shows that if the coupling stiffness and the frequency response function are known, the misalignment can be calculated from the measured vibration. Most of the time, however, these two pieces of information are not known and cannot be measured without shutting down the machine. In such cases, mathematically speaking, even with the assumption

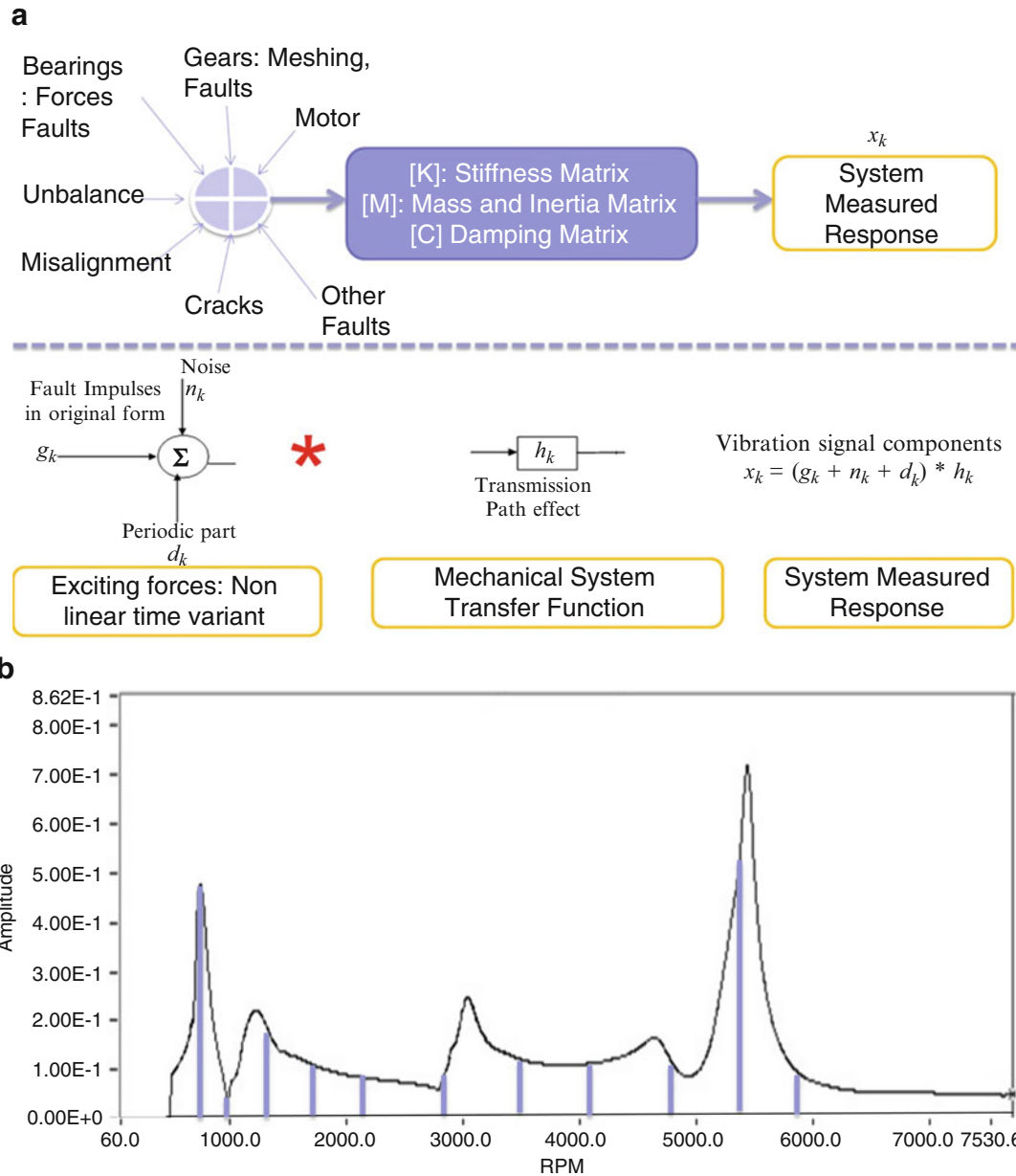


**Fig. 20.2** A force transmission path model resulting in vibration. (a) Force transmission model. (b) Typical FRF of a rotor over a range of frequency

of linearity, the analyst is faced with one equation and 3 unknowns. Therefore, the main problem with successfully detecting misalignment is that the actual machine is not known well enough.

Four different variables are investigated in this study:

- Coupling type,
- Shaft diameter,
- Shaft speed,
- Misalignment type & level.

The four variables investigated in this study can be associated with different components of the measured vibrations. The coupling type changes the coupling stiffness (CS), the shaft diameter changes the frequency response function (FRF) and the misalignment type & level change the misalignment (M). The shaft speed does not affect any of these components directly, however, it can cause the spectrum of the measured vibrations to differ significantly from the spectrum of the forcing

function. Every harmonic of the forcing function is multiplied by the frequency response function at the corresponding frequency values which are determined by the shaft speed. A small harmonic in the forcing function can easily cause a big harmonic in the measured vibrations if it is multiplied by a large value of the frequency response function and vice versa. In this report we will describe the effect of coupling stiffness in details.

## 20.3 Experiment

All tests were conducted on a Machinery Fault Simulator™ (MFS). An 8-channel data acquisition system was used for recording the data. Vibrations were monitored with accelerometers placed at 7 different locations on the MFS. Figure 20.3 shows the measurement setup while Table 20.1 lists all the locations, directions, channel numbers and abbreviated legends used to identify the sensors. The actual shaft speeds deviated slightly from the target speed settings in the experimental design.

Investigating 3 types of couplings, 3 shaft diameters, 3 shaft speeds and 2 types and 3 levels of misalignment results in 162 vibration signals for each of the 7 sensors. In order to avoid lengthiness and confusion, only the most important results and effects of the investigated variables are presented. Table 20.2 summarizes the applied values of these variables to show a clear picture of the systematic experiment design.

The data were acquired using SpectraQuest's own hardware and software developed in-house. The spectral settings included a maximum frequency of 2000 Hz and a spectral resolution of 3200 lines. Sixteen blocks were applied for averaging

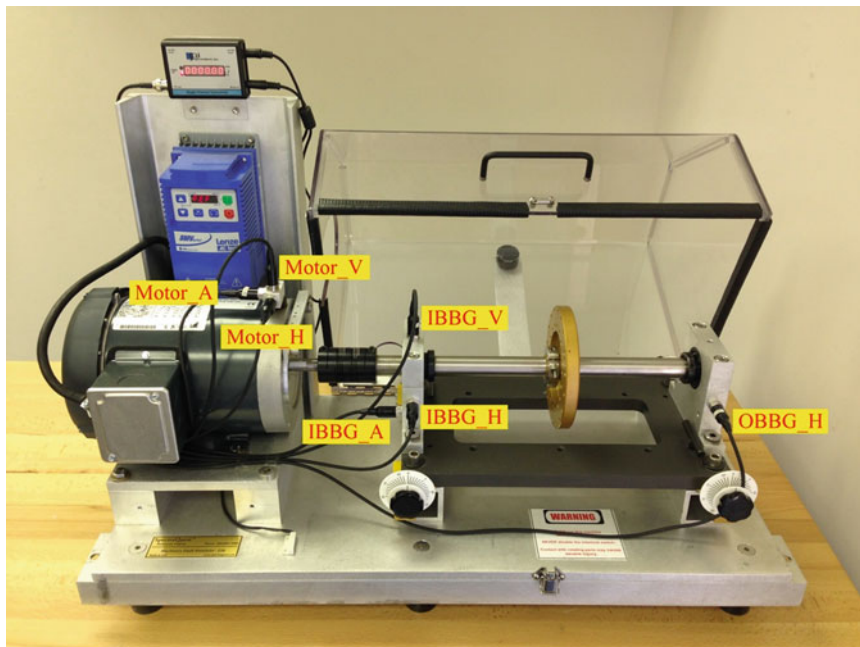


**Fig. 20.3** Measurement setup

**Table 20.1** Sensor locations

Channel	Location	Direction	Legend
1	–	–	Tach
2	Motor	Horizontal	Motor_H
3		Vertical	Motor_V
4		Axial	Motor_A
5	Inboard bearing	Horizontal	IBBG_H
6		Vertical	IBBG_V
7		Axial	IBBG_A
8	Outboard bearing	Horizontal	OBBG_H

**Table 20.2** Investigated variables

<b>Coupling type</b>	Rubber	
	Spiral	
	Rigid	
<b>Shaft diameter</b>	1/2"	
	3/4"	
	1"	
<b>Shaft speed</b>	1750 rpm	
	3880 rpm	
	5170 rpm	
<b>Misalignment type &amp; level</b>	Parallel	5 mils
		15 mils
		25 mils
	Angular	0.03°
		0.10°
		0.17°

**Fig. 20.4** Coupling types used in the study: rubber, spiral & rigid

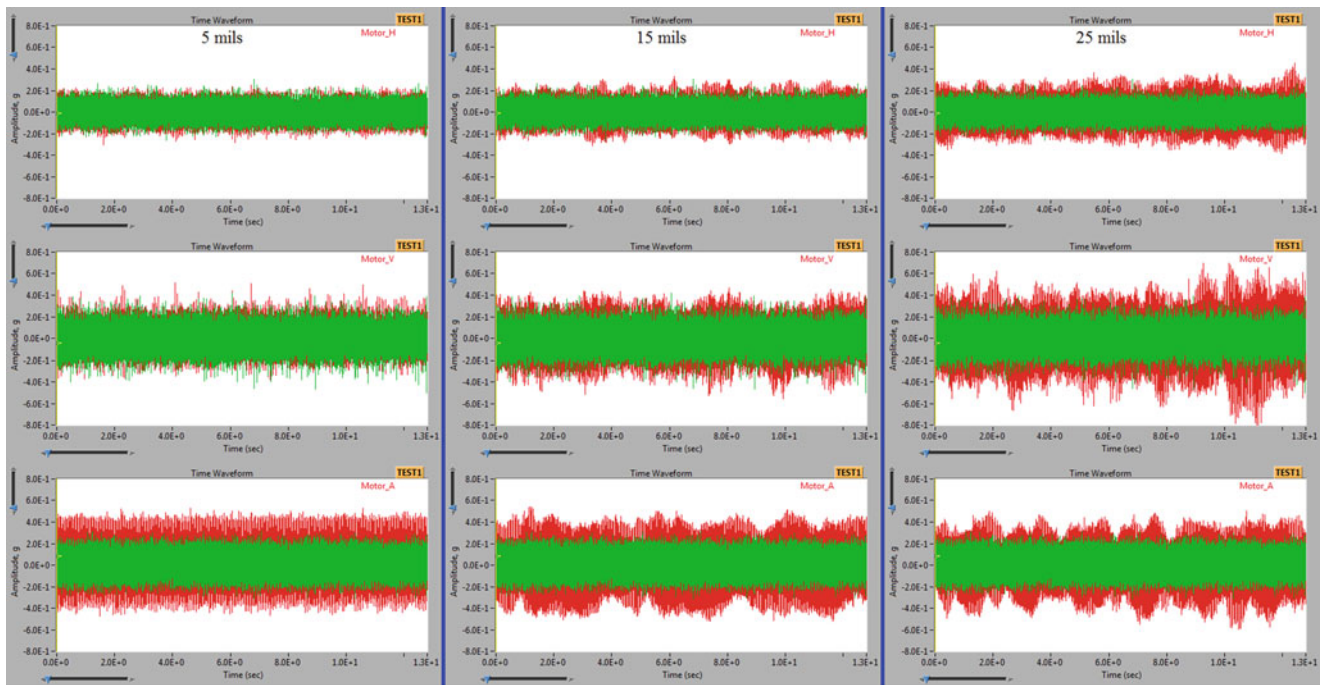
and refining the resolution of the recorded data. In order to preserve information in the high frequency region, acceleration was used as the primary unit of the recorded vibrations.

Figure 20.4 presents the couplings used in this study. It can be concluded that certain harmonics can be associated with certain coupling types. The structural geometry of a coupling can give the analyst an idea of harmonics to look for, however, this tool is not always reliable either.

## 20.4 Results

The following diagrams attempt to clarify the confusing picture of misalignment in a systematic way. The columns always show the investigated variable, the rows always present the different spatial directions: horizontal, vertical and axial – from top to bottom – respectively.

Figure 20.5 clearly shows that the vibration level increases in the horizontal and vertical directions as the level of misalignment increases, however, the rate at which the vibration level increases is not linear. The axial direction displays a surprising result. The vibration level is more or less constant, regardless of the level of misalignment, which makes it very difficult to assess the level of misalignment just by looking at the axial sensor. Nevertheless, an increased vibration level is a direct consequence of many kinds of faults and it is not a unique indicator of shaft misalignment whatsoever. Additionally, many factories do not possess baseline vibration data, which makes it even more difficult to detect faults, since one does not have the data for the faultless configuration to compare the new measurements with. However, there is a clear amplitude modulation in Fig. 20.5 in almost every case which is not present in the aligned configuration, but it is missing in



**Fig. 20.5** Time signal of parallel misalignment in red, alignment in green (motor side). Coupling type: spiral, shaft speed: 1750 rpm, shaft diameter:  $\frac{3}{4}$ "

the axial direction when the misalignment is only 5 mils. The phenomenon of amplitude modulation brings the behavior of misalignment somewhat closer to understanding, but this property does not remain consistent as other variables change.

Figure 20.6 shows much more consistency. The vibration level clearly increases with the level of misalignment, and amplitude modulation is present in every case. It is also important to notice that the vibrations on the rotor side are almost twice as much in amplitude than those on the motor side. After concluding an increased vibration level and some amplitude modulation, it is useful to examine the spectra of these signals for further analysis. However, it is important to keep in mind that all the results refer to a specific coupling type, shaft speed, shaft diameter and misalignment type. Varying at least one of these parameters can drastically change the picture which will be presented later in this paper.

According to Figs. 20.7 and 20.8, the most significant peak at 5 mils is at 3X, which can be related to the structure and geometry of the applied coupling type (spiral) which will be discussed later. Increasing the level of misalignment introduces 6X and 9X peaks which are higher harmonics of 3X. This phenomenon indicates nonlinearities in the system. The 4X peak becomes prominent at 15 mils, whose presence is more difficult to explain by the geometry of the applied coupling. While vibration amplitudes were bigger on the rotor side, harmonics are generally higher on the motor side. Harmonics in the axial direction are not to be neglected; they are often even larger than the corresponding radial ones. Investigating the spectra of vibration signals provides the analyst with much better insight than examining the time waveforms alone. The level of misalignment is still difficult to estimate (especially in the absence of baseline data), but the presence of the misalignment itself is much more prominent in the frequency domain.

Figures 20.9 and 20.10 clearly show that the spiral coupling is designed to be more forgiving towards angular misalignment. The overall misaligned vibration amplitude is so low that it can barely be seen behind the baseline data. The  $0.10^\circ$  case yields surprising results; the reason for the excessive vibrations (compared to the other two investigated levels of misalignment) is not well understood. Amplitude modulation is present in angular misalignment as well.

The time waveforms provide very little, if any, help to detect angular misalignment in the case of a spiral coupling. The geometry and design of this coupling type stands behind this phenomenon, but one must resort to the spectra in order to draw some more useful information from the recorded data.

The diagrams above show the differences between the three types of couplings used in this study. In order to investigate the behavior of each coupling, the frequency domain proves to contain more useful information, however, it is also beneficial to see the vibration level in the time domain.

Judging by Figs. 20.11 and 20.12, it cannot be said in general that – keeping the level of misalignment constant – a stiffer coupling always results in a higher vibration level, because it very much depends on the sensor location. For example,



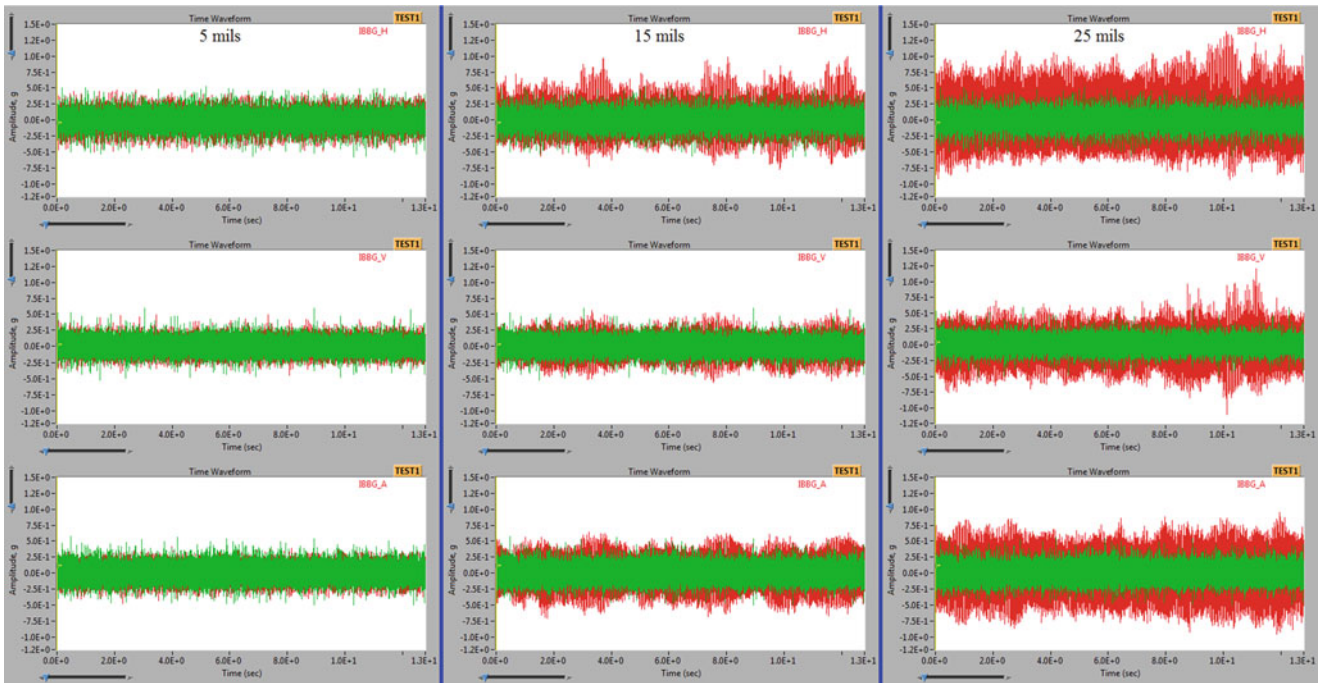


**Fig. 20.6** Time signal of parallel misalignment in red, alignment in green (rotor side). Coupling type: spiral, shaft speed: 1750 rpm, shaft diameter: 3/4"



**Fig. 20.7** Spectrum of parallel misalignment in red, alignment in green (motor side). Coupling type: spiral, shaft speed: 1750 rpm, shaft diameter: 3/4"

the stiffest (rigid) coupling produces the most vibration at Motor\_V, but also generates the least vibration at IBBG\_H. Theoretically, according to (20.3), applying the same level of misalignment to a stiffer coupling produces a greater forcing function which – traveling through the same structural transmission path and therefore the same FRF – should result in a higher vibration level, but reality does not always follow this basic principle. Using the time domain only, it is very difficult to successfully detect misalignment. The spectrum, however, provides fairly good information on the structure and the geometry

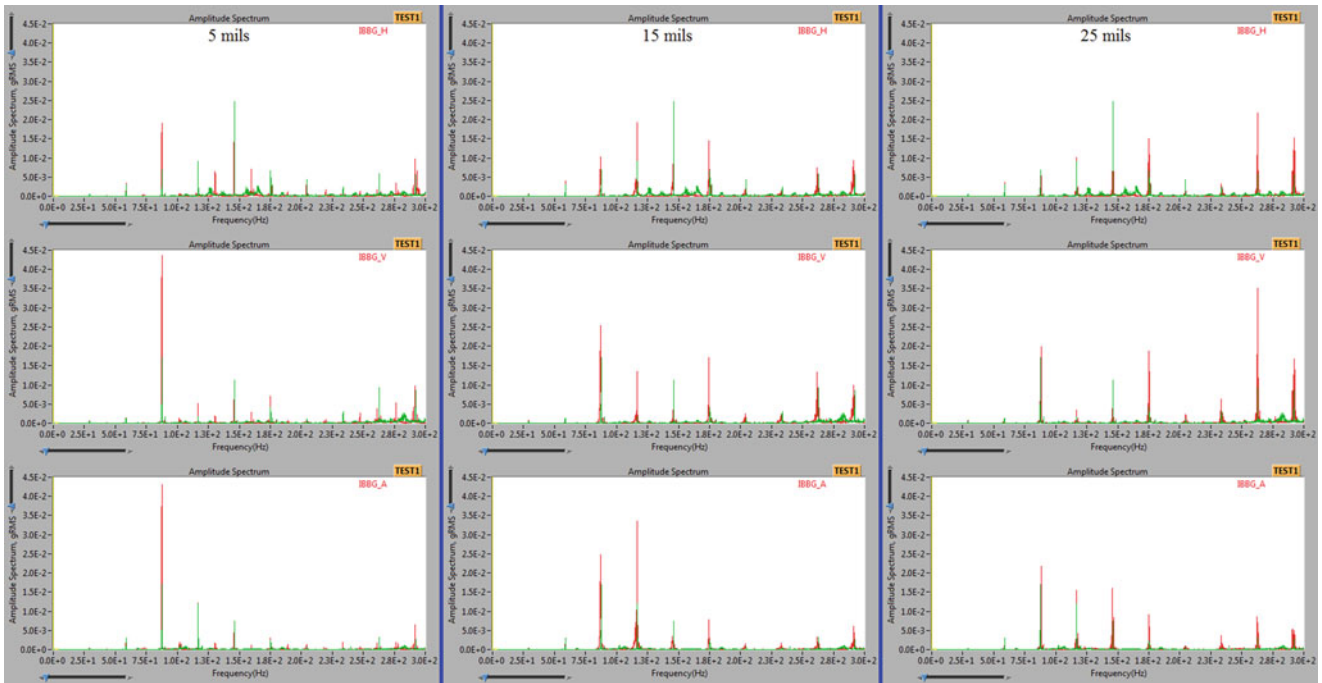


**Fig. 20.8** Spectrum of parallel misalignment in red, alignment in green (rotor side). Coupling type: spiral, shaft speed: 1750 rpm, shaft diameter: 3/4"

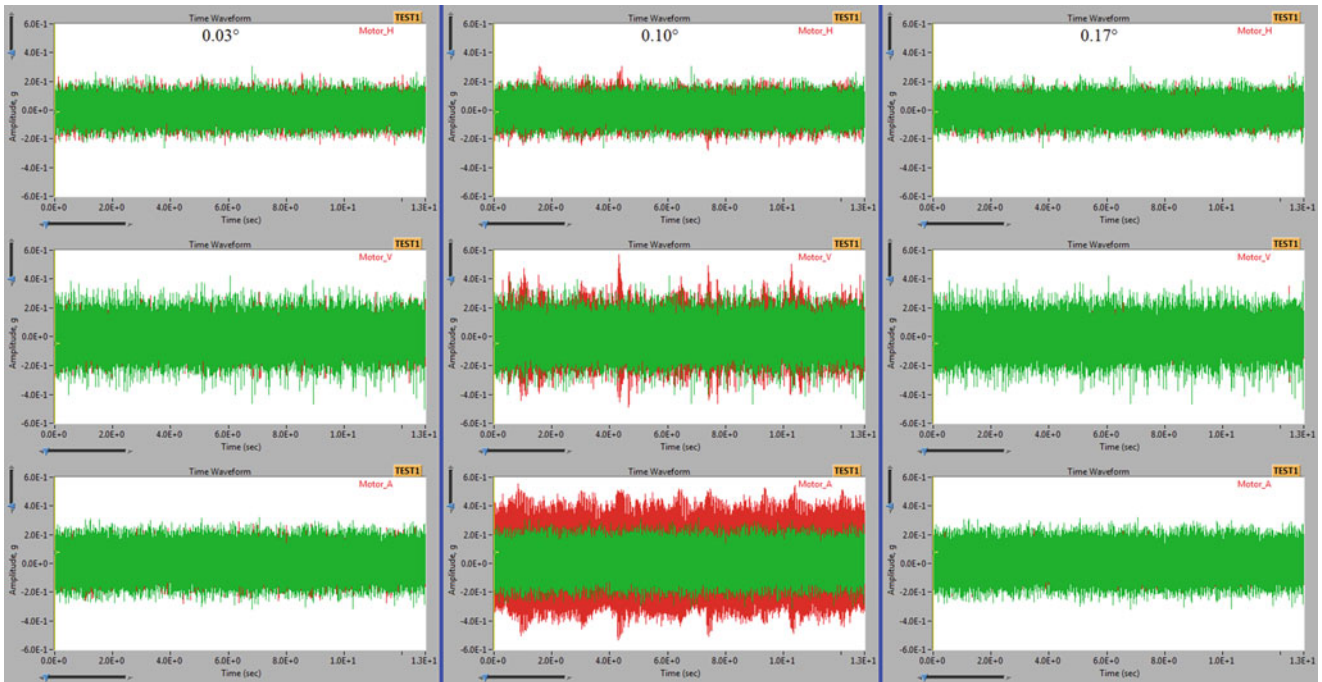


**Fig. 20.9** Time signal of angular misalignment in red, alignment in green (motor side). Coupling type: spiral, shaft speed: 1750 rpm, shaft diameter: 3/4"

of the applied coupling type. For example, the spiral coupling has spring-like grooves which make this type of coupling more forgiving to angular misalignment. If one looks at these grooves carefully, it can be seen that the number of grooves along the coupling follow a distinct pattern. In one revolution of the coupling, the number of grooves changes in the following manner: 8–6–8–6–8–6. The geometry of the coupling is more complicated than that, but as a first approximation, this means that the

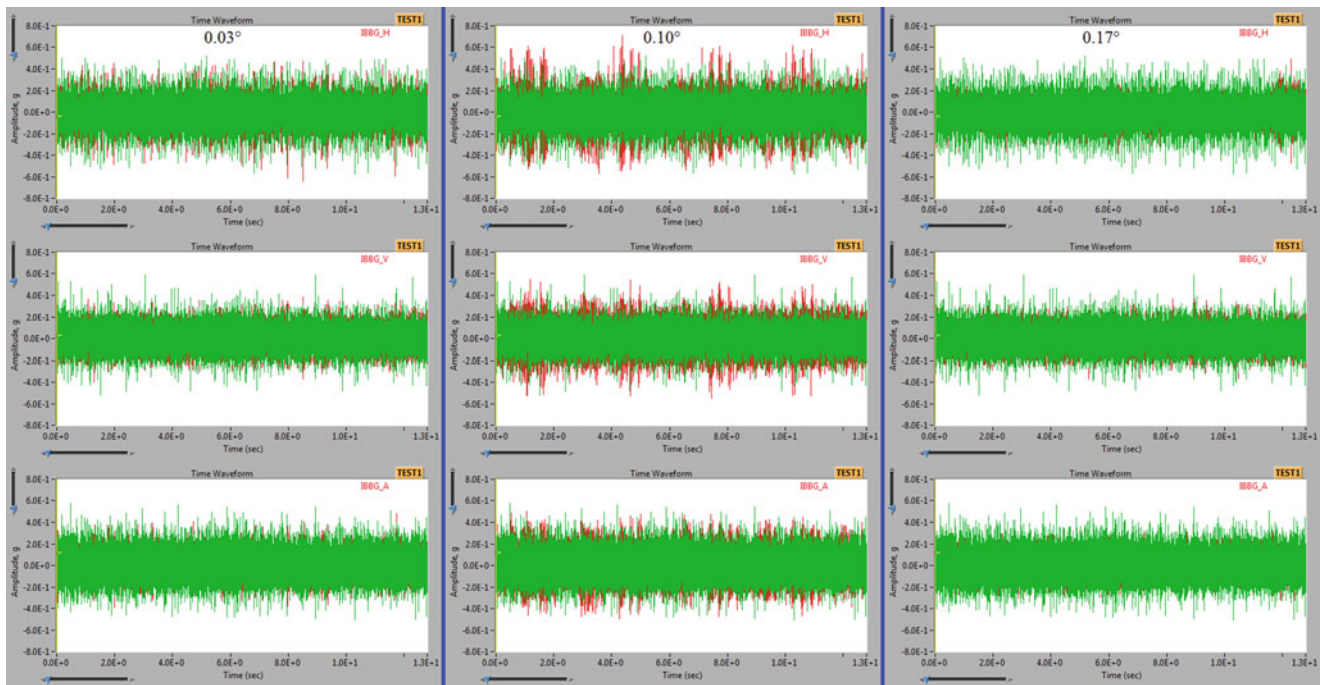


**Fig. 20.10** Time signal of angular misalignment in red, alignment in green (rotor side). Coupling type: spiral, shaft speed: 1750 rpm, shaft diameter:  $\frac{3}{4}$ "

stiffness of the spiral coupling changes six times per revolution, taking up a value corresponding to 6 grooves 3 times and another one corresponding to 8 grooves 3 times as well. As it was mentioned before, the stiffness properties of a coupling as a function of rotation angle are very helpful to detect misalignment, but most of the time, factories do not possess this information. If one measured the stiffness characteristics of the spiral, there would be a definite 3X component with its harmonics directly corresponding to the changing number of grooves. Although this goes through the FRF before reaching the vibration sensors, but apart from the unfortunate scenario of multiplying the 3X component of the forcing function by a very small value of the FRF, it should be detectable in the vibration spectrum.

Therefore the coupling geometry plays a very important role in successfully detecting misalignment. The complete stiffness function might not be available most of the time, but the vibration analyst can at least have an idea of the dominant harmonics just by carefully examining the coupling. This does not require the shutdown of the machine, but merely the specifications or a double of the applied coupling.

The rigid coupling shows moderate peaks at 2X, 4X and 6X and a significant one at 5X. Examining the geometry of the coupling, though, the presence of the 5X component is hard to explain. It is difficult to suspect this harmonic without actually measuring the stiffness of the coupling as a function of rotation angle. This is when practical experience in condition monitoring and vibration analysis becomes very important. The presence of 2X and its harmonics are much easier to identify by the geometry of the coupling, but the reason for 5X remains elusive.

## 20.5 Conclusions

The coupling type has probably the most significant effect on the arising vibrations and it can help a great deal to successfully detect misalignment. The structural geometry of the coupling gives away numerous properties of its spectral behavior. Looking for periodic features such as screw or grooves can help the analyst identify the fault of misalignment even without actually measuring the coupling's stiffness as a function of rotation angle, which would require the shutdown of the machine. Problems occur when these characteristic features are difficult to identify by the geometry of coupling alone, or the coupling is very close to being axisymmetric. In such cases, the analyst has to rely on his practical experience. It is also possible to measure the stiffness of the applied coupling's replica, which does not require the shutdown of the machine, but provides the analyst with very useful information on detecting misalignment. Additionally, keeping every other variable constant, a stiffer coupling is expected to produce more vibration, but some exceptions were also presented in this paper, and the correlation does not seem to be linear and simple.

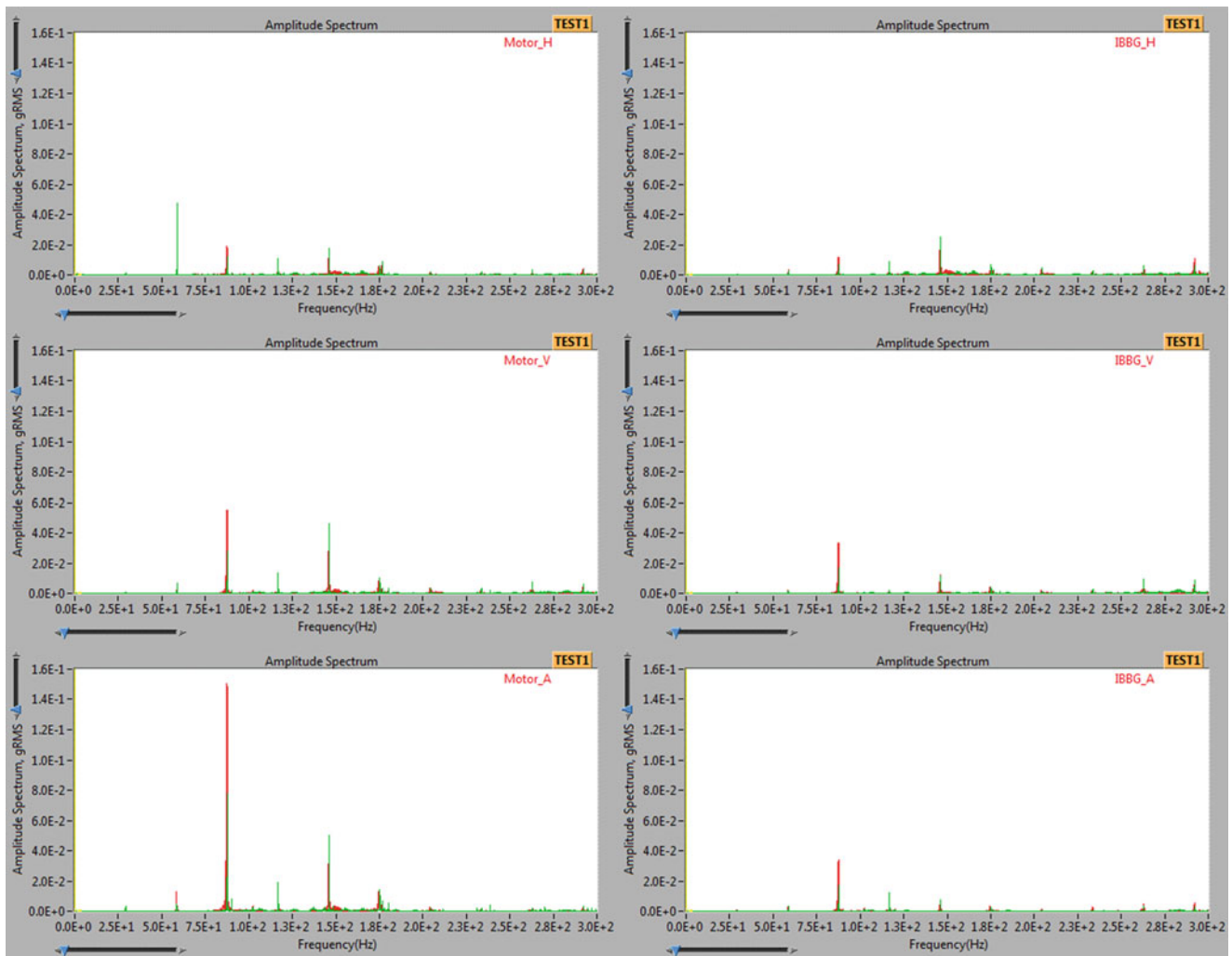


**Fig. 20.11** Spectrum of moderate angular misalignment of  $0.10^\circ$  in red, alignment in green. Coupling type: spiral, shaft speed: 1750 rpm, shaft diameter:  $\frac{3}{4}$ "

Axial vibrations and harmonics are often the greatest, but at least always comparable with the radial ones. This phenomenon helps distinguish misalignment from unbalance, which is a very important result. Unbalance produces a centrifugal force which causes radial vibrations [1, 2]. 1X vibrations were deliberately ignored in this study, because they are significant indicators of other important faults like unbalance and bent shaft. However, axial vibrations were really outstanding and it is highly recommended to look at them carefully when misalignment is suspected.

The results clearly indicate a significant variation in the vibration spectra as a function of operating and design conditions. Both the amplitude of the dominant peak and its location along the frequency axis change in a complex manner. The data indicate that it is not possible to conclude that the cause of real world machinery malfunction is shaft misalignment just by looking at a single vibration spectrum at one operating condition [2, 3]. A careful examination is necessary to differentiate misalignment from other sources of vibration. Since misalignment vibration seems to be a strong function of coupling type and shaft speed, a detailed rotor dynamics model might be needed to develop a predictive model for misalignment vibration spectra. The misalignment phenomenon is definitely nonlinear and very complex. More work is needed to develop simpler rules for diagnosing shaft misalignment of rotating machinery.

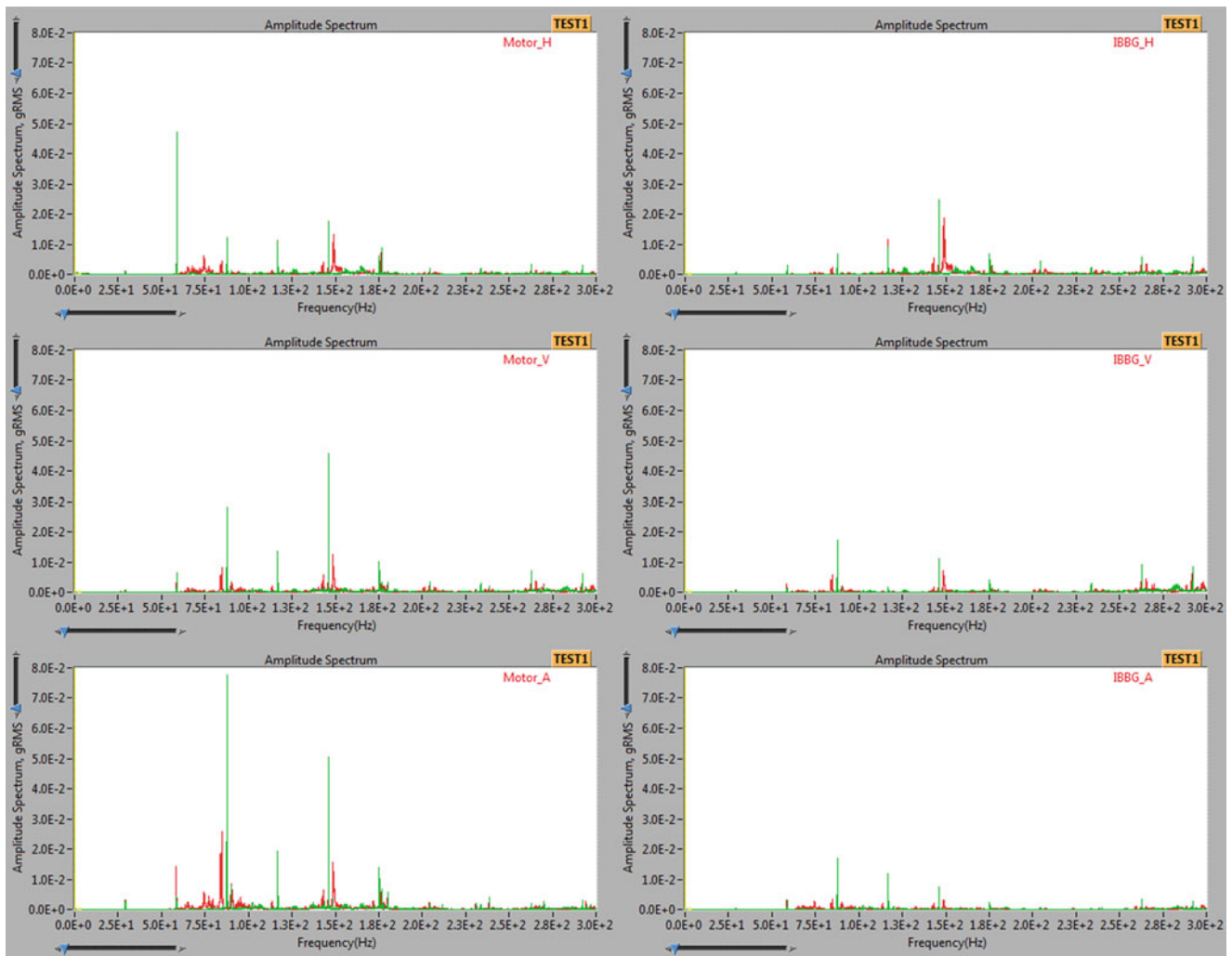


**Fig. 20.12** Spectrum of severe angular misalignment of  $0.17^\circ$  in red, alignment in green. Coupling type: spiral, shaft speed: 1750 rpm, shaft diameter:  $\frac{3}{4}$ "

## References

1. Piotrowski, J.: Shaft Alignment Handbook, 2nd edn. Marcel Dekker, Inc, New York (1995)
2. Jackson, C.: Mini Course Notes, Sixteenth Annual Meeting, Vibration Institute, Williamsburg, VA, June 9–11 (1992)
3. Guy, Eshleman, Jackson: 12th Annual Meeting Proceedings, Vibration Institute, Nashville, TN, May 25–27 (1988)
4. Ganeriwala, S., Patel, S., Hartung, H.: Observations Concerning Misalignment Vibration Signatures, SpectraQuest Technote (2005)



# Chapter 21

## Parametric Experimental Modal Analysis of a Modern Violin Based on a Guarneri del Gesù Model

Elvio Bonisoli, Marco Casazza, Domenico Lisitano, and Luca Dimauro

**Abstract** Mechanical effects and dynamic behaviour of a modern violin, built on a Guarneri del Gesù model, were examined via parametric experimental modal analysis. The soundpost, a mobile component of a violin, has a particular relevance for the final acoustic performance, even if its dimensions are extremely small. Therefore, the aim of this first research is to understand the violin sensitivity to the soundpost position considering its influence on the overall structural-vibrational behaviour.

Experimental modal analysis was performed in six different configurations, related to different positions of the soundpost inside the violin, including both the outer possible locations and optimal position, generally defined by the violinist according only to the perceived best acoustic performance. Six “Signature” modes were identified and tracked in all configurations, comparing mode shapes, damping and natural frequencies of involved modes, in order to find a correlation between mechanical vibrations and acoustic performance of the instrument.

The effects of the soundpost position on the modal properties of the “Signature” mode shapes are highlighted and discussed. Finally, the potential role of soundpost as a practical engineering tool to improve the signature and sound quality is discussed.

**Keywords** Soundpost parametric analysis · Structural vibrations · “Signature” modes · MAC index · Roving hammer tests

### 21.1 Introduction

In the last decades there has been a greater interest in the study of vibrational dynamics and acoustics performance of musical instruments with harmonic case [1–3], such as violins. Violin acoustic properties are the result of a complex vibrational phenomenon, strongly influenced by materials, geometrical proportions and construction details of the violin itself. Obviously, environmental conditions, as well as other factors, should be included to fully describe the final sound perception. However, the attention is limited here to the source of sound production, i.e. the violin and its vibrational behaviour. The instrument geometry is almost bilaterally symmetrical, except for the presence of bassbar and soundpost, which are embedded into the instrument body. In particular, the bass bar is a shaped piece of wood placed under the top plate, whose position is fixed during the building process, while the soundpost is a small and mobile spruce wood cylinder, linking the top and the back plates. The former introduces a linearly distributed constraint, while the latter element is responsible for a punctual modification on the instrument acoustics. Shellen in [1] described the acoustic functions of the two components. The bassbar introduces a dissymmetry and tones are increased. However, its main acoustical aim is to keep the upper and lower bouts of the top plate in step with the left foot of the bridge. From a mechanical point of view, it enhances the distribution of forces generated by the tensed strings. The soundpost is necessary to transmit the top plate motion to the back, or better, to reduce locally the cancelling motion of the top plate [4]. Its displacement around a neutral and theoretically best position, related to instrument proportions and defined along centuries of violin-making art, allows to balance the sound power among the strings, contributing partially to the definition of the final instrument tone quality. Violin makers ‘learn’, through a learning-by-doing process, how to adapt the shaping of the bassbar and to find the appropriate position for the

---

E. Bonisoli (✉) · D. Lisitano · L. Dimauro  
Politecnico di Torino, Department of Mechanical and Aerospace Engineering, Torino, Italy  
e-mail: [elvio.bonisoli@polito.it](mailto:elvio.bonisoli@polito.it); [domenico.lisitano@polito.it](mailto:domenico.lisitano@polito.it); [luca.dimauro@polito.it](mailto:luca.dimauro@polito.it)

M. Casazza  
University of Naples “Parthenope”, Department of Engineering, Centro Direzionale, Naples, Italy  
e-mail: [marco.casazza@uniparthenope.it](mailto:marco.casazza@uniparthenope.it)

soundpost, in order to obtain the desired acoustical performance, depending on the quality of materials. Moreover, violin makers fix the position of the soundpost on the basis of the sound output perceived by the violin player. Apart from an ideal best position for the soundpost, which is defined only on the basis of the instrument proportions, no practical indications were ever defined for violin-makers in order to support the building and set-up process in a more rigorous way.

Recently, Bissinger proposed an analysis of the mechanical and acoustical consequences of removal of the soundpost, using an Experimental Modal Analysis (EMA) applied to a violin with and without soundpost [5–6]. The obtained experimental results were used to define a very simple acoustic model of the violin, considering both the radiative properties of the violin normal modes and its mechanical properties. Marshall numerically evaluated the modal properties of a violin without strings [7], analysing not only bending modes, but also air and plate modes. In [5] was shown how the soundpost location produces a phase difference for both top and back plates. In [8] Bissinger focused his attention on modal-acoustic radiation measurements on several quality-rated violins, in order to find any evident difference in the five “signature” modes below 600 Hz, but no evident differences were found among very fine and the worst violins. Zhang et al. [9] studied the effects on modal behaviour of the cello bridge due to soundpost characteristics and position. In particular, they discussed the modification of the bridge centre of rotation at different frequencies. This work showed that the instantaneous centre moves from the soundpost side of the bridge at low frequency toward the bass bar side at higher frequencies.

As concern new millennium research activity, it is of particular interest the computational Finite-Element Analysis (FEM) to investigate the effects of material and isotropic properties on plates modes [10], as well as the possibility of using composite materials as substitutes for traditional wood in making top plates [11].

Gough showed how the violin acoustic quality is related to the vibrations and acoustic properties of the body shell of the instrument [12–14]. He detected an evident difference in natural frequency consequently to a transverse offset of soundpost position.

While the bassbar effects were widely studied, almost no experimental work has been developed to investigate the effects of soundpost position on the global vibration behaviour of violins. Since millimetric changes of the soundpost position produce surprising modifications changes in the acoustic of the instrument, as known from the empirical experience of violin makers and players, a correlation between different modal parameters and violin acoustic behaviour could be expected. Usually, depending on the sound perception, violin players require to the violin maker to slightly modify the sound post position. Therefore, the main aim of the present work is to analyse how the position of this element influences mode shapes, natural frequencies and damping ratio of the instrument. Nonetheless, until now no references are available to violin makers to show in the simplest possible way how the position of sound post can affect the violin vibrational behaviour.

The paper is organised as follow: in §21.2 the experimental setup adopt for the EMA is presented. In §21.3 the experimental modal parameters for the “Centre” configuration are presented and compared with the other configurations. The effects of the soundpost position on the “Signature” modes are discussed. Finally, some considerations are highlighted in the conclusion.

## 21.2 Experimental Setup

The instrument, object of the parametric EMA, is a contemporary violin, handcrafted by the violin-maker Enzo Cena (Torino, Italy, 2011) on a 1730 Guarneri del Gesù model. The mass of the violin is 0.33 kg (Fig. 21.1).

Several wood kinds were used in the production of the various components. In particular, karst spruce for the top plate and the soundpost, maple for the back plate, ribs and neck, and ebony was used for the fingerboard. The use of different density woods, along with their anisotropy and non-homogeneity, lend violin a mechanical and acoustic behaviour, strongly correlated and influenced by properties of each single component.

All the tests were performed in free-free conditions, suspending the violin with an elastic band (Fig. 21.1). Roving hammer test for modal analysis was performed for the six configurations. The violin is excited with a soft plastic tip and its response is measured using six accelerometers. Mono-axial accelerometers were positioned above the plates lungs and a tri-axial accelerometer was placed in the neck of violin (Fig. 21.2).

The violin was excited in 49 points in one direction (except for the point on the scroll excited in two directions). The points were chosen to obtain a good compromise between geometry representation and expected violin modal behaviour. Some perimetric points (three nodes for each arching, the corners and the centre of the c-rib) were selected approximating the real geometry in the best possible way. Some points are added on the lungs of front and back plates and other two nodes at the bridge base in order to identify modes of the thinnest part of plates. Few other points were selected on the fingerboard and neck. The reference geometry for the EMA tests is shown in Fig. 21.3.



**Fig. 21.1** Violin and setup



**Fig. 21.2** Accelerometers locations

The violin is analysed in six different configurations related to the position of the sound post. The soundpost of the actual violin is a 50 mm-long movable spruce cylinder of approximately 0.7 g and 6 mm diameter. It is placed just behind the E-string bridge foot, between the top and back plates of the violin.

The different configurations (Table 21.1) were defined with respect to a reference point, centred under the right foot of the bridge, i.e. the reference point used by violin makers as ideal position for the sound post.

According to Fig. 21.4, other four configurations were obtained shifting the soundpost position respectively on the left, top, right and below with respect to the reference point. An additional configuration is the “Optimal” point from an acoustical point of view. The position of the soundpost is accurately manually changed by the violin-maker (Fig. 21.5). The



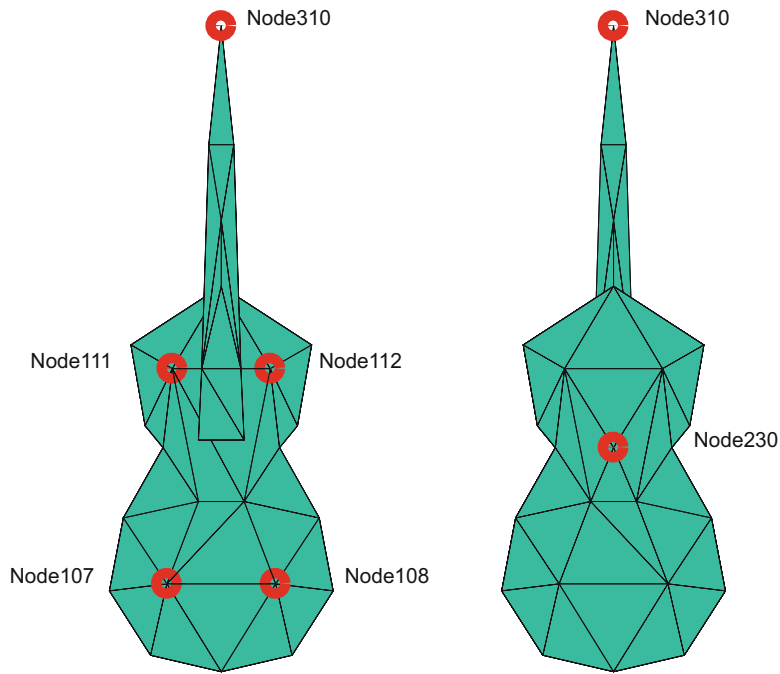


**Fig. 21.3** Reference geometry for experimental tests: front view (left) and bottom view (right)

**Table 21.1** Soundpost position

Configuration	Soundpost ref. system	
	X [mm]	Y [mm]
Central, C	0.0	0.0
Optimal, O	+1.0	0.0
1	+2.0	0.0
2	0.0	+2.0
3	-2.0	0.0
4	0.0	-2.0

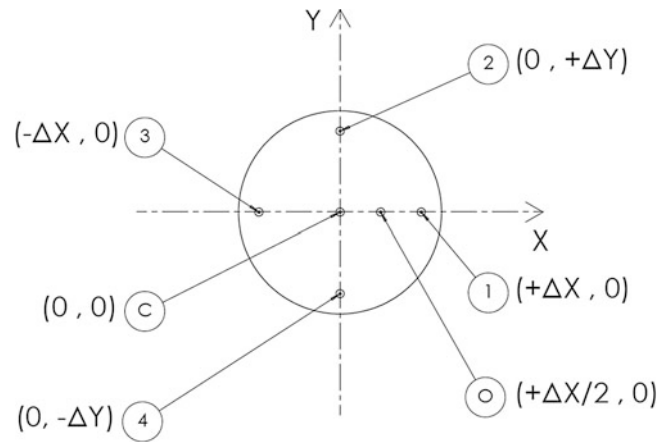


**Fig. 21.4** Soundpost locations



**Fig. 21.5** Soundpost position measuring

location of the soundpost in the different configurations, shown in Fig. 21.4, is expected to have the following effects on the instrument:

- C (0, 0): reference point for the manufacturer;
- (+ $\Delta X/2$ , 0): optimal point for instrument performance;
- 1 (+ $\Delta X$ , 0): increment of soundpost stress (due to minor space between the two plates), with a perceived sound more intense toward acute strings (E and A strings);
- 2 (0, + $\Delta Y$ ): the perceived sound is less loud, with an effect that might result closer to the vowel “U” (International Phonetic Alphabet: u);
- 3 ( $-\Delta X$ , 0): decrement of soundpost stress (due to major space between the two plates), with a perceived sound more intense toward lower-frequency strings (D and G strings). Usually this configuration is not adopted, since it increases the bass bar effect;
- 4 (0,  $-\Delta Y$ ): louder sound, with a perceived effect usually compared to a “more open” sound, close to the open vowel “A” (International Phonetic Alphabet: a).

### 21.3 Identification of Modal Properties and Configuration Comparison

For all the analysed configurations, the identifications were performed on the frequency range 0 ÷ 1024 Hz, using PolyMAX algorithm [15]. In the reference configuration, i.e. the Centre configuration, 59 modes were identified (Table 21.2).

To compare the mode shapes, the well-known Modal Assurance Criterion (MAC) is adopted. It is defined as the normalised scalar product between two modes  $j$ , and  $k$ ; hence it results equal to 100% if two modes are parallel, while it reaches 0% if they are orthogonal:

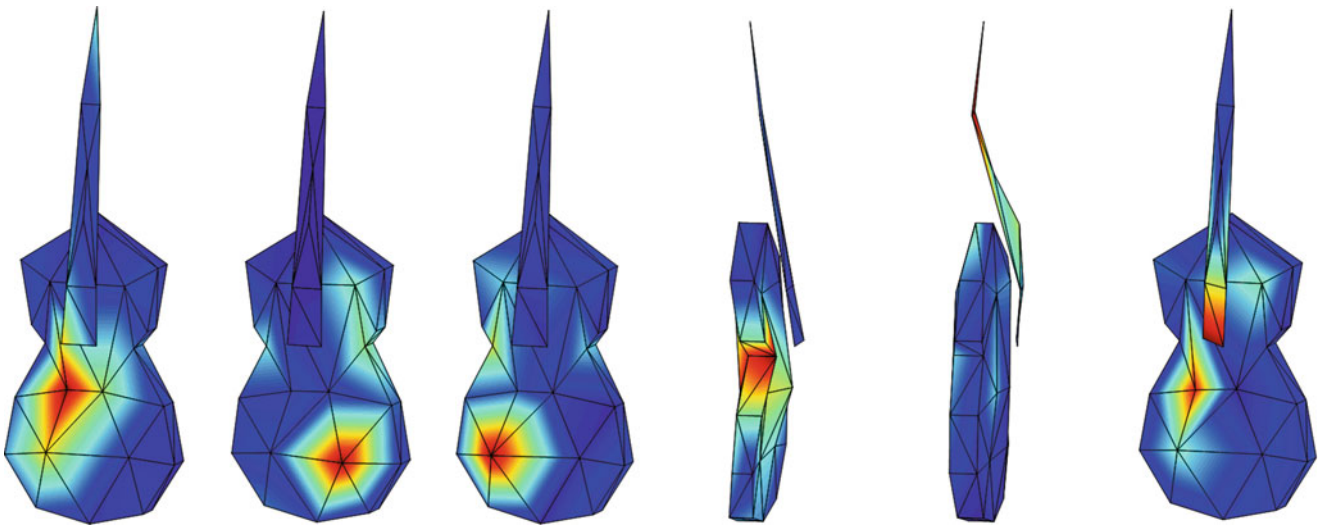
$$MAC_{j,k} = \frac{[\boldsymbol{\varphi}_j^T \boldsymbol{\varphi}_k]^2}{[\boldsymbol{\varphi}_j^T \boldsymbol{\varphi}_j][\boldsymbol{\varphi}_k^T \boldsymbol{\varphi}_k]} \quad (21.1)$$

The Auto-MAC matrix shown in Fig. 21.7, hence the comparison between the family of modes of the same configuration, proves that the mode shapes are quite orthogonal and the synthesized FRFs (Fig. 21.8) results quite near to the experimental ones. Therefore, the dynamics behaviour of the violin is well represented with this set of mode shapes.

In this work, we focus our attention only on the “Signature” mode shapes and their tracking between the configurations. In particular, six “Signature” mode shapes are detected (bold in Table 21.2). Modes 25 and 26 are respectively the breathing of right and left bottom lung of top plate (Fig. 21.6 2–3). Modes 28 and 44 are two bending modes, including also the fingerboard, on  $x$ - $z$  plane (Fig. 21.6 4–5). Modes 15 and 49 could be considered as two torsional mode shapes (Fig. 21.6 1 and 6). The former involves mainly the zone of the violin bridge and the C-rib, while the latter is the torsional mode of the

**Table 21.2** Experimental identified modes conf. Centre

Mode	Freq. [Hz]	$\zeta$ [%]	Mode	Freq. [Hz]	$\zeta$ [%]	Mode	Freq. [Hz]	$\zeta$ [%]
1	0.75	0.08	23	319.55	1.90	45	686.65	0.81
2	0.75	0.01	24	342.26	2.97	46	702.23	1.18
3	0.75	0.07	<b>25</b>	<b>352.57</b>	<b>3.37</b>	47	715.23	1.41
4	2.24	0.02	<b>26</b>	<b>366.64</b>	<b>0.17</b>	48	720.35	1.08
5	2.98	0.02	27	393.21	3.36	<b>49</b>	<b>733.92</b>	<b>0.19</b>
6	6.75	0.09	<b>28</b>	<b>423.33</b>	<b>2.16</b>	50	737.45	0.21
7	71.14	22.04	29	445.69	7.54	51	740.03	1.98
8	92.98	7.01	30	461.78	1.78	52	755.45	1.53
9	99.52	2.86	31	469.88	2.35	53	798.12	2.47
10	125.23	7.36	32	490.15	2.38	54	807.95	2.85
11	136.37	0.86	33	506.57	2.44	55	827.00	1.92
12	152.29	0.90	34	521.27	1.97	56	856.72	2.74
13	158.02	2.97	35	527.36	3.27	57	868.64	0.16
14	162.32	5.97	36	536.53	1.99	58	870.81	0.08
<b>15</b>	<b>182.91</b>	<b>0.05</b>	37	551.40	0.09	59	876.11	0.09
16	204.72	0.76	38	582.21	0.11	60	893.84	1.11
17	245.57	0.79	39	598.87	1.86	61	918.74	0.16
18	269.05	2.96	40	620.23	1.29	62	920.25	3.41
19	276.88	2.03	41	645.69	0.52	63	950.13	2.55
20	282.87	3.91	42	658.17	1.61	64	971.92	1.48
21	291.17	0.37	43	677.29	4.08	65	995.66	2.38
22	313.24	3.44	<b>44</b>	<b>682.68</b>	<b>1.30</b>			

**Fig. 21.6** Experimental “Signature” modes (from left to right): (15)  $f_n=183$  Hz; (25)  $f_n=353$  Hz; (26)  $f_n=367$  Hz; (28)  $f_n=423$  Hz; (44)  $f_n=683$  Hz; (49)  $f_n=734$  Hz

whole structure, including the fingerboard. Mode 49 is found close to the bridge ‘squat’ mode (i.e. 710 Hz), which is related to non-linear bridge behaviour [16].

The Auto-MAC of the Centre configuration is shown in Fig. 21.7. Some  $2 \times 2$  pattern along the diagonal are observable. They are the results of very similar mode shapes with different local behaviour. In particular, several modes involving the top and back plates are highly correlated.

In Fig. 21.8 the auto-inertance of the node corresponding to the right bottom lung of the top plate is shown. The frequencies related to the “Signature” modes are highlighted with coloured vertical lines.

The major peak for the experimental FRF at 350 Hz corresponds to the second “Signature” mode. The synthesized dash-dot red curve is obtained through:

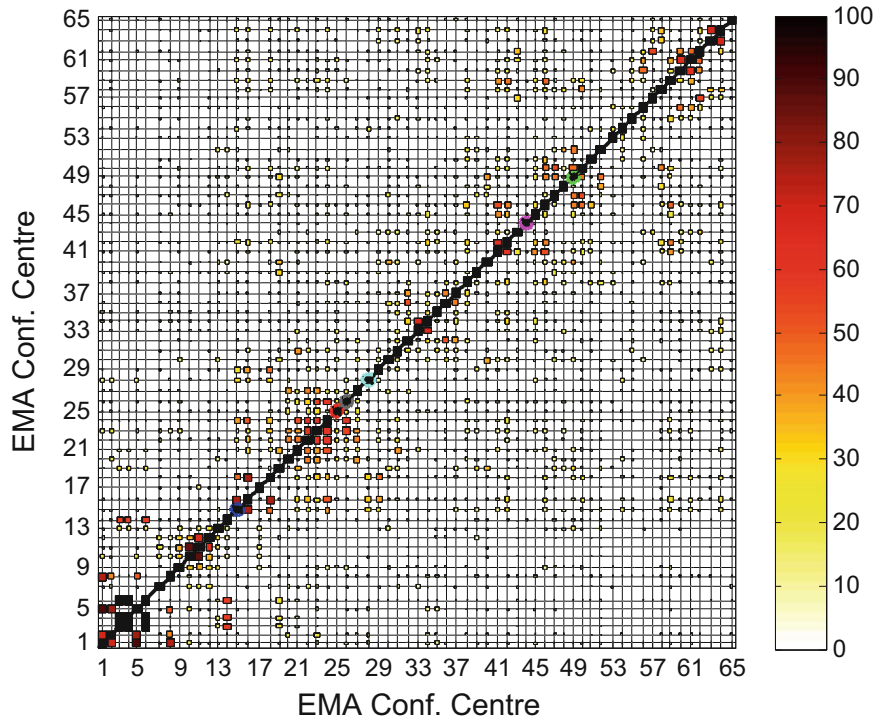


Fig. 21.7 Experimental mode shapes Auto-MAC

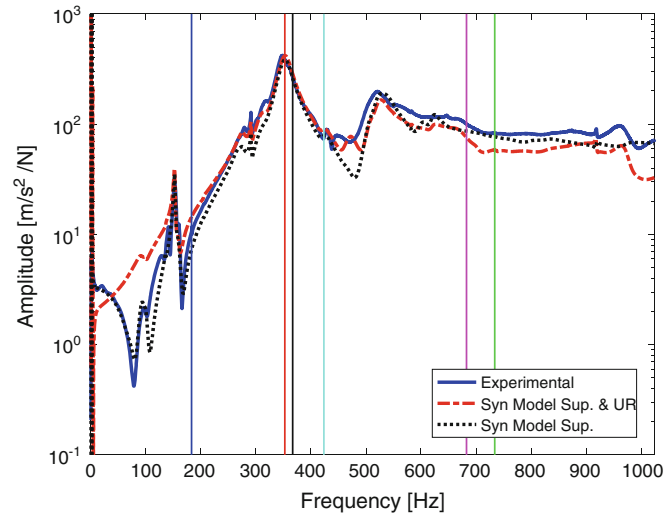
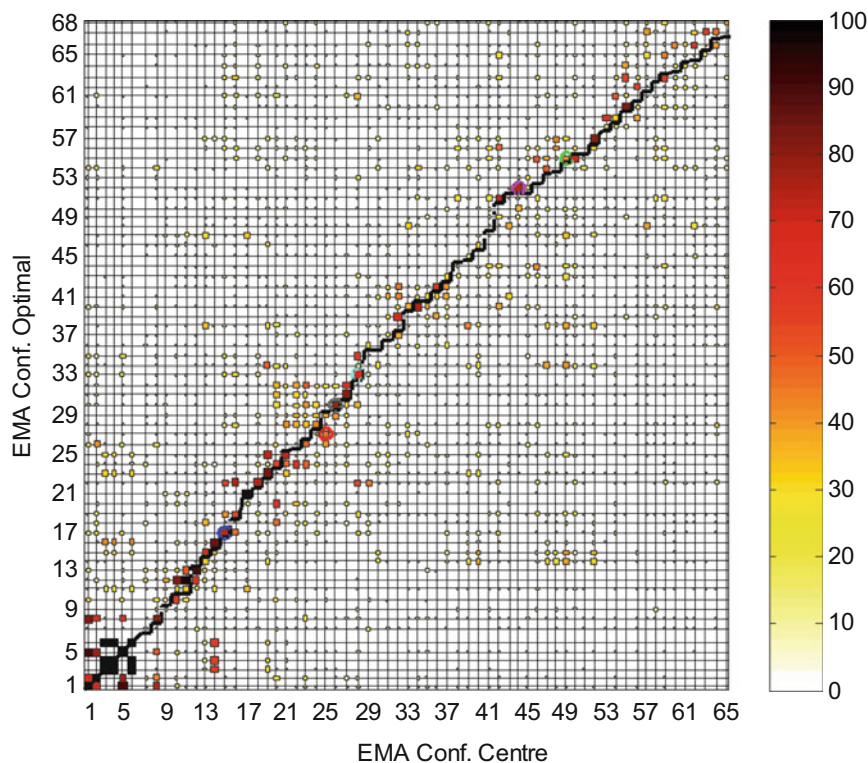


Fig. 21.8 Auto-inertance right bottom lung on front plate

$$A_{j,k}(\omega) = \frac{\ddot{x}_j(\omega)}{F_k(\omega)} = -\omega^2 \frac{x_j(\omega)}{F_k(\omega)} = \sum_{r=1}^n \frac{-\omega^2 \phi_j^{(r)} \phi_k^{(r)}}{(\omega_r^2 + 2i\zeta_r \omega_r \omega - \omega^2)} - [LR] + \omega^2 [UR] \quad (21.2)$$

where  $[LR]$  and  $[UR]$  are respectively lower and the upper residuals [15]. The dot-dot black line was obtained using the same Eq. (21.2), but neglecting terms related to the residuals. This last curve is obtained coupling the modal superposition with the rigid body modes of the violin, this lets to fit, at low frequency, the synthesized FRF with the experimental one.

The identification of modal parameters extraction was performed also on the other configurations.



**Fig. 21.9** MAC Centre vs Optimal

For all other configurations 59 mode shapes are identified, except for conf. Optimal in which 68 modes were detected. As example the MAC between configurations Centre and Optimal is presented in Fig. 21.9. The presence of a marked diagonal indicates that the two configurations are not too much different. Most of the modes are correlated very well, especially the six “Signature” mode shapes.

In Fig. 21.10 a MAC detail focusing only on these “Signature” modes is presented. It is possible to see a stiffer behaviour of the Optimal configuration with respect to the Centre one for five of the six “Signature” modes. The breathing mode of right bottom lung on the top plane presents a low MAC value; this is a confirmation that the soundpost has a relevant effect in the structural vibroacoustic behaviour of the instrument.

Figure 21.11 shows the experimental inertances of right bottom lungs on top plate for all six analysed configurations. The vertical thick coloured lines indicate the natural frequencies of the six “Signature” modes detected in the configuration corresponding to the central position of soundpost, while the rectangular areas represent the “Signature” natural frequencies variation ranges among the six configurations. The soundpost seems not to have any visible effect on the experimental FRF up to 400 Hz, especially for the peaks of the first two “Signature” modes. At higher frequency the response of the violin is quite different.

The extracted “Signature” mode shapes of the six configurations are compared in Fig. 21.12. The mode shapes of each configuration are grouped in relation to their behaviour and compared. The correlation inside the group is quite high for the first three “Signature” mode shapes and slightly lower for higher frequencies mode shapes. The correlation outside the group is very low, as expected. The fourth “Signature” mode, namely the bending mode in the longitudinal plane, presents an evident correlation with the bridge torsional mode and the breathing mode of right bottom lung on top plate.

The trend of natural frequencies along  $x$  direction of soundpost positions (Fig. 21.13) seems to have a common behaviour: for horizontal movements of the soundpost the frequency decreases from left (conf. 3) to the centre; while, moving to the optimal one, it increases for five of the six “Signature” modes. Instead, in the  $y$  direction, no particular trends were detected.

Figure 21.14 shows the trend of damping ratios. For each “Signature” mode the damping ratio changes within a range of 0.2–2%. A decrement in damping ratio involves five of the six “Signature” modes, when the soundpost is moved from the central position to the optimal one. This can be correlated with an improvement in the acoustic power of the instrument.

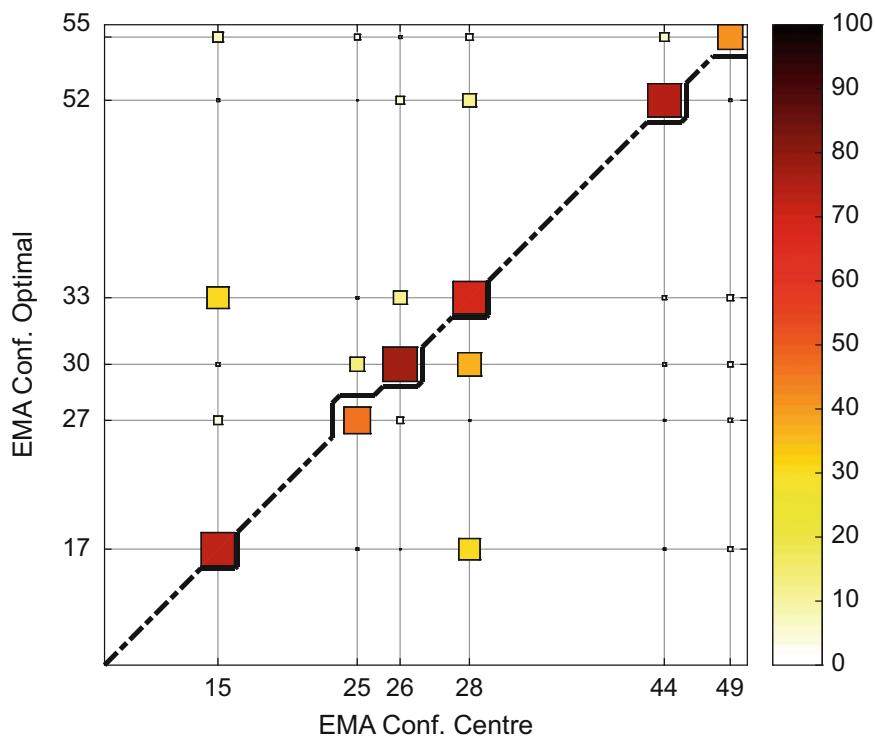


Fig. 21.10 “Signature” modes MAC detail Centre vs Optimal

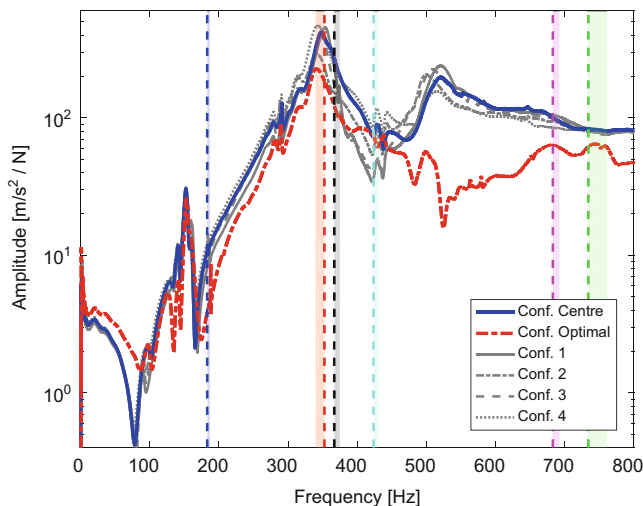


Fig. 21.11 Comparison auto-inertances of inferior right lungs on top plate

### 21.4 Conclusion

A parametric experimental modal analysis was performed on a Guarneri del Gesù violin. The parameter taken in consideration was the position of the soundpost, to evaluate its effect on the vibrational properties of the analysed system. Six different configurations, with different locations of the soundpost, were investigated. The adjustment of the soundpost position is very important for the acoustic performance of the instrument. Each player prefers a slightly different position of the soundpost for best exploit the instrument performances.

Six “Signature” modes of the violin have been identified in each configuration and compared, in order to understand the effect of the soundpost position of the instrument modal behaviour.

Some considerations result:

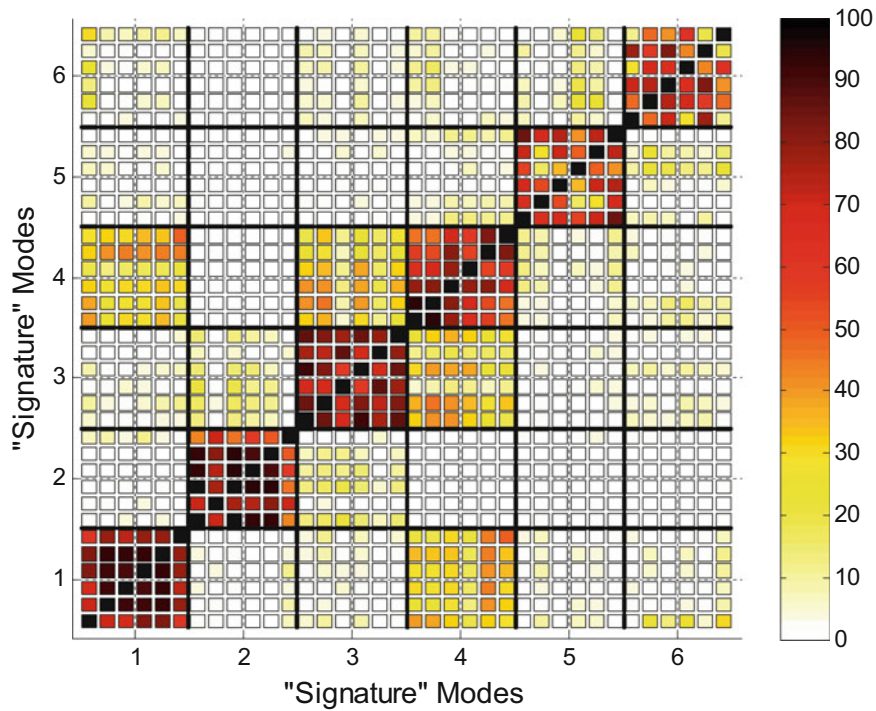


Fig. 21.12 MAC between experimental “Signature” mode shapes groups

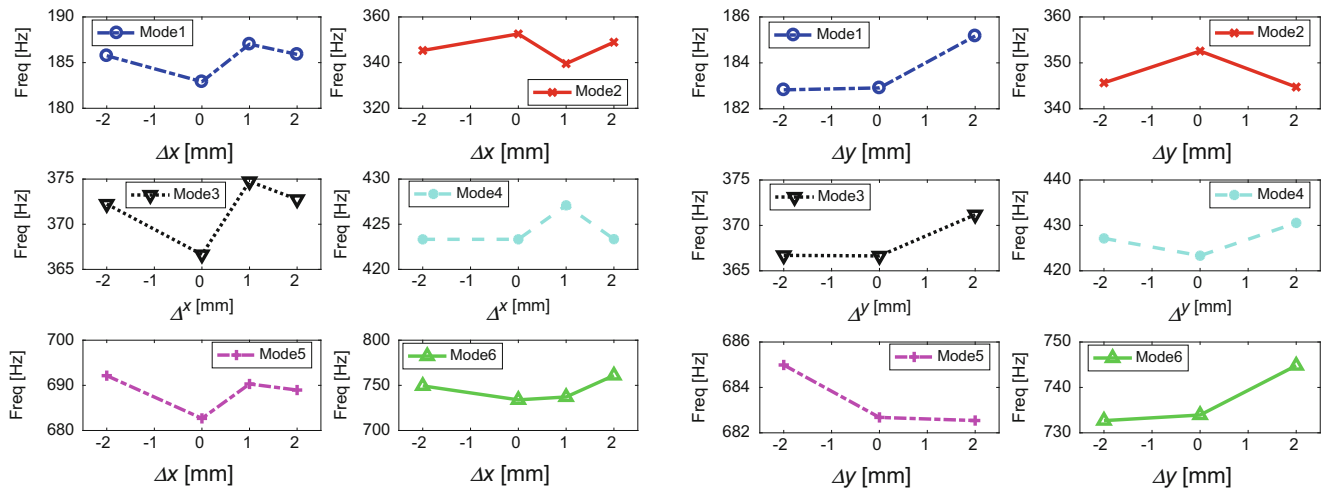


Fig. 21.13 Frequency trend in x (left) and y (right) directions

- the natural frequencies increase when the soundpost is in the optimal position,
- the damping is the lowest in the optimal position.

Both these considerations are coherent with the players’ opinion, considering the “optimal” configuration the best for the instrument performances.

The optimal configuration results as the one in which the natural frequencies of the “Signature” modes are the closest to the standard music note frequencies; their correlation is shown in Table 21.3. The most interesting fact is that the frequencies related to E and F notes are the most recurring. These frequencies are close, as lower octave harmonics, to the one known as “bridge hill” (being a broad peak response of good violins in the vicinity of 2.5 kHz) [17].

It is important to stress here the fact that the violin player requirements depend on their perception, thus, further psychoacoustic considerations should be integrated in a final step, based on this research.

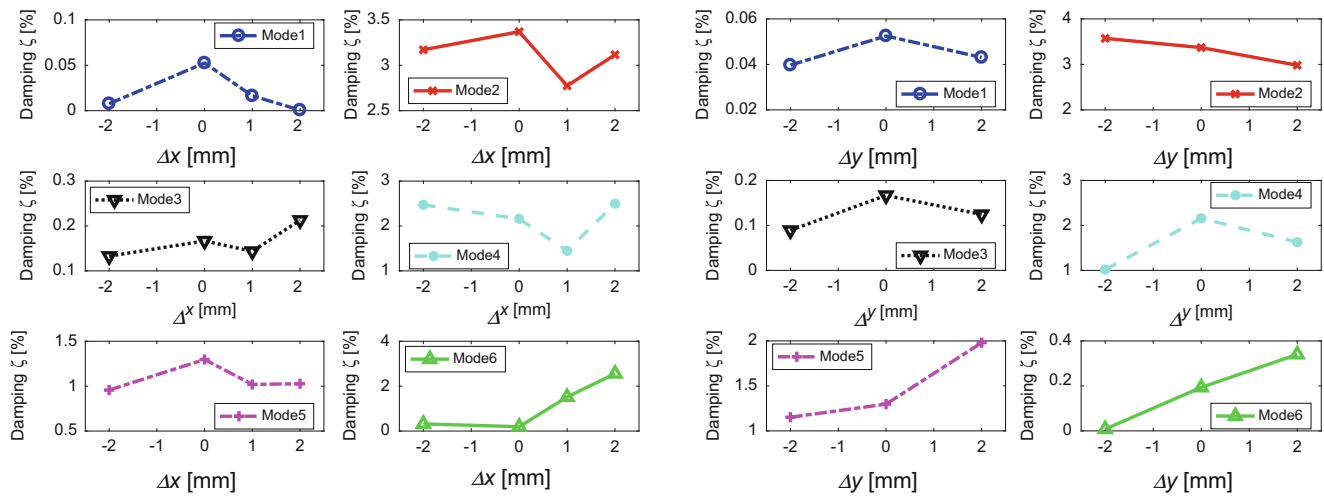


**Fig. 21.14** Damping trend in x (left) and y (right) directions

**Table 21.3** “Signature” mode shapes conf. Optimal and notes frequencies correlation

Mode	Frequency [Hz]	Note	Standard frequency [Hz]
17	187.03	F#3	185
27	339.55	E4 – F4	330–349
30	374.74	F#4	370
33	427.00	A4	440
52	690.78	F5	698
55	738.08	F#5	740

A numerical model of the violin, considering the involved material orthotropy, is ongoing. The present work will let to validate the numerical model and perform much more accurate parametric analysis to better understand the common trend of the modal parameters changing the soundpost location and to relate them with the acoustic performance through an objective law.

A validated parametric model of the violin could become a very useful engineering tool to predict the best soundpost location in order to shift the “Signature” modes natural frequency as much as possible close to the standard note frequencies.

**Acknowledgements** The authors wish to acknowledge the technical and experienced support provided by Simone Geroso from LMS-Siemens industry; Kistler for the additional hardware provided and Enzo Cena (president, Accademia Liuteria Piemontese “S. Filippo”, Turin). Enzo suggestions, combined with his wealth of experience concerning violins, have been extensively useful to understand the violin behaviour.

## References

- Bissinger, G., Oliver, D.: 3-D laser vibrometry on legendary old Italian violins. *Sound Vib.* **41**, 10–14 (2007)
- Schleske, M.: Eigenmodes of vibration in the working process of a violin. *Catgut Acoust. Soc. J.* **3**(1), 2–8 (1996)
- Woodhouse, J.: Body vibration of the violin – what can a maker expert to control. *Catgut Acoust. Soc. J.* **4**(5), 43–49 (2002)
- Schelleng, J.C.: The action of the soundpost. *Catgut Acoust. Soc. Newsl.* **16**, 11–15 (1971)
- Bissinger, G.: The influence of the soundpost on the mechanical motions of the violin. In: *Proceedings of the 12th IMAC*, pp. 294–300. Bethel (1994)
- Bissinger, G.: Some mechanical and acoustical consequences of the violin soundpost. *J. Acoust. Soc. Am.* **97**(5), 3154–3164 (1995)
- Marshall, K.D.: Modal analysis of a violin. *J. Acoust. Soc. Am.* **77**(2), 695–709 (1985)
- Bissinger, G.: Structural acoustics of good and bad violins. *J. Acoust. Soc. Am.* **124**(3), 1764–1773 (2008)
- Zhang, A., Woodhouse, J., Stoppani, G.: Motion of the cello bridge. *J. Acoust. Soc. Am.* **140**(4), 2636–2645 (2016)
- Gough, C.E.: The violin: Chladni patterns, plates, shells and sounds. *Eur. Phys. J. Spec. Top.* **145**, 77–101 (2007)
- Lu Y.: Comparison of finite element method and modal analysis of violin top plate. PhD Thesis, Schulich School of Music, McGill University, Montreal, Canada (2013)
- Gough, C.E.: Measurement, modelling and synthesis of violin vibrato sounds. *Acta Acustica United with Acustica.* **92**(2), 229–240 (2005)
- Gough, C.E.: Violin acoustics. *Acoust. Today.* **12**(2), 22–30 (2016)
- <http://acousticstoday.org/supplementary-text-violinacoustics-colin-e-gough/>



15. Peeters, B., Van der Auweraer, H., Guillaume, P., Leuridan, J.: The PolyMAX frequency-domain method: a new standard for modal parameter estimation? *Shock. Vib.* **11**, 395–409 (2004)
16. Bissinger, G.: The violin bridge as filter. *J. Acoust. Soc. Am.* 482–491 (2006)
17. Woodhouse, J.: On the bridge hill of the violin. *Acta Acustica United with Acustica.* **91**(1), 155–165 (2005)



# Chapter 22

## Influence of the Harmonics on the Modal Behavior of Wind Turbine Drivetrains

N. Gioia, P. J. Daems, C. Peeters, M. El-Kafafy, P. Guillaume, and J. Helsen

**Abstract** In the last decades, noise, vibration and harshness (NVH) problems became critical issues to be tackled by the wind industry. They have been caused by the upscaling trend that has imposed bigger (not quasi-static) loads on turbine subcomponents: the dynamic loads are significantly influencing the fatigue life of the wind turbine components and the tonalities generated. To validate complex simulation models, it is of high interest to continuously track the modal parameters of the fundamental modes of a wind turbine during operating conditions. At this purpose, operational modal analysis (OMA) represents a powerful tool.

The work investigates and implements a completely automated OMA technique for continuously tracking the modes of a wind turbine drive train under normal operating conditions. The methodologies implemented are illustrated using data acquired during a long-term monitoring campaign of an offshore wind turbine. Modal estimation is based on the state-of-the-art pLSCF algorithm. To make it suitable for continuous analysis, the algorithm is improved by eliminating all the human interactions required. The procedure is then coupled with a method that automatically tracks the modal parameters along different data sets. Since this work focuses on the application of OMA on rotating machines, harmonics need to be dealt with. At this purpose, the use of a cepstrum lifter is analyzed and implemented. Modal estimates obtained from an automated analysis on stand still data and rotating turbine data are compared. The data coming from the rotating machine are pre-processed by means of a cepstrum-based procedure. It is shown that the automatic procedure is able to detect modes close to narrow harmonic components, while it still fails in case of broader harmonics. The cepstrum lifter is able to properly filter out also the harmonics influencing broader frequency bands, making OMA possible on the complete frequency band of interest.

**Keywords** Automatic Operational Modal Analysis · Harmonics · Cepstrum Analysis · Rotating Machineries · Wind Turbine Drivetrain

### Nomenclature

MAC      Modal Assurance Criterion  
OMA      Operational Modal Analysis  
p-LSFD   Poly-Reference Least\_Squares Frequency-Domain estimator

### 22.1 Introduction

One of the main design issues in the field of rotating machineries is the susceptibility of the structures to vibrations and the generation of tonalities. Therefore, design values such as the modal parameters (i.e. eigenfrequencies, damping ratios, mode shapes and modal scaling factors) are fundamental for the design. The experimental verification of these parameters

---

N. Gioia (✉) · P. J. Daems · C. Peeters · P. Guillaume · J. Helsen  
Vrije Universiteit Brussel (VUB), Brussel, Belgium  
e-mail: [ngioia@vub.be](mailto:ngioia@vub.be)

M. El-Kafafy  
Vrije Universiteit Brussel (VUB), Brussel, Belgium  
Helwan University, Cairo, Egypt

is essential for model validation and for guaranteeing the safety and reliability of the structure [1]. Since damping and boundary conditions depend on the vibrations amplitude and the modal parameters depend on the (rotating) speed of the structure or the parts, it is important to experimentally verify the design values in normal operating conditions, i.e. around the operating point. At this purpose, Operational Modal Analysis (OMA) represents a powerful tool: it allows to extract the modal parameters from the dynamic response of the structure to unmeasured operational forces. However, this method is based on several assumptions which are not always fulfilled in case of rotating machineries. This is the main reason why new techniques need to be explored. One of the key issues affecting the application of OMA on rotating machineries is the presence of harmonics: the lack of insights in the system force input makes the results of the parameters estimation sensitive to the excitation acting on the structure. Indeed, if the input is not a white noise signal, the output of the parameter estimation is a combination of structural modes and components already present into the input signal (e.g. harmonics), giving erroneous results [2, 3].

This topic is particularly interesting for wind energy application. Wind turbines operate in extreme environments that result in highly variable operating conditions that induce important mechanical stresses on the main components. Moreover, the so-called upscaling trend (the increase of the size of the turbines to produce more energy and in a more efficient way) registered in the last years has caused a significant increase of the loads acting on the different components of the machines, causing premature component failures and a not complete understanding of the dynamics of the machine [4]. It is in this context that the extraction of the modal parameters from the operating turbines becomes significantly important. The industrial design process currently implemented comprises component-level-testing and full-scale machine testing both in laboratory environments and in the field. These tests are generally performed over short periods trying to catch specific operating conditions to be tested. What is missing is a continuous insight into the behavior of the machines during their overall lifetime and under each operating condition [5]. The lack of information concerning the behaviour of the machines under every possible operating condition does not allow the solution of the previously explained problems causing not efficiently optimized machines and higher operational and maintenance costs. The industry could then move towards a new kind of designing process where the decisions on how to improve the models are taken based on what can be learnt from the information acquired on several machines that are already operating to catch every possible operating condition. What is needed to achieve this objective is an automatic algorithm that is able to continuously process a stream of data.

The research focusses on the identification of the modal parameters of the wind turbine drivetrain, one of the main important and critical components of the machine. The work performed aims then to deal with the problem of harmonics. At this purpose, a pre-processing methodology extensively described in literature for reducing the influence of the harmonics from the vibration data has been investigated and implemented: the use of a cepstrum-based time domain signal editing procedure. Both the pre-processing step and the OMA algorithms has been improved in order to make them completely automatic and allow the continuous analysis of a stream of data. The methodology implemented has been tested on real vibration data coming from an operating off-shore wind turbine.

## 22.2 Theoretical Background

### 22.2.1 Poly Least Square Complex Frequency Domain Estimator

The Poly-reference Least-Square Complex Frequency-Domain (p-LSCF) method consists is a frequency-domain Modal analysis method that requires as primary data the output spectra of the system under analysis [6]. This method is based on the assumption that the excitation to the system is a white noise spectrum signal. Under this assumption is indeed possible to model the output spectra exactly in the same way used for the frequency response functions (FRFs)  $H(\omega)$ :

$$H(\omega) = \sum_{i=1}^n \frac{\{v_i\} \langle l_i^T \rangle}{j\omega - \lambda_i} + \frac{\{v_i^*\} \langle l_i^H \rangle}{j\omega - \lambda_i^*} \quad (22.1)$$

Where  $n$  is the number of complex conjugate mode pairs,  $*$  is the complex conjugate operator,  $T$  is the transpose of a matrix,  $H$  is the complex conjugate transpose (Hermitian) of a matrix,  $\{v_i\}$  is the mode shape vector of the mode  $i$ ,  $\langle l_i^T \rangle$  the modal participation factors of the mode  $i$  and  $\lambda_i$  are the poles of the system (occurring in complex conjugate pairs). The poles are linked to the resonance frequencies and the damping ratios of the system by means of the following relation:

$$\lambda_i, \lambda_i^* = -\xi_i \omega_i \pm j \sqrt{1 - \xi_i^2} \omega_i \quad (22.2)$$

The relationship between the input spectra  $[S_{UU}(\omega)]$  and the output spectra  $[S_{yy}(\omega)]$  of a system represented by the FRF  $H(\omega)$  is described by:

$$[S_{yy}] = [H(\omega)] [S_{UU}(\omega)] [H(\omega)]^H \quad (22.3)$$

In case of output-only analysis, the auto-spectra are the only available information. The most important consequence of assuming the input signal as a white noise excitation is that the power spectrum of the input signal is constant; therefore  $S_{UU}(\omega) = S_{UU}$  [6]. Considering this assumption and combining Eqs. (22.1) and (22.3) it is possible to write the modal decomposition of the output spectrum matrix as following:

$$S_{yy}(\omega) = \sum_{i=1}^n \frac{\{v_i\} \langle g_i \rangle}{j\omega - \lambda_i} + \frac{\{v_i^*\} \langle g_i^* \rangle}{j\omega - \lambda_i^*} + \frac{\{g_i\} \langle v_i \rangle}{-j\omega - \lambda_i} + \frac{\{g_i^*\} \langle v_i^* \rangle}{j\omega - \lambda_i^*} \quad (22.4)$$

Where  $g_i$  are the operational reference factors, which replace the participation factors in case of output-only analysis. A right matrix model (Eq. 22.5) is then used to fit the measured FRFs data. The use of the right matrix model as parametric model has the advantage that the participation factors are available when constructing the stabilization diagram, thus a clearer stabilization diagram is generated, on which closely spaced modes are separated.

$$[H(\omega)] = [B(\omega)] [A(\omega)]^{-1} \quad (22.5)$$

Where  $H(\omega) \in \mathbb{C}^{l \times m}$  is the FRF matrix containing the FRFs between all  $m$  inputs and all  $l$  outputs,  $B(\omega) \in \mathbb{C}^{l \times m}$  is the numerator matrix polynomial and  $A(\omega) \in \mathbb{C}^{m \times m}$  is the denominator matrix polynomial.

The results of the fitting of the measured FRFs data by means of a parametric model, are represented in the *stabilization diagram* [7]. The measured FRFs data are fitted with increasing model order models and the poles estimated for a certain model order are compared to the poles estimated for the lower model order. If their differences are within pre-set limits, the pole is labelled as stable one. The spurious numerical modes will not stabilize at all during this iteration procedure and they can be then easily sorted out of the modal parameter estimates. The stabilization diagram shows how the poles stabilize for increasing model orders and it allows the analyst to distinguish the physical modes from the spurious ones.

### 22.2.2 Cepstrum Analysis for Operational Modal Analysis

During this research cepstrum analysis has been used to reduce the influence of the harmonics from the output data. Cepstrum analysis has been defined for the first time [8] as the ‘‘Power spectrum of the logarithm of the power spectrum’’, and originally it has been used for detection of echoes in seismic analysis or for speech analysis. The original formulation of the (power) cepstrum was:

$$C_p(\tau) = |\mathfrak{J} \{ \log(F_{xx}(f)) \}|^2 \quad (22.6)$$

With the advent of the Fast Fourier Transform (FFT) a new type of cepstrum has been obtained: by retaining the phase in all the operations, the ‘‘complex cepstrum’’ (4.2) has been defined as the inverse Fourier transform of the complex logarithm of the complex spectrum [9]. This new definition of cepstrum was thus reversible to the time domain.

$$C_c(\tau) = \mathfrak{J}^{-1} \{ \log(F_{xx}(f)) \} = \mathfrak{J}^{-1} \{ \ln(A(f)) + j\phi(f) \} \quad (22.7)$$

By setting the phase to zero in the Eq. 4.2, the formulation of the real cepstrum has been obtained:

$$C_r(\tau) = \mathfrak{J}^{-1} \{ \ln(A(f)) \} \quad (22.8)$$

The possibility of coming back to the time domain showed the cepstrum analysis as a powerful tool for editing signals in the time domain. Especially after that it has been realized that there are many situations in which the editing can be carried out by modifying the amplitude only, thus using the real cepstrum: the modified amplitude spectrum can be combined with the original phase spectrum to generate the edited time-domain signal.

The application of this time-domain signal editing procedure in OMA application finds its reason in the fact that the information about all the modes are concentrated at low quefrequency [9]. Applying a short-pass lifter (an exponential window on the real cepstrum) greatly enhances the modal information with respect to anything else: it allows to remove all the components at higher quefrequencies keeping the modal information of the signal. The only distortion introduced at lower quefrequency (thus on the interesting part of the signal) is the addition of a known amount of damping, that can be easily removed from the damping value estimated by an OMA procedure by means of the following equation:

$$\xi_r = \xi_m - \frac{1}{2\pi f_r \tau} \quad (22.9)$$

where, for each estimated mode,  $\xi_r$  is the real damping [%],  $\xi_m$  is the measured damping [%],  $f_r$  is the real frequency [Hz] and  $\tau$  is the time constant of the exponential window [s].

The cepstrum lifter has been applied on a signal on which speed correction has been performed: a virtual resampling of the signal allows to switch from time domain (samples every  $\Delta t$  seconds) to the angular domain (samples every  $\Delta\theta$ ), reducing the effects of the speed fluctuation and narrowing the frequency band excited by the harmonics.

## 22.3 Methodology

The two procedures described have been combined in order to be able to automatically apply OMA on a stream of vibration data coming from rotating machines.

To make the Poly-Reference Least-Square Frequency-Domain (p-LSFD) estimator automatic, the main algorithm-analyst interaction has been eliminated by substituting the classical stabilization diagram [10] with a clustering method that autonomously interprets the information collected in the stabilization diagram. In this work a clustering analysis has been used in order to group the poles showing stable characteristics (i.e. representative of the same mode). The physical modes have been then selected automatically exploiting statistical characteristics of the generated clusters (Fig. 22.1).

The algorithm used to obtain the modal model from one data set has been then coupled with an automatic tracking algorithm [11]. The latter automatically tracks the estimates of the modal parameters extracted from different data sets, allowing the analysis of the modal behavior evolution over longer periods. The algorithm compares the modal parameters estimated from a generic record to the modes set of a reference record. The comparison will be made in terms of modal assurance criterion (MAC) and poles value. The MAC value measures how coherent is the estimated mode with respect to the reference one in terms of mode shapes, while the pole value indicates how close is the estimated mode to the reference one in terms of frequency and damping. First a subset of modes that show a cross MAC value (calculated with respect to the reference mode) higher than a threshold value imposed by the analyst is selected. Then the closest modes to the reference one in terms of frequency and damping are selected form this subset.

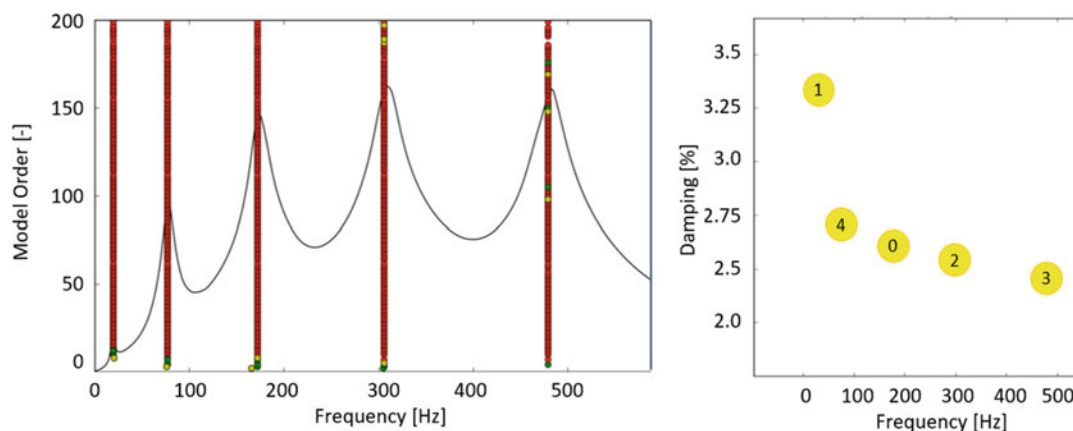


**Fig. 22.1** Classical stabilization diagram and corresponding results from clustering analysis (Data from the simulated response of a doubly supported beam used to validate the implemented procedure)

**Fig. 22.2** Effect of the application of the cepstrum lifter with different cut-off quefrequency values in correspondence of harmonics peaks in the spectrum (Axis values hidden for confidentiality reason)

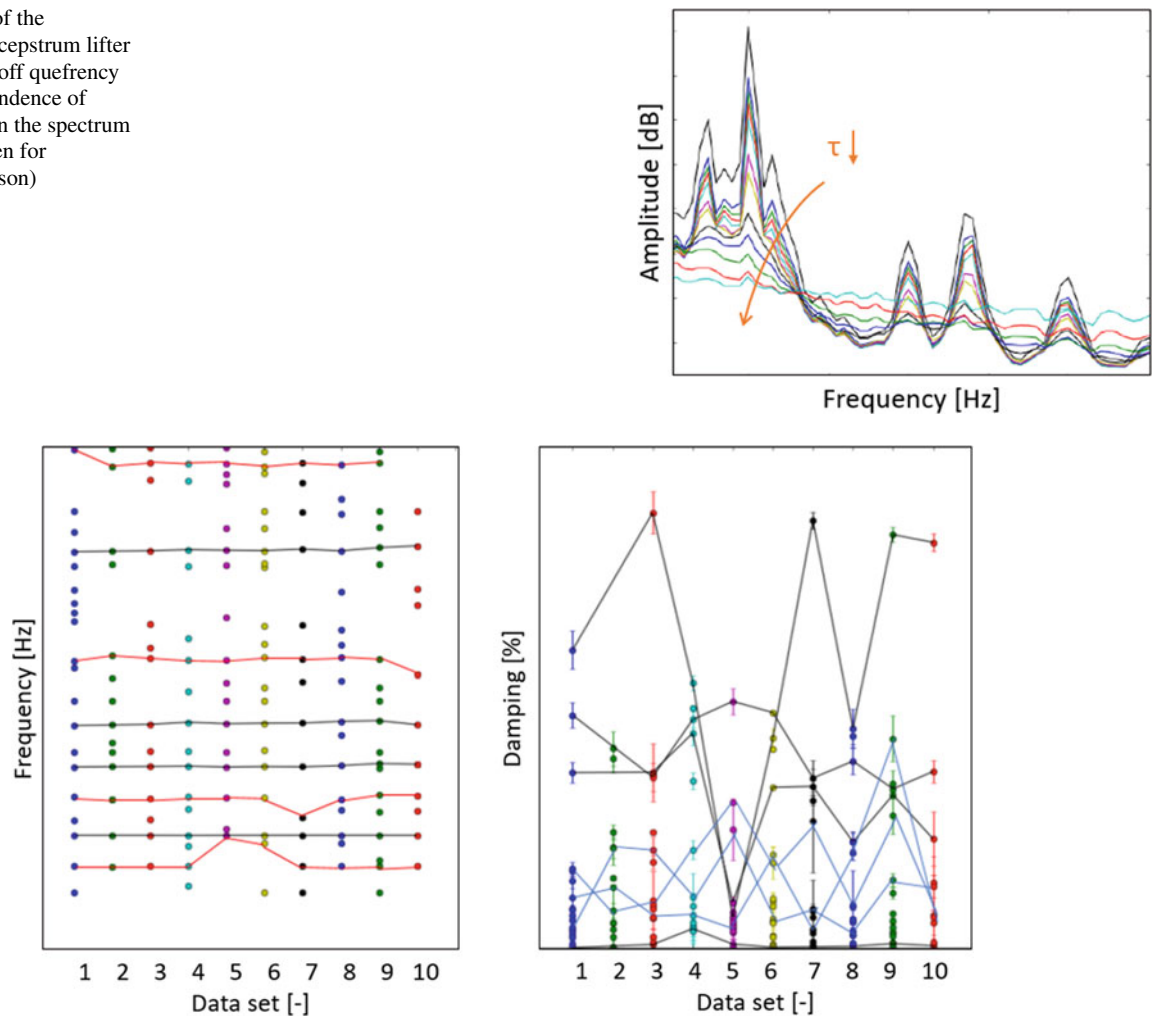


**Fig. 22.3** Results of the tracking procedure on stand still data (Axis values hidden for confidentiality reasons)

Secondly the use of the cepstrum analysis to reduce the influence of the harmonics in the output signals has been investigated and implemented. Since the methodology requires the definition of a parameter depending on the characteristics of the signal, an automatic method to define it has been implemented and coupled to the state-of-the-art algorithm. The required parameter is the cut-off quefrequency, i.e. the time constant of the exponential window applied in the quefrequency domain. The automatic selection of this value is based on the analysis of the effect of this signal editing procedure in the frequency bands identified as the ones containing the harmonic, particularly what is observed is the reduction of the energy consequent to the use of the lifter. In Fig. 22.2, the results for different values of this parameter ( $\tau$ ) are shown.

## 22.4 Results

The methodology described in the previous paragraph has been applied on vibration data coming from the drivetrain of an offshore wind turbine for which a long-term condition monitoring campaign has been performed.

In order to test the automatic tracking of the modal parameters, a subset of the measured data where the wind turbine is in stand still condition has been analyzed. The reason of choosing stand still data is to start analyzing the simplest case possible: in this condition the harmonics do not dominate the spectrum, thus the hypothesis on which OMA is based on are satisfied and modal parameter estimation can be done in a reliable way. Eleven consecutive data sets of 10 min each are selected from the acquired data sets, using as a discriminant the rotor speed that must be lower than a certain value. Within the data sets selected for the analysis, the signal with the lower rotational speed has been selected as reference for the tracking procedure.

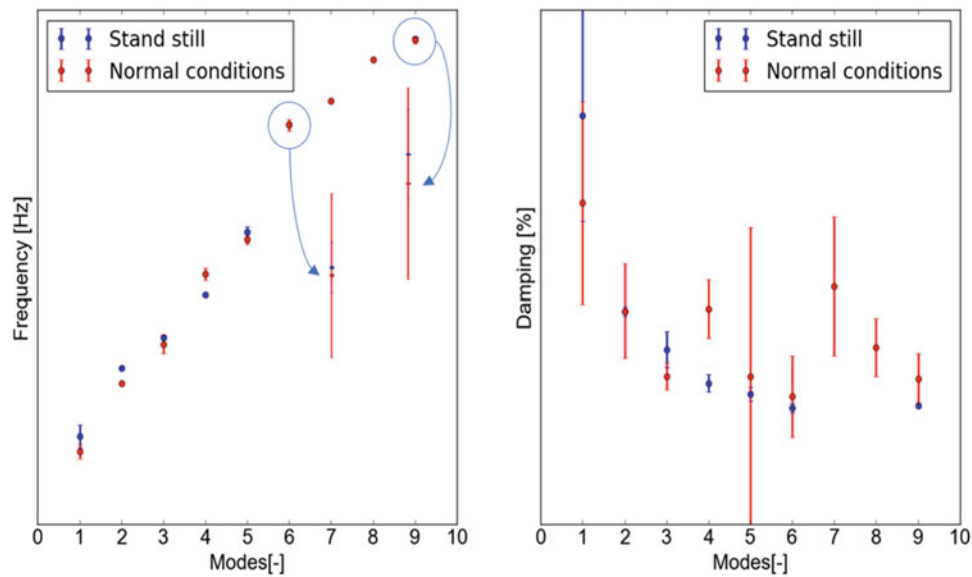


**Fig. 22.4** Comparison of the tracking procedure applied on data coming from the same machine acquired with the machine in stand still condition or in normal operating conditions (Axis values hidden for confidentiality reasons)

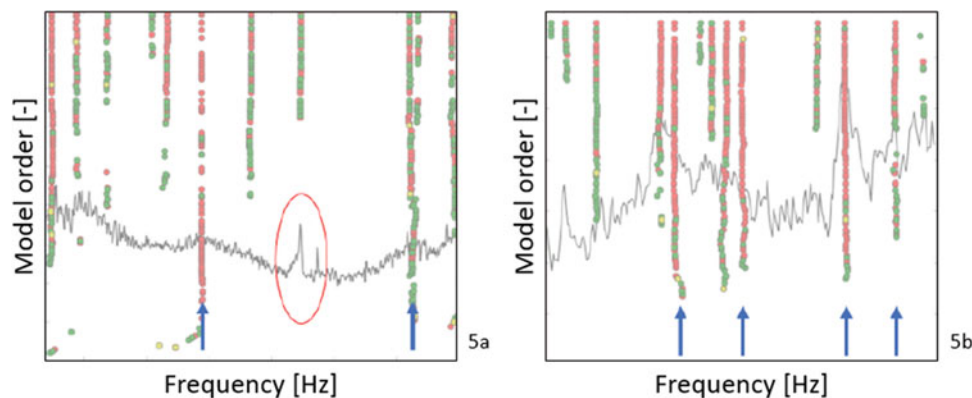


**Fig. 22.5** Stabilization diagram from stand still data (a) and from operational condition data edited by means of a cepstrum lifter (b) (Axis values hidden for confidentiality reasons)

The advantage of having the results from the stand still data is that they allow to have a term of comparison to assess the goodness of the use of the cepstrum lifter. The results of the modal parameters tracking procedure are shown in Fig. 22.3. The estimates in terms of frequency and damping are plotted (vertically aligned dots) for each data set (on the x-axis). On the top of the estimates, horizontal lines are plotted. They represent the result of the tracking procedure: each line touches the estimates that present consistent values along different data sets. It can be noticed that the damping values are less consistent than the frequency values, registering higher variability. This result is expected, since generally the damping value is a modal parameter highly affected by the ambient conditions [12].

Afterwards the cepstrum lifter has been used to pre-process 7 data sets coming from the turbine in normal operating conditions, i.e. when generating energy. The edited signals have been used as input for the automatic tracking algorithm in order to apply OMA on data from which the influence of the harmonics have been reduced.

A comparison has been performed between the results coming from the tracking procedure on stand still data and normal operating condition data. To do so the results of each tracking procedure have been processed in order to obtain punctual values and error bands of the modal parameters: for each estimate the average and the standard deviation have been calculated considering the values obtained for each data set. The result of this comparison in terms of both resonance frequencies and damping ratio is shown in Fig. 22.4.

From Fig. 22.4 it can be noticed that the results from the two different methodologies are comparable, showing the correctness of the Cepstrum analysis in pre-processing the data. It is interesting to notice that two modes, the numbers 7 and 8, show up only when normal operating condition data are used. Analyzing the classical stabilization diagram in the

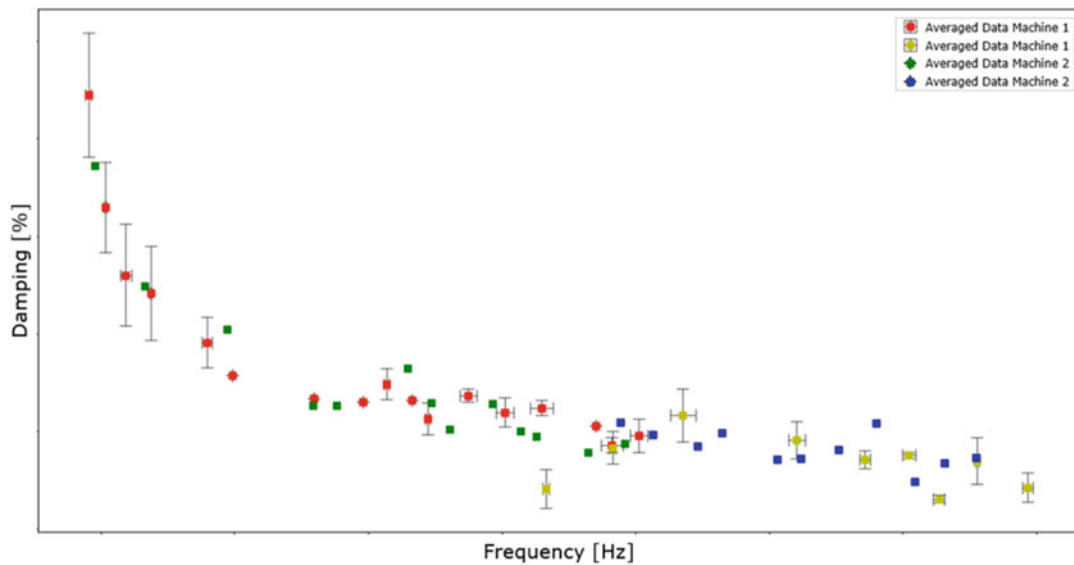


**Fig. 22.6** Collection of the results coming from different analysis performed on data sets acquired on different machines while operating in normal operating conditions. (Axis values hidden for confidentiality reasons)

frequency band of interest, it can be noticed that this is due to a presence of a harmonic (narrow and higher pick in Fig. 22.5a) that masks the modes around it. Indeed, in Fig. 22.5b it can be noticed that the harmonic has been filtered out by the use of the cepstrum analysis and two stable modes show up. These results show the correctness and the utility of the use of Cepstrum to clean the signal from the presence of the harmonics. Indeed, when the turbine is in stand still condition, the harmonics from the gearbox (generated by the shafts and the gears) are avoided, but other harmonics coming from the components in the nacelle can still be present. The use of the cepstrum lifter allows to avoid any presence of harmonics and to apply OMA on a broader frequency band and in a reliable way.

Once the validity of the proposed methodology is shown, several datasets coming from different machines have been analyzed, obtaining the results (in terms of natural frequencies and damping ratios) shown in Fig. 22.6. Again, the average values and the error bars have been calculated considering the values of the estimates coming from different data sets. The different colors of the dots represent the results of the analysis performed on data coming different machines in order to test the robustness of the method with respect to the input parameters.

The error bars on the frequency bands have been increased of an increasing factor of three, in order to make them appreciable on the graph. Also from these results it can be seen the higher variability of the damping (with respect to the one of the frequency) mentioned earlier.

## 22.5 Conclusions

Two different problems have been faced during this research: (i) the generation of an automatic modal parameter estimation algorithm and (ii) dealing with of the problem of harmonics affecting operational modal analysis when applied to rotating machines. In order to allow the continuous processing of the data, the state-of-the-art algorithm for operational modal analysis (p-LSFD) has been implemented in a programming language capable of being coupled with machine learning algorithms and big data storage systems. During the implementation, the algorithm has been improved, in order to increase the information available for building the stabilization diagram and make the selection of the stable poles completely automatic. The algorithm is then coupled with an automatic tracking method that allows to extend the analysis of the modal behaviour of the turbine to longer periods, i.e. tracking the evolution of the estimates over different data sets. To be able to deal with the harmonics, the cepstrum-based time domain signal editing procedure has been investigated and implemented.

Two kinds of data set are selected, each of them suitable for the two different procedures analyzed: data from turbine in stand still conditions are processed with classical OMA, data from the rotating turbine at higher speed are processed with classical OMA after having used the cepstrum lifter to edit the raw data. The results coming from the two analyses have been compared in order to observe the effect of the application of the cepstrum lifter on the raw data.



Once the correctness of the procedure has been assessed, the analysis has been extended to a longer period and to data sets coming from different machines. In this way it was possible to test the robustness of the proposed method. All the obtained results have shown a good consistency of the estimates in terms of resonance frequencies and damping ratios.

The future work associated to this research is to make the overall procedure even more automatic, to the end of continuously analyze the vibration data coming from the gearbox on real time basis. The first step towards this automation is coupling the algorithm coded for automatically tracking the modal parameters to a logical algorithm able to understand the kind of data analyzed (data coming from the turbine is stand still conditions or in normal operating conditions) and, based on that, decide which one of the two analyzed procedures to apply. The scope of this automation is to combine the results of operational modal analysis with the available SCADA data, in order to investigate the influence of environmental and operational conditions on the modal behavior of wind turbine drive.

**Acknowledgment** This research was performed in the framework of the ongoing research project HYMOP funded by VLAIO Vlaanderen, furthermore we want to acknowledge our partners in acquiring the data.

## Bibliography

1. Reynders, E.: System identification methods for (operational) modal analysis: review and comparison. *Arch. Comput. Meth. Eng.* **19**(1), 51–124 (2012)
2. Cornelis, B., Janssens, K., Van der Auweraer, H., Peeters, B.: Removing disturbing harmonics in operational modal analysis. In: *Proceedings of International Modal Analysis Conference, Copenhagen* (2007)
3. Schlombs, R., Hundecq, C., Fenselau, C., Gade, S.: Operational Modal Analysis on a wind turbine gearbox. In: *Conference and Exposition on Structural Dynamics* (2009)
4. Vanhollebeke, F., Vandepitte, D., Desmet, W., Helsen, J.: Some trend and challenges in wind turbine upscaling. In: *Proceedings of iSMA International Conference On Noise And Vibration* (2012)
5. Shantz, C., Gerhard, K., Donnal, J., Moon, J., Sievenpiper, B., Leeb, S., Thomas, K.: Retrofittable machine condition and structural excitation monitoring from the terminal box. *IEEE Sens. J.* **16**, 1224–1232 (2016)
6. Van der Auweraer, H., Peeters, B.: PolyMAX: a revolution in operational modal analysis. In: *1st International Operational Modal Analysis Conference (IOMAC), Copenhagen, Apr* (2005)
7. Peeters, B., Lowet, G., Van der Auweraer, H., Leuridan, J.: A new procedure for modal parameter estimation. *Sound Vib.* **38**(1), 24–29 (2004)
8. Bogert, B.: The quefrency analysis of time series for echoes: cepstrum, pseudo-autocovariance, cross-cepstrum, and saphe cracking. In: *Proceedings of the Symposium on Time Series Analysis* (1963)
9. Randal, R.B.: A history of cepstrum analysis and its application to mechanical problems. *Mech. Syst. Signal Process.* **97**, 3–19 (2016)
10. Peeters, B., Van Der Auweraer, H.: Discriminating physical poles from mathematical poles in high order systems: use and automation of the stabilization diagram. In: *Proceedings of IMTC 2004, the IEEE Instrumentation And Measurement Technology Conference, Como* (2004)
11. El-Kafafy, M., Colanero, L., Gioia, N., Devriendt, C., Guillaume, P., Helsen, J.: Modal parameter estimation of an offshore wind turbine using measured acceleration signals from the drive train. *Struct. Health Monit. Damage Detect.* **7**, 41–48 (2017)
12. Shirzadeh, R., De Sitter, G., Devriendt, C., Weijtjens, W.: Classifying resonance frequencies and damping values of an offshore wind turbine on a monopile foundation for different operational conditions. In: *Proceedings of EWEA* (2014)



# Chapter 23

## The Influence of Geometrical Correlation in Modal Validation Using Automated 3D Metrology

Tarun Teja Mallareddy, Daniel J. Alarcón, Sarah Schneider, and Peter G. Blaschke

**Abstract** Structural analysis is a major part of all manufacturing and testing industries. The need for high level accuracy of the results in the testing field has increased progressively, resulting in development of advanced state of art techniques. In order to acquire the vibrational characteristics of a structure, a detailed Finite Element Analysis (FEA) modelling is performed. Also, Experimental Modal Analysis (EMA) is conducted to extract the dynamic characteristics of a structure. The results obtained from both the processes are correlated for validation purposes. Based on the correlation (good or bad) the structural analysis is validated. In most cases the correlation is not satisfactory; it is mainly because of the boundary conditions that differ in FE and EMA.

This research study explains in detail how important the boundary conditions are for modal validation. But the most imperative part, as the first step of correlation, is the geometry analysis. If the geometrical correlation is not accurate, the later part of correlation will turn out to be an assumption based on inaccuracies. Assumption of a geometrical correlation, without being sure of the differences, will lead to inaccurate results for validation.

A reference plate is tested and simulated by using EMA and FEA techniques respectively. EMA is conducted by using a 3D SLDV for measuring the output response and the input force of excitation is induced by a Scalable Automatic Modal hammer (SAM). This plate is then scanned using ATOS Triple Scan II GOM 3D geometry scanner. The scanned results are compared with the FE model of the reference plate.

The results presented show the importance of geometrical correlation for modal validation and provide results of deviations that were observed on a reference plate. With these conclusions, working on modal validation can be developed by reducing the inaccuracies for the presentation of correlation.

**Keywords** Experimental modal analysis · Impact modal testing · Validation · Geometrical correlation · 3D geometry scanner · FE · Non-mass loaded impact

### Nomenclature

CAD	Computer Aided Design
EMA	Experimental Modal Analysis
FEA	Finite Element Analysis
SAM	Scalable Automatic Modal Hammer
3D SLDV	3D Scanning Laser Doppler Vibrometer

---

T. T. Mallareddy (✉) · D. J. Alarcón · S. Schneider  
Technical University of Applied Sciences Wildau, Wildau, Germany  
e-mail: [mallareddy@th-wildau.de](mailto:mallareddy@th-wildau.de)

P. G. Blaschke  
Technical University of Applied Sciences Wildau, Wildau, Germany  
NV Tech Design GmbH, Steinheim, Germany

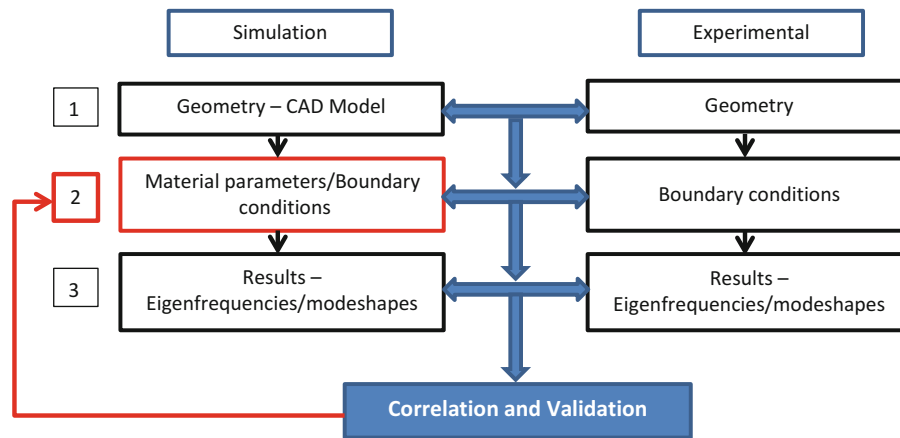


Fig. 23.1 Representation of phases in correlation between simulation and experimental results

## 23.1 Introduction

The current advanced state of art, in the field of structure analysis, for validation of a structure is to correlate the experimental results with the simulation results. This will remain unchanged for several years until a different and effective method or model for validation technique is developed. First and foremost objective is to overcome the challenges in validating the simulated structure where several assumptions lead to inaccurate correlation results [1]. This research paper deals with one important criterion – the geometrical correlation – that is often considered as an assumption and the importance of which is overlooked. The aerospace and automotive NVH industries have developed cycles of correlation and validation during the last years by updating the parameters of the FEA models with experimental vibrational data usually derived from experimental modal analysis (EMA). This is done in order to create a validated dynamic model, but the industries are currently facing a lot of challenges [2].

Firstly, an introduction of the current procedure for the correlation of experimental and simulation tests is given in Fig. 23.1. Generally, the three important steps in a correlation are geometrical correlation, correlation of material parameters/boundary conditions and finally the correlation of the results. The geometrical correlation deals with a CAD model which is created by measuring the geometrical specifications of the experimented structure. After which, the material parameters of the structure and the boundary conditions are defined with specified meshing conditions in the CAD model. The model is then solved for results in terms of the dynamic characteristics/ modal parameters. These results are then correlated with the experimental results and based on this correlation the simulation model is updated for validation as shown in Fig. 23.1 [2]. This process is termed as modal updating.

As shown in the Fig. 23.1, the high priority of importance, to achieve the best correlation, is given in the phase number 2. Most of the research is focused in phase 2, where the material properties and the boundary conditions are modified (mostly trial and error) to achieve the good correlation standards in the results.

But all of this research done in the phase 2 is based on an assumption that the created CAD model is of the exact geometrical dimensions as the tested structure, i.e. assuming a good correlation in phase 1, the geometrical correlation. This is a crucial part of the correlation which is, in most cases, neglected. A small change in the geometry of a structure will affect its dynamic characteristics. And if the structure is a highly non-linear material, then the change in geometry of the structure assuredly influences the end results. A deeper explanation of the influence of the geometry on the eigenfrequencies of a structure is given below with the help of two equations:

Stiffness ‘k’ of a rectangular plate is given by,

$$k = AE/L \quad (23.1)$$

‘A’ represents the cross-sectional area, ‘L’ represents the length of the plate and ‘E’ is the Young’s modulus of steel. Based on the Eq. 23.1, it is clear that the change in length and the area of cross section influences the stiffness value to vary. The square root of the ratio of stiffness and mass ‘m’ is defined as the natural frequency/eigenfrequency ‘ $\omega_n$ ’ of the system.

$$\omega_n = \sqrt{k/m} \text{ rad/s} \quad (23.2)$$

Based on the Eqs. 23.1 and 23.2, it can be deduced that the change in dimensions of a structure will change its eigenfrequencies.

## 23.2 Materials and Methods

A brass metal plate is used for EMA and FE simulation. The plate weighs 398 g with dimensions of  $78 \times 60 \times 10$  mm (LxBxH). The brass plate is placed on a foam mat to create a free vibrational boundary condition. EMA is conducted by utilizing Scalable Automatic Modal hammer (SAM) (Noise-Vibration-Technology, Steinheim a.d. Murr, Germany) for the force input and a 3D SLDV to measure the output vibrational response. The CAD model of the brass plate is developed in ANSYS. This software is used to solve the structure for eigenfrequencies and modeshapes. The suitable material parameters and the suitable boundary conditions (according to the EMA conditions) are given as per the pre-requisite (Fig. 23.2).

An ATOS Triple Scan II (GOM mbh; Braunschweig, Germany) 3D geometry scanner is used to scan the brass plate. This 3D scanner is the advanced geometrical data acquisition system that has a level of accuracy in micrometers. The system is complemented with the software ATOS Professional that enables an automatic scanning of a test piece in 3D. GOM Inspect software is used for analyzing the scanned model with the modeled CAD Data.

## 23.3 Results and Discussion: Correlation of Modal Parameters Obtained by EMA and FEA

The two methods of analysis are shown in Fig. 23.2. The initial comparison of modal parameters of any structure obtained by EMA and FE, will display differences. One of the obvious reasons for this being the difference in boundary conditions, where the simulated model is in the free space whereas the experimented model is placed on a foam mat or suspended by fishing lines (in order to create free-free conditions). This will lead to the change in boundary conditions in the CAD model or the inclusion of the supposed effects of foam bed or the wire by means of soft springs in the FE model. Also the material parameters in the simulation are continuously iterated in order to get the best correlation with the experimental results. The entire research is focused on the boundary conditions, mesh conditions and the material parameters.

Similarly, the results obtained by testing the brass plate are compared with the FE simulations, especially in terms of eigenfrequencies. The initial observation showed the variation in eigenfrequencies at different modes of the structure. The boundary conditions and the material parameters were iteratively optimized to bridge the gap between the eigenfrequencies of the brass plate. After repeated attempts, suitable conditions were acquired and the correlation was satisfactory. The eigenfrequency differences at every mode were significantly reduced to a very less percentage. But, is this correlation

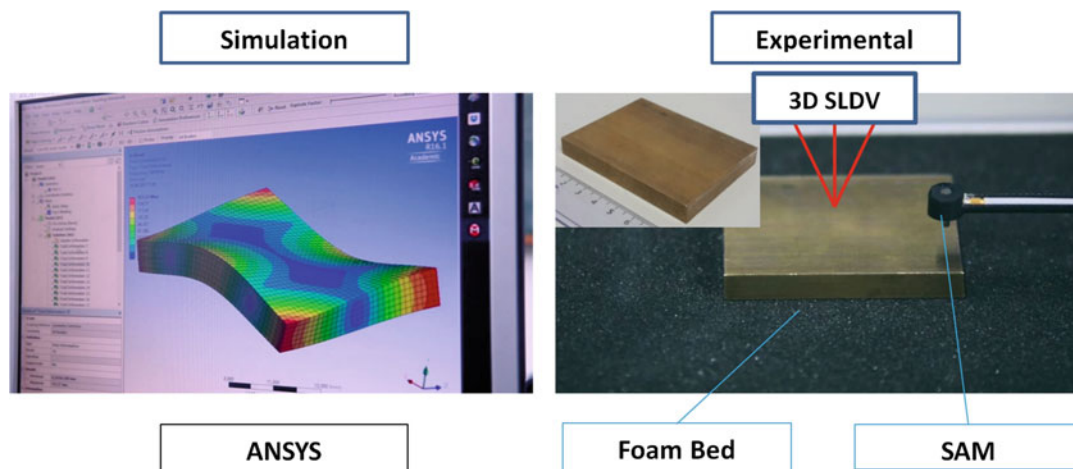


**Fig. 23.2** (left) FE model of the brass plate using ANSYS. (Right) EMA of the brass plate using 3D SLDV and the SAM

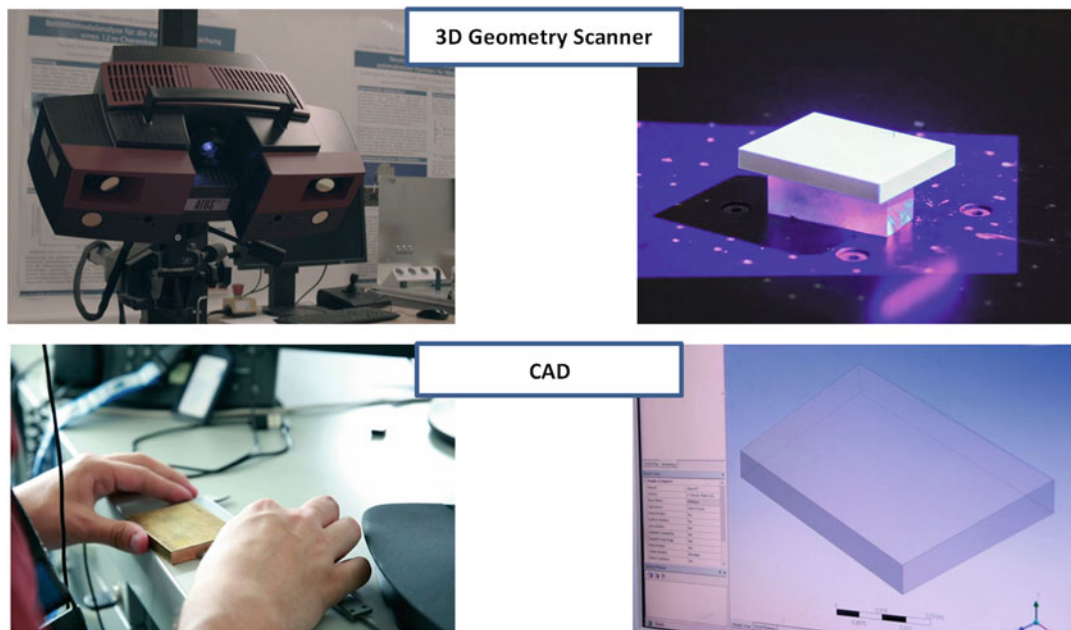


**Fig. 23.3** (Top) 3D geometry scanning of the brass plate using ATOS Triple Scan Metrology. (Bottom) CAD model of the tested structure, created by measuring its dimensions with a caliper (resolution:  $\pm 0.05$  mm)

accurate? This work is completely based on an assumption that the dimensions of the CAD model are similar to the tested structure.

### 23.4 Results and Discussion: The Influence of the Geometrical Correlation

The CAD model for simulation is created by measuring the dimensions of the brass plate as shown in the Fig. 23.3 (bottom), just like the CAD model of any structure. This brass plate is then scanned for the real dimensions by using the ATOS Triple Scan II 3D geometry scanner system as shown in Fig. 23.3 (top).

The obtained scan data and the modelled CAD data is imported in the GOM Inspect program as shown in the Fig. 23.4 (top). After the successful uploading of the data into the program an overlay function of both the models are carried out (Fig. 23.4 – bottom left). After a successful overlay the two CAD and scan data are compared. The initial observation in the Fig. 23.4 (bottom right) shows that there a significant difference between the two models. This reveals that the CAD dimensions are not similar to the tested brass plate and there is a deviation in the geometry.

The ATOS Inspection software also enables the CAD comparison and also the deviations among the two models can be calculated.

For example, in Fig. 23.5 the red region shows the positive deviation in a higher value, of the scan model to the CAD model. The blue region shows the negative deviation in a higher value, of the scan model to the CAD model. The green region shows no difference in the geometry among the two models. So the observation clearly proves that the CAD model used for simulation has an inaccurate correlation with the actual brass plate.

It is very important to have a good geometrical correlation, as this is the first step in the correlation and validation process in structural analysis. If the first step of the correlation is inaccurate, the rest of the steps will have a negative impact as shown in Fig. 23.6.

### 23.5 Conclusions

In order to develop a validated dynamic model, it is imperative to have a good correlation in the geometry level as well as in the level of material parameters and boundary conditions as shown in Fig. 23.7. The influence of change in geometry of the

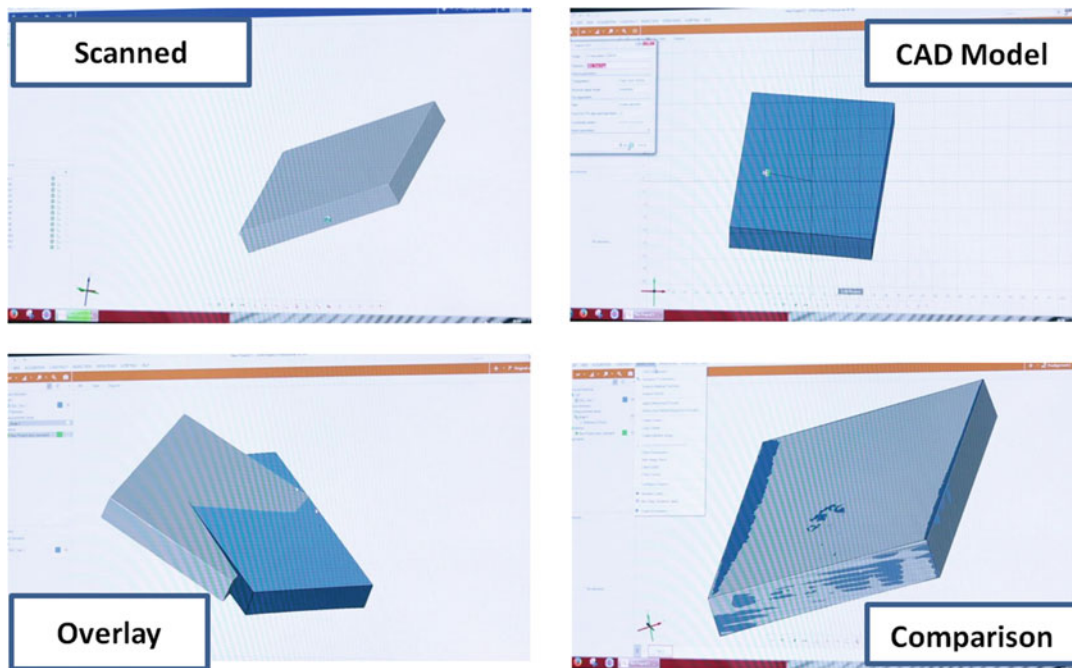


**Fig. 23.4** The comparison of the scan and the CAD data using the GOM Inspect software

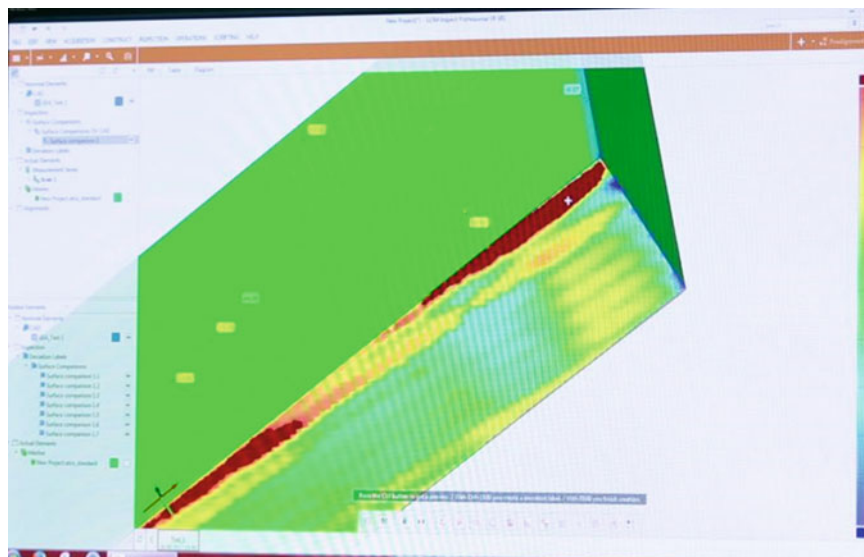


**Fig. 23.5** The comparison of CAD deviations in geometry

structure is a decisive factor in changing its modal parameters. If the geometrical correlation is neglected or assumed to be good, the inaccuracies in the first step will make the entire correlation and validation inaccurate. The R&D field of structural analysis in every industry, on the whole, has a greater responsibility of the structure's quality assurance. The development of a validated dynamic model of a structure is fast-becoming a very important tool, for sensitivity analysis of various parameters, for differentiating between good and damaged structures etc. Geometrical correlation is a very influential factor and needs to be considered in this process of modal validation.

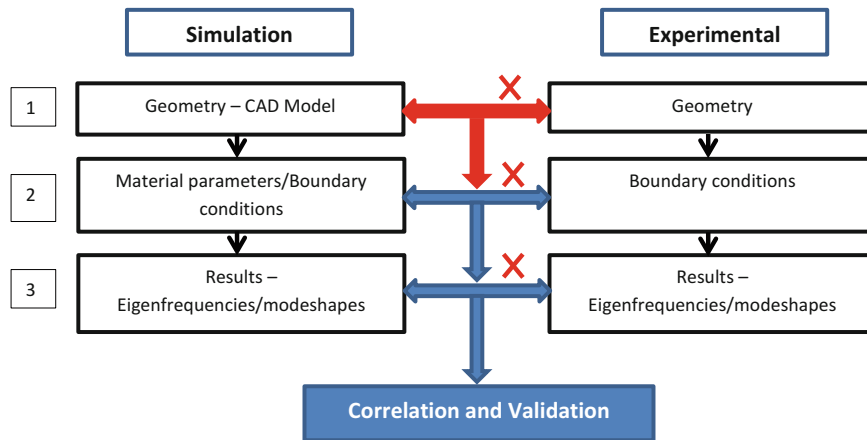


Fig. 23.6 The representation of the correlation of simulation and experimental results showing the influence of geometrical correlation

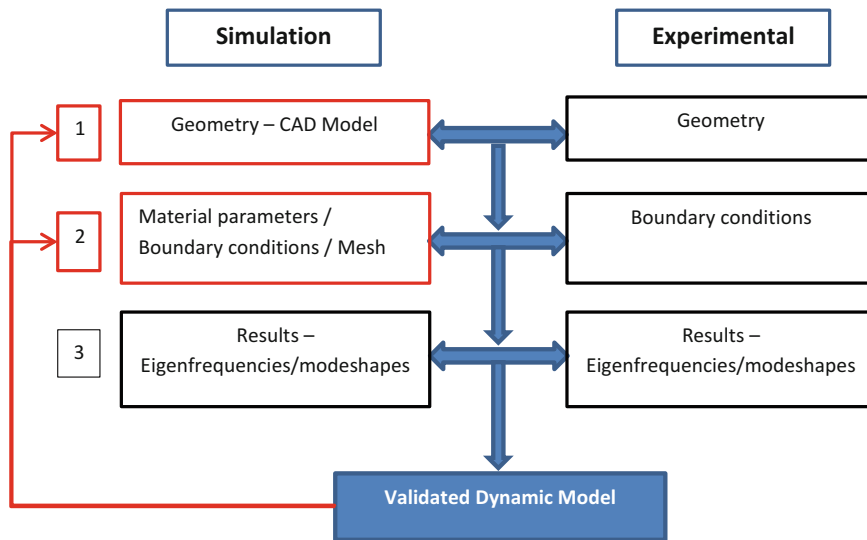


Fig. 23.7 The representation of the correlation of simulation and experimental results for deriving a validated dynamic model

**References**

1. Berman, A.: Inherently incomplete finite element model and its effects on model updating. *AIAA J.* **38**(11), 2142–2146 (2000)
2. Blaschke, P., Schneider, T.: Reactionless test to identify dynamic Young’s modulus and damping of isotropic plastic materials. *Topics Modal Anal. Proc. XXXI Int. Modal Anal. Conf.* **7**, 511–516 (2014)